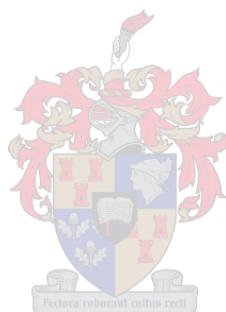


**Use of the *N,N*-dialkyl-*N'*-benzoyl(thio)selenoureas as
single source precursors for the synthesis of
semiconducting quantum dots**

Jocelyn Catherine Bruce

A dissertation submitted to Stellenbosch University



In fulfilment of the requirements for the degree of
Doctor of Philosophy

Promoter: Klaus R. Koch

December 2008

Declaration

By submitting this thesis electronically, I declare that the entirety of the work contained therein is my own, original work, that I am the owner of the copyright thereof (unless to the extent explicitly otherwise stated) and that I have not previously in its entirety or in part submitted it for obtaining any qualification.

Date: December 2008

Abstract

The successful preparation and structural characterization of a number of *N,N*-dialkyl-*N'*-benzoyl(thio)selenourea ligands is described; where the intermolecular interactions are characterized by the presence of Resonance Assisted Hydrogen Bonding (RAHB), π - π interactions between neighbouring benzene residues only being evident amongst the longer alkyl chain derivatives. The first structural characterization of an asymmetrically substituted *N,N*-dialkyl-*N'*-benzoylselenourea ligand reveals an increased stability of the *Z* isomer in the solid state, this being reflected by the sulfur analogue. Attempts to synthesise *N,N*-dicyclohexyl-*N'*-benzoylselenourea led to the isolation and structural characterization of a novel 1,3,5-oxaselenazine salt and dicyclohexylaminobenzoate. The first structural characterization of a “bipodal” *N,N*-dialkyl-*N'*-benzoylselenourea ligand, 3,3,3',3'-tetrabutyl-1,1'-isophthaloylbis(selenourea), reveals RAHB in the crystal lattice similar to that exhibited by the “monopodal” analogue, *N,N*-dibutyl-*N'*-benzoylselenourea.

The successful complexation of the *N,N*-dialkyl-*N'*-benzoyl(thio)selenourea ligands to a number of different transition metal ions is reported allowing the preparation of several potential single source precursors. Coordination through the O and Se/S donor atoms to Pd(II) results in the formation of square planar metal complexes, with a *cis* conformation, several of which could be structurally characterized. In particular, the first structural elucidation of an asymmetrically substituted *N,N*-dialkyl-*N'*-benzoylselenourea metal complex, *cis*-bis(*N*-benzyl-*N*-methyl-*N'*-benzoylselenoureato)palladium(II) indicates the increased stability of the *EZ* isomer in the solid state. Structural elucidation of the novel (*N,N*-diphenyl-*N'*-benzoylselenoureato)cadmium(II) reveals a bimetallic complex in the solid state, where the expected 2:1 ligand : metal ratio is maintained, and the two Cd(II) centres are 5 and 6 coordinated, with O and Se donor atoms. Multinuclear Nuclear Magnetic Resonance (NMR) Spectroscopy has been employed in the thorough characterisation of the potential single source precursors, ⁷⁷Se NMR spectroscopy indicating a decreased shielding of the ⁷⁷Se nucleus as the “hardness” of the central metal ion increases *i.e.* Pd(II) > Zn(II) > Cd(II). Use of ¹¹³Cd NMR spectroscopy indicates the preferential binding of *N,N*-diethyl-*N'*-benzoylselenourea to Cd(II) over that of its sulfur analogue, and initial studies suggest a form of chelate metathesis taking place in solution. ³¹P NMR spectroscopy is used to gain insight into the formation of *cis*-bis(*N,N*-diethyl-*N'*-benzoylselenoureato)Pt(II).

Thermolysis of (*N,N*-diethyl-*N'*-benzoylselenoureato)cadmium(II) and its sulfur analogue led to the successful synthesis of CdSe and CdS quantum dots respectively, where thermolysis over a range of temperatures allows a degree of size control over the resulting nanoparticles. The effect of precursor alkyl chain length on nanoparticle morphology was investigated for both the *N,N*-dialkyl-*N'*-benzoylthio- and -selenoureas. A correlation between the two for the (*N,N*-dialkyl-*N'*-benzoylselenoureato)Cd(II) complexes is described and possible growth mechanisms are discussed. Preliminary investigations into the use of other *N,N*-dialkyl-*N'*-benzoyl(thio)selenourea metal complexes as single source precursors reveal that both (*N,N*-diethyl-*N'*-benzoylselenoureato)Zn(II) and its sulfur analogue show potential as single source precursors for the formation of ZnO and ZnS nanoparticles respectively. Initial studies into the use of *N,N*-dialkyl-*N'*-benzoyl(thio)selenourea metal complexes as single source precursors for the synthesis of core-shell nanoparticles is briefly described.

The Aerosol Assisted Chemical Vapour Deposition (AACVD) of several *N,N*-dialkyl-*N'*-benzoyl(thio)selenourea metal complexes is reported, where both (*N,N*-diethyl-*N'*-benzoylselenoureato)Cd(II) and its sulfur analogue allow the deposition of crystalline CdSe and CdS respectively. The AACVD of (*N,N*-diethyl-*N'*-benzoylselenoureato)Zn(II) leads to the deposition of crystalline ZnSe, ZnS being deposited by (*N,N*-diethyl-*N'*-

benzoylthioureato)Zn(II). The deposition of heazewoodite (Ni_3S_2) with varying morphologies results from the AACVD of *cis*-bis(*N,N*-diethyl-*N'*-benzoylthioureato)Ni(II). Thermal annealing of the amorphous material deposited by the AACVD of *cis*-bis(*N,N*-diethyl-*N'*-benzoylthioureato)Pd(II), allows the formation of highly crystalline palladium. The deposition of metallic platinum using *cis*-bis(*N,N*-diethyl-*N'*-benzoylthioureato)Pt(II) is described as well as the deposition of crystalline $\text{Pd}_{17}\text{Se}_{15}$ from *cis*-bis(*N,N*-diethyl-*N'*-benzoylselenoureato)Pd(II). This, to the best of our knowledge, is the first time that AACVD has been performed, using the *N,N*-dialkyl-*N'*-benzoyl(thio)selenourea metal complexes as single source precursors, in addition, we believe it to be the first time that palladium selenide has been deposited using the AACVD technique.

Opsomming

Die suksesvolle sintese en strukturele karakterisering van mere *N,N*-dialkiel-*N'*-bensoïel(tio)selenoëreum ligande is beskryf; waar die intermolekulêre interaksies gekarakteriseer word deur die teenwoordigheid van Resonans Bemiddelde Waterstof Binding (RBWB), π - π interaksies tussen aangrensende bensien residuë kom net voor in ligande met langer alkiel groepe. Die eerste strukturele karakterisering van 'n assimetriese gesubstitueerde *N,N*-dialkiel-*N'*-bensoïelselenoëreum ligand dui op die verhoogde stabiliteit van die *Z* isomeer in die vaste toestand, 'n soortgelyke observasie is moontlik vir die swaai analoog. Pogings om *N,N*-disikloheksieel-*N'*-bensoïelselenoëreum te sintetiseer het gelei tot die isolering van 'n nuwe 1,3,5-oksaselenasien derivaat sowel as disikloheksieelaminobensoaat. Die eerste strukturele karakterisering van 'n "bipodale" *N,N*-dialkiel-*N'*-bensoïelselenoëreum ligand, 3,3,3',3'-tetrabutiel-1,1'-isofalioëlbis(selenoëreum) dui op die teenwoordigheid van RBWB in die kristal struktuur, op 'n soortgelyke manier as die "monopodale" analoog, *N,N*-dibutiel-*N'*-bensoïelselenoëreum. Die suksesvolle sintese van *N,N*-dialkiel-*N'*-bensoïel(tio)selenoëreum komplekse met verskeie metal ione as moontlike enkel oorsprong voorafgaande verbindings is gerapporteer. Koordinasie met Pd(II) vind plaas deur die O en Se/S donor atome en lei tot die vorming van vierkantigplanêre komplekse met 'n *cis* konformasie. Sekere van hierdie komplekse is kristallografies gekarakteriseer. In besonder, die eerste strukturele karakterisering van 'n assimetriese gesubstitueerde *N,N*-dialkiel-*N'*-bensoïelselenoëreum kompleks, naamlik *cis*-bis(*N*-metiel-*N*-bensiel-*N'*-bensoïelselenoëreato)Pd(II), bring die verhoogde stabiliteit van die *EZ* isomeer in die vaste toestand te voorskyn. Kristallografiese karakterisering van die nuwe (*N,N*-difeniël-*N'*-bensoïelselenoëreato)Cd(II) dui op die formasie van 'n bimetalliese kompleks in die vaste toestand waar die verwagde 2:1 ligand:metaal verhouding behoue bly en die twee sentrale Cd(II) ione is 5 en 6 gekoördineer met Se en O donor atome. Kern Magnetiese Resonans Spektroskopie (KMR) is gebruik om die enkel oorsprong voorafgaande verbindings ten volle te karakteriseer. ^{77}Se KMR dui op 'n vermindering in die beskerming van die ^{77}Se nukleus soos die sentrale metaal ioon harder word bv. Pd(II) > Zn(II) > Cd(II). Die gebruik van ^{113}Cd KMR dui op 'n voorkeur van Cd(II) vir *N,N*-ditiel-*N'*-bensoïelselenoëreum oor die swaai analoog en die moontlikheid van kelaat omruiling in oplossing. ^{31}P KMR is gebruik om die kompleksvorming van *cis*-bis(*N,N*-ditiel-*N'*-bensoïelselenoëreato)Pt(II) te bestudeer.

Termoliese van (*N,N*-ditiel-*N'*-bensoïelselenoëreato)Cd(II) en sy swaai analoog lei tot die suksesvolle sintese van CdSe and CdS kwantum deeltjies, waar termoliese oor 'n temperatuur reeks 'n mate van grootte beheer oor die nanopartikels moontlik maak. Die effek van alkiel lengte in die voorafgaande verbindings op die nanopartikel vorm is ondersoek vir albei die *N,N*-dialkiel-*N'*-bensoïeltio- en selenoëreum. 'N korrelasie tussen die twee is beskryf vir die *N,N*-dialkiel-*N'*-bensoïelselenoëreume en moontlike groei meganismes is bespreek. Voorlopige ondersoek in die

gebruik van ander *N,N*-dialkiel-*N'*-bensoïel(tio)selenoïëreum metaal komplekse as enkel oorsprong voorafgaande verbindings bewys dat altwee (*N,N*-dietiël-*N'*-bensoïelselenoïëreato)Zn(II) en sy swaal analoog potensiaal dui op die vorming van onderskuidelik ZnO en ZnS nanopartikels. Die gebruik van *N,N*-dialkiel-*N'*-bensoïel(tio)selenoïëreum metaal komplekse vir die bereiding van kern/dop nanopartikels is beskryf.

Die Aerosol Bemiddelde Chemiese Damp Deposisie (ABCDD) van verskeie *N,N*-dialkiel-*N'*-bensoïel(tio)selenoïëreum metaal komplekse is gerapporteer, waar beide (*N,N*-dietiël-*N'*-bensoïelselenoïëreato)Cd(II) en (*N,N*-dietiël-*N'*-bensoïeltioïëreato)Cd(II) gebruik kan word vir die deposisie van kristallyne CdSe en CdS. Die (ABCDD) van (*N,N*-dietiël-*N'*-bensoïelselenoïëreato)Zn(II) lei tot die deposisie van kristallyne ZnSe, ZnS kan gedeponeer word deur die gebruik van (*N,N*-dietiël-*N'*-bensoïeltioïëreato)Zn(II). Die deposisie van heazelwoodite (Ni_3S_2) met verskeie vorme is moontlik deur die (ABCDD) van *cis*-bis(*N,N*-dietiël-*N'*-bensoïeltioïëreato)Ni(II). Termiese behandeling van die material gedeponeer deur *cis*-bis(*N,N*-dietiël-*N'*-bensoïeltioïëreato)Pd(II) lei tot die vorming van kristallyne palladium. Kristallyne platinum is gevorm deur die (ABCDD) van *cis*-bis(*N,N*-dietiël-*N'*-bensoïeltioïëreato)Pt(II), so wel as kristallyne $\text{Pd}_{17}\text{Se}_{15}$ van *cis*-bis(*N,N*-dietiël-*N'*-bensoïelselenoïëreato)Pd(II). Dit is, tot die beste van ons wete, die eerste keer dat die ABCDD van *N,N*-dialkiel-*N'*-bensoïel(tio)selenoïëreum metaal komplekse bestudeer is so wel as die eerste keer dat $\text{Pd}_{17}\text{Se}_{15}$ gedeponeer is deur gebruik te maak van die ABCDD tegniek.

*Omnia candida bellaque
Ingentia animalia parvulaque
Omnia sapientia mirabilia
Haec omnia fecit Dominus Deus*

Acknowledgements

Gratias tibi ago, Domine, qui mihi dedisti facultatem copiamque me hunc opusculum conficere

I would sincerely like to thank my promoter Professor Koch for his enthusiasm and encouragement throughout the course of this work.

Staff and students of the PGM research group for providing a fun filled and pleasant working environment – *vir seker!*

Staff and students of the Department of Chemistry and Polymer Science, University of Stellenbosch

Professor Neerish Revaprasadu and his research group at the University of Zululand

Professor Paul O'Brien and the "POB" research group at the University of Manchester

My husband Leon, family and friends for their continued support, interest and encouragement throughout the course of this work.

The University of Stellenbosch, Harry Crossley Foundation, National Research Foundation and Angloplatinum.

The work described in this thesis has been presented in the following forms:

Papers:

- Bruce, J.C., Revaprasadu, N., Koch, K.R., *New Journal of Chemistry*, **2007**, 31, 1647.
- Bruce, J.C., Koch, K.R., *Acta Crystallographica, Section C*, **2008**, C64, m1.
- Stockmann, S., Bruce, J.C., Miller, J., Koch, K.R., *Acta Crystallographica, Section C*, **2008**, C64, o166.

Oral presentations:

- Cape Organometallic Symposium, Breakwater Lodge, Cape Town, October 2005. Awarded the best student oral presentation at the meeting.
- XXXVIIth International Conference on Coordination Chemistry, Cape Town, 13 – 18 August 2006.
- 38th Convention of the South African Chemical Institute, Durban, 3 – 8 December 2006
- Oral lecture given at the University of Zululand, Empangeni, 10 May 2008

Poster presentations:

- NanoAfrica Conference, Cape Town, 26 – 29 November 2006
- ICMR workshop, Richards Bay, 29 July - 1 August 2007

CONTENTS

Abstract

Opsomming

Acknowledgements

Contents

Chapter 1	General Introduction	
1.1	An overview of quantum dots	2
1.1.1	Theoretical considerations	2
1.1.2	Optical properties of quantum dots	3
1.1.3	Potential applications of quantum dots	4
1.1.4	Methods of quantum dot synthesis	5
1.2	Single source precursor synopsis	6
1.3	General coordination chemistry of the <i>N,N</i> -dialkyl- <i>N'</i> -aryl(thio)selenoureas	8
1.4	Objectives and thesis outline	12
	References	14
Chapter 2	Synthesis and characterization of <i>N,N</i>-dialkyl-<i>N'</i>-benzoyl(thio)selenourea ligands and their complexation with selected transition metal ions	19
2.1	Introduction	20
2.2	Experimental	20
2.2.1	Synthesis and characterization of <i>N,N</i> -dialkyl- <i>N'</i> -benzoylselenoureas	20
2.2.2	Synthesis and characterization of <i>N,N</i> -dialkyl- <i>N'</i> -benzoylthioureas	22
2.2.3	Synthesis and characterization of <i>N,N</i> -dialkyl- <i>N'</i> -benzoylselenourea metal complexes	24
2.2.3.1	<i>N,N</i> -dialkyl- <i>N'</i> -benzoylselenourea Cd(II) complexes	24
2.2.3.2	<i>N,N</i> -dialkyl- <i>N'</i> -benzoylselenourea Pd(II) complexes	26
2.2.3.3	<i>N,N</i> -dialkyl- <i>N'</i> -benzoylselenourea Zn(II) complex	27
2.2.3.4	<i>N,N</i> -dialkyl- <i>N'</i> -benzoylselenourea Pt(II) complex	28
2.2.3.5	3,3,3',3'-tetraethyl-1,1'-isophthaloylbis(selenourea) metal complexes	28
2.2.4	Synthesis and characterization of <i>N,N</i> -dialkyl- <i>N'</i> -benzoylthiourea metal complexes	29
2.2.4.1	<i>N,N</i> -dialkyl- <i>N'</i> -benzoylthiourea Cd(II) complexes	29
2.2.4.2	<i>N,N</i> -dialkyl- <i>N'</i> -benzoylthiourea Pd(II) complexes	30
2.2.4.3	<i>N,N</i> -dialkyl- <i>N'</i> -benzoylthiourea Pt(II) and Zn(II) complexes	31
2.2.4.4	“Solventless” synthesis	32
2.2.4.5	“Mixed ligand” Cd(II) complex	33

2.2.4.6	3,3,3',3'-tetra(<i>n</i> -butyl)-1,1'-terephthaloylbis(thiourea) Pd(II) complex	33
2.2.5	General methods and instrumentation	34
2.2.6	Crystallography and Structure refinement	35
2.3	Results and Discussion	36
2.3.1	Crystal and molecular structures of <i>N,N</i> -dialkyl- <i>N'</i> -benzoylselenourea ligands	36
2.3.1.1	Crystal and molecular structure of <i>N,N</i> -diethyl- <i>N'</i> -benzoylselenourea, HL _{Se} ^{1a}	36
2.3.1.2	Crystal and molecular structure of <i>N,N</i> -dibutyl- <i>N'</i> -benzoylselenourea, HL _{Se} ^{1b}	37
2.3.1.3	Crystal and molecular structure of <i>N,N</i> -dihexyl- <i>N'</i> -benzoylselenourea, HL _{Se} ^{1c}	38
2.3.1.4	Crystal and molecular structure of <i>N,N</i> -dioctyl- <i>N'</i> -benzoylselenourea, HL _{Se} ^{1d}	39
2.3.1.5	Crystal and molecular structure of <i>N</i> -methyl- <i>N</i> -benzyl- <i>N'</i> -benzoylselenourea, HL _{Se} ^{1e}	40
2.3.1.6	Crystal and molecular structure of <i>N,N</i> -didecyl- <i>N'</i> -benzoylselenourea, HL _{Se} ^{1f}	41
2.3.1.7	Crystal and molecular structure of <i>N,N</i> -diphenyl- <i>N'</i> -benzoylselenourea, HL _{Se} ^{1g}	42
2.3.1.8	Crystal and molecular structure of an oxaselenazine derivative, 18a and dicyclohexylaminobenzoate, 18b	46
2.3.1.9	Synthesis and structural characterization of 3,3,3',3'-tetraalkyl-1,1'-phenylenedicarbonylbis(selenourea) ligands	54
2.3.2	Crystal and molecular structures of <i>N,N</i> -dialkyl- <i>N'</i> -benzoylthiourea ligands	57
2.3.2.1	Crystal and molecular structure of <i>N,N</i> -dihexyl- <i>N'</i> -benzoylthiourea, HL _S ^{2c}	57
2.3.2.2	Crystal and molecular structure of <i>N,N</i> -dioctyl- <i>N'</i> -benzoylthiourea, HL _S ^{2d}	58
2.3.2.3	Crystal and molecular structure of <i>N</i> -methyl- <i>N</i> -benzyl- <i>N'</i> -benzoylthiourea, HL _S ^{2e}	59
2.3.2.4	Crystal and molecular structure of <i>N,N</i> -dicyclohexyl- <i>N'</i> -benzoylthiourea, HL _S ^{2g}	59
2.3.3	Crystal and molecular structures of <i>N,N</i> -dialkyl- <i>N'</i> -benzoylselenourea metal complexes	62
2.3.3.1	Crystal and molecular structure of <i>cis</i> -bis(<i>N,N</i> -diethyl- <i>N'</i> -benzoylselenoureato)-palladium(II), <i>cis</i> -[Pd ^{II} (L ^{1a} - Se , O) ₂], 112	63
2.3.3.2	Crystal and molecular structure of <i>cis</i> -bis(<i>N,N</i> -dibutyl- <i>N'</i> -benzoylselenoureato)-palladium(II), <i>cis</i> -[Pd ^{II} (L ^{1b} - Se , O) ₂], 122	64
2.3.3.3	Crystal and molecular structure of <i>cis</i> -bis(<i>N</i> -benzyl- <i>N</i> -methyl- <i>N'</i> -benzoylselenoureato)palladium(II), <i>cis</i> -[Pd ^{II} (L ^{1e} - Se , O) ₂], 152	64
2.3.3.4	Crystal and molecular structure of (<i>N,N</i> -diphenyl- <i>N'</i> -benzoylselenoureato)-cadmium(II), [Cd ^{II} (L ^{1g} - Se , O) ₂], 171	66
2.3.3.5	Synthesis of 3,3,3',3'-tetraalkyl-1,1'-phenylenedicarbonylbis(selenourea) metal complexes	71
2.3.4	Crystal and molecular structures of <i>N,N</i> -dialkyl- <i>N'</i> -benzoylthiourea metal complexes	71
2.3.4.1	Crystal and molecular structure of <i>cis</i> -bis(<i>N,N</i> -dibutyl- <i>N'</i> -benzoylthioureato)-palladium(II), <i>cis</i> -[Pd ^{II} (L ^{2b} - S , O) ₂], 222	71
2.3.4.2	Crystal and molecular structure of <i>cis</i> -bis(<i>N,N</i> -dihexyl- <i>N'</i> -benzoylthioureato)-palladium(II), <i>cis</i> -[Pd ^{II} (L ^{2c} - S , O) ₂], 232	72
2.3.4.3	Crystal and molecular structure of <i>cis</i> -bis(<i>N</i> -morpholine- <i>N'</i> -benzoylthioureato)-palladium(II), <i>cis</i> -[Pd ^{II} (L ^{2f} - S , O) ₂], 262	73
2.3.4.4	Crystal and molecular structure of 3,3,3',3'-tetra(<i>n</i> -butyl)-1,1'-terephthaloylbis(thioureato)	

	palladium (II), <i>cis</i> -[Pd ^{II} ₃ (L ^{m2b} -S,O) ₃], 22222	75
2.3.5	Characterization of ligands and metal complexes by Nuclear Magnetic Resonance Spectroscopy	77
2.3.5.1	¹³ C NMR Spectroscopy	77
2.3.5.2	<i>N</i> -methyl- <i>N</i> -benzyl- <i>N'</i> -benzoyl(thio)selenoureas and their Cd(II) and Pd(II) metal complexes	79
2.3.5.3	⁷⁷ Se NMR Spectroscopy	81
2.3.5.4	¹¹³ Cd NMR Spectroscopy	83
2.3.5.5	³¹ P NMR Spectroscopy	85
2.3.6	Thermogravimetric analysis of <i>N,N</i> -dialkyl- <i>N'</i> -benzoyl(thio)selenourea metal complexes	88
2.3.6.1	Thermogravimetric analysis of <i>N,N</i> -dialkyl- <i>N'</i> -benzoylselenourea metal complexes	88
2.3.6.2	Thermogravimetric analysis of <i>N,N</i> -dialkyl- <i>N'</i> -benzoylthiourea metal complexes	90
2.4	Conclusion	95
	References	96
Chapter 3	Use of the <i>N,N</i>-dialkyl-<i>N'</i>-benzoyl(thio)selenourea metal complexes as single source precursors for the synthesis of semiconducting quantum dots and other materials	100
3.1	Introduction	101
3.2	Experimental	101
3.2.1	General methods and instrumentation	101
3.2.2	Nanoparticle synthesis	102
3.2.2.1	Proof of Principle studies	102
3.2.2.2	Temperature dependence studies	102
3.2.2.3	Alkyl chain length studies	102
3.2.2.4	Concentration dependence studies	103
3.2.2.5	Selected precursor thermolysis	103
3.2.2.6	Core-shell particle synthesis	103
3.2.3	Quantum yield determination	104
3.3	Results and Discussion	105
3.3.1	'Proof of principle' studies	105
3.3.1.1	Synthesis of CdSe nanoparticles	105
3.3.1.2	Synthesis of CdS nanoparticles	106
3.3.2	Temperature dependence studies	107
3.3.2.1	Synthesis of CdSe nanoparticles	107
3.3.2.2	Synthesis of CdS nanoparticles	109
3.3.3	Alkyl chain length studies	112

3.3.3.1	Synthesis of CdSe nanoparticles	112
3.3.3.2	Varying temperature thermolysis of $[\text{Cd}^{\text{II}}(\text{L}^{\text{1d}}-\text{Se},\text{O})_2]$	120
3.3.3.3	Synthesis of CdS nanoparticles	128
3.3.4	Concentration dependence studies	131
3.3.4.1	Synthesis of CdSe nanoparticles	131
3.3.4.2	Synthesis of CdS nanoparticles	132
3.3.5	Selected precursor thermolysis	135
3.3.5.1	Thermolysis of $[\text{Cd}^{\text{II}}(\text{L}^{\text{1a}}-\text{Se},\text{O})(\text{L}^{\text{2a}}-\text{S},\text{O})]$, 11211	135
3.3.5.2	Thermolysis of $[\text{Zn}^{\text{II}}(\text{L}^{\text{1a}}-\text{Se},\text{O})_2]$, 113	138
3.3.5.3	Thermolysis of $[\text{Zn}^{\text{II}}(\text{L}^{\text{2a}}-\text{S},\text{O})_2]$, 213	140
3.3.5.4	Thermolysis of <i>cis</i> - $[\text{Ni}^{\text{II}}(\text{L}^{\text{2a}}-\text{S},\text{O})_2]$, 215	142
3.3.5.5	Thermolysis of $[\text{Co}^{\text{III}}(\text{L}^{\text{2a}}-\text{S},\text{O})_3]$, 216	142
3.3.5.6	Thermolysis of <i>cis</i> - $[\text{Pd}^{\text{II}}(\text{L}^{\text{2a}}-\text{S},\text{O})_2]$, 212	143
3.3.5.7	Thermolysis of <i>cis</i> - $[\text{Pt}^{\text{II}}(\text{L}^{\text{2a}}-\text{S},\text{O})_2]$, 214	144
3.3.5.8	Thermolysis of <i>cis</i> - $[\text{Pd}^{\text{II}}(\text{L}^{\text{1a}}-\text{Se},\text{O})_2]$, 112	145
3.3.6	Core-shell nanoparticle synthesis	147
3.3.6.1	Synthesis of CdSe/CdS nanoparticles	147
3.3.6.2	Synthesis of CdSe/ZnS nanoparticles	149
3.3.6.3	Synthesis of CdSe/ZnSe nanoparticles	151
3.4	Conclusion	153
	References	155
Chapter 4	Use of the <i>N,N</i>-dialkyl-<i>N'</i>-benzoyl(thio)selenourea metal complexes as single source precursors for the Aerosol Assisted Chemical Vapour Deposition (AACVD) of CdSe, CdS, ZnSe, ZnS and other materials.	158
4.1	Introduction	159
4.2	Experimental	161
4.2.1	General methods and instrumentation	161
4.2.2	Deposition conditions	162
4.2.2.1	Deposition using $[\text{Cd}^{\text{II}}(\text{L}^{\text{1a-e}}-\text{Se},\text{O})_2]$	162
4.2.2.2	Deposition using $[\text{Cd}^{\text{II}}(\text{L}^{\text{2a-e}}-\text{S},\text{O})_2]$	162
4.2.2.3	Deposition using $[\text{Zn}^{\text{II}}(\text{L}^{\text{1a}}-\text{Se},\text{O})_2]$	162
4.2.2.4	Deposition using $[\text{Zn}^{\text{II}}(\text{L}^{\text{2a}}-\text{S},\text{O})_2]$	162
4.2.2.5	Deposition using <i>cis</i> - $[\text{Ni}^{\text{II}}(\text{L}^{\text{2a}}-\text{S},\text{O})_2]$	162
4.2.2.6	Deposition using <i>cis</i> - $[\text{Pd}^{\text{II}}(\text{L}^{\text{2a}}-\text{S},\text{O})_2]$	162
4.2.2.7	Deposition using <i>cis</i> - $[\text{Pt}^{\text{II}}(\text{L}^{\text{2a}}-\text{S},\text{O})_2]$	162
4.2.2.8	Deposition using <i>cis</i> - $[\text{Pd}^{\text{II}}(\text{L}^{\text{1a}}-\text{Se},\text{O})_2]$	162
4.3	Results and Discussion	163
4.3.1	Deposition of CdSe	163

4.3.1.1	Deposition using $[\text{Cd}^{\text{II}}(\text{L}^{1\text{a}}\text{-Se},\text{O})_2]$	163
4.3.1.2	Deposition using $[\text{Cd}^{\text{II}}(\text{L}^{1\text{b-e}}\text{-Se},\text{O})_2]$	167
4.3.2	Deposition of CdS	168
4.3.2.1	Deposition using $[\text{Cd}^{\text{II}}(\text{L}^{2\text{a}}\text{-S},\text{O})_2]$	168
4.3.2.2	Deposition using $[\text{Cd}^{\text{II}}(\text{L}^{2\text{b-e}}\text{-S},\text{O})_2]$	170
4.3.3	Deposition of ZnSe	171
4.3.4	Deposition of ZnS	174
4.3.5	Deposition of Ni_3S_2	177
4.3.6	Deposition using <i>cis</i> - $[\text{Pd}^{\text{II}}(\text{L}^{2\text{a}}\text{-S},\text{O})_2]$	179
4.3.7	Deposition using <i>cis</i> - $[\text{Pt}^{\text{II}}(\text{L}^{2\text{a}}\text{-S},\text{O})_2]$	182
4.3.8	Deposition of $\text{Pd}_{17}\text{Se}_{15}$	184
4.4	Conclusions	187
	References	189
Chapter 5	Conclusions	191
Addendum A	Cadmium(II) complexes of <i>N,N</i>-diethyl-<i>N'</i>-benzoyl(thio)selenourea as single-source precursors for the preparation of CdS and CdSe nanoparticles	
	Jocelyn C. Bruce, Neerish Revaprasadu, Klaus R. Koch	
	<i>New Journal of Chemistry</i> , 2007 , 31, 1-7.	197
Addendum B	<i>N</i>-benzoyl-<i>N',N'</i>-dibutylselenourea and its <i>cis</i>-$[\text{Pd}(\text{L-Se},\text{O})_2]$ complex	
	Jocelyn C. Bruce, Klaus R. Koch	
	<i>Acta Crystallographica Section C</i> , 2008 , C64, 1, m1-m4.	205
Addendum C	Bipodal 1,1'-acyl-3,3,3',3'-tetraalkylbis(thiourea) ligands with flexible C₃, C₄ and C₆ spacer groups	
	Susanne Stockmann, Jocelyn C. Bruce, Jorn Miller and Klaus R. Koch	
	<i>Acta Crystallographica Section C</i> , 2008 , C64, o166-o170.	210
Addendum D	Titanoxycarbene complexes of Ti(IV) with O- and N- donor ligands	
	Stefan D. Nogai, Oliver Schuster, Jocelyn Bruce and Helgard G. Raubenheimer	
	<i>New Journal of Chemistry</i> , 2008 , 32, 540-546.	216

Chapter 1

General Introduction

The work in this thesis is divided into three areas of focus. The first (**Chapter 2**) describes the preparation, spectroscopic and solid state characterization of a series of *N,N*-dialkyl-*N'*-benzoyl(thio)selenourea ligands and their metal complexes. The second focus area (**Chapter 3**) describes the use of selected *N,N*-dialkyl-*N'*-benzoyl(thio)selenourea metal complexes as single source precursors for the preparation of semiconducting quantum dots as well as other materials. In this section, a possible correlation between precursor alkyl chain length and nanoparticle morphology is also discussed. The single source precursors are taken further in the final section (**Chapter 4**) where their employment in thin film preparation using Aerosol Assisted Chemical Vapour Deposition (AACVD) is described.

“We are about to be able to build things that work on the smallest possible length scales, atom by atom, with the ultimate level of finesse. These little nanothings and the technology that assembles and manipulates them will revolutionise our industries and our lives.” Chemist and Nobel Laureate Richard Smalley spoke these words in 1999 illustrating the impact made on the scientific and general community by materials with critical dimensions. The work described in this thesis focuses mainly on II-VI quantum dots, although a significant impact has been made by nanoparticles of all types.

1.1 An overview of quantum dots

The intense interest in quantum dots is largely two fold. Firstly, these nanoparticles possess unique size dependant optical and electronic properties, and secondly, the number of surface atoms increases considerably as the nanoparticle size decreases allowing influence over the nanoparticle properties by altering the nature of the surface atoms. These two phenomena allow quantum dots a vast myriad of applications and are responsible for the significant research interest in these particles.^[1]

1.1.1 Theoretical considerations

In general the term nanoparticle refers to particles containing a couple of hundred to a couple of thousand atoms, where materials in this size regime (1-100 nm) bridge the gap between individual atoms and the solid state.^[2] Semiconducting materials with confinement in 1 dimension are referred to as 2D quantum wells, confinement in 2 dimensions as 1D quantum wires, and confinement in 3 dimensions as (0D) quantum dots.^[3] The reduced dimensions of quantum dots relative to the exciton radius of the bulk material, and large surface to volume ratio are responsible for the unique properties of these particles.^[1] In the bulk material (see Refs [4-8] for properties of semiconductors) the conduction and valence bands are seen as continuous, however as the nanoparticle dimensions decrease, the valence and conduction bands split giving rise to discrete energy levels (Fig. 1.1). In semiconductors, promotion of an electron to the valence band results in a hole in the conduction band (considered as a particle with its own positive charge and effective mass) where both electrons and holes are considered to be charge carriers. When they approach each other they form an exciton, delocalized within the crystal lattice, where the Bohr radius of the exciton is effectively the distance between the electron and the hole. The physical size of quantum dots is smaller than the actual Bohr exciton radius and the charge carriers are considered quantum mechanically as “particles in a box”. In addition to discrete energy levels in the valence and conduction bands, the coulombic interaction between the electron and hole must be taken into consideration, leading to their state of higher kinetic energy than in the bulk. The consequent increase in the band gap is manifested in the optical spectra and the size dependant nature of this phenomenon leads to the potential applications of these particles.

Several calculations of the size quantization effects have been proposed and most are based on the “particle in a box assumption”, variations occurring through choice of the boundary conditions and complexity.^[9-13] Perhaps the most well known is that of Brus, who proposed the following equation to calculate the 1st excitonic energy state in quantum dots.^[14, 15]

$$E_g(\mathbf{R}) = E_g(\mathbf{R}=\infty) + \frac{\hbar^2\pi^2}{2\mathbf{R}^2} \left(\frac{1}{m_e^-} + \frac{1}{m_h^+} \right) - \frac{1.8e^2}{\epsilon\mathbf{R}} \quad (1)$$

where R is the radius of the particle, m_e and m_h are the effective masses of the electron and hole respectively and ϵ is the bulk optical dielectric coefficient. The first term in the equation is the band gap of the bulk semiconductor, the second corresponds to the sum of the confinement energy for the electron and the hole and the third describes the coulomb interaction energy.^[16, 17] It is apparent that the coulomb term shifts $E(R)$ to smaller energy as R , while the quantum localisation terms shift $E(R)$ to higher energy as R^2 resulting in the apparent band gap increase for a small enough R .^[16]

This rather elementary model fails to recognise two important effects in real nanocrystallites. Firstly the coupling of electronic states to vibrations, in other words, it assumes that both the excited and ground state geometries are similar. Secondly, the crystallite surface structure is not taken into account, *i.e.* it assumes that the potential energy outside the nanocrystal is infinite and hence the electron and hole are always found within the nanocrystal. This is not always the case in practise as electrons and holes can localize on surface sites after partial excitation.^[17] In addition to these points, the nanocrystal is always assumed spherical and the interior is assumed to be of uniform medium.^[18] A further uncertainty in this and other models is the assumption that the effective masses as well as the dielectric constants are size independent.^[1, 3] Despite these limitations, the Brus equation does provide relatively accurate particle sizes, for nanoparticles larger than approximately 7 nm.

1.1.2 Optical properties of quantum dots

The effects of quantum confinement on semiconducting materials can be observed by monitoring the optical absorption spectrum. The band gap energy is related to the excitation of an electron from the valence to the conduction band, resulting from the absorption of a photon. As with all electronic transitions, selection rules apply, where for semiconductors, conservation of the wave vector k , is necessary.^[19] Semiconducting materials where this selection rule is observed are called direct band gap semiconductors, and they exhibit large absorption coefficients. In semiconducting materials where conservation of the wave vector is not observed, the lowest electronic transition (between the valence and conduction bands) is formally forbidden hence they exhibit small absorption coefficients.^[19] As mentioned in the previous section, experimentally the increased band gap of quantum dots is manifested in the absorption spectra by a blue shift in the absorption edge relative to that of the bulk material. As the particle size decreases, overlap between wave functions of the confined charge carriers increases and therefore so does the oscillator strength. The directly proportional relationship between the absorption coefficient and oscillator strength results in decreasing particle size not only leading to a blue shift in the exciton peak, but also an increase in the molar absorption coefficient, where this effect has been investigated in detail for CdS quantum dots.^[19-21]

Whilst the effect of quantum confinement on the absorption spectra of quantum dots is understood with relative ease, the situation with their emission is somewhat more complex. Investigating and understanding the emission of semiconducting nanoparticles is of particular interest for materials such as CdSe, where the emission energy falls within the visible spectrum allowing a variety of potential applications.^[2] Ideally, quantum dot emission should occur through the radiative recombination of an electron in the conduction band with a hole in the valence band leading to the release of a photon, however experimental findings frequently indicate greater complexity in understanding the nature of emission. Likely explanations have led to the nature of the emitting state becoming something of a contentious issue. The models most frequently used to explain observed phenomena are clearly described in references [22-27]. Possible complications will therefore only briefly be discussed here. Defects resulting from lattice mismatch, dangling bonds, or sulfur vacancies (in the case of CdS), lead to the presence of

trapped states (Fig. 1.1). These localized energy minima can trap the excited holes or electrons, rendering them less available for radiative recombination and decreasing the emission efficiency of the quantum dots. In addition, emission wavelengths other than the desired band edge frequency are often observed where studies on CdS nanocrystals have indicated the presence of a red emission (+/- 700 nm) due to sulfur vacancies, and free-carrier recombination giving rise to a weak green fluorescence (515 nm).^[28]

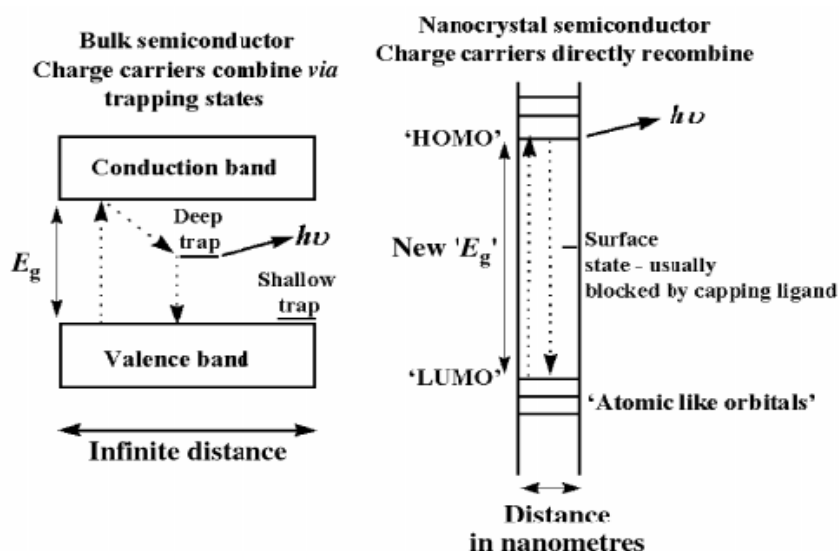


Fig. 1.1 Simplified schematic diagram illustrating energy states of a bulk semiconductor with those of a quantum dot. Taken from Ref [24].

This can be avoided or at least minimized by surface passivation thereby reducing the possibility of charge carriers being trapped. This includes capping of the quantum dots, by materials with a higher band gap, *i.e.* preparation of CdS coated CdSe nanoparticles,^[29] as well as use of coordinating solvents such as trioctylphosphine oxide.^[2] In well passivated quantum dots however, the emission maximum blue shifts with decreasing particle size allowing their potential application as lasers, dyes and fluorescent indicators.^[3]

1.1.3 Potential applications of quantum dots

The unique optical and electronic properties of semiconducting quantum dots allows their potential application in a wide variety of disciplines. Many organic compounds find applications as fluorescent dyes, and generally exhibit quantum yields in the region of 0.6. Where semiconducting quantum dots exhibit sufficient surface passivation, quantum yields in this region can be attained.^[30] Bruchez *et al.* have used silica coated semiconductor nanocrystals in the preparation of fluorescent probes which could find applications in biological staining and diagnostics. Their tests involved the fluorescent labelling of 3T3 mouse fibroblast cells using silica coated CdSe/CdS nanoparticles, where improvements in emission efficiency and spectral width were noted.^[31] The use of quantum dots in this context generally holds several advantages over the more conventional organic dyes as they are less susceptible to photobleaching, where a comparative study revealed photobleaching within 10 minutes for the organic dye Rhodamine B, with CdSe quantum dots taking over 4 hours.^[32, 33] In addition, given that a monodisperse quantum dot sample is used, a very narrow emission spectrum (fwhm ~ 40 nm) can be obtained, making quantum dots ideal for applications where emission overlap needs to be minimized.^[3, 31, 34] Semiconducting quantum dots have been used as optical probes to monitor biocatalytic transformations, where the CdS/ZnS quantum dots used in the study

could have potential as sensors for tyrosinase activity.^[35] More recently, Patolsky *et. al.* have reported on the use of CdSe/ZnS nanoparticles as photochemical centres to investigate the replication of DNA using Fluorescence Resonance Energy Transfer (FRET).^[36] Further details on the use of nanomaterials in bioimaging can be found in a recent review.^[37]

Differences in redox potential between the bulk material and that under quantum confinement gives rise to a number of interesting possibilities where the use of nanosized CdSe particles has been shown to result in the reduction of CO₂ to form formic acid,^[38] as well as the photoirradiation of CdS or ZnS containing polyurea films resulting in the generation of hydrogen.^[39] Metal sulfide and metal oxide nanoparticles have been employed as catalysts in the photoinitiated polymerisation of vinylic monomers and methylmethacrylate.^[40, 41] Semiconducting quantum dots also show potential in the field of solar energy conversion, where Alivisatos and co-workers reported the synthesis of efficient hybrid solar cells making use of semiconductor nanorods, where the nanorod radius could be used to alter the band gap and nanorod length could be used to tune the distance of electron transport through the thin film device.^[42] Nanoparticles find potential applications as novel materials in optical telecommunication systems, where nanocrystalline HgTe in aqueous solution has been found to exhibit emission in the 1.3-1.5 μm wavelength region.^[43] A colloidal nanocrystal of cadmium selenide has allowed the preparation of a single-electron transistor,^[44] and in a separate study, the preparation of single-electron transistors employed SiO₂/Si substrates and CdSe nanocrystals.^[45]

Fairly recently Coe *et. al.* have reported on the synthesis of an organic/inorganic hybrid light-emitting diode (LED) exhibiting a 25-fold enhancement in luminescence efficiency.^[46] Combination of the semiconducting polymer PPV, poly(*p*-phenylenevinylene), and CdS capped CdSe nanoparticles has led to the formation of LED's able to emit from red to green wavelengths and exhibiting quantum yields of up to 0.22 %.^[47] Semiconducting nanoparticles also find potential application in lasers, where narrowband stimulated emission of CdSe quantum dots could be observed, and as expected, nanoparticle size could be used to allow a degree of wavelength selectivity.^[48] Quantum dots have also been employed in the preparation of semiconducting films containing *p*-paraphenylene vinylene (PPV) and CdE (E = S, Se) nanocrystallites, and the synthesis of hybrid organic/inorganic electroluminescence devices.^[49]

1.1.4 Methods of quantum dot synthesis

The different synthetic methods for the preparation of semiconducting quantum dots have recently been reviewed,^[24, 50-52] and are briefly described here. The ideal preparation should produce pure, crystalline quantum dots with monodisperse size and shape and with an independently derivatized surface.^[22] In general, quantum dot synthesis can be divided into four broad categories. Gas phase preparation,^[53] colloidal synthesis,^[16, 20, 54, 55] synthesis in confined matrices^[56-61] and organometallic precursors routes, where the work in this thesis will focus on the latter.

The use of metal organic compounds overcomes several of the limitations exhibited by alternative synthetic routes where gas phase preparations frequently result in particle agglomeration, and size polydispersity.^[1] Colloidal routes are not accessible for the synthesis of all semiconducting materials due to air and moisture sensitivity *e.g.* GaAs and high temperature instability of the colloids complicates annealing resulting in poorly crystalline material. Difficulties associated with preparations in confined matrices include particle size limitations based on the host structure and its removal following nanoparticle formation.^[1] Use of organometallic precursors circumvents several of these drawbacks. In a landmark paper describing the preparation of CdS, CdSe and CdTe quantum dots Bawendi

et.al. used separate metal and chalcogen sources. Injection of Me_2Cd suspended in tri-*n*-octylphosphine (TOP) and TOPE (where E = S, Se, Te) into a hot (230-260 °C) coordinating solvent, tri-*n*-octylphosphine oxide (TOPO)^[62] resulted in a short burst of nucleation followed by slow growth and annealing consistent with Ostwald ripening (Fig. 1.2).^[22]

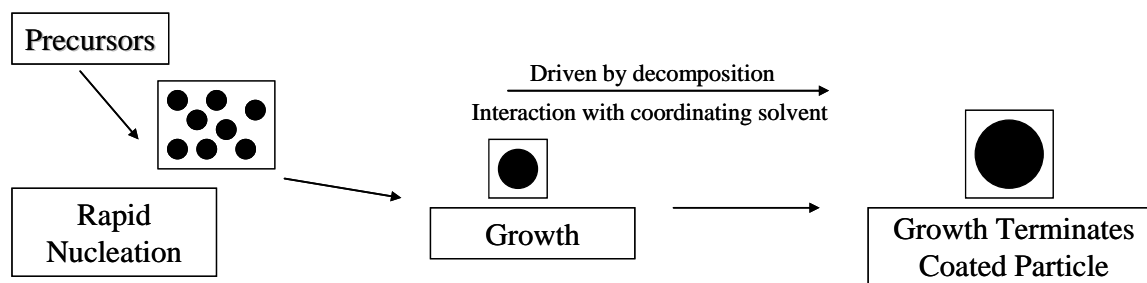


Fig. 1.2 Schematic diagram of nanoparticle growth stages using a one-pot synthesis, Ref [1].

The use of TOPO allowed a measure of control over the growth process, the stabilization of the resulting colloidal dispersion as well as the electronic passivation of the semiconducting surface.^[24] Addition of a non solvent (methanol) resulted in flocculation of the nanoparticles and removal of excess TOP and TOPO allowing isolation of the TOPO capped nanoparticles. The particle size distribution could be reasonably controlled using temperature, where higher temperatures produced larger particles.^[19] Fairly monodisperse, well passivated and highly crystalline nanoparticles could be prepared using this method. However, disadvantages to the method include the use of toxic and pyrophoric metal alkyls at high temperatures. For example, $\text{Cd}(\text{CH}_3)_2$ is highly toxic, unstable at room temperature, pyrophoric, expensive and explosive at elevated temperatures making its use as a precursor particularly hazardous.^[63] This can be avoided by making use of single source precursors, where the metal-chalcogen bond has already been formed. Brennan *et.al.* published one of the first reports describing the preparation of CdSe nanoparticles from the thermolysis of $[\text{Cd}(\text{SePh})_2]_2[\text{Et}_2\text{PCH}_2\text{CH}_2\text{PEt}_2]$.^[64] Soon after, work by O'Brien and co-workers elegantly made use of a variety of single source precursors but focussed on the preparation of thin films using MOCVD (this is discussed further in Chapter 4).^[65] However, in the late 1990's CdS and CdSe were successfully synthesised following the thermolysis of dithio- and diselenocarbamate cadmium(II) complexes in trioctylphosphine oxide (TOPO),^[66, 67] and since then a variety of different single source precursors have been employed.

The work described in this thesis makes use of a particular class of coordination compounds namely the *N,N*-dialkyl-*N'*-benzoyl(thio)selenoureas as single source precursors for the preparation of quantum dots and in order to place their use in context, a brief review of other single source precursors is given below, several of which are shown in Fig 1.3.

1.2 Single source precursor synopsis

Bis(hexylmethylthio- and diselenocarbamato)Cd(II) and Zn(II) metal complexes have been used in the synthesis of CdS, CdSe as well as ZnS and ZnSe nanoparticles.^[68] Thermolysis of bis(diethylthiocarbamato)Zn(II) and bis(methylhexylthiocarbamato)Cd(II) in the presence of MnCl_2 led to the formation of Mn-doped ZnS and CdS nanoparticles with significantly different emission spectra to undoped nanoparticles, the ZnS nanoparticles being more stable to the Mn-doping than their Cd counterparts.^[69] The longer chain precursor, $[\text{Cd}\{\text{S}_2\text{CNMe}(\text{C}_{18}\text{H}_{37})\}_2]$ also yields CdS nanoparticles however, in this case cubically phased material is obtained at lower temperatures (150

– 250 °C) and thermolysis at 300 °C gives hexagonally phased nanoparticles.^[70] Use of the closely related *N*-alkyldithiocarbamate complexes, $[\text{Cd}(\text{S}_2\text{CNHC}_{12}\text{H}_{25})_2]$ and $[\text{Zn}(\text{S}_2\text{CNHC}_6\text{H}_{13})_2]$ has resulted in the formation of hexagonally phased CdS and cubically phased ZnS nanoparticles.^[71] Bis(methylhexyldiselenocarbamato)Cd(II) has successfully been employed for the synthesis of CdSe nanoparticles following 250 °C thermolysis,^[72] and work by Chunggaze and co-workers indicates that subtle alteration in the substituents at the nitrogen atom of these complexes can affect the thermal decomposition of the metal complexes.^[73] The employment of dithio-diselenocarbamate complexes as single source precursors is not limited to d^{10} metal complexes (*i.e.* Cd(II) and Zn(II)) as bismuth sulfide nanoparticles have been synthesised using $[\text{Bi}(\text{S}_2\text{CNMe}^n\text{Octadecyl})_3]$.^[72]

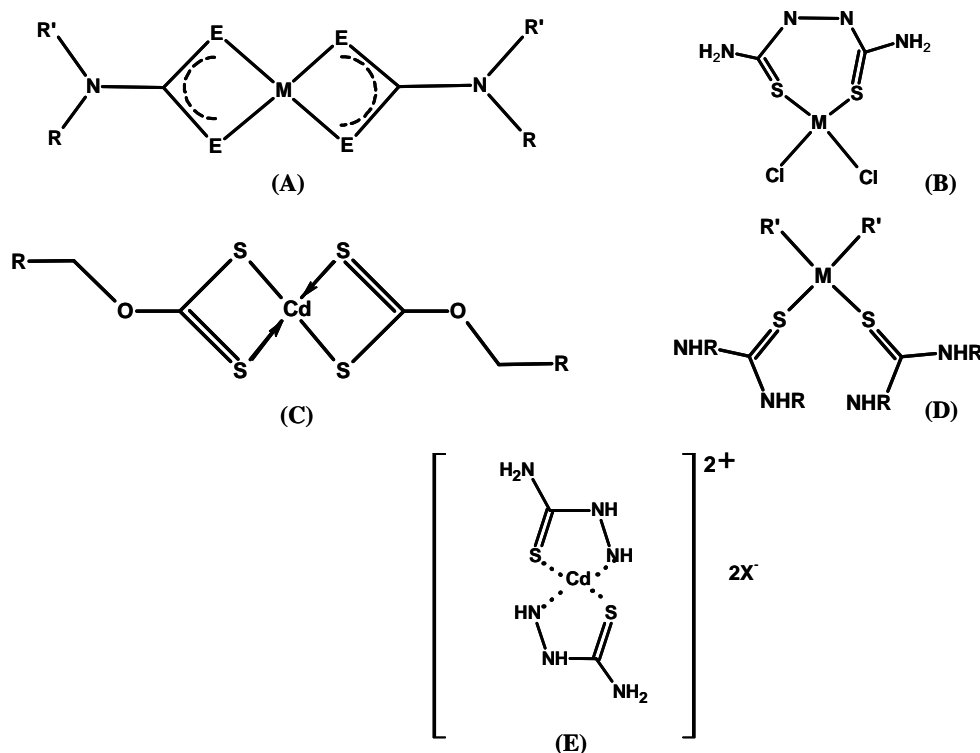


Fig. 1.3 Selected structures of single source precursors, where (A) = bis(methylhexyldithio(seleno)carbamato)M(II) where E = S, Se, M = Cd, Zn, R = Me and R' = Hex,^[68, 74] (B) = Cd(II) complex of dithiobiurea where M = Cd,^[74] (C) = Cd ethylxanthate,^[75, 76] (D) = thiourea precursors where R' = Cl, M = Cd, R = ethyl,^[77] methyl,^[78] phenyl,^[78] (E) = Cd(II) thiosemicarbazide.^[79]

PbS nanoparticles with differing morphologies have been synthesised using $\text{Pb}(\text{SCNEt}_2)_2$.^[80] Both InS and InSe nanoparticles have formed from the thermal decomposition of tris(diethyldithio-diselenocarbamato)indium(III) complexes^[81] and to the best of our knowledge, the only report detailing the synthesis of PtS and PdS nanoparticles by the single source precursor approach, made use of Pt(II) and Pd(II) complexes of bis(methylhexyldithiocarbamate).^[82]

Cadmium ethylxanthate as a single source precursor was initially reported to give spherical CdS nanoparticles, 3.9–4.2 nm in diameter,^[75] however extensive study of this precursor by Li and co-workers allowed the synthesis of hexagonally phased rods, as well as bipodal and tripodal structures. The morphology of the resulting nanoparticles was controlled by delicately balancing the thermodynamic and kinetic growth regimes using reaction conditions such as precursor concentration, reaction temperature and reaction time.^[76] Longer alkyl chain derivatives such as hexadecylxanthates have also been used and found to yield cubically phased CdS nanoparticles. Thermolysis of hexadecylxanthate complexes with various transition metal ions has allowed the synthesis of ZnS, PbS, HgS, CuS,

NiS and MnS nanoparticles.^[83] The Cd(II) complex of dithiobiurea yields irregularly shaped CdS nanoparticles at low injection temperatures, and more spherically shaped nanoparticles following relatively high temperature thermolysis.^[84] Cadmium thiosemicarbazide yields CdS nanorods following 280 °C thermolysis,^[79] where the CdS obtained from both dithiobiurea and thiosemicarbazide derivatives is hexagonally phased. Thermolysis of a Cd(II) complex of *N,N'*-bis(thiocarbamoyl)hydrazine at 280 °C allowed the synthesis of CdS nanoparticles.^[85] Cd(II) complexes of *N,N*-dialkyl thioureas have been investigated where *N,N*-dioctyl-, *N,N*-dicyclohexyl- and *N,N*-diisopropylthiourea complexes were investigated and the morphology of the resulting CdS nanoparticles found to be influenced by the alkyl chain length of the precursor.^[86]

The formation of quantumly confined EuS nanoparticles following the thermal decomposition of Na[Eu(S₂CEt₂)₄]·3.5H₂O has recently been reported by Hasegawa and co-workers.^[87] Selenocarboxylate complexes such as [(Ph₃P)₃Ag₂(SeC(O)Ph)₂] and M(SeCOPh)₂(tmeda), where M = Cd, Zn and tmeda = tetramethylethylenediamine, have been employed in the synthesis of Ag₂Se, CdSe and ZnSe nanoparticles respectively.^[88, 89]

The use of single source precursors is not limited to coordination complexes as Cumberland *et. al.* have recently used inorganic clusters such as Li₄[Cd₁₀Se₄(SPh)₁₆] and related compounds for the synthesis of CdSe and ZnSe nanoparticles.^[90] Nanodimensional Fe, Ni, Co and Mn oxides have been formed from the thermolysis of the various metal acetylacetonate complexes where hexadecylamine (HDA) was used as both solvent and capping agent.^[91]

From the brief review above it is evident that a variety of coordination complexes have been employed as single source precursors. In general fairly high thermolysis temperatures (ranging from 200 to 300 °C) are necessary to achieve nucleation and consequent nanoparticle growth from the majority of these compounds. In addition, the systematic study of precursor structure on the resulting nanoparticle morphology is not usually reported. In recent years, our research group has investigated coordination compounds based on the *N,N*-dialkyl-*N'*-aryl(thio)selenoureas and a brief summary of these compounds, their properties and potential applications is given below.

1.3 General coordination chemistry of the *N,N*-dialkyl-*N'*-aryl(thio)selenoureas

Compounds based on the *N,N*-dialkyl-*N'*-arylselenourea motif (Fig. 1.4 where E = Se) were first reported by Douglass in 1937 and involved the addition of benzoyl chloride to KSeCN followed by an amine, yielding the product in a simple one-pot procedure.^[92] The first reports of their abilities to complex transition metal ions emerged 38 years later,^[93] and since then several reports documenting complexation to a wide variety of transition metal ions have appeared.^[94-99] Structures involving metal complexes of *N,N*-diethyl-*N'*-benzoylselenourea of Zn(II),^[100] Cd(II),^[101] Tl(I),^[102] Co(III),^[103] Ni(II),^[104] Pb(II),^[105] and In(III)^[106] have been reported. In the majority of cases, loss of the selenoamidic proton accompanies coordination through the O and Se donor atoms to the central metal ion. Structural characterizations of *cis*-Bis[*N,N*-diisobutyl-*N'*-(2-fluoro)benzoylselenoureaato]Pd(II) and its difluoro analogue indicate that complexation to *d*⁸ metal ions results in the formation of square-planar metal complexes with a predominantly *cis* conformation, indeed to the best of our knowledge, no mention has been made of a *trans* species.^[107, 108] Studies concerning restricted rotation about the C-NR₂ bond have been investigated for a range of ligands and their metal chelates,^[95, 109-112] as have the mass spectra of several metal complexes and ligands.^[98, 99] *N,N*-diethyl-*N'*-benzoylselenourea and its dibutyl analogue have been shown to extract a myriad of transition metal ions from an aqueous into an organic phase and the chromatographic separation of the resulting metal chelates

investigated.^[113, 114] Whilst there are several reports on the single crystal characterizations of metal complexes, until 2005 those of only two ligands, *N,N*-diethyl-*N'*-(2-fluoro)benzoylselenourea and *N,N*-diisobutyl-*N'*-(2-fluoro)benzoylselenourea, were known.^[107]

The preparation of a series of *N*-monoalkyl-*N'*-aroylselenoureas (where R = H and alkyl, Fig. 1.4) has been reported although their complexation behaviour has not been investigated.^[92, 115]

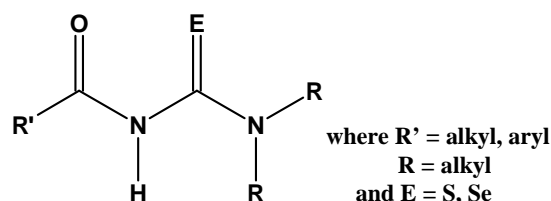


Fig. 1.4 General structure of *N,N*-dialkyl-*N'*-alkyl(aryl)chalcogenourea motif.

A single report describes the preparation of 'bipodal' ligands where two acylselenourea motifs are linked through a spacer molecule, this being either a *meta*- or *para*-substituted phenyl ring (Fig. 1.5). Spacer rigidity and the preferred *cis* coordination of these ligands to d^8 metal ions allows their self-assembly to form square-planar metallamacrocycles with 2:2 and 3:3 metal:ligand ratios, using *meta*- and *para*-substituted 'spacers' respectively (Fig. 1.5).^[116]

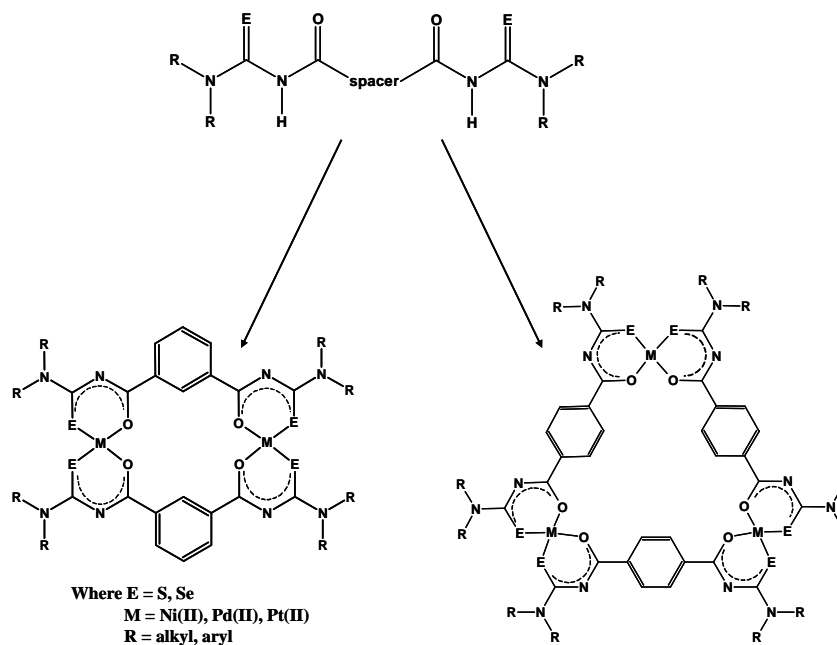


Fig. 1.5 Reaction scheme illustrating formation of 2:2 and 3:3 metallamacrocycles from *meta*- and *para*-substituted 3,3,3',3'-tetraalkyl-1,1'-phenylenedicarbonylbis(chalcogen)urea ligands. (Adapted from Ref [117]).

In relative terms there are very few reports detailing the behaviour of the *N,N*-dialkyl-*N'*-arylselenoureas, the majority of which have originated from a single laboratory over the past decades. Little variation has been reported with regards to the R group substituents, which is surprising given the vast potential these hold to tailor both ligand and metal complex properties. In addition, little mention has been made of potential applications of either the ligands or their chelates. This may partly be ascribed to the lower stability of the *N,N*-dialkyl-*N'*-arylselenoureas relative to their thiourea counterparts which are described below.

The facile synthesis of *N,N*-dialkyl-*N'*-arylthioureas (Fig. 1.4 E = S) analogous to that of that of their Se counterparts was reported by Douglass and Dains.^[118] Numerous reports detail coordination to a host of transition metal ions including Cu(II),^[119] Co(III),^[120] Ag(I),^[121] Hg(II),^[122] Au(III),^[123] Ni(II),^[124] Pd(II)^[125] and Pt(II).^[126] Of the three potential donor atoms, coordination usually takes place through S and O, although isolated cases of S, N donor atom combinations have been reported, and monodentate coordination through S can occur.^[127] Several potential applications have been investigated and their behaviour as possible antimalarial^[128] anticancer^[126, 129-131], antifungal^[132, 133] and antitumour^[134] agents has been documented. *N,N*-dialkyl-*N'*-arylthioureas were found to selectively extract Platinum Group Metal ions (PGM's) over those of base metals copper, iron and nickel^[135] leading to their potential application as selective complexing agents for the trace enrichment of the PGM's.^[136] Later reports enlarged on this to show the separation of Rh(III), Pd(II) and Pt(II) complexes using RP-HPLC, this being affected by altering the R group substituents to tailor the solubility of the resulting chelates.^[137] Further R group modifications have allowed the synthesis of more hydrophilic compounds^[138] and the addition of fluorescent tags^[139] for the potential trace determination of the PGM's.^[140, 141]

Significantly more has been reported about monoalkylthioureas (H_2L) than their selenium counterparts and in compounds of the type H_2L the potentially coordinating O atom is locked in an intramolecular hydrogen bond with the N-H group and consequently only monodentate coordination through the S occurs in metal complexes involving d^8 metal ions.^[142] This allows the presence of geometric isomers, $[Pt(H_2L-S)_2X_2]$ where the *cis* conformer is favoured in systems where ($X = Cl$)^[143] while the bromo- and iodo-complexes favour the *trans*.^[142, 144] Differing modes of coordination are also reflected in the dialkylthioureas where protonation mediated interchange between mono- and bidentate coordination has been investigated (Fig. 1.6).^[145]

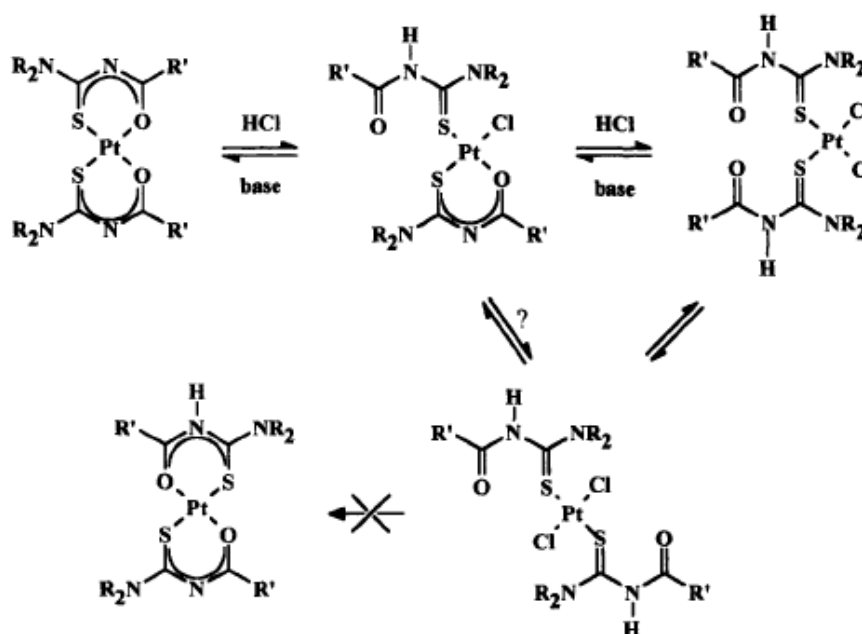


Fig. 1.6 Effects of *conc* HL addition to *cis*-[Pt(Lⁿ-S,O)₂] complex solutions in CDCl₃ ($n = 1-3$).^[145]

Interestingly only a single structural characterization of a *trans*- [Pt(L-S,O)₂] metal complex has been reported,^[146] and the nature of this isomerisation has only recently been elucidated. Complexes of the type *cis*-[M^(II)(L-S,O)₂] where M = Pt, Pd (L represents the deprotonated ligand; S and O, indicating coordination through the sulfur and

oxygen atoms respectively) undergo a photoinduced isomerisation to form the *trans* isomer in the presence of visible light whilst the rate of the reverse process is thought to be temperature dependant.^[147]

'Bipodal' derivatives of the *N,N*-dialkyl-*N'*-arylthioureas (Fig. 1.5 where E = S) were reported as early as 1965,^[148] and significantly more work has been reported on these types of complexes, than on their selenium analogues. More recently, work based on *meta*- and *para*-substituted phenyl ring spacers has shown that with d^8 metal ions, such ligands undergo 'self assembly' to form 2:2 and 3:3 metallamacrocycles (Fig. 1.5).^[149-151] The pyridine adducts of 2:2 and 3:3 Ni(II) complexes of 3,3,3',3'-tetraethyl-1,1'-phenylenedicarbonylbisthioureas have been investigated and exhibit interesting host-guest chemistry in the solid state.^[117, 152] The corresponding diiodoplatinum(IV) adducts have also been prepared and structurally characterized following electrochemically induced oxidative addition of I₂ to the corresponding 2:2 and 3:3 Pt(II) complexes of 3,3,3',3'-tetraethyl-1,1'-isophthaloylbis(thiourea) and 3,3,3',3'-tetraethyl-1,1'-terephthaloylbis(thiourea).^[153] A similar bipodal ligand with a 2,6-substituted pyridine ring as spacer and its AgI coordination polymer has recently been described.^[154] The presence of a rigid 'spacer' molecule is not mandatory as Konig *et al.* reported the synthesis of a variety of 3,3,3',3'-tetraalkyl-1,1'-alkanediolylbis(thioureas) and the Ni(II), Cu(II), Pd(II) and Pt(II) metal complexes of 3,3,3',3'-tetraethyl-1,1'-adipoylbis(thiourea), although no definitive structural characterization of such complexes is available.^[155] In this context we recently reported the first crystallographic characterisation of bipodal ligands with flexible spacer groups.^{[156]*}

Thermal decomposition of the *N,N*-dialkyl-*N'*-benzoylselenoureas (HL_{Se}¹) and their metal complexes ([M^{II}(L¹-Se,O)₂]) has not been investigated to our knowledge, although reports of the S analogues (HL_S²) indicate the formation of metal sulfide residues following thermal decomposition of the metal chelates [M^{II}(L²-S,O)₂].^[157-159] Of particular interest is the formation of cadmium sulfide following the thermal decomposition of *N,N*-dipropyl-*N'*-(benzoylthioureato)Cd(II).^[158] Several coordination compounds such as cadmium ethylxanthate^[75] and cadmium dithiocarbamates^[67] showing similar properties have been used as single source precursors for the preparation of nanosized semiconducting materials such as CdS and CdSe, suggesting that (*N,N*-dialkyl-*N'*-benzoylthioureato)Cd(II) complexes as well as their Se analogues, may be employed in a similar fashion. Further, the thermal decomposition of these chelates with other metal ions such as Pd(II) and Pt(II) could lead to the formation of different materials with interesting properties.

Previous studies on semiconducting quantum dots, particularly CdS and CdSe have focussed on preparations yielding a degree of size control and an increase in monodispersity.^[160] Recently, the focus has shifted to the attainment of morphology control. Comprehensive studies using separate metal and chalcogen sources have indicated that morphology control in these systems is a result of a delicate balance between nucleation and growth, as well as kinetic or thermodynamic control of the growth regime. Various influencing parameters such as monomer concentration, surfactant ratio and reaction temperature can be used to attain the desired shape.^[161-164] Whilst these studies allow morphology control using separate precursor solutions, few investigations have reported the use of single source precursors, even though a wide variety of shapes have been observed using this synthetic method. Scholes and co-workers have studied the thermal decomposition of various precursors in an attempt to relate these to the obtained morphologies,^[160] whilst Pradhan and Efrima report the influence of precursor concentration and annealing temperature on nanoparticle morphology using the single source precursor synthetic method.^[165] Reports

* Reference [155] is included as Addendum C.

by O'Brien and co-workers indicate that alteration of precursor substituents could influence the properties of the resulting nanomaterials.^[72] To date however, there is no systematic investigation into the effect of single source precursor substituents on the resulting nanoparticle morphology.

1.4 Objectives and thesis outline

The main aim of the research described in this thesis was to investigate the effect that alteration in the alkyl chain lengths of the (*N,N*-dialkyl-*N'*-benzoyl(thio)selenoureato)Cd(II) single source precursors would have on the resultant nanoparticle morphology.

Secondary aims were to study the thermolysis of (*N,N*-diethyl-*N'*-benzoyl(thio)selenoureato)M(II) metal complexes (where M = Pt(II), Pd(II), Zn(II)) and the nature of the resulting material, as well as to investigate the use of *N,N*-dialkyl-*N'*-benzoyl(thio)selenourea metal complexes as single source precursors for the Aerosol Assisted Chemical Vapour Deposition (AACVD) of thin films.

Initially, the synthesis of “bipodal” thio- and selenourea metal complexes were of interest as the reduced stability of the resulting selenourea metallamacrocycles was expected to lead to lower thermolysis temperatures and interesting morphologies however the costly nature of preparation and limited yields restricted the use of these compounds as single source precursors, therefore only their preparation and structural characterization are reported.

The preparation and novel structural characterization of a series of *N,N*-dialkyl-*N'*-benzoyl(thio)selenourea ligands as well as their coordination to selected metal ions including Cd(II) and Pd(II) is described in **Chapter 2**. The following page lists the names, codes and structures of the synthesized compounds. This chapter also describes the first structural characterization of a “bipodal” selenourea ligand. Multinuclear NMR (Nuclear Magnetic Resonance) spectroscopy of selected ligands and their metal complexes are reported as well as the thermal decomposition profiles of several *N,N*-dialkyl-*N'*-benzoyl(thio)selenourea metal complexes.

Chapter 3 focuses on the use of the *N,N*-dialkyl-*N'*-benzoyl(thio)selenourea Cd(II) complexes as single source precursors for the preparation of CdS and CdSe quantum dots. The thermolysis of (*N,N*-dioctyl-*N'*-benzoylselenoureato)Cd(II) results in the formation of anisotropic tripodal CdSe nanoparticle and possible growth mechanisms are discussed. The thermolysis of a number of different *N,N*-dialkyl-*N'*-benzoylthiourea metal complexes is examined and preliminary experiments into the synthesis of core/shell nanoparticles are described.

Use of the *N,N*-dialkyl-*N'*-benzoyl(thio)selenourea metal complexes as single source precursors for the preparation of thin films using AACVD is outlined in **Chapter 4**. The deposition of crystalline platinum from *cis*-(*N,N*-diethyl-*N'*-benzoylthioureato)Pt(II) as well as the first AACVD of crystalline Pd₁₇Se₁₅ from *cis*-(*N,N*-diethyl-*N'*-benzoylselenoureato)Pd(II) are described.

A summary of the research described in the preceding chapters is given in **Chapter 5** and the most notable findings are highlighted.

Table 1.1 Summary of synthesized ligands, nomenclature, shorthand notation and numerical codes used in this thesis.

Where E = Se		Structure	Where E = S	
Shorthand notation and code	Name		Name	Shorthand notation and code
HL _{Se} ^{1a}	11 <i>N,N</i> -diethyl- <i>N'</i> -benzoylselenourea:		<i>N,N</i> -diethyl- <i>N'</i> -benzoylthiourea:	21 HL _S ^{2a}
HL _{Se} ^{1b}	12 <i>N,N</i> -dibutyl- <i>N'</i> -benzoylselenourea		<i>N,N</i> -dibutyl- <i>N'</i> -benzoylthiourea	22 HL _S ^{2b}
HL _{Se} ^{1c}	13 <i>N,N</i> -dihexyl- <i>N'</i> -benzoylselenourea		<i>N,N</i> -dihexyl- <i>N'</i> -benzoylselenourea	23 HL _S ^{2c}
HL _{Se} ^{1d}	14 <i>N,N</i> -dioctyl- <i>N'</i> -benzoylselenourea		<i>N,N</i> -dioctyl- <i>N'</i> -benzoylthiourea	24 HL _S ^{2d}
HL _{Se} ^{1e}	15 <i>N</i> -benzyl- <i>N</i> -methyl- <i>N'</i> -benzoylselenourea		<i>N</i> -benzyl- <i>N</i> -methyl- <i>N'</i> -benzoylthiourea:	25 HL _S ^{2e}
HL _{Se} ^{1f}	16 <i>N,N</i> -didecyl- <i>N'</i> -benzoylselenourea		<i>N</i> -morpholine- <i>N'</i> -benzoylthiourea	26 HL _S ^{2f}
HL _{Se} ^{1g}	17 <i>N,N</i> -diphenyl- <i>N'</i> -benzoylselenourea		<i>N,N</i> -dicyclohexyl- <i>N'</i> -benzoylthiourea	27 HL _S ^{2g}

The shorthand notation of the *N,N*-dialkyl-*N'*-benzoyl(thio)selenourea ligands is composed of the letters HL, indicating the presence of the central N-H atom. The subscript (Se or S) refers to the identity of the second coordinating atom, the superscript (1) denotes the selenoureas and (2) refers to the thioureas. The second letter of the superscript *i.e.* a,b,c refers to the identity of the amine residue, where (a) = ethyl, (b) = butyl etc. The trend between the Se and S containing ligands is consistent from (a-e), but the identity of (f) and (g) differ for the two series as depicted in Table 1.

The shorthand notation of the two “bipodal” ligands synthesised is similar where H₂L^{m1a} refers to 3,3,3',3'-tetraethyl-1,1'-isophthaloylbis(selenourea), H₂L indicating the presence of the two N-H atoms, *m* referring to the

meta substitution of the central phenyl ring, (1) indicating a selenourea, and (a) the presence of the diethyl residue. Similarly, H₂L^{m1b} refers to 3,3,3',3'-tetrabutyl-1,1'-isophthaloylbis(selenourea).

Table 1.2 Summary of synthesised metal complexes, shorthand notation and numerical codes used in this thesis.

<i>N,N</i> -dialkyl- <i>N'</i> -benzoylthioureas			<i>N,N</i> -dialkyl- <i>N'</i> -benzoylselenoureas		
Shorthand notation and code	Central metal ion in complex	Ligand used in complex synthesis	Central metal ion in complex	Shorthand notation and code	
[Cd ^{II} (L ^{1a} -Se,O) ₂]	111	Cd(II)	<i>N,N</i> -diethyl- <i>N'</i> -benzoyl(thio)selenourea	Cd(II)	211 [Cd ^{II} (L ^{2a} -S,O) ₂]
<i>cis</i> -[Pd ^{II} (L ^{1a} -Se,O) ₂]	112	Pd(II)		Pd(II)	212 <i>cis</i> -[Pd ^{II} (L ^{2a} -S,O) ₂]
[Zn ^{II} (L ^{1a} -Se,O) ₂]	113	Zn(II)		Zn(II)	213 [Zn ^{II} (L ^{2a} -S,O) ₂]
				Pt(II)	214 <i>cis</i> -[Pt ^{II} (L ^{2a} -S,O) ₂]
				Ni(II)	215 <i>cis</i> -[Ni ^{II} (L ^{2a} -S,O) ₂]
				Co(III)	216 [Co ^{III} (L ^{2a} -S,O) ₃]
[Cd ^{II} (L ^{1b} -Se,O) ₂]	121	Cd(II)	<i>N,N</i> -dibutyl- <i>N'</i> -benzoyl(thio)selenourea	Cd(II)	221 [Cd ^{II} (L ^{2b} -S,O) ₂]
<i>cis</i> -[Pd ^{II} (L ^{1b} -Se,O) ₂]	122	Pd(II)		Pd(II)	222 <i>cis</i> -[Pd ^{II} (L ^{2b} -S,O) ₂]
[Cd ^{II} (L ^{1c} -Se,O) ₂]	131	Cd(II)	<i>N,N</i> -dihexyl- <i>N'</i> -benzoyl(thio)selenourea	Cd(II)	231 [Cd ^{II} (L ^{2c} -S,O) ₂]
<i>cis</i> -[Pd ^{II} (L ^{1c} -Se,O) ₂]	132	Pd(II)		Pd(II)	232 <i>cis</i> -[Pd ^{II} (L ^{2c} -S,O) ₂]
[Cd ^{II} (L ^{1d} -Se,O) ₂]	141	Cd(II)	<i>N,N</i> -dioctyl- <i>N'</i> -benzoyl(thio)selenourea	Cd(II)	241 [Cd ^{II} (L ^{2d} -S,O) ₂]
<i>cis</i> -[Pd ^{II} (L ^{1d} -Se,O) ₂]	142	Pd(II)		Pd(II)	242 <i>cis</i> -[Pd ^{II} (L ^{2d} -S,O) ₂]
[Cd ^{II} (L ^{1e} -Se,O) ₂]	151	Cd(II)	<i>N</i> -benzyl- <i>N</i> -methyl- <i>N'</i> -benzoyl(thio)selenourea	Cd(II)	251 [Cd ^{II} (L ^{2e} -S,O) ₂]
<i>cis</i> -[Pd ^{II} (L ^{1e} -Se,O) ₂]	152	Pd(II)		Pd(II)	252 <i>cis</i> -[Pd ^{II} (L ^{2e} -S,O) ₂]
[Cd ^{II} (L ^{1f} -Se,O) ₂]	161	Cd(II)	<i>N,N</i> -didecyl- <i>N'</i> -benzoylselenourea	Pd(II)	262 <i>cis</i> -[Pd ^{II} (L ^{2f} -S,O) ₂]
<i>cis</i> -[Pd ^{II} (L ^{1f} -Se,O) ₂]	162	Pd(II)			
[Cd ^{II} (L ^{1g} -Se,O) ₂]	171	Cd(II)	<i>N,N</i> -diphenyl- <i>N'</i> -benzoylselenourea	<i>N,N</i> -dicyclohexyl- <i>N'</i> -benzoylthiourea	-

The shorthand notation used for the “mixed ligand” complex, (*N,N*-diethyl-*N'*-benzoylselenoureaato,*N,N*-diethyl-*N'*-benzoylthioureaato)Cd(II) is [Cd^{II}(L^{1a}-Se,O)(L^{2a}-S,O)], **11211**.

The notation of the synthesised metallamacrocyclic complexes, closely follows that of their “monopodal” analogues, where *cis*-[Pd^{II}₂(L^{m1a}-Se,O)₂], **11112** is used for 3,3,3',3'-tetraethyl-1,1'-isophthaloylbis(selenoureaato)palladium(II), and *cis*-[Pt^{II}₂(L^{m1a}-Se,O)₂], **11114** refers to the Pt(II) analogue. The convention is maintained for the sulfur containing complex where *cis*-[Pd^{II}₃(L^{m2b}-S,O)₃], **22222** refers to 3,3,3',3'-tetra(*n*-butyl)-1,1'-terephthaloylbis(thioureaato)palladium(II).

References

- [1] M. Malik, P. O'Brien, N. Revaprasadu, *Phosphorus, Sulfur and Silicon and the Related Elements* **2005**, *180*, 689.
- [2] V. I. Klimov, *Los Alamos Science* **2003**, *28*, 214.
- [3] C. J. Murphy, *Analytical Chemistry* **2002**, *74*, 520A.
- [4] W. C. Dunlap, *An Introduction to semiconductors*, Wiley, New York, **1957**.
- [5] P. O'Brien, A. C. Jones, *CVD of compounds semiconductors: precursor synthesis, development and applications*, Weinheim, New York, **1997**.
- [6] R. P. Nanavati, *An Introduction to Semiconductor Electronics*, McGraw-Hill Book Company, New York, **1963**.
- [7] R. F. Pierret, *Semiconductor fundamentals, Vol. 1*, Second ed., Addison-Wesley Publishing company, New York, **1988**.
- [8] P. Y. Yu, M. Cardona, *Fundamentals of Semiconductors*, Springer-Verlag, Berlin, **1996**.

- [9] Y. Nosaka, *Journal of Physical Chemistry* **1991**, 95, 5054.
- [10] Y. Wang, N. Herron, *Journal of Physical Chemistry* **1991**, 95, 525.
- [11] L.-W. Wang, A. Zunger, *Physical Review B: Condensed Matter* **1996**, 53, 9579.
- [12] M. V. R. Krishna, R. A. Friesner, *Journal of Chemical Physics* **1991**, 95, 8309.
- [13] P. E. Lippens, M. Lannoo, *Physical Review B*: **1989**, 39, 10935.
- [14] L. E. Brus, *Journal of Chemical Physics* **1983**, 79, 5566.
- [15] L. Brus, *Journal of Physical Chemistry* **1986**, 90, 2555.
- [16] A. Hagfeldt, M. Graetzel, *Chemical Reviews (Washington, D. C.)* **1995**, 95, 49.
- [17] M. L. Steigerwald, L. E. Brus, *Accounts of Chemical Research* **1990**, 23, 183.
- [18] T. Kippeny, L. A. Swafford, S. J. Rosenthal, *Journal of Chemical Education* **2002**, 79, 1094.
- [19] T. Trindade, P. O'Brien, N. L. Pickett, *Chemistry of Materials* **2001**, 13, 3843.
- [20] T. Vossmeier, L. Katsikas, M. Giersig, I. G. Popovic, K. Diesner, A. Chemseddine, A. Eychmueller, H. Weller, *Journal of Physical Chemistry* **1994**, 98, 7665.
- [21] A. P. Alivisatos, *Science (Washington, D. C.)* **1996**, 271, 933.
- [22] M. A. Malik, P. O'Brien, N. Revaprasadu, *South African Journal of Science* **2000**, 96, 55.
- [23] N. Chestnoy, T. D. Harris, R. Hull, L. E. Brus, *Journal of Physical Chemistry* **1986**, 90, 3393.
- [24] M. Green, P. O'Brien, *Chemical Communications (Cambridge, United Kingdom)* **1999**, 2235.
- [25] M. Nirmal, B. O. Dabbousi, M. G. Bawendi, M. J.J., J. K. Trautman, T. D. Harris, L. E. Brus, *Nature (London)* **1996**, 383, 802.
- [26] M. Nirmal, D. J. Norris, M. Kuno, M. G. Bawendi*, A. L. Efros, M. Rosen, *Physical review letters* **1995**, 75, 3728.
- [27] A. L. Efros, M. Rosen, M. Kuno, M. Nirmal, D. J. Norris, M. G. Bawendi*, *Physical Review B*: **1996**, 54, 4843.
- [28] J. J. Ramsden, M. Gratzel, *J. Chem. SOC., Faraday Trans. 1*, **1984**, 80, 919.
- [29] N. Revaprasadu, M. Azad Malik, P. O'Brien, G. Wakefield, *Chemical Communications (Cambridge, United Kingdom)* **1999**, 1573.
- [30] M. A. Hines, G.-S. Philippe, *Journal of Physical Chemistry* **1996**, 100, 468.
- [31] M. Bruchez, Jr., M. Moronne, P. Gin, S. Weiss, A. P. Alivisatos, *Science (Washington, D. C.)* **1998**, 281, 2013.
- [32] D. Gerion, F. Pinaud, S. C. Williams, W. J. Parak, D. Zanchet, S. Weiss, A. P. Alivisatos, *Journal of Physical Chemistry B* **2001**, 105, 8861.
- [33] W. C. W. Chan, S. Nie, *Science (Washington, D. C.)* **1998**, 281, 2016.
- [34] B. O. Dabbousi, J. Rodriguez-Viejo, F. V. Mikulec, J. R. Heine, H. Mattoussi, R. Ober, K. F. Jensen, M. G. Bawendi, *Journal of Physical Chemistry B* **1997**, 101, 9463.
- [35] R. Gill, R. Freeman, J.-P. Xu, I. Willner, S. Winograd, I. Shweky, U. Banin, *J Am Chem Soc FIELD Full Journal Title:Journal of the American Chemical Society* **2006**, 128, 15376.
- [36] F. Patolsky, R. Gill, Y. Weizmann, T. Mokari, U. Banin, I. Willner, *Journal of the American Chemical Society* **2003**, 13918.
- [37] F. Pinaud, X. Michalet, L. A. Bentolila, J. M. Tsay, S. Doose, J. J. Li, G. Iyer, S. Weiss, *Biomaterials* **2006**, 27, 1679.
- [38] J. Nedeljkovic, M. T. Nenadovic, O. I. Mieie, A. J. Nozik, *Journal of Physical Chemistry* **1986**, 90, 12.
- [39] S. Shiojiri, T. Hirai, I. Komasa, *Chemical Communications (Cambridge, United Kingdom)* **1998**, 1439.
- [40] A. J. Hoffman, G. Mills, H. Yee, M. R. Hoffman, *Journal of Physical Chemistry* **1992**, 96, 5546.
- [41] A. J. Hoffman, H. Yee, G. Mills, M. R. Hoffman, *Journal of Physical Chemistry* **1992**, 96, 5540.
- [42] W. U. Huynh, J. J. Dittmer, A. P. Alivisatos, *Science (Washington, DC, United States)* **2002**, 295, 2425.
- [43] M. T. Harrison, S. V. Kershaw, M. G. Burt, A. Rogach, A. Eychmuller, H. Weller, *Journal of Materials Chemistry* **1999**, 9, 2721.
- [44] D. L. Klein, R. Roth, A. K. L. Lim, A. P. Alivisatos, P. L. McEuen, *Nature (London)* **1997**, 389, 699.
- [45] H. Weller, *Angew Chem Int Ed Engl FIELD Full Journal Title:Angewandte Chemie (International ed. in English)* **1998**, 37, 1658.
- [46] S. Coe, W.-K. Woo, M. Bawendi, V. Bulovic, *Nature (London, United Kingdom)* **2002**, 420, 800.
- [47] M. C. Schlamp, X. Peng, A. P. Alivisatos, *Journal of Applied Physics* **1997**, 82, 5837.
- [48] V. I. Klimov, A. A. Mikhailovsky, S. Xu, A. Malko, J. A. Hollingsworth, C. A. Leatherdale, H. J. Eisler, M. G. Bawendi, *Science (Washington, D. C.)* **2000**, 290, 314.
- [49] V. L. Colvin, M. C. Schlamp, A. P. Alivisatos, *Nature (London)* **1994**, 370, 354.
- [50] L. B. Cushing, L. V. Kolesnichenko, J. C. O'Connor, *Chemical reviews* **2004**, 104, 3893.
- [51] D. Crouch, S. Norager, P. O'Brien, J.-H. Park, N. Pickett, *Philosophical Transactions of the Royal Society of London, Series A: Mathematical, Physical and Engineering Sciences* **2003**, 361, 297.
- [52] J. A. Dahl, B. L. Maddux, J. E. Hutchison, *Chemical reviews* **2007**, 107, 2228.

- [53] P. C. Sercel, W. A. Saunders, H. A. Atwater, K. J. Vahala, R. C. Flagan, *Applied Physics Letters* **1992**, *61*, 696.
- [54] A. Henglein, *Chemical Reviews (Washington, DC, United States)* **1989**, *89*, 1861.
- [55] L. Spanhel, H. Weller, A. Henglein, *Journal of the American Chemical Society* **1987**, *109*, 6632.
- [56] T. Cassagneau, G. B. Hix, D. J. Jones, P. Maireles-Torres, M. Rhomari, J. Roziere, *Journal of Materials Chemistry* **1994**, *4*, 189.
- [57] K. M. Choi, K. J. Shea, *Journal of Physical Chemistry* **1994**, *98*, 3207.
- [58] K. M. Choi, K. J. Shea, *Journal of the American Chemical Society* **1994**, *116*, 9052.
- [59] H. J. Watzke, J. H. G. Fendler, *Journal of Physical Chemistry* **1987**, *91*, 854.
- [60] Y. Wang, N. Herron, *Journal of Physical Chemistry* **1987**, *91*, 257.
- [61] T. Abe, Y. Tachibana, T. Uematsu, M. Iwamoto, *Journal of the Chemical Society, Chemical Communications (Cambridge, United Kingdom)* **1995**, 1617.
- [62] C. B. Murray, D. J. Norris, M. G. Bawendi, *Journal of the American Chemical Society* **1993**, *115*, 8706.
- [63] Z. A. Peng, X. Peng, *Journal of the American Chemical Society* **2001**, *123*, 183.
- [64] J. G. Brennan., T. Siegrist., P. J. Carroll, S. M. Stuczynski., L. E. Brus, M. L. Steigerwald, *Journal of the American Chemical Society* **1989**, *111*, 4141.
- [65] M. A. Malik, P. O'Brien, *Chemistry of Materials* **1991**, *3*, 999.
- [66] B. Ludolph, M. A. Malik, P. O'Brien, N. Revaprasadu, *Chemical Communications (Cambridge, United Kingdom)* **1998**, 1849.
- [67] T. Trindade, P. O'Brien, X.-m. Zhang, *Chemistry of Materials* **1997**, *9*, 523.
- [68] M. A. Malik, N. Revaprasadu, P. O'Brien, *Chemistry of Materials* **2001**, *13*, 913.
- [69] M. A. Malik, P. O'Brien, N. Revaprasadu, *Journal of Materials Chemistry* **2001**, *11*, 2382.
- [70] M. Lazell, P. O'Brien, *Chemical Communications (Cambridge, United Kingdom)* **1999**, 2041.
- [71] A. A. Memon, M. Afzaal, M. A. Malik, C. Q. Nguyen, P. O'Brien, J. Raftery, *Dalton Transactions* **2006**, 4499.
- [72] M. Lazell, S. J. Norager, P. O'Brien, N. Revaprasadu, *Materials Science & Engineering, C: Biomimetic and Supramolecular Systems* **2001**, *C16*, 129.
- [73] M. Chunggaze, M. A. Malik, P. O'Brien, *Journal of Materials Chemistry* **1999**, *9*, 2433.
- [74] P. S. Nair, T. Radhakrishnan, N. Revaprasadu, P. O'Brien, *Materials Science and Technology* **2005**, *21*, 237.
- [75] P. S. Nair, T. Radhakrishnan, N. Revaprasadu, G. Kolawole, P. O'Brien, *Journal of Materials Chemistry* **2002**, *12*, 2722.
- [76] Y. Li, X. Li, C. Yang, Y. Li, *Journal of Materials Chemistry* **2003**, *13*, 2641.
- [77] M. J. Moloto, N. Revaprasadu, P. O'Brien, M. A. Malik, *Journal of Materials Science: Materials in Electronics* **2004**, *15*, 313.
- [78] M. J. Moloto, M. A. Malik, P. O'Brien, M. Motevalli, G. A. Kolawole, *Polyhedron* **2003**, *22*, 595.
- [79] P. S. Nair, T. Radhakrishnan, N. Revaprasadu, G. A. Kolawole, P. O'Brien, *Chemical Communications (United Kingdom)* **2002**, 564.
- [80] S.-M. Lee, Y. W. Jun, S.N. Cho, J. Cheon, *Journal of the American Chemical Society* **2002**, *124*, 11244.
- [81] N. Revaprasadu, M. A. Malik, J. Carstens, P. O'Brien, *Journal of Materials Chemistry* **1999**, *9*, 2885.
- [82] M. A. Malik, P. O'Brien, N. Revaprasadu, *Journal of Materials Chemistry* **2002**, *12*, 92.
- [83] N. Pradhan, B. Katz, S. Efrima, *Journal of Physical Chemistry B* **2003**, *107*, 13843.
- [84] P. S. Nair, T. Radhakrishnan, N. Revaprasadu, G. A. Kolawole, P. O'Brien, *Polyhedron* **2003**, *22*, 3129.
- [85] P. S. Nair, N. Revaprasadu, T. Radhakrishnan, G. A. Kolawole, *Journal of Materials Chemistry* **2001**, *11*, 1555.
- [86] P. S. Nair, M. M. Chili, T. Radhakrishnan, N. Revaprasadu, P. Christian, P. O'Brien, *South African Journal of Science* **2005**, *101*, 466.
- [87] Y. Hasegawa, M. Afzaal, P. O'Brien, Y. Wada, S. Yanagida, *Chemical Communications (Cambridge, United Kingdom)* **2005**, 242.
- [88] M. T. Ng, C. Boothroyd, J. J. Vittal, *Chemical Communications (Cambridge, United Kingdom)* **2005**, 3820.
- [89] G. Kedarnath, L. B. Kumbhare, V. K. Jain, P. P. Phadnis, M. Nethaji, *Dalton Transactions* **2006**, 2714.
- [90] S. L. Cumberland, K. M. Hanif, A. Javier, G. A. Khitrov, G. F. Strouse, S. M. Woessner, C. S. Yun, *Chemistry of Materials* **2002**, *14*, 1576.
- [91] Y. Li, M. Afzaal, P. O'Brien, *Journal of Materials Chemistry* **2006**, *16*, 2175.
- [92] I. B. Douglass, *Journal of the American Chemical Society* **1937**, *59*, 740.
- [93] L. Beyer, R. Kirmse, E. Hoyer, *Zeitschrift fuer Chemie* **1975**, *15*, 197.
- [94] R. Kirmse, L. Beyer, E. Hoyer, *Zeitschrift fuer Chemie* **1975**, *15*, 454.
- [95] L. Beyer, S. Behrendt, E. Kleinpeter, R. Borsdorf, E. Hoyer, *Zeitschrift fuer Anorganische und Allgemeine Chemie* **1977**, *437*, 282.
- [96] R. Kirmse, L. Beyer, E. Hoyer, *Chemical Physics Letters* **1977**, *49*, 544.

- [97] Y. V. Salyn, E. K. Zumadilov, V. I. Nefedov, R. Scheibe, G. Leonhardt, L. Beyer, E. Hoyer, *Zeitschrift fuer Anorganische und Allgemeine Chemie* **1977**, 432, 275.
- [98] L. Beyer, R. Herzsuh, F. Dietze, F. Hoepfner, E. Hoyer, *Zeitschrift fuer Anorganische und Allgemeine Chemie* **1979**, 458, 33.
- [99] J. Stach, R. Herzsuh, R. Kirmse, L. Beyer, J. Hartung, *Zeitschrift fuer Anorganische und Allgemeine Chemie* **1984**, 514, 223.
- [100] W. Bensch, M. Schuster, *Zeitschrift fuer Anorganische und Allgemeine Chemie* **1993**, 619, 786.
- [101] W. Bensch, M. Schuster, *Zeitschrift fuer Anorganische und Allgemeine Chemie* **1993**, 619, 791.
- [102] W. Bensch, M. Schuster, *Zeitschrift fuer Anorganische und Allgemeine Chemie* **1993**, 619, 1689.
- [103] W. Bensch, M. Schuster, *Zeitschrift fuer Anorganische und Allgemeine Chemie* **1994**, 620, 1479.
- [104] W. Bensch, M. Schuster, *Zeitschrift fuer Anorganische und Allgemeine Chemie* **1994**, 620, 177.
- [105] M. Schuster, W. Bensch, *Zeitschrift fuer Naturforschung, B: Chemical Sciences* **1994**, 49, 1615.
- [106] M. Schuster, W. Bensch, *Zeitschrift fuer Anorganische und Allgemeine Chemie* **1994**, 620, 737.
- [107] M. Kampf, R. Richter, L. Hennig, A. Eidner, J. Baldamus, R. Kirmse, *Zeitschrift fuer Anorganische und Allgemeine Chemie* **2004**, 630, 2677.
- [108] M. Kampf, R. Richter, J. Griebel, A. Weller, R. Kirmse, *Zeitschrift fuer Anorganische und Allgemeine Chemie* **2005**, 631, 698.
- [109] E. Kleinpeter, L. Beyer, *Journal fuer Praktische Chemie (Leipzig)* **1975**, 317, 938.
- [110] E. Kleinpeter, S. Behrendt, L. Beyer, *Zeitschrift fuer Anorganische und Allgemeine Chemie* **1982**, 495, 105.
- [111] E. Kleinpeter, S. Behrendt, L. Beyer, W. Dietzsch, R. Borsdorf, *Journal fuer Praktische Chemie (Leipzig)* **1982**, 324, 29.
- [112] F. Dietze, J. Lerchner, S. Schmidt, L. Beyer, R. Koehler, *Zeitschrift fuer Anorganische und Allgemeine Chemie* **1991**, 600, 37.
- [113] M. Schuster, K. H. Koenig, *Fresenius' Zeitschrift fuer Analytische Chemie* **1987**, 327, 102.
- [114] M. Schuster, K. H. Koenig, *Fresenius' Zeitschrift fuer Analytische Chemie* **1988**, 331, 383.
- [115] M. Koketsu, Y. Yamamura, H. Aoki, H. Ishihara, *Phosphorus, Sulfur and Silicon and the Related Elements* **2006**, 181, 2699.
- [116] R. Kohler, R. Kirmse, R. Richter, J. Sieler, E. Hoyer, L. Beyer, *Zeitschrift fuer Anorganische und Allgemeine Chemie* **1986**, 537, 133.
- [117] O. Hallale, S. A. Bourne, K. R. Koch, *CrystEngComm* **2005**, 7, 161.
- [118] I. B. Douglass, F. B. Dains, *Journal of the American Chemical Society* **1934**, 56, 1408.
- [119] J. Stach, R. Kirmse, A. Heinrich, W. Dietzsch, J. Hartung, L. Beyer, *Zeitschrift fuer Chemie* **1983**, 23, 453.
- [120] L. Beyer, E. Hoyer, H. Hennig, R. Kirmse, H. Hartmann, J. Liebscher, *Journal fuer Praktische Chemie (Leipzig)* **1975**, 317, 829.
- [121] R. Richter, F. Dietze, S. Schmidt, E. Hoyer, W. Poll, D. Mootz, *Zeitschrift fuer Anorganische und Allgemeine Chemie* **1997**, 623, 135.
- [122] R. Richter, J. Sieler, L. Beyer, O. Lindqvist, L. Anderson, *Zeitschrift fuer Anorganische und Allgemeine Chemie* **1985**, 522, 171.
- [123] W. Bensch, M. Schuster, *Zeitschrift fuer Anorganische und Allgemeine Chemie* **1992**, 611, 95.
- [124] J. Sieler, R. Richter, E. Hoyer, L. Beyer, R. Koehler, *Zeitschrift fuer Anorganische und Allgemeine Chemie* **1991**, 603, 25.
- [125] M. Dominguez, E. Antico, L. Beyer, A. Aguirre, S. Garcia-Granda, V. Salvado, *Polyhedron* **2002**, 21, 1429.
- [126] C. Sacht, M. S. Datt, S. Otto, A. Roodt, *Dalton Transactions* **2000**, 727.
- [127] K. R. Koch, *Coordination Chemistry Reviews* **2001**, 216-217, 473.
- [128] T. J. Egan, K. R. Koch, P. L. Swan, C. Clarkson, D. A. Van Schalkwyk, P. J. Smith, *Journal of Medicinal Chemistry* **2004**, 47, 2926.
- [129] Y.-S. Wu, R. Koch Klaus, R. Abratt Valerie, H. Klump Horst, *Archives of biochemistry and biophysics* **2005**, 440, 28.
- [130] W. Hernandez, E. Spodine, J. C. Munoz, L. Beyer, U. Schroeder, J. Ferreira, M. Pavani, *Bioinorganic Chemistry and Applications* **2003**, 1, 271.
- [131] A. Rodger, K. K. Patel, K. J. Sanders, M. Datt, C. Sacht, M. J. Hannon, *Journal of the Chemical Society, Dalton Transactions* **2002**, 3656.
- [132] Z. Weiqun, Y. Wen, L. Xie, X. Cheng, *Journal of Inorganic Biochemistry* **2005**, 99, 1314.
- [133] R. Del Campo, J. J. Criado, R. Gheorghe, F. J. Gonzalez, M. R. Hermosa, F. Sanz, J. L. Manzano, E. Monte, E. Rodriguez-Fernandez, *Journal of Inorganic Biochemistry* **2004**, 98, 1307.
- [134] W. Hernandez, E. Spodine, L. Beyer, U. Schroeder, R. Richter, J. Ferreira, M. Pavani, *Bioinorganic Chemistry and Applications* **2005**, 3, 299.
- [135] K. H. Koenig, M. Schuster, B. Steinbrech, G. Schneeweis, R. Schlodder, *Fresenius' Zeitschrift fuer Analytische Chemie* **1985**, 321, 457.

- [136] M. Schuster, *Fresenius' Journal of Analytical Chemistry* **1992**, 342, 791.
- [137] A. N. Mautjana, J. D. S. Miller, A. Gie, S. A. Bourne, K. R. Koch, *Dalton Transactions* **2003**, 1952.
- [138] K. R. Koch, C. Sacht, S. Bourne, *Inorganica Chimica Acta* **1995**, 232, 109.
- [139] J. Bricks, K. Rurack, R. Radeglia, G. Reck, B. Schulz, H. Sonnenschein, U. Resch-Genger, *Journal of the Chemical Society Perkin Transactions* **2000**, 2, 1209.
- [140] M. Schuster, E. Unterreitmaier, *Fresenius' Journal of Analytical Chemistry* **1993**, 346, 630.
- [141] E. Unterraitmaier, M. Schuster, *Analitica Chimica Acta* **1995**, 309, 339.
- [142] A. N. Westra, C. Esterhuysen, K. R. Koch, *Acta Crystallographica, Section C: Crystal Structure Communications* **2004**, C60, m395.
- [143] S. Bourne, K. R. Koch, *Dalton Transactions* **1993**, 2071.
- [144] K. R. Koch, Y. Wang, A. Coetzee, *Journal of the Chemical Society, Dalton Transactions: Inorganic Chemistry* **1999**, 1013.
- [145] K. R. Koch, S. Bourne, *Journal of Molecular Structure* **1998**, 441, 11.
- [146] K. R. Koch, J. du Toit, M. R. Caira, C. Sacht, *Journal of the Chemical Society, Dalton Transactions: Inorganic Chemistry (1972-1999)* **1994**, 785.
- [147] D. Hanekom, J. M. McKenzie, N. M. Derix, K. R. Koch, *Chemical Communications (Cambridge, United Kingdom)* **2005**, 767.
- [148] J. Goerdeler, K. Stadelbauer, *Chemische Berichte* **1965**, 98, 1556.
- [149] R. Koehler, R. Kirmse, R. Richter, J. Sieler, E. Hoyer, L. Beyer, *Zeitschrift fuer Anorganische und Allgemeine Chemie* **1986**, 537, 133.
- [150] K. R. Koch, S. A. Bourne, A. Coetzee, J. Miller, *Journal of the Chemical Society, Dalton Transactions: Inorganic Chemistry* **1999**, 3157.
- [151] K. R. Koch, O. Hallale, S. A. Bourne, J. Miller, J. Bacsá, *Journal of Molecular Structure* **2001**, 561, 185.
- [152] O. Hallale, S. A. Bourne, K. R. Koch, *New Journal of Chemistry* **2005**, 29, 1416.
- [153] N. Westra Arjan, A. Bourne Susan, R. Koch Klaus, *Dalton Trans* **2005**, 2916.
- [154] U. Schroder, L. Beyer, J. Sieler, *Inorganic Chemistry Communications* **2000**, 3, 630.
- [155] K. H. Koenig, M. Kuge, L. Kaul, H. J. Pletsch, *Chemische Berichte* **1987**, 120, 1251.
- [156] S. Stockmann, J. C. Bruce, J. Miller, K. R. Koch, *Acta Crystallographica, Section C* **2008**, C64, o166.
- [157] M. Merdivan, R. S. Aygun, N. Kulcu, *Journal of Thermal Analysis* **1997**, 48, 1423.
- [158] M. Merdivan, F. Karipcin, N. Kulcu, R. S. Aygun, *Journal of Thermal Analysis and Calorimetry* **1999**, 58, 551.
- [159] N. Ozpazan, H. Arslan, T. Ozpazan, N. Ozdes, N. Kulcu, *Thermochimica Acta* **2000**, 343, 127.
- [160] P. S. Nair, G. D. Scholes, *Journal of Materials Chemistry* **2006**, 16, 467.
- [161] L. Manna, E. C. Scher, A. P. Alivisatos, *Journal of the American Chemical Society* **2000**, 122, 12700.
- [162] X. Peng, U. Manna, W. Yang, J. Wickham, E. Scher, A. Kadavanich, A. P. Alivisatos, *Nature (London)* **2000**, 404, 59.
- [163] Z. A. Peng, X. Peng, *Journal of the American Chemical Society* **2001**, 123, 1389.
- [164] Z. A. Peng, X. Peng, *Journal of the American Chemical Society* **2002**, 124, 3343.
- [165] N. Pradhan, S. Efrima, *Journal of the American Chemical Society* **2003**, 125, 2050.

Chapter 2

Synthesis and characterization of *N,N*-dialkyl-*N'*-benzoyl(thio)selenourea ligands and their complexation with selected transition metal ions.*

The synthesis and structural characterization of several *N,N*-dialkyl-*N'*-benzoylselenourea and *N,N*-dialkyl-*N'*-benzoylthiourea ligands is reported. The attempted synthesis of *N,N*-dicyclohexyl-*N'*-benzoylselenourea resulted in the formation of a 1,3,5 oxaselenazine derivative and crystallographically characterized dicyclohexylaminobenzoate. The coordination of *N,N*-dialkyl-*N'*-benzoylselenourea ligands to several transition metal ions is described as well as that of their sulfur analogues. The structural characterization of several Pd(II) complexes is detailed in addition to that of a unique (*N,N*-diphenyl-*N'*-benzoylselenoureato)Cd(II) complex. The structural characterization of the metallamacrocyclic 3,3,3',3'-tetra(*n*-butyl)-1,1'-terephthaloylbis(thioureato)Pd(II) is also described. Multinuclear NMR spectroscopy of selected ligands and their metal complexes allows the determination of $^1J(^{13}\text{C}-^{77}\text{Se})$ coupling constants for a number of metal complexes and the relative metal ion dependant shielding of the ^{77}Se nucleus upon complexation. The NMR active ^{31}P nucleus is used as a probe to illustrate the coordination of *N,N*-diethyl-*N'*-benzoylselenourea to a Pt(II) centre, despite the inability to isolate a bis chelate of this type. Thermal decomposition of *N,N*-dialkyl-*N'*-benzoylselenourea metal complexes and their sulfur analogues is reported, where the residual constitution can be used as an indication of nanoparticle composition.

* Sections of this chapter are based on the papers:

J. C. Bruce, K. R. Koch, *Acta Cryst C*, 2008, C64, m1 – m4.

J. C. Bruce, N. Revaprasadu, K. R. Koch, *New J. Chem.*, 2007, 31 (9), 1647-1653.

2.1 Introduction

As outlined in Chapter 1, several reports on the preparation of quantum dots using single source precursors have indicated that precursor alkyl chain length may effect the resultant nanoparticle morphology. We here report the synthesis of *N,N*-dialkyl-*N'*-benzoyl(thio)selenoureas with systematic chain length variations and the preparation and structural characterization of selected metal complexes for use as single source precursors. Whilst alkyl chain length variations are reported for symmetrically substituted *N,N*-dialkyl-*N'*-benzoyl(thio)selenoureas, the preparation of asymmetrically substituted *N,N*-dialkyl-*N'*-benzoyl(thio)selenoureas is also reported, to investigate a possible influence over nanoparticle morphology. In order to simplify the complex preparation, the “solventless” synthesis of *N,N*-dialkyl-*N'*-benzoyl(thio)selenourea metal complexes was briefly investigated. This proved to be very successful for the preparation of *cis*-bis(*N,N*-dialkyl-*N'*-benzoylthioureato)Pd(II) complexes as well as their Cd(II) counterparts, however further work will be required for the fine tuning of suitable conditions for the preparation of *N,N*-dialkyl-*N'*-benzoylselenourea metal complexes, although initial results showed promise. The first structural characterization of a “bipodal” *N,N*-dialkyl-*N'*-benzoylselenourea ligand is reported, as well as that of the related 3,3,3',3'-tetra(*n*-butyl)-1,1'-terephthaloylbis(thioureato)Pd(II) metal complex. However, poor yields and the cost of the metal salt used in synthesis precluded the use of *N,N*-dialkyl-*N'*-benzoyl(thio)selenourea metallamacrocycles as single source precursors.

2.2 Experimental

2.2.1 Synthesis and characterization of *N,N*-dialkyl-*N'*-benzoylselenoureas

N,N-diethyl-*N'*-benzoylselenourea (**HL^{1a}**, **11**), *N,N*-dibutyl-*N'*-benzoylselenourea (**HL^{1b}**, **12**), *N,N*-dihexyl-*N'*-benzoylselenourea (**HL^{1c}**, **13**), *N,N*-dioctyl-*N'*-benzoylselenourea (**HL^{1d}**, **14**), *N*-benzyl-*N*-methyl-*N'*-benzoylselenourea (**HL^{1e}**, **15**), *N,N*-didecyl-*N'*-benzoylselenourea (**HL^{1f}**, **16**), *N,N*-diphenyl-*N'*-benzoylselenourea (**HL^{1g}**, **17**) were synthesized according to the method reported by Douglass for the synthesis of *N,N*-diethyl-*N'*-benzoylselenourea.^[1] In general the *N,N*-dialkyl-*N'*-benzoylselenoureas were found to be less stable and could be isolated in lower yields than the corresponding *N,N*-dialkyl-*N'*-benzoylthioureas. The scale of the reaction was also found to influence the yield of the *N,N*-dialkyl-*N'*-benzoylselenoureas and the best results were obtained using approximately 26 mmol reactions. The bipodal ligands 3,3,3',3'-tetraethyl-1,1'-isophthaloylbis(selenourea) (**H₂L^{m1a}**, **1111**) and 3,3,3',3'-tetra(*n*-butyl)-1,1'-isophthaloylbis(selenourea) (**H₂L^{m1b}**, **1212**) were synthesized according to the method described by Kohler *et. al.*^[72]

***N,N*-diethyl-*N'*-benzoylselenourea, HL^{1a}, 11:** Yield (39.0 %). mp 111.1-112.5 °C. Found: C, 51.0; H, 5.7; N, 9.9. C₁₂H₁₆N₂OSe requires C, 50.9; H, 5.7; N, 9.9 %. δ_H (400 MHz; CDCl₃): 1.30 (t, 3H, ³J_{HH} = 7.2, H10/H12), 1.40 (t, 3H, ³J_{HH} = 7.0, H10/H12), 3.59 (q, 2H, ³J_{HH} = 7.2, H9/H11), 4.13 (q, 2H, ³J_{HH} = 7.0, H9/H11), 7.46 (multiplet, 2H, H3, H5), 7.57 (t, 1H, ³J_{HH} = 7.4, H4), 7.83 (d, 2H, ³J_{HH} = 7.6, H2, H6), 8.59 (br s, 1H, N-H). δ_C (101 MHz; CDCl₃): 11.7, 12.8 (C10, C12), 48.4, 51.2 (C9, C11), 127.8 (C3, C5), 128.8 (C2, C6), 132.6 (C1),

132.9 (C4), 162.2 (C7), 180.4 (C8), $^1J(^{13}\text{C}-^{77}\text{Se}) = 220.3$. δ_{Se} (76 MHz; CDCl_3): 483.1. TLC (silica gel, CHCl_3): $R_f = 0.58$

***N,N*-dibutyl-*N'*-benzoylselenourea, HL^{1b}, 12:** Yield (57.5 %). mp 119.5-121.0 °C. Found: C, 56.6; H, 7.1; N, 8.2. $\text{C}_{16}\text{H}_{22}\text{N}_2\text{OSe}$ requires C, 56.6; H, 7.1; N, 8.3 %. δ_{H} (400 MHz; CDCl_3): 0.90 (t, 3H, $^3J_{\text{HH}} = 7.4$, H12/H16), 0.99 (t, 3H, $^3J_{\text{HH}} = 7.4$, H12/H16), 1.28 (m, 2H, $^3J_{\text{HH}} = 7.5$, H11/H15), 1.45 (m, 2H, $^3J_{\text{HH}} = 7.5$, H11/H15), 1.67 (q, 2H, $^3J_{\text{HH}} = 7.4$, H10/H14), 1.83 (q, 2H, $^3J_{\text{HH}} = 7.4$, H10/H14), 3.55 (t, 2H, $^3J_{\text{HH}} = 7.4$, H9/H13), 4.08 (t, 2H, $^3J_{\text{HH}} = 7.6$, H9/H13), 7.46 (t, 2H, H3, H5), 7.57 (t, 1H, H4), 7.83 (d, 2H, H2, H6), 8.54 (br s, 1H, N-H). δ_{C} (101 MHz, CDCl_3): 13.6, 13.8 (C12, C16), 19.9, 20.0 (C15, C11), 28.7, 29.7 (C14, C10), 53.7, 56.4 (C13, C9), 127.8 (C3, C5), 128.8 (C2, C6), 132.5 (C1), 133.0 (C4), 162.1 (C7), 180.9 (C8), $^1J(^{77}\text{Se}-^{13}\text{C}) = 222.14$. δ_{Se} (76 MHz; CDCl_3): 482.5. TLC (silica gel, CHCl_3): $R_f = 0.75$.

***N,N*-dihexyl-*N'*-benzoylselenourea, HL^{1c}, 13:** Yield (51.7 %). mp 65.0-66.8 °C. Found: C, 59.9; H, 8.1; N, 7.3. $\text{C}_{20}\text{H}_{32}\text{N}_2\text{OSe}$ requires C, 60.7; H, 8.2; N, 7.1 %. δ_{H} (400 MHz; CDCl_3): 0.83 (t, 3H, $^3J_{\text{HH}} = 6.8$, H20/H14), 0.89 (t, 3H, $^3J_{\text{HH}} = 6.2$, H20/H14), 1.30 (unres m, 12H, H11-H13, H17-H19), 1.66 (q, 2H, $^3J_{\text{HH}} = 7.1$, H10/H16), 1.83 (q, 2H, $^3J_{\text{HH}} = 7.5$, H10/H16), 3.52 (t, 2H, $^3J_{\text{HH}} = 6.3$, H9/H15), 4.04 (t, 2H, $^3J_{\text{HH}} = 7.7$, H9/H15), 7.45 (t, 2H, H3, H5), 7.56 (t, 1H, H4), 7.83 (d, 2H, H2, H6), 8.64 (br s, 1H, N-H). δ_{C} (101 MHz, CDCl_3): 13.8, 13.9 (C14, C20), 22.3, 22.4 (C13, C19), 26.2, 26.3 (C11, C17), 26.5, 27.5 (C10, C16), 31.2, 31.3 (C12, C18), 53.9, 56.6 (C9, C15), 127.8 (C3, C5), 128.7 (C2, C6), 132.4 (C1), 132.8 (C4), 162.0 (C7), 180.8 (C8), $^1J(^{77}\text{Se}-^{13}\text{C}) = 221.59$. δ_{Se} (76 MHz; CDCl_3): 482.0. TLC (silica gel, CHCl_3): $R_f = 0.85$.

***N,N*-dioctyl-*N'*-benzoylselenourea, HL^{1d}, 14:** Yield (70.0 %). mp 64.3-65.8 °C. Found: C, 63.0; H, 8.6; N, 5.7. $\text{C}_{24}\text{H}_{40}\text{N}_2\text{OSe}$ requires C, 63.8; H, 8.9; N, 6.2 %. δ_{H} (400 MHz; CDCl_3): 0.87 (unres m, 6H, H16 and H24), 1.25 (unres m, 20H, H11-H15, H19-H23), 1.68 (q, 2H, $^3J_{\text{HH}} = 7.3$, H10/H18), 1.85 (q, 2H, $^3J_{\text{HH}} = 7.5$, H10/H18), 3.54 (unres t, 2H, H9/H17), 4.06 (t, 2H, $^3J_{\text{HH}} = 7.6$, H9/H17), 7.48 (t, 2H, H3, H5), 7.58 (t, 1H, H4), 7.84 (d, 2H, H2, H6), 8.52 (br s, 1H, N-H). δ_{C} (101 MHz, CDCl_3): 14.0, 14.1 (C16, C24), 22.5, 22.6 (C15, C23), 26.6 (C10/C18), 26.7, 26.8 (C11, C17), 27.7 (C10/C18), 29.0, 29.1 (C13, C21), 29.2, 29.2 (C12, C20), 31.7, 31.8 (C14, C22), 54.1, 56.8 (C9, C17), 127.9 (C3, C5), 128.9 (C2, C6), 132.6 (C1), 133.0 (C4), 162.0 (C7), 180.8 (C8). $^1J(^{77}\text{Se}-^{13}\text{C}) = 217.88$. δ_{Se} (76 MHz; CDCl_3): 480.8. TLC (silica gel, CHCl_3): $R_f = 0.85$.

***N*-benzyl-*N*-methyl-*N'*-benzoylselenourea, HL^{1e}, 15:** Yield (19.0 %). mp 147.4-148.6 °C. Found: C, 56.7; H, 4.6; N, 8.7. $\text{C}_{16}\text{H}_{16}\text{N}_2\text{OSe}$ requires C, 58.0; H, 4.9; N, 8.5 %. δ_{H} (400 MHz; CDCl_3): 3.10 (s, 3H, H9(Z)), 3.38 (s, 3H, H9(E)), 4.76 (s, 2H, H10(E)), 5.39 (s, 2H, H10(Z)), 7.2 – 7.88 (10H, m, H2-H6, H12-H16 (E and Z)), 8.7 (s, 1H, N-H(Z)), 8.8 (s, 1H, N-H(E)). δ_{C} (101 MHz, CDCl_3): 41.0 (C9(Z)), 45.4 (C9(E)), 60.0 (C10(E)), 63.0 (C10(Z)), 127.8 – 134.3 (C1-C6 (E and Z), C11-C16 (E and Z)), 162.1 (C7(Z)), 162.3 (C7(E)), 182.0 (C8(E)), 182.9 (C8(Z)). $^1J(^{77}\text{Se}-^{13}\text{C}) = 221.66$ (Z isomer), 220.55 (E isomer). δ_{Se} (76 MHz; CDCl_3): 465.17 (Z), 513.13 (E). TLC (silica gel, CHCl_3): $R_f = 0.50$.

***N,N*-didecyl-*N'*-benzoylselenourea, HL^{1f}, 16:** Yield (53.9 %). mp 65.6 – 67.2 °C. Found: C, 66.2; H, 9.2; N, 5.1. $\text{C}_{28}\text{H}_{48}\text{N}_2\text{OSe}$ requires C, 66.3; H, 9.5; N, 5.5 %. δ_{H} (400 MHz; CDCl_3): 0.86 (unres m, 6H, H18 and H28), 1.23 (unres m, 28H, H11-H17, H21-H27), 1.67 (q, 2H, $^3J_{\text{HH}} = 7.0$, H10/H20), 1.84 (q, 2H, $^3J_{\text{HH}} = 7.1$, H10/H20), 3.52 (t, 2H, $^3J_{\text{HH}} = 6.7$, H9/H19), 4.06 (t, 2H, $^3J_{\text{HH}} = 7.5$, H9/H19), 7.47 (t, 2H, H3, H5), 7.57 (t, 1H, H4), 7.83 (d, 2H, H2, H6), 8.57 (br s, 1H, N-H). δ_{C} (101 MHz, CDCl_3): 14.0, 14.1 (C18, C28), 22.5, 22.6 (C17, C27), 26.6 (C10/C20), 26.7, 26.8 (C11, C21), 27.6 (C10/C20), 29.0, 29.1, 29.2, 29.2, 29.3, 29.4, 29.4, 29.5 (C12-15 and C22-C25), 31.7,

31.8 (C16, C26), 54.0, 56.7 (C9, C19), 127.8 (C3, C5), 128.8 (C2, C6), 132.5 (C1), 132.9 (C4), 162.0 (C7), 180.8 (C8). $^1J(^{77}\text{Se}-^{13}\text{C}) = 220.12$. δ_{Se} (76 MHz; CDCl_3): 484.1. TLC (silica gel, CHCl_3): $R_f = 0.87$.

N,N*-diphenyl-*N'*-benzoylselenourea, HL^{1g} , **17*: Yield (36.0 %). mp 133.7 – 134.1 °C. Found: C, 63.1; H, 4.2; N, 7.3. $\text{C}_{20}\text{H}_{16}\text{N}_2\text{OSe}$ requires C, 63.4; H, 4.2; N, 7.4 %. δ_{H} (400 MHz; CDCl_3): 7.39 (m, 12H), 7.51 (m, 1H, H4/H13/H18), 7.64 (m, 2H, H4/H13/H18), 9.07 (br s, 1H, *N-H*). δ_{C} (101 MHz, CDCl_3): 127.6, 127.7, 128.7, 129.3, 129.6, 132.3, 132.9 (C1-C6, C9-C14, C15-C20), 160.7 (C7), 185.2 (C8). $^1J(^{77}\text{Se}-^{13}\text{C}) = 217.79$. δ_{Se} (76 MHz; CDCl_3): 659.9.

3,3,3',3'-tetraethyl-1,1'-isophthaloylbis(selenourea), H_2L^{m1a} , **1111**: Yield (22.0 %). mp 142.0-143.6 °C. Found: C, 44.4, H, 5.3, N, 11.4. $\text{C}_{18}\text{H}_{26}\text{N}_4\text{O}_2\text{Se}_2$ requires C, 44.3, H, 5.4, N, 11.5 %. δ_{H} (400 MHz; CDCl_3): δ 1.31 (t, 6H, $^3J_{\text{HH}} = 7.2$, H34, H36/H54, H56), 1.39 (t, 6H, $^3J_{\text{HH}} = 7.2$, H34, H36/H54, H56), 3.60 (q, 4H, $^3J_{\text{HH}} = 7.1$, H33, H35/ H53, H55), 4.12 (q, 4H, $^3J_{\text{HH}} = 7.1$, H33, H35/ H53, H55), 7.54 (t, 1H, $^3J_{\text{HH}} = 7.8$, H1), 8.00 (d, 2H, $^3J_{\text{HH}} = 7.0$, H2, H6), 8.34 (s, 1H, H4), 9.2-9.3 (br, 2H, *N-H*). δ_{C} (101 MHz; CDCl_3): 11.6 (C34, C36/ C54, C56), 12.9 (C34, C36/ C54, C56), 48.1 (C33, C35/ C53, C55), 50.9 (C33, C35/ C53, C55), 127.0 (C1), 129.4 (C4), 132.6 (C2, C6), 132.9 (C3, C5), 161.9 (C51, C31), 180.4 (C32, C52). $^1J(^{77}\text{Se}-^{13}\text{C}) = 220.15$, δ_{Se} (76 MHz; CDCl_3): 495.06

3,3,3',3'-tetra(*n*-butyl)-1,1'-isophthaloylbis(selenourea), H_2L^{m1b} , **1212**: Yield (11 %). mp 134.0-136.3 °C. Found: C, 52.4; H, 7.15; N, 8.9. $\text{C}_{26}\text{H}_{42}\text{N}_4\text{O}_2\text{Se}_2$ requires C, 52.0; H, 7.05; N, 9.3 %. δ_{H} (400 MHz; CDCl_3): δ 0.89 (t, 6H, $^3J_{\text{HH}} = 7.3$, H36, H310/H66, H610), 0.98 (t, 6H, $^3J_{\text{HH}} = 7.4$, H36, H310/H66, H610), 1.21 (s, 4H, $^3J_{\text{HH}} = 7.5$, H35, H39/ H65, H69), 1.44 (s, 4H, $^3J_{\text{HH}} = 7.5$, H35, H39/ H65, H69), 1.67 (q, 4H, $^3J_{\text{HH}} = 7.6$, H34, H38, H64, H68), 1.84 (q, 4H, $^3J_{\text{HH}} = 7.4$, H34, H38, H64, H68), 3.51 (t, 4H, $^3J_{\text{HH}} = 7.2$, H33, H37, H63, H67), 4.07 (t, 4H, $^3J_{\text{HH}} = 7.5$, H33, H37, H63, H67), 7.57 (t, 1H, H1), 8.01 (d, 2H, H2, H6), 8.29 (s, 1H, H4), 9.14 (br s, 2H, *N-H*). δ_{C} (101 MHz; CDCl_3): 13.6 (C36, C310/ C66, C610), 13.8 (C36, C310/ C66, C610), 19.9 (C35, C39/C65, C69), 20.0 (C35, C39/C65, C69), 28.5 (C34, C38/C64, C68), 29.7 (C34, C38/C64, C68), 53.7 (C33, C37/C63, C67), 56.3 (C33, C37/C63, C67), 126.9 (C1), 129.6 (C4), 132.4 (C2, C6), 133.0 (C3, C5), 161.2 (C31, C61), 180.6 (C32, C62).

2.2.2 Synthesis and characterization of *N,N*-dialkyl-*N'*-benzoylthioureas

N,N-diethyl-*N'*-benzoylthiourea (HL^{2a} , **21**), *N,N*-dibutyl-*N'*-benzoylthiourea (HL^{2b} , **22**), *N,N*-dihexyl-*N'*-benzoylthiourea (HL^{2c} , **23**), *N,N*-dioctyl-*N'*-benzoylthiourea (HL^{2d} , **24**), *N*-benzyl-*N*-methyl-*N'*-benzoylthiourea (HL^{2e} , **25**), *N*-morpholine-*N'*-benzoylthiourea (HL^{2f} , **26**) were synthesized and characterized according to the method described by Douglass and Dains.^[27] The bipodal ligand, 3,3,3',3'-tetra(*n*-butyl)-1,1'-terephthaloylbis(thiourea) (H_2L^{p2b} , **2222**) was also synthesized using this method.

N,N*-diethyl-*N'*-benzoylthiourea, HL^{2a} , **21*: Yield (87.0 %). mp 96.2 – 97.8 °C Found: C, 61.8; H, 5.9; N, 11.4. $\text{C}_{12}\text{H}_{16}\text{N}_2\text{OS}$ requires C, 61.1; H, 6.8; N, 11.9 %. δ_{H} (400 MHz; CDCl_3): 1.28 (unres t, 3H, H10/H12), 1.35 (unres t, 3H, H10/H12), 3.59 (unres q, 2H, H9/H11), 4.02 (unres q, 2H, H9/H11), 7.45 (multiplet, 2H, H3, H5), 7.56 (t, 1H, $^3J_{\text{HH}} = 7.5$ and $^4J_{\text{HH}} = 1.3$, H4), 7.82 (d, 2H, $^3J_{\text{HH}} = 7.5$, H2, H6), 8.40 (br s, 1H, *N-H*). δ_{C} (101 MHz; CDCl_3): 11.4, 13.1 (C10, C12), 47.7, 47.9 (C9, C11), 127.8 (C3, C5), 128.8 (C2, C6), 132.6 (C1), 132.8 (C4), 163.7 (C7) 179.2 (C8). TLC (silica gel, CHCl_3): $R_f = 0.53$.

***N,N*-dibutyl-*N'*-benzoylthiourea, HL^{2b}, 22:** Yield (83.1 %). mp 92.6-94.3 °C. Found: C, 65.7; H, 8.3; N, 8.6; S, 10.7. C₁₆H₂₂N₂OS requires C, 65.8; H, 8.2; N, 9.6; S, 11.0 %. δ_{H} (400 MHz; CDCl₃): 0.90 (t, 3H, $^3J_{\text{HH}} = 7.3$, H12/H16), 0.98 (t, 3H, $^3J_{\text{HH}} = 7.3$, H12/H16), 1.28 (m, 2H, $^3J_{\text{HH}} = 7.5$, H11/H15), 1.44 (m, 2H, $^3J_{\text{HH}} = 7.5$, H11/H15), 1.65 (q, 2H, $^3J_{\text{HH}} = 7.3$, H10/H14), 1.79 (q, 2H, $^3J_{\text{HH}} = 7.5$, H10/H14), 3.55 (t, 2H, $^3J_{\text{HH}} = 7.1$, H9/H13), 3.96 (t, 2H, $^3J_{\text{HH}} = 7.5$, H9/H13), 7.45 (t, 2H, H3, H5), 7.56 (t, 1H, H4), 7.83 (d, 2H, H2, H6), 8.35 (br s, 1H, *N-H*). δ_{C} (101 MHz, CDCl₃): 13.7, 13.8 (C12, C16), 20.0 (C15, C11), 28.4, 30.1 (C14, C10), 53.0, 53.2 (C13, C9), 127.7 (C3, C5), 128.8 (C2, C6), 132.6 (C1), 132.8 (C4), 163.5 (C7), 179.7 (C8). TLC (silica gel, CHCl₃): R_f = 0.81.

***N,N*-dihexyl-*N'*-benzoylthiourea, HL^{2c}, 23:** Yield (45.0 %). mp 58.9-60.5 °C. Found: C, 68.8; H, 9.5; N, 9.7; S, 8.1 %. C₂₀H₃₂N₂OS requires C, 68.9; H, 9.3; N, 8.0; S, 9.2 %. δ_{H} (400 MHz; CDCl₃): 0.83 (t, 3H, $^3J_{\text{HH}} = 6.0$, H20/H14), 0.89 (t, 3H, $^3J_{\text{HH}} = 6.5$, H20/H14), 1.33 (unres m, 12H, H11-H13, H17-H19), 1.65 (unres q, 2H, H10/H16), 1.79 (q, 2H, $^3J_{\text{HH}} = 7.4$, H10/H16), 3.51 (t, 2H, $^3J_{\text{HH}} = 7.4$, H9/H15), 3.94 (t, 2H, $^3J_{\text{HH}} = 7.6$, H9/H15), 7.44 (t, 2H, H3, H5), 7.53 (t, 1H, H4), 7.81 (d, 2H, H2, H6), 8.46 (br s, 1H, *N-H*). δ_{C} (101 MHz, CDCl₃): 13.8, 13.9 (C14, C20), 22.4, 22.5 (C13, C19), 26.2, (C10/C16), 26.3 (C11, C17), 27.9 (C10/C16), 31.3, 31.4 (C12, C18), 53.2, 53.5 (C9, C15), 127.7 (C3, C5), 128.7 (C2, C6), 132.6 (C1), 132.7 (C4), 163.5 (C7), 179.6 (C8). TLC (silica gel, CHCl₃): R_f = 0.79.

***N,N*-dioctyl-*N'*-benzoylthiourea, HL^{2d}, 24:** Yield 98.0 %. m.p. 54.9 – 56.5 °C. Found: C, 71.2; H, 9.9; N, 6.7; S, 7.9. C₂₄H₄₀N₂OS requires C, 71.3; H, 10.0; N, 6.9; S, 7.9 %. δ_{H} (400 MHz; CDCl₃): 0.87 (unres m, 6H, H16 and H24), 1.25 (unres m, 20H, H11-H15, H19-H23), 1.68 (unres q, 2H, H10/H18), 1.82 (unres q, 2H, H10/H18), 3.53, (t, 2H, $^3J_{\text{HH}} = 7.3$, H9/H17), 3.94 (t, 2H, $^3J_{\text{HH}} = 7.6$, H9/H17), 7.48 (t, 2H, H3, H5), 7.58 (t, 1H, H4), 7.83 (d, 2H, H2, H6), 8.21 (br s, 1H, *N-H*). δ_{C} (101 MHz, CDCl₃): 14.0, 14.1 (C16, C24), 22.5, 22.6 (C15, C23), 26.4 (C10/C18), 26.8 (C11, C17), 28.0 (C10/C18), 29.0, 29.1 (C13, C21), 29.2, 29.3 (C12, C20), 31.7, 31.8 (C14, C22), 53.4, 53.6 (C9, C17), 127.7 (C3, C5), 128.9 (C2, C6), 132.7 (C1), 132.9 (C4), 163.5 (C7), 179.6 (C8). TLC (silica gel, CHCl₃): R_f = 0.89.

***N*-benzyl-*N*-methyl-*N'*-benzoylthiourea, HL^{2e}, 25:** Yield (83.2 %). mp 130.5-132.0 °C. Found: C, 67.6; H, 5.6; N, 9.7; S, 10.9. C₁₆H₁₆N₂OS requires C, 67.6; H, 5.7; N, 9.9; S, 11.3 %. δ_{H} (400 MHz; CDCl₃): 3.15 (s, 3H, H9(Z)), 3.31 (s, 3H, H9(E)), 4.77 (s, 2H, H10(E)), 5.28 (s, 2H, H10(Z)), 7.2 – 7.88 (10H, m, H2-H6, H12-H16 (E and Z)), 8.75 (s, 2H, *N-H*(E and Z)). δ_{C} (101 MHz, CDCl₃): 40.3 (C9(Z)), 42.1 (C9(E)), 59.1 (C10(E)), 59.5 (C10(Z)), 127.9 – 135.1 (C1-C6 (E and Z), C11-C16 (E and Z)), 163.5 (C7(Z)), 163.8 (C7(E)), 180.5 (C8(E)), 181.4 (C8(Z)). TLC (silica gel, CHCl₃): R_f = 0.58.

***N*-morpholine-*N'*-benzoylthiourea, HL^{2f}, 26:** Yield (76.2 %). mp 143.7 – 145 °C. Found: C, 57.4; H, 5.1; N, 10.4; S, 13.1. C₁₂H₁₄N₂O₂S requires C, 57.6; H, 5.6; N, 11.2; S, 12.8 %.(These values have been calculated for morpholine and are correct) δ_{H} (400 MHz; CDCl₃): 3.61 (br s, 2H), 3.78 (br s, 4H), 4.18 (br s, 2H, H9-H12), 7.46 (multiplet, 2H, H3, H5), 7.57 (t, 1H, H4), 7.82 (d, 2H, H2, H6), 8.66 (br s, 1H, *N-H*). δ_{C} (101 MHz; CDCl₃): 51.4, 52.3 (C9, C11), 66.1 (C10, C12), 127.9 (C3, C5), 129.0 (C2, C6), 132.3 (C1), 133.2 (C4), 163.5 (C7) 179.5 (C8).

***N,N*-dicyclohexyl-*N'*-benzoylthiourea, HL^{2g}, 27:** Yield (69.4 %). m.p. 118.6 – 120.0 °C. Found: C, 69.6; H, 7.4; N, 7.7; S, 8.6. C₂₀H₂₈N₂OS requires C, 70.1; H, 7.7; N, 8.2; S, 9.4 %. δ_{H} (400 MHz; CDCl₃): 1.56 – 1.85 (unres m, 22H, H9 - H20), 7.45 (t, 2H, H3, H5), 7.55 (t, 1H, H4), 7.90 (d, 2H, H2, H6). δ_{C} (101 MHz, CDCl₃): 27.0, 27.8, 30.8, 32.7, 63.4, 65.1 (C9-C20), 129.8 (C2, C6), 130.4 (C3, C5), 134.0 (C4), 135.7 (C1), 166.8 (C7), 183.3 (C8).

3,3,3',3'-tetra(*n*-butyl)-1,1'-terephthaloylbis(thiourea), H_2L^{p2b} , **2222: Yield (42.8 %). mp 147.3 – 148.8 °C. Found: C, 61.5; H, 8.4; N, 11.1; S, 12.1. $C_{26}H_{42}N_4O_2S_2$ requires C, 61.7; H, 8.3; N, 11.1; S, 12.7 %. δ_H (400 MHz; $CDCl_3$): δ 0.90 (t, 6H, $^3J_{HH} = 7.3$, H36, H310/H66, H610), 0.98 (t, 6H, $^3J_{HH} = 7.3$, H36, H310/H66, H610), 1.28 (s, 4H, $^3J_{HH} = 7.3$, H35, H39/ H65, H69), 1.43 (s, 4H, $^3J_{HH} = 7.3$, H35, H39/ H65, H69), 1.66 (q, 4H, $^3J_{HH} = 6.9$, H34, H38, H64, H68), 1.79 (q, 4H, $^3J_{HH} = 7.2$, H34, H38, H64, H68), 3.55 (t, 4H, $^3J_{HH} = 7.3$, H33, H37, H63, H67), 3.95 (t, 4H, $^3J_{HH} = 7.5$, H33, H37, H63, H67), 7.93 (s, 4H, H1, H2, H4, H5). δ_C (101 MHz; $CDCl_3$): 13.7 (C36, C310/ C66, C610), 13.8 (C36, C310/ C66, C610), 20.0 (C35, C39, C65, C69), 28.4 (C34, C38/C64, C68), 30.2 (C34, C38/C64, C68), 52.9 (C33, C37/C63, C67), 53.1 (C33, C37/C63, C67), 128.3 (C1, C2, C4, C5), 136.4 (C3, C6), 163.0 (C31, C61), 179.7 (C32, C62).**

2.2.3 Synthesis and characterization of *N,N*-dialkyl-*N'*-benzoylselenourea metal complexes

2.2.3.1 *N,N*-dialkyl-*N'*-benzoylselenourea Cd(II) complexes

The Cd^{II} complexes of HL^{1a} , $[Cd^{II}(L^{1a}-Se,O)_2]$ **111**, HL^{1b} , $[Cd^{II}(L^{1b}-Se,O)_2]$ **121**, HL^{1c} , $[Cd^{II}(L^{1c}-Se,O)_2]$ **131**, HL^{1d} , $[Cd^{II}(L^{1d}-Se,O)_2]$ **141**, HL^{1e} , $[Cd^{II}(L^{1e}-Se,O)_2]$ **151**, HL^{1f} , $[Cd^{II}(L^{1f}-Se,O)_2]$ **161**, HL^{1g} , $[Cd^{II}(L^{1g}-Se,O)_2]$ **171** were synthesized according to the method described by Bensch and Schuster for the synthesis of (*N,N*-diethyl-*N'*-benzoylthiourea)Cd(II), $[Cd^{II}(L^{1a}-Se,O)_2]$.^[10]

On recrystallization from a chloroform, ethanol mixture, **111**, **151** and **171** were isolated as solid, microcrystalline material however the longer alkyl chain derivatives, **121**, **131**, **141** and **161** could be isolated only as oily semi-solid material.

(*N,N*-diethyl-*N'*-benzoylselenourea)cadmium(II), $[Cd^{II}(L^{1a}-Se,O)_2]$ **111**: Yield (78.5 %). mp 160.1-161.5 °C. Found: C, 42.7; H, 4.4; N, 8.2. $C_{24}H_{30}N_4O_2Se_2Cd$ requires C, 42.6; H, 4.4; N, 8.3 %. δ_H (400 MHz; $CDCl_3$): 1.24 (t, 6H, $^3J_{HH} = 7.1$, H10A/B or H12A/B), 1.35 (t, 6H, $^3J_{HH} = 7.1$, H10A/B or H12A/B), 3.78 (q, 4H, $^3J_{HH} = 7.1$, H9A/B or H11A/B), 3.98 (q, 4H, $^3J_{HH} = 7.1$, H9A/B or H11A/B), 7.33 (multiplet, 4H, H3A and B, H5A and B), 7.44 (t, 2H, $^3J_{HH} = 7.3$, $^4J_{HH} = 2.0$, H4A and B), 8.07 (d, 4H, $^3J_{HH} = 7.8$, H2A and B, H6A and B). δ_C (101 MHz, $CDCl_3$): 13.0, 13.5 (C10A and B, C12A and B), 45.8, 48.0 (C9A and B, C11A and B), 127.6 (C3A and B, C5A and B), 129.5 (C2A and B, C6A and B), 131.1 (C4A and B), 137.9 (C1A and B), 167.8 (C8A and B), 170.9 (C7A and B), $^1J(^{13}C-^{77}Se) = 164.9$. δ_{Se} (76 MHz; $CDCl_3$): 47. δ_{Cd} (89 MHz; $CDCl_3$): -240. TLC (silica gel, $CHCl_3$): $R_f = 0.42$.

(*N,N*-dibutyl-*N'*-benzoylselenourea)cadmium(II), $[Cd^{II}(L^{1b}-Se,O)_2]$ **121**: Yield (85.5 %). Found: C, 48.7, H, 5.8, N, 6.8. $C_{32}H_{46}N_4O_2Se_2Cd$ requires C, 48.7, H, 5.9, N, 7.1 %. δ_H (400 MHz; $CDCl_3$): 0.88 (t, 6H, $^3J_{HH} = 7.4$, H12A/B or H16A/B), 0.99 (t, 6H, $^3J_{HH} = 7.4$, H12A/B or H16A/B), 1.30 (q, 4H, $^3J_{HH} = 7.5$, H11A/B or H15A/B), 1.40 (q, 4H, $^3J_{HH} = 7.5$, H11A/B or H15A/B), 1.64 (q, 4H, $^3J_{HH} = 7.8$, H10A/B or H14A/B), 1.78 (q, 4H, $^3J_{HH} = 7.8$, H10A/B or H14A/B), 3.70 (t, 4H, $^3J_{HH} = 7.6$, H9A/B or H13A/B), 3.90 (t, 4H, $^3J_{HH} = 7.9$, H9A/B or H13A/B), 7.32 (t, 4H, H3A and B, H5A and B), 7.42 (t, 2H, $^3J_{HH} = 7.4$, $^4J_{HH} = 2.0$, H4A and B), 8.05 (d, 4H, H2A and B, H6A and B). δ_C (101 MHz, $CDCl_3$): 13.8, 13.9 (C12A and B, C16A and B), 20.1, 20.2 (C11A and B, C15A and B), 29.9, 30.2 (C10A and B, C14A and B), 51.5, 53.7 (C9A and B, C13A and B), 127.7 (C3A and B, C5A and B), 129.3 (C2A and B, C6A and B), 131.2 (C4A and B), 137.6 (C1A and B), 169.1 (C8A and B), 170.0 (C7A and B). δ_{Se} (76 MHz; $CDCl_3$): 49. δ_{Cd} (89 MHz; $CDCl_3$): -236. TLC (silica gel, $CHCl_3$): $R_f = 0.59$.

(*N,N*-dihexyl-*N'*-benzoylselenoureato)cadmium(II), [Cd^{II}(L^{Ic}-Se,O)₂] **131**: Yield (94.7 %). Found: C, 54.7; H, 7.0; N, 6.3. C₄₀H₆₂N₄O₂Se₂Cd requires C, 53.3; H, 6.9; N, 6.2 %. δ_{H} (400 MHz; CDCl₃): 0.83 (t, 6H, $^3J_{\text{HH}} = 6.8$, H14A/B or H20A/B), 0.92 (t, 6H, $^3J_{\text{HH}} = 6.6$, H14A/B or H20A/B), 1.33 (unres m, 24H, H11A and B-H13A and B, H17A and B-H19A and B), 1.63 (unres q, 4H, H10A/B or H16A/B), 1.76 (unres q, 4H, H10A/B or H16A/B), 3.57 (t, 4H, $^3J_{\text{HH}} = 7.7$, H9A/B or H15A/B), 3.85 (t, 4H, $^3J_{\text{HH}} = 7.9$, H9A/B or H15A/B), 7.25 (t, 4H, H3A and B, H5A and B), 7.38 (t, 2H, H4A and B), 7.97 (d, 4H, H2A and B, H6A and B). δ_{C} (101 MHz, CDCl₃): 13.8, 13.9 (C14A and B, C20A and B), 22.3, 22.5 (C13A and B, C19A and B), 26.4, 26.5 (C11A and B, C17A and B), 27.5, 27.6 (C10A and B, C16A and B), 31.2, 31.3 (C12A and B, C18A and B), 52.1, 54.4 (C9A and B, C15A and B), 127.5 (C3A and B, C5A and B), 129.0 (C2A and B, C6A and B), 131.0 (C4A and B), 136.7 (C1A and B), 168.5 (C8A and B), 173.2 (C7A and B). δ_{Se} (76 MHz; CDCl₃): 53. TLC (silica gel, CHCl₃): R_f = 0.79.

(*N,N*-dioctyl-*N'*-benzoylselenoureato)cadmium(II), [Cd^{II}(L^{Id}-Se,O)₂] **141**: Yield (98.2 %). Found: C, 57.3; H, 7.8; N, 5.8. C₄₈H₇₈N₄O₂Se₂Cd requires C, 56.9; H, 7.8; N, 5.5 %. δ_{H} (400 MHz; CDCl₃): 0.81 (unres t, 6H, H16A/B or H24A/B), 0.86 (unres t, 6H, H16A/B or H24A/B), 1.24 (unres m, 40H, H11A and B-H15A and B, H19A and B, H23A and B), 1.63 (unres q, 4H, H10A/B or H18A/B), 1.75 (unres q, 4H, H10A/B or H18A/B), 3.61 (t, 4H, $^3J_{\text{HH}} = 7.8$, H9A/B or H17A/B), 3.85 (t, 4H, $^3J_{\text{HH}} = 7.9$, H9A/B or H17A/B), 7.29 (t, 4H, H3A and B, H5A and B), 7.41 (t, 2H, H4A and B), 8.01 (d, 4H, H2A and B, H6A and B). δ_{C} (101 MHz, CDCl₃): 14.0, 14.1 (C16A and B, C24A and B), 22.3, 22.4 (C15A and B, C23A and B), 26.7, 26.9 (C11A and B, C19A and B), 27.6, 27.9 (C10A and B, C18A and B), 28.9, 29.0 (C13A and B, C21A and B), 29.1, 29.2 (C12A and B, C20A and B), 31.5, 31.6 (C14A and B, C22A and B), 52.0, 54.2 (C9A and B, C17A and B), 127.9 (C3A and B, C5A and B), 129.4 (C2A and B, C6A and B), 131.4 (C4A and B), 137.4 (C1A and B), 169.7 (C8A and B), 171.2 (C7A and B). TLC (silica gel, CHCl₃): R_f = 0.85.

(*N*-benzyl-*N*-methyl-*N'*-benzoylselenoureato)cadmium(II), [Cd^{II}(L^{Ie}-Se,O)₂] **151**: Yield (96.7 %). mp 86 – 90 °C. Found: C, 50.0; H, 4.1; N, 7.2. C₃₂H₃₀N₄O₂Se₂Cd requires C, 49.7; H, 3.9; N, 7.3 %. δ_{H} (400 MHz; CDCl₃): 3.20 (s, 6H, H9(*EE*, *E*(*EZ*))), 3.40 (s, 6H, H9(*ZZ*, *Z*(*EZ*))), 5.01 (s, 4H, H10(*EE*, *E*(*EZ*))), 5.22 (s, 4H, H10(*ZZ*, *Z*(*EZ*))), 7.26 – 8.12 (20H, m, H2-H6, H12-H16 (*EE*, *ZZ* and *EZ*)). δ_{C} (101 MHz, CDCl₃): 38.2 (C9(*EE*, *E*(*EZ*))), 40.8 (C9(*ZZ*, *Z*(*EZ*))), 55.8 (C10(*ZZ*, *Z*(*EZ*))), 58.4 (C10(*EE*, *E*(*EZ*))), 127.6 – 137.6 (C1-C6, C11-C16 (*EE*, *ZZ* and *EZ*)), 169.0 (C8(*EE*, *E*(*EZ*))), 169.9 (C8(*ZZ*, *Z*(*EZ*))), 171.8 (C7(*EE*, *E*(*EZ*))), 172.4 (C7(*ZZ*, *Z*(*EZ*))). δ_{Se} (76 MHz; CDCl₃): 58, 83. TLC (silica gel, CHCl₃): R_f = 0.44.

(*N,N*-didecyl-*N'*-benzoylselenoureato)cadmium(II), [Cd^{II}(L^{If}-Se,O)₂] **161**: Yield (92.6 %). Found: C, 60.0 ; H, 7.7 ; N, 4.6. C₅₆H₉₄N₄O₂Se₂Cd requires C, 59.8; H, 8.3; N, 5.0 %. δ_{H} (400 MHz; CDCl₃): 0.86 (unres t, 6H, H18A/B or H28A/B), 0.88 (unres t, 6H, H18A/B or H28A/B), 1.28 (unres m, 56H, H11A and B-H17A and B, H21A and B, H27A and B), 1.66 (unres q, 4H, H10A/B or H20A/B), 1.80 (unres q, 4H, H10A/B or H20A/B), 3.68 (t, 4H, $^3J_{\text{HH}} = 7.7$, H9A/B or H19A/B), 3.89 (t, 4H, $^3J_{\text{HH}} = 7.8$, H9A/B or H19A/B), 7.32 (t, 4H, H3A and B, H5A and B), 7.41 (t, 2H, H4A and B), 8.05 (d, 4H, H2A and B, H6A and B). δ_{C} (101 MHz, CDCl₃): 14.0, 14.1 (C18A and B, C28A and B), 22.6, 22.7 (C17A and B, C27A and B), 26.9, 27.0 (C11A and B, C21A and B), 27.8, 28.3 (C10A and B, C20A and B), 29.2, 29.2, 29.3, 29.4, 29.5, 29.5, 29.6, 29.6 (C12-C15A and B and C22-C25A and B), 31.8, 31.9 (C16A and B, C26A and B), 51.8, 53.9 (C9A and B, C19A and B), 127.7 (C3A and B, C5A and B), 129.4 (C2A and B, C6A and B), 131.1 (C4A and B), 137.7 (C1A and B), 168.3 (C8A and B), 170.3 (C7A and B). TLC (silica gel, CHCl₃): R_f = 0.84.

(*N,N*-diphenyl-*N'*-benzoylselenoureato)cadmium(II), [Cd^{II}(L^{Ig}-Se,O)₂] **171**: Yield (80.0 %). mp 173.5 – 175.1 °C. Found: C, 54.7; H, 3.4; N, 6.0. C₄₀H₃₀N₄O₂Se₂Cd requires C, 55.2; H, 3.5; N, 6.5 %. δ_{H} (400 MHz; CDCl₃): 7.18 (m, 4H), 7.27 (m, 4H), 7.36 (m, 18H), 7.72 (m, 4H). δ_{C} (101 MHz, CDCl₃): 127.6, 127.9, 128.7, 129.3, 130.1, 132.1, 137.3 (C1-C6 (A and B), C9-C14 (A and B), C15-C20 (A and B)), 167.4 (C8A and B), 174.8 (C7A and B).

2.2.3.2 *N,N*-dialkyl-*N'*-benzoylselenourea Pd(II) complexes

The Pd^{II} complexes of the *N,N*-dialkyl-*N'*-benzoylselenoureas **HL^{Ia}**, *cis*-[Pd^{II}(L^{Ia}-Se,O)₂] **112**, **HL^{Ib}**, *cis*-[Pd^{II}(L^{Ib}-Se,O)₂] **122**, **HL^{Ic}**, *cis*-[Pd^{II}(L^{Ic}-Se,O)₂] **132**, **HL^{Id}**, *cis*-[Pd^{II}(L^{Id}-Se,O)₂] **142**, **HL^{Ie}**, *cis*-[Pd^{II}(L^{Ie}-Se,O)₂] **152**, **HL^{If}** *cis*-[Pd^{II}(L^{If}-Se,O)₂] **162**, were synthesized using a solvent extraction mechanism, based on that reported by Shuster and Konig.^[23] Briefly, a chloroform solution (25 ml) of the appropriate ligand (0.612 mmol) was shaken together with an aqueous solution (25 ml) of K₂PdCl₄ (0.306 mmol). A lightening in colour of the brown aqueous solution was accompanied by the darkening of the yellow organic layer, to give an orange solution. The mixture was washed with a sodium acetate solution (1.22 mmol, 10 ml), and the organic layer separated and dried over sodium sulphate. Filtration and slow evaporation of the solvent afforded the complexes in good yield.

cis-bis(*N,N*-diethyl-*N'*-benzoylselenoureato)palladium(II), *cis*-[Pd^{II}(L^{Ia}-Se,O)₂] **112**: Yield (87.4 %). mp 120.5–122.1 °C. Found: C, 43.2; H, 4.5; N, 8.3. C₂₄H₃₀N₄O₂Se₂Pd requires C, 43.0; H, 4.5; N, 8.4 %. δ_{H} (400 MHz; CDCl₃): 1.28 (t, 6H, ³J_{HH} = 7.2, H10A/B or H12A/B), 1.35 (t, 6H, ³J_{HH} = 7.2, H10A/B or H12A/B), 3.86 (multiplet, 8H, H9A and B, H11A and B), 7.40 (multiplet, 4H, H3A and B, H5A and B), 7.49 (t, 2H, H4A and B), 8.25 (d, 4H, H2A and B, H6A and B). δ_{C} (101 MHz, CDCl₃): 13.0, 13.1 (C10A and B, C12A and B), 46.2, 49.0 (C9A and B, C11A and B), 127.9 (C3A and B, C5A and B), 129.7 (C2A and B, C6A and B), 131.5 (C4A and B), 137.2 (C1A and B), 165.7 (C8 A and B), 171.0 (C7 A and B). ¹J(¹³C-⁷⁷Se) = 181.3. δ_{Se} (76 MHz; CDCl₃): 291.6.

cis-bis(*N,N*-dibutyl-*N'*-benzoylselenoureato)palladium(II), *cis*-[Pd^{II}(L^{Ib}-Se,O)₂] **122**: Yield (94.2 %). mp 150.5–151.4 °C. Found: C, 49.1, H, 5.8, N, 7.1. C₃₂H₄₆N₄O₂Se₂Pd requires C, 49.1, H, 5.9, N, 7.2 %. δ_{H} (400 MHz; CDCl₃): 0.93 (t, 6H, ³J_{HH} = 7.4, H12A/B or H16A/B), 0.98 (t, 6H, ³J_{HH} = 7.4, H12A/B or H16A/B), 1.38 (m, 8H, ³J_{HH} = 7.6, H11A and B, H15A and B), 1.67 (q, 4H, ³J_{HH} = 7.7, H10A/B or H14A/B), 1.76 (q, 4H, ³J_{HH} = 7.8, H10A/B or H14A/B), 3.78 (m, 8H, ³J_{HH} = 7.8, H9A and B, H13A and B), 7.40 (t, 4H, H3A and B, H5A and B), 7.49 (t, 2H, H4A and B), 8.23 (d, 4H, H2A and B, H6A and B). δ_{C} (101 MHz, CDCl₃): 13.8, 13.9 (C12A and B, C16A and B), 20.2, 20.3 (C11A and B, C15A and B), 29.9, 30.0 (C10A and B, C14A and B), 51.8, 54.7 (C9A and B, C13A and B), 127.9 (C3A and B, C5A and B), 129.7 (C2A and B, C6A and B), 131.4 (C4A and B), 137.2 (C1A and B), 166.7 (C8A and B), 170.8 (C7A and B). ¹J(⁷⁷Se-¹³C) = 176.53. δ_{Se} (76 MHz; CDCl₃): 301.3.

cis-bis(*N,N*-dihexyl-*N'*-benzoylselenoureato)palladium(II), *cis*-[Pd^{II}(L^{Ic}-Se,O)₂] **132**: Yield (82.3 %). mp 68.2 – 69.8 °C. Found: C, 52.2; H, 6.9; N, 6.3. C₄₀H₆₂N₄O₂Se₂Pd requires C, 53.7; H, 7.0; N, 6.3 %. δ_{H} (400 MHz; CDCl₃): 0.87 (unres t, 6H, H14A/B or H20A/B), 0.90 (unres t, 6H, H14A/B or H20A/B), 1.34 (unres m, 24H, H11A and B-H13A and B, H17A and B-H19A and B), 1.69 (unres q, 4H, H10A/B or H16A/B), 1.78 (unres q, 4H, H10A/B or H16A/B), 3.78 (unres m, 8H, H9A and B, H15A and B), 7.39 (t, 4H, H3A and B, H5A and B), 7.48 (t, 2H, H4A and B), 8.22 (d, 4H, H2A and B, H6A and B). δ_{C} (101 MHz, CDCl₃): 13.9, 14.0 (C14A and B, C20A and B), 22.5, 22.6, (C13A and B, C19A and B), 26.6, 26.7 (C11A and B, C17A and B), 27.7, 27.9 (C10A and B, C16A and B), 31.4,

31.5, (C12A and B, C18A and B), 52.1, 54.9 (C9A and B, C15A and B), 127.9 (C3A and B, C5A and B), 129.7 (C2A and B, C6A and B), 131.3 (C4A and B), 137.2 (C1A and B), 166.0 (C8A and B), 170.8 (C7A and B). $^1J(^{77}\text{Se}-^{13}\text{C})$ 176.37. δ_{Se} (76 MHz; CDCl_3): 299.7.

cis-bis(*N,N*-dioctyl-*N'*-benzoylselenoureato)palladium(II), *cis*-[Pd^{II}(L^{1d}-Se,O)₂] **142**: Yield (68.7 %). mp 64.0-65.7 °C. Found: C, 56.6; H, 7.6; N, 5.7. C₄₈H₇₈N₄O₂Se₂Pd requires C, 57.2; H, 7.8; N, 5.6 %. δ_{H} (400 MHz; CDCl_3): 0.86 (unres t, 6H, H16A/B or H24A/B), 0.89 (unres t, 6H, H16A/B or H24A/B), 1.31 (unres m, 40H, H11A and B-H15A and B, H19A and B, H23A and B), 1.69 (unres q, 4H, H10A/B or H18A/B), 1.78 (unres q, 4H, H10A/B or H18A/B), 3.78 (unres m, 8H, H9A and B and H17A and B), 7.39 (t, 4H, H3A and B, H5A and B), 7.47 (t, 2H, H4A and B), 8.23 (d, 4H, H2A and B, H6A and B). δ_{C} (101 MHz, CDCl_3): 14.0, 14.1 (C16A and B, C24A and B), 22.5, 22.6, (C15A and B, C23A and B), 26.9, 27.1 (C11A and B, C19 A and B), 27.7, 27.9 (C10A and B, C18A and B), 29.0, 29.1 (C13A and B, C21A and B), 29.2, 29.3 (C12A and B, C20A and B), 31.7, 31.8 (C14A and B, C22A and B), 52.1, 54.9 (C9A and B, C17A and B), 127.9 (C3A and B, C5A and B), 129.7 (C2A and B, C6A and B), 131.4 (C4A and B), 137.3 (C1A and B), 166.0 (C8A and B), 170.8 (C7A and B). $^1J(^{77}\text{Se}-^{13}\text{C}) = 175.83$. δ_{Se} (76 MHz; CDCl_3): 300.4.

cis-bis(*N*-benzyl-*N*-methyl-*N'*-benzoylselenoureato)palladium(II), *cis*-[Pd^{II}(L^{1e}-Se,O)₂] **152**: Yield (77.5 %). mp 169.5-170.5 °C. Found: C, 49.1; H, 4.2; N, 6.8. C₃₂H₃₀N₄O₂Se₂Pd requires C, 50.1; H, 3.9; N, 7.3 %. δ_{H} (400 MHz; CDCl_3): 3.33 (br s, H, H9(Z(EZ), EE)), 3.34 (s, H, H9(E(EZ))), 3.36 (s, H, H9(ZZ)), 5.15 (s, H, H10(EE)), 5.17 (s, H, H10(E(EZ))), 5.18 (s, H, H10(Z(EZ))), 5.19 (s, H, H10(ZZ)), 7.30 – 8.31 (H, m, H2-H6, H12-H16 (EE, ZZ and EZ)). δ_{C} (101 MHz, CDCl_3): 38.7 (C9(EE, E(EZ))), 41.2 (C9(Z(EZ))), 41.3 (C9(ZZ)), 55.9 (C10(ZZ), Z(EZ)), 59.5 (C10(E(EZ))), 59.6 (C10(EE)), 127.4 – 137.0 (C1-C6, C11-C16 (EE, ZZ and EZ)), 167.7 (C8(E(EZ))), 167.8 (C8(EE)), 168.4 (C8(ZZ)), 168.5 (C8(Z(EZ))), 171.7 (C7(Z(EZ))), 171.8 (C7(ZZ)), 171.9 (C7(EE)), 172.0 (C7(E(EZ))). δ_{Se} (76 MHz; CDCl_3): 291.9 (EE), 292.7 (E(EZ)), 319.5 (Z(EZ)), 319.8 (ZZ).

cis-bis(*N,N*-didecyl-*N'*-benzoylselenoureato)palladium(II), *cis*-[Pd^{II}(L^{1f}-Se,O)₂] **162**: Yield (98.5 %). mp 55.5 – 57.0 °C Found: C, 58.0; H, 7.13; N, 4.9. C₅₆H₉₄N₄O₂Se₂Pd requires C, 60.1; H, 8.4; N, 5.0 %. δ_{H} (400 MHz; CDCl_3): 0.88 (unres t, 12H, H18A/B and H28A/B), 1.28 (unres m, 56H, H11A and B-H17A and B, H21A and B, H27A and B), 1.70 (unres q, 4H, H10A/B or H20A/B), 1.78 (unres q, 4H, H10A/B or H20A/B), 3.78 (unres m, 8H, H9A/B and H19A/B), 7.39 (t, 4H, H3A and B, H5A and B), 7.47 (t, 2H, H4A and B), 8.23 (d, 4H, H2A and B, H6A and B). δ_{C} (101 MHz, CDCl_3): 14.0, 14.1 (C18A and B, C28A and B), 22.6, 22.7, (C17A and B, C27A and B), 26.9, 27.0 (C11A and B, C21A and B), 27.7, 27.9 (C10A and B, C20A and B), 29.2, 29.3, 29.3, 29.4, 29.5, (C12-15A and B, C22-25A and B), 31.8, 31.9 (16A and B, C26A and B), 52.1, 54.9 (C9A and B, C19A and B), 127.9 (C3A and B, C5A and B), 129.7 (C2A and B, C6A and B), 131.4 (C4A and B), 137.2 (C1A and B), 166.0 (C8A and B), 170.8 (C7A and B). $^1J(^{77}\text{Se}-^{13}\text{C}) = 176.00$. δ_{Se} (76 MHz; CDCl_3): 301.9.

2.2.3.3 *N,N*-dialkyl-*N'*-benzoylselenourea Zn(II) complex

The Zn^{II} complex of HL^{1a}, [Zn^{II}(L^{1a}-Se,O)₂] **113** was synthesized according to the method described by Bensch and Schuster.^[9]

(*N,N*-diethyl-*N'*-benzoylselenoureato)zinc(II): Yield (68.4 %). mp 106.0-107.5 °C. Found: C, 44.8; H, 4.7; N, 8.7. C₂₄H₃₀N₄O₂Se₂Zn requires C, 45.8; H, 4.8; N, 8.9 %. δ_{H} (400 MHz; CDCl_3): 1.30 (t, 6H, $^3J_{\text{HH}} = 7.1$,

H10A/B or H12A/B), 1.38 (t, 6H, $^3J_{\text{HH}} = 7.1$, H10A/B or H12A/B), 3.88 (q, 4H, $^3J_{\text{HH}} = 7.1$, H9A/B or H11A/B), 4.00 (q, 4H, $^3J_{\text{HH}} = 7.1$, H9A/B or H11A/B), 7.36 (multiplet, 4H, H3A and B, H5A and B), 7.46 (t, 2H, $^3J_{\text{HH}} = 7.3$, $^4J_{\text{HH}} = 2.0$, H4A and B), 8.16 (d, 4H, $^3J_{\text{HH}} = 7.1$, H2A and B, H6A and B). δ_{C} (101 MHz, CDCl_3): 13.1, 13.2 (C10A and B, C12A and B), 46.0, 47.9 (C9A and B, C11A and B), 127.7 (C3A and B, C5A and B), 129.5 (C2A and B, C6A and B), 131.5 (C4A and B), 137.9 (C1A and B), 170.3 (C8A and B), 171.5 (C7A and B), $^1J(^{13}\text{C}-^{77}\text{Se}) = 166.6$. δ_{Se} (76 MHz; CDCl_3): 67.6

2.2.3.4 *N,N*-dialkyl-*N'*-benzoylselenourea Pt(II) complex

Several attempts were made to synthesise *cis*-bis(*N,N*-diethyl-*N'*-benzoylselenourea)platinum(II). Two earlier reports exist, mentioning the preparation of this complex from ethanolic solution similar to the procedure followed for Cd(II) complex synthesis,^[22, 23] however the absence of experimental evidence (NMR spectroscopy and elemental analysis) and structural characterization of any Pt(II)/(IV) complex involving the *N,N*-dialkyl-*N'*-benzoylselenoureas, suggests that this synthesis is not facile. Solvent combinations of dioxane and water as well as acetonitrile and water, the latter usually successful for the synthesis of Pt(II) complexes of the sulfur analogues using K_2PtCl_4 yielded only a black precipitate, metallic in appearance, suggestive of decomposition. The black residue obtained was analysed using Transmission Electron Microscopy (TEM) and spherical particles were clearly visible, ranging from 300 nm to 1000 nm in diameter. Energy Dispersive X-ray Spectroscopy (EDAX) analysis indicated the presence of both Pt and Se. More gentle techniques were also attempted; an extraction synthesis similar to that used for the Pd(II) complex preparations was examined, but met with little success most likely due to the lower lability of Pt(II) relative to that of Pd(II). An *in situ* synthesis was then performed in an NMR tube in an attempt to gain spectroscopic evidence of the coordination of the O and Se donor atoms to the Pt(II) metal centre and these results are described in Section 2.3.5.5.

2.2.3.5 3,3,3',3'-tetraethyl-1,1'-isophthaloylbis(selenourea) metal complexes

The Pd(II) and Pt(II) complexes of 3,3,3',3'-tetraethyl-1,1'-isophthaloylbis(selenourea) (**11112** and **11114** respectively) were synthesized according to previously described methods.^[46] Limited solubility in a variety of solvents precluded characterization by NMR.

3,3,3',3'-tetraethyl-1,1'-isophthaloylbis(selenourea) palladium(II), *cis*-[Pd^{II}₂(L^{m1a}-Se,O)₂] **11112**: Yield (22.1 %) mp decomp > 250 °C. Found: C, 36.2, H, 4.0, N, 9.6. C₃₆H₅₀N₈O₄Se₄Pd₂ requires C, 36.4, H, 4.2, N, 9.4 %.

3,3,3',3'-tetraethyl-1,1'-isophthaloylbis(selenourea) platinum(II), *cis*-[Pt^{II}₂(L^{m1a}-Se,O)₂] **11114**: Yield (80.0 %) mp 163.0 – 164.7 °C. Found: C, 31.6, H, 3.5, N, 8.1. C₃₆H₅₀N₈O₄Se₄Pt₂ requires C, 31.7, H, 3.7, N, 8.2 %.

2.2.4 Synthesis and characterization of *N,N*-dialkyl-*N'*-benzoylthiourea metal complexes

2.2.4.1 *N,N*-dialkyl-*N'*-benzoylthiourea Cd(II) complexes

The Cd^{II} complexes of **HL**^{2a}, [Cd^{II}(**L**^{2a}-S,**O**)₂] **211**, **HL**^{2b}, [Cd^{II}(**L**^{2b}-S,**O**)₂] **221**, **HL**^{2c}, [Cd^{II}(**L**^{2c}-S,**O**)₂] **231**, **HL**^{2d}, [Cd^{II}(**L**^{2d}-S,**O**)₂] **241**, **HL**^{2e}, [Cd^{II}(**L**^{2e}-S,**O**)₂] **251**, were synthesized according to previously described methods.^[73] As with the selenourea derivatives, **211** and **251** yielded solid microcrystalline material upon recrystallization and the longer alkyl chain derivatives, **221**, **231**, **241** were isolated as oily semi-solid material.

(*N,N*-diethyl-*N'*-benzoylthioureato)cadmium(II), [Cd^{II}(**L**^{2a}-S,**O**)₂] **211**: Yield (92.7 %). mp 158.0-159.5 °C Found: C, 49.3; H, 5.1; N, 9.5; S, 10.8. C₂₄H₃₀N₄O₂S₂Cd requires C, 49.4; H, 5.2; N, 9.7; S, 11.0 %. δ_H (400 MHz; CDCl₃): 1.17 (t, 6H, ³J_{HH} = 7.1, H10A/B or H12A/B), 1.26 (t, 6H, ³J_{HH} = 7.1, H10A/B or H12A/B), 3.70 (q, 4H, ³J_{HH} = 7.1, H9A/B or H11A/B), 3.84 (q, 4H, ³J_{HH} = 7.1, H9A/B or H11A/B), 7.29 (multiplet, 4H, H3A and B, H5A and B), 7.39 (t, 2H, ³J_{HH} = 7.4, H4A and B), 8.03 (d, 4H, ³J_{HH} = 7.1, H2A and B, H6A and B). δ_C (101 MHz, CDCl₃): 12.9, 13.0 (C10A and B, C12A and B), 45.7, 46.1 (C9A and B, C11A and B), 127.5 (C3A and B, C5A and B), 129.4 (C2A and B, C6A and B), 130.8 (C4A and B), 138.1 (C1A and B), 170.9 (C8A and B), 176.6 (C7A and B). δ_{Cd} (89 MHz; CDCl₃): -275. TLC (silica gel, CHCl₃): R_f = 0.56.

(*N,N*-dibutyl-*N'*-benzoylthioureato)cadmium(II), [Cd^{II}(**L**^{2b}-S,**O**)₂] **221**: Yield (87.7 %). Found: C, 63.7, H, 7.3, N, 8.6, S, 10.0. C₃₂H₄₆N₄O₂S₂Cd requires C, 55.2; H, 6.7; N, 8.1; S, 9.2 %. δ_H (400 MHz; CDCl₃): 0.95 (t, 6H, ³J_{HH} = 7.4, H12A/B or H16A/B), 1.03 (t, 6H, ³J_{HH} = 7.4, H12A/B or H16A/B), 1.35 (q, 4H, ³J_{HH} = 7.5, H11A/B or H15A/B), 1.43 (q, 4H, ³J_{HH} = 7.6, H11A/B or H15A/B), 1.68 (q, 4H, ³J_{HH} = 7.5, H10A/B or H14A/B), 1.79 (q, 4H, ³J_{HH} = 7.5, H10A/B or H14A/B), 3.66 (t, 4H, ³J_{HH} = 7.5, H9A/B or H13A/B), 3.89 (t, 4H, ³J_{HH} = 7.8, H9A/B or H13A/B), 7.35 (t, 4H, H3A and B, H5A and B), 7.47 (t, 2H, ³J_{HH} = 7.4, ⁴J_{HH} = 2.0, H4A and B), 8.05 (d, 4H, H2A and B, H6A and B). δ_C (101 MHz, CDCl₃): 13.7, 13.8 (C12A and B, C16A and B), 20.1, 20.2 (C11A and B, C15A and B), 29.3, 29.9 (C10A and B, C14A and B), 51.7, 52.0 (C9A and B, C13A and B), 127.7 (C3A and B, C5A and B), 129.0 (C2A and B, C6A and B), 131.1 (C4A and B), 136.8 (C1A and B), 168.7 (C8A and B), 178.7 (C7A and B). δ_{Cd} (89 MHz; CDCl₃): -229. TLC (silica gel, CHCl₃): R_f = 0.76.

N,N-dihexyl-*N'*-benzoylthioureato)cadmium(II), [Cd^{II}(**L**^{2c}-S,**O**)₂] **231**: Yield 89.9 %. Found: C, 65.7; H, 8.2; N, 6.5; S, 8.3. C₄₀H₆₂N₄O₂S₂Cd requires C, 59.5; H, 7.7; N, 6.9; S, 7.9 %. δ_H (400 MHz; CDCl₃): 0.83 (t, 6H, ³J_{HH} = 6.9, H14A/B or H20A/B), 0.89 (t, 6H, ³J_{HH} = 6.6, H14A/B or H20A/B), 1.24 (unres m, 24H, H11A and B-H13A and B, H17A and B-H19A and B), 1.63 (unres q, 4H, H10A/B or H16A/B), 1.76 (unres q, 4H, H10A/B or H16A/B), 3.53 (t, 4H, ³J_{HH} = 7.5, H9A/B or H15A/B), 3.88 (t, 4H, ³J_{HH} = 7.6, H9A/B or H15A/B), 7.38 (t, 4H, H3A and B, H5A and B), 7.49 (t, 2H, H4A and B), 7.87 (d, 4H, H2A and B, H6A and B). δ_C (101 MHz, CDCl₃): 13.9, 14.0 (C14A and B, C20A and B), 22.5, 22.6 (C13A and B, C19A and B), 26.5 (C11A and B, C17A and B), 26.7, 27.9 (C10A and B, C16A and B), 31.4, 31.5 (C12A and B, C18A and B), 52.8, 53.1 (C9A and B, C15A and B), 128.2 (C3A and B, C5A and B), 128.4 (C2A and B, C6A and B), 132.2 (C4A and B), 134.3 (C1A and B), 165.6 (C8A and B), 179.5 (C7A and B). δ_{Cd} (89 MHz; CDCl₃): -229. TLC (silica gel, CHCl₃): R_f = 0.70

(*N,N*-dioctyl-*N'*-benzoylthioureato)cadmium(II), [Cd^{II}(**L**^{2d}-S,**O**)₂] **241**: Yield 87.5 %. Found: C, 69.2; H, 9.1; N, 6.1; S, 6.9. C₄₈H₇₈N₄O₂S₂Cd requires C, 62.7; H, 8.6; N, 6.1; S, 7.0 %. δ_H (400 MHz; CDCl₃): 0.85 (unres t, 6H, H16A/B or H24A/B), 0.89 (unres t, 6H, H16A/B or H24A/B), 1.28 (unres m, 40H, H11A and B-H15A and B, H19A and B, H23A and B), 1.63 (unres q, 4H, H10A/B or H18A/B), 1.75 (unres q, 4H, H10A/B or H18A/B), 3.51 (t, 4H,

$^3J_{\text{HH}} = 5.5$, H9A/B or H17A/B), 3.85, (t, 4H, $^3J_{\text{HH}} = 7.7$, H9A/B or H17A/B), 7.36 (t, 4H, H3A and B, H5A and B), 7.47 (t, 2H, H4A and B), 7.89 (d, 4H, H2A and B, H6A and B). δ_{C} (101 MHz, CDCl_3): 14.0, 14.1 (C16A and B, C24A and B), 22.5, 22.6, (C15A and B, C23A and B), 26.8, (C10A/B, C18A/B), 26.9, (C11A and B, C19 A and B), 27.9, (C10A/B, C18A/B), 29.1, 29.2, (C13A and B, C21A and B), 29.2, 29.3, (C12A and B, C20A and B), 31.7, 31.8 (C14A and B, C22A and B), 52.7, 53.0 (C9A and B, C17A and B), 128.2 (C3A and B, C5A and B), 128.5 (C2A and B, C6A and B), 131.9 (C4A and B), 134.8 (C1A and B), 166.3 (C8A and B), 179.4 (C7A and B). δ_{Cd} (89 MHz; CDCl_3): -231. TLC (silica gel, CHCl_3): $R_f = 0.83$

(*N*-benzyl-*N*-methyl-*N'*-benzoylthioureato)cadmium(II), $[\text{Cd}^{\text{II}}(\text{L}^{2\text{e}}-\text{S},\text{O})_2]$ **251**: Yield (75.1 %). mp 118 – 120.5 °C. Found: C, 63.1; H, 4.9; N, 8.1; S, 10.5. $\text{C}_{32}\text{H}_{30}\text{N}_4\text{O}_2\text{S}_2\text{Cd}$ requires C, 56.6; H, 4.5; N, 8.3; S, 9.4 %. δ_{H} (400 MHz; CDCl_3): 3.12 (s, 6H, H9(*EE*, *E(EZ)*)), 3.27 (s, 6H, H9(*ZZ*, *Z(EZ)*)), 4.84 (s, 4H, H10(*EE*, *E(EZ)*)), 5.22 (s, 4H, H10(*ZZ*, *Z(EZ)*)), 7.22 – 7.93 (20H, m, H2-H6, H12-H16 (*EE*, *ZZ* and *EZ*)). δ_{C} (101 MHz, CDCl_3): 39.7 (C9(*ZZ*, *Z(EZ)*)), 40.1 (C9(*EE*, *E(EZ)*)), 57.0 (C10(*EE*, *E(EZ)*)), 58.7 (C10(*ZZ*, *Z(EZ)*)), 127.7 – 135.9 (C1-C6, C11-C16 (*EE*, *ZZ* and *EZ*)), 166.1 (C8(*ZZ*, *Z(EZ)*)), 168.7 (C8(*ZZ*, *Z(EZ)*)), 180.4 (C7(*EE*, *E(EZ)*)), 180.8 (C7(*ZZ*, *Z(EZ)*). TLC (silica gel, CHCl_3): $R_f = 0.55$.

2.2.4.2 *N,N*-dialkyl-*N'*-benzoylthiourea Pd(II) complexes

Pd^{II} complexes of the *N,N*-dialkyl-*N'*-benzoylthioureas **HL**^{2a}, *cis*- $[\text{Pd}^{\text{II}}(\text{L}^{2\text{a}}-\text{S},\text{O})_2]$ **212**, **HL**^{2b}, *cis*- $[\text{Pd}^{\text{II}}(\text{L}^{2\text{b}}-\text{S},\text{O})_2]$ **222**, **HL**^{2c}, *cis*- $[\text{Pd}^{\text{II}}(\text{L}^{2\text{c}}-\text{S},\text{O})_2]$ **232**, **HL**^{2d}, *cis*- $[\text{Pd}^{\text{II}}(\text{L}^{2\text{d}}-\text{S},\text{O})_2]$ **242**, **HL**^{2e}, *cis*- $[\text{Pd}^{\text{II}}(\text{L}^{2\text{e}}-\text{S},\text{O})_2]$ **252**, were synthesized using the solvent extraction mechanism previously described for the corresponding *N,N*-dialkyl-*N'*-benzoylselenoureas.

***cis*-bis(*N,N*-diethyl-*N'*-benzoylthioureato)palladium(II)**, *cis*- $[\text{Pd}^{\text{II}}(\text{L}^{2\text{a}}-\text{S},\text{O})_2]$ **212**: Yield (90.2 %). mp 156.7-157.4 °C. Found: C, 49.8; H, 5.2; N, 9.6. $\text{C}_{24}\text{H}_{30}\text{N}_4\text{O}_2\text{S}_2\text{Pd}$ requires C, 50.0; H, 5.2; N, 9.7 %. δ_{H} (400 MHz; CDCl_3): 1.28 (t, 6H, $^3J_{\text{HH}} = 7.1$, H10A/B or H12A/B), 1.34 (t, 6H, $^3J_{\text{HH}} = 7.2$, H10A/B or H12A/B), 3.87 (m, 8H, H9A and B or H11A and B), 7.42 (t, 4H, H3A and B, H5A and B), 7.49 (t, 2H, $^3J_{\text{HH}} = 7.4$, $^2J_{\text{HH}} = 2.4$, H4A and B), 8.24 (d, 4H, H2A and B, H6A and B). δ_{C} (101 MHz, CDCl_3): 12.7, 13.1 (C10A and B, C12A and B), 46.0, 47.2 (C9A and B, C11A and B), 127.9 (C3A and B, C5A and B), 129.7 (C2A and B, C6A and B), 131.4 (C4A and B), 137.1 (C1A and B), 170.6 (C8A and B), 171.1 (C7A and B).

***cis*-bis(*N,N*-dibutyl-*N'*-benzoylthioureato)palladium(II)**, *cis*- $[\text{Pd}^{\text{II}}(\text{L}^{2\text{b}}-\text{S},\text{O})_2]$ **222**: Yield (88.4 %). mp 146.0-147.7 °C. Found: C, 53.9; H, 7.1; N, 7.7; S, 7.9. $\text{C}_{32}\text{H}_{46}\text{N}_4\text{O}_2\text{S}_2\text{Pd}$ requires C, 55.8; H, 6.7; N, 8.1; S, 9.3 %. δ_{H} (400 MHz; CDCl_3): 0.97 (m, 12H, H12A and B and H16A and B), 1.40 (m, 8H, H11A and B, H15A and B), 1.70 (m, 8H, H10A and B and H14A and B), 3.80 (m, 8H, H9A and B, H13A and B), 7.41 (t, 4H, H3A and B, H5A and B), 7.49 (t, 2H, H4A and B), 8.24 (d, 4H, H2A and B, H6A and B). δ_{C} (101 MHz, CDCl_3): 13.8, 13.9 (C12A and B, C16A and B), 20.2, 20.3 (C11A and B, C15A and B), 29.5, 30.0 (C10A and B, C14A and B), 51.6, 52.8 (C9A and B, C13A and B), 127.9 (C3A and B, C5A and B), 129.7 (C2A and B, C6A and B), 131.4 (C4A and B), 137.1 (C1A and B), 170.4 (C8A and B), 171.5 (C7A and B).

***cis*-bis(*N,N*-dihexyl-*N'*-benzoylthioureato)palladium(II)**, *cis*- $[\text{Pd}^{\text{II}}(\text{L}^{2\text{c}}-\text{S},\text{O})_2]$ **232**: Yield 94.9 %. m.p. 86.7 – 88.1 °C. Found: C, 58.5; H, 8.1; N, 7.8; S, 7.9. $\text{C}_{40}\text{H}_{62}\text{N}_4\text{O}_2\text{S}_2\text{Pd}$ requires C, 59.9; H, 7.8; N, 7.0; S, 8.0 %. δ_{H} (400 MHz; CDCl_3): 0.87 (unres t, 6H, H14A/B or H20A/B), 0.91 (unres t, 6H, H14A/B or H20A/B), 1.32 (unres m, 24H, H11A

and B-H13A and B, H17A and B-H19A and B), 1.70 (unres q, 4H, H10A/B or H16A/B), 1.77 (unres q, 4H, H10A/B or H16A/B), 3.77 (unres m, 8H, H9A and B, H15A and B), 7.41 (t, 4H, H3A and B, H5A and B), 7.48 (t, 2H, H4A and B), 8.24 (d, 4H, H2A and B, H6A and B). δ_C (101 MHz, CDCl₃): 13.9, 14.0 (C14A and B, C20A and B), 22.6, (C13A and B, C19A and B), 26.6, 26.7, (C11A and B, C17A and B), 27.3, 27.9, (C10A and B, C16A and B), 31.5, 31.6, (C12A and B, C18A and B), 51.9, 53.1 (C9A and B, C15A and B), 127.9 (C3A and B, C5A and B), 129.7 (C2A and B, C6A and B), 131.4 (C4A and B), 137.1 (C1A and B), 170.4 (C8A and B), 171.5 (C7A and B).

cis-bis(*N,N*-dioctyl-*N'*-benzoylthioureato)palladium(II), *cis*-[Pd^{II}(L^{2d}-S,O)₂] **242**: Yield 98.0 %. m.p. 95.2 – 97.0 °C. Found: C, 61.5; H, 7.8; N, 5.2; S, 6.0. C₄₈H₇₈N₄O₂S₂Pd requires C, 63.1; H, 8.6; N, 6.1; S, 7.0 %. δ_H (400 MHz; CDCl₃): 0.86 (unres t, 6H, H16A/B or H24A/B), 0.89 (unres t, 6H, H16A/B or H24A/B), 1.31 (unres m, 40H, H11A and B-H15A and B, H19A and B, H23A and B), 1.70 (unres q, 4H, H10A/B or H18A/B), 1.76 (unres q, 4H, H10A/B or H18A/B), 3.78 (unres m, 8H, H9A and B and H17A and B), 7.40 (t, 4H, H3A and B, H5A and B), 7.48 (t, 2H, H4A and B), 8.23 (d, 4H, H2A and B, H6A and B). δ_C (101 MHz, CDCl₃): 14.0, 14.1 (C16A and B, C24A and B), 22.5, 22.6, (C15A and B, C23A and B), 27.0, 27.1, (C11A and B, C19 A and B), 27.4, 27.9, (C10A and B, C18A and B), 29.2, 29.2, (C13A and B, C21A and B), 29.3, 29.4, (C12A and B, C20A and B), 31.7, 31.8 (C14A and B, C22A and B), 51.9, 53.1 (C9A and B, C17A and B), 127.9 (C3A and B, C5A and B), 129.7 (C2A and B, C6A and B), 131.4 (C4A and B), 137.1 (C1A and B), 170.4 (C8A and B), 171.5 (C7A and B).

cis-bis(*N*-benzyl-*N*-methyl-*N'*-benzoylthioureato)palladium(II), *cis*-[Pd^{II}(L^{2e}-S,O)₂] **252**: Yield (89.0 %). mp 203.6 – 204.8 °C. Found: C, 55.5; H, 4.2; N, 7.4; S, 9.1. C₃₂H₃₀N₄O₂S₂Pd requires C, 57.1; H, 4.5; N, 8.3; S, 9.5 %. δ_H (400 MHz; CDCl₃): 3.29 (s, H9(ZE)), 3.33 (s, H9(ZZ)), 3.35 (s, H9(EE)), 3.37 (s, H9(E(EZ))), 5.12 (s, H10(EE)), 5.16 (s, H10(E(EZ))), 5.20 (s, H10(ZE)), 5.22 (s, H10(ZZ)), 7.30 – 8.31 (m, H2-H6, H12-H16 (EE, ZZ and EZ)). δ_C (101 MHz, CDCl₃): 38.6 (C9(EE, E(EZ))), 39.7 (C9(ZE)), 39.8 (C9(ZZ)), 55.7 (C10(ZZ, Z(EZ))), 57.6 (C10(E(EZ))), 57.7 (C10(EE)), 127.4 – 136.8 (C1-C6, C11-C16 (EE, ZZ and EZ)), 171.1 (C8(ZE)), 171.2 (C8(ZZ)), 171.4 (C8(EE)), 171.5 (C8(E(EZ))), 173.0 (C7(E(EZ))), 173.0 (C7(EE)), 173.1 (C7(ZZ)), 173.2 (C7(ZE)).

2.2.4.3 *N,N*-dialkyl-*N'*-benzoylthiourea Pt(II) and Zn(II) complexes

The Zn^{II} and Pt^{II} complexes of HL^{2a}, [Zn^{II}(L^{2a}-S,O)₂] **213** and *cis*-[Pt^{II}(L^{2a}-S,O)₂] **214** respectively were synthesized and purified according to previously reported methods.^[36, 73]

(*N,N*-diethyl-*N'*-benzoylthioureato)zinc(II), [Zn^{II}(L^{2a}-S,O)₂] **213**: Yield (53.7 %). mp 78.5-79.8 °C. Found: C, 53.2; H, 5.6; N, 10.1; S, 11.8. C₂₄H₃₀N₄O₂S₂Zn requires C, 53.8; H, 5.6; N, 10.4; S, 11.9 %. δ_H (400 MHz; CDCl₃): 1.31 (t, 6H, ³J_{HH} = 7.0, H10A/B or H12A/B), 1.36 (t, 6H, ³J_{HH} = 7.1, H10A/B or H12A/B), 3.88 (q, 4H, ³J_{HH} = 7.1, H9A/B or H11A/B), 3.96 (q, 4H, ³J_{HH} = 7.1, H9A/B or H11A/B), 7.38 (m, 4H, H3A and B, H5A and B), 7.47 (t, 2H, ³J_{HH} = 7.3, ⁴J_{HH} = 2.0, H4A and B), 8.18 (m, 4H, H2A and B, H6A and B). δ_C (101 MHz, CDCl₃): 12.7, 13.2 (C10A and B, C12A and B), 45.8, 45.9 (C9A and B, C11A and B), 127.7 (C3A and B, C5A and B), 129.4 (C2A and B, C6A and B), 131.4 (C4A and B), 138.0 (C1A and B), 171.8 (C8A and B), 176.2 (C7A and B).

***cis*-bis(*N,N*-diethyl-*N'*-benzoylthioureato)platinum(II), *cis*-[Pt^{II}(L^{2a}-S,O)₂] 214:** Yield (94.9 %). mp 169.7-171.2 °C. Found: C, 43.5; H, 4.5; N, 8.4. C₂₄H₃₀N₄O₂S₂Pt requires C, 43.3; H, 4.5; N, 8.4 %. δ_{H} (400 MHz; CDCl₃): 1.28 (t, 6H, ³J_{HH} = 7.0, H10A/B or H12A/B), 1.34 (t, 6H, ³J_{HH} = 7.2, H10A/B or H12A/B), 3.77 (q, 4H, ³J_{HH} = 7.1, H9A/B or H11A/B), 3.83 (q, 4H, ³J_{HH} = 7.2, H9A/B or H11A/B), 7.42 (multiplet, 4H, H3A and B, H5A and B), 7.52 (t, 2H, H4A and B), 8.26 (d, 4H, H2A and B, H6A and B). δ_{C} (101 MHz, CDCl₃): 12.4, 13.1 (C10A and B, C12A and B), 45.9, 47.0 (C9A and B, C11A and B), 128.0 (C3A and B, C5A and B), 129.3 (C2A and B, C6A and B), 131.3 (C4A and B), 137.6 (C1A and B), 167.0 (C8A and B), 168.4 (C7A and B).

2.2.4.4 “Solventless” synthesis

Ni^{II} and Co^{III} complexes of HL^{2a}, *cis*-[Ni^{II}(L^{2a}-S,O)₂] 215 and [Co^{III}(L^{2a}-S,O)₃] 216 as well as the Pd^{II} complex of HL^{2f}, *cis*-[Pd^{II}(L^{2f}-S,O)₂] 262 were synthesized using a novel “solventless” synthesis.

***cis*-bis(*N,N*-diethyl-*N'*-benzoylthioureato)nickel(II), *cis*-[Ni^{II}(L^{2a}-S,O)₂] 215:**

Ligand (0.76 mmol) and base (CH₃COO⁻Na⁺·3H₂O, 1.5 mmol) were ground together using a mortar and pestle with a few drops of MeCN to form a white paste. A slight molar excess of NiSO₄·7H₂O (0.40 mmol) was added to the mixture, followed by more MeCN and grinding. Within a few seconds the colour of the Ni^{II} salt changed from green to red brown. Excess base and metal ions were removed by washing with water, centrifugation and drying yielded the desired complex.

Yield (67.2 %). mp 138.4-139.2 °C. Found: C, 54.4; H, 5.8; N, 10.2; S, 12.7. C₂₄H₃₀N₄O₂S₂Ni requires C, 54.5; H, 5.7; N, 10.6; S, 12.1 %. δ_{H} (400 MHz; CDCl₃): 1.27 (m, 12H, H10A and B or H12A and B), 3.78 (m, 8H, H9A and B or H11A and B), 7.34 (m, 4H, H3A and B, H5A and B), 7.47 (t, 2H, H4A and B), 8.13 (d, 4H, H2A and B, H6A and B). δ_{C} (101 MHz, CDCl₃): 12.5, 13.1 (C10A and B, C12A and B), 45.5, 46.1 (C9A and B, C11A and B), 127.9 (C3A and B, C5A and B), 129.2 (C2A and B, C6A and B), 131.3 (C4A and B), 136.7 (C1A and B), 172.4 (C8A and B), 172.5 (C7A and B).

(*N,N*-diethyl-*N'*-benzoylthioureato)cobalt(III), [Co^{III}(L^{2a}-S,O)₃] 216:

Ligand (0.78 mmol) and base (CH₃COO⁻Na⁺·3H₂O, 2.0 mmol) were ground together using a mortar and pestle with a few drops of MeCN to form a white paste. A slight molar excess of CoSO₄·7H₂O (0.27 mmol) was added to the mixture, followed by more MeCN and grinding. Within a few seconds the colour of the Co^{II} salt changed from pink to green. Excess base and metal ions were removed by washing with water, centrifugation and drying yielded the desired complex.

Yield (69.7 %). mp 166.4-167.9 °C. Found: C, 56.5; H, 5.9; N, 10.2; S, 12.8. C₃₆H₄₅N₆O₃S₃Co requires C, 56.6; H, 5.9; N, 10.9; S, 12.6 %. δ_{H} (400 MHz; CDCl₃): 1.18 (t, 9H, H10A/B/C or H12A/B/C), 1.25 (t, 9H, H10A/B/C or H12A/B/C), 3.83 (m, 12H, H9A,B and C and H11A, B and C), 7.29 (m, 6H, H3A,B and C, H5A,B and C), 7.39 (t, 3H, H4A,B and C), 8.15 (d, 6H, H2A,B and C, H6A,B and C). δ_{C} (101 MHz, CDCl₃): 12.9, 13.2 (C10A,B and C, C12A,B and C), 45.4, 45.6 (C9A,B and C, C11A,B and C), 127.4 (C3A,B and C, C5A,B and C), 129.5 (C2A,B and C, C6A,B and C), 130.8 (C4A,B and C), 138.7 (C1A,B and C), 174.7 (C8A,B and C), 175.1 (C7A,B and C).

It is worth noting here that the initial Co^{II} salt must have been oxidized to Co^{III} to form the desired metal complex. This was not the case when MeOH was used to moisten the reaction mixture. Whilst the above mentioned colour

change did indeed occur, paramagnetic “impurities” indicate that the oxidation process was not complete. Varying the use of MeCN to MeOH did not appear to affect the formation of the d^8 metal complexes.

***cis*-bis(*N*-morpholine-*N'*-benzoylthioureato)palladium(II), *cis*-[Pd^{II}(L^{2f}-S,O)₂] **262**:**

Ligand (0.14 mmol) and base (NaHCO₃, 0.28 mmol) were ground together using a mortar and pestle with a few drops of MeOH to form a paste. A slight molar excess of K₂PdCl₄ (0.08 mmol) was added to the mixture, followed by more MeOH and grinding. Excess base and metal ions were removed by washing with water, centrifugation and drying yielded the desired complex.

Yield (66%). mp 217.3 – 218.6 °C. Found: C, 47.1; H, 4.0; N, 10.2; S, 11.3. C₂₄H₂₆N₄O₄S₂Pd requires C, 47.6; H, 4.3; N, 9.3; S, 10.6 %. δ_H (400 MHz; CDCl₃): 3.79 (s, 8H, H9A and B, H11A and B), 4.20 (d, 8H, H10A and B, H12A and B), 7.43 (multiplet, 4H, H3A and B, H5A and B), 7.51 (t, 2H, H4A and B), 8.21 (unres m, 4H, H2A and B, H6A and B). δ_C (101 MHz, CDCl₃): 47.4, 49.8 (C9A and B, C11A and B), 66.4, 66.6 (C10A and B, C12A and B), 128.0 (C3A and B, C5A and B), 129.6 (C2A and B, C6A and B), 131.9 (C4A and B), 136.6 (C1A and B), 172.0 (C8A and B), 172.3 (C7A and B).

2.2.4.5 “Mixed ligand” Cd(II) complex

A “mixed ligand” Cd(II) metal complex was also synthesised using the method reported for the synthesis of the (*N,N*-diethyl-*N'*-benzoylselenoureato)cadmium(II).^[10]

(*N,N*-diethyl-*N'*-benzoylselenoureato,*N,N*-diethyl-*N'*-benzoylthioureato)Cd(II), [Cd^{II}(L^{1a}-Se,O)(L^{2a}-S,O)]

11211: Yield (81.6 %). mp 149.6 – 151.8 °C Found: C, 45.2, H, 4.6, N, 8.2, S, 3.7. C₂₄H₃₀N₄O₂SSeCd requires C, 45.8; H, 4.8; N, 8.9; S, 5.1 %. δ_H (400 MHz; CDCl₃): 1.20 (unres m, 6H, H10A/B or H12A/B), 1.30 (unres m, 6H, H10A/B or H12A/B), 3.72 (unres m, 4H, H9A/B or H11A/B), 3.91 (unres m, 4H, H9A/B or H11A/B), 7.32 (multiplet, 4H, H3A and B, H5A and B), 7.41 (m, 2H, H4A and B), 8.05 (m, 4H, H2A and B, H6A and B). δ_C (101 MHz, CDCl₃): 12.9, (C10B/C12B), 13.0 (C10A/C12A), 13.1, (C10B/C12B), 13.5 (C10A/C12A), 45.8 (C9A/B, C11A/B), 46.3 (C9B/C11B), 48.0 (C9A/C11A), 127.5 (C3A, C5A), 127.6 (C3B, C5B), 129.3 (C2B, C6B), 129.5 (C2A, C6A), 130.9 (C4B), 131.1 (C4A), 137.8 (C1B), 137.9 (C1A), 167.7 (C8A), 170.3 (C8B), 171.0 (C7A), 176.9 (C7B). δ_{Se} (76 MHz; CDCl₃): 47.3. δ_{Cd} (89 MHz; CDCl₃): -242. Where ring A refers to selenourea and ring B to thiourea resonances.

2.2.4.6 3,3,3',3'-tetra(*n*-butyl)-1,1'-terephthaloylbis(thiourea) Pd(II) complex

The Pd(II) complex of 3,3,3',3'-tetra(*n*-butyl)-1,1'-terephthaloylbis(thiourea) (**22222**) was synthesized using the solvent extraction method described for the monopedal derivatives.

3,3,3',3'-tetra(*n*-butyl)-1,1'-terephthaloylbis(thioureato)palladium(II), *cis*-[Pd^{II}₃(L^{m2b}-S,O)₃], **22222:**

Yield (95.3 %). mp 277.5 – 279 °C. Found: C, 50.3; H, 6.2; N, 8.6; S, 9.6. C₇₈H₁₂₀N₁₂O₆S₆Pd·CH₃CH₂OH·CHCl₃ requires C, 49.1; H, 6.4; N, 8.5; S, 9.7 %. δ_H (400 MHz; CDCl₃): δ 0.96 (m, 36H, H36, H310, H66, H610), 1.39 (m, 24H, H35, H39, H65, H69), 1.72 (m, 24H, H34, H38, H64, H68), 3.79 (m, 24H, H33, H37, H63, H67), 8.31 (s, 12H, H1, H2, H4, H5). δ_C (101 MHz; CDCl₃): 13.8 (C36, C310/ C66, C610), 13.9 (C36, C310/ C66, C610), 20.2 (C35, C39, C65, C69), 20.3 (C35, C39, C65, C69), 29.5 (C34, C38/C64, C68), 29.9 (C34, C38/C64, C68), 51.7 (C33,

C37/C63, C67), 52.8 (C33, C37/C63, C67), 129.3 (C1, C2, C4, C5), 139.7 (C3, C6), 169.7 (C32, C62), 171.3 (C31, C61).

2.2.5 General methods and instrumentation

All reagents and solvents were commercially available, and used without further purification excluding the acetone used in ligand synthesis, which was distilled before use, as well as the KSeCN and KSCN which were dried in a vacuum oven at 70 °C prior to use.

¹H and ¹³C NMR spectra were recorded on either a 400 MHz Varian^{Unity} Inova spectrometer equipped with an Oxford magnet (9.4 T) operating at 400 MHz for ¹H and 100 MHz for ¹³C or a 600 MHz Varian^{Unity} Inova spectrometer equipped with an Oxford magnet (14.09 T) operating at 600 MHz for ¹H and 150 MHz for ¹³C. All samples were measured in deuterated chloroform at concentrations in the order of 10⁻² M. Proton chemical shifts are quoted relative to the residual CHCl₃ solvent resonance at 7.26 ppm, and ¹³C chemical shifts relative to the CDCl₃ triplet at 77.0 ppm. (centre peak). *J* values are given in Hz. HSQC and HMQC spectra were collected with pulse sequences developed by the Darmstadt NMR application laboratory of Varian GmbH (ghsqc_da and ghmqc_da respectively). HMQC spectra were optimized for ³J_{H-C} couplings. All resonances were assigned by making use of chemical shift values, proton coupling constants where suitable, H-H COSY, and C-H GHSQC and GHMCQ relationships giving single and multiple C-H bond correlations respectively. ¹⁹⁵Pt spectra were run at 30 °C and externally referenced to 500 mg/cm³ H₂PtCl₆ in 30% (v/v) D₂O/1M HCl. ⁷⁷Se NMR were run at 25 °C and externally referenced to a 0.1-0.2 M solution of KSeCN with the following solvent ratios: 0.5 ml CDCl₃/2.5 ml DMSO.^[74] ¹¹³Cd NMR were run at 25 °C and externally referenced to a 4.5 M aqueous soln of Cd(NO₃)₂·4H₂O.^[75, 76] ³¹P NMR were run 25 °C and externally referenced to H₃PO₄.

Elemental analyses were performed on a Heraeus Universal Combustion Analyser, Model CHN-Micro courtesy of the University of Cape Town. On several occasions throughout the course of this work, great difficulty was experienced in obtaining accurate elemental analysis results. Several crystalline compounds were analysed at the University of Stellenbosch using an EA Euro 3000 instrument, however these results exhibited even less consistency than those obtained using the Heraeus instrument.

Melting points were obtained using an Electrothermal digital melting point apparatus. Model Nm IA9300.

Thermogravimetric analyses (TGA) of selected compounds were performed using a TG Instruments Q500 thermogravimetric analyser where the samples were maintained in a nitrogen atmosphere and heated at a rate of 10 °/min.

Selected metal complexes were heated in a Labofurn Model 3A Ramp controller furnace under N₂, in small glass crucibles inside a quartz reactor. The heating rate was programmed to reach 450 °C within 60 minutes, followed by a further 4 hours of heating at this temperature.

Powder X-ray diffraction was performed using a Bruker D8 ADVANCE with Bragg-Brentano geometry instrument with a Cu radiation source and dynamic scintillation detector.

Energy Dispersive X-Ray Spectroscopy used was attached to a Leo 1430VP Scanning Electron Microscope.

2.2.6 Crystallography and Structure refinement

Data collection for single-crystal determinations were performed on a SMART APEX CCD (Bruker-Nonius). Cell refinement and data reduction was performed using SAINT (Bruker-Nonius). Initial structure solutions were performed using SHELXS 97 and atomic positions were located from a difference fourier map. The refinement method was full matrix least squares on F^2 using SHELXL 97. Molecular graphics were generated *via* XSeed using POV-Ray. All hydrogen atoms were placed in geometrically calculated positions with C–H = 0.99 Å, (for –CH₂); 0.98 Å, (for –CH₃); 0.95 Å, (for phenyl) and refined using a riding model with $U_{\text{iso}}(\text{H}) = 1.2 U_{\text{eq}}$ (parent), for –CH₂ and phenyl or $U_{\text{iso}}(\text{H}) = 1.5 U_{\text{eq}}$ (parent) for –CH₃.

2.3 Results and Discussion

As previously mentioned, the *N,N*-dialkyl-*N'*-benzoylselenoureas were found to be less stable than the corresponding *N,N*-dialkyl-*N'*-benzoylthioureas. Whilst a wide variety of acyl- and aroyl-thioureas could be synthesized, attempts to isolate *N,N*-dialkyl-*N'*-acylselenoureas were unsuccessful and in retrospect this is not surprising as almost all the literature reporting the synthesis of these compounds refers to the preparation of *N'*-benzoyl derivatives.^[1, 2, 9, 10, 22] In general, if the benzoylselenoureas were isolated from solution within approximately 48 hours, fair yields could be obtained, however extended periods of standing frequently resulted in the development of a red colour accompanied with a foul smell, suggesting further reaction or decomposition and consequently very low product yields. It has previously been noted that the larger atomic size of selenium, allows Se containing compounds an increased polarizability making them “less stable” than their S analogues.^[77] Offensive smelling by-products in these reactions have also been reported^[1] as has the development of red coloured by-products, although no mention was made of possible structures.^[77, 78]

2.3.1 Crystal and molecular structures of *N,N*-dialkyl-*N'*-benzoylselenourea ligands

Several *N,N*-dialkyl-*N'*-benzoylselenourea solid state structures are discussed in this section, and the crystal and refinement data for each is given in Table 2.34 at the end of the section.

2.3.1.1 Crystal and molecular structure of *N,N*-diethyl-*N'*-benzoylselenourea, HL_{Se}^{1a}

Despite several structural characterizations of various metal complexes of *N,N*-diethyl-*N'*-benzoylselenourea being reported, no structural elucidation of the ligand, HL_{Se}^{1a} could be found.^[11-15] Recrystallization from an ethanolic solution yielded suitable crystals and the molecular structure of HL_{Se}^{1a} is shown in Fig. 2.31 (A). Relevant bond lengths and torsion angles are given in Table 2.31. Fig. 2.31 (B) shows the intermolecular hydrogen bonding exhibited by this ligand, where the selenoamidic proton is involved in a weak hydrogen bond with the selenium atom of a neighbouring molecule (symmetry code 1-*x*, 1-*y*, -*z*) N(H)⋯Se = 2.70 Å, N – Se = 3.532 (2) Å and Se⋯H-N = 168.4°. The selenoamidic proton of this molecule in turn, forms a weak hydrogen bond with the selenium atom of the original molecule, so resulting in a weakly hydrogen bonded dimer in the crystal structure.^[79] Interestingly, this hydrogen bonding is quite different to that exhibited by the sulfur analogue (HL_S2a)^[80] in which hydrogen bonding takes place between the thioamidic proton and the oxygen atom of a neighbouring molecule, leading to chains of hydrogen bonded molecules parallel to the *b* axis in the crystal lattice and no evidence of “dimerisation” displayed by the selenium analogue is evident. In HL_S^{2a} four molecules are present in the asymmetric unit and the average hydrogen bonding distances are N(H)⋯O = 2.03 Å, N – O = 2.870 (3) Å and 6⋯H-N = 161°.

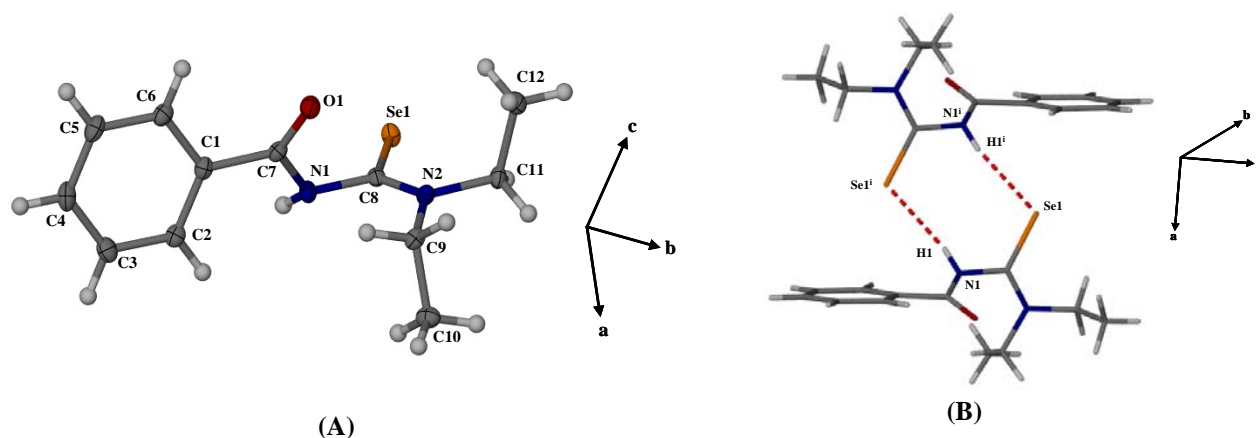


Fig. 2.31 The molecular structure of *N,N*-diethyl-*N'*-benzoylselenourea $\text{HL}_{\text{Se}}^{1a}$ with atom numbering scheme shown, displacement ellipsoids are drawn at the 50 % probability level (A) and intermolecular hydrogen bonding exhibited by $\text{HL}_{\text{Se}}^{1a}$. [Symmetry code (i) $1-x, 1-y, -z$.] (B).

2.3.1.2 Crystal and molecular structure of *N,N*-dibutyl-*N'*-benzoylselenourea, $\text{HL}_{\text{Se}}^{1b}$

Crystals of *N,N*-dibutyl-*N'*-benzoylselenourea, $\text{HL}_{\text{Se}}^{1b}$ (Fig. 2.32(A)) were grown from a saturated ethanolic solution and crystallized in the space group $P2_1/c$. Relevant bond lengths and torsion angles are given in Table 2.31. As shown in Fig. 2.32 (B), the molecules of $\text{HL}_{\text{Se}}^{1b}$ are linked through a hydrogen bond between the selenoamidic proton of one molecule and the Se atom of its neighbour at $(-x, 1-y, 1-z)$, with $\text{N}-\text{H}\cdots\text{Se} = 2.756 \text{ \AA}$, $\text{N}\cdots\text{Se} = 3.538 (2) \text{ \AA}$ and $\text{Se}\cdots\text{H}-\text{N} = 159^\circ$ so giving rise to a dimer linked through such hydrogen bonds in the crystal structure, in a similar fashion to that of $\text{HL}_{\text{Se}}^{1a}$. This dimer forms an eight-membered ring structure where the atoms $\text{H1}/\text{N1}/\text{C8}/\text{Se1}/\text{H1}^i/\text{N1}^i/\text{C8}^i/\text{Se}^i$ [symmetry code: (i) $(-x, 1-y, 1-z)$] lie in a plane with a maximum deviation of 0.119

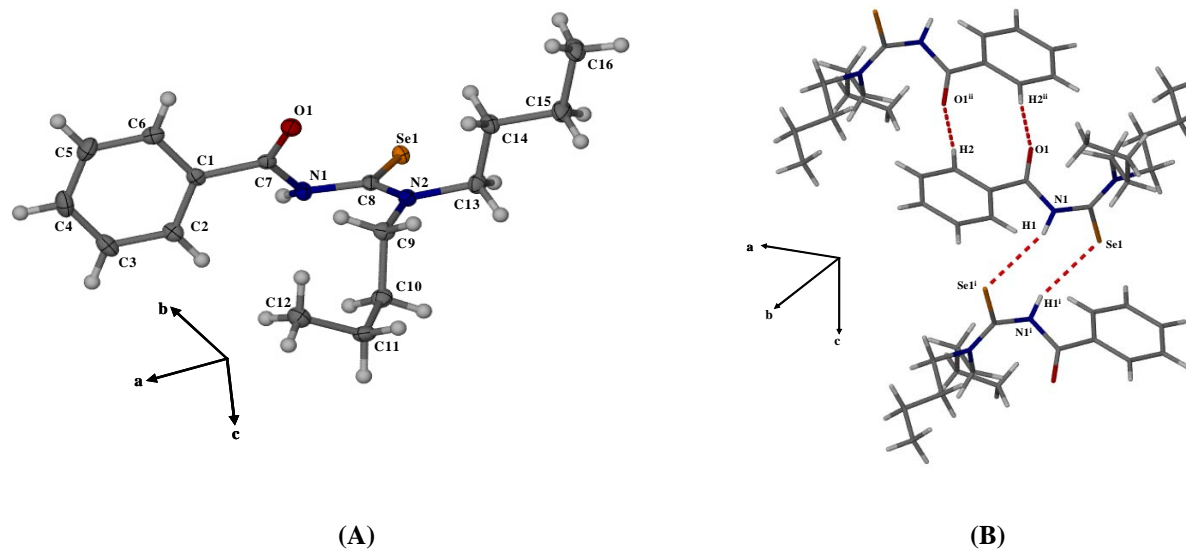


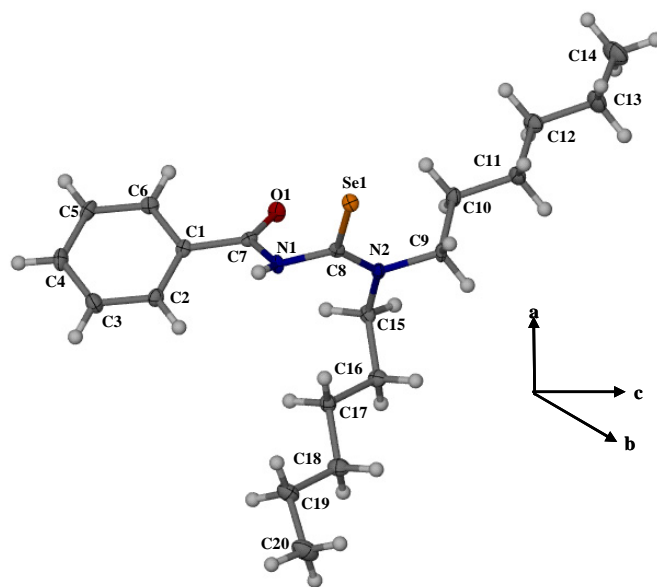
Fig. 2.32 The molecular structure of *N,N*-dibutyl-*N'*-benzoylselenourea $\text{HL}_{\text{Se}}^{1b}$ with atom numbering scheme shown, displacement ellipsoids are drawn at the 50 % probability level (A) and intermolecular hydrogen bonding exhibited by $\text{HL}_{\text{Se}}^{1b}$. [Symmetry codes (i) $1-x, 1-y, -z$, (ii) $-x, 1-y, -z$] (B).

A second dimeric hydrogen bond is present in $\text{HL}_{\text{Se}}^{1b}$ between the carbonyl O atom and an H atom on the benzene residue at $(-x, 1-y, -z)$, with $\text{C6}-\text{H6}\cdots\text{O1} = 2.481 \text{ \AA}$, $\text{C6}\cdots\text{O1} = 3.407 (3) \text{ \AA}$ and $\text{O1}\cdots\text{H6}-\text{C6} = 173.7^\circ$. Similarly to the first dimer, this forms a ten-membered ring structure where the atoms $\text{O1}/\text{C7}/\text{C1}/\text{C6}/\text{H6}/\text{O1}^{\text{ii}}/\text{C7}^{\text{ii}}/\text{C1}^{\text{ii}}/\text{C6}^{\text{ii}}/\text{H6}^{\text{ii}}$ [symmetry code: (ii) $-x, 1-y, -z$] again lie in a plane, with a maximum deviation of $0.241 (2) \text{ \AA}$ for atom O1, the

angle between these two planes being $82.36(2)^\circ$. It is interesting to note that the second hydrogen bond is not evident in the solid-state structures of any other *N,N*-dialkyl-*N'*-benzoylselenoureas that were analysed. These two dimers give rise to the hydrogen-bonded chains shown in Fig. 2.32 (B) that form in the direction of the *c* axis. There is little interaction apparent between these chains.^[81]

2.3.1.3 Crystal and molecular structure of *N,N*-dihexyl-*N'*-benzoylselenourea, $\text{HL}_{\text{Se}}^{1c}$

N,N-dihexyl-*N'*-benzoylselenourea, $\text{HL}_{\text{Se}}^{1c}$ was also successfully crystallized from ethanol and Fig. 2.33 (A) shows the molecular structure Fig. 2.33 (B) illustrating the various intermolecular interactions. Similarly to the previous two molecular structures, $\text{HL}_{\text{Se}}^{1c}$ exhibits intermolecular hydrogen bonding between the selenoamidic proton of one molecule and the Se atom of its neighbour at $(-x, 1-y, 1-z)$, with $\text{N-H} \cdots \text{Se} = 2.77(4) \text{ \AA}$, $\text{N} \cdots \text{Se} = 3.533(3) \text{ \AA}$ and $\text{Se} \cdots \text{H-N} = 153^\circ$ so giving rise to a dimer linked through such hydrogen bonds in the crystal structure. Interestingly, $\text{HL}_{\text{Se}}^{1c}$ also exhibits a $\pi - \pi$ stacking interaction between the benzene residues of two neighbouring molecules. A plane defined between the 6 aromatic carbons C1/C2/C3/C4/C5/C6 exhibited a root mean square (r.m.s.) deviation of 0.0063 with C6 exhibiting the largest deviation of 0.008 (3) \AA . The average interplanar spacing between two neighbouring residues [symmetry code (ii) $-x, -y, 1-z$] is 3.4732 (26) \AA . No evidence of similar interactions could be found in the structures of $\text{HL}_{\text{Se}}^{1a}$ and $\text{HL}_{\text{Se}}^{1b}$.



(A)

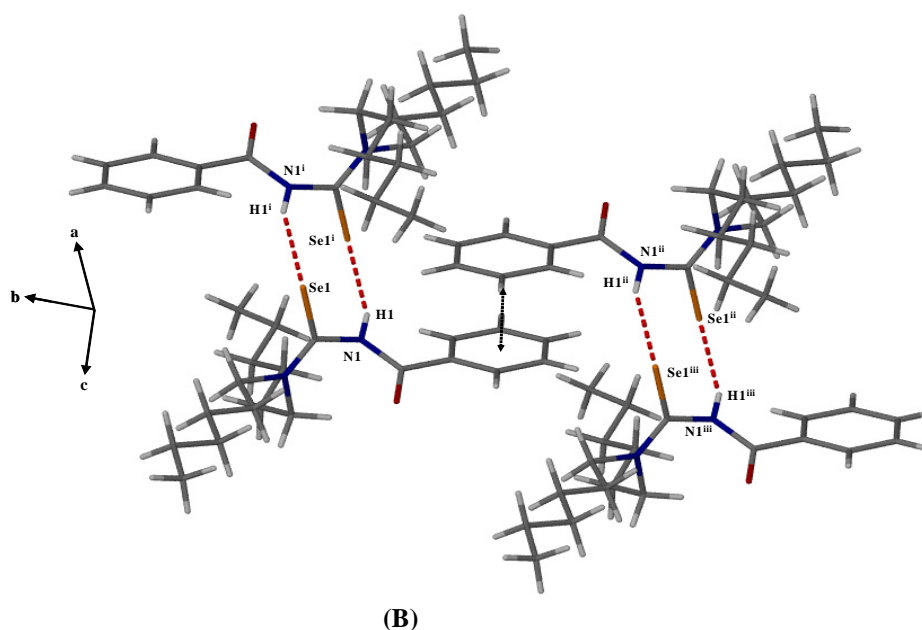
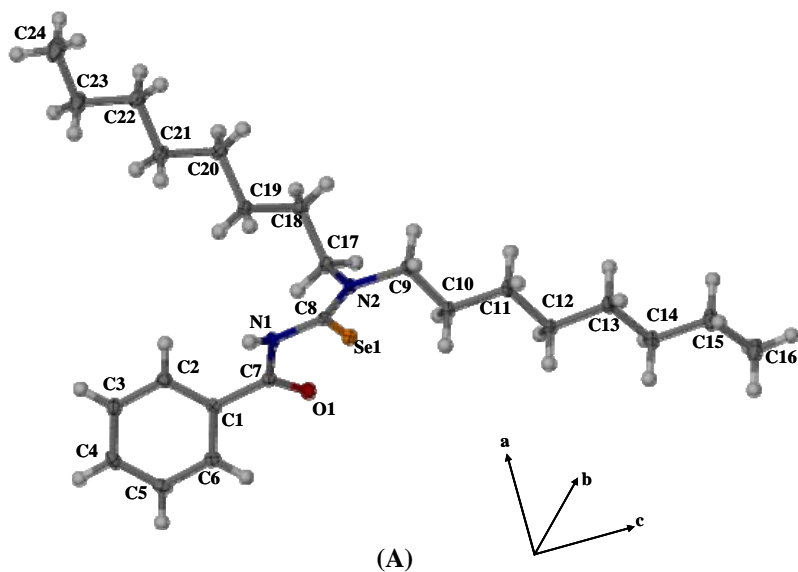


Fig. 2.33 The molecular structure of *N,N*-dihexyl-*N'*-benzoylselenourea $\text{HL}_{\text{Se}}^{1c}$ with atom numbering scheme shown, displacement ellipsoids are drawn at the 50 % probability level (A) and intermolecular hydrogen bonding exhibited by $\text{HL}_{\text{Se}}^{1c}$ as well as $\pi - \pi$ interactions. [Symmetry codes (i) $-x, 1-y, 1-z$, (ii) $-x, -y, 1-z$, (iii) $x, y-1, z$] (B).

2.3.1.4 Crystal and molecular structure of *N,N*-dioctyl-*N'*-benzoylselenourea, $\text{HL}_{\text{Se}}^{1d}$

Recrystallization of *N,N*-dioctyl-*N'*-benzoylselenourea, $\text{HL}_{\text{Se}}^{1d}$ from ethanol yielded crystals suitable for analysis and Fig 2.34 (A and B) illustrate the molecular structure and intermolecular interactions respectively.

$\text{HL}_{\text{Se}}^{1d}$ displays intermolecular hydrogen bonding between the selenoamidic proton of one molecule and the Se atom of its neighbour at $(2-x, 3-y, 1-z)$, with $\text{N-H} \cdots \text{Se} = 2.85(2) \text{ \AA}$, $\text{N} \cdots \text{Se} = 3.553(2) \text{ \AA}$ and $\text{Se} \cdots \text{H-N} = 149(2)^\circ$, giving rise to the expected hydrogen bonded dimer. Similar to $\text{HL}_{\text{Se}}^{1c}$, the dioctyl derivative ($\text{HL}_{\text{Se}}^{1d}$) also exhibits a $\pi - \pi$ interaction between the benzene residues of two neighbouring molecules. A plane defined by the 6 aromatic carbons C1/C2/C3/C4/C5/C6 exhibited a r.m.s. deviation of 0.0038, C3 this time giving rise to the maximum deviation of



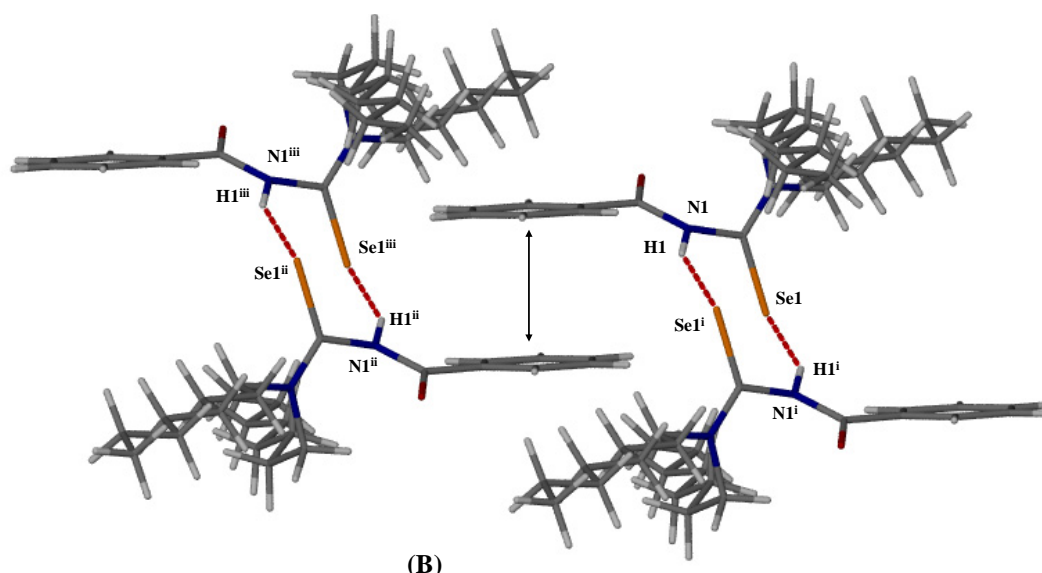


Fig. 2.34 The molecular structure of *N,N*-dioctyl-*N'*-benzoylselenourea $\text{HL}_{\text{Se}}^{1\text{d}}$ with atom numbering scheme shown, displacement ellipsoids are drawn at the 50 % probability level (A) and intermolecular hydrogen bonding exhibited by $\text{HL}_{\text{Se}}^{1\text{d}}$ as well as $\pi - \pi$ interactions. [Symmetry codes (i) $2-x, 3-y, 1-z$, (ii) $-x, 2-y, 1-z$, (iii) $x, y-1, z$] (B).

0.0057 (14) Å. The average interplanar spacing between two neighbouring residues [symmetry code (ii) $-x, 2-y, 1-z$] was found to be 3.4718 (159) Å, this distance being comparable to that displayed in $\text{HL}_{\text{Se}}^{1\text{c}}$.

2.3.1.5 Crystal and molecular structure of *N*-methyl-*N*-benzyl-*N'*-benzoylselenourea, $\text{HL}_{\text{Se}}^{1\text{e}}$

Selected bond lengths and torsion angles of the solid state structures of the *N,N*-dialkyl-*N'*-benzoylselenourea ligands will be discussed following section 2.3.1.7 however the partial double bond character of the (E)C-NR₂ bond (where E = S, Se) needs to briefly be discussed here. The (E)C-NR₂ bond length in these and other related solid state structures is consistently shorter than the average C-N single bond length of 1.472 Å, but longer than that expected for a double bond.^[82] This results in partial double bond character and limited rotation about this bond, where a degree of magnetic inequivalence arises in the amine residues. Where an asymmetrically substituted amine is used ($\text{HL}_{\text{Se}}^{1\text{e}}$ and $\text{HL}_{\text{S}}^{2\text{e}}$) the formation of *E* and *Z* isomers occurs as shown in Fig. 2.35.^[83] The NMR spectroscopy of these ligands and their metal complexes will be discussed in more detail in section 2.3.5.2.

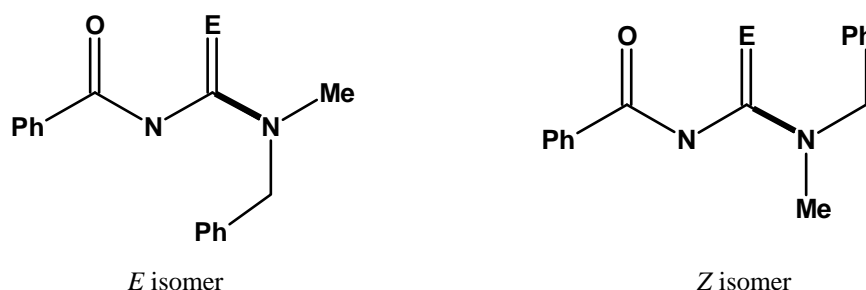


Fig. 2.35 *E* and *Z* isomerisation exhibited by *N*-methyl-*N*-benzyl-*N'*-benzoylseleno-thioureas where E = Se, S.

Crystals of *N*-methyl-*N*-benzyl-*N'*-benzoylselenourea, $\text{HL}_{\text{Se}}^{1e}$ were grown from ethanolic solution and analysed. Fig. 2.36 (A and B) illustrate the molecular structure and intermolecular interactions.

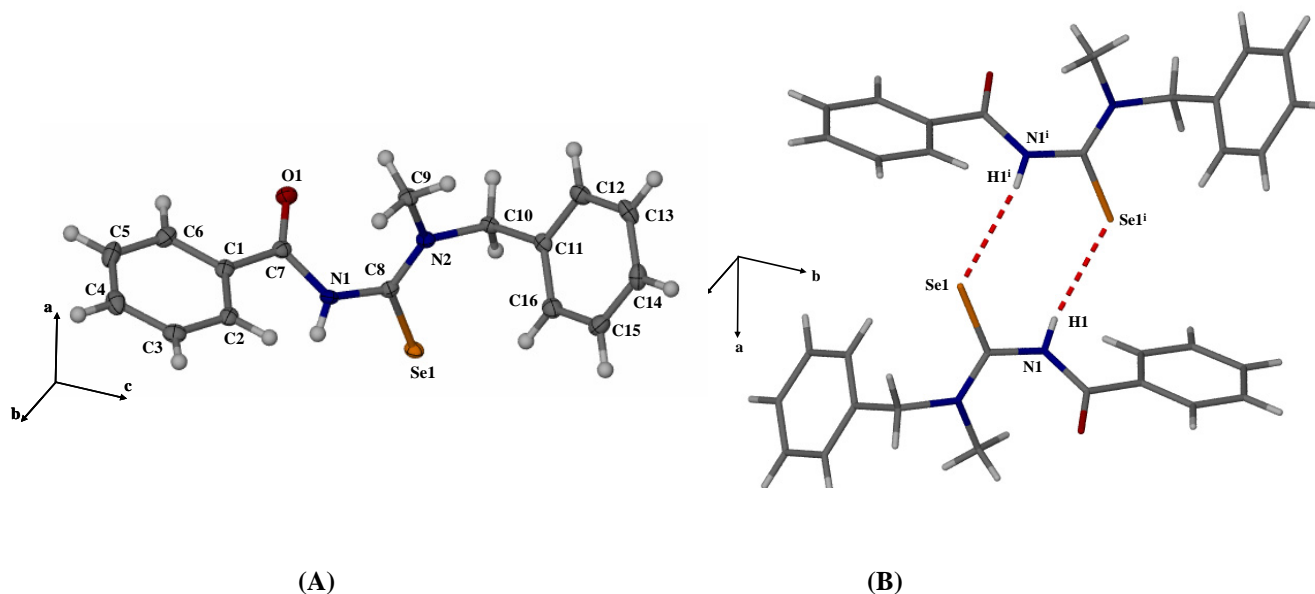


Fig. 2.36 The molecular structure of *N*-methyl-*N*-benzyl-*N'*-benzoylselenourea, $\text{HL}_{\text{Se}}^{1e}$ with atom numbering scheme shown, displacement ellipsoids are drawn at the 50 % probability level (A) and (B) intermolecular hydrogen bonding exhibited by $\text{HL}_{\text{Se}}^{1e}$. [Symmetry code (i) 1-*x*, 1-*y*, 1-*z*.]

From Fig. 2.36 (A) it is apparent that the *Z* isomer of $\text{HL}_{\text{Se}}^{1e}$ is the most stable in the solid state. To the best of our knowledge, this is the first time that a structural characterization of an asymmetrically substituted benzoylselenourea has been reported. Interestingly, despite the presence of two benzene residues in this molecule, no $\pi - \pi$ interactions exhibited by the longer alkyl chain analogues were evident in the crystal lattice of this molecule. The intermolecular hydrogen bonding between the selenoamidic proton of one molecule and the Se atom of its neighbour at (1-*x*, 1-*y*, 1-*z*), leading to dimer formation, was however maintained, where $\text{N-H} \cdots \text{Se} = 2.73$ (3) Å, $\text{N} \cdots \text{Se} = 3.503$ (2) Å and $\text{Se} \cdots \text{H-N} = 169$ (2) °.

2.3.1.6 Crystal and molecular structure of *N,N*-didecyl-*N'*-benzoylselenourea, $\text{HL}_{\text{Se}}^{1f}$

Crystals of *N,N*-didecyl-*N'*-benzoylselenourea, $\text{HL}_{\text{Se}}^{1f}$ suitable for single crystal analysis were isolated from ethanolic solution and the molecular structure and intermolecular interactions exhibited by the compound are shown in Fig. 2.37 (A and B). In keeping with the trend exhibited by the longer alkyl chain derivatives, $\text{HL}_{\text{Se}}^{1f}$ displays two types of intermolecular interactions. Hydrogen bonding between the selenoamidic proton of one molecule and the Se atom of a neighbouring molecule (1-*x*, 2-*y*, -*z*), with $\text{N-H} \cdots \text{Se} = 2.80$ (2) Å, $\text{N} \cdots \text{Se} = 3.519$ (2) Å and $\text{Se} \cdots \text{H-N} = 152.9$ (2) °, giving rise to the expected dimer formation, as well as $\pi - \pi$ stacking interactions between the benzene residues of two neighbouring molecules. A plane defined by the 6 aromatic carbons C1/C2/C3/C4/C5/C6 exhibited a r.m.s. deviation of 0.0091, C6 giving rise to the maximum deviation of 0.0122 (13) Å. The average interplanar spacing between two neighbouring benzene residues [symmetry code (ii) 1-*x*, 1-*y*, -*z*] is 3.4292 (116) Å, this distance being slightly smaller than that displayed in both $\text{HL}_{\text{Se}}^{1c}$ and $\text{HL}_{\text{Se}}^{1d}$.

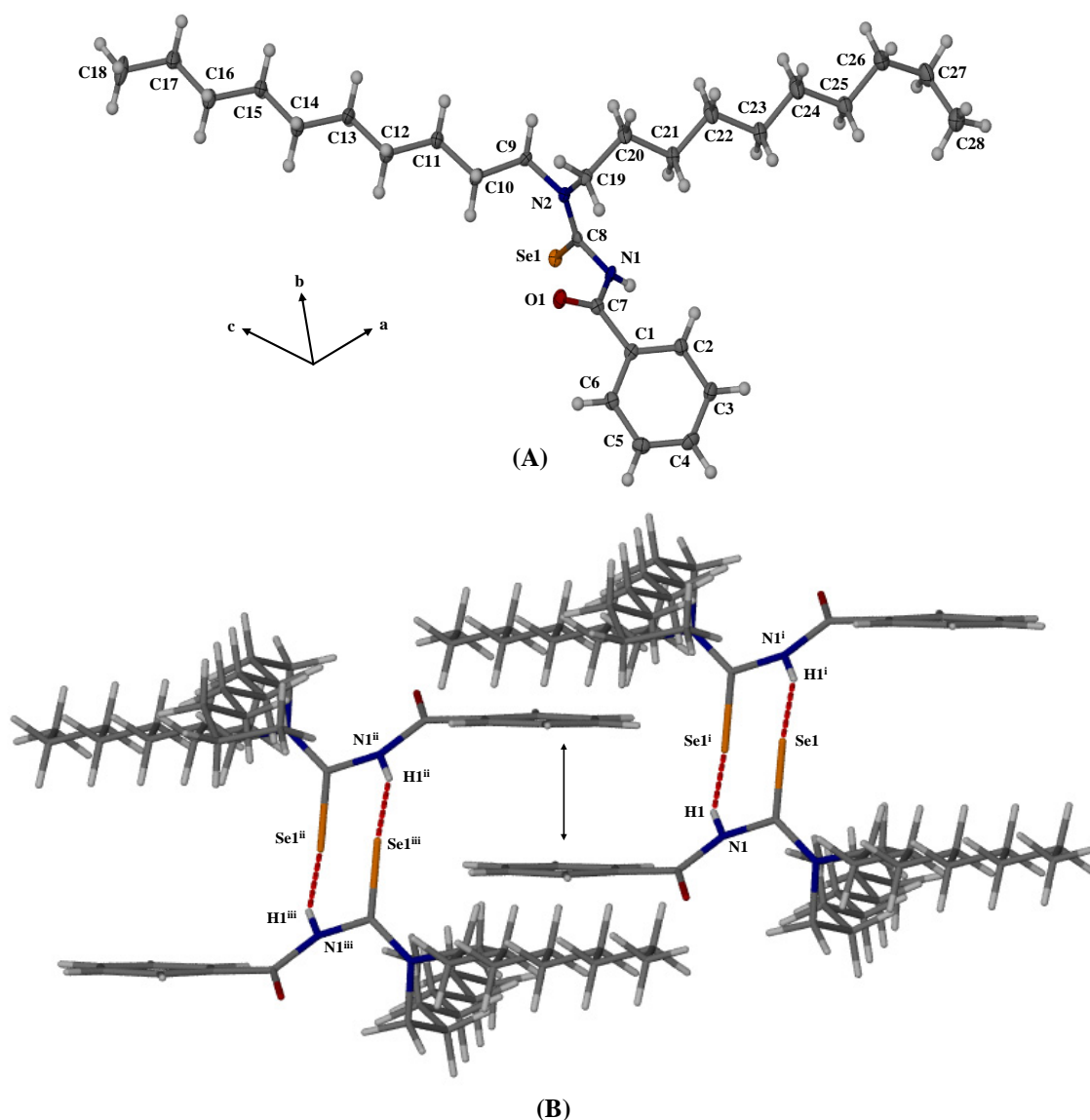


Fig. 2.37 The molecular structure of *N,N*-didecyl-*N'*-benzoylselenourea $\text{HL}_{\text{Se}}^{1f}$ with atom numbering scheme shown, displacement ellipsoids are drawn at the 50 % probability level (A) and intermolecular hydrogen bonding exhibited by $\text{HL}_{\text{Se}}^{1f}$ as well as $\pi - \pi$ interactions. [Symmetry codes (i) 1-*x*, 2-*y*, -*z*, (ii) 1-*x*, 1-*y*, -*z*, (iii) *x*, *y*-1, *z*] (B).

2.3.1.7 Crystal and molecular structure of *N,N*-diphenyl-*N'*-benzoylselenourea, $\text{HL}_{\text{Se}}^{1g}$

N,N-diphenyl-*N'*-benzoylselenourea, $\text{HL}_{\text{Se}}^{1g}$ crystals isolated from ethanolic solution were analysed by single crystal X-ray diffraction. Fig. 2.38 (A and B) shows the molecular structure as well as the interesting intermolecular interactions exhibited by this molecule.

$\text{HL}_{\text{Se}}^{1g}$ is the only compound in the benzoylselenourea ligand series which does not exhibit an intermolecular hydrogen bond between the selenoamidic proton and the Se atom of a neighbouring molecule. An intermolecular hydrogen bond between the carbonyl O atom and an H atom on a neighbouring benzene residue (1-*x*, 1-*y*, 1-*z*), with $\text{C6}\cdots\text{H6}\cdots\text{O1} = 2.40 \text{ \AA}$, $\text{C6}\cdots\text{O1} = 3.282(5) \text{ \AA}$ and $\text{O1}\cdots\text{H6}\cdots\text{C6} = 154.2^\circ$ is found instead. This is slightly shorter than the similar bond exhibited by $\text{HL}_{\text{Se}}^{1b}$ with a $\text{C6}\cdots\text{O1}$ distance of $3.407(3) \text{ \AA}$ and a slightly larger $\text{O1}\cdots\text{H6}\cdots\text{C6}$ angle of 173.7° .^[81] Interestingly $\text{HL}_{\text{Se}}^{1g}$ displays a short interaction between two neighbouring Se atoms (1-*x*, *y*, $\frac{1}{2}$ -*z*) with a

distance of 2.3237 (9) Å. This compares most favourably with previously reported Se-Se single bond distances in the range 2.3 – 2.447 Å,^[84, 85] and this interaction can therefore be classified as a bond. As will be discussed in Section 2.3.5.3, there is clear NMR evidence that the Se-Se bond persists in solution and therefore this molecule may be more correctly referred to as a diselenide.

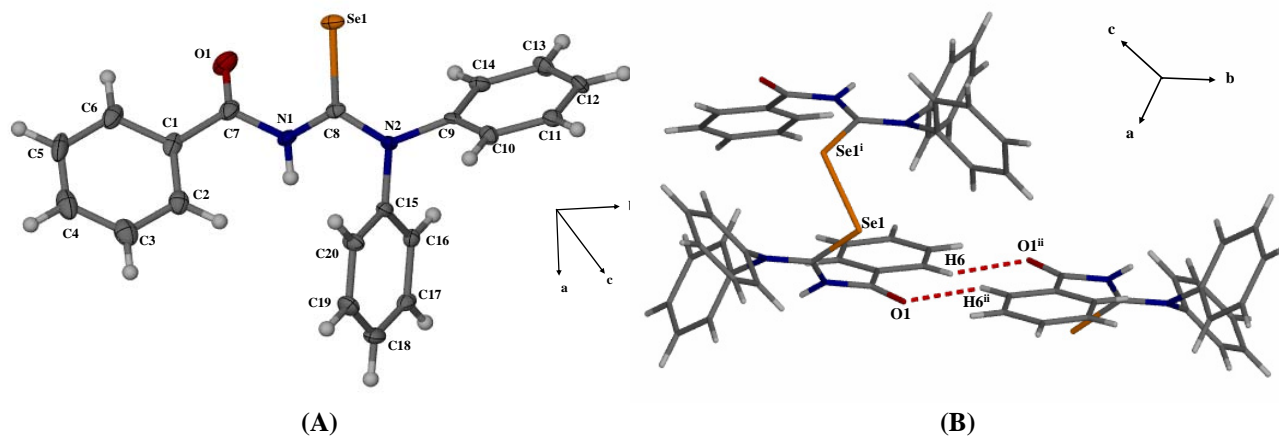


Fig. 2.38 The molecular structure of *N,N*-diphenyl-*N'*-benzoylselenourea $\text{HL}_{\text{Se}}^{1g}$ with atom numbering scheme shown, displacement ellipsoids are drawn at the 50 % probability level (A) and intermolecular hydrogen bonding exhibited by $\text{HL}_{\text{Se}}^{1g}$ as well as an intermolecular Se-Se bond. [Symmetry codes (i) 1-*x*, *y*, 1/2-*z*, (ii) 1-*x*, 1-*y*, 1-*z*.](B).

Previously, it has been found that 1-methyl-4-imidazoline-2-selone is unstable under aerobic conditions and can readily be oxidized to form the diselenide.^[86] Several studies on the more closely related 6-*n*-propyl-2-selenouracil and its alkyl derivatives have led to the formation of diselenides following acetone recrystallization of 6-*n*-propyl- and -ethyl-2-selenouracil iodine adducts (Fig. 2.39). Interestingly the diselenides formed were uncharged and not dications (which have previously been reported for related structures).^[87] Se-Se bond distances reported for the -ethyl- and -propyl- derivatives, [*N*-(6'-ethyl-4'-pyrimidone)(6-ethyl-2-selenouracil)(Se-Se)] and [*N*-(6'-*n*-propyl-4'-pyrimidone)(6-*n*-propyl-2-selenouracil)₂(Se-Se)], were 2.4328 (9) and 2.4427 (6) Å respectively,^[88] falling within the range reported for other diselenoamides (2.34 – 2.59 Å).^[89-92] The 2.3237 (9) Å observed in $\text{HL}_{\text{Se}}^{1g}$ is however slightly shorter than the lower limit of this range, strongly suggesting a Se-Se bond.

The bond order^[93] calculated for the range of bond lengths exhibited by the diselenoamides varies from 1.0330–0.4592, the bond order calculated for the Se-Se bond in $\text{HL}_{\text{Se}}^{1g}$ is 1.0890* validating its classification as a “diselenide” rather than a “selenourea”. The C-Se bond lengths for the diselenoamides range between 1.874 and 1.952 Å, where the 1.966 (3) Å in $\text{HL}_{\text{Se}}^{1g}$ falls slightly outside the upper limit of this range. Where the diselenoamides do not display an inversion centre, the C-Se-Se-C torsion angle varies between 50.67 and 93.1 °,^[89, 94] the 93.5 ° displayed by $\text{HL}_{\text{Se}}^{1g}$ compares well to this range.

* Bond order calculated using $n = 10^{(2.35-d) / 0.71}$, where *n* = bond order, *d* = Se-Se bond distance. Taken from Ref [87].

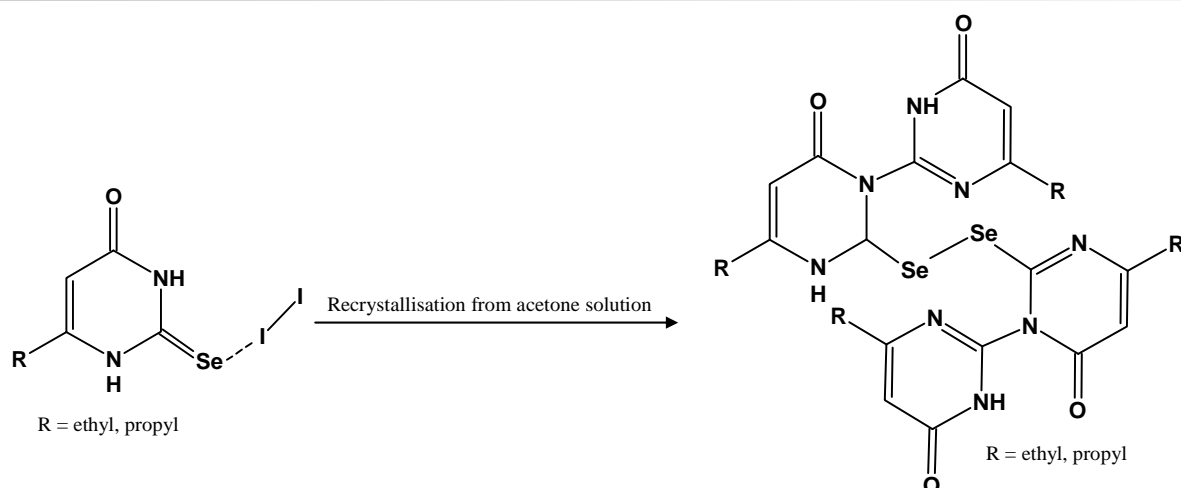


Fig. 2.39. Graphical representation of diselenide formation. Adapted from Ref.[88] by Antoniadis and co-workers.

In the context of this work, the presence of the diselenide oxidation product is consistent with results previously obtained by Grimmacher, where attempts were made to isolate Cu(II) complexes of the related *N*-alkyl-*N'*-benzoylthioureas. Spectroscopic evidence was obtained suggesting the formation of a disulfide as a by-product (Fig. 2.310), the Cu(I) complex of the desired ligand also being isolated.^[95]

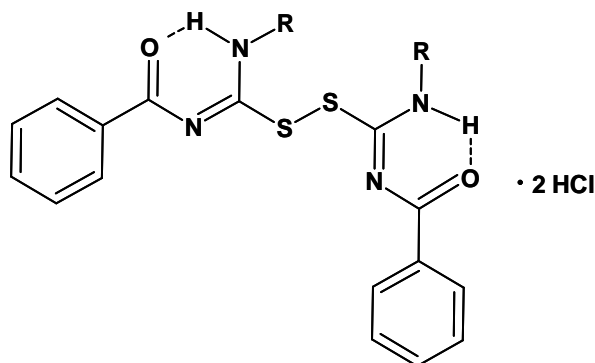


Fig. 2.310 Schematic representation of the hydrochloride disulfide derivative, one of the by-products isolated from reaction of *N*-alkyl-*N'*-benzoylthioureas with Cu(II) acetate. Adapted from Ref [95].

It is noteworthy that no evidence of diselenide formation was apparent when dialkylamines were used in the ligand synthesis, suggesting that the diphenylamine residue may have electronically contributed in some way to the formation of the diselenide, $\text{HL}_{\text{Se}}^{1g}$. Dissociation constants of all the dialkylamines used were not readily available, however there is a relatively small difference in *pK*_a values of diethylamine (10.49) and *n*-ethylamine (10.81), justifying a comparison between the *pK*_a values of the monoalkylamines, these being readily available.^[96] The *pK*_a values of the alkylamines vary little with alkyl chain length and fall in the range 10.64 (*n*-decylamine) – 10.81 (*n*-ethylamine). Remarkably, that of diphenylamine is 0.79, clearly showing a greatly reduced basicity relative to its alkyl analogues. Initially this was thought to partly rationalize the formation of $\text{HL}_{\text{Se}}^{1g}$, however a recent report by Kampf *et al.* has documented a similar diselenidic structure, Bis[diisobutylamino-(2-fluoro)benzoylimino-methylselenide].^[16] The *pK*_a of diisopropylamine is 10.96, a similar value being likely for diisobutylamine, and therefore it is probable that other factors also play a role in the formation of these species. The formation of $\text{HL}_{\text{Se}}^{1g}$ implies that the *N,N*-dialkyl-*N'*-benzoylselenoureas are sensitive to oxidation and partly explains the lower yields obtained for these compounds, as well as the difficulty in forming certain metal complexes as quantitatively as their

sulfur analogues. This is an interesting phenomenon and deserves further systematic study, which was beyond the scope of this work.

Selected bond lengths and angles for compounds **11-18a** are listed in Table 2.31. Those for compounds **11-17** are discussed below and the synthesis and bond lengths of **18a** are discussed in section 2.3.1.8. Table 2.31 shows that the (O)C-N, N-C(Se) and (Se)C-NR₂ bonds are all shorter than the average C-N single bond length of 1.472 (5) Å.^[82] Similar observations have been made for the *N,N*-dialkyl-*N'*-aroylthioureas for which the C-N bond lengths decrease in the order N-C(E) > (O)C-N > E(C)-NR₂, where E = S and this trend appears to largely be maintained for this series, where E = Se.^[97] *N,N*-diphenyl-*N'*-benzoylselenourea, HL_{Se}^{1g} is however an exception to this trend where (O)C-N > N-C(Se) > Se(C)-NR₂, the N-C(Se) bond being particularly short (1.274 (5) Å) relative to that observed in the other compounds. HL_{Se}^{1g} also exhibits a significantly longer C=Se bond of 1.966 (3) Å, comparable to a C-Se bond length, relative to the average C=Se bond length of 1.840 Å seen in the other compounds, however this can be understood in light of the intermolecular Se-Se bond unique to the ligand in the series. The relative orientations of the O and Se atoms can be defined using the following torsion angles: O-C(O)-N(H)-C(Se) and C(O)-N(H)-C(Se)-Se. Data in Table 2.31 indicates that compounds **11-16** exhibit largely opposing orientations of these two atoms however in HL_{Se}^{1g} these atoms are more aligned than in the dialkyl analogues.

Table 2.31 Selected bond lengths (Å) and torsion angles (°) for compounds **11-17** and **18a**.

Compound	C=O	C=Se	(O)C-N	N-C(Se)	(Se)C-NR ₂	O-C(O)-N(H)-C(Se)	C(O)-N(H)-C(Se)-Se
HL _{Se} ^{1a} 11	1.221 (2)	1.834 (2)	1.388 (2)	1.416 (2)	1.320 (2)	-6.8 (2)	-108.3 (1)
HL _{Se} ^{1b} 12	1.212 (3)	1.848 (2)	1.397 (3)	1.399 (3)	1.314 (3)	0.5 (4)	121.1 (2)
HL _{Se} ^{1c} 13	1.224 (2)	1.836 (2)	1.377 (3)	1.410 (3)	1.318 (3)	13.1 (3)	107.4 (2)
HL _{Se} ^{1d} 14	1.216 (2)	1.839 (2)	1.380 (2)	1.410 (2)	1.315 (2)	-11.1 (3)	-110.8 (2)
HL _{Se} ^{1e} 15	1.220 (2)	1.844 (2)	1.383 (3)	1.392 (2)	1.324 (2)	6.1 (3)	-128.5 (2)
HL _{Se} ^{1f} 16	1.218 (2)	1.838 (2)	1.378 (2)	1.407 (2)	1.315 (2)	-14.3 (3)	-107.6 (2)
HL _{Se} ^{1g} 17	1.215 (5)	1.966 (3)	1.386 (5)	1.274 (5)	1.361 (4)	49.6 (6)	2.0 (5)
L _{Se} ^{1h} 18a	1.328 (3)	1.919 (3)	1.333 (3)	1.326 (4)	1.324 (4)	-	-

Table 2.32 shows the hydrogen bonding data of compounds **11-17**. The Se[⋯]H-N dimeric hydrogen bonds are all of comparable length although the Donor-H[⋯]Acceptor angles differ somewhat, HL_{Se}^{1d} exhibiting the smallest of 149 (2) ° and HL_{Se}^{1c} the largest at 169 (2) °. In terms of hydrogen bonding, the benzoylselenourea moiety consists of a donor– acceptor pair connected by a delocalized π-system reflected in the shorter amide and acyl-substituted C–N bonds. The dimer formation evident in the crystal lattices of HL_{Se}^{1a-f} therefore represents as example of resonance-assisted hydrogen bonding (RAHB) or π-bond cooperativity.^[98] In the case of the *N,N*-dialkyl-*N'*-benzoylselenoureas, the selenoamide N-H group becomes a stronger proton donor as the selenium atom accepts a hydrogen bond, this being due to the stabilisation of the zwitterionic resonance form as shown in Fig. 2.3.11(A and B) . This, to the best of our knowledge, is the first time that this observation has been made regarding the *N,N*-dialkyl-*N'*-benzoylselenoureas.

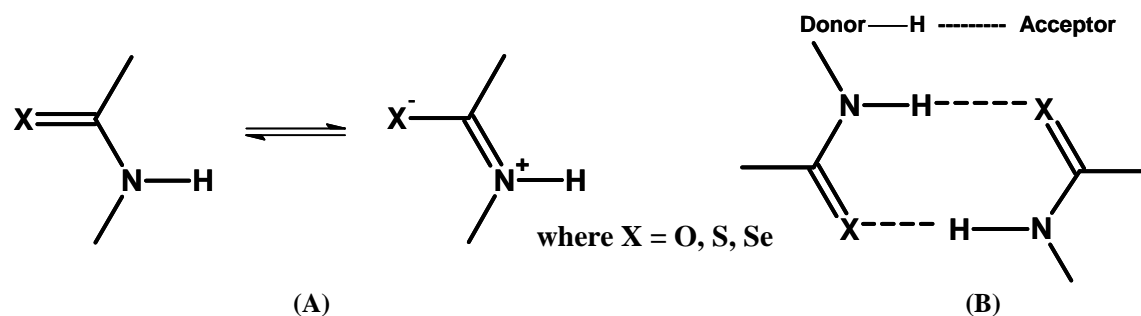


Fig. 2.3.11 Zwitterionic resonance form of selenoamide moiety (A), and its stabilisation through Resonance Assisted Hydrogen Bonding, RAHB, (B). Adapted from Ref.^[99].

Table 2.32 Hydrogen-bond geometry (Å, °) for **11-17**

	Donor—H...Acceptor	Donor—H	H...Acceptor	Donor...Acceptor	Donor—H...Acceptor
HL _{Se} ^{1a} 11	N1-H1...Se1 ⁱ (i) 1-x, 1-y, -z	0.85	2.70	3.532 (2)	168.4
HL _{Se} ^{1b} 12	N1-H1...Se1 ⁱ (i) 1-x, 1-y, -z C6-H6...O1 ⁱⁱ	0.84 (2)	2.74 (2)	3.539 (2)	158 (3)
	(ii) -x, 1-y, -z	0.93	2.48	3.407 (3)	173.8
HL _{Se} ^{1c} 13	N1 - H1...Se1 ⁱ (i) -x, 1-y, 1-z	0.83 (4)	2.77 (4)	3.533(3)	153 (3)
HL _{Se} ^{1d} 14	N1-H1...Se1 ⁱ (i) 2-x, 3-y, 1-z	0.80 (2)	2.85 (2)	3.553 (2)	149 (2)
HL _{Se} ^{1e} 15	N1-H1...Se1 ⁱ (i) 1-x, 1-y, 1-z	0.78 (3)	2.73 (3)	3.503 (2)	169 (2)
HL _{Se} ^{1f} 16	N1-H1...Se1 ⁱ (i) 1-x, 2-y, -z	0.79 (2)	2.80 (2)	3.519 (2)	152.9 (2)
HL _{Se} ^{1g} 17	C6-H6...O1 ⁱⁱ (ii) 1-x, 1-y, 1-z	0.95	2.40	3.282 (5)	154.2

2.3.1.8 Crystal and molecular structure of an oxaselenazine derivative, **18a** and dicyclohexylaminobenzoate, **18b**

The synthesis of *N,N*-dicyclohexyl-*N'*-benzoylselenourea HL_{Se}^{1h}, **18**, was attempted employing the reaction procedure used for the synthesis of compounds **11-17**, however the reaction and products differed substantially to those observed for compounds **11-17**.

Addition of benzoyl chloride to an anhydrous acetone solution of KSeCN resulted in a yellow solution and white precipitate. This indicated the formation of the isoselenocyanate intermediate with subsequent precipitation of KCl as observed in compounds **11-17**. Shortly after dicyclohexylamine addition however, formation of a brown oil was noted. This was extracted with dichloromethane and single crystal X-ray diffraction analysis of the red - brown crystals obtained following evaporation of this material from a dichloromethane / ethanol mixture resulted in the structure shown in Fig. 2.312. Unfortunately the structure solution is of poor quality, although it is evident that two molecules of a benzoylselenourea derivative are present in the asymmetric unit as well as three molecules of ethanol and two of selenocyanate residues. The molecular structure indicates that *N,N*-dicyclohexyl-*N'*-benzoylselenourea formation most likely occurred, but that the subsequent addition of a carbon atom and an amine residue resulted in the 6 membered ring structure, **18a** shown in Fig.2.312. The averaged values of selected bond lengths are shown in Table 2.31.

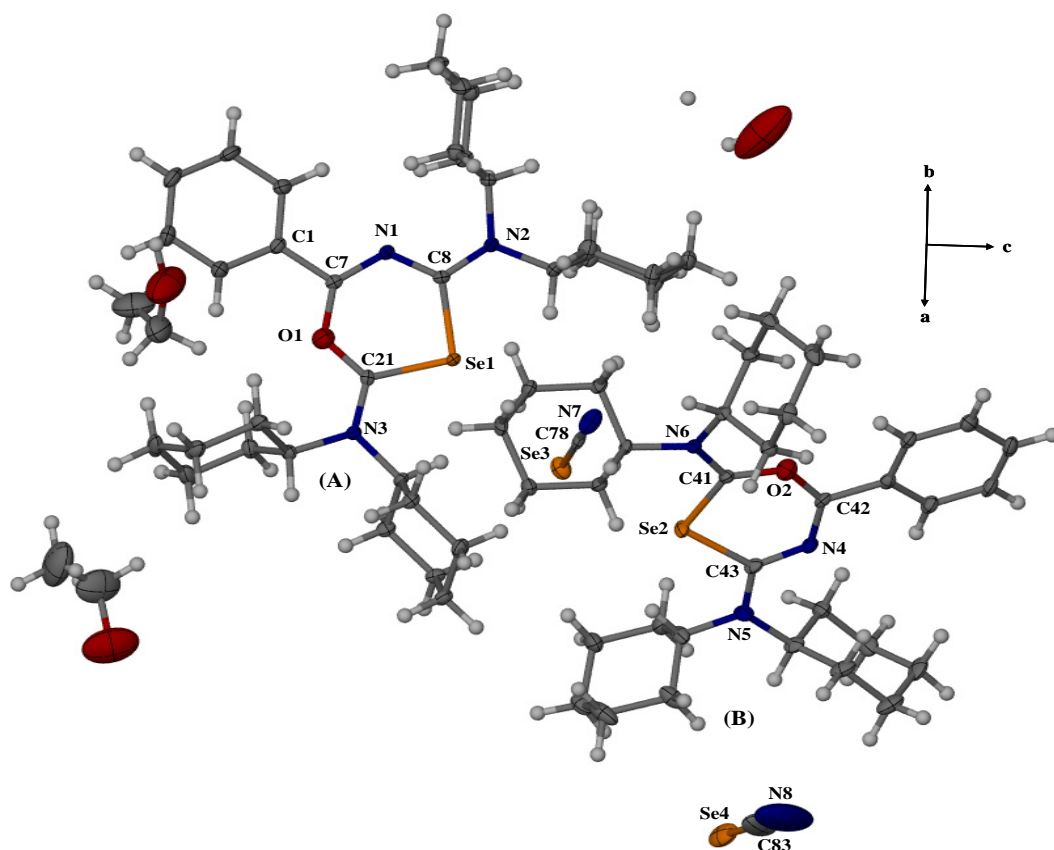


Fig. 2.312 Molecular structure of 1,3,5-oxaselenazine derivative **18a**, with selected atom numbering shown. Displacement ellipsoids are drawn at the 50 % probability level.

The C-O bond lengths of **18a** have an average length of 1.328 (3) Å and are longer than the average 1.219 Å of the C=O bonds of **11-17**. Similarly, the C-Se bonds of **18a** exhibit an average length of 1.919 (3) Å, this being longer than the average C=Se bond of 1.840 Å exhibited by compounds **11-17**. These observations indicate that both the C-O and C-Se bonds in **18a** are single bonds. Interestingly, the (O)C-N and N-C(Se) average bond lengths in **18a** are significantly shorter than their counterparts in compounds **11-17**. The average (O)C-N bond length in **18a** being 1.333 (3) Å, relative to that of 1.384 Å for **11-17**, and the average N-C(Se) bond lengths in **18a** of 1.326 (4) Å also being shorter than the average length of 1.406 Å exhibited by compounds **11-17**. These observations suggest that both the (O)C-N and N-C(Se) bonds are double bonds. The (Se)C-NR₂ bond lengths are comparable to those of compounds **11-17** in Table 2.31. The 6 ring atoms, C8/N1/C7/O1/C21/Se1, in Fig. 2.312 (A) and C43/N4/C42/O2/C41/Se2, in Fig. 2.312 (B) are both planar, however the r.m.s. deviation differs at 0.0350 for molecule (A), a maximum deviation of -0.0492 (12) Å exhibited by Se1 and 0.5168 for molecule (B), a maximum deviation of -0.7758 (11) Å exhibited by Se2.

A Cambridge Crystallographic Structural Database (CCSD) search revealed no record of any other 6 membered ring structures similar to that in Fig. 2.312. One report however described the synthesis of related 6 membered ring structures (1,3,5-oxachalcogenazines) where C atoms were substituted at positions 2 and 6 as opposed to the N atoms in our structure, these being synthesized from treatment of a seleno- or thioamide with an aliphatic aldehyde in the presence of a Lewis base (BF₃OEt₂) although no structural characterization was given.^[100] The absence of a selenoamidic proton in the crystal structure of **18a** as well as the corresponding proton resonance in the ¹H NMR spectrum and short (O)C-N and N-C(Se) bonds suggest the presence of an unsaturated nitrogen atom and this compound could therefore be classified as a 1,3,5-oxaselenazine. The two selenocyanate residues associated with

the 1,3,5-oxaselenazine molecules A and B are linear, with average Se-C bond lengths of 1.771 Å, and average C-N bond lengths of 1.148 Å. This implies single Se-C bonds and C ≡ N triple bonds, as the averaged length of 1.148 Å compares well with the 1.155 Å reported for the (S-C≡N)⁻ species.^[82] As previously mentioned the short (O)C-N and N-C(Se) bonds imply an unsaturated, nitrogen atom, with a positive charge. The linear selenocyanate residues with the given bond lengths suggest the presence of a negatively charged, Se-C≡N⁻ species. As there are two selenocyanate residues associated with the two 1,3,5-oxaselenazine molecules (A and B), a salt has been isolated in the solid state.

A proposed reaction mechanism is outlined below.

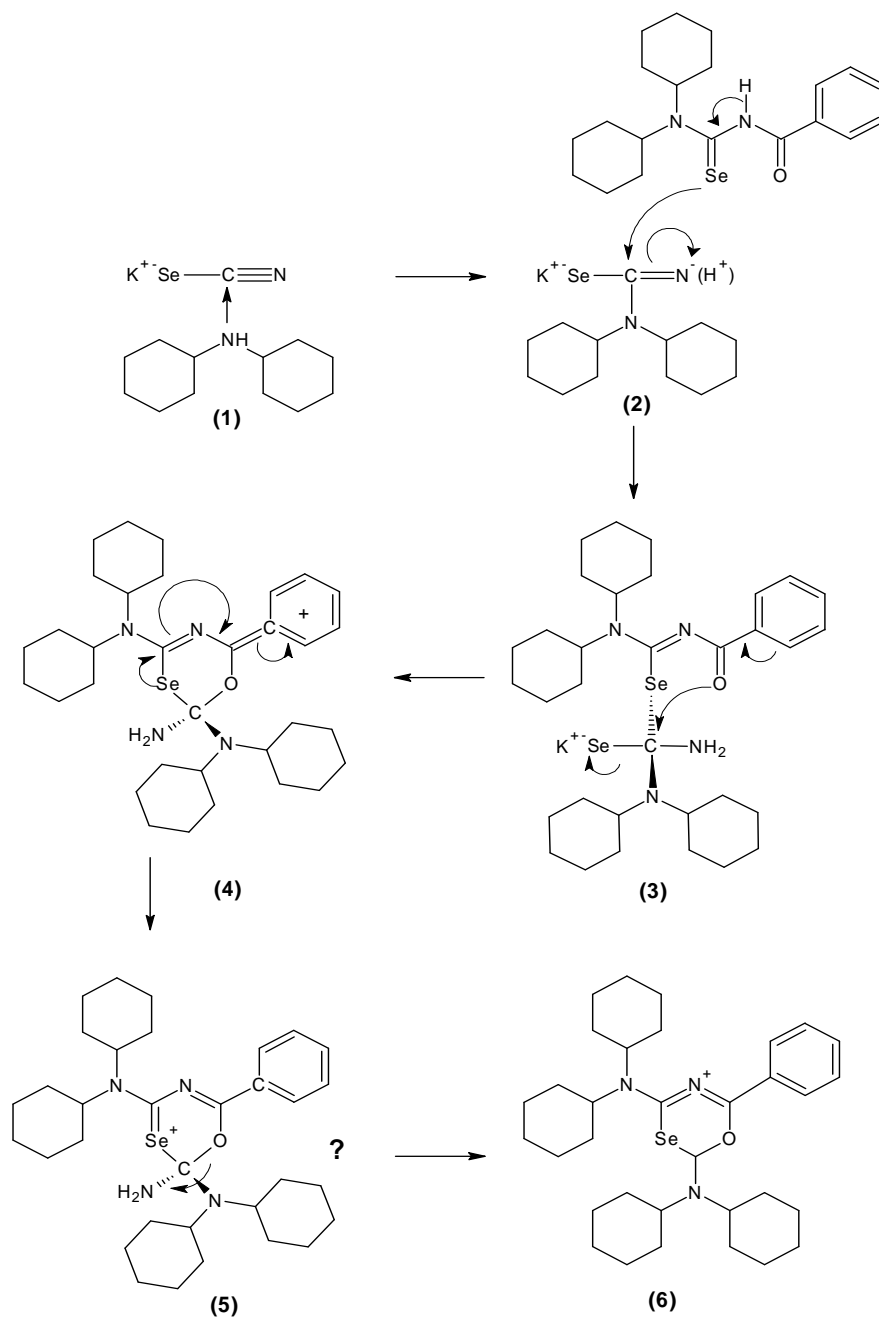


Fig. 2.313

Proposed reaction mechanism for the formation of the 1,3,5-oxaselenazine derivative, 18a.

Nucleophilic attack by the amine residue on potassium selenocyanate leads to the formation of the intermediate species shown in Fig. 2.313 (step 2). A second nucleophilic attack by the selenium atom of *N,N*-dicyclohexyl-*N'*-benzoylselenourea occurs at the same carbon atom (step 2, Fig. 2.313) and through a series of rearrangements, removal of K^+Se^- is affected (steps 3 and 4) to lead to the intermediate species shown in step 5. It is not certain how the rearrangement depicted in step 5 leads to the formation of the oxaselenazine species in step 6, but this may be facilitated by the presence of a hydride, although how this would form in the reaction mixture is not certain. A complete mechanistic study of the formation of **18a** is beyond the scope of this work however the formation of an oxaselenazine salt does seem likely. Attempts to recrystallise this material in order to gain a better quality structure proved unsuccessful.

From the same attempted synthesis of *N,N*-dicyclohexyl-*N'*-benzoylselenourea HL_{Se}^{lh} , **18**, colourless crystalline material was also isolated from the reaction mixture and analysed yielding the following molecular structure (Fig. 2.314). The asymmetric unit consists of two dicyclohexylamine and two benzoic acid residues involved in hydrogen bonding. Table 2.33 shows the hydrogen bond length similarity, indicating the formation of a salt, as opposed to co-crystallization of dicyclohexylamine and benzoic acid. This is confirmed by the relatively high melting point (205.7 – 207.6 °C), where benzoic acid melts between 121 and 125 °C and dicyclohexylamine is a liquid at room temperature.^[101] The hydrogen bonding leads to the formation of a 12 membered ring structure where atoms O1/O2/O3/O4/C1/C8 lie in a plane with a r.m.s. deviation of 0.0095, a maximum deviation of 0.0152 (7) Å being exhibited by O4, N1 lying -1.0635 (16) Å below and N2, 1.0933 (16) Å above this plane.

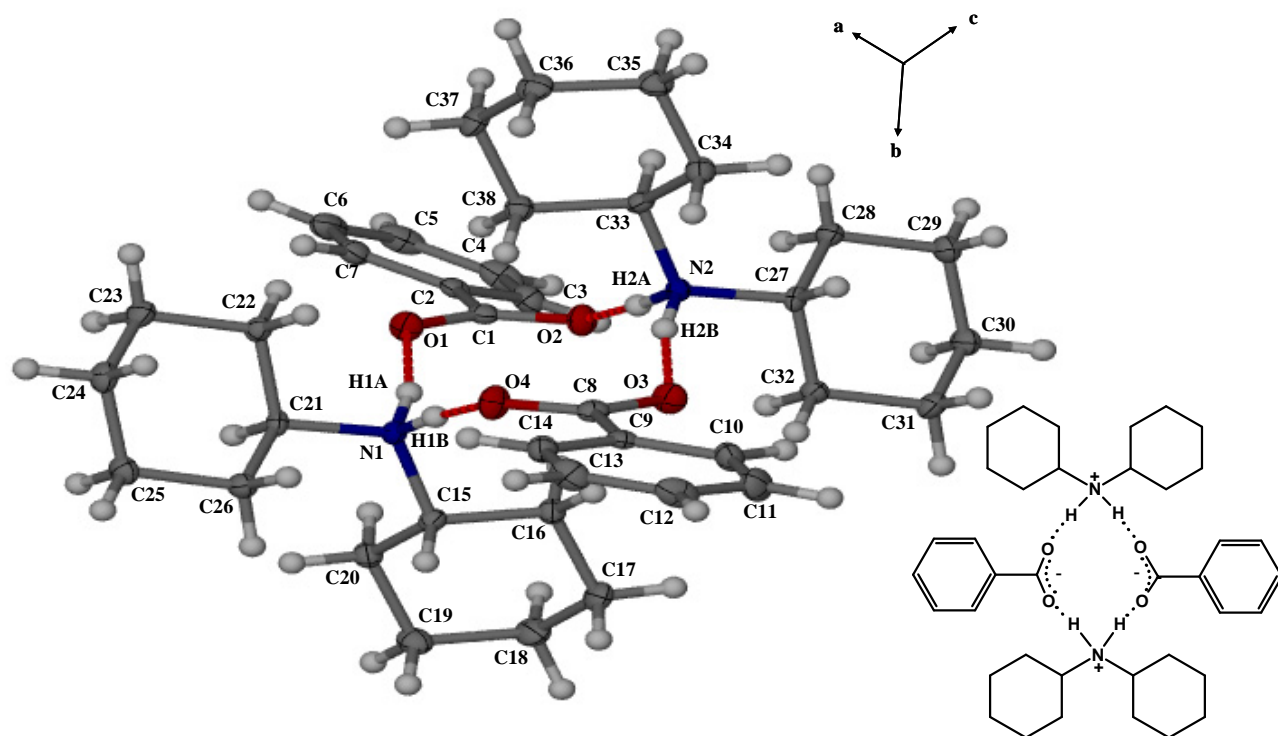


Fig. 2.314 Molecular structure of dicyclohexylaminobenzoate, **18b**, with atom numbering scheme shown, displacement ellipsoids are drawn at the 50 % probability level.

Interestingly, C16 and C38 lie directly opposite each other on either side of this plane, where C16 lies $-2.3945(15)$ Å below and C38, $2.4401(15)$ Å above the O1/O2/O3/O4/C1/C8 plane. As expected the two benzene residues are planar, C2/C3/C4/C5/C6/C7 exhibiting a r.m.s. deviation of 0.0100, a maximum deviation of 0.0136(11) for C6 and atoms C9/C10/C11/C12/C13/C14 exhibiting a r.m.s. deviation of 0.0066, a maximum deviation of 0.0092(11) for C11 where the two planes lie at an angle of $15.31(0.08)^\circ$ relative to each other. Fig. 2.315 illustrates the unit cell packing of **18b** viewed down the *a* axis where the 12 membered hydrogen bonded rings can clearly be seen, however the close proximity of C16 and C38 to the O1/O2/O3/O4/C1/C8 plane precludes the formation of hydrogen bonded channels throughout the crystal lattice.

To confirm the nature of this unexpected product, dicyclohexylaminobenzoate was separately synthesized by allowing slow evaporation of a methanol solution containing equimolar amounts of dicyclohexylamine and benzoic acid. The X-Ray powder diffraction pattern (XPRD) of the resulting material was experimentally obtained and found to closely resemble that generated from the crystallographic data thereby confirming its identity.(Fig. 2.316).

Table 2.33 Hydrogen-bond geometry (Å, °) for **18b**

<i>D</i> —H... <i>A</i>	<i>D</i> —H	H... <i>A</i>	<i>D</i> ... <i>A</i>	<i>D</i> —H... <i>A</i>
N1-H1A...O1	0.981	1.750	2.715	167.22
N1-H1B...O4	0.943	1.788	2.717	167.77
N2-H2A...O2	0.984	1.755	2.728	169.42
N2-H2B...O3	0.943	1.763	2.690	167.14

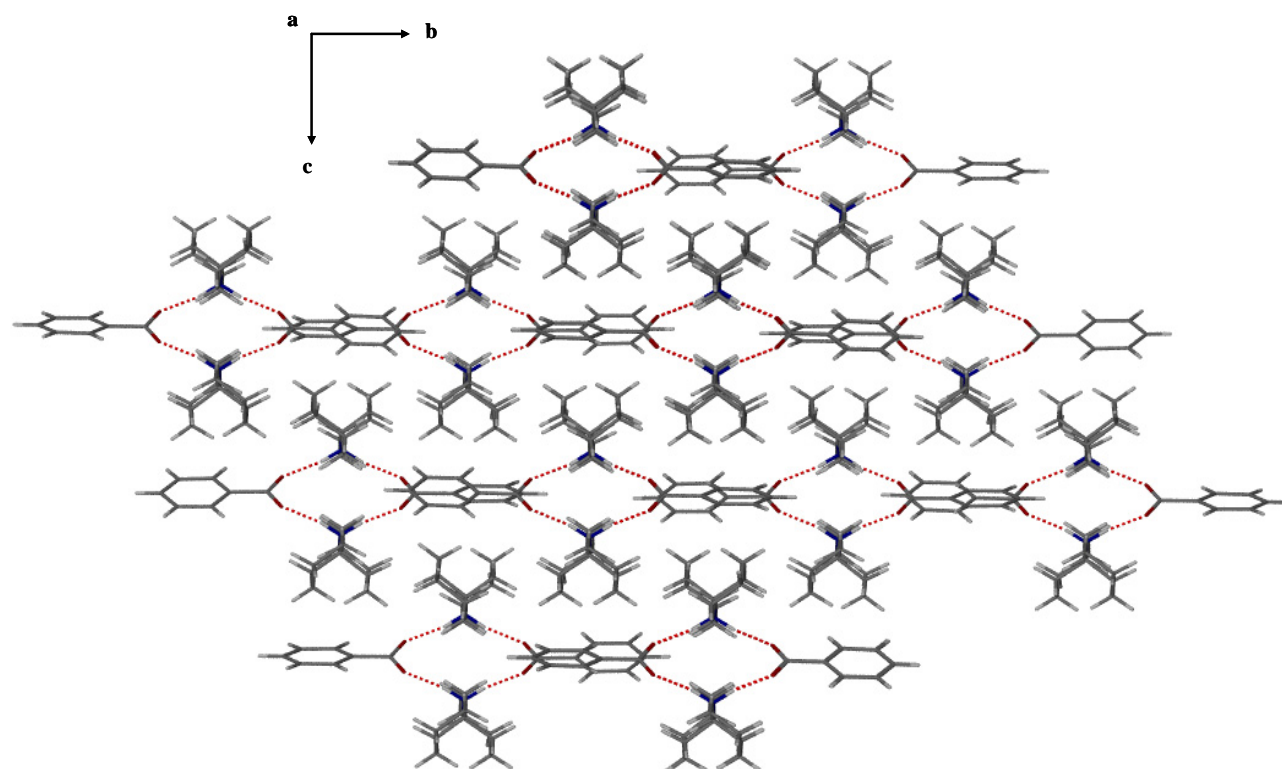


Fig. 2.315

Unit cell packing of dicyclohexylaminobenzoate (**18b**), viewed down the *a* axis. Dotted lines indicate hydrogen bonding between the O atoms of the benzoic acid residues and the N atoms of the dicyclohexylamine residues.

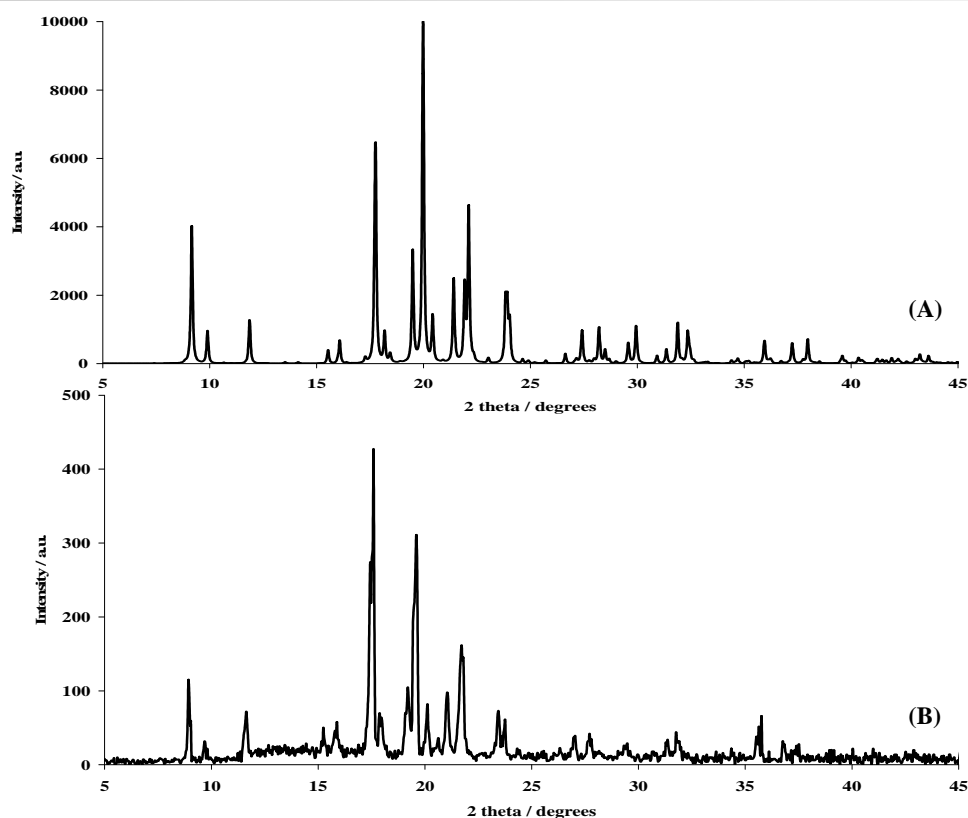


Fig. 2.316 XPRD patterns of dicyclohexylaminobenzoate obtained from (A) crystallographic data and (B) independently synthesized sample.

A review of literature in this area revealed that the hydrogen bonded networks in organic salts comprising secondary amines and carboxylic acids have previously been studied in the context of organogelators^[102, 103] and that the structural characterization of dicyclohexylaminobenzoate has been reported.^[104] At least two forms of hydrogen bonding are possible when considering secondary amines and carboxylic acids (Fig. 2.317) the one being zero dimensional and the other giving rise to one dimensional hydrogen bonded networks. Organic salts presenting the latter motif have been found to exhibit gelling properties with a variety of organic solvents.^[102]

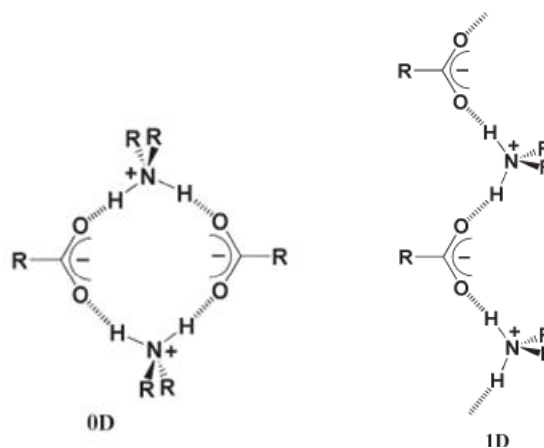


Fig. 2.317 Possible hydrogen bonding motifs when considering secondary amines and monocarboxylic acids; leading to 0D and 1D structures.^[102]

The precise mechanism by which these two unexpected products, **18a** and **18b**, formed has not been established, however it is evident that hydrolysis of the benzoyl chloride must have taken place to allow the organic salt formation, **18b**. Two molar equivalents of selenocyanate would remain, and it is interesting that two SeCN

molecules are associated in the crystal lattice of the 1,3,5-oxaselenazine derivative **18a**. Another look at pK_a values of the amines provides little clarification as that of dicyclohexylamine is 10.8,^[105] clearly within the range of the dialkylamines where no evidence of this phenomenon was observed.

As in the case of HL_{se}^{1g} it would appear that the choice of amine is important in *N,N*-dialkyl-*N'*-benzoylselenourea ligand synthesis as the substituents can affect a significant influence on the reaction course and subsequent products.

Table 2.34 Crystal and structure refinement data for compounds **11-17**.

Compound	HL _{Se} ^{1a} , 11	HL _{Se} ^{1b} , 12	HL _{Se} ^{1c} , 13	HL _{Se} ^{1d} , 14	HL _{Se} ^{1e} , 15	HL _{Se} ^{1f} , 16	HL _{Se} ^{1g} , 17
Empirical Formula	C ₁₂ H ₁₆ N ₂ OSe	C ₁₆ H ₂₄ N ₂ OSe	C ₂₀ H ₃₂ N ₂ OSe	C ₂₄ H ₄₀ N ₂ OSe	C ₁₆ H ₁₆ N ₂ OSe	C ₂₈ H ₄₈ N ₂ OSe	C ₂₀ H ₁₆ N ₂ OSe
Formula Weight /gmol ⁻¹	283.2314	339.33	395.44	451.54	331.27	507.64	379.31
Crystal system	monoclinic	monoclinic	monoclinic	monoclinic	monoclinic		monoclinic
Space Group	C2/c	P2 ₁ /c	P2 ₁ /c	P2 ₁ /c	P2 ₁ /c	P2 ₁ /n	C2/c
Unit cell dimensions							
<i>a</i> / Å	20.562 (4)	10.388 (2)	10.703 (2)	12.599 (1)	11.273 (1)	16.664 (2)	17.782 (4)
<i>b</i> / Å	8.442 (2)	15.715 (3)	9.390 (1)	9.5106 (8)	4.8510 (5)	9.2373 (9)	10.427 (2)
<i>c</i> / Å	14.824 (3)	10.152 (2)	20.521 (3)	20.387 (2)	26.095 (3)	19.432 (2)	18.193 (4)
β / °	106.93 (3)	98.423 (3)	90.156 (2)	99.345 (2)	92.487 (2)	110.133 (2)	99.49 (3)
<i>V</i> / Å ³	2461.7 (9)	1639.4 (5)	2062.4 (5)	2410.4 (4)	1425.7 (3)	2808.5 (5)	3327.0 (12)
<i>Z</i>	8	4	4	4	4	4	8
<i>μ</i> / mm ⁻¹	3.032	2.289	1.829	1.574	2.630	1.358	2.265
<i>T</i> / K	173 (2)	273 (2)	100 (2)	100 (2)	173 (2)	100 (2)	173 (2)
Reflections collected / unique	7430/ 2851	10228/3775	18083/3840	15027/5659	8616/3379	16057/5763	10101/3844
Data / restraints / parameters	2851/0/148	3031/0/187	3246/0/223	4775/0/259	2954/0/190	4922/0/295	3014/0/217
Goodness-of-fit on <i>F</i> ²	1.095	1.025	1.041	1.044	1.055	1.093	1.041
Final <i>R</i> indices [I>2σ (I)]	2.28, 5.85 %	3.71, 8.00 %	2.82, 6.46 %	2.91, 7.05 %	2.99, 7.07 %	3.33, 8.04 %	5.40, 12.09 %
<i>R</i> indices (all data)	R = 0.0247 wR ₂ = 0.0592	R = 0.0510 wR ₂ = 0.0853	R = 0.0382 wR ₂ = 0.0689	R = 0.0356 wR ₂ = 0.0737	R = 0.0363 wR ₂ = 0.0736	R = 0.0408 wR ₂ = 0.0836	R = 0.0735 wR ₂ = 0.1295

Table 2.35 Crystal and structure refinement data for compounds **18a**, **b** and **1212**.

Compound	HL _{Se} ^{1b} , 18a	18b	H ₂ L _{Se} ^{m1b} , 1212
Empirical Formula		C ₃₈ H ₅₈ N ₂ O ₄	C ₂₆ H ₄₂ N ₄ O ₂ Se ₂
Formula Weight /g mol ⁻¹		606.86	600.56
Crystal system	triclinic	monoclinic	monoclinic
Space Group	<i>P</i> -1	<i>P</i> 2 ₁ / <i>n</i>	<i>P</i> 2 ₁
Unit cell dimensions			
<i>a</i> / Å	14.7704 (12)	11.2984 (10)	7.2012 (14)
<i>b</i> / Å	14.9390 (12)	19.9801 (18)	17.739 (4)
<i>c</i> / Å	18.9488 (15)	15.2549 (14)	11.334 (2)
	104.5400 (10)		
β / °	91.4160 (10)	102.9200 (10)	103.24 (3)
	116.3610 (10)		
<i>V</i> / Å ³	3581.4 (5)	3356.5 (5)	1409.4 (5)
<i>Z</i>	8	6	2
μ / mm ⁻¹	2.106	0.115	2.652
<i>T</i> / K	100 (2)	100 (2)	173 (2)
Reflections collected / unique	39997/14677	19551/6827	8808/5877
Data / restraints / parameters	12167/0/816	4695/0/417	5371/1/312
Goodness-of-fit on <i>F</i> ²	1.047	1.050	1.002
Final <i>R</i> indices [<i>I</i> > 2 σ (<i>I</i>)]	4.11, 9.98 %	4.90, 12.85 %	4.37, 10.40 %
<i>R</i> indices (all data)	<i>R</i> = 0.0522 <i>wR</i> 2 = 0.1054	<i>R</i> = 0.0730 <i>wR</i> 2 = 0.1440	<i>R</i> = 0.0467 <i>wR</i> 2 = 0.1050

2.3.1.9 Synthesis and structural characterization of 3,3,3',3'-tetraalkyl-1,1'-phenylenedicarbonylbis(selenourea) ligands

In general, synthesis of 3,3,3',3'-tetraalkyl-1,1'-phenylenedicarbonylbis(selenourea) derivatives proved to be significantly more complex than their monopodal analogues. Several attempts were made to synthesize 3,3,3',3'-tetraethyl-1,1'-terephthaloylbis(selenourea) however these were met with little success. Synthesis of *meta*-substituted derivatives proved more fruitful where 3,3,3',3'-tetraethyl-1,1'-isophthaloylbis(selenourea) was successfully isolated and characterized although despite several attempts, structural characterization was not possible. A crystal structure of its longer alkyl chain analogue was possible however where crystals of 3,3,3',3'-tetra(*n*-butyl)-1,1'-isophthaloylbis(selenourea), H₂L^{m1b}, **1212** suitable for single crystal X-ray diffraction analysis, were isolated from an ethanol solution and Fig. 2.318 (A and B) illustrates the molecular structure and intermolecular hydrogen bonding displayed by this ligand. Crystal and refinement data for this structure is given in Table 2.35.

As in the monopodal analogue (HL_{Se}^{1b}) an intermolecular hydrogen bond is formed between the selenoamidic proton of one molecule and the Se atom of a neighbouring molecule at (*x*-1, *y*, *z*) with N – H[⋯]Se = 2.62 Å, N[⋯]Se = 3.458 (3) Å and Se[⋯]H-N = 158.7 °. This molecule in turn, forms a hydrogen bond between the selenoamidic proton and Se atom of the original molecule with N – H[⋯]Se = 2.66 Å, N[⋯]Se = 3.506 (4) Å and Se[⋯]H-N = 162.3 ° leading to the dimerisation we have come to expect from compounds of this type. The second acylselenourea moiety in the molecule is involved in similar hydrogen bonding with the neighbouring molecule at (1+*x*, *y*, *z*), the hydrogen bond parameters being comparable to those reported for the monopodal derivatives. As for the monopodal analogue (HL_{Se}^{1b}), these intermolecular interactions can be classified as Resonance Assisted Hydrogen Bonding (RAHB) and lead to chains of hydrogen bonded units in the crystal lattice.^[98] Selected bond lengths and torsion angles are given in Table 2.36 where they are evidently similar to those of HL_{Se}^{1b}.

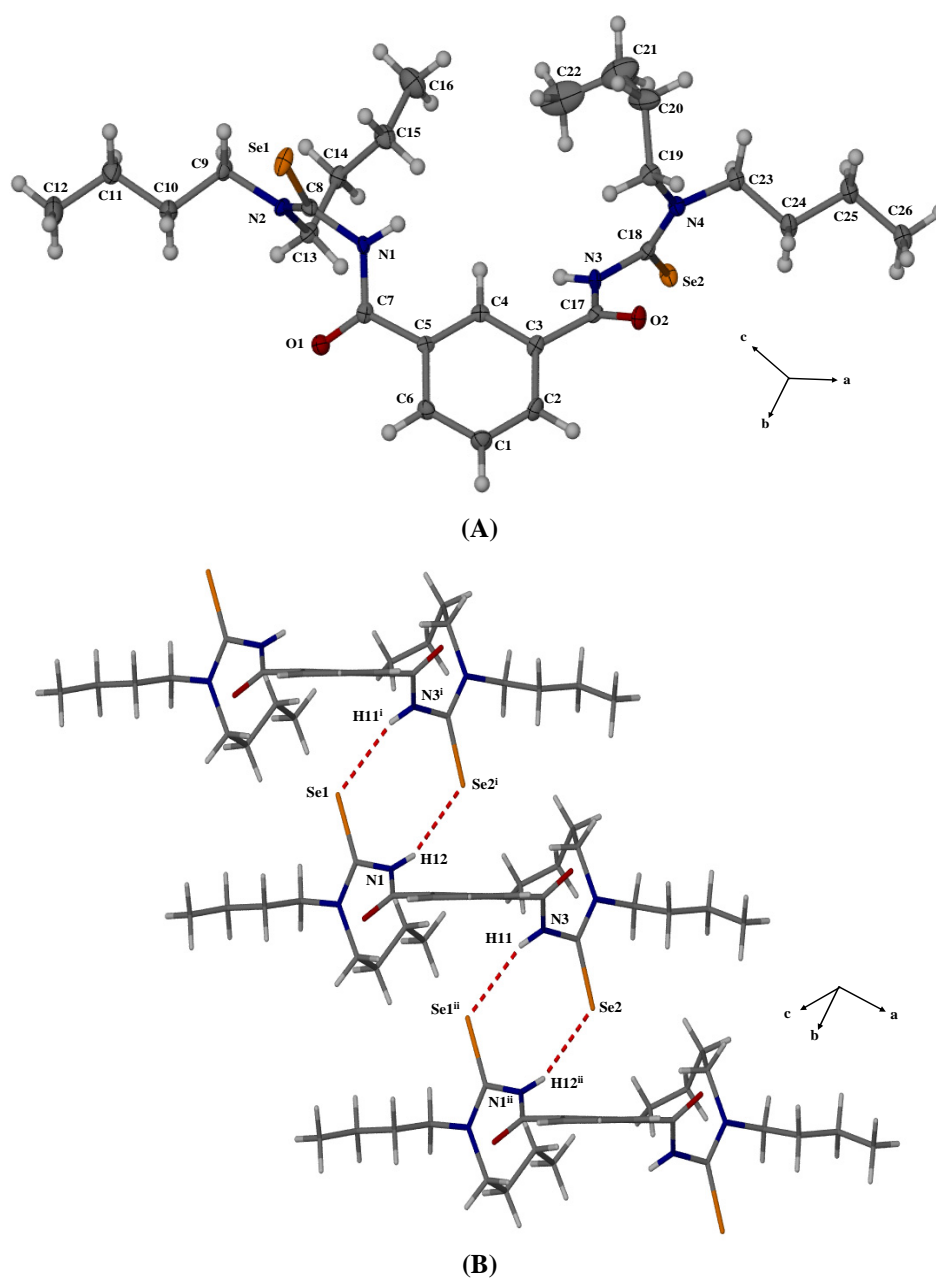


Fig. 2.318 Molecular structure of 3,3,3',3'-tetra(*n*-butyl)-1,1'-isophthaloylbis(selenourea), $\text{H}_2\text{LSe}^{m1b}$ with atom numbering scheme shown. Displacement ellipsoids are drawn at the 50 % probability level (A) and intermolecular hydrogen bonding exhibited by $\text{H}_2\text{LSe}^{m1b}$. [Symmetry codes (i) $x-1, y, z$, (ii) $1+x, y, z$] (B).

Table 2.36 Selected bond lengths (Å) and torsion angles (°) for compounds HLSe^{1b} and $\text{H}_2\text{LSe}^{m1b}$.

Compound	C=O	C=Se	(O)C-N	N-C(Se)	(Se)C-NR ₂	O-C(O)-N(H)-C(Se)	C(O)-N(H)-C(Se)-Se
HLSe^{1b} 12	1.212 (3)	1.848 (2)	1.397 (3)	1.399 (3)	1.314 (3)	0.5 (4)	121.1 (2)
$\text{H}_2\text{LSe}^{m1b}$	1.220 (5)	1.836 (4)	1.368 (6)	1.406 (5)	1.319 (5)	5.8 (6)	117.0 (4)
$\text{H}_2\text{LSe}^{m1b}$	1.206 (5)	1.844 (4)	1.392 (5)	1.411 (5)	1.317 (6)	4.8 (6)	125.0 (4)

In summary, recrystallization of the *N,N*-dialkyl-*N'*-benzoylselenoureas from ethanol proved to be the most successful method for obtaining crystals of these compounds suitable for single crystal X-ray diffraction analysis. The dominant intermolecular interaction exhibited by the *N,N*-dialkyl-*N'*-benzoylselenoureas analysed in the solid state is Resonance Assisted Hydrogen Bonding (RAHB), this occurring between the selenoamidic proton of one molecule and the Se atom of a neighbouring molecule. In the case of HL_{Se}^{1a} RAHB is the only intermolecular interaction observed in the solid state structure. The dibutyl analogue, HL_{Se}^{1b}, exhibits RAHB as well as a second hydrogen bond between the carbonyl O atom and an H atom on the benzene residue of a neighbouring molecule. This second hydrogen bond is present in only one other of the structures analysed. As the alkyl chain length of the ligands increase, HL_{Se}^{1c}, HL_{Se}^{1d} and HL_{Se}^{1f}, the RAHB is maintained, but π - π interactions are also exhibited between the benzene residues of two neighbouring molecules. The dihexyl and dioctyl derivatives, HL_{Se}^{1c} and HL_{Se}^{1d} display similar interplanar separations between the benzene residues of 3.4732 (26) and 3.4718 (159) Å respectively whereas that of the didecyl derivative, HL_{Se}^{1f}, is slightly shorter at 3.4292 (116) Å. The asymmetrically substituted HL_{Se}^{1e} contains two benzene residues, but interestingly exhibits no evidence of π - π interactions in the solid state, only RAHB similar to that exhibited by HL_{Se}^{1a-d,f}. Structural elucidation of *N,N*-diphenyl-*N'*-benzoylselenourea, HL_{Se}^{1g} reveals a Se-Se distance of 2.3237 (9) Å with a neighbouring molecule, justifying its classification as a diselenide rather than a selenourea. The RAHB exhibited by the majority of ligands in this series is not displayed by HL_{Se}^{1g}, rather a hydrogen bond between the carbonyl O atom and an H atom on the benzene residue, reminiscent of that displayed by HL_{Se}^{1b} is exhibited by the structure. Attempts to synthesize *N,N*-dicyclohexyl-*N'*-benzoylselenourea resulted in the isolation of two distinct products, both of which could be structurally characterized. Crystallographic analysis of a red crystalline material revealed the formation of a 1,3,5-oxaselenazine salt that has, to the best of our knowledge, not previously been structurally characterized. Crystallographic analysis of a white crystalline material revealed the formation of dicyclohexylaminobenzoate, its identity being confirmed with a separate synthesis of the material exhibiting an identical powder X-Ray diffraction pattern. Several attempts to synthesize the bipodal 3,3,3',3'-tetraalkyl-1,1'-terephthaloylbis(selenourea) ligands were met with little success, however synthesis of the 3,3,3',3'-tetraethyl-1,1'-isophthaloylbis(selenourea) isomer, were more successful. 3,3,3',3'-tetra(*n*-butyl)-1,1'-isophthaloylbis(selenourea) was also successfully synthesized and could be structurally characterized, where RAHB is exhibited between neighbouring molecules in a fashion similar to that displayed by the monopodal analogue.

2.3.2 Crystal and molecular structures of *N,N*-dialkyl-*N'*-benzoylthiourea ligands

Several *N,N*-dialkyl-*N'*-benzoylthiourea solid state structures are discussed in this section, and the crystal and refinement data for each is given in Table 2.39 at the end of the section. Solid state characterizations of *N,N*-diethyl-*N'*-benzoylthiourea HL^{2a} [106] and *N,N*-dibutyl-*N'*-*p*-chlorobenzoylthiourea have previously been reported and for the sake of comparison, this data has been included in Table 2.37.

2.3.2.1 Crystal and molecular structure of *N,N*-dihexyl-*N'*-benzoylthiourea, HL_S^{2c}

Crystals of *N,N*-dihexyl-*N'*-benzoylthiourea, HL_S^{2c} isolated following recrystallization from an acetone, water solvent mixture were analysed by single crystal X-ray diffraction. Fig. 2.319 (A and B) illustrates the molecular structure as well as the intermolecular interactions exhibited by this compound.

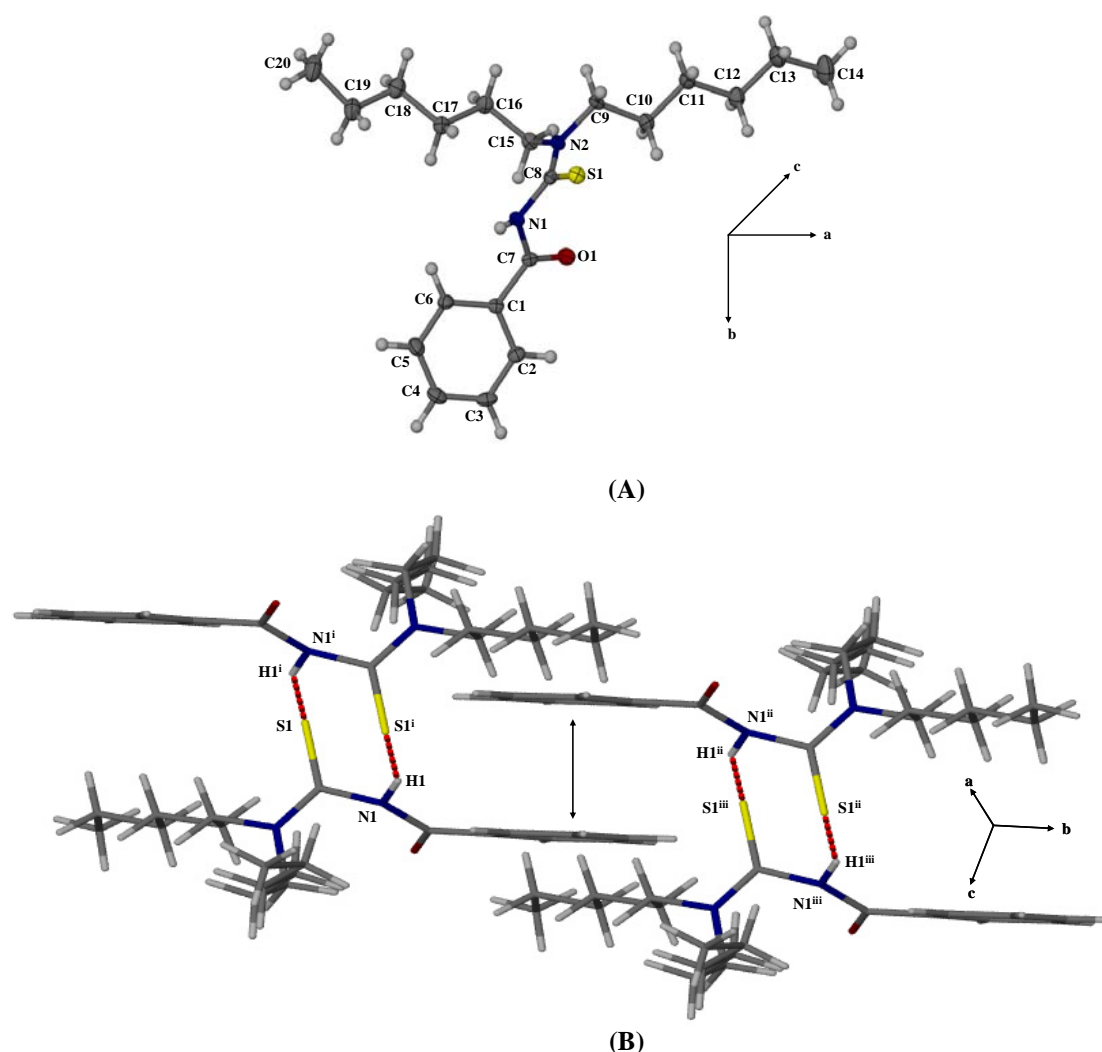


Fig 2.319 The molecular structure of *N,N*-dihexyl-*N'*-benzoylthiourea HL_S^{2c} with atom numbering scheme shown, displacement ellipsoids are drawn at the 50 % probability level (A) and intermolecular hydrogen bonding exhibited by HL_S^{2c} as well as $\pi - \pi$ interactions. [Symmetry codes (i) $2-x, 1-y, 2-z$, (ii) $2-x, 2-y, 2-z$, (iii) $x, 1+y, z$] (B).

Similarly to its selenium analogue, HL_S^{2c} exhibits intermolecular hydrogen bonding between the thioamidic proton of one molecule and the sulfur atom of its neighbour at $(2-x, 1-y, 2-z)$, with $N-H \cdots S = 2.72(2) \text{ \AA}$, $N \cdots S = 3.428(2) \text{ \AA}$ and $S \cdots H-N = 146.7(2)^\circ$ so giving rise to a dimer linked through such hydrogen bonds in the crystal structure.

HL_S^{2c} also displays the $\pi - \pi$ interactions exhibited by HL_{Se}^{1c} where a plane defined between the 6 aromatic carbons C1/C2/C3/C4/C5/C6 exhibited a root mean square deviation of 0.0056 with C6 exhibiting the largest deviation of 0.0080 (11) Å; these values comparing very closely with those obtained for HL_{Se}^{1c} . The average interplanar spacing between planes defined by the 6 aromatic carbons in neighbouring benzene residues (2-x, 2-y, 2-z) was found to be 3.4527 (34) Å.

2.3.2.2 Crystal and molecular structure of *N,N*-dioctyl-*N'*-benzoylthiourea, HL_S^{2d}

Recrystallization from an acetone, water mixture also yielded single crystals of *N,N*-dioctyl-*N'*-benzoylthiourea HL_S^{2d} and the molecular structure and intermolecular interactions are shown in Fig. 2.320 (A and B).

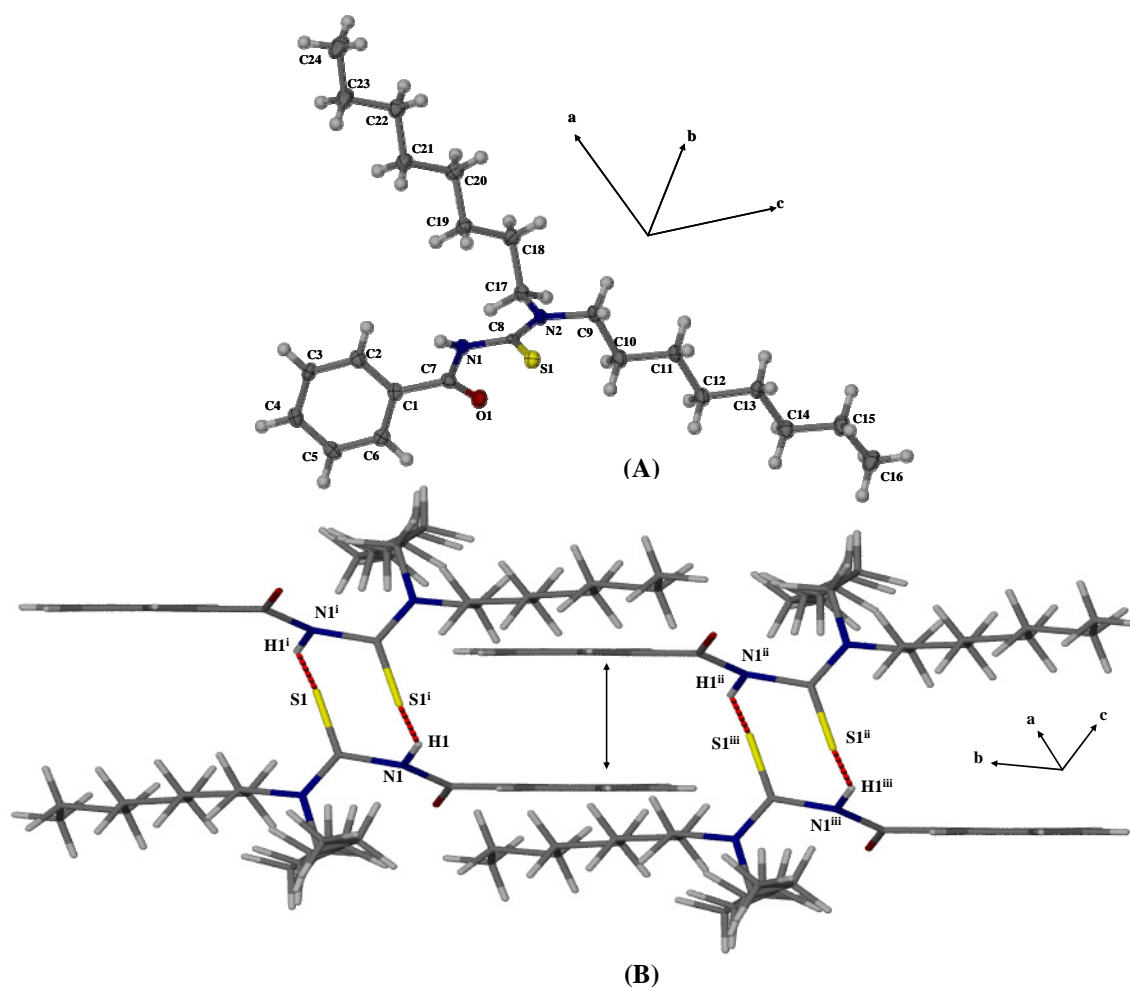


Fig 2.320 The molecular structure of *N,N*-dioctyl-*N'*-benzoylthiourea HL_S^{2d} with atom numbering scheme shown, displacement ellipsoids are drawn at the 50 % probability level (A) and intermolecular hydrogen bonding exhibited by HL_S^{2d} as well as $\pi - \pi$ interactions. [Symmetry codes (i) -x, 1-y, 1-z, (ii) -x, -y, 1-z, (iii) x, y-1, z] (B).

As its selenium counterpart, HL_S^{2d} exhibits intermolecular hydrogen bonding between the thioamidic proton and the sulfur atom of its neighbour at (-x, 1-y, 1-z) with $\text{N-H}\cdots\text{S} = 2.69$ (4) Å, $\text{N}\cdots\text{S} = 3.467$ (3) Å and $\text{S}\cdots\text{H-N} = 148$ (3) °. This hydrogen bonding leads to the dimeric structure similar to that observed in HL_{Se}^{1d} . Once again $\pi - \pi$ interactions between two neighbouring benzene residues are present with an interplanar spacing of 3.4424 (177) Å; the plane being that defined by C1/C2/C3/C4/C5/C6 with a root mean square deviation of 0.0072 and a maximum deviation from planarity by C6 of -0.0115 (26).

2.3.2.3 Crystal and molecular structure of *N*-methyl-*N*-benzyl-*N'*-benzoylthiourea, HL_S^{2e}

N-methyl-*N*-benzyl-*N'*-benzoylthiourea HL_S^{2e} crystallized from an acetone,-water mixture for which the molecular structure together with the intermolecular interactions are shown in Fig. 2.321 (A and B).

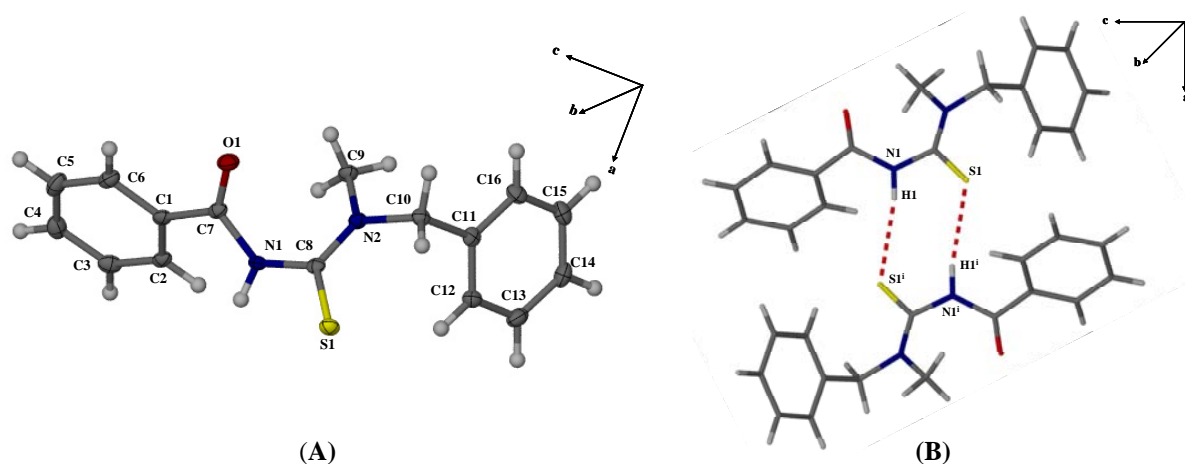


Fig. 2.321 The molecular structure of *N*-methyl-*N*-benzyl-*N'*-benzoylthiourea HL_S^{2e} with atom numbering scheme shown, displacement ellipsoids are drawn at the 50 % probability level (A) and intermolecular hydrogen bonding exhibited by HL_S^{2e}. [Symmetry code (i) 1-x, 1-y, 1-z.]

Interestingly, HL_S^{2e} is similar to HL_{Se}^{1e} in that the *Z* isomer appears to be the more stable in the solid state. An intermolecular hydrogen bond is present between the thioamidic proton and the sulfur atom of its neighbour at (1-x, 1-y, 1-z) with N-H[⋯]S = 2.48 Å, N[⋯]S = 3.422 (2) Å and S[⋯]H-N = 165.9 °. This hydrogen bond is markedly shorter than those of HL_S^{2c} and HL_S^{2d} and the Donor[⋯]Acceptor angle is also slightly larger relative to the 146.7 (2) and 148 (3) ° displayed by HL_S^{2c} and HL_S^{2d} respectively, making it tempting to speculate about the presence of the π – π interactions and the size of this angle, as HL_S^{2e} does not exhibit the same intermolecular interactions displayed by HL_S^{2c} and HL_S^{2d}.

2.3.2.4 Crystal and molecular structure of *N,N*-dicyclohexyl-*N'*-benzoylthiourea, HL_S^{2g}

Yellow crystals of *N,N*-dicyclohexyl-*N'*-benzoylthiourea HL_S^{2g} were isolated from an acetone, water solvent mixture and analysed to reveal a very interesting structure (Fig. 2.322).

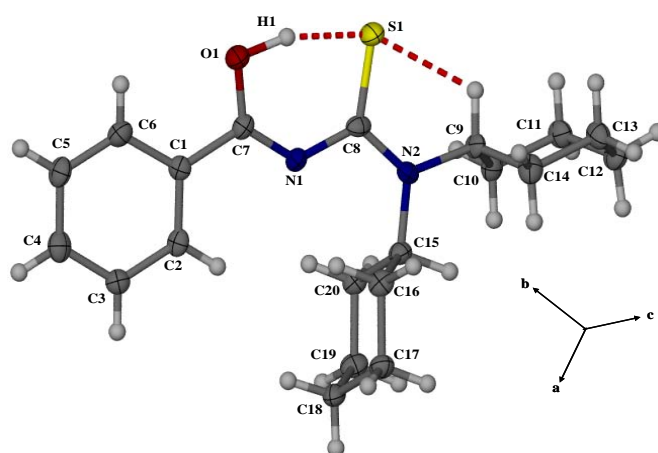


Fig. 2.322 The molecular structure of *N,N*-dicyclohexyl-*N'*-benzoylthiourea HL_S^{2g} with atom numbering scheme shown, displacement ellipsoids are drawn at the 50 % probability level.

The acylthiourea moiety allows for the formation of resonance structures as shown in Fig.2.323. It is therefore possible that a form of keto-enol tautomerism may occur in which the thioamidic proton is located on either the sulfur or oxygen atoms rather than the central nitrogen atom. During the elucidation of HL_S^{1a-g} and HL_S^{2c-e} , the thioamidic proton (generally attached to the nitrogen atom) could frequently be located from the difference fourier map, however this was not possible with HL_S^{2g} , rather there appeared to be unassigned electron density surrounding the carbonyl O atom and the hydrogen atom could be located from the difference fourier map in this area.

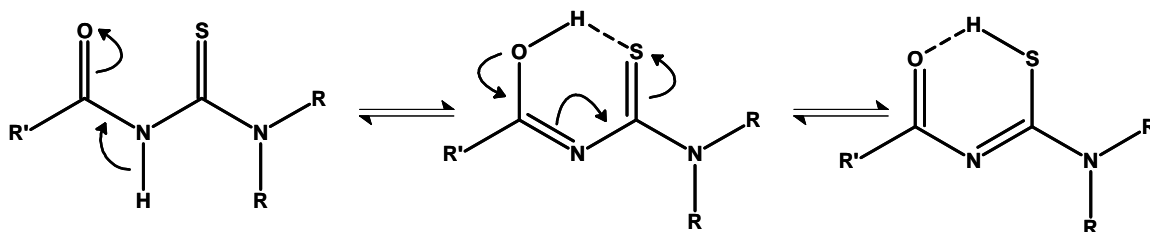


Fig. 2.323 Resonance structures of *N,N*-dialkyl-*N'*-acyl(aryl)thioureas where R = any alkyl group and R' = acyl or aryl moiety.

Table 2.37 shows the particularly short (O)C-N bond length of 1.293 (4) Å in HL_S^{2g} compared to the average (O)C-N bond length of 1.382 (3) Å for HL_S^{2c-e} . In addition, the C=O and C=S bonds of 1.321 (4) and 1.716 (3) Å respectively are slightly longer than the average C=O and C=S bonds of 1.220 (3) and 1.682 (3) Å for ligands HL_S^{2c-e} . The molecular structure of HL_S^{2g} is therefore shown as the “enol” form of the ligand in Fig. 2.322 with an O-H bond length of 0.92 (5) Å and an S-H distance of 1.96(5) Å. This is also, to the best of our knowledge the first time that the donor atoms O and S appear to be in the same plane where the torsion angles O-C(O)-N(H)-C(S) and C(O)-N(H)-C(S)-S exhibit values of -1.4 (5) and -6.9 (4) ° respectively. A plane defined by the atoms H1/O1/C7/N1/C8/S1 exhibits a r.m.s. deviation of 0.0470 Å, where the maximum deviation is exhibited by S1 (-0.0656 (174) Å). Intermolecular $\pi - \pi$ interactions appear to be present in the crystal lattice of HL_S^{2g} (Fig. 2.324 (A)) where a plane defined by C1/C2/C3/C4/C5/C6 exhibits a r.m.s. deviation of 0.0067, the maximum deviation of 0.0100 (25) being displayed by C6; the interplanar spacing between the benzene residues of neighbouring molecules (symmetry code: 2-x, 1-y, -z) is 3.3253 (317) Å.

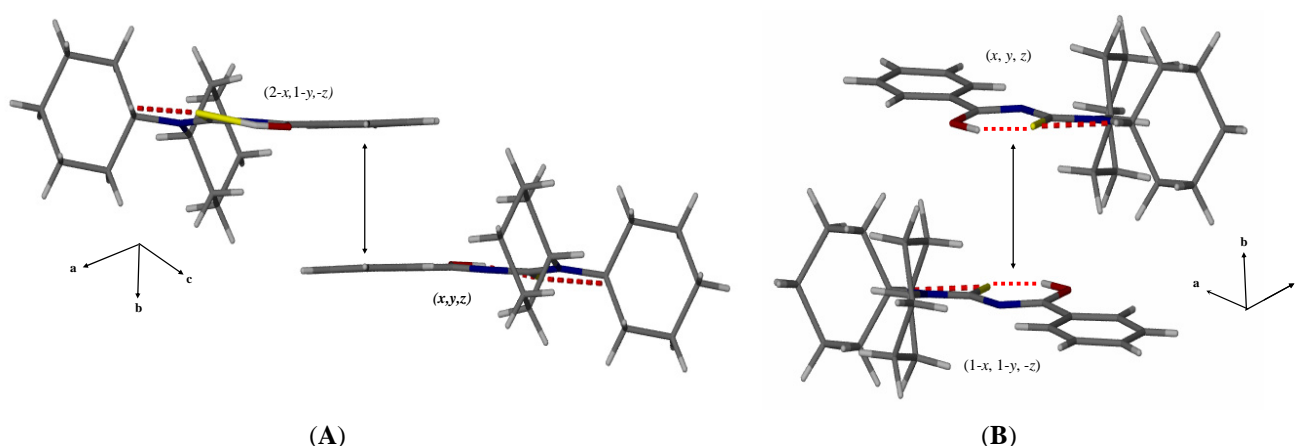


Fig. 2.324 $\pi - \pi$ interactions displayed by *N,N*-dicyclohexyl-*N'*-benzoylthiourea HL_S^{2g} (A) and short contact between chelate rings of HL_S^{2g} (B).

Further evidence of electronic delocalization in the acylthiourea moiety is found in the N-C(S) and (S)-C-NR₂ bond lengths where the latter is significantly longer than the corresponding bonds in the dialkyl analogues. It is therefore likely that a certain amount of aromatic character is present in the acylthiourea moiety and this is lent further

credence by the short distance between the planes (H1/O1/C7/N1/C8/S1) of neighbouring molecules (symmetry code 1-x, 1-y, -z) being 3.7075 (296) Å (Fig. 2.324 (B)).

Table 2.37 shows selected bond lengths and torsion angles of compounds **21**, **23-25** and **27**. No structural characterization of HL_S^{2b} **22**, could be found however that of the *para*-chloro analogue has recently been reported^[107] and is included in Table 2.37 for the purposes of comparison. Similarly to the selenium analogues the (O)C-N, N-C(S) and (S)C-NR₂ bonds are all shorter than the average C-N single bond length of 1.472 (5) Å; the bond lengths decreasing in the order N-C(S) > (O)C-N > S(C)-NR₂.^{[82][97]}

Table 2.37 Selected bond lengths (Å) and torsion angles (°) for compounds **21-25**, **27**.

Compound	C=O	C=S	(O)C-N	N-C(S)	(S)C-NR ₂	O-C(O)-N(H)-C(S)	C(O)-N(H)-C(S)-S
HL _S ^{2a} 21 ^[106]	1.230 (3)	1.672 (3)	1.362 (4)	1.448 (4)	1.320 (4)	-12.5 (4)	-100.4 (3)
<i>p</i> -Cl analogue of HL _S ^{2b} 22 ^[107]	1.215 (3)	1.677 (2)	1.382 (3)	1.410 (3)	1.328 (3)	-1.10	120.68
HL _S ^{2c} 23	1.216 (2)	1.683 (2)	1.379 (2)	1.411 (2)	1.322 (2)	-12.1 (2)	-108.9 (2)
HL _S ^{2d} 24	1.222 (4)	1.676 (3)	1.382 (4)	1.420 (4)	1.312 (4)	-11.9 (5)	-109.4 (3)
HL _S ^{2e} 25	1.222 (2)	1.686 (2)	1.386 (2)	1.401 (2)	1.329 (2)	-6.3 (3)	128.9 (2)
HL _S ^{2g} 27	1.321 (4)	1.716 (3)	1.293 (4)	1.391 (4)	1.338 (4)	-1.4 (5)	-6.9 (4)

HL_S^{2a} displays a particularly long N-C(S) bond of 1.448 (4) Å as well as a longer C=O bond length of 1.230 (3) Å. This can be understood in the light of the intermolecular hydrogen bonding displayed by this compound between the thioamidic proton and the carbonyl oxygen atom of a neighbouring molecule being quite different to that of the other compounds in the series. The relative orientations of the O and S atoms can be defined using the following torsion angles: O-C(O)-N(H)-C(S) and C(O)-N(H)-C(S)-S and Table 2.37 indicates that compounds **21-25** exhibit largely opposing orientations of these two atoms.

Table 2.38 shows the hydrogen bonding data of compounds **23-25**. The S[⋯]H-N dimeric hydrogen bonds are all of comparable length although the Donor-H[⋯]Acceptor angles differ somewhat, HL_S^{2c} and HL_S^{2d} exhibiting similar angles of 147 (2) and 148 (3) ° respectively and HL_S^{2e} the largest at 165.93 °. In terms of hydrogen bonding, the benzoylthiourea moiety, like the selenourea, consists of a donor-acceptor pair connected by a delocalized π-system reflected in the shorter amide and acyl-substituted C-N bonds. The formation of dimers in the crystal lattice therefore represents as example of resonance-assisted hydrogen bonding (RAHB) or π bonding cooperativity.^[99]

Table 2.38 Hydrogen-bond geometry (Å, °) for **23-25**

	D—H [⋯] A	D—H	H [⋯] A	D [⋯] A	D—H [⋯] A
HL _S ^{2c} 23	N1—H1 [⋯] S1 ⁱ (i) = 2-x, 1-y, 2-z	0.81 (2)	2.72 (2)	3.428 (2)	147 (2)
HL _S ^{2d} 24	N1—H1 [⋯] S1 ⁱ (i) = -x, 1-y, 1-z	0.87 (4)	2.69 (4)	3.467 (3)	148 (3)
HL _S ^{2e} 25	N1—H1 [⋯] S1 ⁱ (i) = 1-x, 1-y, 1-z	0.962	2.480	3.422 (2)	165.93

Generally, it appears as though the intermolecular interactions exhibited by both the *N,N*-dialkyl-*N'*-benzoylselenourea and *N,N*-dialkyl-*N'*-benzoylthiourea ligands are similar, where HL_{Se}^{1c} and HL_{Se}^{1d} exhibit RAHB and intermolecular π – π interactions between the benzene residues of neighbouring molecules as do their sulfur analogues, HL_S^{2c} and HL_S^{2d}. In addition, the asymmetrically substituted HL_{Se}^{1e} and HL_S^{2e} both exhibit the *Z* isomer as the most stable in the solid state, and RAHB similar to their symmetrically substituted analogues. It is interesting

to note that in the synthesis of *N,N*-dicyclohexyl-*N'*-benzoylselenourea and its sulfur analogue, interesting solid state structures were obtained. In the case of *N,N*-dicyclohexyl-*N'*-benzoylselenourea, the ligand could not be isolated, but the 1,3,5-oxaselenazine salt **18a** was obtained and in the case of *N,N*-dicyclohexyl-*N'*-benzoylthiourea HL_S^{2g} a tautomeric form of the ligand was isolated in the solid state. This suggests that the choice of amine in the synthesis of both the selenium and sulfur containing ligands has significant influence over the final product obtained. The crystal structure analysis of 3,3,3',3'-tetra(*n*-butyl)-1,1'-isophthaloylbis(selenourea) reveals intermolecular interactions similar to those exhibited by the monopodal analogue, HL^{1b}, where RAHB occurs between the selenoamidic protons and selenium atoms of neighbouring molecules leading to chains of hydrogen bonded units in the crystal lattice. Despite several attempts, synthesis of the isomeric 3,3,3',3'-tetra(*n*-butyl)-1,1'-terephthaloylbis(selenourea) was not possible indicating the differing stabilities of compounds of this type.

Table 2.39 Crystal and structure refinement data for compounds **23-25, 27**.

Compound	HL _S ^{2c} , 23	HL _S ^{2d} , 24	HL _S ^{2e} , 25	HL _S ^{2g} , 27
Empirical Formula	C ₂₀ H ₃₂ N ₂ OS	C ₂₄ H ₄₀ N ₂ OS	C ₁₆ H ₁₆ N ₂ OS	C ₂₀ H ₂₈ N ₂ OS
Formula Weight /gmol ⁻¹	348.30	404.64	284.37	344.50
Crystal system	monoclinic	monoclinic	monoclinic	monoclinic
Space Group	<i>P</i> 2 ₁ / <i>c</i>			
Unit cell dimensions				
<i>a</i> / Å	10.650 (7)	12.5783 (16)	11.208 (2)	10.7337 (16)
<i>b</i> / Å	9.394 (6)	9.4801 (12)	4.8285 (9)	11.9260(18)
<i>c</i> / Å	20.311 (12)	20.192 (3)	26.039 (5)	14.338 (2)
β / °	90.053 (12)	99.423 (2)	92.474 (4)	98.797 (2)
<i>V</i> / Å ³	2032 (2)	2375.3 (5)	1407.9 (5)	1813.8 (5)
<i>Z</i>	4	4	4	4
μ / mm ⁻¹	0.168	0.152	0.227	0.188
<i>T</i> / K	100 (2)	100 (2)	100 (2)	273 (2)
Reflections collected / unique	12602/4788	13893 / 5494	8483/3317	11037/4189
Data / restraints / parameters	3761/0/223	3707/0/259	2557/0/186	2881/0/225
Goodness-of-fit on <i>F</i> ²	1.028	1.117	1.011	1.196
Final <i>R</i> indices [<i>I</i> > 2σ(<i>I</i>)]	5.22, 12.82 %	7.04, 12.20 %	5.02, 10.70%	0.0546, 11.70 %
<i>R</i> indices (all data)	<i>R</i> = 0.0685 <i>wR</i> ₂ = 0.1397	<i>R</i> = 0.1195 <i>wR</i> ₂ = 0.1799	<i>R</i> = 0.0711 <i>wR</i> ₂ = 0.1168	<i>R</i> = 0.0979 <i>wR</i> ₂ = 0.1804

2.3.3 Crystal and molecular structures of *N,N*-dialkyl-*N'*-benzoylselenourea metal complexes

Complex synthesis of the *cis*-bis(*N,N*-dialkyl-*N'*-benzoylselenoureaato)palladium(II) complexes discussed in this section was performed using a method of solvent extraction. This method is described in detail in Section 2.2.3.2 and therefore only briefly summarised here.

In general, 2 molar equivalents of the appropriate ligand were dissolved in dichloromethane, followed by the addition of an aqueous solution containing one molar equivalent of the metal salt, K₂PdCl₄ and an excess of the base, sodium acetate. Vigorous shaking of the biphasic solvent system in a separating funnel allowed the formation of the metal complex in the organic phase, this being extracted, dried and the majority of solvent removed by evaporation to allow the isolation of the final product. Crystal and refinement data for the crystal structures discussed in this section are summarised in Table 2.313 at the end of the section.

2.3.3.1 Crystal and molecular structure of *cis*-bis(*N,N*-diethyl-*N'*-benzoylselenoureato)palladium(II), *cis*-[Pd^{II}(L^{1a}-Se,O)₂], **112**

Recrystallization of *cis*-bis(*N,N*-diethyl-*N'*-benzoylselenoureato)palladium(II), *cis*-[Pd^{II}(L^{1a}-Se,O)₂] **112** yielded crystals suitable for single crystal X-ray diffraction analysis and the molecular structure as well as the crystal packing are illustrated in Fig 2.325 (A and B). Similarly to the sulfur analogue, *cis*-bis(*N,N*-diethyl-*N'*-benzoylthioureato)palladium(II)^[34], loss of the H atom from HL_{Se}^{1a} allows coordination to take place through the O and Se atoms and the compound crystallizes out in the *cis*-square-planar conformation. The atoms in the coordination sphere of *cis*-[Pd^{II}(L^{1a}-Se,O)₂] all lie in a plane (Se1A/Se1B/O1A/O1B/Pd1) with a root mean square deviation of 0.0052, and a maximum deviation of 0.0071 (6) exhibited by Pd1. By comparison, the chelate rings however differ slightly, with the nitrogen atom (N1A) in ring A lying -0.564 (3) Å below the coordination plane and the corresponding atom in ring B (N1B) lying 0.831 (3) Å above the coordination plane. Interestingly the chelate rings exhibit significantly differing degrees of planarity, where for ring A, a plane defined by the atoms Se1A/C8A/N1A/C7A/O1A has a root mean squared deviation of 0.1874, the largest deviation being that of O1A (-0.194 (1) Å). Similar atoms in ring B, Se1B/C8B/N1B/C7A/O1B, are clearly more planar where the root mean squared deviation is only 0.0318, the maximum being for C7B (-0.0537 (17)). The coordination plane defined by atoms Se1A/Se1B/O1A/O1B/Pd1 and chelate plane defined by the atoms in chelate ring A, Se1A/C8A/N1A/C7A/O1A, lie at an angle of 21.48 (7) ° to each other and that of the coordination plane, Se1A/Se1B/O1A/O1B/Pd1, and chelate plane defined by the atoms in chelate ring B, Se1B/C8B/N1B/C7A/O1B, at 23.18 (6) °; so allowing the molecule to describe a shallow “S” shape (Fig. 2.325(B)). Selected bond lengths and angles of this structure are summarised in Table 2.310 and discussed later in the section.

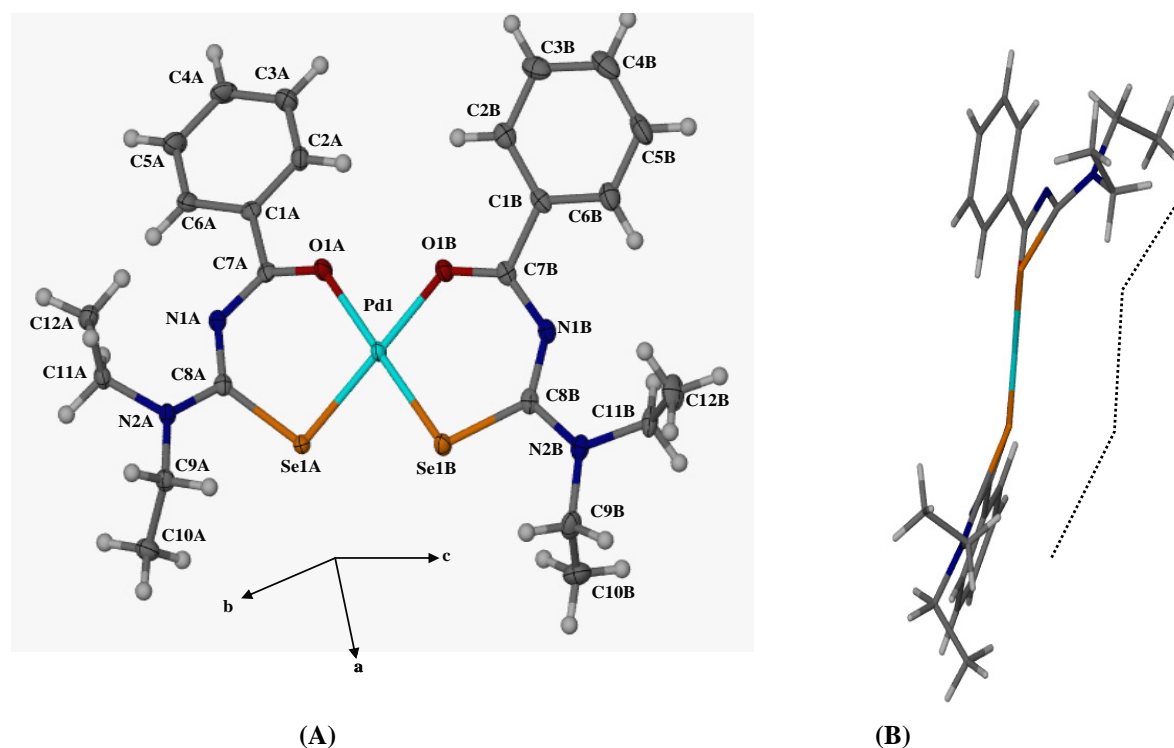


Fig. 2.325 The molecular structure of *cis*-bis(*N,N*-diethyl-*N'*-benzoylselenoureato)palladium(II), *cis*-[Pd^{II}(L^{1a}-Se,O)₂] **112** with atom numbering scheme shown, displacement ellipsoids are drawn at the 50 % probability level (A) and side view of complex illustrating “S” shape described by the compound (B).

2.3.3.2 Crystal and molecular structure of *cis*-bis(*N,N*-dibutyl-*N'*-benzoylselenoureato)palladium(II), *cis*-[Pd^{II}(L^{1b}-Se,O)₂], **122**

Slow evaporation from a chloroform, ethanol solvent mixture yielded crystals of *cis*-bis(*N,N*-dibutyl-*N'*-benzoylselenoureato)palladium(II), *cis*-[Pd^{II}(L^{1b}-Se,O)₂] **122** suitable for single crystal X-ray diffraction analysis. The molecular structure and packing diagram are shown in Fig. 2.326 (A and B) respectively. The generally expected mode of coordination of HL_{Se}^{1b} with loss of the selenoamidic proton and yielding a *cis*-square-planar complex is observed. The four donor atoms and Pd metal centre lie in a single coordination plane involving atoms Se1A/O1A/Pd1/Se1B/O1B with a mean deviation from planarity of only 0.026 Å, the maximum being for O1B (-0.0324 (5) Å). The two chelate rings are twisted at an angle of 4.6 (1) ° relative to each other and deviate slightly from perfect planarity with mean deviations of 0.096 and 0.085 Å for atoms Se1A/C8A/N1A/C7A/O1A and Se1B/C8B/N1B/C7B/O1B, respectively. The reduced planarity in the chelate rings is reflected in a puckering of the C7A/N1A/C8A and C7B/N1B/C8B planes, with atoms N1A and N1B respectively lying 0.486 (2) Å below and 0.336 (2) Å above the coordination plane, these distances being significantly less than the corresponding distances in the diethyl analogue. The coordination plane and chelate plane defined by the atoms in chelate ring A lie at an angle of 15.63 (6) ° to each other and that of the coordination plane and chelate plane defined by the atoms in ring B at 11.48 (7) °; these angles being significantly smaller than those exhibited by the diethyl analogue, HL_{Se}^{1a} describing a much shallower “S” shape than HL_{Se}^{1a}.

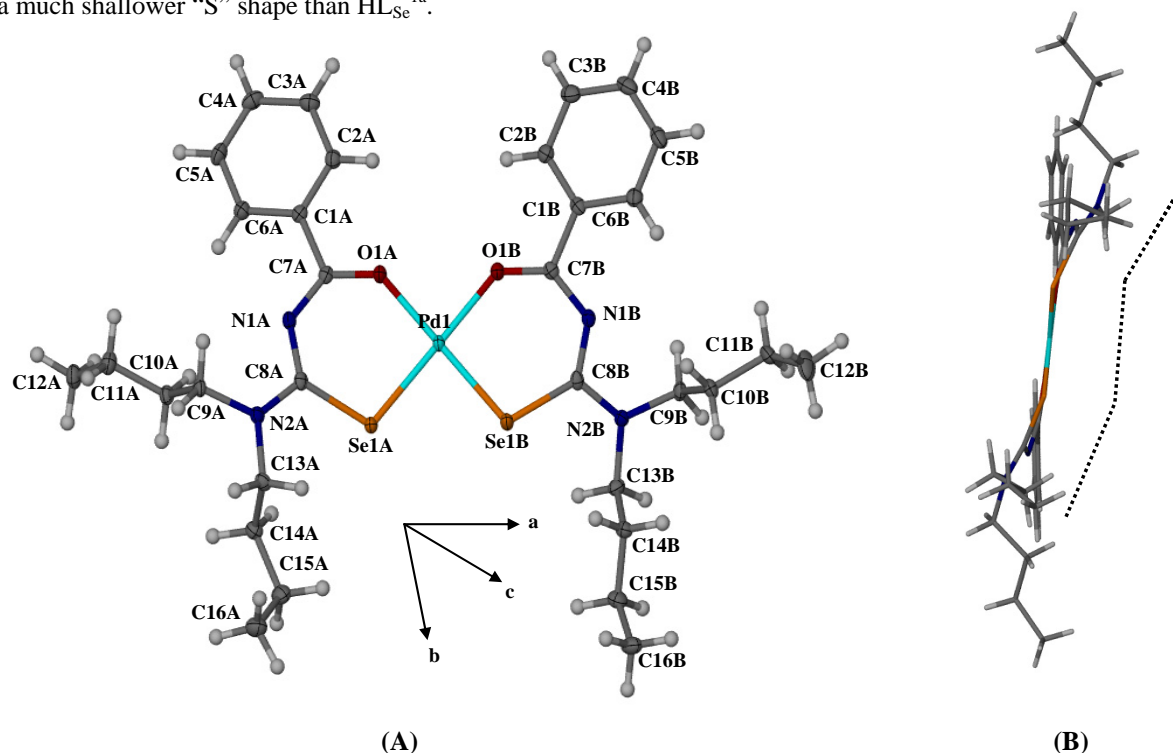


Fig. 2.326 The molecular structure of *cis*-bis(*N,N*-dibutyl-*N'*-benzoylselenoureato)palladium(II), *cis*-[Pd^{II}(L^{1b}-Se,O)₂] **122** with atom numbering scheme shown, displacement ellipsoids are drawn at the 50 % probability level (A) and and side view of complex illustrating shallow “S” shape described by the compound (B).

2.3.3.3 Crystal and molecular structure of *cis*-bis(*N*-benzyl-*N*-methyl-*N'*-benzoylselenoureato)palladium(II), *cis*-[Pd^{II}(L^{1c}-Se,O)₂], **152**

Crystals of *cis*-bis(*N*-benzyl-*N*-methyl-*N'*-benzoylselenoureato)palladium(II), *cis*-[Pd^{II}(L^{1c}-Se,O)₂] **152** were isolated from an NMR tube and analysed using single crystal X-ray diffraction. Unfortunately the structure is of

poor quality and several atoms classified as “non-positive definite” are shown as spheres and not thermal ellipsoids in Fig. 2.327. Despite the poor quality of the structure the basic geometry of the complex is easily discernable and several important observations can be made. As usual the complex has a *cis* configuration and coordination takes place through the Se and O donor atoms leading to a square planar metal complex. As previously seen in Section 2.3.1.5, the *Z* isomer is favoured by the ligand in the solid state. Interestingly, it would appear that the *EZ* isomer of the palladium complex is the most stable in the solid state. In *cis*-[Pd^{II}(L^{1e}-Se,O)₂] **152** chelate ring A displays Se1A and the phenyl ring on the same side of the C8A-N2A partial double bond (*Z* configuration) whereas chelate ring B displays Se1B and the phenyl ring on either side of the C8B-N2B partial double bond (*E* configuration) giving rise to the *EZ* configuration. Efforts to recrystallise a better quality crystal of this compound to confirm the observations proved unsuccessful, however this is, to the best of our knowledge, the first structural characterization of an asymmetrically substituted *N,N*-dialkyl-*N'*-benzoylselenourea palladium complex. In the related *N,N*-dialkyl-*N'*-benzoylthioureas, Mtongana *et. al.* obtained the structural analysis of a platinum (II) complex, *cis*-bis(*N*-pentyl-*N'*-(4-methoxy-phenyl)-*N'*-2,2-dimethylpropanoylthioureato)platinum(II) in the solid state, and interestingly, this complex exhibited the *ZZ* isomer as the most stable in the solid state.^[83]

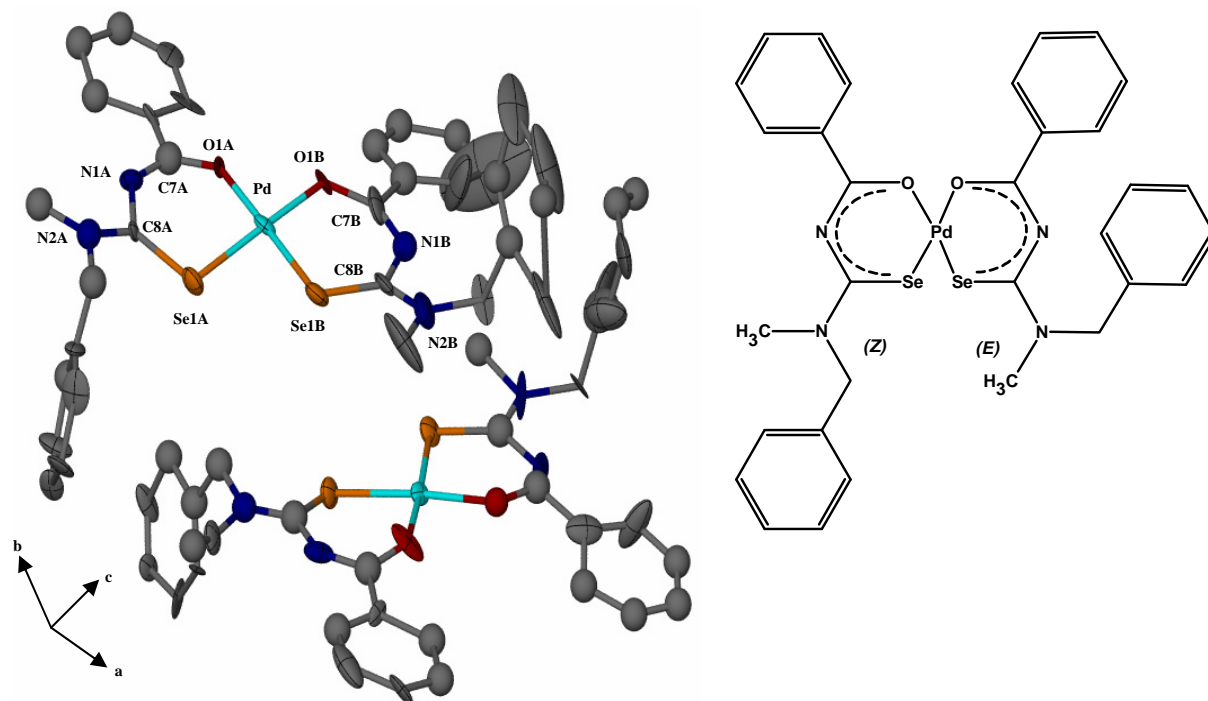


Fig. 2.327 The molecular structure of *cis*-bis(*N*-benzyl-*N*-methyl-*N'*-benzoylselenoureato)palladium(II), *cis*-[Pd^{II}(L^{1e}-Se,O)₂] **152** with selected atom numbers shown.

Table 2.310 Selected geometric parameters (Å, °) for compounds **11**, **12**, **15**, **112**, **122** and **152**.

	HL ^s ^{1a} 11	<i>cis</i> -[Pd ^{II} (L ^{1a} -Se,O) ₂] 112		HL ^s ^{1b} 12	<i>cis</i> -[Pd ^{II} (L ^{1b} -Se,O) ₂] 122		HL ^s ^{1e} 15	<i>cis</i> -[Pd ^{II} (L ^{1e} -Se,O) ₂] 152	
		Ring A	Ring B		Ring A	Ring B		Ring A	Ring B
Pd-O		2.0587 (17)	2.0360 (17)		2.0395 (12)	2.0439 (12)		1.96 (3)	2.00 (4)
C=O	1.221(2)	1.268 (3)	1.263 (3)	1.212 (3)	1.266 (2)	1.260 (2)	1.220 (2)	1.33 (5)	1.46 (6)
(O)C-N	1.388(2)	1.331 (3)	1.336 (3)	1.397 (3)	1.329 (2)	1.335 (2)	1.383 (3)	1.34 (5)	1.17 (6)
N-C(Se)	1.416(2)	1.329 (3)	1.332 (3)	1.399 (3)	1.333 (2)	1.334 (2)	1.392 (2)	1.42 (6)	1.45 (6)
C=Se	1.834(2)	1.915 (2)	1.908 (2)	1.848 (2)	1.9076 (17)	1.9006 (16)	1.844 (2)	1.84 (4)	1.83 (5)
(Se)C-NR ₂	1.320(2)	1.334 (3)	1.347 (2)	1.314 (3)	1.341 (2)	1.338 (2)	1.324 (2)	1.33 (6)	1.28 (7)
Pd-Se		2.3581 (2)	2.3391 (6)		2.3489 (3)	2.3411 (3)		2.344 (6)	2.374 (6)
O-Pd-Se		93.37 (5)	93.99 (5)		93.12 (3)	93.59 (4)		94.5 (10)	97.7 (10)

The Pd-O and Pd-Se bonds of *cis*-[Pd^{II}(L^{1a}-Se,O)₂] and *cis*-[Pd^{II}(L^{1b}-Se,O)₂] compare well with those previously reported for bis[*N'*-(2-fluorobenzoyl)-*N,N*-diisobutylselenoureato]palladium(II)^[16] where the average Pd-O bond length = 2.0645 (3) Å and Pd-Se bond length = 2.356 (1) Å, as well as the difluoro analogue, *N,N*-diisobutyl-*N'*-(2,6-difluoro)benzoylselenourea, where Pd-O = 2.0755 (2) and Pd-Se = 2.357 (1) average bond lengths were reported.^[17] The C=O and C=Se bond lengths in the Pd(II) complexes are somewhat longer than in the corresponding ligands as a result of a slight loss of double bond character in these bonds, presumably due to electronic delocalization in the six-membered chelate ring of the metal complex. The relative reduction in the C=Se bond order of HL^{1a}, HL^{1b} and HL^{1e} on coordination to Pd(II) in the respective complexes is reflected by a reduction of the ¹*J*(⁷⁷Se-¹³C) coupling constants details of which will be discussed in Section 2.3.5.1. The electron delocalization in the chelate rings of the Pd(II) complexes is further shown by the slight shortening of the *endo* C-N bond lengths ((O)C-N and N-C(Se)) as well as the slight lengthening of the *exo* C-N bond ((Se)C-NR₂) relative to those in the uncoordinated ligands.

2.3.3.4 Crystal and molecular structure of (*N,N*-diphenyl-*N'*-benzoylselenoureato)cadmium(II), [Cd^{II}(L^{1g}-Se,O)₂], **171**

Slow evaporation from an ethanol solution yielded crystals of (*N,N*-diphenyl-*N'*-benzoylselenoureato)cadmium(II), [Cd^{II}(L^{1g}-Se,O)₂] **171**, the molecular structure of which is shown in Fig. 2.328.

Remarkably, this compound contains two metal centres, and the metal : ligand ratio of 1:2 that would be expected in a Cd(II) complex, is maintained in the structure. The coordination environment of the two cadmium ions however appear to be quite distinct, (Fig. 2.328 inset). Cd(2) is a six coordinate metal centre, being bound to three Se and three O atoms, while Cd(1) was initially thought to be only 4 coordinate, being bound to Se1A, Se1C, Se1D and O1A. However, a bond has been defined between Cd(1) and O1D as the interatomic distance of 2.6935 (20) Å is only slightly longer than the O1D-Cd(2) bond of 2.6420 (20) Å, the distance between O1C and Cd(1) of 3.5160 (20) Å is thought to be too long to justify a bond, so that Cd(1) appears to be a 5 coordinate metal centre. Chelate rings A and B bind to Cd(1) and Cd(2) respectively in the expected fashion of these compounds, however chelate C has a shared Se atom between both Cd metal centres. Chelate D in turn, shares both its coordinating atoms (O and Se) between the metal centres.

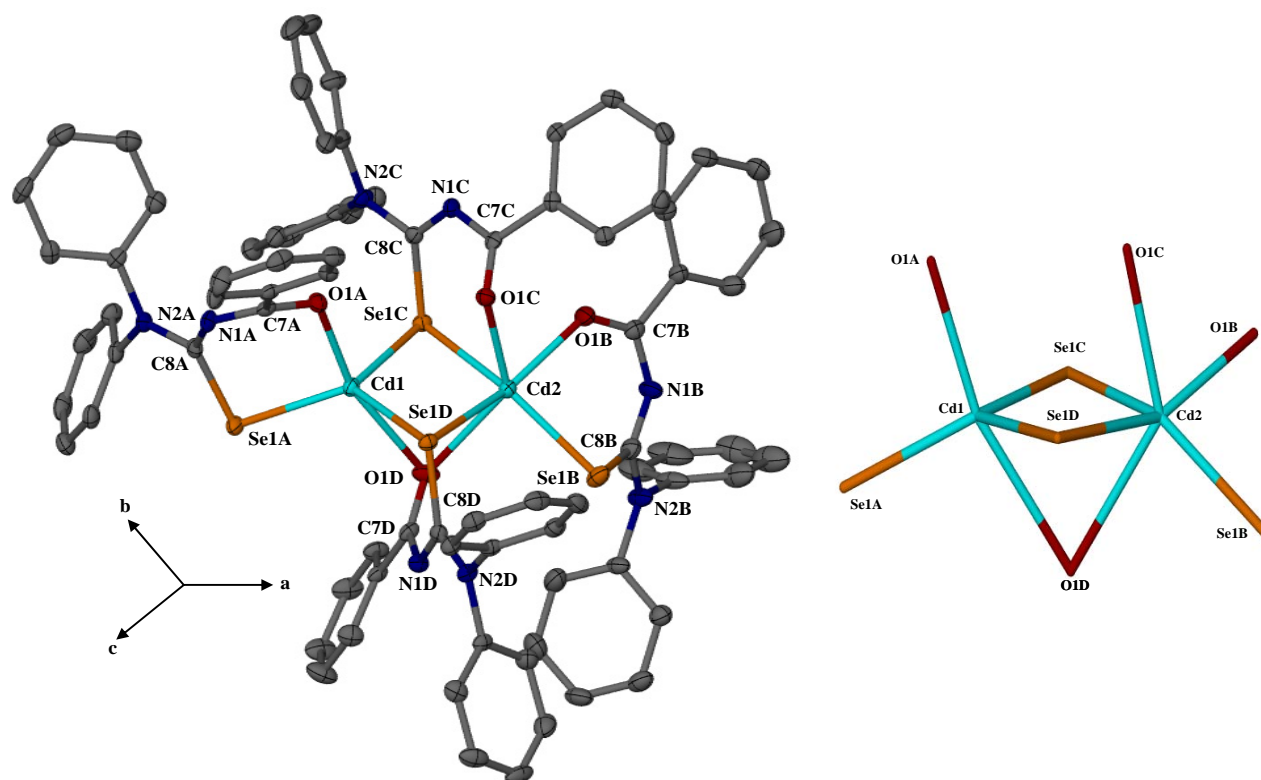


Fig. 2.328 The molecular structure of (*N,N*-diphenyl-*N'*-benzoylselenoureato)cadmium(II), $[\text{Cd}^{\text{II}}(\text{L}^{1\text{g}}\text{-Se},\text{O})_2]$ **171**, with selected atom numbering shown, displacement ellipsoids are drawn at the 50 % probability level, hydrogen atoms have been omitted for clarity. Inset shows the differing coordination of the two Cd metal centres.

The two central Cd atoms, Se1C and Se1D lie in a plane with a mean deviation of 0.0765 Å. O1A and O1C lie 2.0141 (20) Å and 2.2099 (20) Å respectively, above this plane, Se1B and Se1A being -1.3992 (8) Å and -1.0822 (7) Å below this plane, O1C lies only 0.768 (2) Å above this plane. The intramolecular Cd-Cd distance of 3.2603 (10) Å is slightly larger than the sum of the Van der Waal's radii.

Table 2.311 Selected bond lengths (Å) for $\text{HL}_{\text{Se}}^{1\text{g}}$ **17**, $[\text{Cd}^{\text{II}}(\text{L}^{1\text{g}}\text{-Se},\text{O})_2]$ **171**, $\text{HL}^{1\text{a}}$ **11**, and $[\text{Cd}^{\text{II}}(\text{L}^{1\text{a}}\text{-Se},\text{O})_2]$ **111**

Compound	C=O	C=Se	(O)C-N	N-C(Se)	(Se)C-NR ₂	
$\text{HL}_{\text{Se}}^{1\text{g}}$, 17	1.215 (5)	1.966 (3)	1.386 (5)	1.274 (5)	1.361 (4)	
$[\text{Cd}^{\text{II}}(\text{L}^{1\text{g}}\text{-Se},\text{O})_2]$ 171	1.261 (3)	1.906 (3)	1.326 (3)	1.323 (3)	1.356 (3)	Chelate ring A
	1.251 (3)	1.908 (3)	1.345 (3)	1.308 (3)	1.352 (3)	Chelate ring B
	1.238 (3)	1.940 (3)	1.361 (3)	1.298 (3)	1.364 (3)	Chelate ring C
	1.246 (3)	1.924 (3)	1.357 (3)	1.316 (3)	1.344 (3)	Chelate ring D
	1.249 (3)	1.920 (3)	1.347 (3)	1.311 (3)	1.354 (3)	Chelate average
$\text{HL}_{\text{Se}}^{1\text{a}}$, 11	1.221 (2)	1.834 (2)	1.388 (2)	1.416 (2)	1.320 (2)	
$[\text{Cd}^{\text{II}}(\text{L}^{1\text{a}}\text{-Se},\text{O})_2]$ 111	1.257 (3)	1.908 (3)	1.325 (4)	1.326 (4)	1.335 (4)	Chelate ring A
	1.287 (3)	1.911 (3)	1.309 (3)	1.337 (3)	1.324 (4)	Chelate ring B
	1.272 (3)	1.910 (3)	1.317 (4)	1.332 (4)	1.330 (4)	Chelate average

Table 2.311 shows selected bond lengths in the chelate rings A-D as well as the average of these distances for easy comparison with those of the ligand $\text{HL}_{\text{Se}}^{1\text{g}}$ **17**. As for the Pd (II) complexes, the C=O bond length is lengthened in the Cd chelate relative to the uncoordinated ligand indicating a reduction in electron density and the presence of

only a partial C-O double bond. Interestingly the inverse is observed for the C=Se bond, where the average distance in the chelate (1.920 (3) Å) is shorter than that in $\text{HL}_{\text{Se}}^{1g}$ (1.966 (3) Å), however this can be rationalized in the light of the Se-Se bond present in the ligand (Section 2.3.1.7) reducing the double bond character of the C=Se bond to that of a single bond, and electron density being restored in the chelate allowing a shortening of this bond. The electron delocalization in the chelate rings is shown by the slight shortening of the (O)C-N and (Se)C-NR₂ bond lengths relative to the corresponding bonds in the unbound ligand, $\text{HL}_{\text{Se}}^{1g}$.

Three of the Cd-O bond lengths (Cd1-O1A, Cd2-O1B/O1C) fall in the range 2.254 (2) – 2.327 (2), the remaining two Cd-O bonds being the longest, between the shared O1D atom and the two Cd metal centres (Table 2.312). As expected the shared Se atoms (Se1C, Se1D) exhibit slightly longer Cd-Se bonds than those atoms bound to only a single metal centre (Se1A, Se1B). The five coordinate metal centre, Cd(1), has a geometry that can be described as distorted trigonal bipyramidal, given the following angles: O1D-Cd1-O1A = 162.72 (6) °, Se1D-Cd1-Se1C = 109.03 (3) °, Se1D-Cd1-Se1A = 123.42 (3) °, Se1C-Cd1-Se1A = 123.98 (2) °. If the Cd(1)-Se1D distance of 2.8367 (8) Å is considered too long to warrant classification as a formal bond, the Cd(2) metal centre will also be 5 coordinate, however the geometry resembles square pyramidal rather than the trigonal bipyramidal seen in Cd(1) where Cd(2) lies 0.8483 (8) Å above a plane defined by Se1C/O1D/Se1B/O1B with a r.m.s of 0.0843 Å. The angle between O1C and this plane is 86.93 ° and O1B-Cd2-Se1B = 85.96 (6) °, O1B-Cd2-Se1C = 86.53 (6) °, Se1B-Cd2-O1D = 92.27 (5) °, Se1C-Cd2-O1D = 69.70 (5) °.

Dimeric cadmium(II) solid state structures are not unknown^[108] and Kedarnath *et al.* have previously reported the structural elucidation of trimeric $[\text{Cd}_3(\text{OAc})_2(\text{SeCH}_2\text{CH}_2\text{NMe}_2)_4]$ where two metal centres are 6 coordinate and symmetrically equivalent, the central metal ion being four coordinate.^[109] Vittal *et al.* have also reported a 5 coordinate metal centre displaying distorted trigonal bipyramidal geometry similar to that of Cd(1) in $[\text{Cd}^{\text{II}}(\text{L}^{1g}\text{-Se},\text{O})_2]$ **171**, with three Se and two O donor atoms.^[110]

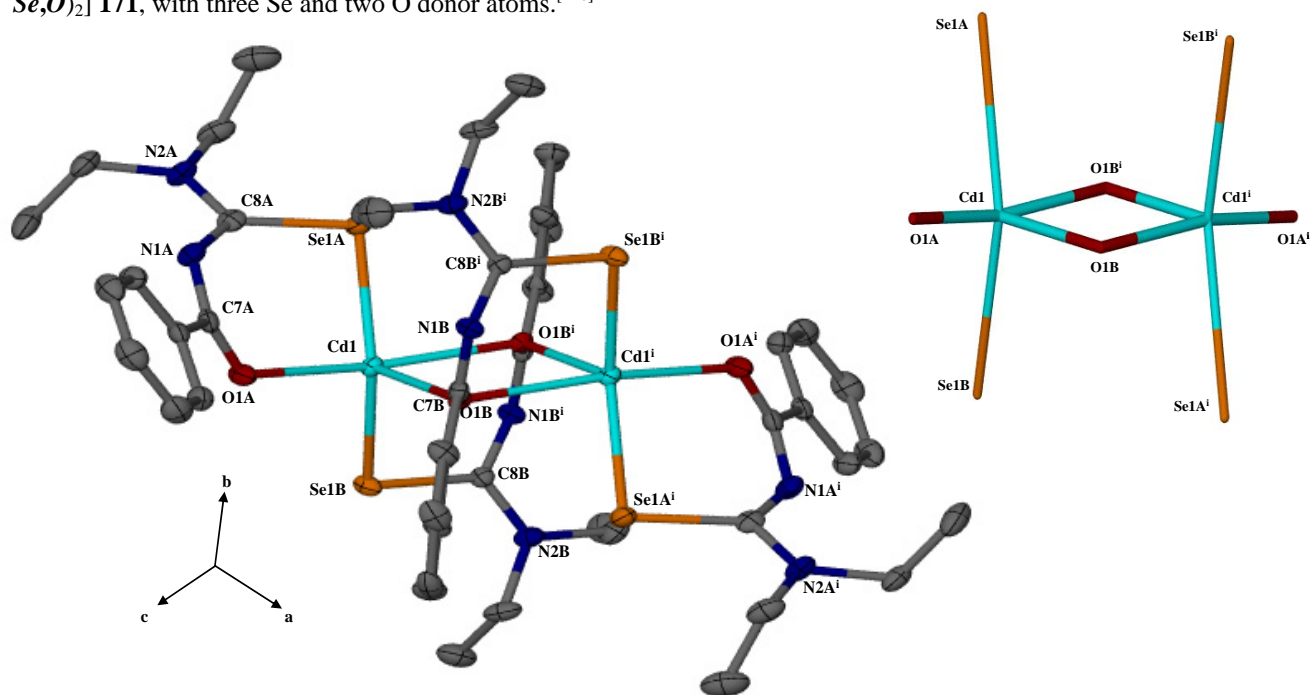


Fig. 2.329

The molecular structure of (*N,N*-diethyl-*N'*-benzoylselenoureato)cadmium(II), $[\text{Cd}^{\text{II}}(\text{L}^{1a}\text{-Se},\text{O})_2]$ **111**, with selected atom numbering shown, displacement ellipsoids are drawn at the 50 % probability level, hydrogen atoms have been omitted for clarity, [Symmetry code (i) 1-*x*, 1-*y*, -*z*]. Inset shows coordination environment of Cd metal centres.

Table 2.311 Shows the bond lengths of $\text{HL}_{\text{Se}}^{\text{Ia}}$ and $[\text{Cd}^{\text{II}}(\text{L}^{\text{Ia}}\text{-Se},\text{O})_2]$ **111**, the structure of which was initially published by Bensch and Schuster in 1993.^[10] Our analysis of the same complex yielded a slightly better data set and for this reason the bond distances and angles quoted in Table 2.311 and Table 2.312 are those that we obtained. The molecular structure of $[\text{Cd}^{\text{II}}(\text{L}^{\text{Ia}}\text{-Se},\text{O})_2]$ is shown in Fig 2.329; approximately half the molecule is present in the asymmetric unit, the remainder being generated by the symmetry code $(-x, 1-y, 1-z)$. It is interesting to note that where $[\text{Cd}^{\text{II}}(\text{L}^{\text{Ia}}\text{-Se},\text{O})_2]$ **171** had two bridging Se atoms, Se1C and Se1D, the diethyl analogue has two bridging O atoms and the Cd metal centre can be described as having distorted trigonal bipyramidal geometry with $\text{O1A-Cd1-O1B}^{\text{i}} = 168.19(6)^\circ$, $\text{O1A-Cd1-O1B} = 92.70(7)^\circ$, $\text{O1B-Cd1-O1B}^{\text{i}} = 79.72(7)^\circ$ and $\text{Se1A-Cd1-Se1B} = 145.40(1)^\circ$. Similarly to $[\text{Cd}^{\text{II}}(\text{L}^{\text{Ia}}\text{-Se},\text{O})_2]$ **171**, the C=O bond length is increased relative to that in the ligand and this time the C=Se bond does likewise. Electron delocalization in the chelate ring is evident from the shortening of the (O)C-N and N-C(Se) bonds in the chelate relative to those in the uncoordinated ligand. Interestingly, the (Se)C-NR₂ bond is slightly lengthened in the chelate, whereas in the diphenyl analogue, the N-C(Se) exhibits this phenomenon. It is worth mentioning here that the structural characterization of the sulfur analogue has been reported and that the coordination sphere of the Cd metal centre is very similar to that of the Se derivative.^[80] From these structures, it may be concluded that the nature of the ligand substituents has a significant impact on the resulting solid state structures of the metal complexes.

Table 2.312 Selected geometric parameters of $[\text{Cd}^{\text{II}}(\text{L}^{\text{Ia}}\text{-Se},\text{O})_2]$ **171** and $[\text{Cd}^{\text{II}}(\text{L}^{\text{Ia}}\text{-Se},\text{O})_2]$ **111** (Å, °).

$[\text{Cd}^{\text{II}}(\text{L}^{\text{Ia}}\text{-Se},\text{O})_2]$ 171 , Cd1		$[\text{Cd}^{\text{II}}(\text{L}^{\text{Ia}}\text{-Se},\text{O})_2]$ 171 , Cd2		$[\text{Cd}^{\text{II}}(\text{L}^{\text{Ia}}\text{-Se},\text{O})_2]$ 111	
Distance / Angle		Distance / Angle		Distance / Angle	
Cd1-O1A	2.254 (2)	Cd2-O1B	2.327 (2)	Cd1-O1A	2.271 (2)
Cd1-O1D	2.694 (2)	Cd2-O1C	2.363 (2)	Cd1-O1B	2.270 (2)
Cd1-Se1A	2.5678 (8)	Cd2-O1D	2.642 (2)	Cd1-O1B ⁱ	2.430 (2)
Cd1-Se1C	2.6582 (7)	Cd2-Se1B	2.5694 (8)	Cd1-Se1A	2.5716 (4)
Cd1-Se1D	2.6424 (7)	Cd2-Se1C	2.7020 (8)	Cd1-Se1B	2.5931 (4)
		Cd2-Se1D	2.8367 (8)		
Se1D-Cd1-Se1C	109.03 (3)	O1C-Cd2-O1D	128.65 (6)	Se1A-Cd1-O1A	90.49 (5)
Se1D-Cd1-O1A	95.66 (5)	O1C-Cd2-Se1D	75.24 (5)	Se1A-Cd1-Se1B	145.40 (1)
Se1D-Cd1-Se1A	123.42 (3)	O1C-Cd2-Se1B	131.21 (5)	Se1A-Cd1-O1B	108.70 (5)
Se1D-Cd1-O1D	73.94 (5)	O1C-Cd2-O1B	82.29 (7)	Se1A-Cd1-O1B ⁱ	83.49 (4)
Se1C-Cd1-O1A	102.08 (5)	O1C-Cd2-Se1C	80.65 (5)	O1A-Cd1-O1B ⁱ	168.19 (6)
Se1C-Cd1-O1D	69.54 (5)	O1B-Cd2-Se1C	86.53 (6)	O1A-Cd1-Se1B	102.64 (5)
Se1A-Cd1-O1A	91.64 (5)	O1B-Cd2-Se1D	153.95 (5)	O1A-Cd1-O1B	92.70 (7)
Se1A-Cd1-O1D	105.59 (5)	O1B-Cd2-O1D	134.02 (7)	O1B-Cd1-Se1B	102.57 (5)
O1D-Cd1-O1A	162.72 (6)	O1B-Cd2-Se1B	85.96 (6)	O1B-Cd1-O1B ⁱ	79.72 (7)
Se1C-Cd1-Se1A	123.98 (2)	Se1C-Cd2-Se1B	145.64 (2)	Se1B-Cd1-O1B ⁱ	87.93 (4)
		Se1C-Cd2-Se1D	102.38 (3)		
		Se1C-Cd2-O1D	69.70 (5)		
		Se1D-Cd2-O1D	71.65 (4)		
		Se1D-Cd2-Se1B	98.94 (3)		
		Se1D-Cd2-O1D	69.69 (5)		
		Se1B-Cd2-O1D	92.27 (5)		

Table 2.313 Crystal and structure refinement data for compounds **112**, **122**, **152**, **171** and **111**.

Compound	<i>cis</i> -[Pd ^{II} (L ^{1a} -Se, <i>O</i>) ₂] 112	<i>cis</i> -[Pd ^{II} (L ^{1b} -Se, <i>O</i>) ₂] 122	<i>cis</i> -[Pd ^{II} (L ^{1c} -Se, <i>O</i>) ₂] 152	[Cd ^{II} (L ^{1e} -Se, <i>O</i>) ₂] 171	[Cd ^{II} (L ^{1a} -Se, <i>O</i>) ₂] 111
Empirical Formula	C ₂₄ H ₃₀ N ₄ O ₂ Se ₂ Pd	C ₃₂ H ₄₆ N ₄ O ₂ Se ₂ Pd	C ₃₂ H ₃₀ N ₄ O ₂ Se ₂ Pd	C ₄₀ H ₃₀ N ₄ O ₂ Se ₂ Cd	C ₂₄ H ₃₀ N ₄ O ₂ Se ₂ Cd
Formula Weight /gmol ⁻¹	670.84	783.05	766.92	869.00	676.84
Crystal system	monoclinic	triclinic	triclinic	triclinic	monoclinic
Space Group	<i>P</i> 2 ₁ / <i>c</i>	<i>P</i> -1	<i>P</i> -1	<i>P</i> -1	<i>P</i> 2 ₁ / <i>n</i>
Unit cell dimensions					
<i>a</i> / Å	11.268 (2)	9.9302 (8)	9.646 (6)	11.288 (2)	12.4416 (13)
<i>b</i> / Å	16.335 (3)	10.9315 (9)	11.842 (8)	16.193 (3)	11.4001 (12)
<i>c</i> / Å	14.326 (3)	15.4119 (13)	26.674 (17)	19.449 (4)	18.687 (2)
α / °		80.216 (1)	90.051 (10)	79.89 (3)	
β / °	104.05 (3)	88.291 (1)	100.221 (11)	87.68 (3)	92.071 (2)
γ / °		81.867 (1)	90.031 (11)	86.73 (3)	
<i>V</i> / Å ³	2558.0 (9)	1632.0 (2)	2999 (3)	3492.3 (12)	2648.7 (5)
<i>Z</i>	4	2	4	4	4
μ / mm ⁻¹	3.599	2.833	3.083	2.751	3.600
<i>T</i> / K	173 (2)	173 (2)	100 (2)	173 (2)	173 (2)
Reflections collected / unique	15748/5892	18809/7329	29277/13149	40672/16098	16366/6151
Data / restraints / parameters	5162/0/302	6802/0/374	5378/0/333	13406/0/883	5184/0/302
Goodness-of-fit on <i>F</i> ²	1.060	1.049	1.803	0.979	0.992
Final <i>R</i> indices [<i>I</i> >2 σ (<i>I</i>)]	2.83, 6.39 %	2.21, 5.54 %	29.31, 58.21 %	3.24, 7.45 %	3.28, 7.08 %
<i>R</i> indices (all data)	<i>RI</i> = 0.0344 <i>wR2</i> = 0.0659	<i>RI</i> = 0.0244 <i>wR2</i> = 0.0563	<i>RI</i> = 0.3994 <i>wR2</i> = 0.6294	<i>RI</i> = 0.0395 <i>wR2</i> = 0.0762	<i>RI</i> = 0.0419 <i>wR2</i> = 0.0746

2.3.3.5 Synthesis of 3,3,3',3'-tetraalkyl-1,1'-phenylenedicarbonylbis(selenourea) metal complexes

Metallamacrocyclic complexes of 3,3,3',3'-tetraalkyl-1,1'-phenylenedicarbonylbis(selenoureas) are not widely reported and only a single paper could be found describing the synthesis of complexes of this type.^[72] Given the successful synthesis of 3,3,3',3'-tetraethyl-1,1'-isophthaloylbis(selenourea) the synthesis of the Pd(II) and Pt(II) metal complexes was attempted using a method reported by Mautjana *et. al.* for related monopodal metal complexes, which is briefly described here.^[46] One molar equivalent of the ligand, 3,3,3',3'-tetraethyl-1,1'-isophthaloylbis(selenourea), was dissolved in acetonitrile, followed by the dropwise addition of four molar equivalents of the base, sodium acetate in aqueous solution. A molar equivalent of the appropriate metal salt (K_2PdCl_4 or K_2PtCl_4), was dissolved in a combination of acetonitrile and water, and slowly added to the reaction mixture, at a slightly elevated temperature (50 °C). Addition of excess water allowed the precipitation of the product, which was isolated by centrifugation and dried under vacuum. In this manner, both the Pd(II), *cis*- $[Pd^{II}_2(L^{m1a}-Se,O)_2]$ and Pt(II) complexes, *cis*- $[Pt^{II}_2(L^{m1a}-Se,O)_2]$ of 3,3,3',3'-tetraethyl-1,1'-isophthaloylbis(selenourea) could be synthesized. The limited solubility of the metallamacrocycles however precluded their analysis by NMR spectroscopy as well as the ability to obtain crystals suitable for single crystal X-ray diffraction analysis. The preparation of *cis*- $[Pt^{II}_2(L^{m1a}-Se,O)_2]$ under these conditions is rather surprising considering the inability to prepare the monopodal derivative using the same procedure. The oxidative addition of the S analogue to form Pt(IV) halogen adducts using an electrolytic synthetic procedure has recently been reported, however attempts to synthesize the analogous Se complex met with little success.^[62]

2.3.4 Crystal and molecular structures of N,N-dialkyl-N'-benzoylthiourea metal complexes

The synthesis of the majority of metal complexes discussed in this section was performed using the method of solvent extraction, previously described for the selenium analogues, (Section 2.2.3.2). Crystal and refinement data for the crystal structures discussed in this section are summarised in Table 2.315 at the end of the section.

2.3.4.1 Crystal and molecular structure of *cis*-bis(*N,N*-dibutyl-*N'*-benzoylthioureato)palladium(II), *cis*- $[Pd^{II}(L^{2b}-S,O)_2]$, **222**

Crystals of *cis*-bis(*N,N*-dibutyl-*N'*-benzoylthioureato)palladium(II), *cis*- $[Pd^{II}(L^{2b}-S,O)_2]$, **222**, were isolated from a binary solvent mixture of dichloromethane and ethanol. Similar to its selenium analogue it is a triclinic structure in the space group *P*-1. Loss of the thioamidic proton allows coordination through the O and S atoms resulting in a square planar complex with a *cis* conformation (Fig. 2.330(A and B)). The coordination sphere is planar where the atoms O1A/S1A/PD1/O1B/S1B exhibit a r.m.s. deviation of 0.0041, the maximum deviation being 0.0073 (10) Å for Pd1, this reflecting observations made for the selenium analogue. Remarkably, N1A and N1B lie only -0.1928 (41) below and 0.3770 (42) above this plane respectively, allowing the chelate to be significantly more planar than *cis*- $[Pd^{II}(L^{1b}-Se,O)_2]$, (Fig 2.326) where the comparable distances are -0.564 (3) and 0.831 (3) Å. The benzene residues are planar as expected where planes defined by the atoms C1A/C2A/C3A/C4/C5A/C6A and C1B/C2B/C3B/C4B/C5B/C6B exhibit r.m.s. deviations of 0.0064 and 0.0061 respectively. They lie at an angle of

8.29 (13) ° relative to each other, larger than the 5.92 (6) ° observed for the selenium analogue. Selected bond lengths and angles are given in Table 2.314.

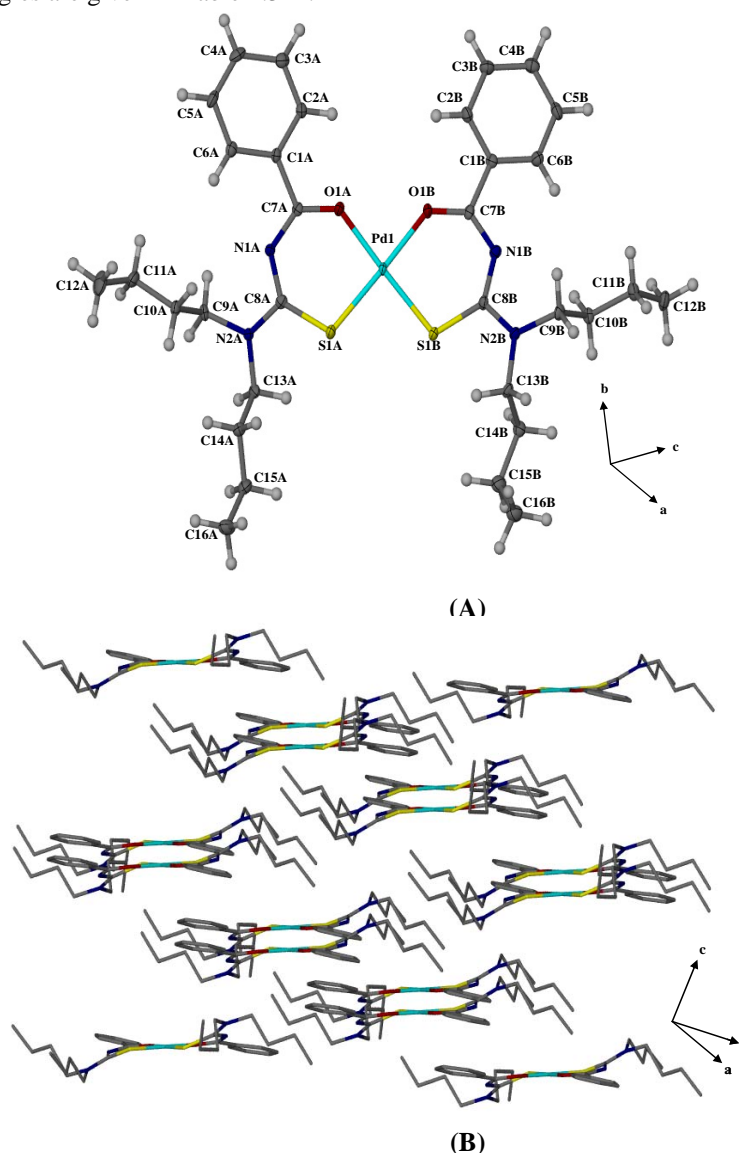


Fig. 2.330 The molecular structure of *cis*-bis(*N,N*-dibutyl-*N'*-benzoylthioureato)palladium(II), *cis*-[Pd^{II}(L^{2b}-S,O)₂] **222** with atom numbering scheme shown, displacement ellipsoids are drawn at the 50 % probability level (A) and crystal packing (B).

2.3.4.2 Crystal and molecular structure of *cis*-bis(*N,N*-dihexyl-*N'*-benzoylthioureato)palladium(II), *cis*-[Pd^{II}(L^{2c}-S,O)₂] **232**

Crystals of *cis*-bis(*N,N*-dihexyl-*N'*-benzoylthioureato)palladium(II), *cis*-[Pd^{II}(L^{2c}-S,O)₂] **232**, were grown by slow pentane diffusion into a saturated chloroform solution of the compound. As for the dibutyl derivative, loss of the thioamidic proton results in square-planar complex formation, in a *cis* conformation where coordination takes place through the O and S donor atoms (Fig. 2.331). The coordination plane is markedly less planar than observed in *cis*-[Pd^{II}(L^{2b}-S,O)₂], O1A and O1B exhibiting maximum deviations of -0.0346 (18) and 0.0345 (18) Å below and above the O1A/S1A/Pd1/O1B/S1B plane respectively, the coordination plane exhibiting a r.m.s. deviation of 0.0296 relative to the 0.0041 observed in *cis*-[Pd^{II}(L^{2b}-S,O)₂]. The reduced planarity is sustained to the nitrogen atoms

where N1A lies $-0.4414(66)$ and N1B $0.4810(64)$ Å above the coordination plane. The $8.29(13)^\circ$ angle between the benzene residues observed in cis -[Pd^{II}(L^{2b}-S,O)₂] is accentuated in the longer chain analogue where the benzene residues lie at $21.08(20)^\circ$ relative to each other. The longer alkyl chains in cis -[Pd^{II}(L^{2c}-S,O)₂] lead to increased thermal motion as is evident from the large ellipsoids in Fig 2.331 however the disorder was not thought sufficient to warrant modeling. Fig 2.331 (B) shows the unit cell packing of cis -[Pd^{II}(L^{2c}-S,O)₂] viewed down the *c* axis where the coordination planes lie at angles of $53.26(6)^\circ$ relative to each other. Selected bond lengths and angles are given in Table 2.314.

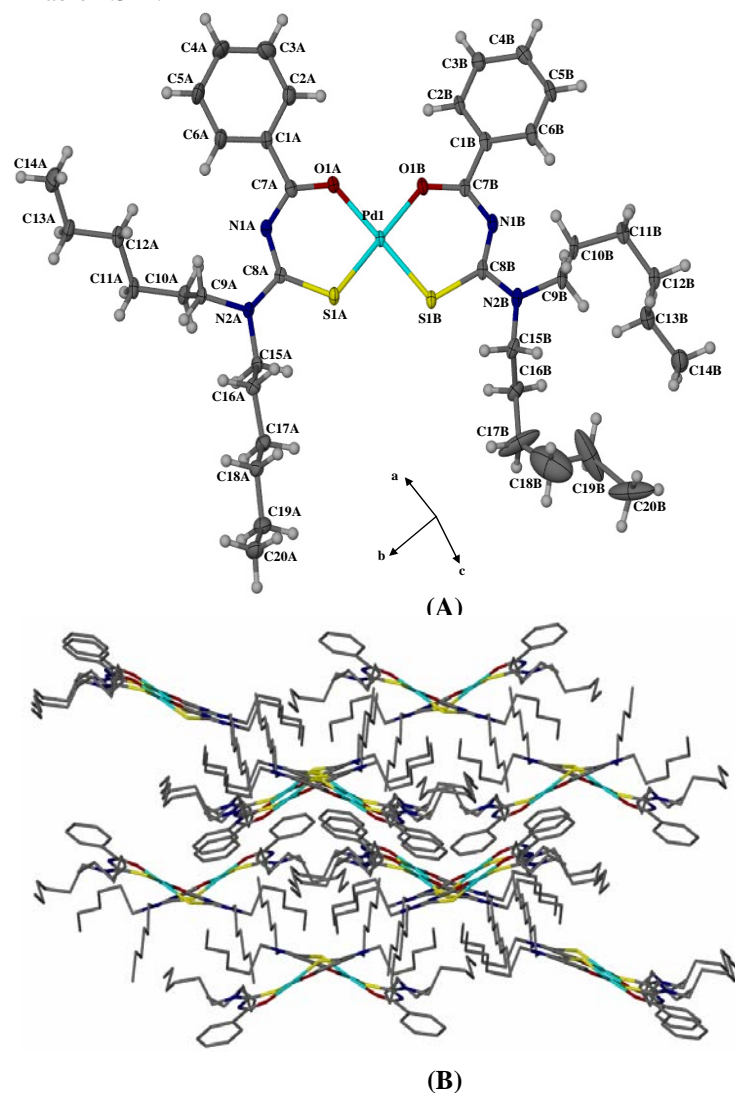


Fig. 2.331 The molecular structure of cis -bis(*N,N*-dihexyl-*N'*-benzoylthioureato)palladium(II), cis -[Pd^{II}(L^{2c}-S,O)₂] **232** with atom numbering scheme shown, displacement ellipsoids are drawn at the 50 % probability level (A) and crystal packing viewed along the *c* axis (B).

2.3.4.3 Crystal and molecular structure of cis -bis(*N*-morpholine-*N'*-benzoylthioureato)palladium(II), cis -[Pd^{II}(L^{2f}-S,O)₂], **262**

Following the “solventless synthesis” (Section 2.2.4.4) of cis -bis(*N*-morpholine-*N'*-benzoylthioureato)palladium(II), cis -[Pd^{II}(L^{2f}-S,O)₂] **262** crystals were isolated from an NMR sample tube of the compound, where the *N*-morpholine-*N'*-benzoylthiourea ligand coordinates to the Pd(II) centre in a fashion similar to that described for the

acyclic alkyl chain derivatives cis -[Pd^{II}(L^{2b}-S,O)₂] and cis -[Pd^{II}(L^{2c}-S,O)₂] (Fig. 2.332 (A and B)). Selected bond lengths and angles are given in Table 2.314. The coordination plane through atoms O1A/S1A/Pd1/O1B/S1B displays the largest r.m.s. of 0.0367 in the series reported here, the maximum deviation of 0.0438 (16) Å being for O1B. This molecule appears to be significantly less planar than the preceding two and this is reflected in the larger distances of the central nitrogen atoms from the coordination plane where N1A lies -0.5701 (59) Å below and N1B 1.0227 (59) Å above the plane. The aromatic residues lie at an angle of 41.57 (22) ° relative to each other, this being the largest distortion from planarity for the series reported here. Atoms S1A/C8A/N1A/C7A/O1A in the chelate plane lie at 17.28 (19) ° to the coordination plane and atoms in the chelate plane S1B/C8B/N1B/C7B/O1B at 30.54 (16) ° to the coordination plane and hence **262** takes on an S shape similar to that described for cis -[Pd^{II}(L^{1a}-Se,O)₂] **112**. The morpholine residues take on the chair conformation as expected.

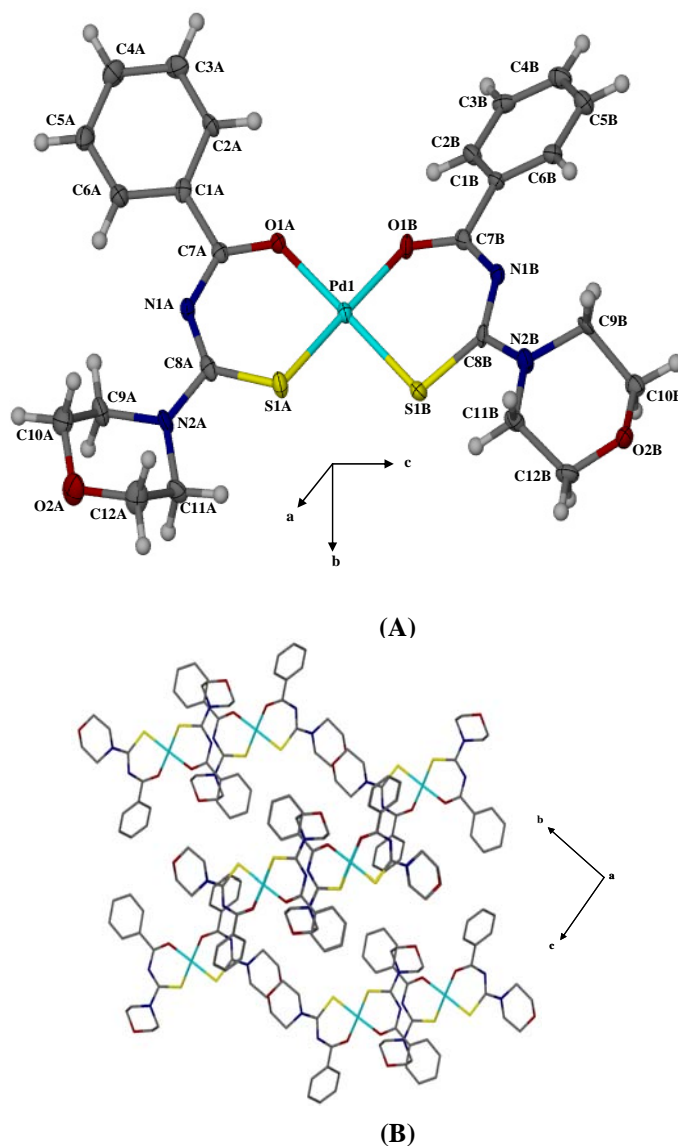


Fig. 2.332 The molecular structure of cis -bis(*N*-morpholine-*N'*-benzoylthioureato)palladium(II), cis -[Pd^{II}(L^{2f}-S,O)₂] **262** with atom numbering scheme shown, displacement ellipsoids are drawn at the 50 % probability level (A) and crystal packing viewed along the *a* axis (B).

Table 2.314 gives selected geometric parameters of each of the Pd(II) complexes as well as those of HL_S^{2c} for comparison. No structural elucidation of *N,N*-dibutyl-*N'*-benzoylthiourea could be found however that of the *para*-

chloro analogue has been reported and selected bond lengths are in Table 2.314,^[107] recently reported bond lengths of *N*-morpholine-*N'*-benzoylthiourea have also been included.^[111] Similarly to the selenium analogues, the carbon – donor atom bond lengths in the chelates relative to those in the uncoordinated ligands are lengthened, reflecting a loss of double bond character, most likely as a result of electronic delocalization in the six-membered ring of the metal complexes. This is further seen by the shortening of the C-N bonds in the chelate ring ((O)C-N and N-C(S)) as well as the lengthening of the (S)-CNR₂ bonds in the complexes relative to those in the ligand. The Pd-S and Pd-O bond lengths all compare well with each other and with those previously reported.^[34]

Table 2.314 Selected geometric parameters (Å, °) for compounds **262**, **26**, **232**, **23**, **222** and the *p*-Cl analogue of **22**.

	<i>p</i> -Cl analogue of HL ^{2b} 22 ^[107]	<i>cis</i> -[Pd ^{II} (L ^{2b} -S,O) ₂] 222		HL ^{2c} 23	<i>cis</i> -[Pd ^{II} (L ^{2c} -S,O) ₂] 232		HL ^{2f} 26 ^[111] ^[112]	<i>cis</i> -[Pd ^{II} (L ^{2f} -S,O) ₂] 262	
		Ring A	Ring B		Ring A	Ring B		Ring A	Ring B
Pd-O		2.010 (2)	2.005 (2)		2.021 (5)	2.022 (4)		2.037 (3)	2.038 (3)
C=O	1.215 (3)	1.272 (4)	1.271 (4)	1.216 (2)	1.287 (8)	1.277 (7)	1.212 (6)	1.273 (6)	1.267 (6)
(O)C-N	1.382 (3)	1.325 (4)	1.326 (4)	1.379 (2)	1.318 (8)	1.319 (8)	1.366 (6)	1.324 (6)	1.331 (6)
N-C(S)	1.410 (3)	1.344 (4)	1.344 (4)	1.411 (2)	1.346 (8)	1.344 (9)	1.422 (6)	1.331 (6)	1.332 (6)
C=S	1.677 (2)	1.732 (4)	1.748 (3)	1.683 (2)	1.738 (6)	1.737 (6)	1.653 (5)	1.725 (5)	1.739 (5)
(S)C-NR ₂	1.328 (3)	1.346 (4)	1.343 (4)	1.322 (2)	1.342 (8)	1.340 (8)	1.324 (6)	1.370 (6)	1.345 (6)
Pd-S		2.2411 (10)	2.2490 (10)		2.2300 (16)	2.2353 (16)		2.2352 (13)	2.2385 (13)
O-Pd-S		84.35 (10)	93.27 (7)		94.22 (14)	93.93 (14)		94.22 (10)	92.16 (10)

2.3.4.4 Crystal and molecular structure of 3,3,3',3'-tetra(*n*-butyl)-1,1'-terephthaloylbis(thiourea)-palladium (II), *cis*-[Pd^{II}₃(L^{m2b}-S,O)₃], **22222**

Synthesis and structural characterization of the Pt(II) complex of 3,3,3',3'-tetra(*n*-butyl)-1,1'-terephthaloylbis(thiourea) has been reported,^[59] however structural characterization of the Pd(II) analogue is unknown. Crystals of *cis*-[Pd^{II}₃(L^{m2b}-S,O)₃], **22222**, were grown from a dichloromethane / ethanol solvent mixture and analysed, Fig. 2.333 illustrating the molecular structure. A significant amount of disorder is present in the structure, particularly due to the presence of solvent molecules associated with the compound and the alkyl chains of the amine residues, however several interesting features can be pointed out. As expected coordination takes place in a *cis* fashion to give an approximately square planar coordination sphere. Interestingly, the macrocyclic ring is rather twisted as depicted by the non-bonded torsion angles through the oxygen atoms O1/O2/O3/O4 = 3.6 °, O3/O4/O5/O6 = -14.8 ° and O5/O6/O1/O2 = 25.6 ° comparable to the 8.6 (5), -16.1 (5) and 22.7 (5) ° reported for the Pt(II) analogue.^[59] The orientations of the aromatic rings can be described in a comparable manner where the non-bonded torsion angles C13/C14/C15/C16 = -13.7 °, C15/C16/C17/C18 = 11.5 and C17/C18/C13/C14 = -2.5 °, equivalent torsion angles of the Pt(II) analogue reported as -1.0 (6), 13.9 (6) and -24.5 (6) °.^[59]

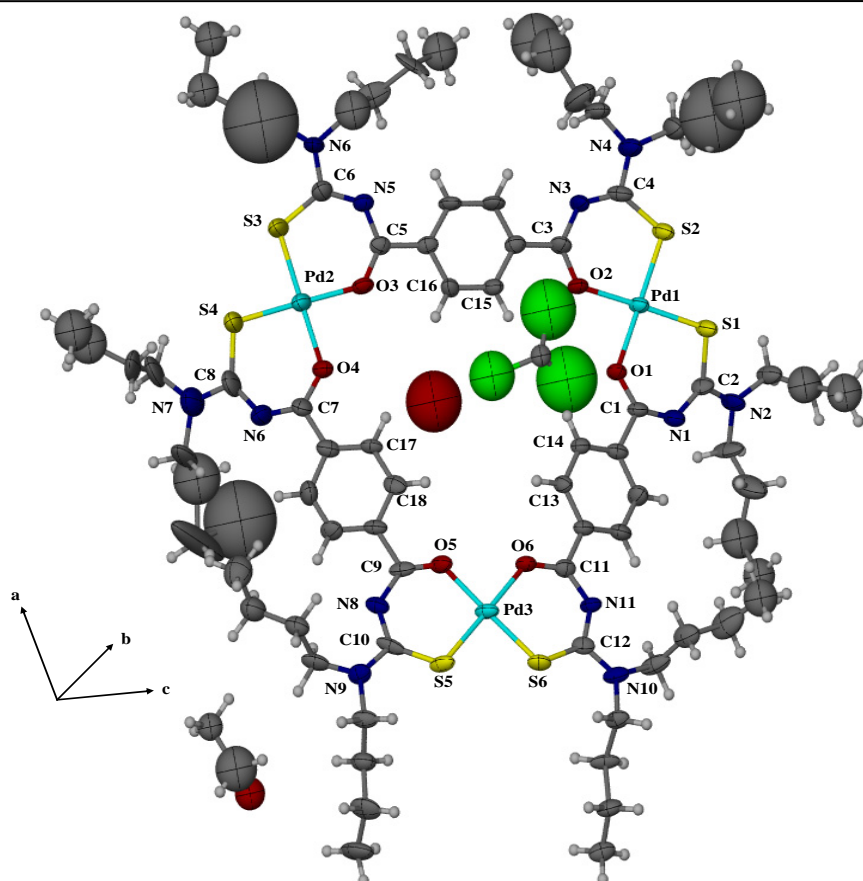


Fig. 2.333 Molecular structure of (3,3,3',3'-tetra(*n*-butyl)-1,1'-terephthaloylbisthioureato)palladium(II), *cis*-[Pd^{II}(L^{m2b}-S,O)₃], **22222**, with selected atomic numbering shown. Displacement ellipsoids are drawn at the 50 % probability level.

Table 2.315 Crystal and structure refinement data for compounds **222**, **232**, **262** and **22222**.

Compound	<i>cis</i> -[Pd ^{II} (L ^{2b} -S,O) ₂] 222	<i>cis</i> -[Pd ^{II} (L ^{2c} -S,O) ₂] 232	[Pd ^{II} (L ^{2f} -S,O) ₂] 262	<i>cis</i> -[Pd ^{II} ₃ (L ^{m2b} -S,O) ₃], 22222
Empirical Formula	C ₃₂ H ₄₆ N ₄ O ₂ S ₂ Pd	C ₄₀ H ₆₂ N ₄ O ₂ S ₂ Pd	C ₂₄ H ₂₆ N ₄ O ₂ S ₂ Pd	
Formula Weight /gmol ⁻¹	689.25	801.46	605.01	
Crystal system	triclinic	Monoclinic	triclinic	Monoclinic
Space Group	<i>P</i> -1	<i>P</i> 2 ₁ / <i>c</i>	<i>P</i> -1	<i>P</i> 2 ₁ / <i>c</i>
Unit cell dimensions				
<i>a</i> / Å	9.855 (2)	8.474 (1)	8.935 (1)	17.353 (2)
<i>b</i> / Å	10.887 (2)	15.646 (2)	11.385 (2)	20.998 (3)
<i>c</i> / Å	15.496 (3)	30.899 (4)	13.878 (2)	26.208 (4)
<i>α</i> / °	79.586 (4)		67.976 (2)	
<i>β</i> / °	89.072 (3)	95.071 (2)	77.604 (2)	94.103 (3)
<i>γ</i> / °	82.363 (4)		68.185 (2)	
<i>V</i> / Å ³	1620.6 (5)	4080.8 (10)	1210.3 (3)	9525 (2)
<i>Z</i>	2	4	2	5
<i>μ</i> / mm ⁻¹	0.736	0.595	0.979	0.963
<i>T</i> / K	100 (2)	100 (2)	173 (2)	100 (2)
Reflections collected / unique	18807 / 7465	46415 / 9807	13543 / 5497	58747/21881
Data / restraints / parameters	5973 / 0 / 371	8490 / 0 / 446	4534 / 0 / 316	8117/0/878
Goodness-of-fit on <i>F</i> ²	1.030	1.285	0.979	0.998
Final <i>R</i> indices [<i>I</i> > 2σ(<i>I</i>)]	5.21, 9.96 %	8.20, 20.22 %	4.37, 8.69 %	10.93, 26.92 %
<i>R</i> indices (all data)	<i>R</i> 1 = 0.0703 <i>wR</i> 2 = 0.1062	<i>R</i> 1 = 0.0946 <i>wR</i> 2 = 0.2125	<i>R</i> 1 = 0.0630 <i>wR</i> 2 = 0.1213	<i>R</i> = 0.2553 <i>wR</i> 2 = 0.3532

2.3.5 Characterization of ligands and metal complexes by Nuclear Magnetic Resonance Spectroscopy

2.3.5.1 ^{13}C NMR Spectroscopy

During the ^{13}C NMR characterization of the *N,N*-dialkyl-*N'*-benzoylselenoureas, a “switch” in the relative chemical shift positions of the carbonyl and selenocarbonyl carbons upon complexation was noted. In the ^{13}C NMR spectrum of the ligands, the selenocarbonyl carbon is deshielded relative to that of the carbonyl carbon atom. Coordination to a metal ion results in the selenocarbonyl carbon resonating upfield relative to the carbonyl carbon, this now being more deshielded than the selenocarbonyl carbon. In addition, the separation between the two resonances is less in the case of the complexes than the uncoordinated ligands.

Similar observations have been made for the *N,N*-dialkyl-*N'*-benzoylthioureas. This phenomenon occurs for a variety of different metal ions, but the extent of the chemical shift displacement is dependant on the nature of the metal centre as well as that of the ligand (*i.e.* Se or S donor atom). Table 2.316 illustrates the extent of these chemical shift displacements for the Pd(II) and Cd(II) metal complexes of both ligand types where the shift displacements (Δ defined as $\delta^{13}\text{C}_{\text{complex}} - \delta^{13}\text{C}_{\text{ligand}}$) are given.

Table 2.316 Chemical shift displacements of selected complexes.

Compound	$\Delta [\delta^{13}\text{C}(\text{O})]/\text{ppm}$	$\Delta [\delta^{13}\text{C}(\text{E})]/\text{ppm}$ where E = S	$\Delta [\delta^{13}\text{C}(\text{O})]/\text{ppm}$	$\Delta [\delta^{13}\text{C}(\text{E})]/\text{ppm}$ where E = Se
<i>cis</i> -[Pd ^{II} (L ^a -E,O) ₂]	7.4	-8.6	8.5	-14.8
<i>cis</i> -[Pd ^{II} (L ^b -E,O) ₂]	8.0	-9.3	8.7	-14.2
<i>cis</i> -[Pd ^{II} (L ^c -E,O) ₂]	8.0	-9.2	8.8	-14.8
<i>cis</i> -[Pd ^{II} (L ^d -E,O) ₂]	8.0	-9.2	8.8	-14.8
<i>cis</i> -[Pd ^{II} (L ^e -E,O) ₂]	9.6	-10.1	9.8	-14.8
<i>cis</i> -[Pd ^{II} (L ^f -E,O) ₂]	8.8	-7.5	8.8	-14.8
[Cd ^{II} (L ^a -E,O) ₂]	12.9	-8.3	8.5	-13.2
[Cd ^{II} (L ^b -E,O) ₂]	15.2	-11.0	7.9	-11.8
[Cd ^{II} (L ^c -E,O) ₂]	16.0	-14.0	8.0	-11.0
[Cd ^{II} (L ^d -E,O) ₂]	15.9	-13.4	8.0	-11.3
[Cd ^{II} (L ^e -E,O) ₂]	17.3	-15.4	9.9	-12.2
[Cd ^{II} (L ^f -E,O) ₂]	-	-	8.3	-12.5

In the Pd(II) complexes displacement of the carbonyl resonance is comparable for both the thio- and selenoureas varying between 7.4 and 9.8 ppm. This is however not the case in the Cd(II) complexes where the displacement for the thioureas, ranging from 12.9 – 17.3 ppm, is on average almost twice that shown by the selenoureas, where these vary between 7.9 and 9.9 ppm. The thiocarbonyl and selenocarbonyl resonances in the Pd(II) complexes differ in their displacements as would be expected, where the selenocarbonyl resonance is the most shielded. This phenomenon is reversed in the Cd(II) metal complexes where on average the thiocarbonyl resonances exhibit the greatest upfield shift, although the difference between the displacements of the C=Se and C=S resonances is less than that shown in the Pd(II) complexes. Table 2.317 records the C=O, C=S and C=Se chemical shift displacements of all the metal complexes of HL_{Se}^{1a} and HL_S^{2a} synthesized in this work. Clear trends are visible in the thioureas, where, as the molecular weight of the *d*⁸ metal ion increases (Ni(II) < Pd(II) < Pt(II)), the chemical shift displacement of the carbonyl carbon decreases, but that of the thiocarbonyl carbon increases. The *d*¹⁰ ions show almost equal chemical shift displacements for C(O), but a slightly larger displacement of C(S) is found for the Cd(II) metal centre. Similar observations can be made for the selenium analogues, however the relative

displacement of C(Se) in the Cd(II) complex is much larger than in the sulfur derivative. Taking into account the decreasing chemical shift displacement of the carbonyl carbons, and increasing displacement of the seleno- and thiocarbonyl carbons moving down the Ni(II) triad (*i.e.* Ni(II), Pd(II), Pt(II)) and Zn(II), Cd(II), and that coordination takes place through the O and S/Se atoms, it has previously been speculated that the displacement values could reflect the relative order of HSAB ‘softness’ of the metal centre in the order Pt(II) > Pd(II) > Ni(II) for the d^8 metal ions and Cd(II) > Zn(II) for the d^{10} metal ions.^[46]

Table 2.317 Chemical shift displacements of selected metal complexes of HL_{Se}^{2a}, **21**.

Complex	$\Delta [\delta^{13}\text{C}(\text{O})]/\text{ppm}$	$\Delta [\delta^{13}\text{C}(\text{E})]/\text{ppm}$ where E = S	$\Delta [\delta^{13}\text{C}(\text{O})]/\text{ppm}$	$\Delta [\delta^{13}\text{C}(\text{E})]/\text{ppm}$ where E = Se
<i>cis</i> -[Ni ^{II} (L ^a -E,O) ₂]	8.8	-6.8	-	-
<i>cis</i> -[Pd ^{II} (L ^a -E,O) ₂]	7.4	-8.6	8.5	-14.8
<i>cis</i> -[Pt ^{II} (L ^a -E,O) ₂]	4.7	-12.2	-	-
[Zn ^{II} (L ^a -E,O) ₂]	12.5	-7.4	9.0	-10.2
[Cd ^{II} (L ^a -E,O) ₂]	12.9	-8.3	8.5	-14.8
[Co ^{II} (L ^a -E,O) ₃]	11.4	-4.5	-	-

Of the six isotopes of selenium, only ⁷⁷Se is NMR active having a natural abundance of 7.58 % and comparable sensitivity to that of ¹³C nucleus for most routine NMR experiments.^[113] This led to the observation of ⁷⁷Se satellites and the determination of the ¹J(¹³C-⁷⁷Se) coupling constants. Fig. 2.334 illustrates the ¹J(¹³C-⁷⁷Se) coupling constants for HL_{Se}^{1a}, its Cd(II), Zn(II) and Pd(II) complexes, where in addition to the ¹J(¹³C-⁷⁷Se) coupling constants the differing chemical shift positions of the carbonyl and selenocarbonyl carbons is clearly visible.

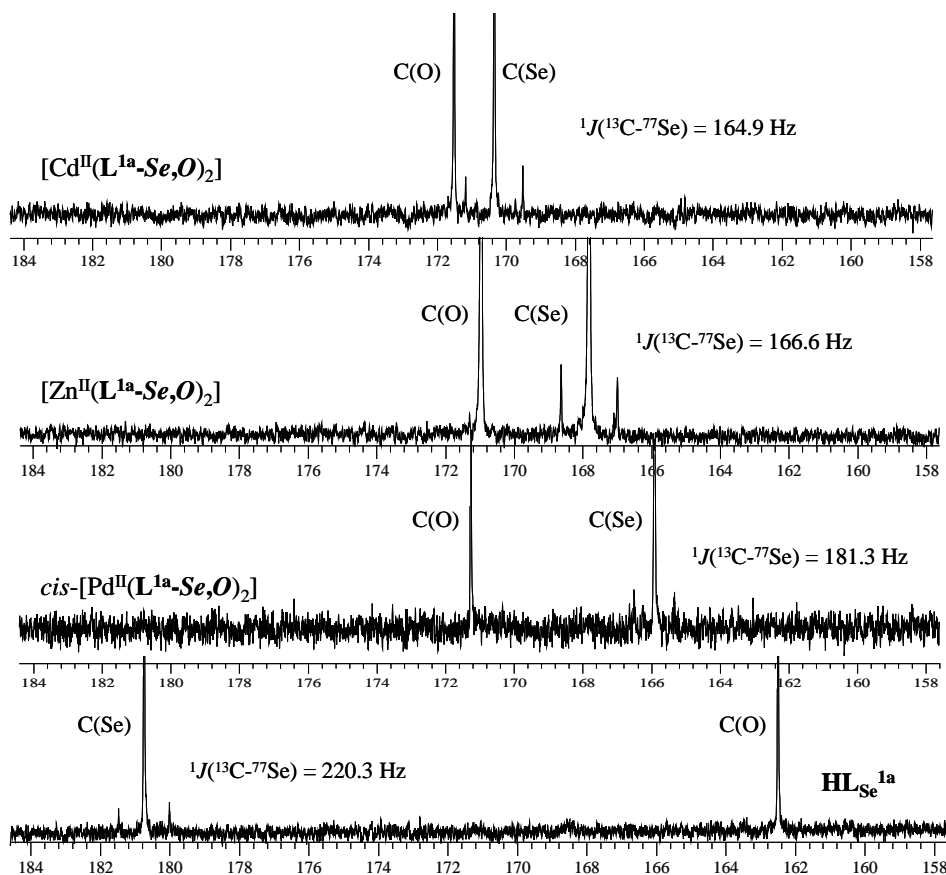


Fig 2.334 ¹³C NMR spectra of HL_{Se}^{1a}, *cis*-[Pd^{II}(L^{1a}-Se,O)₂], [Zn^{II}(L^{1a}-Se,O)₂] and [Cd^{II}(L^{1a}-Se,O)₂] illustrating the relative exchange of chemical shift positions and ¹J(¹³C-⁷⁷Se) coupling.

Table 2.318 Coupling constants of *N,N*-dialkyl-*N'*-benzoylselenoureas and Pd(II) complexes

Compound	Coupling constant /Hz	Compound	Coupling constant /Hz
HL _{Se} ^{1a} 11	220.3	<i>cis</i> -[Pd ^{II} (L ^{1a} -Se,O) ₂] 112	181.3
HL _{Se} ^{1b} 12	222.1	<i>cis</i> -[Pd ^{II} (L ^{1b} -Se,O) ₂] 122	176.5
HL _{Se} ^{1c} 13	221.6	<i>cis</i> -[Pd ^{II} (L ^{1c} -Se,O) ₂] 132	176.4
HL _{Se} ^{1d} 14	217.9	<i>cis</i> -[Pd ^{II} (L ^{1d} -Se,O) ₂] 142	175.8
HL _{Se} ^{1e} 15	221.7 (Z) / 220.6 (E)	<i>cis</i> -[Pd ^{II} (L ^{1e} -Se,O) ₂] 152	-
HL _{Se} ^{1f} 16	220.1	<i>cis</i> -[Pd ^{II} (L ^{1f} -Se,O) ₂] 162	176.0
HL _{Se} ^{1g} 17	217.8	-	-

An average $^1J(^{13}\text{C}-^{77}\text{Se})$ coupling constant of 220.3 Hz is observed for the *N,N*-dialkyl-*N'*-benzoylselenourea ligands, (Table 2.318) this comparing well with those reported for similar compounds.^[114] Interestingly, that observed in HL_{Se}^{1g} (217.8 Hz) is only slightly less than the average which is surprising in the light of the solid state characterization where clear evidence of a reduced C=Se bond order was obtained. Coordination to a metal centre clearly lowers the value of the coupling constant as would be expected given the lengthening of the C=O and C=Se bond lengths observed in the solid state. The majority of the Pd(II) complexes show a coupling constant of 176 Hz, this comparing well with reported values of a related Ni(II) complex where a $^1J(^{13}\text{C}-^{77}\text{Se})$ coupling constant of 180 Hz was reported.^[116] The d^{10} metal complexes, [Zn^{II}(L^{1a}-Se,O)₂] and [Cd^{II}(L^{1a}-Se,O)₂] give lower, but comparable $^1J(^{13}\text{C}-^{77}\text{Se})$ coupling constants of 166.6 and 164.9 Hz respectively, indicating a reduced C=Se bond order for d^{10} metal complexes relative to their d^8 counterparts. The absence of ^{77}Se satellites in the remaining Cd(II) metal complexes, [Cd^{II}(L^{1b-g}-Se,O)₂], precluded the calculation of coupling constants and this is attributed to the lability of the Cd(II) metal ion and the dynamic nature of these complexes in solution, which could not be lifted by cooling to lower temperatures.

2.3.5.2 *N*-methyl-*N*-benzyl-*N'*-benzoyl(thio)selenoureas and their Cd(II) and Pd(II) metal complexes

As previously mentioned in Section 2.3.1.5, the partial double bond character of the (E)C-NR₂ bond (where E = S, Se) results in limited rotation about this bond and a degree of inequivalence arises in the amine residues, leading to the formation of *E* and *Z* isomers where an asymmetrically substituted amine is used. Where coordination takes place to a d^8 metal ion and a square planar metal complex results, this inequivalence is carried over to result in the formation of (*ZZ*), (*EZ*) and (*EE*) isomers as shown in Fig. 2.335.

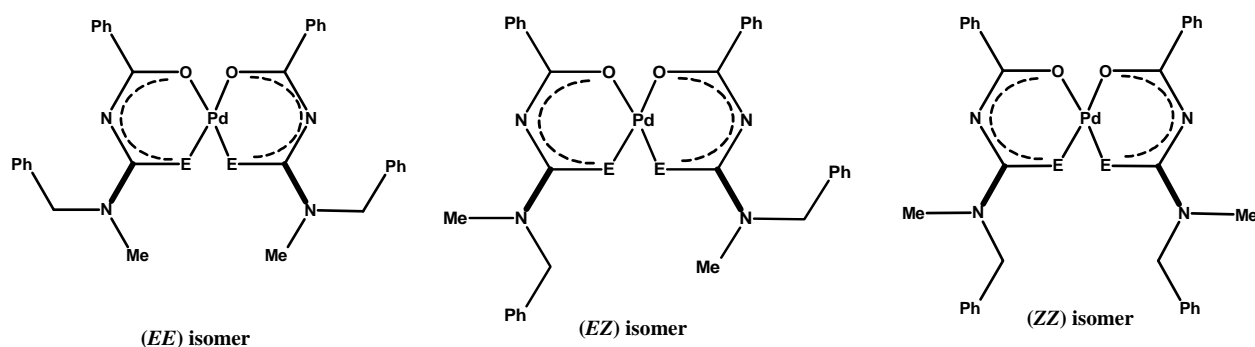


Fig. 2.335 (*EE*), (*EZ*) and (*ZZ*) isomerisation exhibited by *cis*-bis(*N*-methyl-*N*-benzyl-*N'*-benzoyl(thio)selenourea)Pd(II) where E = Se, S.

The presence of these isomers can clearly be seen in both the ^1H and ^{13}C NMR spectra and Fig. 2.336 illustrates the chemical shift positions of the N-CH₃ resonances for the isomers in $\text{HL}_{\text{Se}}^{1e}$, $\text{HL}_{\text{S}}^{2e}$ and $\text{cis}[\text{Pd}^{\text{II}}(\text{L}^{2e}\text{-S},\text{O})_2]$, whilst the N-CH₂- resonance is shown for $\text{cis}[\text{Pd}^{\text{II}}(\text{L}^{1e}\text{-Se},\text{O})_2]$. The isomer assignment of $\text{HL}_{\text{Se}}^{1e}$ and $\text{HL}_{\text{S}}^{2e}$ is made, taking into account the seleno- and thiocarbonyl groups which, because of magnetic anisotropy, should deshield the nuclei coplanar to them.^[115] This results in a downfield shift for the N-CH₂- resonance of the *Z* isomer relative to that of the *E* isomer (not shown) and an upfield shift for the N-CH₃ resonance of the *Z* isomer relative to its *E* counterpart (Fig. 2.336).^[116] These observations closely reflect those made for *N*-methyl-*N*-benzyl-*N'*-pivaloylthiourea following a thorough study of the of the *N,N*-dialkyl-*N'*-pivaloylthiourea ligands and their Pt(II) complexes.^[83] Further evidence for this assignment is obtained from the solid state configurations of both ligands where the *Z* isomer appears to be the most stable and it is therefore likely that the majority species in solution would reflect this.

As previously mentioned, complexation results in electronic delocalization in the chelate ring and a consequent reduction in the C=Se and C=S bond order, complicating the isomer assignment for $\text{cis}[\text{Pd}^{\text{II}}(\text{L}^{1e}\text{-Se},\text{O})_2]$ and its sulfur analogue. However, 4 well separated N-CH₃ resonances are present in $\text{cis}[\text{Pd}^{\text{II}}(\text{L}^{2e}\text{-S},\text{O})_2]$, and the isomer assignment has been made largely based on the relative intensities, where the *ZZ* isomer is the major species in solution, followed by the *EZ* isomer (*E(EZ)* and *Z(EZ)* having similar intensities) and the *EE* isomer being the minor species. Once again, these assignments closely resemble those made for the Pt(II) complex of *N*-methyl-*N*-benzyl-*N'*-pivaloylthiourea, following extensive investigation of complexes of this type.^[83] The ^1H NMR spectrum of the complex $\text{cis}[\text{Pd}^{\text{II}}(\text{L}^{1e}\text{-Se},\text{O})_2]$ does not exhibit 4 well defined N-CH₃ resonances and therefore the N-CH₂-resonances are shown in Fig. 2.336 and used to propose the relative isomer distributions. It is interesting to note that the configurational isomers in both $\text{HL}_{\text{Se}}^{1e}$ and $\text{HL}_{\text{S}}^{2e}$ exhibit similar distributions and this appears to be carried over to the Pd(II) complexes where the relative percentages of the *ZZ*, *EZ* and *EE* isomers for $\text{cis}[\text{Pd}^{\text{II}}(\text{L}^{1e}\text{-Se},\text{O})_2]$ and $\text{cis}[\text{Pd}^{\text{II}}(\text{L}^{2e}\text{-S},\text{O})_2]$ are comparable.

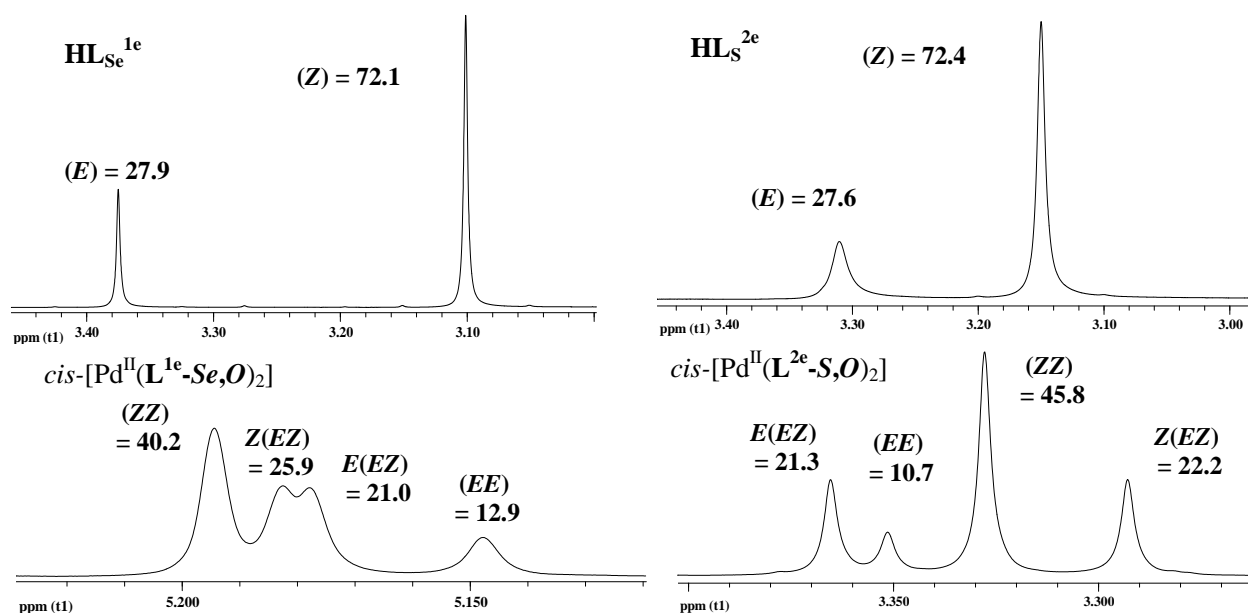


Fig. 2.336 Expansions of ^1H NMR spectra to show N-CH₃ resonances of $\text{HL}_{\text{Se}}^{1e}$, $\text{HL}_{\text{S}}^{2e}$, $\text{cis}[\text{Pd}^{\text{II}}(\text{L}^{2e}\text{-S},\text{O})_2]$ and N-CH₂-resonances of $\text{cis}[\text{Pd}^{\text{II}}(\text{L}^{1e}\text{-Se},\text{O})_2]$ in CDCl_3 at 25 °C. A 1 % error is estimated for the percentage distributions.

The energy difference, ΔG_0 , between 2 isomers can be calculated using Equation 2.1 where $R = 1.9872 \text{ cal.K}^{-1}.\text{mol}^{-1}$, T = temperature at which the peaks are well separated (in our case 298 K was used) and K is the equilibrium

constant which can be calculated using Equation 2.2 where $[Z]$ and $[E]$ are determined using a deconvolution analysis of the peak integrals in the ^1H NMR spectra.^[83]

$$\Delta G_{\text{O}} = -RT \ln K \quad \text{Equation 2.1}$$

$$K = [E]/[Z] \text{ for HL}_{\text{Se}}^{1\text{e}} \text{ and HL}_{\text{S}}^{2\text{e}}, [EE]/[ZZ] \text{ for metal complexes} \quad \text{Equation 2.2}$$

Table 2.319. Selected thermodynamic data for the rotation about the (E)C-NR₂ bond in HL_{Se}^{1e}, HL_S^{2e} and their Cd(II) and Pd(II) metal complexes.

Compound	Isomer % (Z) or (ZZ)	Isomer % (E) or (EE)	K	$\Delta G_{\text{O}(EE-ZZ)}$ kcal/mol
HL _{Se} ^{1e}	72.1	27.9	0.39	0.56
HL _S ^{2e}	72.4	27.6	0.38	0.57
<i>cis</i> -[Pd ^{II} (L ^{1e} -Se,O) ₂]	40.2	12.9	0.32	0.67
<i>cis</i> -[Pd ^{II} (L ^{2e} -S,O) ₂]	45.8	10.7	0.23	0.86

These results are shown in Table 2.319 where it is clear that the energy difference between the *E* and *Z* isomers in both ligands is comparable. Complexation to Pd(II) results in an energy difference between the *ZZ* and *EE* isomers of 0.67 kcal/mol for *cis*-[Pd^{II}(L^{1e}-Se,O)₂] and 0.86 kcal/mol for its sulfur analogue. This suggests that the C-N bond order in the selenourea is lower than that of its sulfur analogue upon complexation to Pd(II).

2.3.5.3 ⁷⁷Se NMR Spectroscopy

As previously mentioned, ⁷⁷Se is the only NMR active selenium isotope having a natural abundance of 7.58 % and comparable sensitivity to that of ¹³C nucleus for most routine NMR experiments.^[113] No common reference has been established for ⁷⁷Se NMR spectroscopy and absolute chemical shift values therefore cover a wide range. Reference [113] lists some of the more common reference materials that have been used, however ⁷⁷Se NMR spectra in this work were obtained by making use of a coaxial insert containing 0.5 ml CDCl₃/2.5 ml DMSO which was referenced to -273 ppm from an external 1 M CH₃SeCH₃ (in CHCl₃).^[117] As suggested by Duddeck, chemical shift values are presented as integers.^[113]

Table 2.320 lists the ⁷⁷Se NMR chemical shift values of the *N,N*-dialkyl-*N'*-benzoylselenourea ligands, as well as those of selected metal complexes, where it is evident that altering the alkyl chain length of the amine residues in HL_{Se}^{1a-d,f} has little effect on the chemical shift position of the ⁷⁷Se nucleus. The isomer assignments of HL_{Se}^{1e} **15**, have been made based on the relative intensities of the resonances where the major isomer (*Z*) appears the most shielded at 466 ppm. Interestingly the chemical shift position of HL_{Se}^{1g} **17** differs to that of the dialkyl derivatives where the ⁷⁷Se nucleus is significantly more deshielded at 660 ppm. This confirms observations made in Section 2.3.1.7 relating to the oxidation of the ligand to form the diselenide. Upon complexation to Pd(II), shielding of ⁷⁷Se nucleus increases and the resonance appears at approx. 300 ppm. Altering the amine residue from diethyl to dibutyl results in a slight downfield shift of the ⁷⁷Se resonance and this is in accordance with reports on the ⁷⁷Se NMR of related Pd(II)diselenocarbamate complexes where R group alteration from ethyl to isobutyl resulted in a 13 ppm downfield shift.^[118]

Table 2.320 ^{77}Se NMR chemical shift positions of selected compounds

Compound	^{77}Se chemical shift position	Compound	^{77}Se chemical shift position
$\text{HL}_{\text{Se}}^{1a}$ 11	483	<i>cis</i> -[Pd ^{II} (L ^{1a} -Se,O) ₂] 112	292
$\text{HL}_{\text{Se}}^{1b}$ 12	483	<i>cis</i> -[Pd ^{II} (L ^{1b} -Se,O) ₂] 122	301
$\text{HL}_{\text{Se}}^{1c}$ 13	482	<i>cis</i> -[Pd ^{II} (L ^{1c} -Se,O) ₂] 132	300
$\text{HL}_{\text{Se}}^{1d}$ 14	481	<i>cis</i> -[Pd ^{II} (L ^{1d} -Se,O) ₂] 142	300
$\text{HL}_{\text{Se}}^{1e}$ 15	466 (<i>Z</i>) and 513 (<i>E</i>)	<i>cis</i> -[Pd ^{II} (L ^{1e} -Se,O) ₂] 152	320, 320 293, 292
$\text{HL}_{\text{Se}}^{1f}$ 16	484	<i>cis</i> -[Pd ^{II} (L ^{1f} -Se,O) ₂] 162	302
$\text{HL}_{\text{Se}}^{1g}$ 17	660	<i>cis</i> -[Pd ^{II} (L ^{1g} -Se,O) ₂] 172	-
[Cd ^{II} (L ^{1a} -Se,O) ₂] 111	47	[Zd ^{II} (L ^{1a} -Se,O) ₂] 113	68
[Cd ^{II} (L ^{1b} -Se,O) ₂] 121	49		
[Cd ^{II} (L ^{1c} -Se,O) ₂] 131	53		
[Cd ^{II} (L ^{1e} -Se,O) ₂] 151	83, 58		
[Cd ^{II} (L ^{1a} -Se,O)(L ^{2a} -S,O)] 11211	47		

In the case of the Pd(Se₂CNR₂)₂ complexes, this was attributed to changes in the mesomeric effect and hence the chemical shielding, however the isobutyl and ethyl groups could affect the steric environments surrounding the selenium atoms and would therefore influence the solvent interactions at these sites. In our case, the smaller chemical shift difference of only 3 ppm can be accounted for by the slight steric difference present between the ethyl and butyl groups. The asymmetrically substituted derivative however (*cis*-[Pd^{II}(L^{1e}-Se,O)₂] **152**) exhibits chemical shift differences almost ten times in magnitude to that of the dibutyl derivative and the greater steric difference between these amine residues can influence the solvent interactions with the ^{77}Se nucleus, accounting for the large chemical shift difference.

Complexation to Cd(II) increases the shielding of the ^{77}Se nucleus even more and in [Cd^{II}(L^{1a}-Se,O)₂] **111** the resonance appears at 47 ppm (Fig. 2.337) Typical $^1J(^{77}\text{Se}-^{113}\text{Cd})$ couplings fall in the range 126-195 Hz however these were not observable for **111**, or indeed any of the other Cd(II) complexes.^[113] ^{77}Se resonances of the complexes $\text{HL}_{\text{Se}}^{1b-f}$ were not easily observable at room temperature and this is thought to be due to the high lability of Cd(II) complexes, exchange being too fast for observation of the nucleus on the NMR time scale. Low temperature NMR studies were undertaken to observe the resonance and Table 2.320 lists the chemical shift values obtained for [Cd^{II}(L^{1b}-Se,O)₂] **121**, [Cd^{II}(L^{1c}-Se,O)₂] **131**, [Cd^{II}(L^{1e}-Se,O)₂] **151** at 233.5 K. The resonances observed however, were very broad and extended analysis times were needed to observe these. Inferences from the chemical shift positions under these conditions should be made with caution as temperature-induced signal shifts for ^{77}Se nucleus have been reported.^[113] These are however strongly dependant on the structure of the compound and corrections for this could not easily be made without a series of experiments being undertaken. Due to the costly nature of low temperature NMR and the relatively limited information that would result, these experiments were not felt to be justified and were accordingly not carried out.

Fig. 2.337 shows the ^{77}Se NMR spectra of $\text{HL}_{\text{Se}}^{1a}$ and its three metal complexes where coordination to Zn(II) resulted in an increase in the shielding of the ^{77}Se nucleus, similar to that for Cd(II). In the related diselenocarbamate complexes, Zn(II) and Cd(II)(Se₂CN-*n*-Bu₂)₂ exhibit chemical shift differences of 48 ppm where the most shielded resonance is that of the Zn(II) complex. The inverse is seen here where the ^{77}Se resonance in [Cd^{II}(L^{1a}-Se,O)₂] **111**, appears 21 ppm upfield to that in the Zn(II) complex. ^{77}Se NMR studies have also been carried out on dichloroselenourea complexes of Zn(II), Cd(II) and Hg(II) where it was found, similarly to our complexes, that the ^{77}Se nucleus is the most shielded in the Cd(II) complex.^[119]

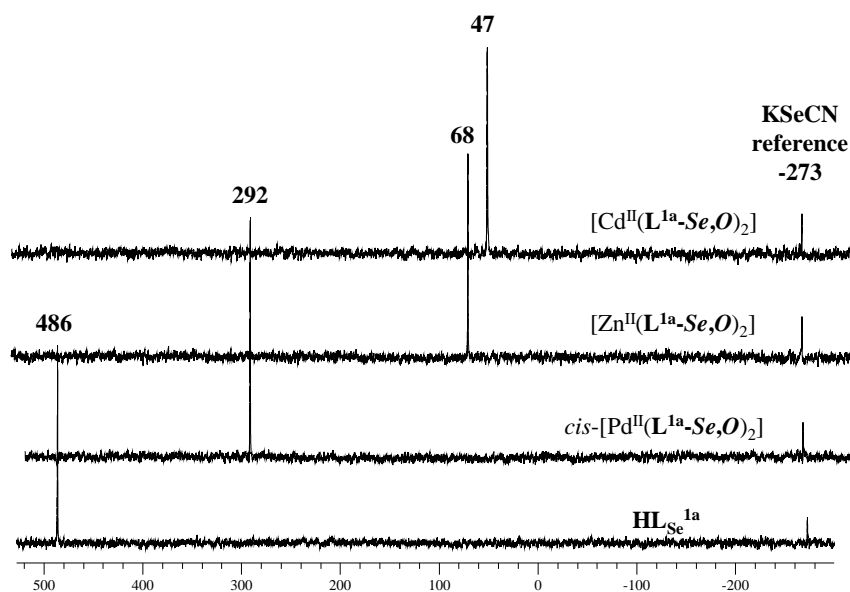


Fig. 2.337 ^{77}Se NMR spectra of $\text{HL}_{\text{Se}}^{1a}$ and its Pd(II), Zn(II) and Cd(II) metal complexes.

2.3.5.4 ^{113}Cd NMR Spectroscopy

Cadmium has two NMR active isotopes, ^{111}Cd and ^{113}Cd , the latter having a 10 % greater sensitivity and therefore instruments settings were optimized for observation of this nucleus.^[120] As with the case of ^{77}Se , the choice of reference material varies greatly, with some of the more common materials including $\text{Cd}(\text{ClO}_4)_2$ and $\text{Cd}(\text{CH}_3)_2$.^[121] Maciel *et al.* reported on the concentration dependence of the ^{113}Cd resonance in 4.5 M and 0.1 M aqueous $\text{Cd}(\text{NO}_3)_2 \cdot 4\text{H}_2\text{O}$, the chemical shift being -3.72 and -49.41 ppm respectively, relative to 0.1M aqueous $\text{Cd}(\text{ClO}_4)_2$.^[75] Due to the availability of this salt, a 4.5 M aqueous solution of $\text{Cd}(\text{NO}_3)_2 \cdot 4\text{H}_2\text{O}$ was carefully weighed out and placed in a coaxial insert which was then used as a reference material. As the lock frequency of the instrument is referenced to $\text{Cd}(\text{CH}_3)_2$, the resonance frequency of the $\text{Cd}(\text{NO}_3)_2 \cdot 4\text{H}_2\text{O}$ insert was adjusted according to the specifications given by Cardin *et al.* resulting in the $\text{Cd}(\text{NO}_3)_2 \cdot 4\text{H}_2\text{O}$ resonance appearing at -692 ppm (Fig. 2.).^[122] Previous studies of tetrahedral complexes have shown a decrease in shielding among the chalcogen donor atoms in the order $\text{O} \gg \text{Se} > \text{S}$,^[123] however Fig. 2.338 shows the $[\text{Cd}^{\text{II}}(\text{L}^{1a}\text{-Se},\text{O})_2]$ resonance 35 ppm downfield to that of the S analogue. This compares closely with solid state measurements on $\text{Cd}(\text{TU})_2\text{Cl}_2$ and $\text{Cd}(\text{SU})_2\text{Cl}_2$ where the ^{113}Cd nucleus in the Se complex resonates 30 ppm downfield to that of its S counterpart.^[119] This suggests that for $[\text{Cd}^{\text{II}}(\text{L}^{1a}\text{-Se},\text{O})_2]$, the paramagnetic contribution to the nuclear shielding constant must dominate over that of the spin-orbit contribution where $\sigma = \sigma_{\text{Dia}} + \sigma_{\text{Para}} + \sigma_{\text{Spin orbit}}$, a larger $\sigma_{\text{Spin orbit}}$ contribution being expected for Se than S.^[124] Se is only slightly less electronegative ($\lambda = 2.55$) than S ($\lambda = 2.58$) and the covalent nature of the Cd-Se bond is likely to be comparable to that of the Cd-S bond. However, orbital overlap of Cd(II) with Se would be expected to be better than with either S or O as the lowest unoccupied molecular orbitals on Se involve the 5s and 4d electron shells and these are the orbitals that are filled in the second row transition metal ion Cd(II), the orbital distortion is therefore less allowing for the increased paramagnetic shielding contribution and the deshielding seen in $[\text{Cd}^{\text{II}}(\text{L}^{1a}\text{-Se},\text{O})_2]$ **111**. Interestingly the ‘mixed ligand complex’, $[\text{Cd}^{\text{II}}(\text{L}^{1a}\text{-Se},\text{O})(\text{L}^{2a}\text{-S},\text{O})]$ **11211** resonance is almost the same as that of $[\text{Cd}^{\text{II}}(\text{L}^{1a}\text{-Se},\text{O})_2]$ **111** and will be discussed in more detail shortly.

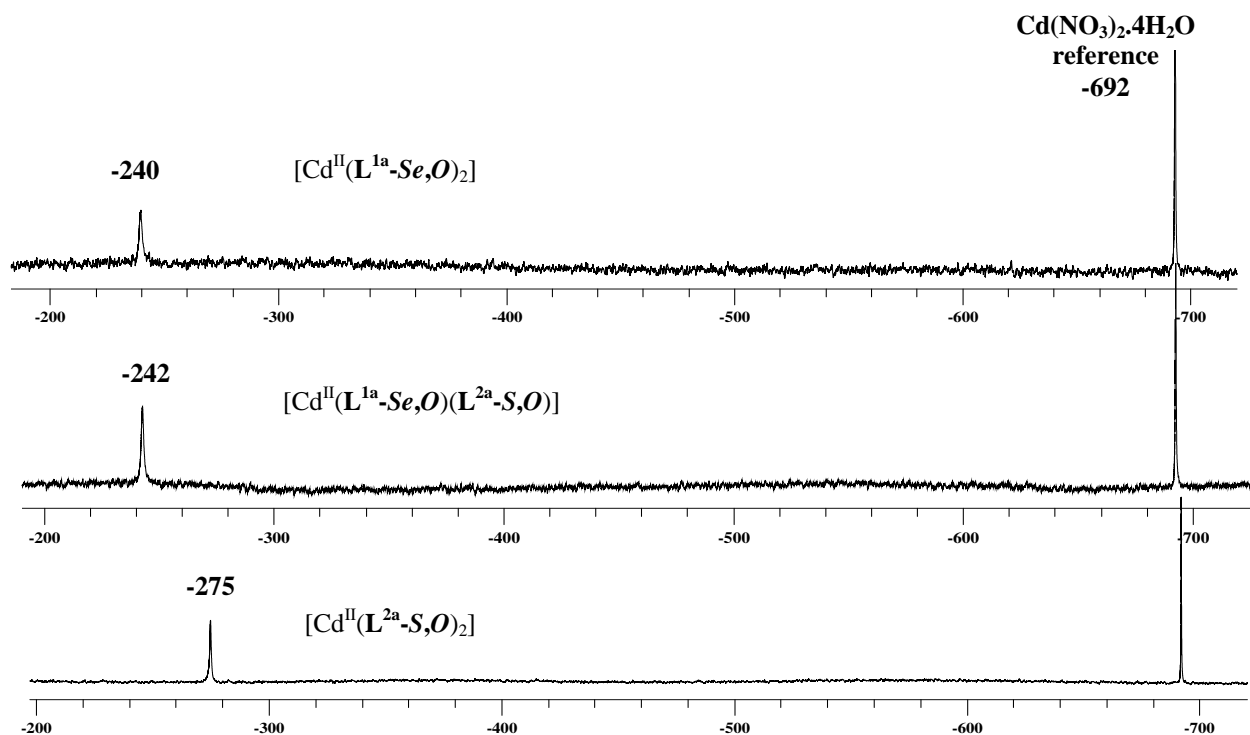


Fig. 2.338 ^{113}Cd NMR spectra of $[\text{Cd}^{\text{II}}(\text{L}^{1\text{a}}\text{-Se},\text{O})_2]$ **111**, $[\text{Cd}^{\text{II}}(\text{L}^{1\text{a}}\text{-Se},\text{O})(\text{L}^{2\text{a}}\text{-S},\text{O})]$ **11211** and $[\text{Cd}^{\text{II}}(\text{L}^{2\text{a}}\text{-S},\text{O})_2]$ **211**

The chemical shift positions of the remaining (*N,N*-dialkyl-*N'*-benzoylthioureato)Cd(II) complexes (Table 2.321) appear to be very similar although distinct to that of the diethyl derivative. It is recognized however that chemical dynamic problems influence ^{113}Cd chemical shifts, making shift analyses somewhat confounding and hence no deductions in terms of structural properties are drawn from this data.^[123] Low temperature NMR experiments were undertaken for the (*N,N*-dialkyl-*N'*-benzoylselenoureato)Cd(II) complexes ($[\text{Cd}^{\text{II}}(\text{L}^{1\text{b}}\text{-Se},\text{O})_2]$ **121** at -236 ppm obtained at 233.5 K) in an attempt to reduce the rate of the exchange process, however very long acquisition times were necessary and as for the ^{77}Se NMR the relatively limited information that would result from the necessary series of experiments did not justify the expenditure and further analysis was not done.

Table 2.321 ^{113}Cd chemical shift positions of selected complexes.

Compound	^{113}Cd chemical shift position	Compound	^{113}Cd chemical shift position
$[\text{Cd}^{\text{II}}(\text{L}^{1\text{a}}\text{-Se},\text{O})_2]$ 111	-240	$[\text{Cd}^{\text{II}}(\text{L}^{2\text{a}}\text{-S},\text{O})_2]$ 211	-275
$[\text{Cd}^{\text{II}}(\text{L}^{1\text{b}}\text{-Se},\text{O})_2]$ 121	-236	$[\text{Cd}^{\text{II}}(\text{L}^{2\text{b}}\text{-S},\text{O})_2]$ 221	-229
$[\text{Cd}^{\text{II}}(\text{L}^{1\text{c}}\text{-Se},\text{O})_2]$ 131	-	$[\text{Cd}^{\text{II}}(\text{L}^{2\text{c}}\text{-S},\text{O})_2]$ 231	-229
$[\text{Cd}^{\text{II}}(\text{L}^{1\text{d}}\text{-Se},\text{O})_2]$ 141	-	$[\text{Cd}^{\text{II}}(\text{L}^{2\text{d}}\text{-S},\text{O})_2]$ 241	-231

As mentioned previously the ^{113}Cd chemical shift positions of $[\text{Cd}^{\text{II}}(\text{L}^{1\text{a}}\text{-Se},\text{O})_2]$ **111**, $[\text{Cd}^{\text{II}}(\text{L}^{1\text{a}}\text{-Se},\text{O})(\text{L}^{2\text{a}}\text{-S},\text{O})]$ **11211** are very similar indicating that the electronic environment of the Cd^{2+} ion in **11211** resembles that of $[\text{Cd}^{\text{II}}(\text{L}^{1\text{a}}\text{-Se},\text{O})_2]$ **111** more than its S analogue. Interestingly, the ^{77}Se chemical shift positions are also very similar, that of both **111** and **11211** resonating at 47 ppm (Table 2.320) and this is reflected in the practically identical $^1J(^{13}\text{C}\text{-}^{77}\text{Se})$ coupling constants of 164.9 and 164.6 Hz respectively. Isolation of a crystal from an NMR sample of **11211** was found to have an identical unit cell to that of $[\text{Cd}^{\text{II}}(\text{L}^{1\text{a}}\text{-Se},\text{O})_2]$ **111**, suggesting a form of chelate metathesis taking place in solution. This phenomenon has recently been studied in the square planar *cis*-bis(*N,N*-dialkyl-*N'*-aroyl(acyl)thioureato)palladium(II) complexes,^[125] however no mention of this could be found in the literature relating to the selenium analogues. To substantiate this further, a molar equivalent of free ligand ($\text{HL}_{\text{Se}}^{1\text{a}}$)

was added to a solution of $[\text{Cd}^{\text{II}}(\text{L}^{\text{1a}}\text{-Se},\text{O})(\text{L}^{\text{2a}}\text{-S},\text{O})]$ **11211** in an NMR tube and the resulting spectra are shown in Fig. 2.339. Only expansions of the carbonyl region are shown, but observations made from this are reflected in the remainder of the spectrum. Fig. 2.339 (B) shows the resonances of the donor atoms surrounding the Cd(II) metal centre in **11211**. Fig. 2.339 (C) shows that obtained following the addition of 1 molar equivalent of $\text{HL}_{\text{Se}}^{\text{1a}}$. The decreased shielding of the thiocarbonyl carbon coupled with the increased shielding of the carbonyl carbon and their relative chemical shift positions implies the loss of coordination of $\text{HL}_{\text{S}}^{\text{2a}}$ to the metal centre and the presence of ‘free ligand’ HL^{2a} (Fig. 2.339(A)). This was confirmed by the addition of $\text{HL}_{\text{S}}^{\text{2a}}$ to the solution Fig. 2.339 (D) illustrating the increased intensity of the C(O) and C(S) resonances of $\text{HL}_{\text{S}}^{\text{2a}}$. The remaining two resonances at 171.1 and 169.5 ppm are attributed to $[\text{Cd}^{\text{II}}(\text{L}^{\text{1a}}\text{-Se},\text{O})_2]$ **111**, as they differ only slightly to the 170.9 and 167.8 ppm exhibited by the separately prepared $[\text{Cd}^{\text{II}}(\text{L}^{\text{1a}}\text{-Se},\text{O})_2]$ **111**. The above results illustrate the increased affinity that Cd(II) exhibits for Se rather than S as a donor atom, as even in the presence of excess $\text{HL}_{\text{S}}^{\text{2a}}$ coordination of the Se analogue occurs. Analogous studies using Pd(II) as a central metal ion could provide interesting insight into the coordinating behaviour of the *N,N*-dialkyl-*N'*-benzoylseleno- and thioureas.

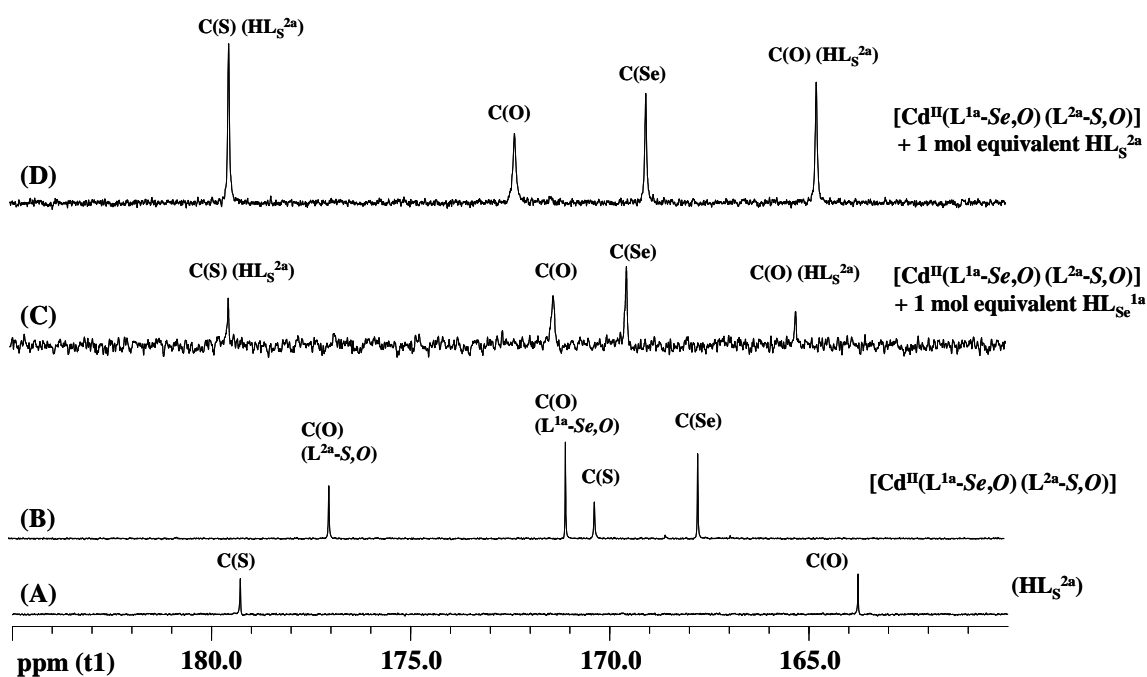


Fig. 2.339 ^{13}C NMR spectra of (A) uncoordinated $\text{HL}_{\text{S}}^{\text{2a}}$, (B) $[\text{Cd}^{\text{II}}(\text{L}^{\text{1a}}\text{-Se},\text{O})(\text{L}^{\text{2a}}\text{-S},\text{O})]$ **11211**, (C) **11211** + 1 molar equivalent of $\text{HL}_{\text{Se}}^{\text{1a}}$ and (D) $[\text{Cd}^{\text{II}}(\text{L}^{\text{1a}}\text{-Se},\text{O})(\text{L}^{\text{2a}}\text{-S},\text{O})]$ **11211** + 2 molar equivalents of $\text{HL}_{\text{Se}}^{\text{1a}}$.

2.3.5.5 ^{31}P NMR Spectroscopy

As described in Section 2.2.3.4 synthesis of *cis*-bis(*N,N*-diethyl-*N'*-benzoylselenoureato)platinum(II) from K_2PtCl_4 as starting material proved to be an onerous task. To establish if coordination of *N,N*-diethyl-*N'*-benzoylselenourea to Pt(II) would occur the following experiment was designed. A Pt(II) complex soluble in organic solvents, $(\text{Bu}_3\text{P})_2\text{PtCl}_2$, was dissolved in CDCl_3 and examined by ^{31}P NMR spectroscopy. (Fig. 2.340 (A)). Addition of a molar equivalent of ligand, $\text{HL}_{\text{Se}}^{\text{1a}}$, and a base (NET_3) in the NMR tube resulted in the ^{31}P spectrum shown in Fig.

2.340 (B)). By monitoring the ^{31}P nucleus, spectroscopic evidence of coordination or the lack thereof could be obtained.

The magnetically equivalent ^{31}P nuclei in the starting compound ($(\text{But}_3\text{P})_2\text{PtCl}_2$) give rise to a single ^{31}P resonance with a $^1J(^{31}\text{P}-^{195}\text{Pt})$ coupling constant of 3518.8 Hz (Fig. 2.340(A)). Following the addition of the $\text{HL}_{\text{Se}}^{1a}$ and NEt_3 some of the starting compound (S.C.) (Fig. 2.340 (B)) is retained in solution, however two large additional resonances appear and these are assigned to the ^{31}P *trans* to the Se atom (P_{Se}) and *trans* to the O atom (P_{O}) (Fig. 2.340(B)), the two ^{31}P nuclei no longer being equivalent due to the unsymmetrical nature of $\text{HL}_{\text{Se}}^{1a}$ resulting in ^{31}P - ^{31}P spin-spin coupling where ($^2J(^{31}\text{P}-^{31}\text{P}) = 20$ Hz). The most deshielded ^{31}P resonance (12.9 ppm) exhibits a smaller $^1J(^{31}\text{P}-^{195}\text{Pt})$ coupling constant of 3008.5 Hz relative to that of 3602.2 Hz exhibited by the more shielded ^{31}P resonance at -6.7 ppm and for this reason has been assigned to P_{Se} . In terms of Pearson's "Principle of Hard and Soft Acids and Bases" (HSAB),^[126] the "softer" Se atom is expected to bind more favourably to the Pt(II) metal centre, labilising the *trans* Pt-P bond so resulting in smaller $^1J(^{31}\text{P}-^{195}\text{Pt})$ couplings, with the opposite effect occurring for P_{O} . Both the $^1J(^{31}\text{P}-^{195}\text{Pt})$ coupling constants and chemical shift positions of the ^{31}P resonances occur within the expected range.^[127-130]

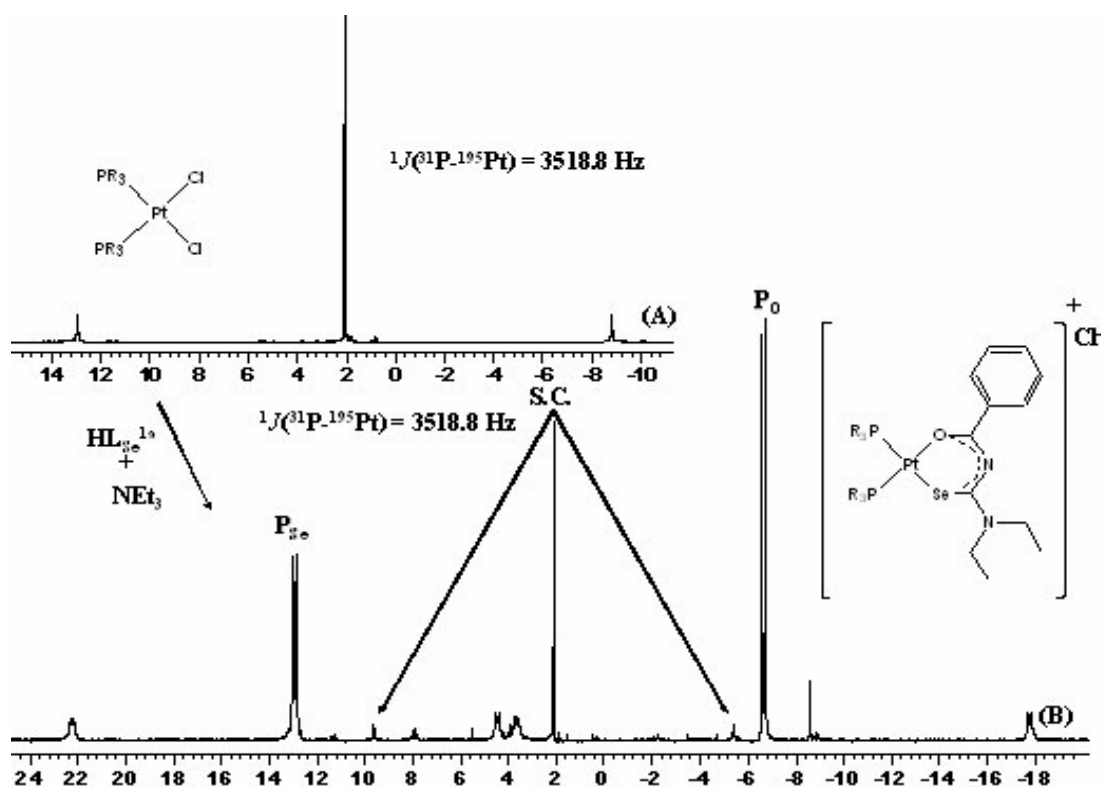


Fig 2.340. ^{31}P NMR spectra of $(\text{But}_3\text{P})_2\text{PtCl}_2$ (S.C.), (A) and that obtained subsequent to addition of $\text{HL}_{\text{Se}}^{1a}$ and NEt_3 (B).

The resonances of P_{O} and P_{Se} both exhibit fine structure which has been attributed to ^{77}Se satellites (Fig. 2.341). This can clearly be resolved in P_{O} ($^2J(^{31}\text{P}-^{77}\text{Se}) = 14$ Hz), but is slightly obscured by the main resonance for P_{Se} however a $^2J(^{31}\text{P}-^{77}\text{Se}) = 65$ Hz can be estimated, these values comparing well with those previously reported for related compounds where $^2J(^{31}\text{P}-^{77}\text{Se})_{\text{cis}} = 11$ Hz and $^2J(^{31}\text{P}-^{77}\text{Se})_{\text{trans}} = 74$ Hz.^[128, 129, 131] As the natural abundance of ^{77}Se is 7.58 % and that of ^{31}P is 100 %, the expected relative intensities of ^{77}Se satellites would be in the region of 0.076. The averaged values found for the P_{O} and P_{Se} resonances varied between 0.06 and 0.1, supporting the assignment of

the fine structure as ^{77}Se satellites. Small quantities of other minor phosphorous containing species are present in solution, however further work is required to identify these. It is evident however, that coordination of *N,N*-diethyl-*N'*-benzoylselenourea to the Pt(II) metal centre did occur, indicating that these complexes may actually be stable in solution. Further work would be necessary however, to enable isolation of the *cis*-bis(*N,N*-diethyl-*N'*-benzoylselenourea)Pt(II) complex.

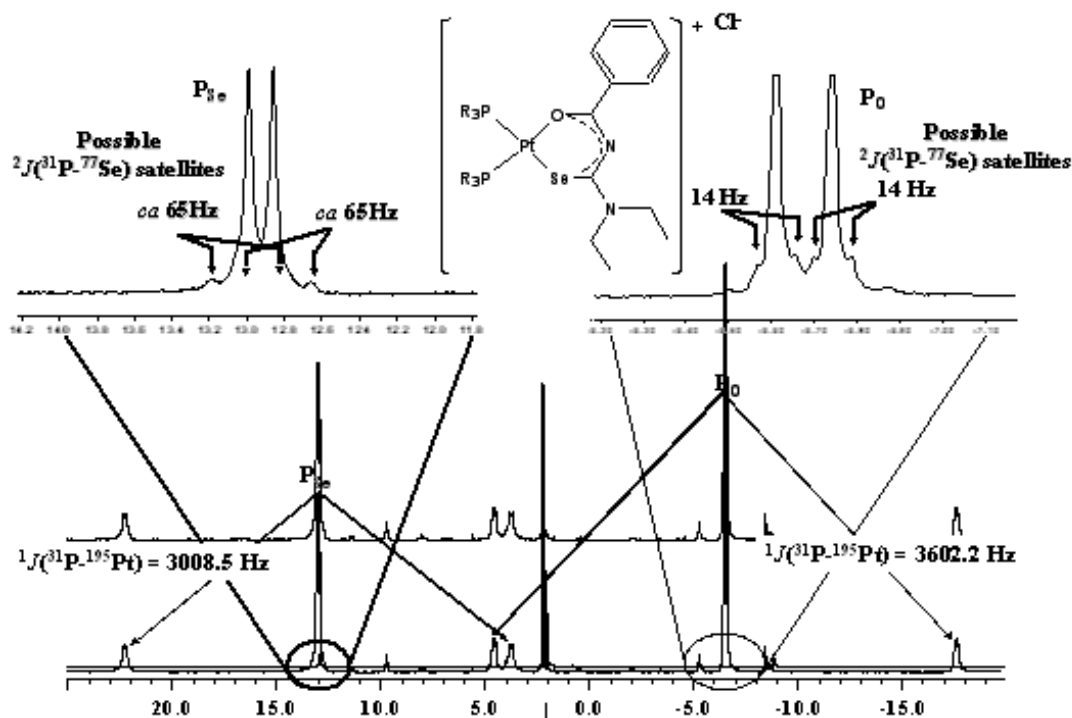


Fig. 2.341 Expansion of ^{31}P NMR spectrum obtained upon addition of $\text{HL}_{\text{Se}}^{1a}$ and NEt_3 to $(\text{But}_3\text{P})_2\text{PtCl}_2$ illustrating $^1J(^{31}\text{P}-^{195}\text{Pt})$ and $^2J(^{31}\text{P}-^{77}\text{Se})$ coupling constants.

The diselenidic nature of $\text{HL}_{\text{Se}}^{1g}$ seen in the solid state, may in part, rationalize the results obtained when the *cis*-bis(*N,N*-diethyl-*N'*-benzoylselenourea)Pt(II) complex synthesis was attempted on a larger scale. $\text{HL}_{\text{Se}}^{1g}$ provides evidence of the reduction potential of ligands of this type and therefore it is possible that in the variety of solvents used, oxidation of the ligand occurred and consequent reduction of the Pt(II) species, born out by the presence each time in solution, of a black metallic like precipitate. It is also possible that the kinetic inertness of PtCl_4^{2-} in aqueous media results in the decomposition of the inherently unstable complex, and this is supported by the fact that use of PdCl_4^{2-} allowed the synthesis of the desired complexes with relative ease. It is therefore likely that use of an organically soluble Pt(II) source (*e.g.* $\text{Pt}(\text{cod})_2$), use of dried solvents and an inert atmosphere would allow the synthesis of *cis*-bis(*N,N*-diethyl-*N'*-benzoylselenourea)Pt(II).

2.3.6 Thermogravimetric analysis of *N,N*-dialkyl-*N'*-benzoyl(thio)selenourea metal complexes

As the synthesis of the *N,N*-dialkyl-*N'*-benzoyl(thio)selenourea metal complexes was performed with a view to their use as single source precursors, a preliminary investigation into the thermal decomposition of selected metal complexes was undertaken. This was in order to gain an insight into the possible material that could be formed from the thermal decomposition of the *N,N*-dialkyl-*N'*-benzoyl(thio)selenourea metal complexes, and the possible composition of the resulting nanoparticles.

2.3.6.1 Thermogravimetric analysis of *N,N*-dialkyl-*N'*-benzoylselenourea metal complexes

The decomposition profiles of $[\text{Cd}^{\text{II}}(\text{L}^{\text{1a}}\text{-Se},\text{O})_2]$, $\text{cis-}[\text{Pd}^{\text{II}}(\text{L}^{\text{1a}}\text{-Se},\text{O})_2]$ and $[\text{Zn}^{\text{II}}(\text{L}^{\text{1a}}\text{-Se},\text{O})_2]$ are shown in Fig. 2.342. To the best of our knowledge there are no reports detailing the thermogravimetric analysis (TGA) of *N,N*-dialkyl-*N'*-benzoylselenourea metal complexes however Merdivan *et al.* have studied several related thiourea complexes and suggest a two step decomposition process for compounds of this type. An initial mass loss corresponding to the elimination of 2 moles of diethylbenzamide followed by the loss of SCN and CN radicals to yield either the metal ion or the metal sulfide this being dependant on the central metal ion.^[66] Assuming a similar decomposition profile for $[\text{Cd}^{\text{II}}(\text{L}^{\text{1a}}\text{-Se},\text{O})_2]$, $\text{cis-}[\text{Pd}^{\text{II}}(\text{L}^{\text{1a}}\text{-Se},\text{O})_2]$ and $[\text{Zn}^{\text{II}}(\text{L}^{\text{1a}}\text{-Se},\text{O})_2]$ allows the calculation of the following mass losses shown in Table 2.322. The poor agreement between the calculated and observed % mass loss values indicates that the decomposition of *N,N*-dialkyl-*N'*-benzoylselenourea metal complexes is distinct to that of their S analogues. Fig. 2.342 shows a 3 step decomposition profile for both $[\text{Cd}^{\text{II}}(\text{L}^{\text{1a}}\text{-Se},\text{O})_2]$ and $\text{cis-}[\text{Pd}^{\text{II}}(\text{L}^{\text{1a}}\text{-Se},\text{O})_2]$, but only a 2 step decomposition profile for $[\text{Zn}^{\text{II}}(\text{L}^{\text{1a}}\text{-Se},\text{O})_2]$. It is also clear that the onset of decomposition and the major mass losses occur at different temperatures for all three complexes where $[\text{Cd}^{\text{II}}(\text{L}^{\text{1a}}\text{-Se},\text{O})_2] < \text{cis-}[\text{Pd}^{\text{II}}(\text{L}^{\text{1a}}\text{-Se},\text{O})_2] <$

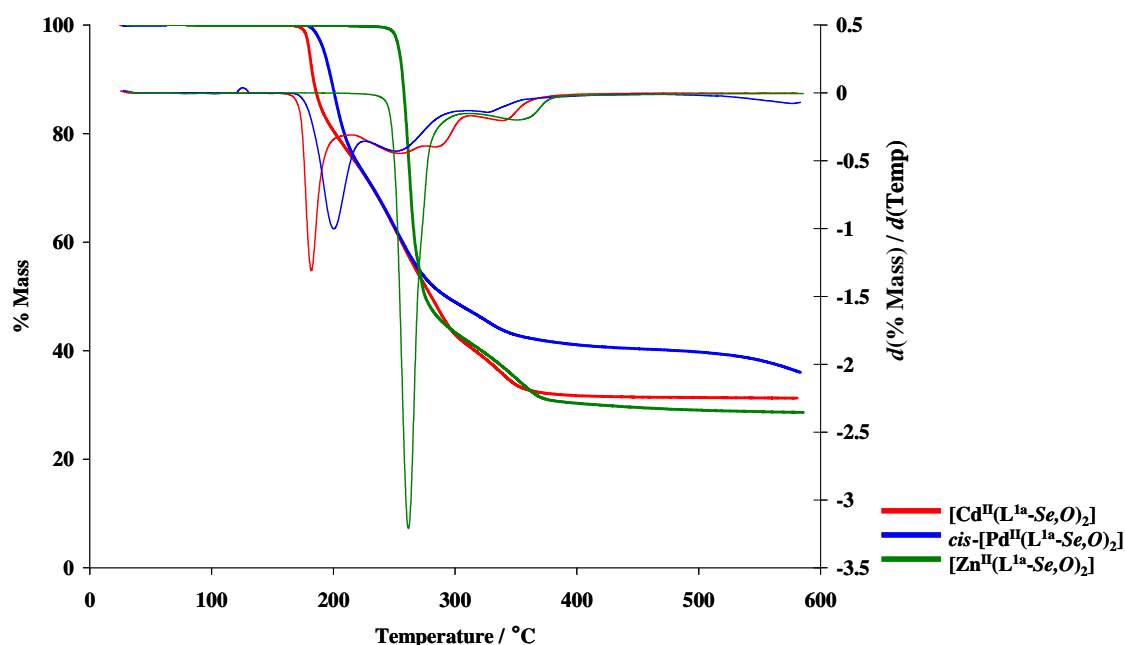


Fig. 2.342 TGA profiles and their first derivatives of $[\text{Cd}^{\text{II}}(\text{L}^{\text{1a}}\text{-Se},\text{O})_2]$, $\text{cis-}[\text{Pd}^{\text{II}}(\text{L}^{\text{1a}}\text{-Se},\text{O})_2]$ and $[\text{Zn}^{\text{II}}(\text{L}^{\text{1a}}\text{-Se},\text{O})_2]$. Analysis was performed using a ramp rate of $10\text{ }^\circ\text{C}/\text{min}$.

Table 2.322 Thermogravimetric data for pyrolytic processes for $[\text{Cd}^{\text{II}}(\text{L}^{\text{Ia}}-\text{Se},\text{O})_2]$, $\text{cis}-[\text{Pd}^{\text{II}}(\text{L}^{\text{Ia}}-\text{Se},\text{O})_2]$ and $[\text{Zn}^{\text{II}}(\text{L}^{\text{Ia}}-\text{Se},\text{O})_2]$.

Complex	Process	Temp range / °C	Mass loss / %	
			Calculated	Observed
$[\text{Cd}^{\text{II}}(\text{L}^{\text{Ia}}-\text{Se},\text{O})_2]$	$[\text{Cd}^{\text{II}}(\text{L}^{\text{Ia}}-\text{Se},\text{O})_2] \longrightarrow 2\text{DEB}$	0-215	52.37	24.22
	$\longrightarrow \text{SeCN} + \text{CN}$	215-312	19.35	35.03
		312-372	-	8.52
$\text{cis}-[\text{Pd}^{\text{II}}(\text{L}^{\text{Ia}}-\text{Se},\text{O})_2]$	$\text{cis}-[\text{Pd}^{\text{II}}(\text{L}^{\text{Ia}}-\text{Se},\text{O})_2] \longrightarrow 2\text{DEB}$	0-226	52.84	27.52
	$\longrightarrow \text{SeCN} + \text{CN}$	226-310	19.53	24.90
		310-354	-	4.95
$[\text{Zn}^{\text{II}}(\text{L}^{\text{Ia}}-\text{Se},\text{O})_2]$	$[\text{Zn}^{\text{II}}(\text{L}^{\text{Ia}}-\text{Se},\text{O})_2] \longrightarrow 2\text{DEB}$	0-310	56.29	58.16
	$\longrightarrow \text{SeCN} + \text{CN}$	310-400	20.80	13.21

* DEB = diethylbenzamide

$[\text{Zn}^{\text{II}}(\text{L}^{\text{Ia}}-\text{Se},\text{O})_2]$ as would be expected given their differing geometries. The higher temperature at which decomposition commences for $[\text{Zn}^{\text{II}}(\text{L}^{\text{Ia}}-\text{Se},\text{O})_2]$ relative to that of $\text{cis}-[\text{Pd}^{\text{II}}(\text{L}^{\text{Ia}}-\text{Se},\text{O})_2]$ and $[\text{Cd}^{\text{II}}(\text{L}^{\text{Ia}}-\text{Se},\text{O})_2]$, suggests an increased thermal stability for this complex relative to the Pd(II) and Cd(II) derivatives. Table 2.323 shows the calculated and observed residual masses assuming the formation of the metal selenide. The best agreement between the two values is seen in $[\text{Cd}^{\text{II}}(\text{L}^{\text{Ia}}-\text{Se},\text{O})_2]$ where it is likely that CdSe is formed. Both $\text{cis}-[\text{Pd}^{\text{II}}(\text{L}^{\text{Ia}}-\text{Se},\text{O})_2]$ and $[\text{Zn}^{\text{II}}(\text{L}^{\text{Ia}}-\text{Se},\text{O})_2]$ display poor agreement between the two values. It is known however that more than one phase of palladium selenide occurs, where the observed residual mass of 35.9 % shows better agreement with the calculated residual masses of 39.4 % and 29.8 % for PdSe_2 and $\text{Pd}_{17}\text{Se}_{15}$ formation respectively.^[130, 132]

Table 2.323 Residual mass % following thermal decomposition of $[\text{Cd}^{\text{II}}(\text{L}^{\text{Ia}}-\text{Se},\text{O})_2]$, $\text{cis}-[\text{Pd}^{\text{II}}(\text{L}^{\text{Ia}}-\text{Se},\text{O})_2]$ and $[\text{Zn}^{\text{II}}(\text{L}^{\text{Ia}}-\text{Se},\text{O})_2]$.

Complex	Temp / °C	Calculated mass / %	Observed residual mass / %
$[\text{Cd}^{\text{II}}(\text{L}^{\text{Ia}}-\text{Se},\text{O})_2]$	~ 580	28.3	31.2
$\text{cis}-[\text{Pd}^{\text{II}}(\text{L}^{\text{Ia}}-\text{Se},\text{O})_2]$	~ 580	27.6	35.9
$[\text{Zn}^{\text{II}}(\text{L}^{\text{Ia}}-\text{Se},\text{O})_2]$	~ 580	22.9	28.6

Following TGA, the residue quantity is too small to allow for PXRD analysis, however to overcome this, a sample of $\text{cis}-[\text{Pd}^{\text{II}}(\text{L}^{\text{Ia}}-\text{Se},\text{O})_2]$ was heated in a furnace to 475 °C using a heating profile as close to that of the TGA as possible. A final temperature of 580 °C was not feasible due to the glass crucible used. The PXRD pattern of the residue obtained in this manner is shown in Fig. 2.343 along with those of library patterns of $\text{Pd}_{17}\text{Se}_{15}$ (red) and PdSe_2 (blue). It is clear that a very crystalline residue was obtained and Energy dispersive X-Ray spectroscopy (EDAX) analysis indicated a Pd : Se ratio of 1 : 1.333. Fig. 2.343 shows that several peaks in both the PdSe_2 and $\text{Pd}_{17}\text{Se}_{15}$ PXRD patterns coincide with those obtained experimentally. Semi quantitative analysis of the data indicates that the residue is composed of 52.9 % $\text{Pd}_{17}\text{Se}_{15}$ and 47.1 % PdSe_2 . As will be shown in Chapter 3 and 4, this could have important implications in the behaviour of $\text{cis}-[\text{Pd}^{\text{II}}(\text{L}^{\text{Ia}}-\text{Se},\text{O})_2]$ as a single source precursor.

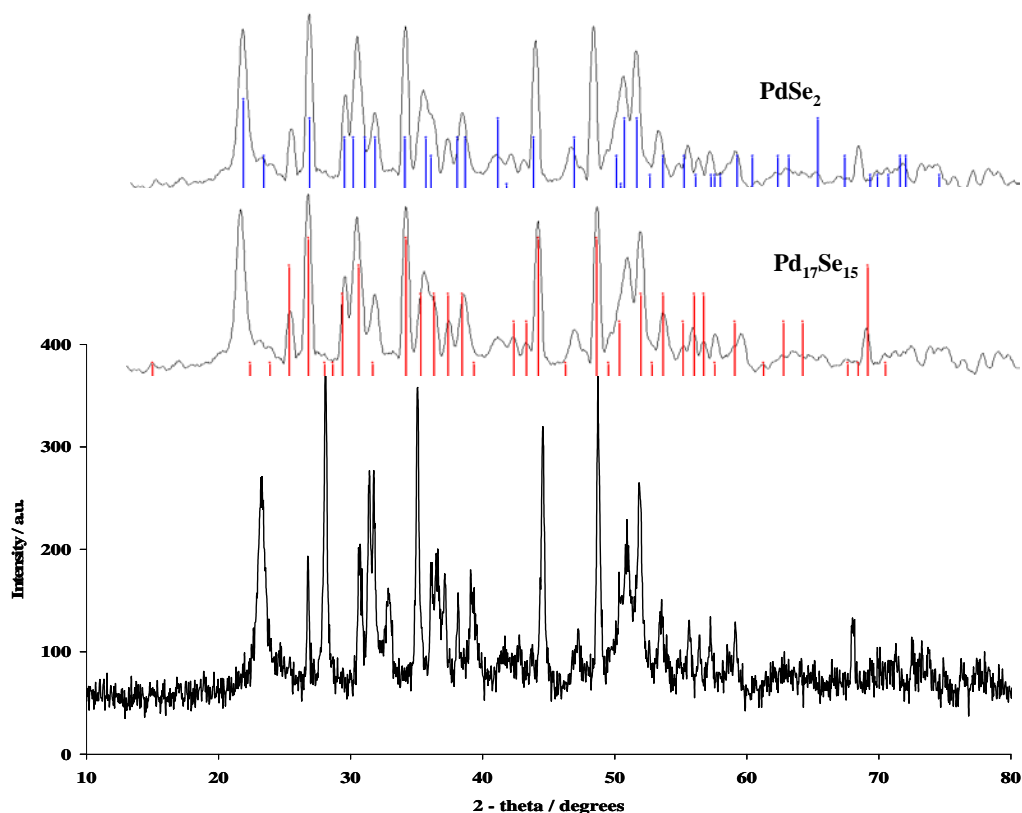


Fig. 2.343 PXRD patterns of PdSe_2 , $\text{Pd}_{17}\text{Se}_{15}$ and that obtained from the residue following furnace decomposition of *cis*- $[\text{Pd}^{\text{II}}(\text{L}^{\text{1a}}\text{-S},\text{O})_2]$.

2.3.6.2 Thermogravimetric analysis of *N,N*-dialkyl-*N'*-benzoylthiourea metal complexes

For facile comparison with Fig. 2.342, the decomposition profiles of $[\text{Cd}^{\text{II}}(\text{L}^{\text{2a}}\text{-S},\text{O})_2]$, *cis*- $[\text{Pd}^{\text{II}}(\text{L}^{\text{2a}}\text{-S},\text{O})_2]$ and $[\text{Zn}^{\text{II}}(\text{L}^{\text{2a}}\text{-S},\text{O})_2]$ are shown in Fig. 2.344. As previously mentioned Merdivan *et al.* suggested a two step decomposition mechanism for *N,N*-dialkyl-*N'*-benzoylthiourea metal complexes and Table 2.324 shows the calculated and observed mass loss percentages assuming this to hold true for $[\text{Cd}^{\text{II}}(\text{L}^{\text{2a}}\text{-S},\text{O})_2]$, *cis*- $[\text{Pd}^{\text{II}}(\text{L}^{\text{2a}}\text{-S},\text{O})_2]$ and $[\text{Zn}^{\text{II}}(\text{L}^{\text{2a}}\text{-S},\text{O})_2]$.

Table 2.324 Thermogravimetric data for pyrolytic processes for $[\text{Cd}^{\text{II}}(\text{L}^{\text{2a}}\text{-S},\text{O})_2]$, *cis*- $[\text{Pd}^{\text{II}}(\text{L}^{\text{2a}}\text{-S},\text{O})_2]$ and $[\text{Zn}^{\text{II}}(\text{L}^{\text{2a}}\text{-S},\text{O})_2]$.

Complex	Process	Temp range / °C	Mass loss / %	
			Calculated	Observed
$[\text{Cd}^{\text{II}}(\text{L}^{\text{2a}}\text{-S},\text{O})_2]$	$[\text{Cd}^{\text{II}}(\text{L}^{\text{2a}}\text{-S},\text{O})_2] \longrightarrow 2\text{DEB}$	0-269	60.80	55.07
	$\longrightarrow \text{SCN} + \text{CN}$	269-331	14.42	8.73
<i>cis</i> - $[\text{Pd}^{\text{II}}(\text{L}^{\text{2a}}\text{-S},\text{O})_2]$	<i>cis</i> - $[\text{Pd}^{\text{II}}(\text{L}^{\text{2a}}\text{-S},\text{O})_2] \longrightarrow 2\text{DEB}$	0-274	61.43	54.17
	$\longrightarrow \text{SCN} + \text{CN}$	274-400	14.57	19.39
$[\text{Zn}^{\text{II}}(\text{L}^{\text{2a}}\text{-S},\text{O})_2]$	$[\text{Zn}^{\text{II}}(\text{L}^{\text{2a}}\text{-S},\text{O})_2] \longrightarrow 2\text{DEB}$	0-310	66.14	67.95
	$\longrightarrow \text{SCN} + \text{CN}$	310-400	15.69	9.20

* DEB = diethylbenzamide

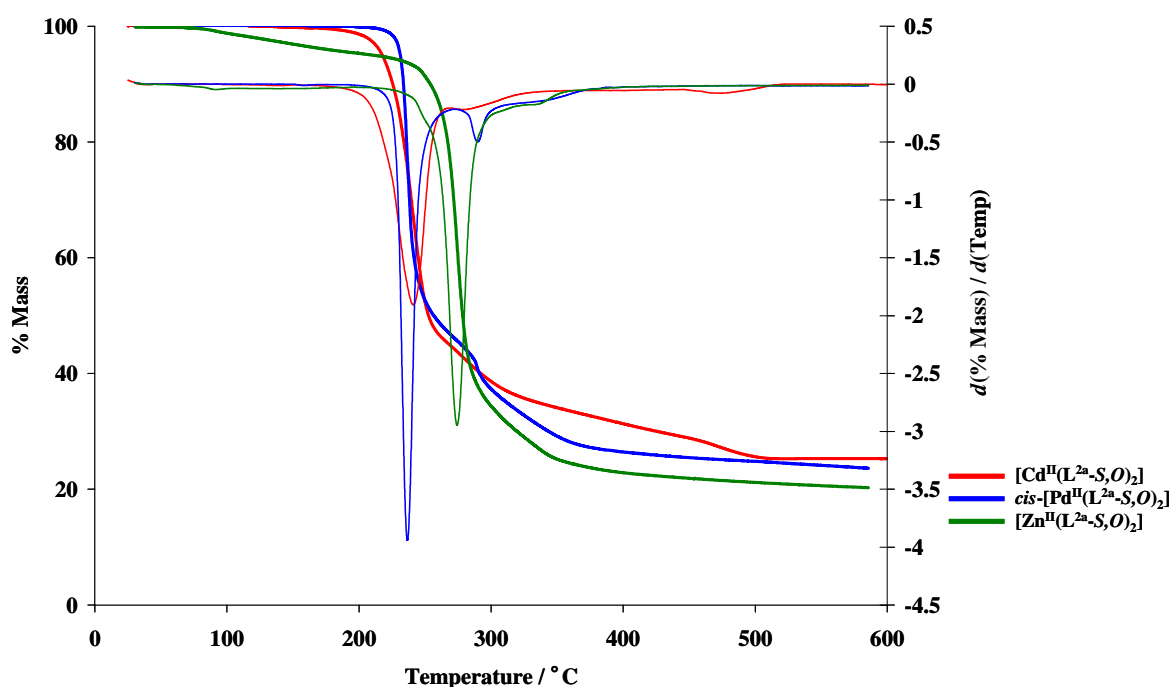


Fig. 2.344 TGA profiles and their first derivatives of $[\text{Cd}^{\text{II}}(\text{L}^{2\text{a}}-\text{S},\text{O})_2]$, $\text{cis}-[\text{Pd}^{\text{II}}(\text{L}^{2\text{a}}-\text{S},\text{O})_2]$ and $[\text{Zn}^{\text{II}}(\text{L}^{2\text{a}}-\text{S},\text{O})_2]$. Analysis was performed using a ramp rate of $10^\circ/\text{min}$.

For all three complexes, agreement between the calculated and observed values is significantly improved relative to the Se analogues. Onset of decomposition occurs at differing temperatures for the three complexes, the trend being similar to that seen in the analogous Se complexes where $[\text{Cd}^{\text{II}}(\text{L}^{2\text{a}}-\text{S},\text{O})_2] < \text{cis}-[\text{Pd}^{\text{II}}(\text{L}^{2\text{a}}-\text{S},\text{O})_2] < [\text{Zn}^{\text{II}}(\text{L}^{2\text{a}}-\text{S},\text{O})_2]$. Interestingly however, the major mass loss in the decomposition of $[\text{Cd}^{\text{II}}(\text{L}^{2\text{a}}-\text{S},\text{O})_2]$ occurs largely over the same temperature range as that of $\text{cis}-[\text{Pd}^{\text{II}}(\text{L}^{2\text{a}}-\text{S},\text{O})_2]$ this being distinct to observations made for the Se analogues. Decomposition onset and the initial major mass losses for $[\text{Cd}^{\text{II}}(\text{L}^{2\text{a}}-\text{S},\text{O})_2]$, $\text{cis}-[\text{Pd}^{\text{II}}(\text{L}^{2\text{a}}-\text{S},\text{O})_2]$ and $[\text{Zn}^{\text{II}}(\text{L}^{2\text{a}}-\text{S},\text{O})_2]$ all occur at higher temperatures than those displayed by their selenourea counterparts suggesting lower thermal stability in the *N,N*-dialkyl-*N'*-benzoylselenourea metal complexes. Table 2.325 shows the calculated and observed residual masses assuming metal sulfide formation. These values show improved agreement relative to those displayed by the Se analogues, suggesting similar decomposition profiles for $[\text{Cd}^{\text{II}}(\text{L}^{2\text{a}}-\text{S},\text{O})_2]$, $\text{cis}-[\text{Pd}^{\text{II}}(\text{L}^{2\text{a}}-\text{S},\text{O})_2]$ and $[\text{Zn}^{\text{II}}(\text{L}^{2\text{a}}-\text{S},\text{O})_2]$ to those suggested by Merdivan *et al.* for related complexes.^[67] In order to confirm the nature of the residue formed following $\text{cis}-[\text{Pd}^{\text{II}}(\text{L}^{2\text{a}}-\text{S},\text{O})_2]$ decomposition, a sample of the complex was heated in a furnace in the same way to that described for its Se counterpart. Fig. 2.345 illustrates the PXRD pattern obtained from the furnace residue. Clearly, the residue contained crystalline material however none of the 2 theta peaks corresponded to those of the reference compounds for PdS or PdS₂ phases. Three separate areas of the sample were analysed using EDAX and the averaged values indicated a Pd : S ratio of 1.15 : 1.

Table 2.325 Residual mass % following thermal decomposition of $[\text{Cd}^{\text{II}}(\text{L}^{2\text{a}}-\text{S},\text{O})_2]$, $\text{cis}-[\text{Pd}^{\text{II}}(\text{L}^{2\text{a}}-\text{S},\text{O})_2]$ and $[\text{Zn}^{\text{II}}(\text{L}^{2\text{a}}-\text{S},\text{O})_2]$.

Complex	Temp / °C	Calculated mass / %	Observed residual mass / %
$[\text{Cd}^{\text{II}}(\text{L}^{2\text{a}}-\text{S},\text{O})_2]$	~ 580	24.78	25.26
$\text{cis}-[\text{Pd}^{\text{II}}(\text{L}^{2\text{a}}-\text{S},\text{O})_2]$	~ 580	23.99	23.61
$[\text{Zn}^{\text{II}}(\text{L}^{2\text{a}}-\text{S},\text{O})_2]$	~ 580	18.17	20.27

This corresponds to a Pd_7S_6 phase, however no previous reports about the existence of such a phase could be found. The inconclusive nature of the residue following thermal decomposition of $\text{cis}[\text{Pd}^{\text{II}}(\text{L}^{2a}\text{-S},\text{O})_2]$ could have important implications for its use as a single source precursor in the preparation of nanosized materials, and this will be discussed further in Chapters 3 and 4.

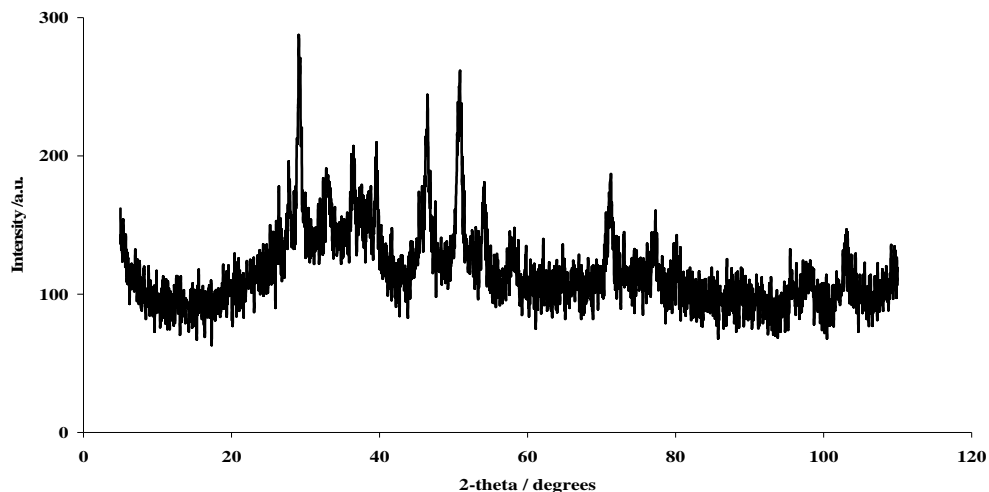


Fig. 2.345 PXRD patterns of residue following furnace decomposition of $\text{cis}[\text{Pd}^{\text{II}}(\text{L}^{2a}\text{-S},\text{O})_2]$.

Decomposition profiles of $\text{cis}[\text{Pt}^{\text{II}}(\text{L}^{2a}\text{-S},\text{O})_2]$, $[\text{Co}^{\text{III}}(\text{L}^{2a}\text{-S},\text{O})_3]$ and $\text{cis}[\text{Ni}^{\text{II}}(\text{L}^{2a}\text{-S},\text{O})_2]$ are shown in Fig. 2.346. The onset of decomposition is comparable for $\text{cis}[\text{Pt}^{\text{II}}(\text{L}^{2a}\text{-S},\text{O})_2]$ and $[\text{Co}^{\text{III}}(\text{L}^{2a}\text{-S},\text{O})_3]$, however that of $\text{cis}[\text{Ni}^{\text{II}}(\text{L}^{2a}\text{-S},\text{O})_2]$ is significantly higher. Comparison with Fig. 2.344 shows the onset of decomposition decreasing in temperature with increasing atomic weight for metal complexes involving the d^8 metal ions where $\text{cis}[\text{Ni}^{\text{II}}(\text{L}^{2a}\text{-S},\text{O})_2] > \text{cis}[\text{Pd}^{\text{II}}(\text{L}^{2a}\text{-S},\text{O})_2] > \text{cis}[\text{Pt}^{\text{II}}(\text{L}^{2a}\text{-S},\text{O})_2]$. As with their Cd(II), Pd(II) and Zn(II) analogues, Table 2.326 shows the calculated and observed mass loss percentages obtained based on a two step decomposition mechanism.

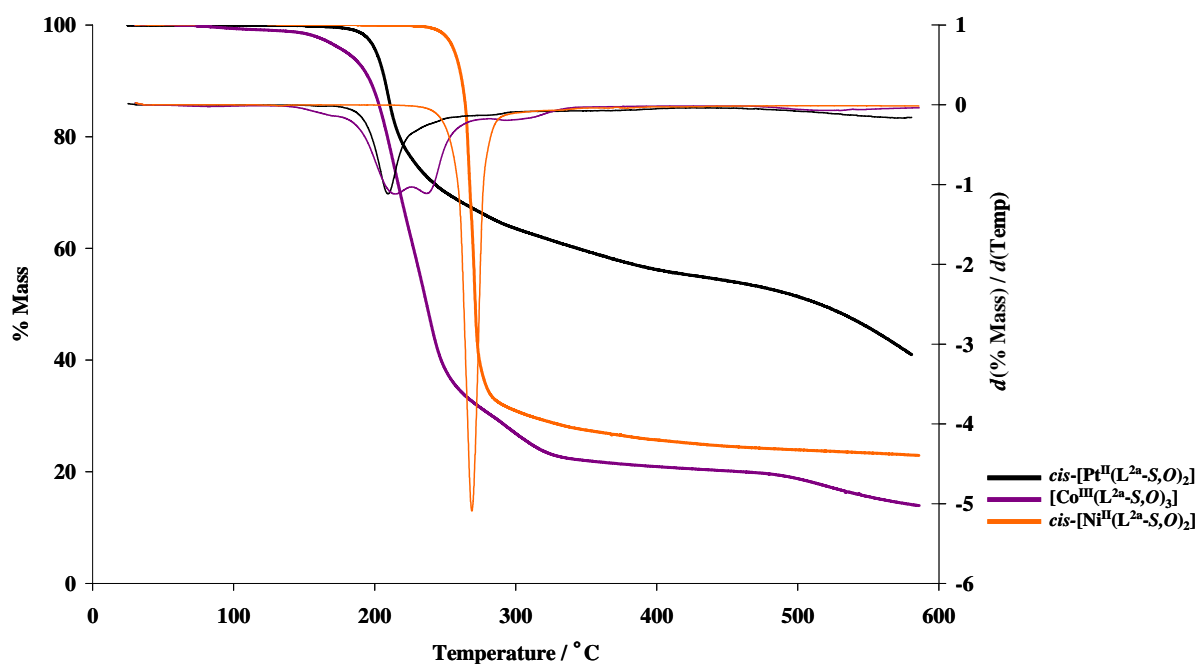


Fig. 2.346 TGA profiles and their first derivatives of $\text{cis}[\text{Pt}^{\text{II}}(\text{L}^{2a}\text{-S},\text{O})_2]$, $[\text{Co}^{\text{III}}(\text{L}^{2a}\text{-S},\text{O})_3]$ and $\text{cis}[\text{Ni}^{\text{II}}(\text{L}^{2a}\text{-S},\text{O})_2]$. Analysis was performed using a ramp rate of $10\text{ }^\circ\text{C}/\text{min}$.

The thermal decomposition of both cis -[Pt^{II}(L^{2a}-S,O)₂] and cis -[Ni^{II}(L^{2a}-S,O)₂] have previously been investigated by Merdivan *et al.*,^[66] their observations indicating the formation of Pt and NiS respectively. Table 2.326 however illustrates the poor agreement between the calculated and observed mass percentages suggesting different decomposition mechanisms. Largely single step decompositions are evident from Fig. 2.346 for both complexes. The thermal decomposition of [Co^{III}(L^{2a}-S,O)₃] has not previously been investigated and exhibits a 3 stage decomposition. Initially the octahedral complex geometry was thought to contribute to its differing decomposition profile from those complexes studied by Merdivan *et al.*, these largely being square-planar, however the decomposition profile of octahedral (*N,N*-diethyl-*N'*-benzoylthioureato)Ru(III) was also reported and found to correspond to those obtained for the square-planar complexes although the final residue corresponded to that of the metal and not the metal sulfide.^[66]

Table 2.326 Thermogravimetric data for pyrolytic processes for [cis-[Pt^{II}(L^{2a}-S,O)₂], [Co^{III}(L^{2a}-S,O)₃] and cis-[Ni^{II}(L^{2a}-S,O)₂].

Complex	Process	Temp range / °C	Mass loss / %	
			Calculated	Observed
[cis-[Pt ^{II} (L ^{2a} -S,O) ₂]	[cis-[Pt ^{II} (L ^{2a} -S,O) ₂] → 2DEB	0-250	53.23	29.92
	→ 2SCN	250-300	17.44	6.53
[Co ^{III} (L ^{2a} -S,O) ₃]	[Co ^{III} (L ^{2a} -S,O) ₃] → 3DEB	0-281	67.16	69.61
	→ 2SCN + CN	281-345	18.59	8.25
cis-[Ni ^{II} (L ^{2a} -S,O) ₂]	cis-[Ni ^{II} (L ^{2a} -S,O) ₂] → 2DEB	0-296	66.87	68.60
	→ SCN + CN	296-585	15.87	8.48

* DEB = diethylbenzamide

The nature of the final residues clarifies these observations somewhat where the calculated values consider the formation of Pt, CoS and NiS. Poor agreement between the calculated and observed values is apparent for each complex. Several phases of nickel sulfide have been reported and as will become apparent in Chapter 4, the residual mass percentage for cis -[Ni^{II}(L^{2a}-S,O)₂] corresponds closely to that of heazelwoodite, a rhombohedral phase of nickel sulfide, Ni₃S₂, where the calculated residual mass is 22.70 %.

Table 2.327 Residual mass % following thermal decomposition of [cis-[Pt^{II}(L^{2a}-S,O)₂], [Co^{III}(L^{2a}-S,O)₃] and cis-[Ni^{II}(L^{2a}-S,O)₂]

Complex	Temp / °C	Calculated mass / %	Observed residual mass / %
[cis-[Pt ^{II} (L ^{2a} -S,O) ₂]	~ 580	29.33	40.34
[Co ^{III} (L ^{2a} -S,O) ₃]	~ 580	11.90	13.90
cis-[Ni ^{II} (L ^{2a} -S,O) ₂]	~ 580	17.26	22.90

The 13.9 % residual mass observed for [Co^{III}(L^{2a}-S,O)₃] does not correspond to the 7.70 % necessary for a Co (0) residue or to the 11.90 % of a CoS residue. It is however in close agreement with the 13.98 % suggesting a CoO₃ residue. The precise mechanism by which this is formed has not been elucidated however the formation of a residue with this composition rather than that of a sulfide, is thought likely given the ‘harder’ nature of the Co(III) metal centre and that of the ‘harder’ O donor atom. As the precise nature of the residues resulting from PGM complex thermolysis was of particular interest, cis -[Pt^{II}(L^{2a}-S,O)₂] was subjected to furnace heating using the same conditions described for cis -[Pd^{II}(L^{1a}-Se,O)₂]. PXRD analysis of the residue is shown in Fig. 2.347. Crystalline material is clearly formed and the 2-theta values correspond closely to that of Pt(0), in keeping with results reported by Merdivan *et al.*^[66] EDAX analysis however indicated a Pt : S ratio of 1 : 1.25 (average of 3 separate areas tested). This rather curious results suggests that amorphous S could in someway be associated with the Pt(0) residue,

however as no crystalline phases of S are evident in the XRD pattern, it is unlikely that the S is incorporated in the crystal lattice, rather it could in some way be associated with the surface of the sample.

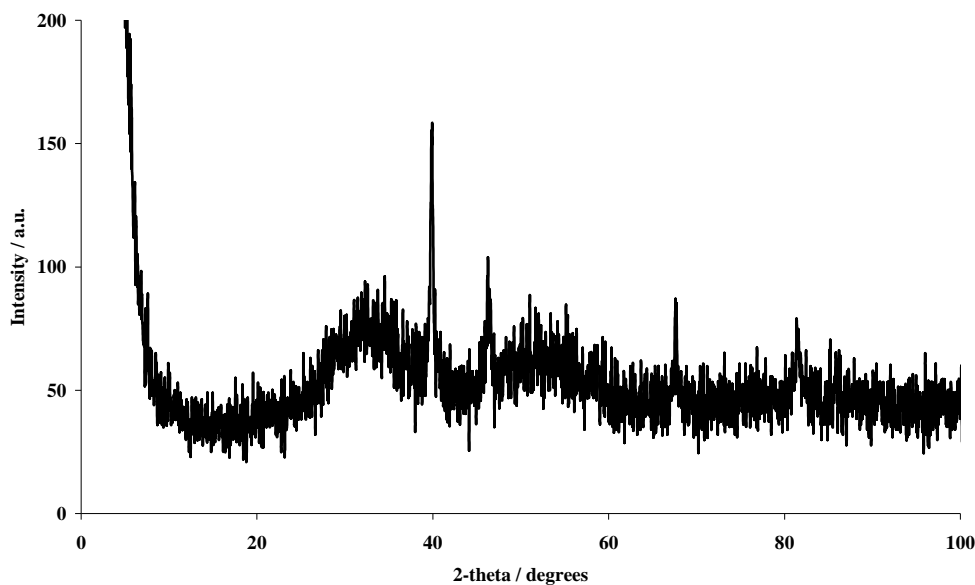


Fig. 2.347 PXRD patterns of residue following furnace decomposition of $\text{cis-}[\text{Pt}^{\text{II}}(\text{L}^{2\text{a}}\text{-S},\text{O})_2]$.

A separate sample of $\text{cis-}[\text{Pt}^{\text{II}}(\text{L}^{2\text{a}}\text{-S},\text{O})_2]$ was heated in different TGA apparatus using a ceramic pan holder and the temperature taken to 950 °C. The results obtained are remarkably similar where the remaining mass percentage at 585 °C is 42.8 %. Interestingly, further mass loss occurs up to 950 °C where the remaining mass percentage is 34.6 % however if a higher temperature could be achieved it is evident from the profile gradient that further mass loss would occur. These results suggest that the mass losses seen above 585 °C could be associated with the slow diffusion of S from the sample surface. This will be discussed further in Chapter 4.

It is worth mentioning here, that calculations based on thermogravimetric analysis, whilst initially helpful, are not always accurate in indicating the nature of the formed residue. Possible reasons for this lie with the technique itself where temperature measurements and mass loss correlations are particularly difficult to accurately determine in the solid state. Solid samples are rife with analysis difficulty given that heat transfer, diffusion and release of decomposition products can only take place from the sample surface, limiting the rate at which this can occur. Decomposition products formed in the centre of the sample have a greater physical distance to overcome before they can be released possibly leading to mass losses not necessarily accurately corresponding to the temperature. Further, thermolysis of the single source precursor during nanoparticle synthesis takes place in a vastly different environment to that inside the TGA apparatus. During thermolysis, removal of decomposition products may be hindered to a greater or lesser degree than seen in the solid state, and different decomposition products may form. TGA can therefore only be used as a guideline to possible nanoparticle composition.

2.4 Conclusion

Several *N,N*-dialkyl-*N'*-benzoyl(thio)selenourea ligands have successfully been synthesized and structurally characterized. *N,N*-diethyl-*N'*-benzoylselenourea exhibits a hydrogen bond between the selenium atom of one molecule and the selenoamidic proton of a neighbouring molecule. A reciprocal hydrogen bond between the Se atom of the second molecule and the selenoamidic proton of the original molecule leads to a form of dimerisation in the solid state known as Resonance Assisted Hydrogen Bonding (RAHB). This type of intermolecular hydrogen bonding was exhibited by the majority of ligand structures characterized in the solid state. In addition to RAHB, *N,N*-dibutyl-*N'*-benzoylselenourea also exhibited an intermolecular hydrogen bond between the carbonyl oxygen atom and a hydrogen atom on the benzene residue of a neighbouring molecule, a reciprocal hydrogen bond leading to the formation of a 10 membered ring structure in the crystal lattice of this compound. The longer alkyl chain derivatives, *N,N*-dihexyl-*N'*-benzoyl(thio)selenourea, *N,N*-dioctyl-*N'*-benzoyl(thio)selenourea and *N,N*-didecyl-*N'*-benzoylselenourea exhibited similar intermolecular interactions, where, in each case, RAHB was present as well as π - π interactions between the benzene residues of neighbouring molecules. Structural characterization of the asymmetrically substituted *N*-benzyl-*N*-methyl-*N'*-benzoyl(thio)selenourea ligands indicate the increased stability of the *Z* isomer in the solid state. Attempted synthesis of *N,N*-dicyclohexyl-*N'*-benzoylselenourea resulted in the formation of two separate products, both of which could be structurally characterized. A 1,3,5-oxaselenazine salt was isolated, this being, to the best of our knowledge, the first time that a structure such as this has been characterized in the solid state. The intermolecular hydrogen bonding of the second product, dicyclohexylaminobenzoate exhibits a 12 membered ring structure in the solid state and the nature of this product could be confirmed from the PXRD pattern of separately prepared material. Solid state characterization of *N,N*-diphenyl-*N'*-benzoylselenourea revealed a particularly short intermolecular Se-Se distance, leading to the classification of this ligand as a diselenide rather than a selenourea. The crystal structure of *N,N*-dicyclohexyl-*N'*-benzoylthiourea indicated the formation of the “enol” resonance structure in the solid state. These results suggest that the choice of amine substituent in the synthesis of *N,N*-dialkyl-*N'*-benzoyl(thio)selenoureas can have a substantial influence over the course of the reaction and the products formed.

The structural characterization of the “bipodal” 3,3,3',3'-tetra(*n*-butyl)-1,1'-isophthaloylbis(selenourea) indicated RAHB between neighbouring molecules in a fashion similar to that exhibited by the “monopodal” derivative *N,N*-dibutyl-*N'*-benzoylselenourea, although no evidence of the second hydrogen bond exhibited by this structure could be found in that of the “bipodal” analogue.

Several potential single source precursors could successfully be synthesized and structural characterizations of *cis*-bis(*N,N*-dibutyl-*N'*-benzoyl(thio)selenoureato)palladium(II), *cis*-bis(*N,N*-dihexyl-*N'*-benzoyl(thio)selenoureato)palladium(II), *cis*-bis(*N*-morpholine-*N'*-benzoylthioureato)palladium(II), and *cis*-bis(*N*-benzyl-*N*-methyl-*N'*-benzoylselenoureato)palladium(II) indicate the formation of square planar metal complexes, where coordination to the d^8 metal centre takes place through the O and E (where E = S, Se) donor atoms. The partial structural characterization of *cis*-bis(*N*-benzyl-*N*-methyl-*N'*-benzoylselenoureato)palladium(II) indicates the increased stability of the *EZ* isomer in the solid state. This, to the best of our knowledge is the first structural elucidation of an asymmetrically substituted selenourea metal complex.

Crystallographic characterization of (*N,N*-diphenyl-*N'*-benzoylselenoureato)cadmium(II) disclosed a bimetallic structure with 5 and 6 coordinated metal centres where a 2 : 1 ligand : metal ratio is maintained, coordination to the metal centres taking place through the O and Se donor atoms as expected.

The solid state characterization of the metallamacrocyclic (3,3,3',3'-tetra(*n*-butyl)-1,1'-terephthaloylbisthioureato)palladium(II) revealed a 3:3 metal : ligand ratio where similarly to the “monopodal” analogue, coordination to the Pd(II) metal centre took place through the O and S donor atoms.

^{13}C NMR spectroscopy revealed a displacement in the relative chemical shift positions of the selenocarbonyl and carbonyl ^{13}C resonances upon coordination to the varying metal ions reflecting the relative “hardness” of the central metal ions, this being in accordance with previous observations made for related *N,N*-dialkyl-*N'*-arylthiureas.

The presence of ^{77}Se satellites in the ^{13}C NMR spectroscopy of $\text{HL}_{\text{Se}}^{1a}$ and $[\text{M}^{\text{II}}(\text{L}^{1a}\text{-Se},\text{O})_2]$, where M = Pd, Cd and Zn, allowed the determination of $^1J(^{13}\text{C}\text{-}^{77}\text{Se})$ coupling constants. The average value of 220.3 Hz exhibited by the ligands and that of 177.2 Hz exhibited by the Pd(II) complexes, reflecting the reduced C=Se bond order in the d^8 metal complexes. In addition the $^1J(^{13}\text{C}\text{-}^{77}\text{Se})$ coupling constant of 164.9 and 166.6 Hz exhibited by the Cd(II) and Zn(II) complexes of $\text{HL}_{\text{Se}}^{1a}$ respectively, indicate an even further reduction of the C=Se bond order upon complexation to the d^{10} metal ions.

Use of an asymmetrically substituted amine during ligand synthesis leads to the formation of *EE*, *EZ* and *ZZ* isomers upon complexation to the Pd(II) metal centre. Analysis of the ^1H NMR spectra of *cis*-bis(*N*-benzyl-*N*-methyl-*N'*-benzoyl(thio)selenoureato)palladium(II) allowed an indication of the relative isomer distributions to be obtained.

Observation of the ^{77}Se nucleus revealed an increase in the nuclear shielding of $[\text{M}^{\text{II}}(\text{L}^{1a}\text{-Se},\text{O})_2]$ as the ‘softness’ of the metal ion increases, *i.e.* Cd(II) > Zn(II) > Pd(II). ^{113}Cd NMR spectroscopy of $[\text{Cd}^{\text{II}}(\text{L}^{1a}\text{-Se},\text{O})_2]$ and $[\text{Cd}^{\text{II}}(\text{L}^{2a}\text{-S},\text{O})_2]$ exhibits deshielding of the Cd nucleus when bound to the selenourea rather than its sulfur analogue. Similarities in the ^{113}Cd chemical shift environment of $[\text{Cd}^{\text{II}}(\text{L}^{1a}\text{-Se},\text{O})_2]$ and $[\text{Cd}^{\text{II}}(\text{L}^{1a}\text{-Se},\text{O})(\text{L}^{2a}\text{-S},\text{O})]$ illustrates the preferential binding of $\text{HL}_{\text{Se}}^{1a}$ to Cd(II) over that of its sulfur analogue ($\text{HL}_{\text{S}}^{2a}$) and preliminary investigations provide support for a form of chelate metathesis taking place in solution.

^{31}P NMR spectroscopy studies indicate that coordination of $\text{HL}_{\text{Se}}^{1a}$ to a Pt(II) metal centre does indeed take place, to form $\text{R}_3\text{PPtC}_6\text{H}_5\text{C}(\text{O})\text{NC}(\text{Se})\text{NEt}_2$ (where R = butyl) suggesting that *cis*-bis(*N,N*-diethyl-*N'*-benzoylselenoureato)Pt(II) may indeed be stable in solution.

Thermal decomposition of $[\text{Cd}^{\text{II}}(\text{L}^{1a}\text{-Se},\text{O})_2]$ and $[\text{Cd}^{\text{II}}(\text{L}^{2a}\text{-S},\text{O})_2]$ suggests the formation of CdSe and CdS residues respectively. Thermal decomposition of *cis*-[Pt $^{\text{II}}$ ($\text{L}^{2a}\text{-S},\text{O}$) $_2$] and *cis*-[Ni $^{\text{II}}$ ($\text{L}^{2a}\text{-S},\text{O}$) $_2$] in turn suggests the formation of Pt(0) and Ni $_3\text{S}_2$, paving the way for thermolysis of these single source precursors which will be discussed in the next chapter.

References

- [1] I. B. Douglass, *Journal of the American Chemical Society* **1937**, 59, 740.
- [2] L. Beyer, R. Kirmse, E. Hoyer, *Zeitschrift fuer Chemie* **1975**, 15, 197.
- [3] R. Kirmse, L. Beyer, E. Hoyer, *Zeitschrift fuer Chemie* **1975**, 15, 454.
- [4] L. Beyer, S. Behrendt, E. Kleinpeter, R. Borsdorf, E. Hoyer, *Zeitschrift fuer Anorganische und Allgemeine Chemie* **1977**, 437, 282.
- [5] R. Kirmse, L. Beyer, E. Hoyer, *Chemical Physics Letters* **1977**, 49, 544.

- [6] Y. V. Salyn, E. K. Zumadilov, V. I. Nefedov, R. Scheibe, G. Leonhardt, L. Beyer, E. Hoyer, *Zeitschrift fuer Anorganische und Allgemeine Chemie* **1977**, 432, 275.
- [7] L. Beyer, R. Herzsuh, F. Dietze, F. Hoepfner, E. Hoyer, *Zeitschrift fuer Anorganische und Allgemeine Chemie* **1979**, 458, 33.
- [8] J. Stach, R. Herzsuh, R. Kirmse, L. Beyer, J. Hartung, *Zeitschrift fuer Anorganische und Allgemeine Chemie* **1984**, 514, 223.
- [9] W. Bensch, M. Schuster, *Zeitschrift fuer Anorganische und Allgemeine Chemie* **1993**, 619, 786.
- [10] W. Bensch, M. Schuster, *Zeitschrift fuer Anorganische und Allgemeine Chemie* **1993**, 619, 791.
- [11] W. Bensch, M. Schuster, *Zeitschrift fuer Anorganische und Allgemeine Chemie* **1993**, 619, 1689.
- [12] W. Bensch, M. Schuster, *Zeitschrift fuer Anorganische und Allgemeine Chemie* **1994**, 620, 1479.
- [13] W. Bensch, M. Schuster, *Zeitschrift fuer Anorganische und Allgemeine Chemie* **1994**, 620, 177.
- [14] M. Schuster, W. Bensch, *Zeitschrift fuer Naturforschung, B: Chemical Sciences* **1994**, 49, 1615.
- [15] M. Schuster, W. Bensch, *Zeitschrift fuer Anorganische und Allgemeine Chemie* **1994**, 620, 737.
- [16] M. Kampf, R. Richter, L. Hennig, A. Eidner, J. Baldamus, R. Kirmse, *Zeitschrift fuer Anorganische und Allgemeine Chemie* **2004**, 630, 2677.
- [17] M. Kampf, R. Richter, J. Griebel, A. Weller, R. Kirmse, *Zeitschrift fuer Anorganische und Allgemeine Chemie* **2005**, 631, 698.
- [18] E. Kleinpeter, L. Beyer, *Journal fuer Praktische Chemie (Leipzig)* **1975**, 317, 938.
- [19] E. Kleinpeter, S. Behrendt, L. Beyer, *Zeitschrift fuer Anorganische und Allgemeine Chemie* **1982**, 495, 105.
- [20] E. Kleinpeter, S. Behrendt, L. Beyer, W. Dietzsch, R. Borsdorf, *Journal fuer Praktische Chemie (Leipzig)* **1982**, 324, 29.
- [21] F. Dietze, J. Lerchner, S. Schmidt, L. Beyer, R. Koehler, *Zeitschrift fuer Anorganische und Allgemeine Chemie* **1991**, 600, 37.
- [22] M. Schuster, K. H. Koenig, *Fresenius' Zeitschrift fuer Analytische Chemie* **1987**, 327, 102.
- [23] M. Schuster, K. H. Koenig, *Fresenius' Zeitschrift fuer Analytische Chemie* **1988**, 331, 383.
- [24] M. Koketsu, Y. Yamamura, H. Aoki, H. Ishihara, *Phosphorus, Sulfur and Silicon and the Related Elements* **2006**, 181, 2699.
- [25] R. Kohler, R. Kirmse, R. Richter, J. Sieler, E. Hoyer, L. Beyer, *Zeitschrift fuer Anorganische und Allgemeine Chemie* **1986**, 537, 133.
- [26] O. Hallale, S. A. Bourne, K. R. Koch, *CrystEngComm* **2005**, 7, 161.
- [27] I. B. Douglass, F. B. Dains, *Journal of the American Chemical Society* **1934**, 56, 1408.
- [28] J. Stach, R. Kirmse, A. Heinrich, W. Dietzsch, J. Hartung, L. Beyer, *Zeitschrift fuer Chemie* **1983**, 23, 453.
- [29] L. Beyer, E. Hoyer, H. Hennig, R. Kirmse, H. Hartmann, J. Liebscher, *Journal fuer Praktische Chemie (Leipzig)* **1975**, 317, 829.
- [30] R. Richter, F. Dietze, S. Schmidt, E. Hoyer, W. Poll, D. Mootz, *Zeitschrift fuer Anorganische und Allgemeine Chemie* **1997**, 623, 135.
- [31] R. Richter, J. Sieler, L. Beyer, O. Lindqvist, L. Anderson, *Zeitschrift fuer Anorganische und Allgemeine Chemie* **1985**, 522, 171.
- [32] W. Bensch, M. Schuster, *Zeitschrift fuer Anorganische und Allgemeine Chemie* **1992**, 611, 95.
- [33] J. Sieler, R. Richter, E. Hoyer, L. Beyer, R. Koehler, *Zeitschrift fuer Anorganische und Allgemeine Chemie* **1991**, 603, 25.
- [34] M. Dominguez, E. Antico, L. Beyer, A. Aguirre, S. Garcia-Granda, V. Salvado, *Polyhedron* **2002**, 21, 1429.
- [35] C. Sacht, M. S. Datt, S. Otto, A. Roodt, *Dalton Transactions* **2000**, 727.
- [36] K. R. Koch, *Coordination Chemistry Reviews* **2001**, 216-217, 473.
- [37] T. J. Egan, K. R. Koch, P. L. Swan, C. Clarkson, D. A. Van Schalkwyk, P. J. Smith, *Journal of Medicinal Chemistry* **2004**, 47, 2926.
- [38] Y.-S. Wu, R. Koch Klaus, R. Abratt Valerie, H. Klump Horst, *Archives of biochemistry and biophysics* **2005**, 440, 28.
- [39] W. Hernandez, E. Spodine, J. C. Munoz, L. Beyer, U. Schroeder, J. Ferreira, M. Pavani, *Bioinorganic Chemistry and Applications* **2003**, 1, 271.
- [40] A. Rodger, K. K. Patel, K. J. Sanders, M. Datt, C. Sacht, M. J. Hannon, *Journal of the Chemical Society, Dalton Transactions* **2002**, 3656.
- [41] Z. Weiqun, Y. Wen, L. Xie, X. Cheng, *Journal of Inorganic Biochemistry* **2005**, 99, 1314.
- [42] R. Del Campo, J. J. Criado, R. Gheorghe, F. J. Gonzalez, M. R. Hermosa, F. Sanz, J. L. Manzano, E. Monte, E. Rodriguez-Fernandez, *Journal of Inorganic Biochemistry* **2004**, 98, 1307.
- [43] W. Hernandez, E. Spodine, L. Beyer, U. Schroeder, R. Richter, J. Ferreira, M. Pavani, *Bioinorganic Chemistry and Applications* **2005**, 3, 299.
- [44] K. H. Koenig, M. Schuster, B. Steinbrech, G. Schneeweis, R. Schlotter, *Fresenius' Zeitschrift fuer Analytische Chemie* **1985**, 321, 457.

- [45] M. Schuster, *Fresenius' Journal of Analytical Chemistry* **1992**, 342, 791.
- [46] A. N. Mautjana, J. D. S. Miller, A. Gie, S. A. Bourne, K. R. Koch, *Dalton Transactions* **2003**, 1952.
- [47] K. R. Koch, C. Sacht, S. Bourne, *Inorganica Chimica Acta* **1995**, 232, 109.
- [48] J. Bricks, K. Rurack, R. Radeglia, G. Reck, B. Schulz, H. Sonnenschein, U. Resch-Genger, *Journal of the Chemical Society Perkin Transactions* **2000**, 2, 1209.
- [49] M. Schuster, E. Unterreitmaier, *Fresenius' Journal of Analytical Chemistry* **1993**, 346, 630.
- [50] E. Unterraitmaier, M. Schuster, *Analitica Chimica Acta* **1995**, 309, 339.
- [51] A. N. Westra, C. Esterhuysen, K. R. Koch, *Acta Crystallographica, Section C: Crystal Structure Communications* **2004**, C60, m395.
- [52] S. Bourne, K. R. Koch, *Dalton Transactions* **1993**, 2071.
- [53] K. R. Koch, Y. Wang, A. Coetzee, *Journal of the Chemical Society, Dalton Transactions: Inorganic Chemistry* **1999**, 1013.
- [54] K. R. Koch, S. Bourne, *Journal of Molecular Structure* **1998**, 441, 11.
- [55] K. R. Koch, J. du Toit, M. R. Caira, C. Sacht, *Journal of the Chemical Society, Dalton Transactions: Inorganic Chemistry (1972-1999)* **1994**, 785.
- [56] D. Hanekom, J. M. McKenzie, N. M. Derix, K. R. Koch, *Chemical Communications (Cambridge, United Kingdom)* **2005**, 767.
- [57] J. Goerdeler, K. Stadelbauer, *Chemische Berichte* **1965**, 98, 1556.
- [58] R. Koehler, R. Kirmse, R. Richter, J. Sieler, E. Hoyer, L. Beyer, *Zeitschrift fuer Anorganische und Allgemeine Chemie* **1986**, 537, 133.
- [59] K. R. Koch, S. A. Bourne, A. Coetzee, J. Miller, *Journal of the Chemical Society, Dalton Transactions: Inorganic Chemistry* **1999**, 3157.
- [60] K. R. Koch, O. Hallale, S. A. Bourne, J. Miller, J. Bacsá, *Journal of Molecular Structure* **2001**, 561, 185.
- [61] O. Hallale, S. A. Bourne, K. R. Koch, *New Journal of Chemistry* **2005**, 29, 1416.
- [62] N. Westra Arjan, A. Bourne Susan, R. Koch Klaus, *Dalton Trans* **2005**, 2916.
- [63] U. Schroder, L. Beyer, J. Sieler, *Inorganic Chemistry Communications* **2000**, 3, 630.
- [64] K. H. Koenig, M. Kuge, L. Kaul, H. J. Pletsch, *Chemische Berichte* **1987**, 120, 1251.
- [65] S. Stockmann, J. C. Bruce, J. Miller, K. R. Koch, *Acta Crystallographica, Section C* **2008**, C64, o166.
- [66] M. Merdivan, R. S. Aygun, N. Kulcu, *Journal of Thermal Analysis* **1997**, 48, 1423.
- [67] M. Merdivan, F. Karipcin, N. Kulcu, R. S. Aygun, *Journal of Thermal Analysis and Calorimetry* **1999**, 58, 551.
- [68] N. Ozpazan, H. Arslan, T. Ozpazan, N. Ozdes, N. Kulcu, *Thermochimica Acta* **2000**, 343, 127.
- [69] P. S. Nair, T. Radhakrishnan, N. Revaprasadu, G. Kolawole, P. O'Brien, *Journal of Materials Chemistry* **2002**, 12, 2722.
- [70] T. Trindade, P. O'Brien, X.-m. Zhang, *Chemistry of Materials* **1997**, 9, 523.
- [71] M. Lazell, S. J. Norager, P. O'Brien, N. Revaprasadu, *Materials Science & Engineering, C: Biomimetic and Supramolecular Systems* **2001**, C16, 129.
- [72] R. Koehler, L. Beyer, R. Richter, J. Sieler, J. Stach, *Zeitschrift fuer Anorganische und Allgemeine Chemie* **1991**, 600, 73.
- [73] L. Beyer, E. Hoyer, J. Liebscher, H. Hartmann, *Zeitschrift fuer Chemie* **1981**, 21, 81.
- [74] W.-H. Pan, J. P. Fackler, Jr., J. A. Kargol, J. L. Burmeister, *Inorganica Chimica Acta* **1980**, 44, L95.
- [75] G. E. B. Maciel, Marie., *Journal of the Chemical Society, Chemical Communications* **1973**, 12, 394.
- [76] A. M. C. Bond, Ray; Ebner, Jennifer; Ellis, S. Richard., *Inorganic Chemistry* **1989**, 28, 4509.
- [77] Y. Zhou, H. Heimgartner, *Helvetica Chimica Acta* **2000**, 83, 539.
- [78] R. Koehler, L. Beyer, M. Moll, A. Hantschmann, R. Richter, J. Sieler, R. Szargan, L. Weber, E. Hoyer, *Tetrahedron* **1990**, 46, 7735.
- [79] J. C. Bruce, N. Revaprasadu, K. R. Koch, *New Journal of Chemistry* **2007**, 31, 1647.
- [80] M. Bolte, L. Fink, *Private Communication to CCDC* **2003**, Crystal Nm CCDC214316.
- [81] J. C. Bruce, K. R. Koch, *Acta Crystallographica, Section C: Crystal Structure Communications* **2008**, C64, m1.
- [82] F. H. Allen, O. Kennard, D. G. Watson, L. Brammer, A. G. Orpen, R. Taylor, *Journal of the Chemical Society, Perkin Transactions 2: Physical Organic Chemistry (1972-1999)* **1987**, S1.
- [83] S. Mtongana, PhD Thesis, University of Stellenbosch (Stellenbosch), **2006**.
- [84] C. thone, P. G. Jones, J. Laube, S. Jager, *Acta Crystallographica, Section C: Crystal Structure Communications* **1998**, C54, 1247.
- [85] G. R. Willey, J. R. Barras, M. D. Rudd, M. G. B. Drew, *Journal of the Chemical Society, Dalton Transactions: Inorganic Chemistry* **1994**, 3025.
- [86] G. Roy, M. Nethaji, G. Mugesh, *Organic & Biomolecular Chemistry* **2006**, 4, 2883.
- [87] F. Bigoli, F. Demartin, P. Deplano, F. A. Devillanova, F. Isaia, V. Lippolis, M. L. Mercuri, M. A. Pellinghelli, E. F. Trogu, *Inorganic Chemistry* **1996**, 35, 3194.

- [88] C. D. Antoniadis, A. J. Blake, S. K. Hadjikakou, N. Hadjiliadis, P. Hubberstey, M. Schroder, C. Wilson, *Acta Crystallographica, Section B: Structural Science* **2006**, B62, 580.
- [89] C. D. Antoniadis, S. K. Hadjikakou, N. Hadjiliadis, A. Papakyriakou, M. Baril, I. S. Butler, *Chemistry--A European Journal* **2006**, 12, 6888.
- [90] W. W. Du Mont, A. Martens, S. Pohl, W. Saak, *Inorganic Chemistry* **1990**, 29, 4847.
- [91] S. Kubiniok, W. W. d. Mont, S. Pohl, W. Saak, *Angewandte Chemie, Int. Ed. Engl.* **1988**, 27, 431.
- [92] V. K. Landry, M. Minoura, K. Pang, D. Buccella, B. V. Kelly, G. Parkin, *Journal of the American Chemical Society* **2006**, 128, 12490.
- [93] L. Pauling, *The Nature of the Chemical Bond*, 3rd ed., Cornell University Press, New York, **1960**.
- [94] G. L. Sommen, A. Linden, H. Heimgartner, *Helvetica Chimica Acta* **2007**, 90, 641.
- [95] T. Grimbacher, University of Cape Town **1995**.
- [96] *CRC Handbook of Chemistry and Physics*, **1998-1999**.
- [97] K. R. Koch, C. Sacht, T. Grimbacher, S. Bourne, *South African Journal of Chemistry* **1995**, 48, 71.
- [98] T. Steiner, *Angewandte Chemie, International Edition* **2002**, 41, 48.
- [99] T. Steiner, *Angewandte Chemie, Int. Ed. Engl.* **2002**, 41, 48.
- [100] I. M. Rafiqul, K. Shimada, S. Aoyagi, Y. Fujisawa, Y. Takikawa, *Tetrahedron Letters* **2004**, 45, 6187.
- [101] Aldrich, *Handbook of Fine Chemicals and Laboratory Equipment* **2007-2008**.
- [102] D. R. Trivedi, A. Ballabh, P. Dastidar, *Journal of Materials Chemistry* **2005**, 15, 2606.
- [103] D. R. Trivedi, P. Dastidar, *Crystal Growth and Design* **2006**, 6, 1022.
- [104] D. R. Trivedi, A. Ballabh, P. Dastidar, B. Ganguly, *European Journal of Chemistry* **2004**, 10, 5311.
- [105] D. Yang, G. Zuccarello, B. R. Mattes, *Macromolecules* **2002**, 35, 5304.
- [106] M. Bolte, L. Fink, **2003**.
- [107] H. Arslan, U. Florke, N. Kulcu, E. Kayhan, *Turkish Journal of Chemistry* **2006**, 30, 429.
- [108] I. P. Gray, A. M. Z. Slawin, J. D. Woollins, *Dalton Transactions* **2005**, 12, 2188.
- [109] G. Kedarnath, S. Dey, V. K. Jain, G. K. Dey, B. Varghese, *Polyhedron* **2006**, 25, 2383.
- [110] M. T. Ng, P. A. W. Dean, J. J. Vittal, *Dalton Transactions* **2004**, 18, 2890.
- [111] S. Cunha, F. C. Macedo, Jr., G. A. N. Costa, M. T. Rodrigues, Jr., R. B. V. Verde, L. C. de Souza Neta, I. Vencato, C. Lariucci, F. P. Sa, *Monatshefte fuer Chemie* **2007**, 138, 511.
- [112] Z. Weiqun, L. Zhu, Y. Zhang, Z. Yu, L. Lu, X. Yang, *Vibrational Spectroscopy* **2004**, 36, 73.
- [113] H. Duddeck, *Progress in NMR Spectroscopy* **1995**, 27, 1.
- [114] J. Sibor, D. Zurek, R. Marek, M. Kutý, O. Humpa, J. Marek, P. Pazdera, *Collection of Czechoslovak Chemical Communications* **1999**, 64, 1673.
- [115] S. N. Balasubrahmanyam, S. N. Bharathi, G. Usha, *Organic Magnetic Resonance* **1983**, 21, 474.
- [116] H.-O. Kalinowski, W. Lubosch, D. Seebach, *Chemische Berichte* **1977**, 110, 3733.
- [117] W. H. Pan, J. P. Fackler, J. A. Kargol, J. L. Burmeister, *Inorganica Chimica Acta* **1980**, 44, L95.
- [118] W. H. Pan, J. P. Fackler, Jr., *Journal of the American Chemical Society* **1978**, 100, 5783.
- [119] A. A. Isab, M. I. M. Wazeer, *Journal of Coordination Chemistry* **2005**, 58, 529.
- [120] R. K. Harris, B. E. Mann, *NMR and the Periodic Table*, Academic Press, London, **1978**.
- [121] T. Axenrod, G. Webb, *Nuclear magnetic resonance spectroscopy of nuclei other than protons*, John Wiley and Sons, Inc, U.S.A., **1974**.
- [122] A. D. E. Cardin, Paul D.; Odom, Jerome D.; Howard, James W., Jr, *Journal of the American Chemical Society* **1975**, 97, 1672.
- [123] M. F. Summers, *Coordination chemistry reviews* **1988**, 86, 43.
- [124] D. M. Burger, *Personal Communication* **2008**.
- [125] L. v. D. Molen, MSc Thesis, University of Stellenbosch (Stellenbosch), **2007**.
- [126] R. G. Pearson, *Journal of Chemical Education* **1968**, 45, 581.
- [127] S. Mtongana, MSc thesis, University of Stellenbosch (Stellenbosch), **2002**.
- [128] S. Dey, V. K. Jain, A. Knoedler, W. Kaim, S. Zalis, *European Journal of Inorganic Chemistry* **2001**, 2965.
- [129] M. Risto, E. M. Jahr, M. S. Hannu-Kuure, R. Oilunkaniemi, R. S. Laitinen, *Journal of Organometallic Chemistry* **2007**, 692, 2193.
- [130] L. B. Kumbhare, V. K. Jain, P. P. Phadnis, M. Nethaji, *Journal of Organometallic Chemistry* **2007**, 692, 1546.
- [131] A. Singhal, V. K. Jain, B. Varghese, E. Tiekink, *Inorganica Chimica Acta* **1999**, 285, 190.
- [132] C. Soulard, X. Rocquefelte, P. E. Petit, M. Evain, S. Jobic, J. P. Itie, P. Munsch, H. J. Koo, M. H. Whangbo, *Inorganic Chemistry* **2004**, 43, 1943.

Chapter 3

Use of the *N,N*-dialkyl-*N'*-benzoyl(thio)selenourea metal complexes as single source precursors for the synthesis of semiconducting quantum dots and other materials.*

The use of (*N,N*-diethyl-*N'*-benzoylselenourea)Cd(II) and (*N,N*-diethyl-*N'*-benzoylthiourea)Cd(II) as single source precursors for the synthesis of CdSe and CdS quantum dots is reported. Varying the thermolysis temperature of these two precursors did not significantly alter the morphology of the resulting nanoparticles. Thermolysis of (*N,N*-dioctyl-*N'*-benzoylselenourea)Cd(II) results in the formation of anisotropic nanoparticles, and an investigation into the effect of thermolysis temperature on the morphology is reported. Possible growth mechanisms for the formation of the observed bipodal and tripodal structures are discussed. Thermolysis of (*N,N*-dioctyl-*N'*-benzoylthiourea)Cd(II) and related metal complexes results in the formation of exclusively spherical CdS nanoparticles. Preliminary investigations into the effect of precursor concentration on nanoparticle morphology are reported. The thermolysis of a number of different *N,N*-diethyl-*N'*-benzoylthiourea metal complexes is examined, where ZnS, Ni_xS_y can potentially be formed. Thermolysis of complexes involving the platinum group metals results in the formation of well defined spherical nanoparticles, and the possible composition of these is discussed. Preliminary experiments in the synthesis of core/shell nanoparticles are described where CdSe/CdS nanoparticles could be successfully synthesised. Attempts to prepare CdSe/ZnSe nanoparticles produced CdSe, CdO, as well as ZnO nanoparticles.

* Sections of this chapter are based on the paper:
J. C. Bruce, N. Revaprasadu, K. R. Koch, *New J. Chem.*, 2007, 31 (9), 1647-1653.

3.1 Introduction

The work in this chapter describes an investigation into the use of the *N,N*-dialkyl-*N'*-benzoylthio- and selenourea metal complexes as single source precursors. The greater reactivity of the *N,N*-dialkyl-*N'*-benzoylselenoureas could allow the decomposition of their metal complexes at temperatures lower than those usually employed for other precursors and the thermolysis of both $[\text{Cd}^{\text{II}}(\text{L}^{\text{1a}}\text{-Se},\text{O})_2]$ and $[\text{Cd}^{\text{II}}(\text{L}^{\text{2a}}\text{-S},\text{O})_2]$ over a range of different temperatures is investigated. As seen in Chapter 2, the *N*-substituents of both the thio- and selenoureas can be altered with relative ease, allowing an investigation into the effect of alkyl chain length in the precursor on the resulting nanoparticle morphology. This has been rigorously investigated in the synthesis of both CdSe and CdS nanoparticles. Coordination of both the thio- and selenoureas takes place with a wide variety of transition metal ions and the potential for the synthesis of nanoparticles with various compositions using these complexes, is vast. Preliminary investigations into the possible formation of a number of different materials is therefore reported where $[\text{Cd}^{\text{II}}(\text{L}^{\text{1a}}\text{-Se},\text{O})(\text{L}^{\text{2a}}\text{-S},\text{O})]$, $[\text{Zn}^{\text{II}}(\text{L}^{\text{1a}}\text{-Se},\text{O})_2]$, $[\text{Zn}^{\text{II}}(\text{L}^{\text{2a}}\text{-S},\text{O})_2]$, *cis*- $[\text{Ni}^{\text{II}}(\text{L}^{\text{2a}}\text{-S},\text{O})_2]$ and $[\text{Co}^{\text{III}}(\text{L}^{\text{2a}}\text{-S},\text{O})_3]$ are separately thermolysed under similar reaction conditions. In this context, the study of PGM related nanoparticles is of particular interest and the thermolysis of *cis*- $[\text{Pd}^{\text{II}}(\text{L}^{\text{2a}}\text{-S},\text{O})_2]$, *cis*- $[\text{Pt}^{\text{II}}(\text{L}^{\text{2a}}\text{-S},\text{O})_2]$ and *cis*- $[\text{Pd}^{\text{II}}(\text{L}^{\text{1a}}\text{-Se},\text{O})_2]$ is investigated. Finally, preliminary examination of the synthesis of differing core/shell nanoparticles is reported.

3.2 Experimental

3.2.1 General methods and instrumentation

Single source precursors were synthesised according to methods described in Chapter 2. All other solvents and reagents were commercially available and used without further purification.

UV-Visible absorption spectra were obtained using an Agilent 8453 spectrometer and quartz cuvettes (1 cm path length) were used. Samples were determined in toluene which was also used as a reference solvent. Band edges were calculated using the linear regression method, where a straight line was fitted to a minimum of 20 data points and the *x*-axis intercept taken as the band edge.

Emission spectra were obtained using a Perkin Elmer LS50B Luminescence Spectrometer where the excitation and emission slit widths were set to 5 and 10 nm, respectively. An excitation wavelength of 350 nm was used unless otherwise stated. As the photostability of nanoparticle solutions such as these has not been established, samples were optically analysed within 12 hours of synthesis to minimise any possible photodegradation.

Powder X-Ray diffraction patterns were recorded on either an Oxford Xcalibur 2 diffractometer using Mo-K α radiation ($\lambda = 0.71073 \text{ \AA}$) at a temperature of 100 K and with X-ray power = 2.0 kW, or a Bruker D8 ADVANCE with Bragg-Brentano geometry instrument with a Cu radiation source and dynamic scintillation detector or a D8 High-Resolution Diffractometer. PXRD data was used to calculate particle size using the Scherrer equation,^[25]

$$\text{where } D = 0.94\lambda / B \cos \theta$$

B = Full Width at Half Maximum height (FWHM) in radians, θ is the angle of diffraction, and λ is the wavelength of the X-rays used (\AA), 0.71073 for Mo-K α radiation and 1.5418 for Cu radiation. In order to convert data obtained from the Oxford Xcalibur machine with Mo-K α radiation to that conventionally found in the literature with Cu radiation, the following conversion was applied, $\theta_{\text{Cu}} = \sin^{-1}(\lambda_{\text{Cu}} / \lambda_{\text{Mo}} \sin \theta_{\text{Mo}})$. In the majority of cases, particle size was calculated using the (220) peak for cubically phased CdS and CdSe.

Transmission electron microscopy (TEM) was performed on either a JEM 1200 EXII (Jeol, Japan) instrument or a LEO 912 Omega (Zeiss, Oberkochen) instrument, fitted with a 2k x 2k digital camera. Samples were prepared by placing a drop of the dilute toluene solution of the sample onto a carbon coated copper grid at room temperature. Excess sample was wicked away using filter paper. Particle size was determined by measuring the diameter of 100 – 300 nanoparticles using a software (freeware) programme called ImageJ.* In the isolated cases where this number of nanoparticles could not clearly be identified, as many nanoparticles as possible were counted, this usually being in the range of 20-50. In order to ensure the precision of these results, the same photograph was analysed on different days and the standard deviation of these consecutive results was found to be less than the standard deviation obtained following the analysis of a single photograph. It should however be mentioned here that in isolated TEM images clear particle boundaries were not always visible, this complicating the particle size determination somewhat.

3.2.2 Nanoparticle synthesis

A typical synthesis proceeded as follows. A specified mass of the precursor complex was dissolved in trioctylphosphine (TOP) and injected into a three-neck flask containing hexadecylamine (HDA) at the specified temperature, under a nitrogen atmosphere. Samples were withdrawn at various time intervals. Following a 60 – 90 min reaction period the solution was cooled to 70 °C and excess methanol added to precipitate the nanoparticles. These were isolated by centrifugation and successively washed (methanol) to remove organic by-products from ligand decomposition and excess capping agent. Nanoparticles were then redispersed in toluene to enable further optical characterisation. No size selective precipitation was performed. Samples subjected to PXRD analysis were dried under vacuum to remove any solvent traces and analysed as dry powders.

3.2.2.1 Proof of Principle studies

Synthesis of CdSe nanoparticles: The precursor, $[\text{Cd}^{\text{II}}(\text{L}^{1\text{a}}-\text{Se},\text{O})_2]$, (0.709 mmol) was suspended in TOP (4.8 ml) and the mixture injected into HDA (6.4 g) at 200 °C, followed by a 40 minute reaction where samples were withdrawn at 10, 20 and 30 minute intervals.

Synthesis of CdS nanoparticles: The precursor, $[\text{Cd}^{\text{II}}(\text{L}^{2\text{a}}-\text{S},\text{O})_2]$, (0.857 mmol) was suspended in TOP (6 ml) and the mixture injected into HDA (6 g) at 200 °C, followed by a 30 minute reaction where samples were withdrawn at 10 and 20 minute intervals.

3.2.2.2 Temperature dependence studies

Synthesis of CdSe nanoparticles: The precursor, $[\text{Cd}^{\text{II}}(\text{L}^{1\text{a}}-\text{Se},\text{O})_2]$, (0.858 mmol) was suspended in TOP (4 ml) and the mixture injected into HDA (5 g) and reacted for 60 min. An initial temperature of 200 °C was used, followed by 100, 125, 150 and 250 °C.

Synthesis of CdS nanoparticles: The precursor, $[\text{Cd}^{\text{II}}(\text{L}^{2\text{a}}-\text{S},\text{O})_2]$, (0.858 mmol) was suspended in TOP (4 ml) and the mixture injected into HDA (5 g) and reacted for 60 min. An initial temperature of 200 °C was used, followed by 125, 150, 240 and 300 °C.

3.2.2.3 Alkyl chain length studies

Synthesis of CdSe nanoparticles: The precursor (0.858 mmol) was suspended in TOP (4 ml) and the mixture injected into HDA (5 g) at 150 °C, reaction times varied between 60 – 90 minutes. Samples were withdrawn at 10, 30, 45 and 60 minute intervals.

* ImageJ: Public domain image processing programme developed at the National Institutes of Health. Can be downloaded free of charge from <http://rsb.info.nih.gov/ij/>

Synthesis of CdS nanoparticles: The precursor (0.858 mmol) was suspended in TOP (4 ml) and the mixture injected into HDA (5 g) at 150 °C, reaction times varied between 60 – 90 minutes. Samples were withdrawn at 10, 30, 45 and 60 minute intervals.

3.2.2.4 Concentration dependence studies

Synthesis of CdSe nanoparticles: The precursor, $[\text{Cd}^{\text{II}}(\text{L}^{\text{1d}}-\text{Se},\text{O})_2]$, (1.715 mmol) was suspended in TOP (4 ml) and the mixture injected into HDA (5 g) at 150 °C, and reacted for 90 minutes. Samples were withdrawn at 10, 30, 45 and 60 minute intervals.

Synthesis of CdS nanoparticles: The precursor, $[\text{Cd}^{\text{II}}(\text{L}^{\text{2a}}-\text{S},\text{O})_2]$, (2.14 mmol) was suspended in TOP (4 ml) and the mixture injected into HDA (5 g) at 150 °C, and reacted for 60 minutes. Samples were withdrawn at 10, 30, 45 and 60 minute intervals. In a second experiment, the precursor, $[\text{Cd}^{\text{II}}(\text{L}^{\text{2a}}-\text{S},\text{O})_2]$, (1.715 mmol) was suspended in TOP (4 ml) and injected into HDA (5 g) at 200 °C, and reacted for 60 minutes. Samples were withdrawn at 10, 30, 45 minute intervals.

3.2.2.5 Selected precursor thermolysis

Thermolysis of $[\text{Cd}^{\text{II}}(\text{L}^{\text{1a}}-\text{Se},\text{O})(\text{L}^{\text{2a}}-\text{S},\text{O})]$: The precursor, $[\text{Cd}^{\text{II}}(\text{L}^{\text{1a}}-\text{Se},\text{O})(\text{L}^{\text{2a}}-\text{S},\text{O})]$, (0.893 mmol) was suspended in TOP (4 ml) and the mixture injected into HDA (5 g) and reacted for 60 minutes. Temperatures of 150 and 175 °C were investigated.

Thermolysis of $[\text{Zn}^{\text{II}}(\text{L}^{\text{1a}}-\text{Se},\text{O})_2]$: The precursor, $[\text{Zn}^{\text{II}}(\text{L}^{\text{1a}}-\text{Se},\text{O})_2]$, (0.858 mmol) was suspended in TOP (4 ml) and the mixture injected into HDA (5 g) at 150 °C followed by a 60 minute reaction.

Thermolysis of $[\text{Zn}^{\text{II}}(\text{L}^{\text{2a}}-\text{S},\text{O})_2]$: The precursor, $[\text{Zn}^{\text{II}}(\text{L}^{\text{2a}}-\text{S},\text{O})_2]$, (0.860 mmol) was suspended in TOP (4 ml) and the mixture injected into HDA (5 g) at 150 °C followed by a 60 minute reaction.

Thermolysis of *cis*- $[\text{Ni}^{\text{II}}(\text{L}^{\text{2a}}-\text{S},\text{O})_2]$: The precursor, *cis*- $[\text{Ni}^{\text{II}}(\text{L}^{\text{2a}}-\text{S},\text{O})_2]$, (0.863 mmol) was suspended in TOP (4 ml) and the mixture injected into HDA (5 g) at 200 °C followed by a 60 minute reaction.

Thermolysis of $[\text{Co}^{\text{III}}(\text{L}^{\text{2a}}-\text{S},\text{O})_3]$: The precursor, $[\text{Co}^{\text{III}}(\text{L}^{\text{2a}}-\text{S},\text{O})_3]$, (0.414 mmol) was suspended in TOP (4 ml) and the mixture injected into HDA (5 g) at 200 °C followed by a 90 minute reaction.

Thermolysis of *cis*- $[\text{Pd}^{\text{II}}(\text{L}^{\text{2a}}-\text{S},\text{O})_2]$: The precursor, *cis*- $[\text{Pd}^{\text{II}}(\text{L}^{\text{2a}}-\text{S},\text{O})_2]$, (0.866 mmol) was suspended in TOP (6 ml) and the mixture injected into HDA (6 g) at 200 °C, followed by a 40 minute reaction.

Thermolysis of *cis*- $[\text{Pt}^{\text{II}}(\text{L}^{\text{2a}}-\text{S},\text{O})_2]$: The precursor, *cis*- $[\text{Pt}^{\text{II}}(\text{L}^{\text{2a}}-\text{S},\text{O})_2]$, (0.601 mmol) was suspended in TOP (5 ml) and the mixture injected into HDA (5 g) at 200 °C, followed by a 40 minute reaction.

Thermolysis of *cis*- $[\text{Pd}^{\text{II}}(\text{L}^{\text{1a}}-\text{Se},\text{O})_2]$: The precursor, *cis*- $[\text{Pd}^{\text{II}}(\text{L}^{\text{1a}}-\text{Se},\text{O})_2]$, (0.745 mmol) was suspended in TOP (6 ml) and the mixture injected into HDA (5.6 g) at 200 °C, followed by a 40 minute reaction.

3.2.2.6 Core-shell particle synthesis

Attempted synthesis of CdSe/CdS nanoparticles: Previously synthesized CdSe nanoparticles (0.5 g) were ‘dissolved’ in HDA (5 g) and heated to 150 °C. $[\text{Cd}^{\text{II}}(\text{L}^{\text{2a}}-\text{S},\text{O})_2]$ (0.5 g) suspended in TOP (4 ml) was injected into this solution and a 60 minute reaction followed.

Attempted synthesis of CdSe/ZnS nanoparticles: $[\text{Cd}^{\text{II}}(\text{L}^{\text{1a}}-\text{Se},\text{O})_2]$ (0.858 mmol) was suspended in TOP (4 ml) and the mixture injected in HDA (5 g) at 150 °C, followed by a 45 minute reaction. $[\text{Zn}^{\text{II}}(\text{L}^{\text{2a}}-\text{S},\text{O})_2]$ (0.858 mmol) suspended in TOP (4 ml) was then injected into this solution followed by a further 45 minute reaction.

Attempted synthesis of CdSe/ZnSe nanoparticles: $[\text{Cd}^{\text{II}}(\text{L}^{\text{1a}}-\text{Se},\text{O})_2]$ (0.858 mmol) was suspended in TOP (2 ml) and injected in HDA (5 g) at 150 °C, followed by a 45 minute reaction. $[\text{Zn}^{\text{II}}(\text{L}^{\text{1a}}-\text{Se},\text{O})_2]$ (0.858 mmol) suspended in TOP (2 ml) was then injected into this solution followed by a further 45 minute reaction.

3.2.3 Quantum yield determination

Quantum yields are generally obtained by reference to that of known substances, and similarly to Pradhan and co-workers, perylene was chosen as a reference substance for this work.^[15] This aromatic compound is known to have a quantum yield of 0.71 in toluene ($\lambda = 414 \text{ nm}$).^[26] In order to avoid concentration errors such as the “inner filter effect” the concentration range of perylene where a linear response between emission intensity and concentration could be observed on the available instrumentation was established and is found to be between 5.0×10^{-8} and $7.5 \times 10^{-7} \text{ M}$. As an excitation wavelength of 350 nm was used in the determination of emission spectra for all CdS and CdSe nanoparticles, the following equation was used to allow for this:^[15]

$$\Phi_{350} = \Phi_{412} \cdot \frac{I_{\text{PL}(350 \text{ nm})}}{I_{\text{PL}(412 \text{ nm})}} \cdot \frac{\text{OD}_{(350 \text{ nm})}}{\text{OD}_{(412 \text{ nm})}} \cdot \frac{R_{\text{s}(412 \text{ nm})}}{R_{\text{s}(350 \text{ nm})}} \cdot \frac{412}{350}$$

where Φ_{350} and Φ_{412} = quantum yield at 350 and 412 nm excitation wavelengths

I_{PL} = measured fluorescence intensity at each wavelength

R_{S} = Intensity of the raman bands of the solvent

OD = optical density at each wavelength

Fifth term, normalizes the raman signals with respect to the wavelength.

In this way the quantum yield of perylene with 350 nm excitation could be calculated as 5.5×10^{-4} . Using the following relationship, the quantum yield of the nanoparticles could be obtained where:^[27-29]

$$\Phi_{\text{u}} = \Phi_{\text{p}} \cdot \frac{\text{Area}_{\text{u}}}{\text{Area}_{\text{p}}} \cdot \frac{(1-10^{-A_{\text{p}}})}{(1-10^{-A_{\text{u}}})}$$

Where Φ_{u} and Φ_{p} = quantum yield of the unknown and perylene solutions respectively

Area_{u} and Area_{p} = area of the emission spectra of the unknown and perylene solutions

A_{u} and A_{p} = absorbance of the unknown and perylene solutions.

As the molar concentration of the nanoparticles can not accurately be determined, solutions were used where the absorbance matched that of the standard perylene solution. In certain cases, dilution of the nanoparticle solutions in a similar ratio to that necessary for the detection of the perylene standard did not allow for the detection of any nanoparticle emission on the instrumentation available. In cases such as these, correction factors based on the necessary dilutions were applied to the above expression to allow for this. It should be noted here that this method of quantum yield determination is not absolute and can only be used as an indication of the relative emission efficiencies, this however is sufficient for the purposes of this work.

3.3 Results and Discussion

Several initial ‘proof of principle’ experiments were necessary to establish if compounds based on the *N,N*-dialkyl-*N'*-benzoylseleno- and -thiourea motif could be used as single source precursors for the synthesis of nanosized material. Owing to the inexpensive and ready availability of Cd(II) salts as well as the relatively well established behaviour of CdSe and CdS under quantum confinement, the synthesis of these two materials from the appropriate precursors was initially undertaken to establish if the compounds synthesised would form CdSe and CdS nanoparticles under the appropriate conditions.

3.3.1 ‘Proof of principle’ studies

3.3.1.1 Synthesis of CdSe nanoparticles

The initial thermolysis of $[\text{Cd}^{\text{II}}(\text{L}^{\text{Ia}}\text{-Se,O})_2]$ yielded very encouraging results, where well formed monodispersed spherical nanoparticles of CdSe with an average size of 3.2 (15) nm are seen in the TEM image, Fig. 3.31(A). The optical spectra obtained are shown in Fig. 3.31 (B) where the absorption spectrum is plotted on the y axis and the emission spectrum on the secondary y axis. A calculated band edge of 636 nm clearly indicates a blue shift relative to that of bulk CdSe which exhibits a band edge at 716 nm.^[30] The emission spectrum shows a close to band edge emission with the FWHM being 50 nm.

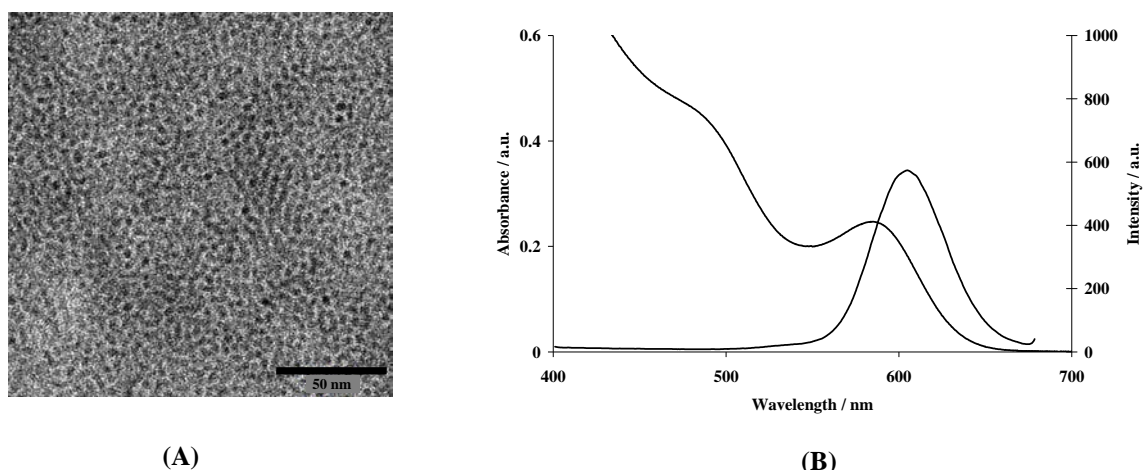


Fig. 3.31 TEM image of CdSe nanoparticles (200 °C, 40 mins) (A) and absorption and emission spectra of CdSe nanoparticles following a 40 minute reaction (B).

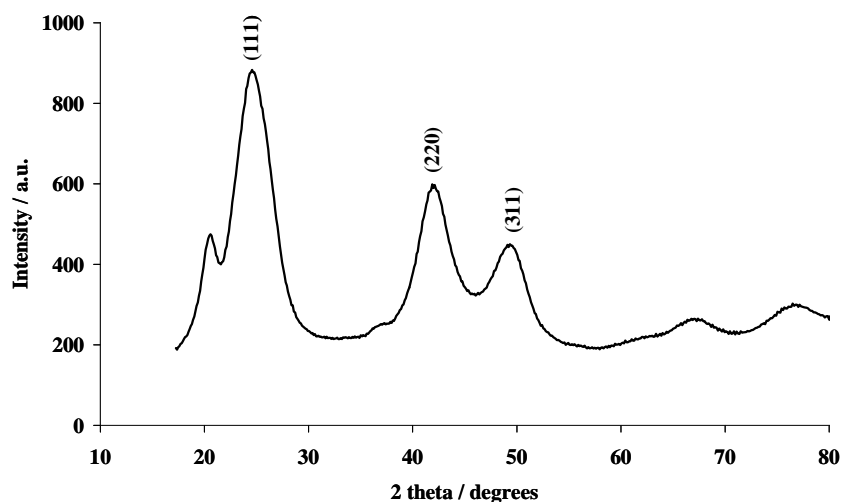


Fig. 3.32 PXRD pattern of cubically phased CdSe nanoparticles (200 °C, 40 mins).

Bulk CdSe has a stable wurtzite phase at room temperature^[31] however both cubic and hexagonal phases are known. The small particle size complicates the assignment of a specific phase and it becomes difficult to exclusively assign a particular phase to the CdSe nanoparticles. Bawendi *et al.* have also reported that a mixture of the two phases is possible for CdSe nanoparticles where one phase can dominate the other.^[32] Fig. 3.32 is however consistent with a predominantly cubic phase, although this may not necessarily be exclusive. The broad peaks in the diffraction pattern are indicative of particles in the nanosize domain and the (111), (220) and (311) peaks are clearly visible.

3.3.1.2 Synthesis of CdS nanoparticles

The initial thermolysis of $[\text{Cd}^{\text{II}}(\text{L}^{2\text{a}}\text{-S},\text{O})_2]$ yielded well formed spherical nanoparticles with an average size of 3.4 (11) nm and are clearly visible in the TEM image obtained following the 30 minute reaction (Fig. 3.33 (A)).

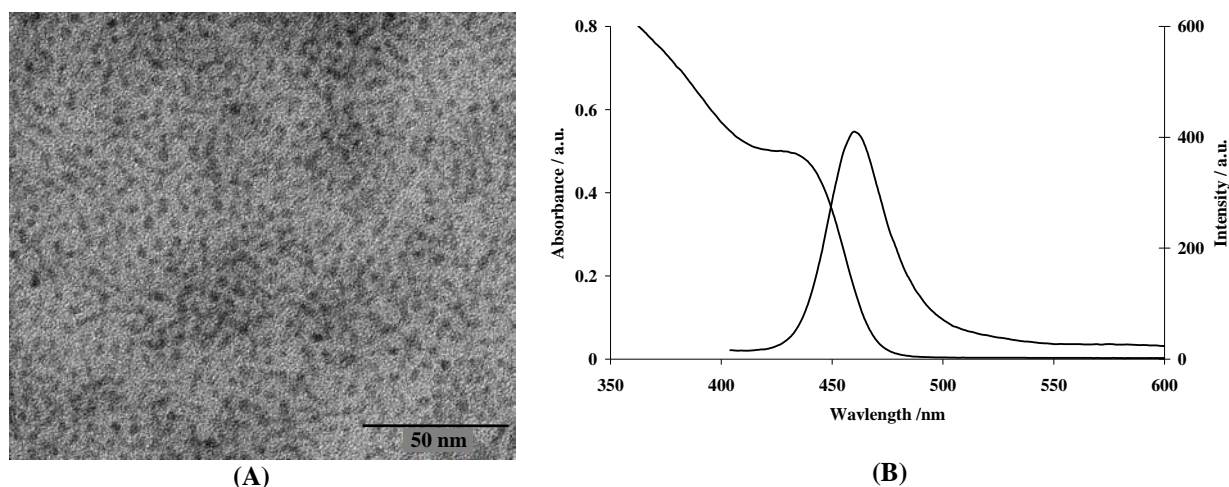


Fig. 3.33 TEM image of CdS nanoparticles (200 °C, 30 mins) (A) and absorption and emission spectra of CdS nanoparticles following a 30 minute reaction (B).

A calculated band edge of 470 nm is clearly blue shifted relative to that of bulk CdS with a band edge of 512 nm,^[30] indicating the formation of quantum dots, Fig. 3.33 (B). As in the formation of CdSe, the emission spectrum shows a close to band edge emission although the FWHM is only 33 nm, significantly smaller than that seen for the CdSe nanoparticles suggesting increased monodispersity in the CdS nanoparticles relative to their Se counterparts. This is reflected in the standard deviations obtained from the TEM images where the 15 % obtained for the CdSe nanoparticles is larger than the 11 % observed for the CdS nanoparticles. These results suggest the presence of Ostwald ripening. In the case of the CdSe nanoparticles, the higher surface free energy of the smaller crystallites allows their dissolution and the slow diffusion of material to the surface of the larger crystallites; the result being the ‘defocusing’ of the size regime manifested by an increased polydispersity observed in the TEM image and the increased FWHM of the emission spectrum. In the case of the CdS nanoparticles, the reaction has ended prior to this stage in the ‘growth cycle’ and consequently the nanoparticles exhibit an increased monodispersity and narrower emission.^[30, 33] It should be noted here that the onset of ‘Ostwald ripening’ is amongst other factors concentration, reaction temperature and time dependant.^[33] Fig. 3.34 shows that, like the CdSe nanoparticles, the CdS nanoparticles have a predominantly cubic phased crystallinity where the broadened (111), (220) and (311) peaks indicate particles in the nanosized regime. This is somewhat unusual given that the bulk phase of CdS like that of CdSe is wurtzite. In addition, thermolysis of Cd(II) complexes based on dithiocarbamate, dithiobiurea, dithiosemicarbazide^[34] and N-alkylthiurea ligand motifs^[35] all result in hexagonally phased CdS nanoparticles.

The encouraging results obtained from the thermolysis of both $[\text{Cd}^{\text{II}}(\text{L}^{\text{1a}}\text{-Se},\text{O})_2]$ and $[\text{Cd}^{\text{II}}(\text{L}^{\text{2a}}\text{-S},\text{O})_2]$ prompted further investigations into the behaviour of these compounds as single source precursors. Memon *et al.* recently reported that thermolysis of N-alkyldithiocarbamate Cd(II) complexes at elevated temperature increased the nanoparticle anisotropy.^[7] Interesting results were reported by Li and co-workers where thermolysis of cadmium ethylxanthate at varying temperatures gave tripodal, bipodal, rod shaped and spherical CdS nanoparticles.^[14] We therefore decided to investigate the effect of temperature on the nanoparticle morphology with regard to the thermolysis of both $[\text{Cd}^{\text{II}}(\text{L}^{\text{1a}}\text{-Se},\text{O})_2]$ and $[\text{Cd}^{\text{II}}(\text{L}^{\text{2a}}\text{-S},\text{O})_2]$.

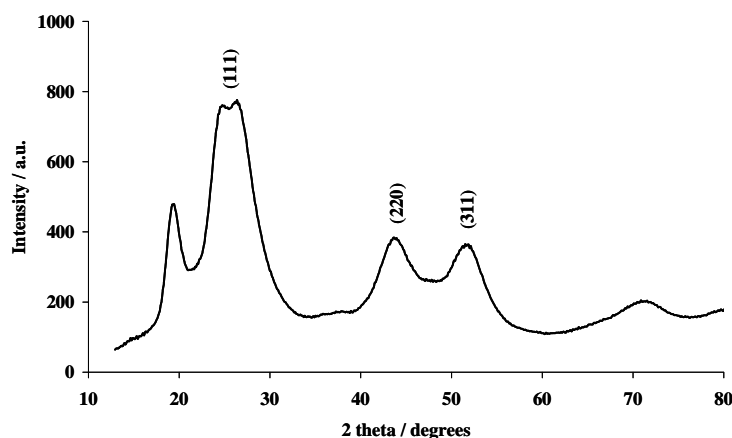


Fig. 3.34 PXRD pattern of CdSe nanoparticles (200 °C, 30 mins).

3.3.2 Temperature dependence studies

3.3.2.1 Synthesis of CdSe nanoparticles

Generally, fairly high reaction temperatures are necessary to allow nucleation and nanoparticle growth from the thermolysis of single source precursors. From a production point of view, it would however be advantageous to achieve nanoparticle growth at lower temperatures. It was therefore decided to incrementally decrease the temperature of thermolysis of $[\text{Cd}^{\text{II}}(\text{L}^{\text{1a}}\text{-Se},\text{O})_2]$. Table 3.31 shows the results obtained following 60 minute reactions at various temperatures and Fig. 3.35 illustrates the optical spectra of the nanoparticles obtained following thermolysis at 100, 150 and 250 °C.

Table 3.31 Properties of CdSe nanoparticles obtained following thermolysis of $[\text{Cd}^{\text{II}}(\text{L}^{\text{1a}}\text{-Se},\text{O})_2]$ at various temperatures.

Temp / °C	Band edge / nm	Band edge / eV	Average size / nm (std. dev. %)*	Average size / nm (Scherrer Eqn ^[25])	FWHM / nm	Emission maxima / nm
100	515	2.41	2.0 (14)	-	46	504 453 [‡]
125	539	2.30	2.2 (13)	1.3	38.5	522.5 451.5 [‡]
150	575	2.15	2.5 (15)	1.7	46	557.5
175	604	2.05	2.6 (17)	1.8	42.5	582
200	639	1.94	3.3 (14)	1.6	50.5	589.5
250	688	1.80	3.8 (15)	1.7	72	611

* from TEM data

[‡]second smaller maximum

It is remarkable that CdSe formation occurred at a temperature as low as 100 °C. Samples were withdrawn from the reaction vessel at this temperature at varying times and showed that the band edge (502 nm) and emission maximum (487 nm) red shifted slightly over time. A second smaller emission maximum appeared at 453 nm, the intensity of which increased with time (Fig. 3.35). This phenomenon was also observed at 125 °C at which temperature the band

edge and emission maxima also red shifted slightly over the 60 minute reaction period. The smaller emission maximum at 453 nm persisted and grew in intensity as the reaction progressed. However the overall intensity of the minor emission band decreased with increasing temperature from 21.5 % of the emission maximum at 100 °C to 8.2 % of the emission maximum at 125 °C and was no longer observable at temperatures > 150 °C. At 150 °C the absorption spectrum obtained from a sample withdrawn 10 minutes into the reaction was very similar to that from a 60 minute sample indicating that nucleation occurs more rapidly at a higher temperature. In general good quality nanoparticles were obtained where reaction temperatures were 150 °C or higher and surprisingly quantum confinement still occurred at 250 °C since the band edge of 699 nm remained blue shifted relative to that of bulk CdSe. The emission at 250 °C broadened significantly over time however, where the 60 minute sample exhibited a FWHM of 72 nm. A second lower wavelength emission in the region of 409 nm also increased in intensity during the course of the reaction from 7.4 % of the emission maximum at 10 minutes to 45.5 % of the emission maximum at 60 minutes.* These observations suggest an increase in the CdSe particle size distribution over time and the possible development of a second size regime of nanoparticles under these reaction conditions (250 °C). These effects are more marked as the temperature of reaction increases as no evidence of similar low wavelength emissions were observable in the optical spectra following thermolysis at 200 °C.

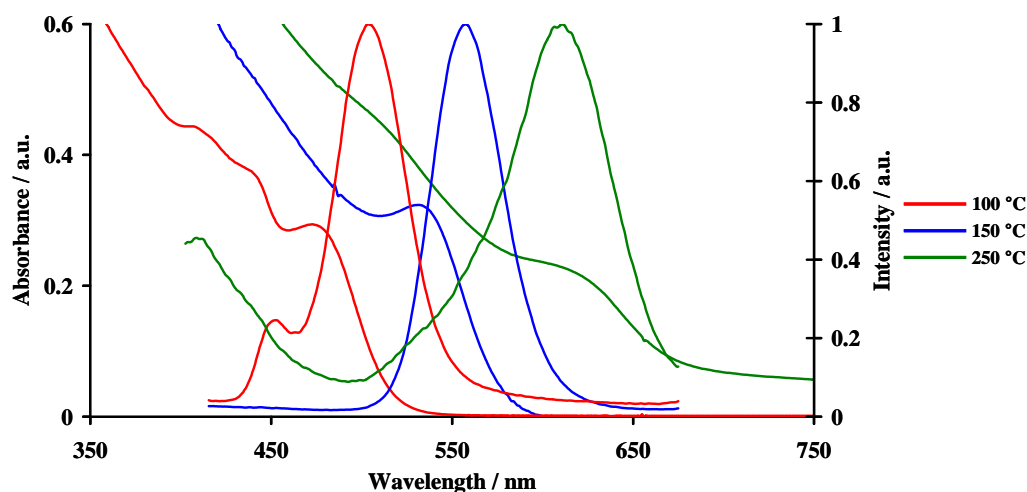


Fig. 3.35 Optical spectra of CdSe nanoparticles obtained following thermolysis of $[\text{Cd}^{\text{II}}(\text{L}^{\text{1a}}\text{-Se},\text{O})_2]$ at 100, 150 and 250 °C.

Particle sizes obtained from the TEM images as well as the (220) peak in the PXRD patterns are shown in Table 3.31. The reduced crystallinity of the nanoparticles obtained at 100 °C precluded particle size estimation and therefore no data is shown. Where the material was of sufficient crystallinity to give a reasonable PXRD pattern, it is evident that cubically phased CdSe is formed. Particle sizes calculated from the PXRD patterns using the Sherrer equation^[25] are consistently smaller than those obtained from the TEM images, although the rough trend of increasing particle size with increasing reaction temperature is consistent with the TEM observations. TEM images of 60 minute samples for each reaction temperature indicated the formation of largely spherical nanoparticles. At temperatures of 150 °C and below, slight evidence of anisotropic growth was present although this was poorly defined and the spherical form dominated. At temperatures above 150 °C evidence of anisotropy was significantly reduced and only spherical nanoparticles were observable. Before discussing the results obtained from $[\text{Cd}^{\text{II}}(\text{L}^{\text{2a}}\text{-$

* Emission spectra are not shown below 400 nm due to interference from the Rayleigh scatter peak or above 675 nm due to interference from the Raman scatter peak.

$S,O)_2]$ thermolysis, the optical properties of the CdSe nanoparticles obtained at varying temperatures deserves some consideration.

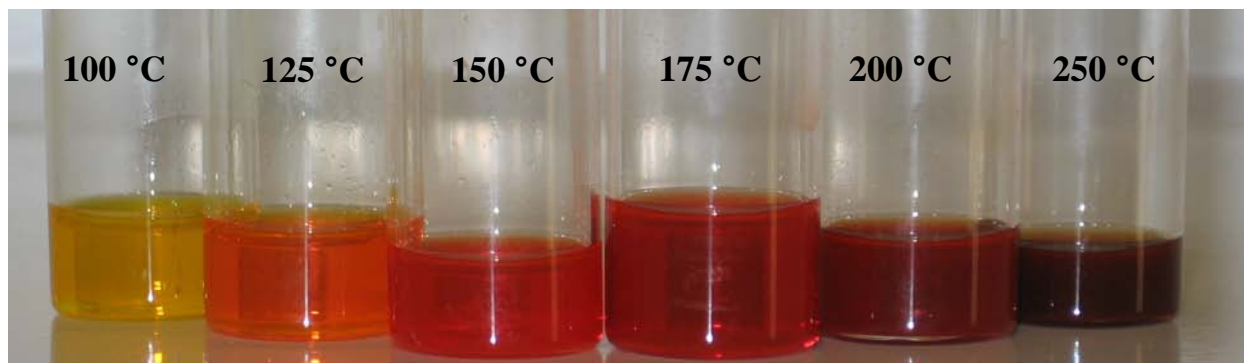


Fig. 3.36 CdSe nanoparticles in toluene following thermolysis of $[Cd^{II}(L^{1a}-Se,O)_2]$ at various temperatures.

A photograph of toluene suspended CdSe nanoparticles obtained from thermolysis of $[Cd^{II}(L^{1a}-Se,O)_2]$ at varying temperatures is shown in Fig. 3.36. The well described size dependant optical properties of CdSe are clearly evident.^[36, 37] The corresponding emission spectra of the samples are shown in Fig. 3.37 where the size dependant emission is beautifully manifest. The smallest nanoparticles synthesised at 100 °C, 2.0 (14) nm in diameter show a 504 nm emission maximum and the largest nanoparticles synthesised at 250 °C, 3.8 (15) nm in diameter exhibit a 611 nm emission maximum. Nanoparticles synthesised at temperatures between these two extremes consequently have emission maxima in the range 504 to 611 nm.

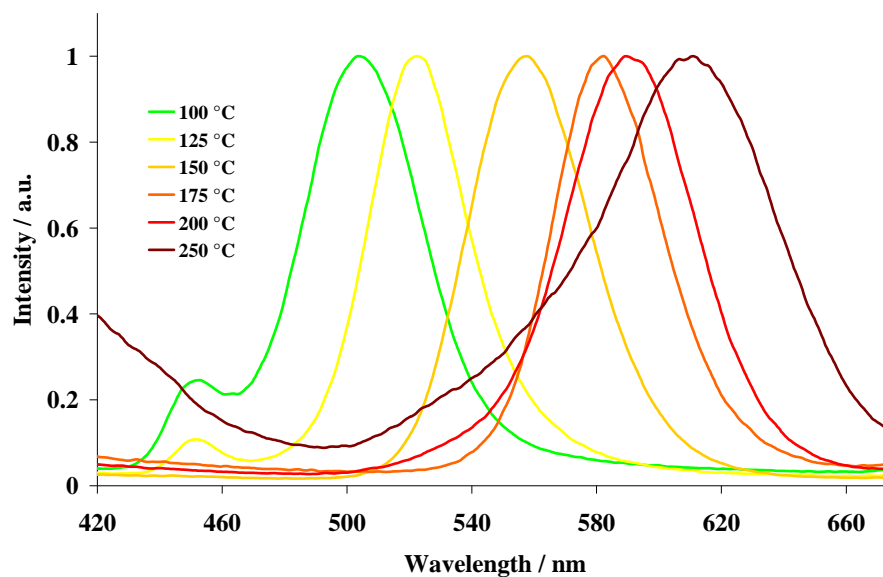


Fig. 3.37 Emission spectra of CdSe nanoparticles obtained following thermolysis of $[Cd^{II}(L^{1a}-Se,O)_2]$ at various temperatures.

3.3.2.2 Synthesis of CdS nanoparticles

The thermolysis of $[Cd^{II}(L^{2a}-S,O)_2]$ was investigated at five different temperatures and Table 3.32 shows the results obtained following 60 minute reactions, Fig. 3.38 illustrates the optical spectra of the nanoparticles obtained following thermolysis at 125, 150 and 240 °C.

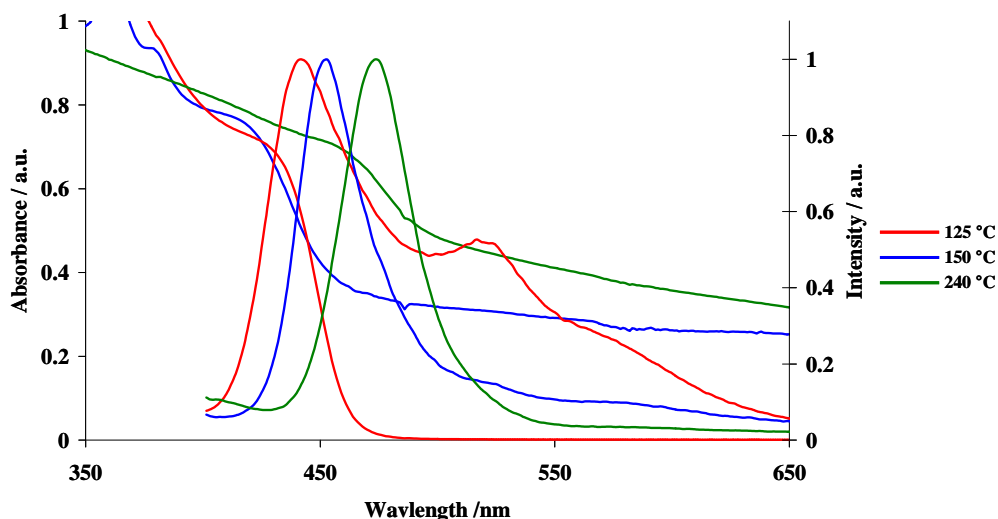
Table 3.32 Properties of CdS nanoparticles obtained following thermolysis of $[\text{Cd}^{\text{II}}(\text{L}^{2\text{a}}-\text{S},\text{O})_2]$ at various temperatures.

Temp / °C	Band edge / nm	Band edge / eV	Average size / nm (std. dev. %)*	Average size / nm (Scherrer Eqn ^[25])	FWHM / nm	Emission maxima / nm
125	480	2.58	3.1 (18)	-	-	441.5 516.5 [‡]
150	464	2.67	3.0 (15)	1.6	35.5	452.5
175	475	2.61	3.1 (15)	-	31.5	459.5
200	494	2.51	3.5 (15)	1.9	31.5	467.0
240	562	2.21	3.9 (13)	-	36.5	474.0
300	599	2.07	6.4 (17)	7.3	45	500.5 398.6 [‡]

* from TEM data

[‡] second smaller maximum

The temperature limit of nanoparticle formation for $[\text{Cd}^{\text{II}}(\text{L}^{2\text{a}}-\text{S},\text{O})_2]$ appears to be higher than that of its selenium analogue, where thermolysis of $[\text{Cd}^{\text{II}}(\text{L}^{2\text{a}}-\text{S},\text{O})_2]$ at 125 °C yields CdS nanoparticles of relatively poor quality. It is likely that at this relatively low decomposition temperature, slow nucleation occurs and this is supported by the yellow colour due to nucleation in the solution only being observed 12 minutes into the reaction, whereas at higher temperatures (200 °C), this yellow colour is immediately observed. Samples withdrawn from the 125 °C reaction mixture at 10 minutes indicate a very broad emission with a maximum at 516 nm. As the reaction progressed a second lower wavelength emission emerged at 442 nm and grew in intensity whilst the longer wavelength emission diminished resulting in the emission spectrum shown in Fig. 3.38 at 60 minutes. These results suggest uneven nucleation at lower temperatures, giving rise to a broad particle size distribution reflected in the higher standard deviation of 18 % and the bimodal emission evident in the emission spectrum. The absence of similar observations following the thermolysis of $[\text{Cd}^{\text{II}}(\text{L}^{1\text{a}}-\text{Se},\text{O})_2]$ at a similar temperature, implies a higher thermal stability of the (*N,N*-diethyl-*N'*-benzoylthioureato)Cd(II) complex relative to its selenium counterpart, under these conditions.

**Fig. 3.38** Optical spectra of CdS nanoparticles obtained following thermolysis of $[\text{Cd}^{\text{II}}(\text{L}^{2\text{a}}-\text{S},\text{O})_2]$ at 125, 150 and 240 °C.

An injection temperature of 150 °C resulted in nanoparticles with the smallest diameter and a band gap of 464 nm. This is significantly blue shifted relative to that of bulk CdS at 515 nm indicating quantum confinement. As with the formation of CdSe, absorption spectra of samples withdrawn from the 150 °C reaction mixture at 10 and 60 minutes were very similar indicating rapid nucleation at the higher temperature. The emission spectrum obtained 10 minutes into the reaction shows clear evidence of a longer wavelength emission however as the reaction time increased the

intensity of this emission decreased significantly and is barely observable after 60 minutes (Fig. 3.38). This indicates that annealing and passivation of the semiconducting surface occurs as the reaction proceeds. At an even higher injection temperature of 240 °C, the reaction becomes uncontrollable as within 20 minutes the particles no longer exhibit quantum confinement. This is in contrast to results obtained for the thermolysis of $[\text{Cd}^{\text{II}}(\text{L}^{\text{Ia}}\text{-Se},\text{O})_2]$ where moderately good quality CdSe nanoparticles form at relatively lower temperatures (100 °C) and retain their quantum confinement up to 250 °C.^[38] As with CdSe, particle sizes are estimated from the (220) peak in the PXRD patterns and are slightly smaller than the estimates obtained from the TEM images. CdS particle sizes for the 125 and 240 °C are not given due to the reduced crystallinity observed in these samples. Similarly to the CdSe nanoparticles, where the crystallinity of the nanoparticles was sufficient to allow reasonable PXRD analysis it is evident that cubically phased material is formed. It is interesting to note that whilst the average diameter of the nanoparticles did vary with the injection temperature, the final morphology of the nanoparticles remained unaltered for both CdS and CdSe. As mentioned in the previous section, the majority of single source precursor complexes involving sulfur containing ligands result in the formation of hexagonally phased CdS, and it was therefore curious that even over a range of temperatures cubically phased material was obtained in our case. Zelaya-Angel and co-workers have studied this phase change in CdS systems deposited onto glass substrates and found evidence of cubic to hexagonal transitions in the region of 300 °C.^[39, 40] Whilst the thermolysis environment is quite different to that of a deposition reaction, $[\text{Cd}^{\text{II}}(\text{L}^{\text{2a}}\text{-S},\text{O})_2]$ was nevertheless injected at 300 °C to observe the effect on the phase of material formed. As expected the optical spectra indicate that the particles no longer exhibit quantum confinement and PXRD analysis still showed the presence of zinc-blende CdS, however the TEM images (Fig. 3.39) revealed some interesting results.

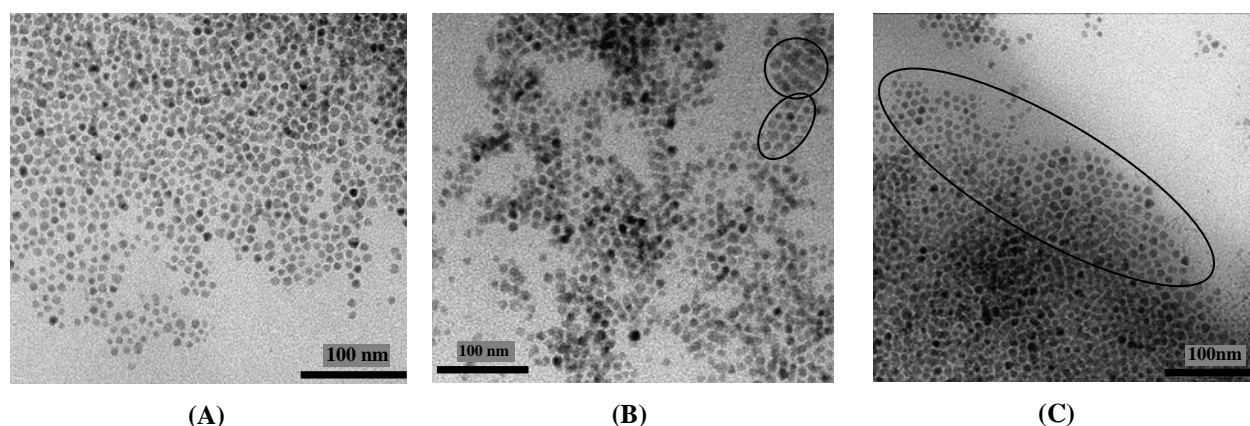


Fig. 3.39 TEM images of CdS nanoparticles obtained following thermolysis of $[\text{Cd}^{\text{II}}(\text{L}^{\text{2a}}\text{-S},\text{O})_2]$ at 300 °C.

Image (A) shows well defined spherical nanoparticles where the larger particle size distribution is reflected in the increased standard deviation reported in Table 3.32. Images (B) and (C) also show spherical particles, however in the highlighted sections, ordered self assembly of the particles into a short range 2D array appears to have occurred. This phenomenon has previously been reported for spherical cobalt nanoparticles^[41] as well as ZnS nanodots.^[42] Li and co-workers report that this phenomenon of self organization is thought to be governed by two main driving forces, van der Waals interactions and dipolar attraction. This suggests that the range and degree of order could be manipulated by evaporation rate^[43] and the use of different solvent combinations as they indeed found to be the case.^[42] Blanton and co-workers have previously worked on CdSe nanocrystals where they measured the dipole moments of colloidal nanocrystals and also observed the presence of charge in solution, as well as a marked increase in conductivity at high nanocrystal volume fractions.^[44] These last two observations could have marked

consequences for the potential application of close packed assemblies of nanocrystals. The measured dipole moment however is thought to arise from the wurtzite CdSe lattice and intuitively rationalises the hexagonal close-packing seen over short distances. In our case however, PXRD patterns indicate cubic CdS, where the presence of a dipole moment is less intuitive, however Shim and Guyot-Sionnest have reported the occurrence of dipole moments in cubically phased material.^[45]

Thermolysis of both $[\text{Cd}^{\text{II}}(\text{L}^{\text{1a}}\text{-Se},\text{O})_2]$ and $[\text{Cd}^{\text{II}}(\text{L}^{\text{2a}}\text{-S},\text{O})_2]$ over a range of temperatures gives largely spherical nanoparticles and therefore little control over the final nanoparticle morphology. These results are in marked contrast to those reported by Li and co-workers^[14] on the decomposition of cadmium ethylxanthate, however this can be rationalized by the hexagonally phased material produced on thermolysis of their precursor and the cubically phased material produced upon decomposition of both $[\text{Cd}^{\text{II}}(\text{L}^{\text{1a}}\text{-Se},\text{O})_2]$ and $[\text{Cd}^{\text{II}}(\text{L}^{\text{2a}}\text{-S},\text{O})_2]$. Thermolysis of both precursors at different temperatures does however allow the synthesis of nanoparticles with a fair degree of size control. Particularly in the case of CdSe, nanoparticle size can be varied between 2.0 (14) and 3.8 (15) nm with a reasonable amount of accuracy. Interestingly, the phase of both CdSe and CdS appears to be independent of temperature over the range studied and examination of the optical spectra shows the formation of good quality nanoparticles from both precursors between 150 and 175 °C.

Lazell and co-workers have also investigated the synthesis of semiconducting nanoparticles via single source precursor thermolysis and found that tailoring the precursor alkyl groups could have a significant influence over the nanoparticles obtained^[8] and for this reason the thermolysis of $[\text{Cd}^{\text{II}}(\text{L}^{\text{1b}}\text{-Se},\text{O})_2]$ **121**, $[\text{Cd}^{\text{II}}(\text{L}^{\text{1c}}\text{-Se},\text{O})_2]$ **131**, $[\text{Cd}^{\text{II}}(\text{L}^{\text{1d}}\text{-Se},\text{O})_2]$ **141**, $[\text{Cd}^{\text{II}}(\text{L}^{\text{1e}}\text{-Se},\text{O})_2]$ **151**, $[\text{Cd}^{\text{II}}(\text{L}^{\text{1f}}\text{-Se},\text{O})_2]$ **161** and their sulfur analogues, $[\text{Cd}^{\text{II}}(\text{L}^{\text{2b}}\text{-S},\text{O})_2]$ **221**, $[\text{Cd}^{\text{II}}(\text{L}^{\text{2c}}\text{-S},\text{O})_2]$ **231**, $[\text{Cd}^{\text{II}}(\text{L}^{\text{2d}}\text{-S},\text{O})_2]$ **241**, and $[\text{Cd}^{\text{II}}(\text{L}^{\text{2e}}\text{-S},\text{O})_2]$ **251** was undertaken. As some of the best quality nanoparticles were obtained at 150 °C for both the diethyl analogues, all precursors were initially injected at this temperature and the results obtained are discussed in the next section.

3.3.3 Alkyl chain length studies

3.3.3.1 Synthesis of CdSe nanoparticles

Equimolar quantities of the precursors, $[\text{Cd}^{\text{II}}(\text{L}^{\text{1b}}\text{-Se},\text{O})_2]$, $[\text{Cd}^{\text{II}}(\text{L}^{\text{1c}}\text{-Se},\text{O})_2]$, $[\text{Cd}^{\text{II}}(\text{L}^{\text{1d}}\text{-Se},\text{O})_2]$, $[\text{Cd}^{\text{II}}(\text{L}^{\text{1e}}\text{-Se},\text{O})_2]$ and $[\text{Cd}^{\text{II}}(\text{L}^{\text{1f}}\text{-Se},\text{O})_2]$ were thermolysed and the absorption spectra of the resulting nanoparticles are shown in Fig.3.310. The previously obtained results from thermolysis of $[\text{Cd}^{\text{II}}(\text{L}^{\text{1a}}\text{-Se},\text{O})_2]$ have been included for comparison. Table 3.33 summarises the properties of the CdSe nanoparticles obtained and clearly shows a decrease in the band edge as the alkyl chain length of the precursor increases where that of (*N,N*-dioctyl-*N'*-benzoylselenoureato)Cd(II), $[\text{Cd}^{\text{II}}(\text{L}^{\text{1d}}\text{-Se},\text{O})_2]$ at 653 nm is significantly red shifted to that of (*N,N*-diethyl-*N'*-benzoylselenoureato)Cd(II), $[\text{Cd}^{\text{II}}(\text{L}^{\text{1a}}\text{-Se},\text{O})_2]$ at 575 nm. This indicates the formation of larger nanoparticles as the alkyl chain length of the precursor increases. The band edge of 599 nm exhibited by nanoparticles obtained from thermolysis of the asymmetrically substituted $[\text{Cd}^{\text{II}}(\text{L}^{\text{1e}}\text{-Se},\text{O})_2]$ lies in between that of nanoparticles obtained following the thermolysis of $[\text{Cd}^{\text{II}}(\text{L}^{\text{1c}}\text{-Se},\text{O})_2]$ and $[\text{Cd}^{\text{II}}(\text{L}^{\text{1d}}\text{-Se},\text{O})_2]$.

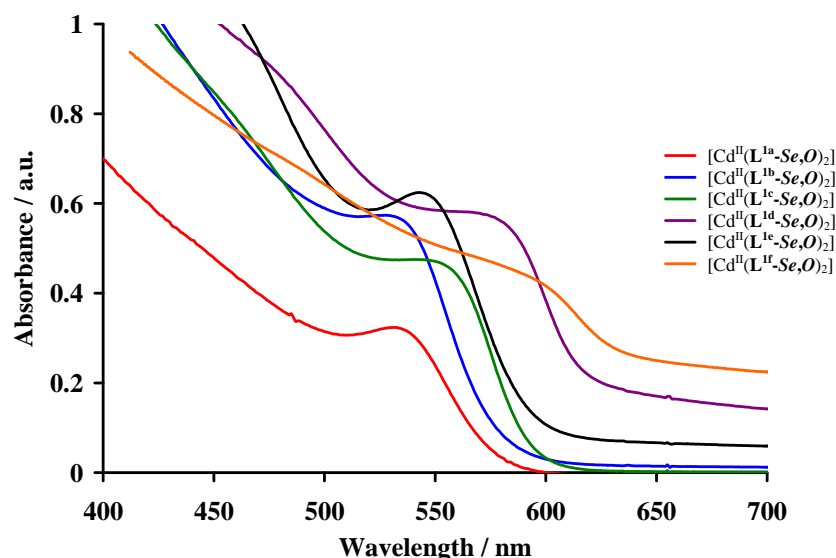


Fig. 3.310 Absorption spectra of CdSe nanoparticles obtained following thermolysis of $[\text{Cd}^{\text{II}}(\text{L}^{\text{Ia}}-\text{Se},\text{O})_2]$, $[\text{Cd}^{\text{II}}(\text{L}^{\text{Ib}}-\text{Se},\text{O})_2]$, $[\text{Cd}^{\text{II}}(\text{L}^{\text{Ic}}-\text{Se},\text{O})_2]$, $[\text{Cd}^{\text{II}}(\text{L}^{\text{Id}}-\text{Se},\text{O})_2]$, $[\text{Cd}^{\text{II}}(\text{L}^{\text{Ie}}-\text{Se},\text{O})_2]$ and $[\text{Cd}^{\text{II}}(\text{L}^{\text{If}}-\text{Se},\text{O})_2]$ at 150 °C.

Table 3.33 Properties of CdSe nanoparticles obtained following thermolysis of $[\text{Cd}^{\text{II}}(\text{L}^{\text{Ia-f}}-\text{Se},\text{O})_2]$ at 150 °C for 60 minutes.

Precursor	Band edge / nm	Band edge / eV	Average size / nm (std. dev. %)*	Average size / nm (Scherrer Eqn ^[25])	FWHM / nm	Emission maxima / nm
$[\text{Cd}^{\text{II}}(\text{L}^{\text{Ia}}-\text{Se},\text{O})_2]$	575	2.15	2.0 (14)	1.7	46	557.5
$[\text{Cd}^{\text{II}}(\text{L}^{\text{Ib}}-\text{Se},\text{O})_2]$	583	2.12	3.4 (17)	4.0	46.5	563.5
$[\text{Cd}^{\text{II}}(\text{L}^{\text{Ic}}-\text{Se},\text{O})_2]$	595	2.08	spherical 3.0 (15) rod length 8.6 (18) rod width 2.3 (18)	3.9	36.5	578
$[\text{Cd}^{\text{II}}(\text{L}^{\text{Id}}-\text{Se},\text{O})_2]$	635	1.95	rod length 10.6 (16) rod width 2.8 (16) tripod length 10.0 (7) tripod width 2.9 (11)	5.4	35	597.5
$[\text{Cd}^{\text{II}}(\text{L}^{\text{Ie}}-\text{Se},\text{O})_2]$	599	2.07	2.7 (12)	3.4	49.5	564
$[\text{Cd}^{\text{II}}(\text{L}^{\text{If}}-\text{Se},\text{O})_2]$	678	1.83	3.9 (13)	4.0	40.5	611

* from TEM data

The red shift observed in the absorption spectra is reflected in the emission spectra where the emission maximum of CdSe nanoparticles obtained following thermolysis of $[\text{Cd}^{\text{II}}(\text{L}^{\text{Id}}-\text{Se},\text{O})_2]$ at 597.5 nm is clearly red shifted to the 557.5 nm obtained from CdSe nanoparticles following thermolysis of $[\text{Cd}^{\text{II}}(\text{L}^{\text{Ia}}-\text{Se},\text{O})_2]$ (Fig. 3.311). This time the emission maximum obtained from nanoparticles following thermolysis of the asymmetrically substituted $[\text{Cd}^{\text{II}}(\text{L}^{\text{Ie}}-\text{Se},\text{O})_2]$ lies in between that of nanoparticles obtained following thermolysis of $[\text{Cd}^{\text{II}}(\text{L}^{\text{Ib}}-\text{Se},\text{O})_2]$ and $[\text{Cd}^{\text{II}}(\text{L}^{\text{Ic}}-\text{Se},\text{O})_2]$. Interestingly the presence of a lower wavelength emission increases in intensity as the alkyl chain length of the precursor increases. Nanoparticles obtained from thermolysis of (*N,N*-dihexyl-*N'*-benzoylselenoureato)Cd(II) $[\text{Cd}^{\text{II}}(\text{L}^{\text{Ic}}-\text{Se},\text{O})_2]$ give the first indication of this emission in the region of 434 nm where the intensity decreases as the reaction proceeds. This is accentuated in nanoparticles obtained following thermolysis of (*N,N*-dioctyl-*N'*-benzoylselenoureato)Cd(II) $[\text{Cd}^{\text{II}}(\text{L}^{\text{Id}}-\text{Se},\text{O})_2]$ and although not reflected here, in results obtained from reactions where twice the molar equivalent of $[\text{Cd}^{\text{II}}(\text{L}^{\text{Id}}-\text{Se},\text{O})_2]$ was used in the reaction, the emission spectra clearly displayed an increased intensity of this shorter wavelength emission. (Section 3.3.4.1) Nanoparticles obtained following thermolysis of (*N,N*-didecyl-*N'*-benzoylselenoureato)Cd(II) $[\text{Cd}^{\text{II}}(\text{L}^{\text{If}}-\text{Se},\text{O})_2]$ exhibit the most intense shorter wavelength emission where 5 minutes after injection, the intensity is 118 % of that at 611 nm. As the reaction proceeds the intensity decreases to become 102 % of that at 611 nm after 30 minutes and finally 37 %

following a 60 minute reaction. The origin of this emission is not clear, and as previously discussed (Chapter 1), the nature of the emitting state in semiconducting quantum dots is not clearly understood. In the CdS system studied and discussed by Brus *et al.*, the presence of trapped states can lead to varying wavelength emissions, where deep traps, originally thought to arise due to sulfur vacancies, usually localised in the band gap, lead to longer wavelength emissions.^[46] In contrast, the shorter wavelength emissions observed here, could arise from shallow trap emissions, shallow traps usually being located near the band edge allowing for an increased energy for radiative recombination.^[47] Ramsden *et al.* also studying the CdS system, reported a shorter wavelength emission attributed to cadmium vacancies, however this occurred in the 513 – 517 nm region, clearly different to the emission observed here.^[48] As this phenomenon appears to increase with the precursor alkyl chain length, it is tempting to suggest a correlation between the two, where the alkyl chains may in some way inhibit the formation of well defined crystalline material leading to the shorter wavelength emission, however as the course of the reaction proceeds, decomposition of the alkyl chains takes place, the crystallinity of the nanoparticle presumably improves and the intensity of the shorter wavelength emission decreases as observed. It is interesting to note that in each case where it is observed the emission appears to be centred around 433 nm and exhibits little shift as the reaction proceeds. The longer wavelength emissions however exhibit slight red shifts as the reactions progress, this behaviour being expected for close to band gap emission.

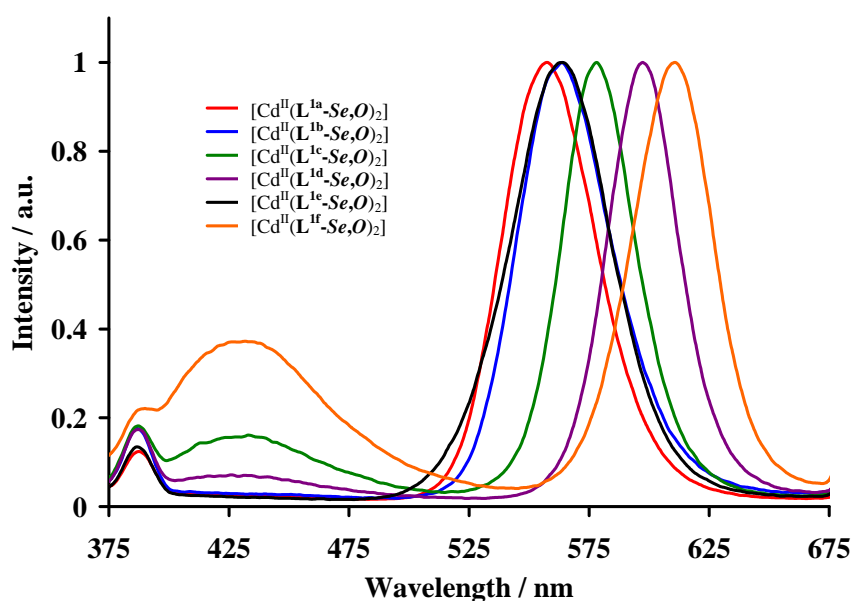


Fig. 3.311 Emission spectra of CdSe nanoparticles obtained following thermolysis of $[\text{Cd}^{\text{II}}(\text{L}^{\text{Ia}}\text{-Se},\text{O})_2]$, $[\text{Cd}^{\text{II}}(\text{L}^{\text{Ib}}\text{-Se},\text{O})_2]$, $[\text{Cd}^{\text{II}}(\text{L}^{\text{Ic}}\text{-Se},\text{O})_2]$, $[\text{Cd}^{\text{II}}(\text{L}^{\text{Id}}\text{-Se},\text{O})_2]$, $[\text{Cd}^{\text{II}}(\text{L}^{\text{Ie}}\text{-Se},\text{O})_2]$ and $[\text{Cd}^{\text{II}}(\text{L}^{\text{If}}\text{-Se},\text{O})_2]$ at 150 °C.

Table 3.33 shows the FWHM for the emission maxima of the nanoparticles obtained following thermolysis of each precursor however they all appear to have comparable values and no trend with alkyl chain length variation is evident.

PXRD patterns obtained for each set of nanoparticles are shown in Fig. 3.312. In each case cubically phased nanoparticles are obtained. Interestingly the intensity of the (220) peak appears to increase relative to that of the (311) peak as the alkyl chain length of the precursor increases. This is rather curious behaviour for a cubically phased system and is more usually associated with hexagonal systems where intensity increases of a particular peak indicate preferential elongation of a particular facet of a nanocrystal or orientation along a particular plane in the

case of nanocrystalline material which has been deposited onto a substrate.^[7] The (220) peak was used in the estimation of particle size and indicates a rough trend of increasing particle size with increasing alkyl chain length in the precursor although this is not as clear as that exhibited by the band edge.

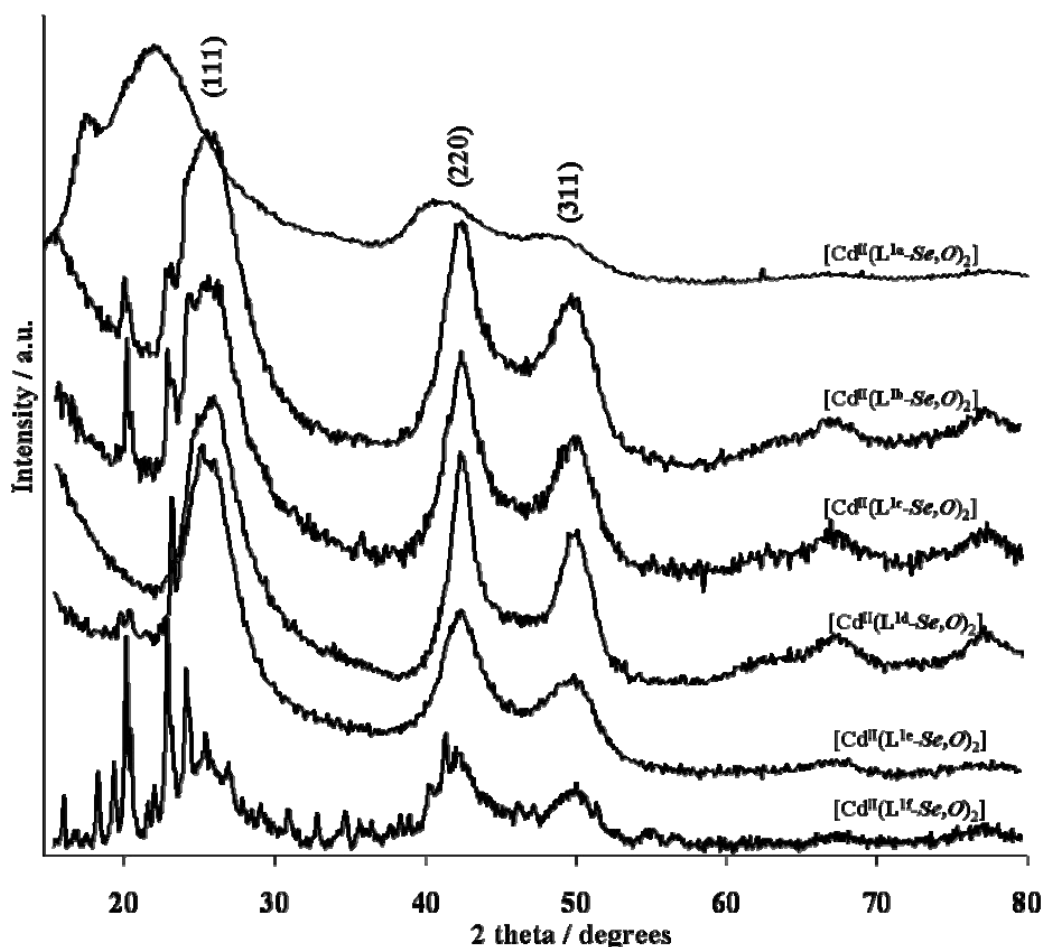


Fig. 3.312 PXRD patterns of CdSe nanoparticles following thermolysis of $[\text{Cd}^{\text{II}}(\text{L}^{\text{Ia}}\text{-Se},\text{O})_2]$, $[\text{Cd}^{\text{II}}(\text{L}^{\text{Ib}}\text{-Se},\text{O})_2]$, $[\text{Cd}^{\text{II}}(\text{L}^{\text{Ic}}\text{-Se},\text{O})_2]$, $[\text{Cd}^{\text{II}}(\text{L}^{\text{Id}}\text{-Se},\text{O})_2]$, $[\text{Cd}^{\text{II}}(\text{L}^{\text{Ie}}\text{-Se},\text{O})_2]$ and $[\text{Cd}^{\text{II}}(\text{L}^{\text{If}}\text{-Se},\text{O})_2]$ at 150 °C.*

The presence of sharp peaks in the low angle region of the PXRD patterns is rather unusual. Again this appears to be correlated with increasing precursor alkyl chain length as no evidence of this crystalline phase is evident in PXRD patterns obtained following thermolysis of $(N,N\text{-diethyl-}N'\text{-benzoylselenoureato})\text{Cd}(\text{II})$. The PXRD pattern of nanoparticles obtained following thermolysis of $[\text{Cd}^{\text{II}}(\text{L}^{\text{Id}}\text{-Se},\text{O})_2]$ do not clearly follow this trend however as described in section 3.3.4.1, results obtained from a reaction using two molar equivalents of the precursor clearly indicated the presence of these low angle peaks. It is therefore likely that there may be some connection between the shorter wavelength emission observed (Fig. 3.311) and these low angle peaks. A full search of the PXRD database was conducted however no identical pattern could be found and therefore the origin of this crystalline material remains somewhat unclear.

The morphology of the CdSe nanoparticles from the various precursors was investigated and selected TEM images are shown in Fig. 3.313.

* The d spacing of the PXRD pattern obtained for CdSe nanoparticles following thermolysis of $[\text{Cd}^{\text{II}}(\text{L}^{\text{Ia}}\text{-Se},\text{O})_2]$ is slightly shifted relative to that obtained for the remaining nanoparticles however analysis of this material was performed on the Oxford Xcalibur machine using Mo radiation whereas that of the remaining nanoparticles was performed using Cu radiation. Slight shifts in the d spacing have been associated with stacking faults and prolate nanoparticles^[30] however these are too small to account for that observed here and it is therefore likely that the sample may not have been correctly mounted for analysis.

Predominantly spherical nanoparticles are evident following thermolysis of $[\text{Cd}^{\text{II}}(\text{L}^{\text{Ib}}\text{-Se},\text{O})_2]$ (Fig. 3.313 (A)) with an average diameter of 3.4 (17) nm, slightly larger than those obtained from the diethyl analogue. Fig. 3.313 (B) illustrates the presence of anisotropy in the nanoparticle morphologies obtained following thermolysis of $[\text{Cd}^{\text{II}}(\text{L}^{\text{Ic}}\text{-Se},\text{O})_2]$ where the average diameter of spherical nanoparticles is 3.0 (15) nm and the average rod length and width = 8.6 (18) and 2.3 (18) nm respectively. Interestingly little evidence of anisotropy is evident in the nanoparticles derived from $[\text{Cd}^{\text{II}}(\text{L}^{\text{Ie}}\text{-Se},\text{O})_2]$ (Fig. 3.313 (D)) where the average particle diameter is 2.7 (12) nm.

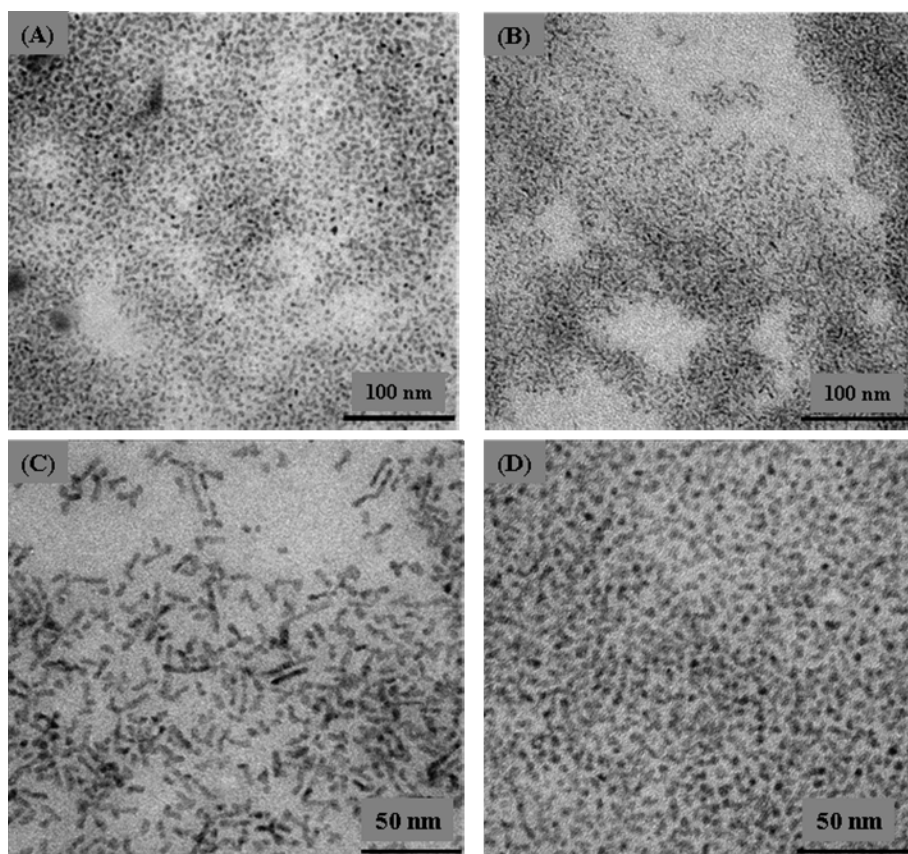


Fig 3.313 TEM images of CdSe nanoparticles obtained following thermolysis of (A) $[\text{Cd}^{\text{II}}(\text{L}^{\text{Ib}}\text{-Se},\text{O})_2]$, (B) $[\text{Cd}^{\text{II}}(\text{L}^{\text{Ic}}\text{-Se},\text{O})_2]$, (C) $[\text{Cd}^{\text{II}}(\text{L}^{\text{Id}}\text{-Se},\text{O})_2]$ and (D) $[\text{Cd}^{\text{II}}(\text{L}^{\text{Ie}}\text{-Se},\text{O})_2]$ at 150 °C.

Nanoparticles obtained following the thermolysis of $[\text{Cd}^{\text{II}}(\text{L}^{\text{Id}}\text{-Se},\text{O})_2]$ (Fig. 3.313 (C)) yield fascinating morphologies, with clear evidence of anisotropic growth. The TEM image illustrates the presence of both nanorods and tripods. Both the nanorods and tripod “arms” have similar lengths, 10.6 (16) and 10.0 (7) respectively (Table 3.33). Fig. 3.314 (A) shows enlarged areas of the TEM image where the tripod morphology can clearly be seen. Fig 3.314 (B) shows a TEM image following “ageing” of the CdSe nanoparticles to observe possible effects on the nanoparticle morphology. The enlarged areas show the presence of tripods and an apparent tetrapod, however this will be discussed in more detail shortly.

The above results appear to indicate that an increase in precursor alkyl chain length leads to an increase in the anisotropy exhibited by the resulting nanoparticles, suggesting that a degree of morphological control can be enforced by alteration of the precursor. To establish if this was the case, *N,N*-didecyl-*N'*-benzoylselenourea $[\text{Cd}^{\text{II}}(\text{L}^{\text{If}}\text{-Se},\text{O})_2]$ was synthesised and thermolysed under identical conditions to those of $[\text{Cd}^{\text{II}}(\text{L}^{\text{Id}}\text{-Se},\text{O})_2]$ in order to observe the morphology of the resulting nanoparticles.

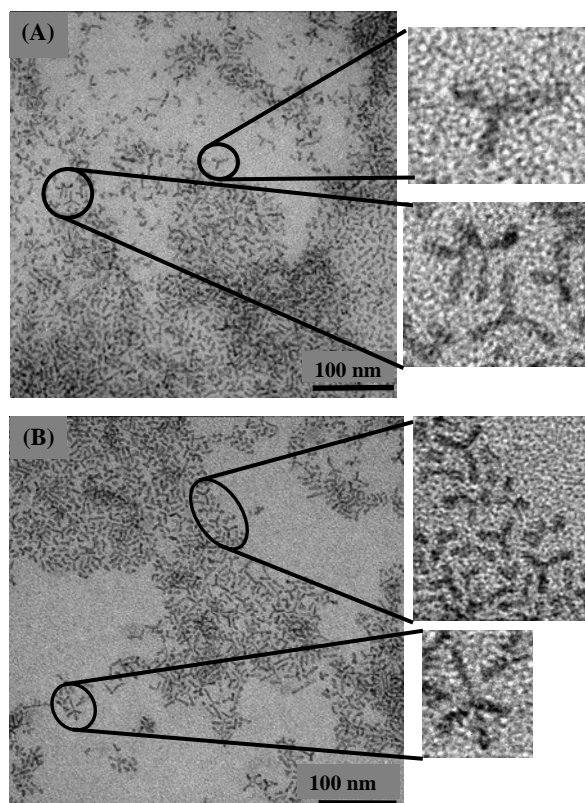


Fig. 3.314 TEM images of CdSe nanoparticles obtained following thermolysis of $[\text{Cd}^{\text{II}}(\text{L}^{1\text{d}}\text{-Se},\text{O})_2]$ where (A) was obtained shortly after CdSe synthesis and (B) following a period of “ageing” for approximately 30 days.

Fig. 3.315 (A) shows the significant reduction in anisotropic growth of CdSe nanoparticles following the thermolysis of $[\text{Cd}^{\text{II}}(\text{L}^{1\text{f}}\text{-Se},\text{O})_2]$. The diameter of the spherical nanoparticles, 3.9 (13) (Table 3.3), is in accordance with the trend of increasing particle size with increasing precursor alkyl chain length. Intriguingly however, no evidence of tripodal or bipodal morphologies could be found. This indicates that the degree of anisotropy may be alkyl chain length dependant; however this is only maintained up to a certain point after which spherical nanoparticles again dominate the morphology. Fig. 3.315 (B-D) shows the anomalous structures seen in sections of the same sample where a degree of self association appears to have occurred, leading to the formation of rather unusual rods. The structures appear to be composed of spherical nanoparticles with an increased density of nanoparticles leading to the formation of what appears to be a boundary giving form to the structure. Inside this a lower density of nanoparticles is present throughout the internal area. Careful examination of several images indicates a differing intensity for the material inside the structures suggesting that this is not the same as that remaining on the grid. The three rod shapes in Fig. 3.315 (D) have an average length of 551.0 (12) nm and width of 106.5 (28) nm. Another image isolated from the sample (not shown) showed the presence of a very long rod (1307.6 nm in length and 91.8 nm in width) possibly composed of three similar length rods attached end to end. Possible reasons for the formation of structures such as these remain very uncertain; evaporation rate of the solvent being the most likely. Interestingly during a second analysis of this sample several weeks after the synthesis, no evidence of these structures could be found suggesting the influence of sample preparation and solvent evaporation rate on their presence. As will be seen in Section 3.3.4.2, the formation of these structures is not limited to CdSe.

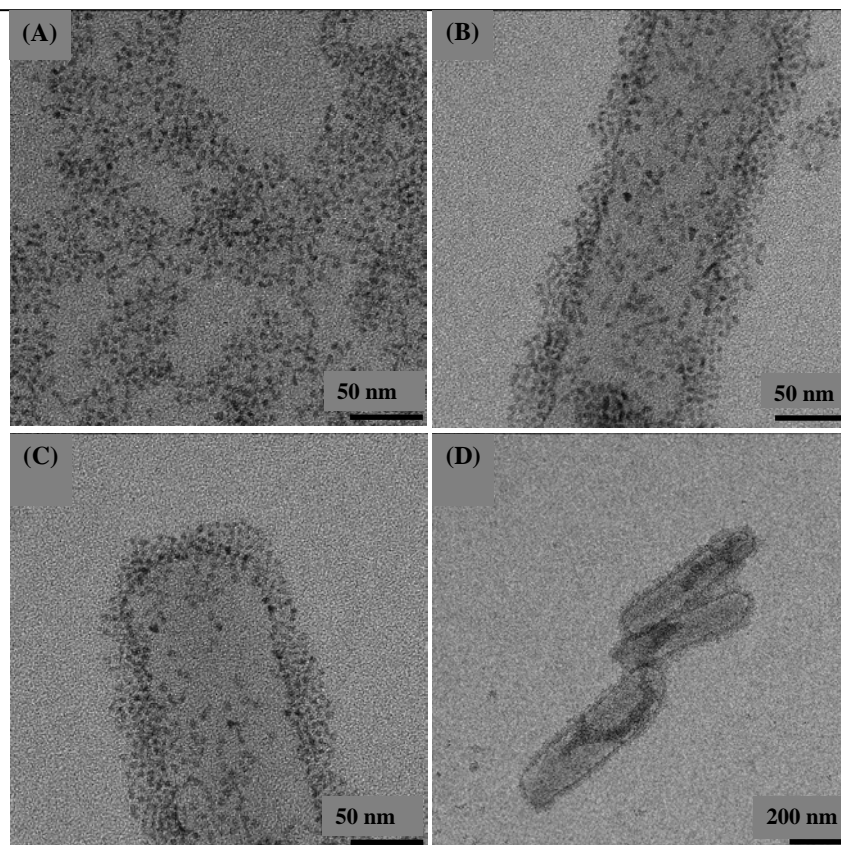


Fig. 3.315 TEM images of CdSe nanoparticles obtained following thermolysis of $[\text{Cd}^{\text{II}}(\text{L}^{\text{II}}\text{-Se},\text{O})_2]$ at 150 °C.

The formation of anisotropic CdSe structures with cubic crystallinity remains something of a conundrum, however Bawendi and co-workers have reported that due to the small size of nanoparticles, the relatively limited number of atoms involved and the presence of stacking faults, a cubic PXRD pattern does not necessarily reflect an underlying cubic structure, however the reverse is true for hexagonal systems, where a wurtzite PXRD pattern strongly suggests wurtzite crystallinity.^[32] It is therefore possible that hexagonally phased material could be present and this would go some way towards explaining the presence of anisotropic CdSe nanoparticles. Fig. 3.316 (A) illustrates the relationship

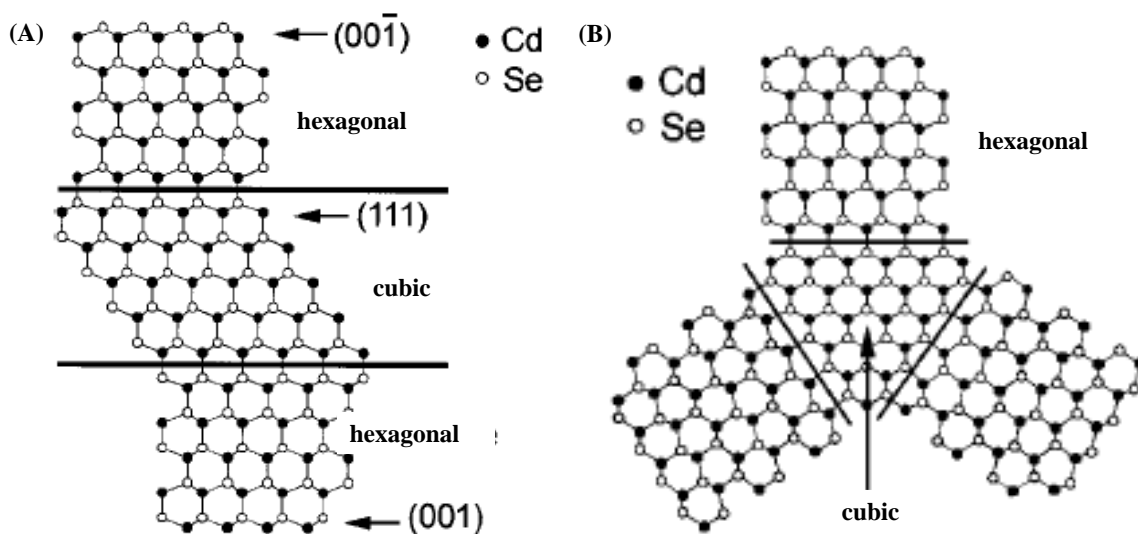


Fig. 3.316 Two dimensional representations showing (A) the relationship between cubic and hexagonal phases, and (B) the structure of a tetrapod with a cubic core and hexagonally phased arms (Adapted from Ref [49]).

between cubically and hexagonally phased material. The (111) face of cubic and the (001) face of the hexagonal phases, both have alternating Cd and Se containing planes, where cubic has an ABCABC type stacking and hexagonal has an ABAB type stacking. The two structures are related by a stacking fault as seen in Fig. 3.316 (A). The formation of multiarmed structures can occur where cubically phased nuclei are initially formed. Epitaxial growth of hexagonally phased “arms” then occurs from the (111) faces of the cubic core as shown in Fig. 3.316 (B). As there are four equivalent (111) faces in a cubically phased core and it is likely that hexagonally phased growth would occur at each with comparable rates, the resulting structure should be a tetrapod. The fourth “arm” in Fig. 3.316 (B) comes out of the page. This should result in a TEM image where a tripod can clearly be seen, however the presence of the fourth arm should manifest as a darker area in the centre of the tripodal structure as the view is along the plane of this fourth arm. Fig. 3.317 illustrates this effect for CdSe (A) and CdS (B) tetrapods.

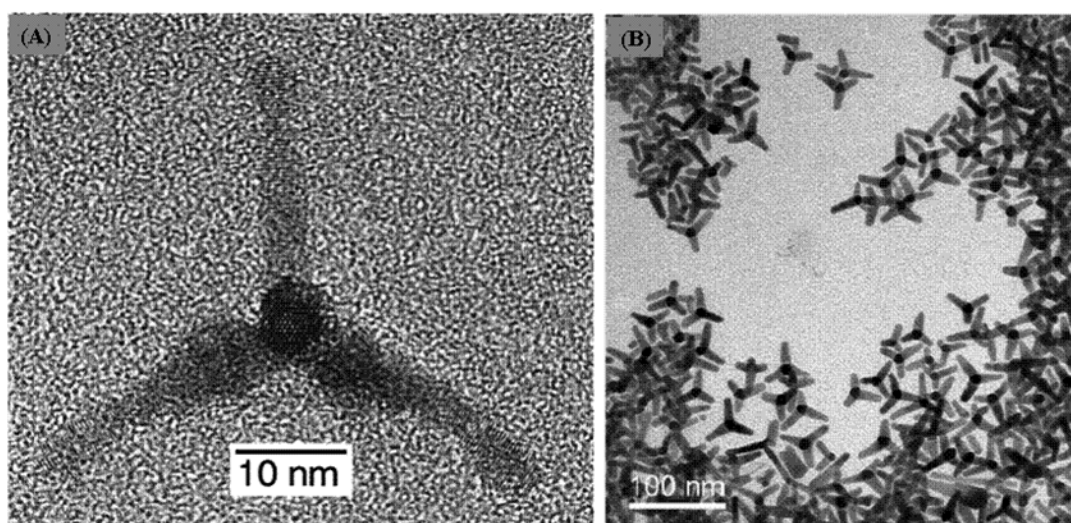


Fig. 3.317 HRTEM image of a typical tetrapod-shaped CdSe nanocrystal looking down the (001) direction of an arm (A) and (B) TEM image of similar CdS tetrapods. Taken from Ref [49] and [50] respectively.

If this growth mechanism applies to the structures observed following thermolysis of $[\text{Cd}^{\text{II}}(\text{L}^{\text{Id}}\text{-Se},\text{O})_2]$, similar images should be obtained, however this is clearly not the case. The single tetrapod that can easily be observed (Fig. 3.314 (B)) exhibits angles between the 4 arms which are intermediate between those expected for a true tripod and a tetrapod. In addition, no consistent evidence of a darkened centre in each of the tripods indicating the presence of a fourth arm could be found. Only 2 analytical techniques remained to give an indication of the growth mechanism. The first, High Resolution Transmission Electron Microscopy (HRTEM) would ideally be able to differentiate between the core and arm lattice planes enabling indexing to determine each phase. As this technique is not yet available in South Africa, a sample was taken to the University of Manchester and analysed, unfortunately however, this degree of resolution could not be obtained. The second technique involves the deconvolution of the PXRD pattern to determine if any hexagonally phased material is present. This was initially thought to be likely given the increased intensity between the (220) and (311) peaks which could correspond to the (103) peak of hexagonally phased material, indicating its presence in the nanocrystals. The software available for this deconvolution was however not readily available in South Africa and the data was also taken to the University of Manchester where it was found to be of insufficient quality to enable an accurate determination of the relative amounts of zinc blende and wurtzite CdSe. As one of the strongest detectors available had been used to collect the PXRD data, pursuing this line of analysis further would be unlikely to yield different results.

It is interesting to note here that in the PXRD patterns (Fig. 3.312) the intensity and sharpness of the (220) relative to that of the (311) peak appears to increase with increasing alkyl chain length of the precursor up to a point for nanoparticles derived from $[\text{Cd}^{\text{II}}(\text{L}^{\text{1d}}\text{-Se},\text{O})_2]$, after which this effect is no longer as noticeable for nanoparticles derived from $[\text{Cd}^{\text{II}}(\text{L}^{\text{1f}}\text{-Se},\text{O})_2]$. This trend reflects that mentioned above for the degree of anisotropy present.

Anisotropic structures from an inherently isotropic system have recently been reported by Berhanu and co-workers where PbS exhibited a range of differing morphologies.^[51] Whilst no tetrapodal structures were reported, bipods, rods, truncated cubes, tripods and prisms amongst others were formed. The varying morphologies were found to be dependant on growth modifier, precursor ratios, precursor concentration as well as solution pH.^[51] Further literature searches revealed a report by Jun *et al.* where multiarmed CdS nanoparticles were formed following the thermal decomposition of $\text{Cd}(\text{S}_2\text{CNET}_2)_2$.^[52] Similarly to the results reported by Manna and co-workers,^[49] a zinc-blende core and wurtzite phased arms were reported. Interestingly however, the presence of bi- and tripodal structures was also noted. Under relatively mild conditions (temperature = 120 °C) tetrapods were almost exclusively formed suggesting even development of the four {111} surfaces of the zinc blende core and growth of the (001) faces of the wurtzite arms. Faster growth observed at higher temperatures (180 °C), resulted in the bi and tripodal structures suggesting that once two or three (001) wurtzite faces have formed on the {111} surface of the zinc blende core, the growth rate of the (001) faces is faster than that of the remaining {111} surface giving rise to the structures observed. In the CdS system studied, very fast growth conditions (300 °C) favoured the formation of wurtzite seeds and hence only 1-D nanorods were formed.^[53]

To further understand our system, thermolysis of $[\text{Cd}^{\text{II}}(\text{L}^{\text{1d}}\text{-Se},\text{O})_2]$ was undertaken for a range of differing temperatures and the results are reported in the next section.

3.3.3.2 Varying temperature thermolysis of $[\text{Cd}^{\text{II}}(\text{L}^{\text{1d}}\text{-Se},\text{O})_2]$

The precursor $[\text{Cd}^{\text{II}}(\text{L}^{\text{1d}}\text{-Se},\text{O})_2]$, was thermolysed at 5 additional temperatures, (80 °C, 100 °C, 125 °C, 175 °C and 200 °C) where the absorption spectra of the resulting nanoparticles, obtained following a 60 minute reaction period, are shown in Fig. 3.318.

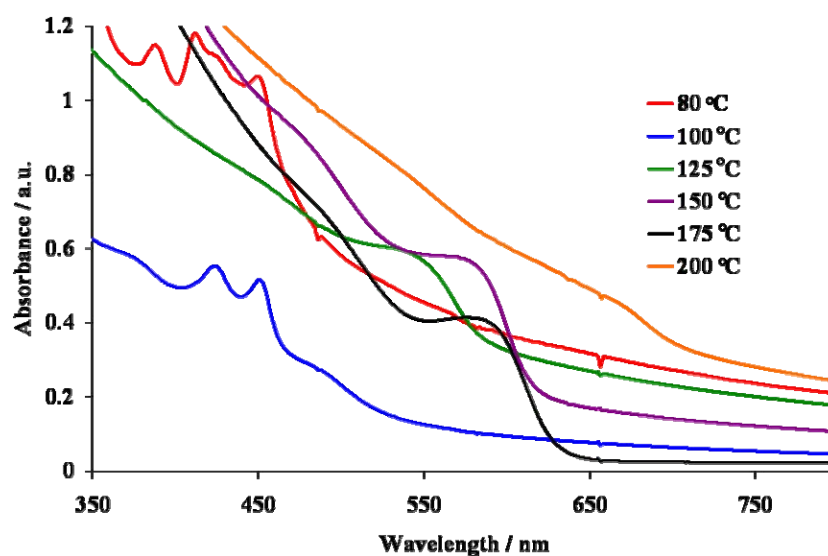


Fig. 3.318 Absorption spectra of CdSe nanoparticles obtained following thermolysis of $[\text{Cd}^{\text{II}}(\text{L}^{\text{1d}}\text{-Se},\text{O})_2]$ at 80, 100, 125, 150, 175 and 200 °C for 60 minutes.

Table 3.34 shows the nanoparticle band edges where the larger band edge values are observed for nanoparticles synthesised at 80 and 100 °C. Interestingly the 60 minute sample obtained at 80 °C appears to have a smaller band gap than that obtained at 100 °C however following a 180 minute reaction at 80 °C the band edge value appears to increase to 2.55 eV (486 nm). A similar effect is observed for the 100 °C sample, where following a 120 minute reaction, the band edge is 2.58 eV (480 nm). Nanoparticle samples obtained at 125, 150 and 175 °C appear to have comparative band edge values these being smaller than those obtained at lower temperatures as expected. Quantum confinement is clearly no longer observed at 200 °C where the band edge of 1.54 eV (805 nm) is red shifted to that of bulk CdSe at 1.73 eV (716 nm).

Table 3.34 Properties of CdSe nanoparticles obtained following thermolysis of $[\text{Cd}^{\text{II}}(\text{L}^{\text{Id}}\text{-Se},\text{O})_2]$ at varying temperatures for 60 minutes.

Temp / °C	Band edge / nm	Band edge / eV	Average size / nm (std. dev. %)*	Average size / nm (Scherrer Eqn ^[25])	FWHM / nm	Emission maxima / nm
80	542	2.29	spherical 3.4 (21) rod length 12.2 (14) rod width 3.0 (12)	-	42	453
100	485	2.55	spherical 2.8 (13)	-	-	457.5 [‡] 495
125	634	1.96	tripod length 7.5 (21) tripod width 2.5 (12)	4.05	36.5	434.5 [‡] 566.5
150	635	1.95	rod length 10.6 (16) rod width 2.8 (16) tripod length 10.0 (7) tripod width 2.9 (11)	5.4	35	597.5
175	635	1.95	spherical 3.8 (14) rod length 11.1 (13) rod width 3.2 (12) tripod length 8.6 (16) tripod width 3.1 (16)	5.0	41	431 [‡] 614
200	805	1.54	spherical 5.3 (6) butterfly width 7.0 (13) butterfly length 12.6 (24) interwing spacing 2.3 (13)	7.1	84	369.5

* from TEM data

[‡] second emission maximum

The normalized emission spectra are shown in Fig. 3.319, values for the emission maxima and FWHM being in Table 3.34. As expected, the general trend for quantumly confined nanoparticles is followed where increasing thermolysis temperature corresponds to an increase in emission wavelength. Curiously the sample obtained following 100 °C thermolysis exhibits a significant lower wavelength emission at 457.5 nm. After 10 minutes, the shorter wavelength emission is 88 % the intensity of that at 489.5 nm, however the intensity increases over time to become 218 % and finally 225.6 % of the longer wavelength emission following a 60 and 120 minute reaction respectively. The longer wavelength emission centred around 495 nm is thought to be the band edge emission as slight red shifts in the emission maxima as the reaction proceeds are observed.

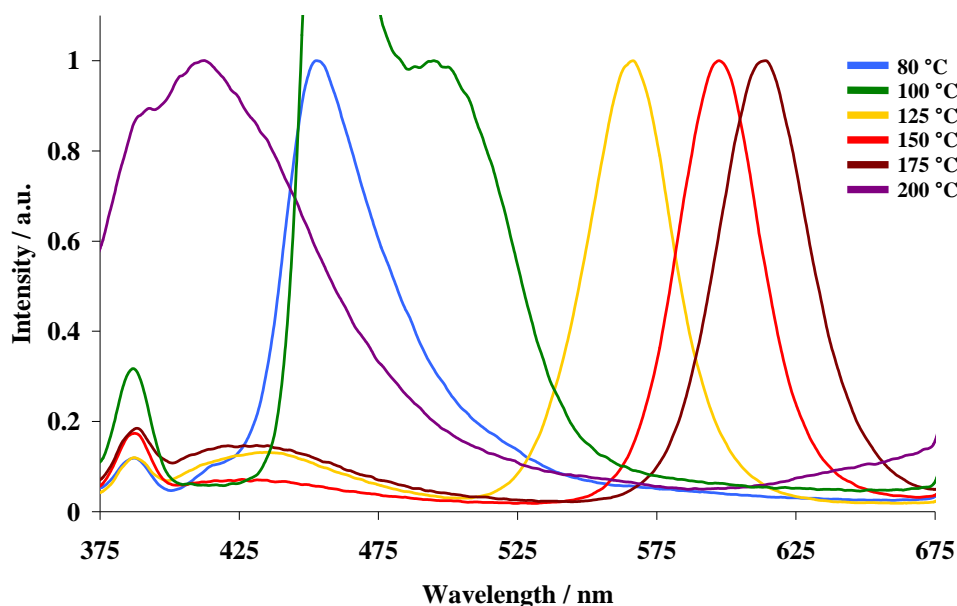


Fig. 3.319 Emission spectra of CdSe nanoparticles obtained following thermolysis of $[\text{Cd}^{\text{II}}(\text{L}^{1\text{d}}-\text{Se},\text{O})_2]$ at 80, 100, 125, 150, 175 and 200 °C for 60 minutes. $\lambda_{\text{Ex}} = 300$ nm for 200 °C sample.

In contrast, the shorter wavelength emission maximum shifts by less than 2 nm as the reaction progresses, and it is therefore unlikely to be band edge related, rather it may indicate shallow trap emission. To confirm the presence of this emission band, the reaction was repeated three times under identical conditions and the observations remain the same. Returning to Fig. 3.37 in section 3.3.2.1, thermolysis of $[\text{Cd}^{\text{II}}(\text{L}^{1\text{a}}-\text{Se},\text{O})_2]$ at 100 °C also gave rise to a shorter wavelength emission at 453 nm that exhibited an increase in intensity as the reaction progressed as previously described. A similar although less marked observation was made for the sample following thermolysis at 125 °C. The observations made from Fig. 3.319 for nanoparticles from the thermolysis of $[\text{Cd}^{\text{II}}(\text{L}^{1\text{d}}-\text{Se},\text{O})_2]$ are very similar and it would appear that an increase in the alkyl chain length of the precursor enhances this phenomenon at least at 100 °C. Thermolysis at 125 °C gives nanoparticles with an emission maximum of 566.5 nm. A less intense shorter wavelength emission is also present, but this decreases in intensity as the reaction proceeds, from being 23 % to 13 % of the of the band edge emission intensity following 10 and 60 minute reactions respectively. A similar effect is seen in CdSe nanoparticles obtained from 175 °C thermolysis where the shorter wavelength emission decreases in intensity from being 43 % to 15 % of the intensity of the band edge emission following a 10 and 60 minute reaction respectively. Interestingly little evidence of this shorter wavelength emission could be seen from the 150 °C reaction. The emission maximum and behaviour over time of this shorter wavelength emission is reminiscent of that seen in Fig. 3.311 for the CdSe nanoparticles obtained from the 150 °C thermolysis of $[\text{Cd}^{\text{II}}(\text{L}^{1\text{c}}-\text{Se},\text{O})_2]$ and $[\text{Cd}^{\text{II}}(\text{L}^{1\text{f}}-\text{Se},\text{O})_2]$. Thermolysis at 200 °C results in a longer wavelength emission at 637 nm, however this is completely overshadowed by the shorter wavelength emission and has disappeared altogether within 5 minutes of the reaction. As the CdSe nanoparticles are no longer quantum dots at this temperature, it is not surprising that following a 60 minute reaction the photoluminescence is completely dominated by the shorter wavelength emission. This is similar to, although more marked, than observations made following the thermolysis of $[\text{Cd}^{\text{II}}(\text{L}^{1\text{a}}-\text{Se},\text{O})_2]$ at 250 °C where a very broad shorter wavelength emission appeared and exhibited an increase in intensity as the reaction progressed.

In general however, the expected increase in emission wavelength with increasing temperature is observed. A photograph of the CdSe nanoparticles synthesised at varying temperatures taken under UV light is shown in Fig. 3.320 and illustrates this clearly. The most right hand sample (barely visible in Fig. 3.320) was obtained following thermolysis of $[\text{Cd}^{\text{II}}(\text{L}^{\text{Id}}-\text{Se},\text{O})_2]$ at 200 °C and illustrates the poor emission obtained from these nanoparticles.

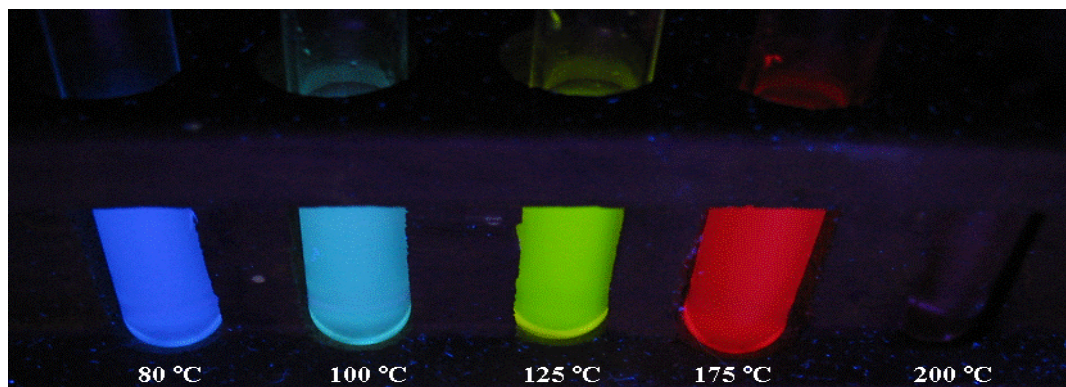


Fig. 3.320 Photograph of toluene suspended CdSe nanoparticles following thermolysis of $[\text{Cd}^{\text{II}}(\text{L}^{\text{Id}}-\text{Se},\text{O})_2]$ at 80, 100, 125, 175 and 200 °C.

The PXRD patterns of the CdSe nanoparticles are shown in Fig. 3.321, where once again it appears as though predominantly cubically phased material is obtained. Thermolysis of $[\text{Cd}^{\text{II}}(\text{L}^{\text{Id}}-\text{Se},\text{O})_2]$ at 80 and 100 °C leads to very poorly crystalline material, however the crystallinity improves as the reaction temperature is increased. In addition the (220) peak appears to increase in relative intensity and sharpness with increasing temperature. As previously observed, the presence of sharp low angle peaks presumably associated with a highly crystalline material is evident at each temperature and no temperature trend is evident.

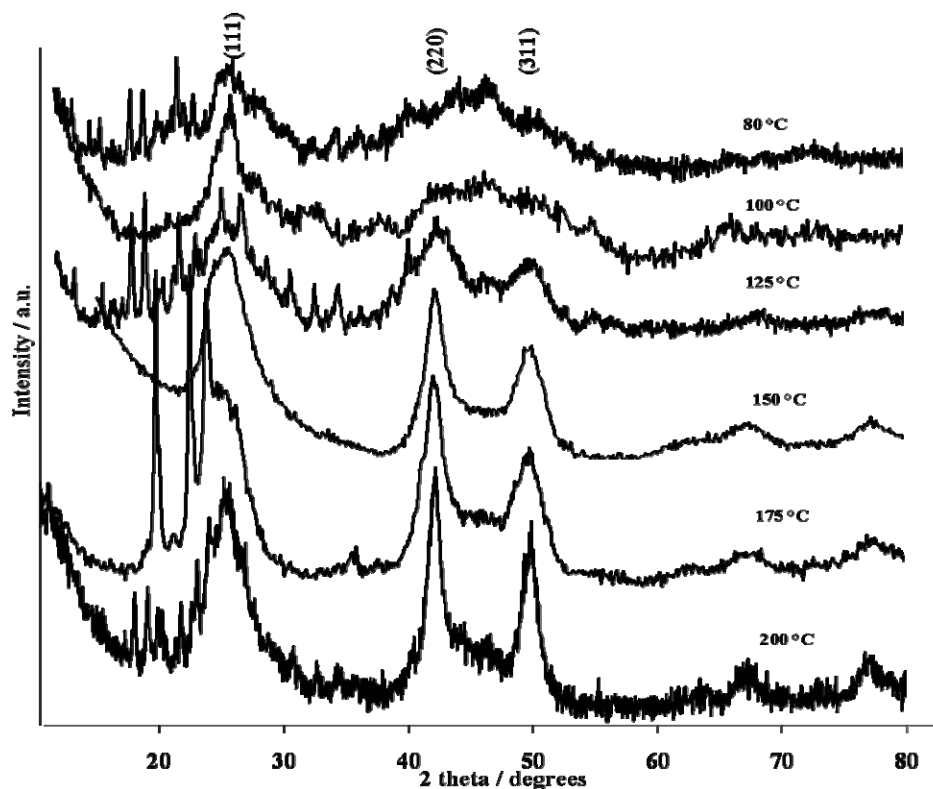


Fig. 3.321 PXRD patterns of CdSe nanoparticles following thermolysis of $[\text{Cd}^{\text{II}}(\text{L}^{\text{Id}}-\text{Se},\text{O})_2]$ at 80, 100, 125, 150, 175 and 200 °C.

The morphology of the CdSe nanoparticles obtained at each temperature is shown in Fig. 3.322. Following an 80 °C thermolysis, largely anisotropic structures are obtained. Spherical nanoparticles are also present however with an average diameter of 3.4 (21) nm. The anisotropic structures are mostly rod shaped (length = 12.2 (14) and width = 3.0 (12)) however isolated structures appear to be tripodal, although the limited resolution of the microscope makes a well defined tripod difficult to observe. At 100 °C, largely agglomerated, predominantly spherical nanoparticles are obtained, with an average diameter of 2.8 (13) nm. This supports observations made for the optical spectra of these nanoparticles where a shorter band edge was observed relative to that for nanoparticles synthesised at 80 °C. The reason for the agglomeration of these nanoparticles is not clear; however the effect was similar at 60 and 180 minute samples and appears to be limited to nanoparticles synthesised at this temperature. Well defined tripods are evident from the 125 °C sample, where both the length (7.5 (21) nm) and width (2.5 (12) nm) appear to be slightly smaller than those obtained for the rods at 80 °C. Interestingly, in the PXRD pattern obtained for nanoparticles from this sample the presence of a broad peak in between the (220) and (311) peaks, suggests that the previously described method of tripodal synthesis may be applicable to these systems. This is because the peak position corresponds to the 2θ value usually associated with the (103) peak in hexagonally phased CdSe. As the 2θ values of the (110) and (112) peaks in hexagonally phased CdSe correspond very closely to the 2θ values of the (220) and (311) peaks in cubically phased CdSe, the existence of the (103) peak could indicate the presence of a second phase. As previously discussed tripodal structures are observed following 150 °C thermolysis and a number of morphologies are obtained following 175 °C thermolysis. Spherical nanoparticles (diameter = 3.8 (14) nm), rods (length = 11.1 (13) nm and width = 3.2 (12) nm) as well as tripods (length 8.6 (16) nm and width 3.1 (16) nm) are clearly evident.

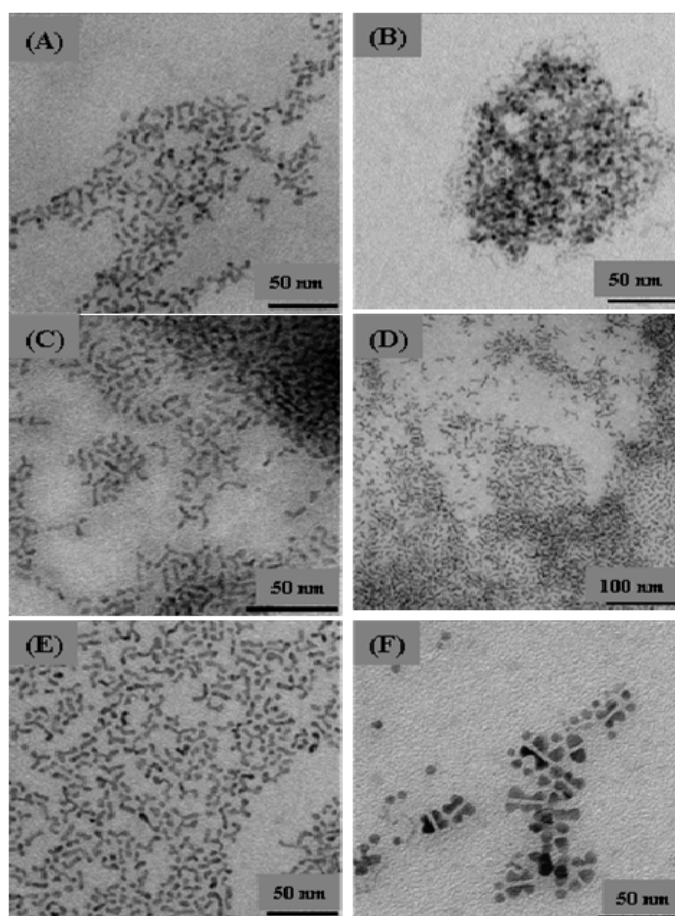


Fig. 3.322

TEM images of CdSe nanoparticles obtained following thermolysis of $[\text{Cd}^{\text{II}}(\text{L}^{\text{Id}}\text{-Se},\text{O})_2]$ at 80, 100, 125, 150, 175 and 200 °C.

Intriguing structures are obtained following thermolysis at 200 °C where apart from spherically shaped particles (diameter = 5.3 (6) nm), nanoparticles with a morphology resembling that of a butterfly are evident. Given the shape and length (12.6 (24) nm) it is likely that these are formed by the agglomeration of two spherical nanoparticles to form one “wing” of the “butterfly”. In Fig. 3.322 (D), a longer structure is also visible where it appears as though 3 nanoparticles have attached to form the structure although this appears to be significantly longer where the average length of both sides = 21.0 (0.05) nm. The reason for the flattened sides in the structures is not clear although the separation distance in various structures appears to be comparable (12.6 (24) nm). It was thought that the capping agent (hexadecylamine) may be responsible for this constant separation distance, however the length of a 16 carbon alkyl chain is approximately 1.89 nm and therefore other factors may be involved in achieving this equidistant separation. It is likely that reaction time plays a significant role in the formation of the “butterfly” structures as TEM analysis of a 10 minute reaction sample, showed only spherical nanoparticles.

The nature of analysing such small material makes it difficult to quantify the degree, if any, of temperature dependant tripodal formation using $[\text{Cd}^{\text{II}}(\text{L}^{\text{1d}}\text{-Se},\text{O})_2]$ as a precursor, however the formation of tripods at least to some extent appears to be possible over a range of different temperatures (125-175 °C).

It is interesting that the degree of anisotropic morphology is significantly increased, over a range of different temperatures, following thermolysis of $[\text{Cd}^{\text{II}}(\text{L}^{\text{1d}}\text{-Se},\text{O})_2]$ as opposed to its shorter alkyl chain analogue $[\text{Cd}^{\text{II}}(\text{L}^{\text{1a}}\text{-Se},\text{O})_2]$. This appears to confirm the possibility of morphology control by tailoring the single source precursor. The mechanism by which this occurs however is not clear. In order to gain a further understanding into this, the thermal decomposition (TGA profiles) of both precursors is revisited.

The TGA profiles and their first derivatives are shown in Fig. 3.323 where approximate three step decomposition profiles are evident for both complexes.

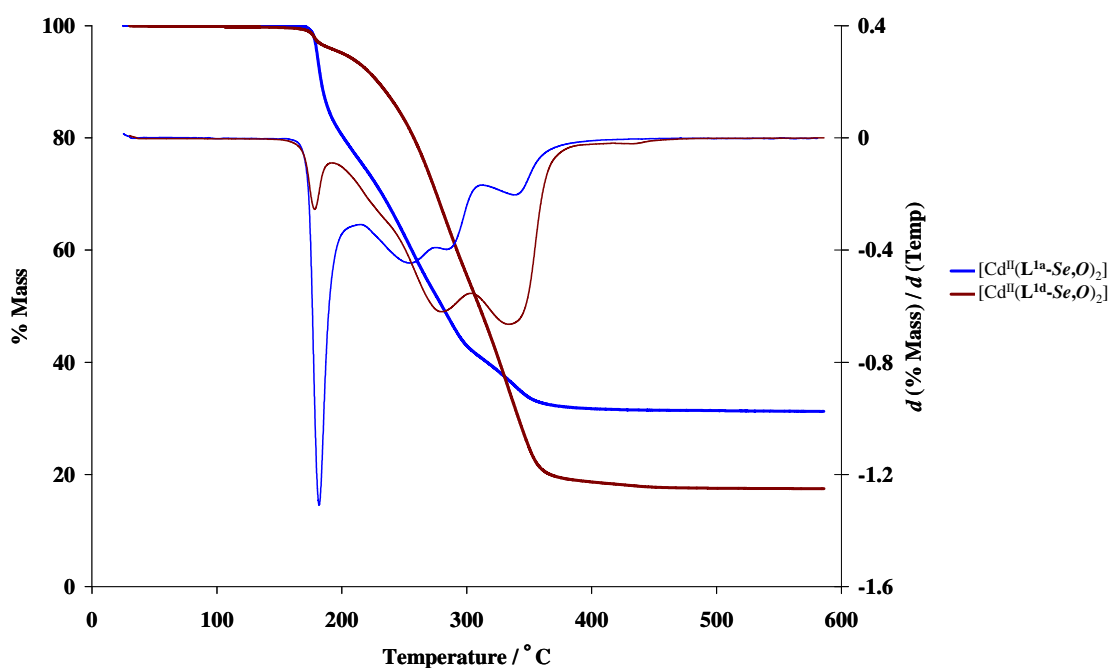


Fig. 3.323 TGA profiles and their first derivatives of $[\text{Cd}^{\text{II}}(\text{L}^{\text{1a}}\text{-Se},\text{O})_2]$ and $[\text{Cd}^{\text{II}}(\text{L}^{\text{1d}}\text{-Se},\text{O})_2]$. Analysis was performed using a ramp rate of 10 °/min.

Whilst the precise mechanism by which decomposition of the (*N,N*-dialkyl-*N'*-benzoylthioureato)Cd(II) complexes occurs is not fully elucidated (Section 2.3.6.2), information about the decomposition can still be obtained. In 1964, Coats and Redfern published a method by which kinetic parameters could be obtained from thermogravimetric data.^[54] Fig. 3.324 shows a plot of $\log_{10}[-\log_{10}(1-\alpha)/T^2]$ against $1/T$, where α = fraction of initial compound decomposed over time and T = temperature (K). The gradient of the plot corresponds to $-E/2.3R$, allowing the relatively facile determination of the activation energy (E) for a particular decomposition. The above derivation is based on the assumption that the decomposition follows that of a first order process.

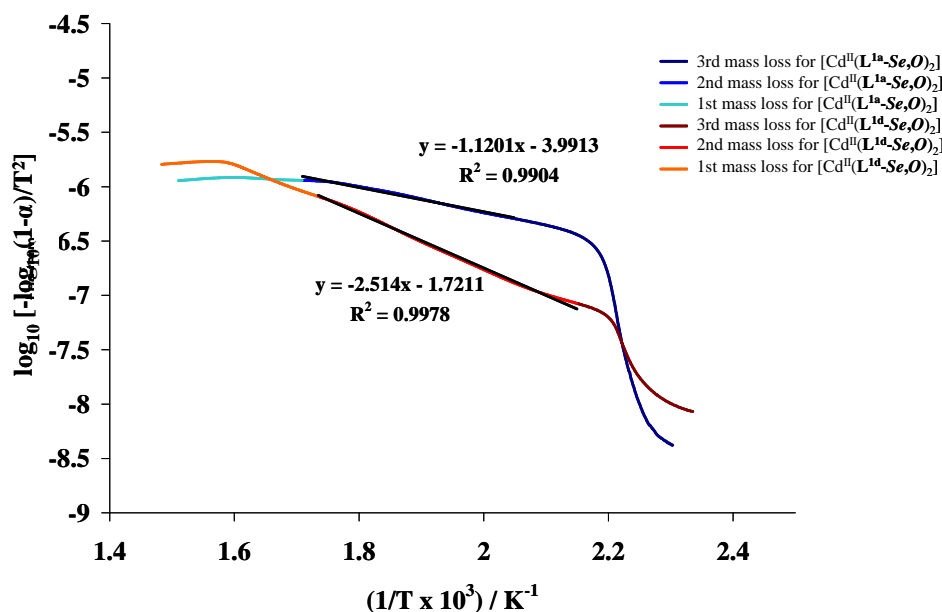


Fig. 3.324 Coats-Redfern analyses of decomposition of $[\text{Cd}^{\text{II}}(\text{L}^{1\text{a}}\text{-Se},\text{O})_2]$ and $[\text{Cd}^{\text{II}}(\text{L}^{1\text{d}}\text{-Se},\text{O})_2]$.

It is clear from the linear sections in Fig. 3.324 that only the 2nd mass losses for both $[\text{Cd}^{\text{II}}(\text{L}^{1\text{a}}\text{-Se},\text{O})_2]$ and $[\text{Cd}^{\text{II}}(\text{L}^{1\text{d}}\text{-Se},\text{O})_2]$ follow a first order reaction and activation energies calculated from this data correspond to 21.4 kJ mol^{-1} for $[\text{Cd}^{\text{II}}(\text{L}^{1\text{a}}\text{-Se},\text{O})_2]$ and more than double that, 48.1 kJ mol^{-1} for $[\text{Cd}^{\text{II}}(\text{L}^{1\text{d}}\text{-Se},\text{O})_2]$. This rather surprising result is in contrast to that recently published by Nair and Scholes.^[55] In this case, the authors determined the activation energies of four different single source precursors, where only one (cadmium thiosemicarbazide) produced anisotropic morphologies, the remaining three producing mostly spherical nanoparticles. These precursors had higher activation energies ranging from $10.9 - 18.2 \text{ kJ mol}^{-1}$, that of the rod producing cadmium thiosemicarbazide being much lower at only 2.1 kJ mol^{-1} . The authors suggest that this lower activation energy allows an increased monomer concentration at the onset of decomposition, relative to the other spherical producing precursors. This gives rise to an environment under kinetic control, which is required for the growth of anisotropic structures. In our case, the reverse is observed, where the mostly spherically producing $[\text{Cd}^{\text{II}}(\text{L}^{1\text{a}}\text{-Se},\text{O})_2]$ exhibits the lower activation energy, and the tripod producing $[\text{Cd}^{\text{II}}(\text{L}^{1\text{d}}\text{-Se},\text{O})_2]$ exhibits slightly more than double this activation energy, suggesting that other factors must play a role in morphology control. It is worth noting here that deductions made by Nair and Scholes are based on hexagonally phased systems, where the differing crystal faces grow at varying rates, thus making the formation of anisotropic structures more easily understood. In our case, the evidence for hexagonally phased material is limited, however if the system is purely cubically phased, a growth regime under kinetic control, should equate to the synthesis of larger spherical nanoparticles as all crystallographic faces should grow at comparable rates. Inferences from the activation energies should therefore be made with caution. It is

possible that the capping agent, hexadecylamine, may contribute to the observations made, as it has previously been noted, that HDA lowers the decomposition temperature of single source precursors. The onset of decomposition for both $[\text{Cd}^{\text{II}}(\text{L}^{\text{1a}}\text{-Se},\text{O})_2]$ and $[\text{Cd}^{\text{II}}(\text{L}^{\text{1d}}\text{-Se},\text{O})_2]$ appears to occur at a similar temperature, however the same effect may be present here, but to differing degrees for both $[\text{Cd}^{\text{II}}(\text{L}^{\text{1a}}\text{-Se},\text{O})_2]$ and $[\text{Cd}^{\text{II}}(\text{L}^{\text{1d}}\text{-Se},\text{O})_2]$.^[15]

Other possible reasons for anisotropic growth include the presence of a reaction by-product as a second surfactant, or capping agent that may act as a structure directing agent.^[55] Ethylenediamine has reportedly behaved as a capping agent,^[56] and nitrogen containing compounds, detected using infrared and elemental analysis, following the thermal decomposition of cadmium thiosemicarbazide have also been thought to contribute to the formation of anisotropic structures. In this context, the possibility of a nitrogen containing species arising from the decomposition of $[\text{Cd}^{\text{II}}(\text{L}^{\text{1d}}\text{-Se},\text{O})_2]$, behaving in a similar fashion seemed likely. In addition, the quantum yield of CdSe nanoparticles obtained following decomposition of $[\text{Cd}^{\text{II}}(\text{L}^{\text{1d}}\text{-Se},\text{O})_2]$ is 8 times larger than that of nanoparticles derived from $[\text{Cd}^{\text{II}}(\text{L}^{\text{1a}}\text{-Se},\text{O})_2]$, suggesting increased surface passivation and the possible presence of a second surfactant leading to the increased emission efficiency of the nanoparticles derived from $[\text{Cd}^{\text{II}}(\text{L}^{\text{1d}}\text{-Se},\text{O})_2]$. To gain further insight into this possibility, elemental analysis of two CdSe nanoparticle samples derived from $[\text{Cd}^{\text{II}}(\text{L}^{\text{1a}}\text{-Se},\text{O})_2]$ and two CdSe nanoparticle samples derived from $[\text{Cd}^{\text{II}}(\text{L}^{\text{1d}}\text{-Se},\text{O})_2]$ were each analysed in duplicate. The mean results indicated that nanoparticles derived from $[\text{Cd}^{\text{II}}(\text{L}^{\text{1a}}\text{-Se},\text{O})_2]$ have a slightly lower nitrogen content, 1.6 % relative to the 3.6 % of nanoparticles derived from $[\text{Cd}^{\text{II}}(\text{L}^{\text{1d}}\text{-Se},\text{O})_2]$. Infrared analysis of both sets of nanoparticles however revealed almost identical spectra, indicative of HDA passivation, with no difference in peak broadness or position to suggest significant differences in the nature of the capping agent.^[55] Given the problematic experience with elemental analysis (Section 2.2), it is improbable that a difference of 2 % can be considered significant, and hence the reason for anisotropic growth may lie elsewhere.

The growth of tetrapodal chalcogenide nanocrystals has recently been investigated by O'Brien and Thomas, where the number of surface atoms is found to decrease when branching takes place. This rather counterintuitive finding means that branching will lead to a lowering in the number of surface atoms in comparison to the growth of another layer on the tetrahedral seed and hence a decrease in the internal energy or maximisation of the lattice energy.^[57] The above findings hold true for both hexagonally and triangularly shaped branches. The calculated size regimes where branching would lead to a maximum change in the percentage of surface atoms is around 3.5 nm for hexagonal and between 2 and 4 nm for triangular branches, where both these value ranges correspond closely to those reported experimentally in the literature. In our case, increasing precursor alkyl chain length resulted in an increase in the particle size and it is therefore likely that decomposition of $[\text{Cd}^{\text{II}}(\text{L}^{\text{1d}}\text{-Se},\text{O})_2]$ could allow the system to reach this size regime whereupon branching of the initial seed takes place to lower the number of surface atoms and hence the internal energy of the system. Conversely, decomposition of $[\text{Cd}^{\text{II}}(\text{L}^{\text{1a}}\text{-Se},\text{O})_2]$ results in smaller nanoparticles, where given the 60 minute reaction period, this size regime is not reached and hence there is little evidence of anisotropic growth.

In summary, alteration of the precursor alkyl chain length does appear to influence the final nanoparticle morphology, in the case of the *N,N*-dialkyl-*N'*-benzoylselenoureas for the formation of CdSe. A similar investigation was therefore undertaken for the *N,N*-dialkyl-*N'*-benzoylthioureas and the formation of CdS.

3.3.3.3 Synthesis of CdS nanoparticles

Equimolar quantities of the precursors, $[\text{Cd}^{\text{II}}(\text{L}^{2\text{b}}-\text{S},\text{O})_2]$, $[\text{Cd}^{\text{II}}(\text{L}^{2\text{c}}-\text{S},\text{O})_2]$, $[\text{Cd}^{\text{II}}(\text{L}^{2\text{d}}-\text{S},\text{O})_2]$ and $[\text{Cd}^{\text{II}}(\text{L}^{2\text{e}}-\text{S},\text{O})_2]$ were thermolysed at 150°C and the absorption spectra of the resulting nanoparticles are shown in Fig.3.325. The previously obtained results from thermolysis of $[\text{Cd}^{\text{II}}(\text{L}^{2\text{a}}-\text{S},\text{O})_2]$ have been included for comparison.

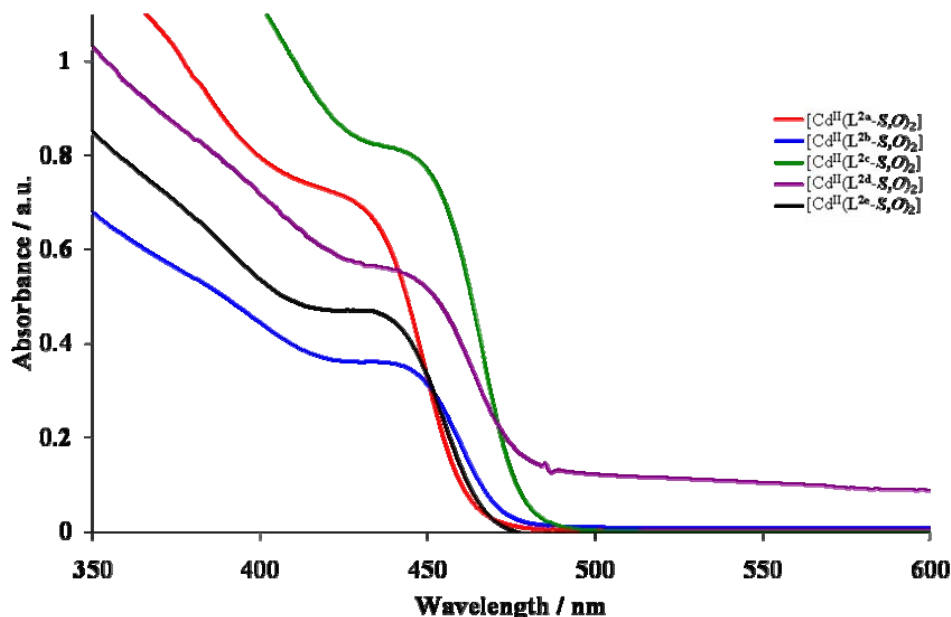


Fig. 3.325 Absorption spectra of CdS nanoparticles obtained following thermolysis of $[\text{Cd}^{\text{II}}(\text{L}^{2\text{a}}-\text{S},\text{O})_2]$, $[\text{Cd}^{\text{II}}(\text{L}^{2\text{b}}-\text{S},\text{O})_2]$, $[\text{Cd}^{\text{II}}(\text{L}^{2\text{c}}-\text{S},\text{O})_2]$, $[\text{Cd}^{\text{II}}(\text{L}^{2\text{d}}-\text{S},\text{O})_2]$ and $[\text{Cd}^{\text{II}}(\text{L}^{2\text{e}}-\text{S},\text{O})_2]$ at 150°C .

Table 3.35 summarises the properties of the CdS nanoparticles obtained. Similarly to the trend observed for the selenium analogues (Table 3.33), a decrease in the band edge is observed with an increase in the alkyl chain length of the precursor. Interestingly, the band edge value obtained for the CdS nanoparticles from the asymmetrically substituted $[\text{Cd}^{\text{II}}(\text{L}^{2\text{e}}-\text{S},\text{O})_2]$ lies in between that of nanoparticles derived from $[\text{Cd}^{\text{II}}(\text{L}^{2\text{a}}-\text{S},\text{O})_2]$ and $[\text{Cd}^{\text{II}}(\text{L}^{2\text{b}}-\text{S},\text{O})_2]$, whereas for the CdSe nanoparticles, the band edge value lies in between that of nanoparticles derived from the longer chain $[\text{Cd}^{\text{II}}(\text{L}^{1\text{c}}-\text{Se},\text{O})_2]$ and $[\text{Cd}^{\text{II}}(\text{L}^{1\text{d}}-\text{Se},\text{O})_2]$. As for the selenium analogues, quantum confinement is conserved in the nanoparticles derived from each precursor.

Fig. 3.326 illustrates the emission spectra, where the trend is slightly different to that observed in Fig. 3.311.

Table 3.35 Properties of CdS nanoparticles obtained following thermolysis of $[\text{Cd}^{\text{II}}(\text{L}^{2\text{a-e}}-\text{S},\text{O})_2]$ at 150°C for 60 minutes.

Precursor	Band edge / nm	Band edge / eV	Average size / nm (std. dev. %)*	Average size / nm (Scherrer Eqn ^[25])	FWHM / nm	Emission maxima / nm
$[\text{Cd}^{\text{II}}(\text{L}^{2\text{a}}-\text{S},\text{O})_2]$	464	2.67	3.0 (15)	1.6	35.5	452.5
$[\text{Cd}^{\text{II}}(\text{L}^{2\text{b}}-\text{S},\text{O})_2]$	475	2.61	3.1 (16)	2.5	42.5	464.5 579 [†]
$[\text{Cd}^{\text{II}}(\text{L}^{2\text{c}}-\text{S},\text{O})_2]$	480	2.58	3.2 (14)	3.4	32.5	470.5
$[\text{Cd}^{\text{II}}(\text{L}^{2\text{d}}-\text{S},\text{O})_2]$	485	2.56	3.1 (13)	3.5	34	467.5
$[\text{Cd}^{\text{II}}(\text{L}^{2\text{e}}-\text{S},\text{O})_2]$	468	2.65	3.1 (14)	3.0	40.5	459.5

* from TEM data

[†] second emission maximum

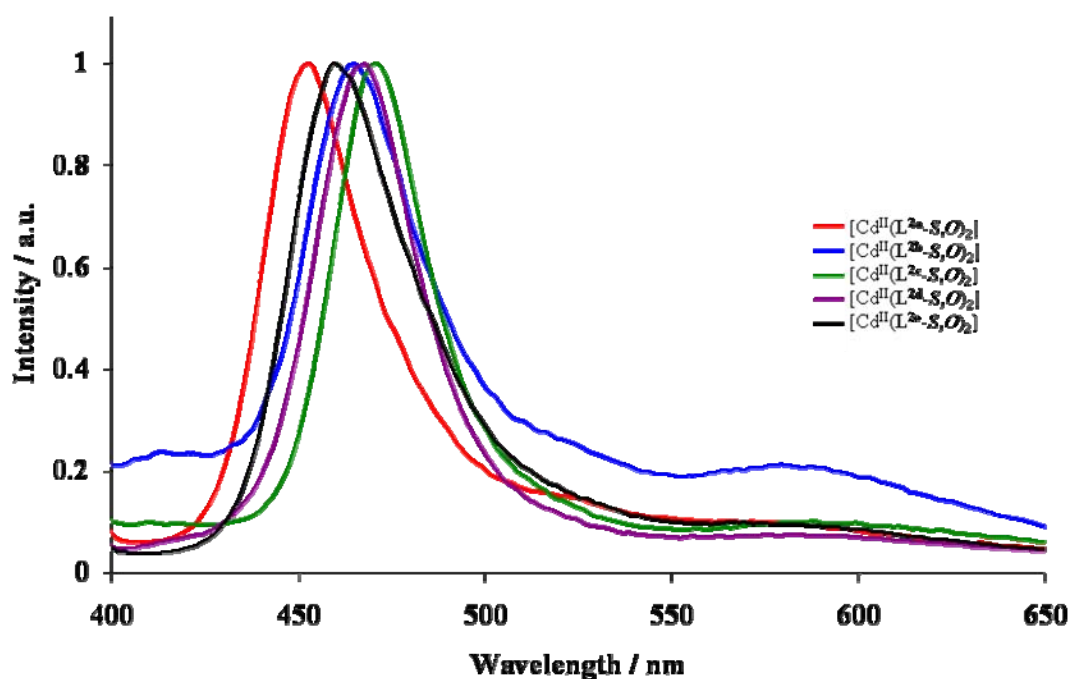


Fig. 3.326 Emission spectra of CdS nanoparticles obtained following thermolysis of $[\text{Cd}^{\text{II}}(\text{L}^{2\text{a}}-\text{S},\text{O})_2]$, $[\text{Cd}^{\text{II}}(\text{L}^{2\text{b}}-\text{S},\text{O})_2]$, $[\text{Cd}^{\text{II}}(\text{L}^{2\text{c}}-\text{S},\text{O})_2]$, $[\text{Cd}^{\text{II}}(\text{L}^{2\text{d}}-\text{S},\text{O})_2]$ and $[\text{Cd}^{\text{II}}(\text{L}^{2\text{e}}-\text{S},\text{O})_2]$ at 150 °C.

The most blue shifted emission maximum is observed for nanoparticles derived from $[\text{Cd}^{\text{II}}(\text{L}^{2\text{a}}-\text{S},\text{O})_2]$, however the largest red shift is exhibited by nanoparticles derived from $[\text{Cd}^{\text{II}}(\text{L}^{2\text{c}}-\text{S},\text{O})_2]$. An emission maximum of only 467.5 nm is exhibited by CdS nanoparticles from the longest chain precursor, $[\text{Cd}^{\text{II}}(\text{L}^{2\text{d}}-\text{S},\text{O})_2]$. It should be noted here, that the CdSe emission maxima span a significantly larger wavelength range (557.5 – 611 nm) than that observed from CdS nanoparticles (452.5 – 470.5 nm), illustrating the increased degree of “tunability” offered by CdSe.^[58] The emission spectrum of nanoparticles obtained following thermolysis of $[\text{Cd}^{\text{II}}(\text{L}^{2\text{b}}-\text{S},\text{O})_2]$ displays a longer wavelength emission centred around 579 nm. The emission spectrum from a sample obtained after a 10 minute reaction time, displayed 3 clear emission maxima of similar intensity at 455.5, 523.5 and 568 nm. The two longer wavelength emissions decreased in intensity as the reaction progressed, and the band edge emission became more intense, where at 60 minutes the intensity of that at 579 nm is only 21.3 % of the band edge emission. Similar although not as striking observations were made for CdS nanoparticles derived from all other precursors at 150 °C. This is reminiscent of the longer wavelength emission discussed in Section 3.3.2.2 and would appear to confirm its temperature dependant nature, rather than being influenced by the nature of the precursor. Interestingly no evidence of the shorter wavelength emission observed in CdSe nanoparticle synthesis (Section 3.3.3.1) is apparent here. As for the CdSe nanoparticles, the FWHM values (Table 3.35) obtained from the CdS nanoparticles do not exhibit a trend with increasing precursor alkyl chain length, it is worth noting however, that the CdS emissions appear in general to be slightly narrower than those of the corresponding CdSe emissions.

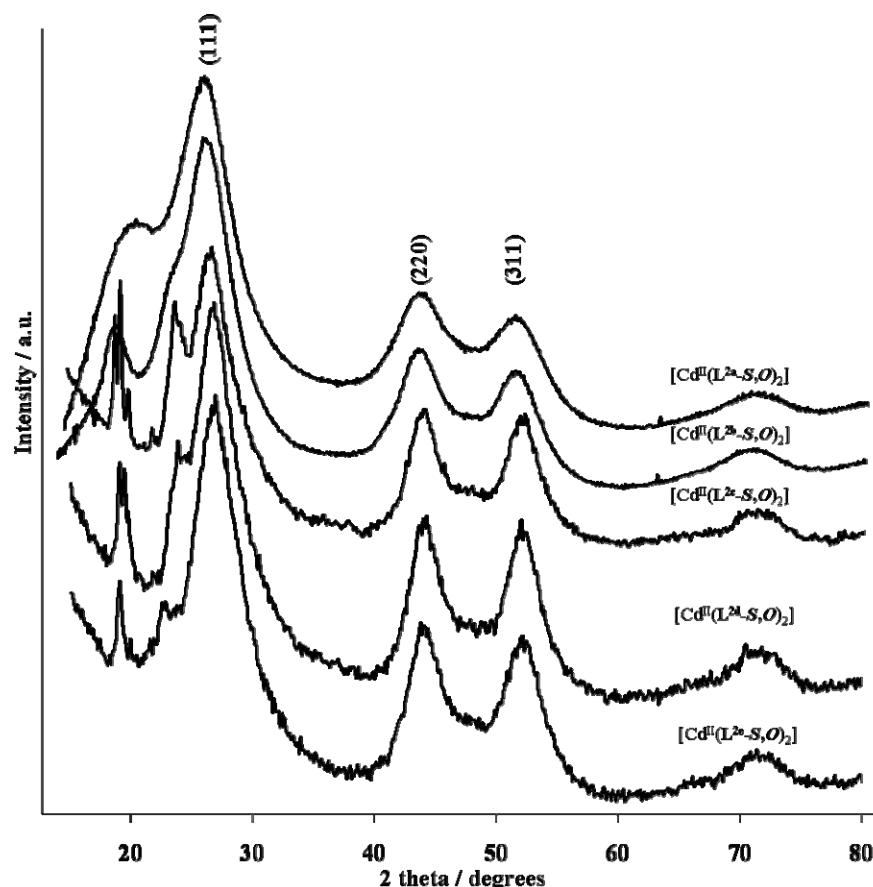


Fig. 3.327 PXRD patterns of CdS nanoparticles obtained following thermolysis of $[\text{Cd}^{\text{II}}(\text{L}^{2\text{a}}-\text{S},\text{O})_2]$, $[\text{Cd}^{\text{II}}(\text{L}^{2\text{b}}-\text{S},\text{O})_2]$, $[\text{Cd}^{\text{II}}(\text{L}^{2\text{c}}-\text{S},\text{O})_2]$, $[\text{Cd}^{\text{II}}(\text{L}^{2\text{d}}-\text{S},\text{O})_2]$ and $[\text{Cd}^{\text{II}}(\text{L}^{2\text{e}}-\text{S},\text{O})_2]$ at 150 °C.

Each precursor gives rise to cubically phased CdS (Fig. 3.327) where unlike the CdSe nanoparticles, the intensity of both the (220) and (311) peaks remain similar with increasing precursor alkyl chain lengths. Particle sizes obtained using the (220) peak, are given in Table 3.35 where a clear trend is evident between increasing particle size and precursor alkyl chain length. Once again, sharp peaks indicative of a highly crystalline material are evident at low angles, these being more clearly evident where the alkyl chain length of the precursor is increased. The degree of this crystalline material however, appears to be slightly less in the CdS nanoparticles than in the corresponding CdSe nanoparticles.

From the TEM data (Fig. 3.328), almost exclusively spherical nanoparticles were formed from all precursors and little evidence of anisotropic growth could be obtained. Where possible, several hundred nanoparticles were counted and the particle sizes obtained are all analogous at 3.1 nm in diameter (Table 3.35).

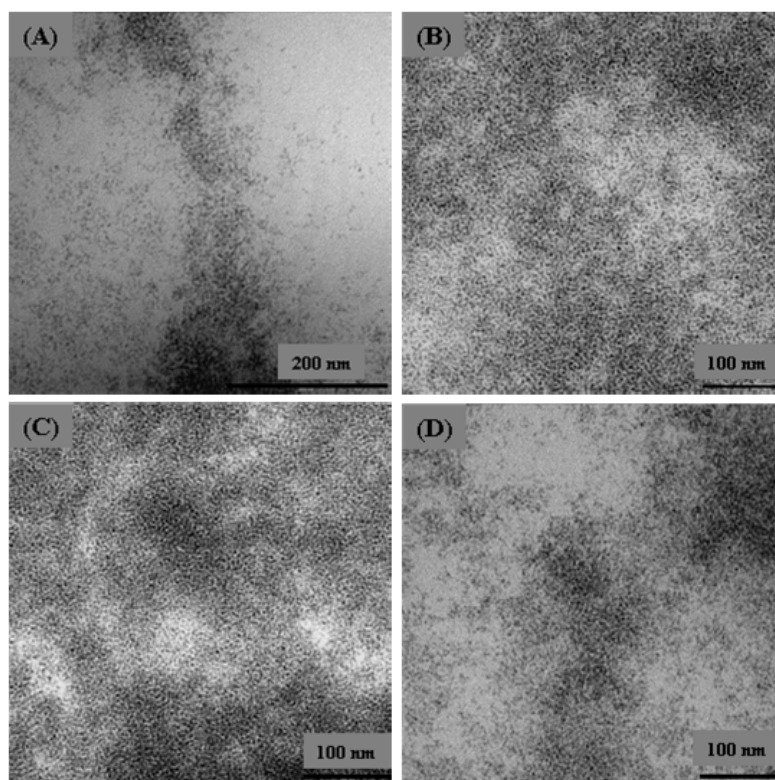


Fig. 3.328 TEM images of CdS nanoparticles obtained following thermolysis of (A) $[\text{Cd}^{\text{II}}(\text{L}^{2\text{b}}\text{-S},\text{O})_2]$, (B) $[\text{Cd}^{\text{II}}(\text{L}^{2\text{c}}\text{-S},\text{O})_2]$, (C) $[\text{Cd}^{\text{II}}(\text{L}^{2\text{d}}\text{-S},\text{O})_2]$ and (D) $[\text{Cd}^{\text{II}}(\text{L}^{2\text{e}}\text{-S},\text{O})_2]$ at 150 °C.

The above results indicate that in the case of the *N,N*-dialkyl-*N'*-benzoylthiourea Cd(II) complexes, increasing alkyl chain length exhibits little morphology control on the resulting CdS nanoparticles. No evidence of the tripodal and bipodal structures observed following thermolysis of $[\text{Cd}^{\text{II}}(\text{L}^{1\text{d}}\text{-Se},\text{O})_2]$ could be found in the nanoparticles derived from the sulfur analogue. The following section describes a brief investigation into the influence of precursor concentration on resulting nanoparticle morphology.

3.3.4 Concentration dependence studies

3.3.4.1 Synthesis of CdSe nanoparticles

In order to raise the chemical potential of the reaction environment, double the concentration of $[\text{Cd}^{\text{II}}(\text{L}^{1\text{d}}\text{-Se},\text{O})_2]$ was thermolysed at 150 °C. It was thought that an increased chemical potential could lead to a growth regime under kinetic control and the possible formation of either longer rods, or tripods with increased rod length. Fig.3.329 illustrates the optical spectra obtained, where the previously obtained results using a lower concentration of $[\text{Cd}^{\text{II}}(\text{L}^{1\text{d}}\text{-Se},\text{O})_2]$ are included (solid line) for comparison purposes. Curiously the increased concentration results in a blue shift in the band edge from 653 nm to 594.7 nm, and this is coupled with a blue shift in the emission maximum from 597.5 nm to 582 nm. As Fig. 3.330 (A) shows, the phase of CdSe is maintained where once again the (220) peak exhibits an increased intensity relative to the (311) peak. Particle sizes obtained from the PXRD data show a smaller particle size of 4.2 nm at the higher precursor concentration relative to that of 5.4 nm obtained using 0.858 mmol of $[\text{Cd}^{\text{II}}(\text{L}^{1\text{d}}\text{-Se},\text{O})_2]$. This trend is reflected in the TEM images (Fig. 3.330 (B)), where the average rod length of 8.7 (14) nm and width (2.4 (16) nm) observed at the higher concentration is smaller than that observed at the lower concentration (rod length = 10.0 (7) nm and width = 2.7 (12) nm). In addition it appears as though fewer rods are present in the TEM images obtained from the 1.715 mmol experiment and spherical nanoparticles with 3.6

(11) nm diameters were clearly visible. It would therefore appear that an increase in monomer concentration leads to smaller nanoparticles however this is contrary to all previous reports describing similar experiments and it is therefore likely that other factors may be playing a role. Unfortunately due to the limited time available in which to complete the project, this experiment could not be repeated to confirm the trends observed.

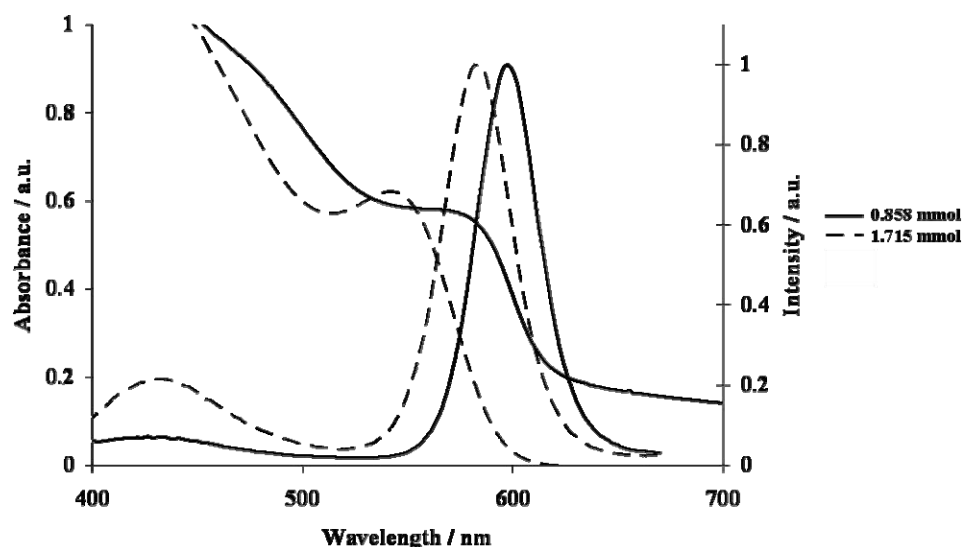


Fig. 3.329 Optical spectra of CdSe nanoparticles obtained following thermolysis of 0.858 mmol and 1.715 mmol of $[\text{Cd}^{\text{II}}(\text{L}^{\text{1d}}\text{-Se},\text{O})_2]$ at 150 °C for 60 minutes.

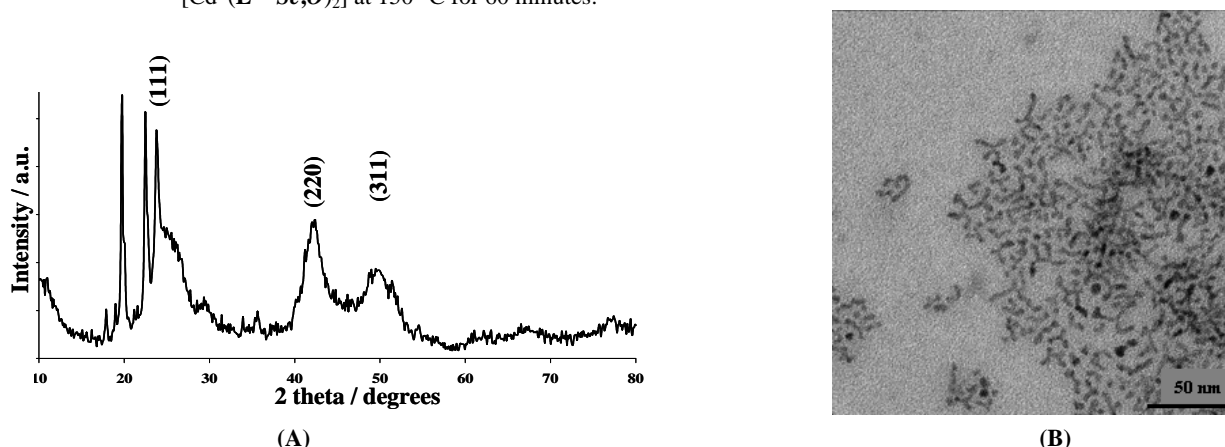


Fig. 3.330 PXRD pattern (A) and TEM image (B) of CdSe nanoparticles obtained following thermolysis of 1.715 mmol of $[\text{Cd}^{\text{II}}(\text{L}^{\text{1d}}\text{-Se},\text{O})_2]$ at 150 °C for 60 minutes.

3.3.4.2 Synthesis of CdS nanoparticles

Similarly to the above experiment, the influence of precursor concentration on nanoparticle morphology was investigated for $[\text{Cd}^{\text{II}}(\text{L}^{\text{2a}}\text{-S},\text{O})_2]$ where more than twice the precursor concentration was injected at 150 °C. From the absorption spectra (Fig. 3.331 (A)) a clear red shift of 16 nm occurred, where the band edge of the CdS nanoparticles obtained from the 2.14 mmol experiment is 480 nm. This is reflected, although to a lesser degree, in the emission spectra where the 0.858 mmol experiment yielded CdS with an emission maximum of 425.5 nm relative to that of the 2.14 mmol experiment of 455.5 nm. A larger FWHM (42.5 nm) is also observed for the higher concentration. The PXRD pattern shows cubically phased CdS and as expected the TEM images (Fig.3.331 (B)) illustrate a spherical morphology. An increase in nanoparticle diameter is observed with increasing precursor

concentration where the 2.14 mmol experiment yields nanoparticles 3.4 (17) nm in diameter, and the 0.858 mmol experiment, nanoparticles 3.0 (15) nm in diameter.

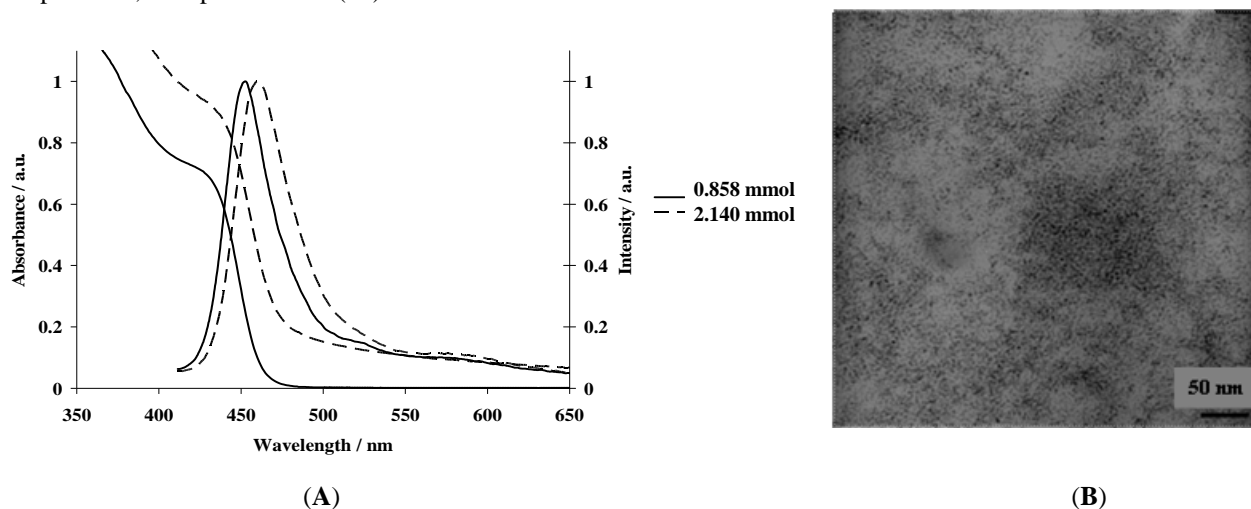


Fig. 3.331 Optical spectra (A) of CdS nanoparticles obtained following thermolysis of 0.858 mmol and 2.140 mmol $[\text{Cd}^{\text{II}}(\text{L}^{2\text{a}}-\text{S},\text{O})_2]$ and TEM image (B) of CdS nanoparticles obtained following 2.140 mmol thermolysis.

Further examination of this precursor was undertaken at a higher temperature (200 °C) where 1.715 mmol of $[\text{Cd}^{\text{II}}(\text{L}^{2\text{a}}-\text{S},\text{O})_2]$ was thermolysed for 60 minutes. The reaction at the higher concentration very quickly becomes uncontrollable at this elevated temperature as within 30 minutes, quantum confinement is no longer observed and the band edge following a 60 minute reaction is 599 nm relative to that of 494 nm from the lower concentration (Fig. 3.332). A less marked red shift is also seen in the emission spectra where the emission maximum at 472 nm is obtained from the more concentrated reaction mixture. Similarly to Fig. 3.331 (A) an increased FWHM of 39.5 nm is observed for CdS nanoparticles from the 2.140 mmol reaction.

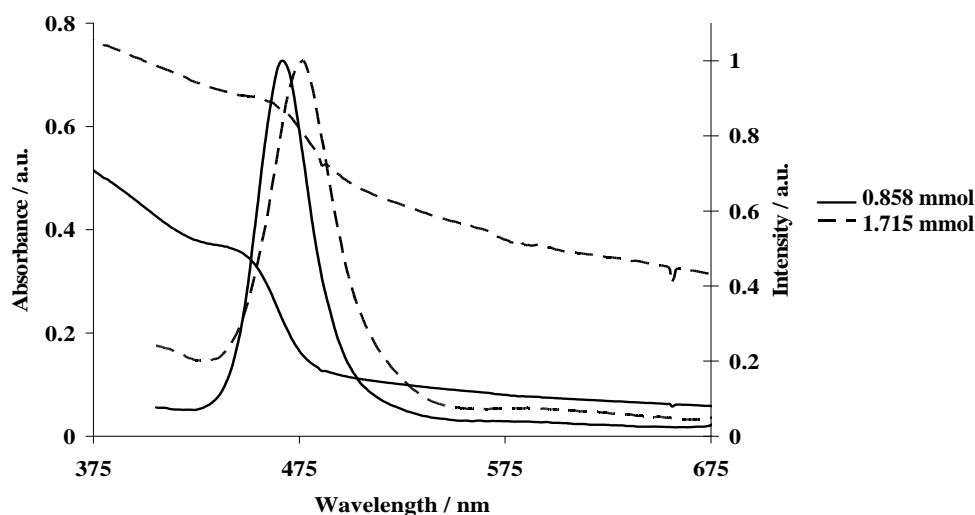


Fig. 3.332 Optical spectra of CdS nanoparticles obtained following thermolysis of 0.858 mmol and 1.715 mmol $[\text{Cd}^{\text{II}}(\text{L}^{2\text{a}}-\text{S},\text{O})_2]$ at 200 °C.

Microscopic analysis yielded some very interesting structures (Fig. 3.333). The CdS nanoparticles are exclusively spherical with diameters of 3.7 (14) nm, slightly larger than those obtained from a less concentrated reaction mixture (3.5 (15) nm), however they appear to undergo a type of “self assembly” to form the large rod-like structures seen in Fig. 3.333. The edges of the rod-like structure appear to be composed of denser regions of the spherical

nanoparticles. At first glance these structures are reminiscent of those observed for CdSe nanoparticles following thermolysis of $[\text{Cd}^{\text{II}}(\text{L}^{\text{H}}\text{-Se},\text{O})_2]$ (Fig. 3.315), possibly caused by solvent evaporation, however closer inspection reveals several interesting differences. The length of the CdS structures is on average significantly shorter (350 nm) than those of the CdSe structures as are the widths of 48 – 91 nm relative to the 87.7 – 141.2 nm observed for the CdSe structures. In addition, the CdS “rods” are less well defined, particularly at each end where no structure boundary is evident and it appears as though nanoparticles are in some kind of dynamic state, either joining or leaving the larger structure. Conversely in the CdSe nanostructures, well defined ends are clearly evident. In the CdS structures, the density of spherical nanoparticles appears to be larger in the body of the structure whereas in the case of CdSe, the edges of the structures appear to have a larger nanoparticle density, whilst the body of the structures are relatively sparsely “populated”. As in the previous case, the mechanism by which these structures are formed remains unclear, but is most likely solvent and evaporation rate dependant.

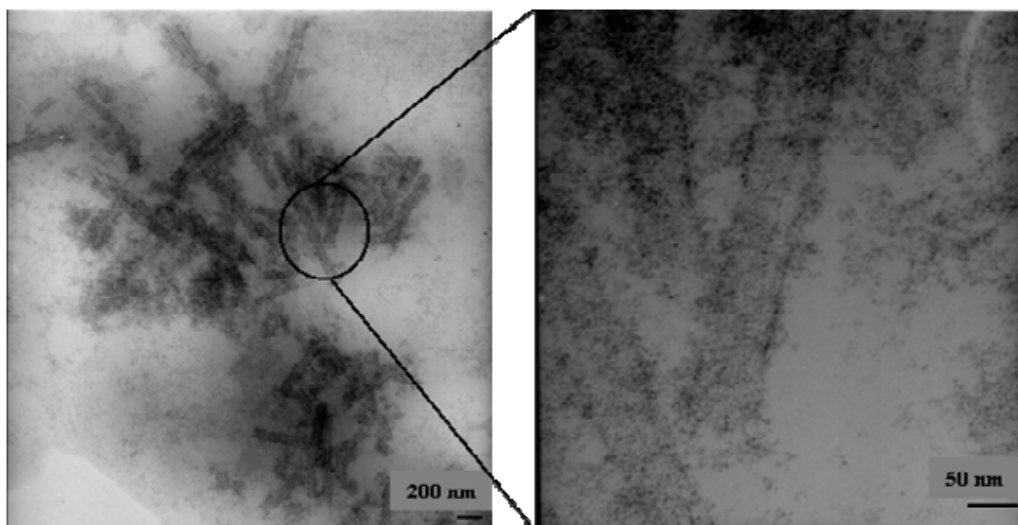


Fig. 3.333 TEM images of CdS nanoparticles obtained following thermolysis of 1.715 mmol $[\text{Cd}^{\text{II}}(\text{L}^{2\text{a}}\text{-S},\text{O})_2]$ at 200 °C.

Solutions containing these structures were left to “age” for a period of approximately 16 weeks after which they were reanalysed using TEM. Fig. 3.334 shows that whilst the above structures are no longer evident, an interesting alteration has taken place over time.

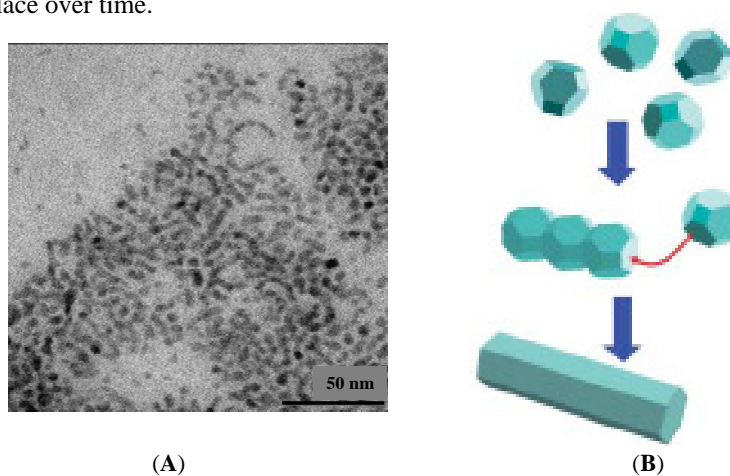


Fig. 3.334 TEM of CdS nanoparticles obtained following thermolysis of 1.715 mmol $[\text{Cd}^{\text{II}}(\text{L}^{2\text{a}}\text{-S},\text{O})_2]$ at 200 °C and a 16 week “ageing” period (A) and (B) pictorial representation of orientated attachment growth mechanism adapted from Ref [59].

Anisotropic structures are clearly visible, where previously, exclusively spherical nanoparticles were observed. The average rod lengths are 8.3 (23) nm and widths 3.0 (18) nm. The rod width is only slightly less than the average diameter of the previously observed spherical nanoparticles (3.7 (14) nm) suggesting that the mechanism of formation could be via “orientated attachment.” This has previously been reported for ZnS as well as CdTe systems^[60, 61] This mechanism of growth can occur when nearly isotropic nanoparticles are initially formed in solution, followed by their combination in a particular direction leading to the formation of anisotropic structures (Fig. 3.334 (B)).^[59] Although the exact driving force of this mechanism is not known it is thought that the coalescence of nanoparticles in this fashion may reduce the overall surface energy of the structure through removal of high energy facets. Despite the apparent crystal lattice symmetry in cubically phased CdS, the presence of dipole-dipole interactions is possible, these being brought about by charging chalcogen surface states.^[45] The magnitude of these interactions were studied in CdSe and ZnSe systems by Shim and Guyot-Sionnest and found to be linearly dependant on the semiconductor core radius.^[45] It is known that weakly coordinating stabilisers can enhance these dipole-dipole interactions. In our case the use of weakly coordinated HDA suggests that this growth mechanism may be responsible for the structures seen here. In addition, this growth mechanism may also be responsible for the formation of the ‘butterfly’ CdSe structures following high temperature thermolysis of $[\text{Cd}^{\text{II}}(\text{L}^{\text{1d}}\text{-Se},\text{O})_2]$ (Fig. 3.322(F)).

The following section describes a preliminary investigation into the thermolysis of a range of different metal complexes. As the *N,N*-dialkyl-*N'*-benzoylseleno- and -thioureas coordinate to a variety of transition metal ions, they are potential single source precursors for a number of different materials. In order to gain some idea of metal complexes with the largest potential, several were separately thermolysed under related conditions and the results are discussed below.

3.3.5 Selected precursor thermolysis

3.3.5.1 Thermolysis of $[\text{Cd}^{\text{II}}(\text{L}^{\text{1a}}\text{-Se},\text{O})(\text{L}^{\text{2a}}\text{-S},\text{O})]$, 11211

The “mixed ligand complex”, (*N,N*-diethyl-*N'*-benzoylselenoureato,*N,N*-diethyl-*N'*-benzoylthioureato)Cd(II), $[\text{Cd}^{\text{II}}(\text{L}^{\text{1a}}\text{-Se},\text{O})(\text{L}^{\text{2a}}\text{-S},\text{O})]$ containing both sulfur and selenium could possibly be used for the synthesis of alloyed nanoparticles of the type CdSe_xS_y . To investigate the possibility of this, the precursor was thermolysed at two different temperatures and the optical spectra are shown in Fig. 3.335. Thermolysis at the lower temperature yielded nanoparticles with a 577 nm band edge and a bimodal emission where the minor emission occurred at 445.5 nm and the most intense emission at 547 nm. The higher energy emission exhibited interesting behaviour as it was not evident in the initial samples withdrawn 10 minutes into the reaction period. As time progressed however it became more intense from 12.4 % relative to that of the emission at lower energy at 30 minutes to 15.4 % at 45 minutes. This was followed by a decrease in relative intensity to 14.1 % as shown in Fig. 3.335 at 60 minutes. Comparison with the optical properties of CdSe and CdS nanoparticles formed from the thermolysis of $[\text{Cd}^{\text{II}}(\text{L}^{\text{1a}}\text{-Se},\text{O})]$ and $[\text{Cd}(\text{L}^{\text{2a}}\text{-S},\text{O})]$, Tables 3.31 and 3.32 respectively, shows that the band edge obtained resembles that of nanoparticles with a higher percentage of CdSe relative to CdS. This is also reflected in the major emission of 547 nm, this being very similar to the wavelength obtained for related CdSe nanoparticles of 557.5 nm. The minor emission however suggests a percentage of CdS formation and its appearance only 30 minutes into the reaction implies differing nucleation rates for the formation of CdS and CdSe under these conditions.

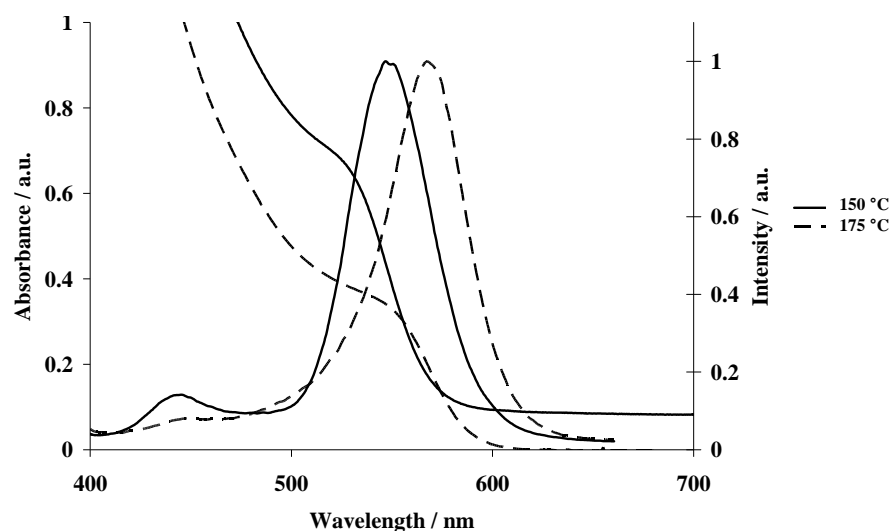


Fig. 3.335 Optical spectra of nanoparticles obtained following 60 minute thermolysis of $[\text{Cd}^{\text{II}}(\text{L}^{1\text{a}}\text{-Se},\text{O})(\text{L}^{2\text{a}}\text{-S},\text{O})]$ at 150 and 175 °C.

These results also suggest the initial and rapid decomposition of the acylselenourea section of the chelate in the precursor resulting in the formation of CdSe as observed. As the reaction progresses the acylthiourea section of the chelate decomposes resulting in the formation of CdS. These observations confirm those made in Chapter 2 where the increased stability of the acylthiourea ligands was noted relative to their selenium counterparts. In addition the Cd metal centre showed preference for the acylselenourea relative to the acylthiourea and it is therefore likely that solvation of the precursor in TOP prior to injection allowed the dissociation of the acylthiourea section of the chelate, where the intermediate species formed may be stabilised by the electron rich TOP. Injection of the mixture would then result in the initial formation of CdSe as the Se donor atom was already bonded to the Cd metal centre. Formation of CdS would require more time as it is likely that a lower percentage of S atoms would be bonded to the Cd metal centre at injection. It should be noted that the relative intensities of the two emission peaks can not be used as an indication of the relative quantities of material as CdSe is generally more emissive than CdS.

Precursor thermolysis at 175 °C resulted in an expected red shift in the band edge (589 nm) this again resembling that of CdSe more than CdS. These results are reflected in the emission spectrum where the major emission is red shifted to 567.5 nm. Interestingly at 60 minutes there is very little evidence of the higher energy emission and the behaviour of this emission band is quite different to that at 150 °C. 10 minutes into the reaction the intensity of this higher energy emission is 21 % relative to that of the major emission and as the reaction proceeds it decreases in intensity to only 8 % of the major emission at 60 minutes. The behaviour of the precursor is therefore quite different at the higher temperature and the rates of CdS and CdSe nucleation may resemble each other more closely under these conditions.

The optical spectra alone however provide very little insight as to the exact nature of the nanoparticles formed, where several possibilities as to their nature exist. Firstly, separate CdS and CdSe nanoparticles could form, secondly, alloyed nanoparticles of the nature CdSe_xS_y could form, these either being homogenous or exhibiting a gradient, and finally although unlikely, core/shell nanoparticles could form where it is possible, given the above observations, that CdSe would be coated by CdS layers.

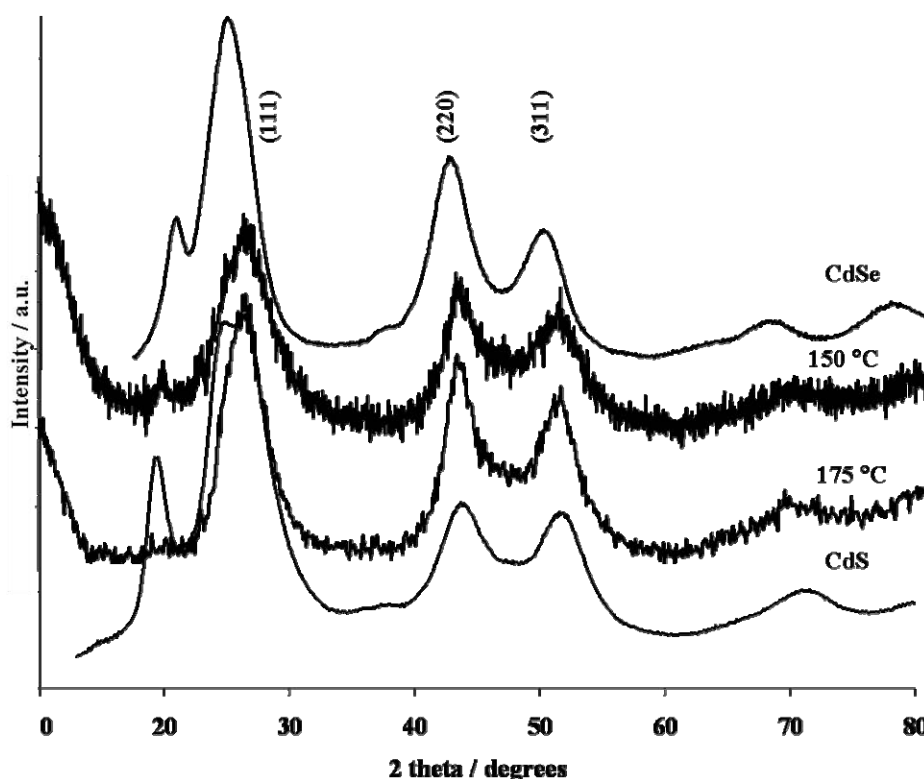
Table 3.36 Properties of nanoparticles obtained following thermolysis of $[\text{Cd}^{\text{II}}(\text{L}^{1\text{a}}\text{-Se},\text{O})(\text{L}^{2\text{a}}\text{-S},\text{O})]$ at 150 and 175 °C for 60 minutes.

Temp. / °C	Band edge / nm	Band edge / eV	Average size / nm (std. dev. %)*	Average size / nm (Scherrer Eqn ^[25])	FWHM / nm	Emission maxima / nm
150	577	2.15	spherical 2.9 (21)	4.0	48	445.5 [‡] 547
175	589	2.10	spherical 3.2 (21) rod length 7.1 (30) rod width 2.5 (12) bipod length 8.2 (12) bipod width 2.7 (12) tripod length 7.4 (21) tripod width 2.5 (12)	4.1	48	567.5

* from TEM data

‡ second emission maximum

The PXRD data is shown in Fig. 3.336 where CdSe and CdS patterns obtained from the 150 °C thermolysis of $[\text{Cd}^{\text{II}}(\text{L}^{1\text{a}}\text{-Se},\text{O})]$ and $[\text{Cd}(\text{L}^{2\text{a}}\text{-S},\text{O})]$ have been included for comparison. It is clear that the nanoparticles obtained from $[\text{Cd}^{\text{II}}(\text{L}^{1\text{a}}\text{-Se},\text{O})(\text{L}^{2\text{a}}\text{-S},\text{O})]$ thermolysis are cubically phased and resemble CdS lattice spacing more closely than that of CdSe. Given the optical properties of the nanoparticles, this observation is rather unexpected. This data does however support the formation of alloyed nanoparticles as separate populations of CdS and CdSe nanoparticles would manifest as a superposition of pure CdS and CdSe patterns.^[62] PXRD patterns of core/shell nanoparticles are also known to be between those of the core and shell material however it is unlikely that this is the case here.

**Fig. 3.336** PXRD patterns of nanoparticles obtained following 150 and 175 °C thermolysis of $[\text{Cd}^{\text{II}}(\text{L}^{1\text{a}}\text{-Se},\text{O})(\text{L}^{2\text{a}}\text{-S},\text{O})]$ as well as CdS and CdSe patterns obtained from the 150 °C thermolysis of $[\text{Cd}(\text{L}^{2\text{a}}\text{-S},\text{O})]$ and $[\text{Cd}^{\text{II}}(\text{L}^{1\text{a}}\text{-Se},\text{O})]$ respectively, for comparison.

The morphology of the resulting nanoparticles was investigated and TEM images are shown in Fig. 3.337. Images obtained from the 150 °C precursor thermolysis were of very poor quality and despite several attempts, beam stability and contrast on the microscope could not be enhanced. It is however possible to conclude that nanophased

material was formed, and most likely a combination of spherical and possibly anisotropic structures although the latter could not be distinguished clearly enough to enable quantification. Several spherical nanoparticles could however be measured and the results are given in Table 3.36. Thermolysis at a higher temperature resulted in larger spherical nanoparticles, confirming observation made from the optical data and PXRD patterns (Table 3.36), and several other interesting morphologies. Numerous, well defined bipod structures could be identified as well as isolated rods and tripods. In each case the length of the anisotropic structures are comparable and in the region of 7.4 nm and the width of each structure is slightly smaller than that of the diameters of the spherical nanoparticles, 2.5 nm relative to 3.2 nm. Unfortunately, the available microscopic resolution was not sufficient to distinguish between CdS and CdSe. In HRTEM instrumentation, the image contrast is dependant on the electron density inside the object. Where the lattice parameters are similar and as it has fewer electrons per unit cell, CdS would therefore be expected to manifest reduced contrast relative to CdSe, and this has previously been used to confirm core/shell structures as opposed to alloys, however with the available instrumentation in South Africa, this resolution can not be attained.^[63]

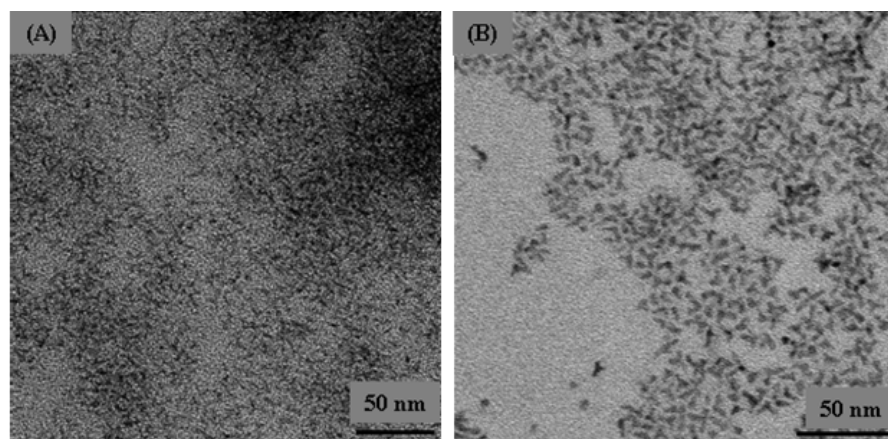


Fig. 3.337 TEM images of nanoparticles obtained following 150 °C (A) and 175 °C (B) thermolysis of $[\text{Cd}^{\text{II}}(\text{L}^{\text{1a}}\text{-Se},\text{O})(\text{L}^{\text{2a}}\text{-S},\text{O})]$.

In conclusion, with the experimental evidence obtained, the exact nature of the nanoparticles formed following thermolysis of $[\text{Cd}^{\text{II}}(\text{L}^{\text{1a}}\text{-Se},\text{O})(\text{L}^{\text{2a}}\text{-S},\text{O})]$ can not be clearly ascertained, however more extensive investigation of the precursor *i.e.* thermolysis at differing temperatures and different concentrations, would yield a larger series of results from which several helpful deductions could be made. It is likely that under these conditions, nanoparticles with differing sizes would be synthesised and the PXRD patterns could confirm initial observations made here, where larger particle sizes, result in a narrowing of the XRD peaks, suggesting the formation of alloyed nanoparticles.^[63] It is interesting to note that attempts at alloyed nanoparticle synthesis usually involve the use of separate metal and chalcogen precursors,^[62, 64] this, to the best of our knowledge, is the first time that this type of synthesis has been attempted using the single source precursor approach.

3.3.5.2 Thermolysis of $[\text{Zn}^{\text{II}}(\text{L}^{\text{1a}}\text{-Se},\text{O})_2]$, 113

Zinc selenide is a wide band gap semiconductor and like its cadmium counterpart it is also a direct band gap semiconductor.^[65] Two stable phases are known, cubic and hexagonal where the band gap sizes are in the region of 2.82 and 2.87 eV respectively.^[66] Very few reports on the synthesis of ZnSe nanoparticles exist,^[67] particularly where the single source precursor approach has been used,^[2, 23] and of these fairly high temperatures (250 °C) have

been necessary to effect precursor decomposition.^[68] Doping of ZnSe has however allowed the synthesis of nanoparticles with a tuneable emission over a wide range of wavelengths.^[65] As the *N,N*-dialkyl-*N'*-benzoylselenourea ligands are well known to coordinate to Zn(II),^[69] the precursor $[\text{Zn}^{\text{II}}(\text{L}^{\text{1a}}\text{-Se,O})_2]$, **113** was synthesised and thermolysed in an attempt to synthesise ZnSe nanoparticles. The PXRD pattern and TEM image of the nanoparticles obtained are shown in Fig. 3.338 (A and B respectively). The low angle peaks in the PXRD pattern are in similar 2 theta positions to the contaminants previously seen and the broader less intense peaks are reminiscent of hexagonally phased ZnSe however the position of the experimental peaks, 56.6, 63.0 and 67.5 ° are significantly shifted to higher angles than those expected for this phase of ZnSe, 46, 50 and 54 °. Further examination of this pattern showed that the experimental peaks correspond very closely to those expected for ZnO (56.6, 62.8 and 67.9 °). The lower angle (100) and (101) reflections are also visible however that of (002) is noticeable in its absence. The small particle size results in the extensive peak broadening visible and the absence of the (002) peak could be attributed to this.^[66]

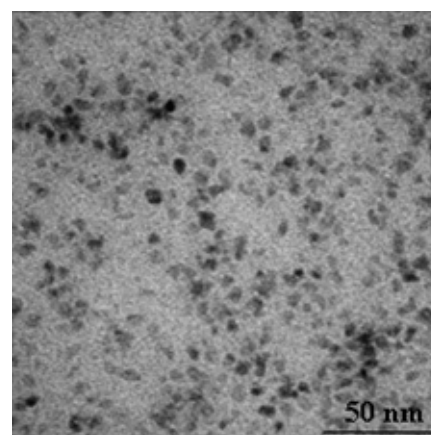
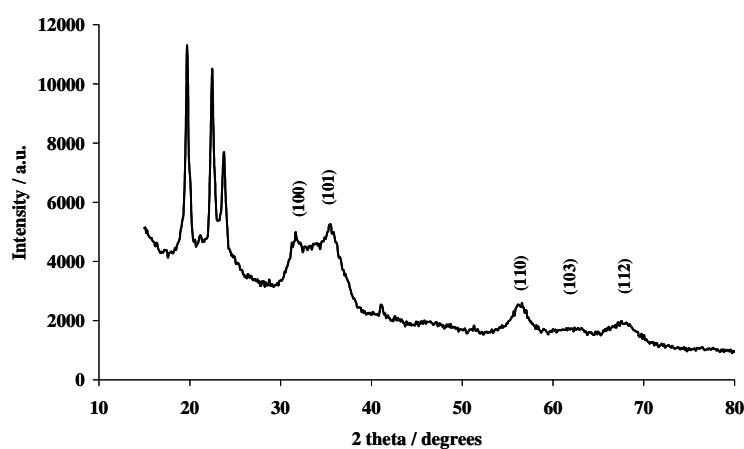


Fig. 3.338 PXRD pattern and TEM image of nanoparticles obtained following thermolysis of $[\text{Zn}^{\text{II}}(\text{L}^{\text{1a}}\text{-Se,O})_2]$ at 150 °C for 60 mins.

The TEM image (Fig. 3.338 (B)) shows well defined spherical nanoparticles 3.4 (16) nm in diameter. Clearly the Zn(II) metal centre shows a preference for the O donor atom as opposed to Se and this can be understood in terms of Pearson's "Hard and Soft Acids and Bases".^[70] The optical properties of the resulting nanoparticles are shown in Fig. 3.339 where a band edge of 367 nm (3.38 eV) was calculated for the 60 minute sample. This is very similar to the 3.37 eV reported for the bulk band gap of ZnO.^[71] The nanoparticles appear to exhibit a bimodal emission centred around 417 and 520 nm and this could indicate 2 sets of emissive nanoparticles or the longer wavelength emission could be attributed to zinc interstitials or oxygen vacancies,^[72] indicating low crystallinity in the nanoparticles where the latter case seems more likely from examination of the PXRD pattern.

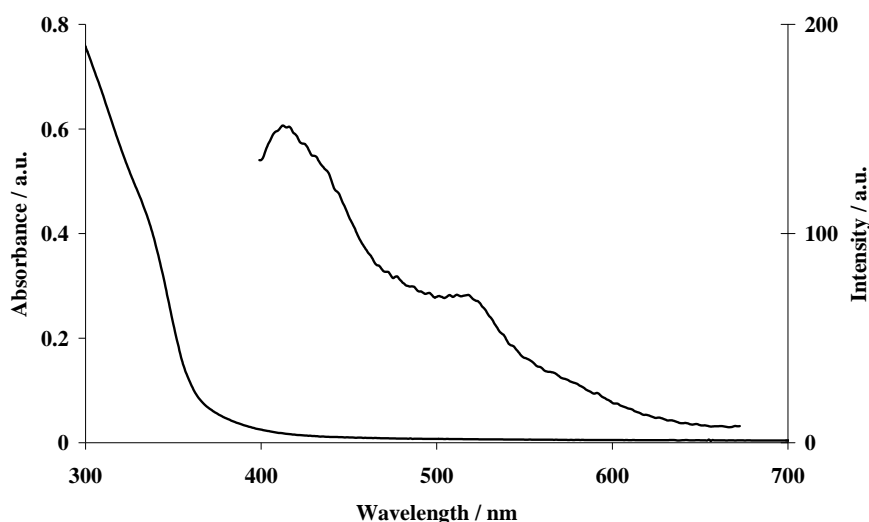


Fig. 3.339 Optical spectra of nanoparticles obtained following thermolysis of $[\text{Zn}^{\text{II}}(\text{L}^{1\text{a}}\text{-Se},\text{O})_2]$ at 150 °C for 60 mins.

The $[\text{Zn}^{\text{II}}(\text{L}^{1\text{a}}\text{-Se},\text{O})_2]$ precursor therefore shows clear potential for the synthesis of Zn chalcogen nanoparticles and variations of reaction conditions could alter the preference of Zn for O or Se donor atoms and could lead to the formation of nanoparticles with very interesting compositions. ZnO nanoparticles have previously been made from thermal decomposition of single source precursors such as zinc ketoacidoximate,^[73] and thin films have been deposited by MOCVD using methylzinc isopropoxide and methylzinc *tert*-butoxide single source precursors.^[74] In many cases, however ZnO synthesis results in emission spectra largely consisting of defect emission bands. Generally it is thought that ZnO with low defect densities could be prepared by using precursors with preformed Zn-O bonds, and given the relatively limited number of single source precursors that have been reported in this context, the potential of $[\text{Zn}^{\text{II}}(\text{L}^{1\text{a}}\text{-Se},\text{O})_2]$ as a single source precursor is vast.

3.3.5.3 Thermolysis of $[\text{Zn}^{\text{II}}(\text{L}^{2\text{a}}\text{-S},\text{O})_2]$, 213

Several reports on the synthesis of ZnS nanoparticles using the single source precursor approach have appeared in recent years, largely concentrating on the use of (*N*-alkyldithiocarbamato)Zn(II) complexes.^[4, 5, 7, 75, 76] Like its selenium counterpart, ZnS has stable sphalerite (cubic) and wurtzite (hexagonal) phases, the former being favoured by the bulk material under ambient conditions with a band gap of 340 nm (3.65 eV). The energy difference between the two structures is very small however and this, and the similarities between the two, allow for the formation of various polytypes that differ only slightly in energy. In addition, the wurtzite phase can be more stable than the cubic phase on the nanoscale.^[77] Yu and co-workers have also found that the ratio of cubic to hexagonally phased material is dependant on nanoparticle size, where nanoparticles containing both phases have been formed.^[60] Given the behaviour of $[\text{Zn}^{\text{II}}(\text{L}^{1\text{a}}\text{-Se},\text{O})_2]$ and the ZnO nanoparticles formed, it was with interest that $[\text{Zn}^{\text{II}}(\text{L}^{2\text{a}}\text{-S},\text{O})_2]$ was thermolysed under similar conditions. The PXRD pattern and TEM image of the resultant nanoparticles are shown in Fig. 3.340.

The broad PXRD peaks make absolute assignment of the phase quite difficult, however the pattern in Fig. 3.340 has been indexed to that of cubically phased ZnS, even though the (220) and (311) reflections do not correspond entirely to those expected for ZnS. The reason for this slight alteration in the *d* spacing is not certain, but may arise from the small size of the nanoparticles. Microscopic analysis reveals small spherical nanoparticles, the average measured size of 2.3 nm (17) comparing well with that calculated from the PXRD data (2.2 nm). The optical spectra of the

nanoparticles are shown in Fig. 3.341 where the band edge of 333 nm is slightly blue shifted relative to that of the bulk material. The emission spectrum of the nanoparticles obtained from a 60 minute reaction shows a very broad emission centred around 420 nm. Given the calculated band edge of 333 nm it is highly unlikely that this is due to band edge emission, but rather to deep trap emission, possibly caused by surface sulfur vacant sites.^[42, 77]

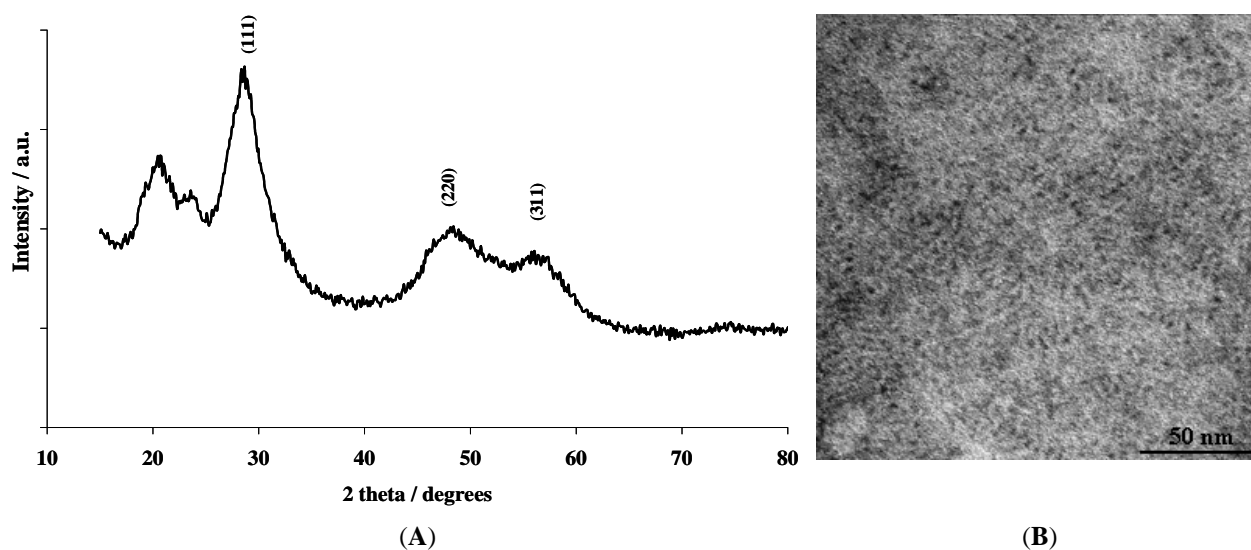


Fig. 3.340 PXRD pattern (A) and TEM image (B) of ZnS nanoparticles obtained following thermolysis of $[\text{Zn}^{\text{II}}(\text{L}^{2\text{a}}\text{-S}, \text{O})_2]$ at 150 °C for 60 minutes.

In this context, the presence of a weak defect band in the 440 nm region has previously been reported to be a common occurrence in the formation of ZnS nanoparticles.^[15] The emission spectrum from nanoparticles obtained 30 minutes into the reaction (dotted line Fig. 3.341) reveals a second shorter wavelength emission at 349.5 nm and this is likely to be the band edge emission. It is interesting that this is the only sample (from 10, 30, 45 and 60 minute samples) that showed this emission.

The complex $[\text{Zn}^{\text{II}}(\text{L}^{2\text{a}}\text{-S}, \text{O})_2]$ can therefore be used as a single source precursor for the synthesis of ZnS nanoparticles and examination of this precursor under varying conditions, could optimise the properties of the resulting nanoparticles.

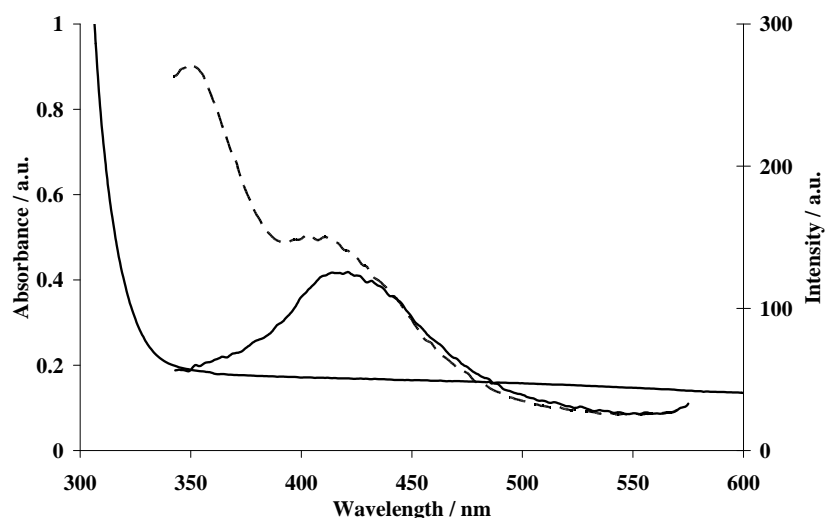


Fig. 3.341 Optical spectra of ZnS nanoparticles obtained following thermolysis of $[\text{Zn}^{\text{II}}(\text{L}^{2\text{a}}\text{-S}, \text{O})_2]$ at 150 °C for 60 minutes, dotted line (-----) illustrates the emission spectrum obtained 30 minutes into the reaction.

3.3.5.4 Thermolysis of $cis\text{-}[\text{Ni}^{\text{II}}(\text{L}^{2a}\text{-S},\text{O})_2]$, 215

As part of our interest in d^8 metal ions, $[\text{Ni}^{\text{II}}(\text{L}^{2a}\text{-S},\text{O})_2]$ was synthesised and thermolysed under similar conditions to those used previously. The PXRD pattern of the resulting material and TEM images are shown in Fig. 3.342 (A and B) respectively.

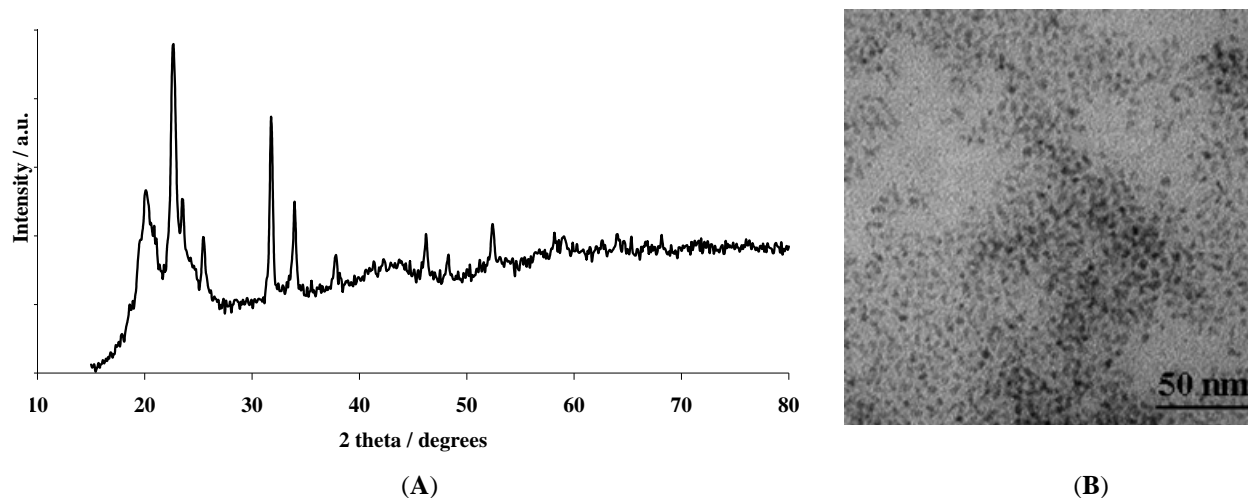


Fig. 3.342 PXRD pattern (A) and TEM image (B) of nanoparticles obtained following thermolysis of $cis\text{-}[\text{Ni}^{\text{II}}(\text{L}^{2a}\text{-S},\text{O})_2]$ at 150 °C for 60 minutes.

Several geological nickel sulfide phases are known and reference PXRD patterns for many of these are available, such as godlevskite (Ni_9S_8), heazelwoodite (Ni_3S_2), millerite (NiS), polydimite (Ni_3S_4), Ni_7S_6 and $\text{Ni}_{17}\text{S}_{18}$. The above PXRD pattern shows several well defined peaks however none of these correspond to any of the above mentioned phases. Given the behaviour of the $[\text{Zn}^{\text{II}}(\text{L}^{1a}\text{-Se},\text{O})_2]$ precursor, nickel oxide phases (NiO_2 and NiO) as well as that of nickel were examined, however once again, no match for the experimental pattern could be found. The exact nature of the formed material is therefore not certain, however the TEM image shows well formed spherical nanoparticles, 3.1 (14) nm in diameter. This complex therefore shows potential as a single source precursor, however further work would be necessary to optimize conditions for the isolation of good quality material. As shown in the next chapter, this is likely to be a phase of nickel sulfide.

3.3.5.5 Thermolysis of $[\text{Co}^{\text{III}}(\text{L}^{2a}\text{-S},\text{O})_3]$, 216

The precursor $[\text{Co}^{\text{III}}(\text{L}^{2a}\text{-S},\text{O})_3]$ was thermolysed under similar reaction conditions to those used previously and a 60 minute reaction period yielded the material whose TEM is shown in Fig. 3.343.

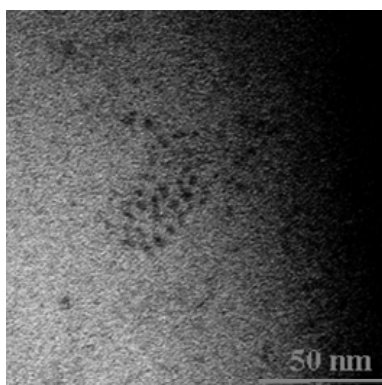


Fig. 3.343 TEM image of nanoparticles obtained following thermolysis of $[\text{Co}^{\text{III}}(\text{L}^{2a}\text{-S},\text{O})_3]$ at 200 °C for 60 minutes.

Spherical nanoparticles, 3.4 (19) nm in diameter can be made out from the image however following PXRD analysis the nanoparticles proved to be largely amorphous making their composition difficult to ascertain. ESI analysis indicated the presence of cobalt and oxygen on the TEM grid, and further examination of this precursor could lead to the optimisation of reaction conditions.

3.3.5.6 Thermolysis of $cis\text{-}[\text{Pd}^{\text{II}}(\text{L}^{2a}\text{-S},\text{O})_2]$, 212

As part of our interest in d^8 metal ions and the PGM's in particular the complex $cis\text{-}[\text{Pd}^{\text{II}}(\text{L}^{2a}\text{-S},\text{O})_2]$ was synthesised and thermolysed under conditions similar to those used previously in the thermolysis of $cis\text{-}[\text{Ni}^{\text{II}}(\text{L}^{2a}\text{-S},\text{O})_2]$. The absorption spectrum obtained from the resulting material as well as a TEM image are shown in Fig. 3.344 (A and B). Very little information has been reported on the synthesis of nanosized PGM chalcogenides and only one documents the formation of PdS nanoparticles using the single source precursor approach.^[12] In this report a band edge of 455 nm (2.71 eV) was recorded for the PdS nanoparticles, and this compares well with that of 454 nm (2.73 eV) obtained from our nanoparticles. Interestingly however, our nanoparticles were found to be non-emissive. This could possibly have arisen from incomplete capping of the nanoparticles, but is most likely related to their poor crystallinity as PXRD analysis indicated the formation of amorphous material. The TEM image shows the formation of very well defined spherical nanoparticles, 2.9 (22) nm in diameter, with a rather large size distribution. ESI analysis indicated the presence of both sulfur and palladium and it is therefore likely that the nanoparticles are a phase of palladium sulfide. Several phases of palladium sulfide are known, *e.g.* Pd₄S, Pd₃S, Pd₁₆S₇, PdS₂ and Zubkov and co-workers calculated the enthalpies of formation of several of these phases, where that of PdS was found to be the most stable.^[78]

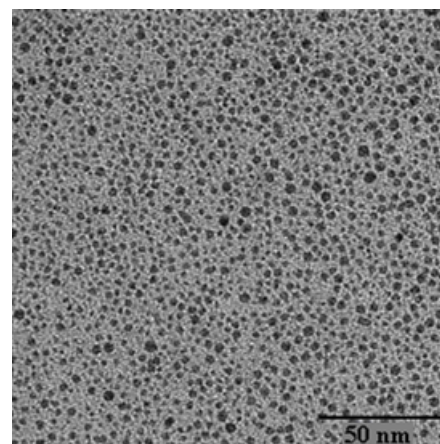
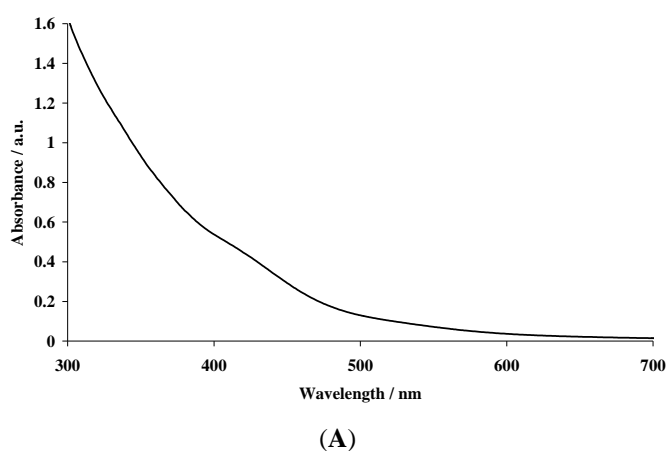


Fig. 3.344 Absorption spectrum (A) and TEM image (B) of nanoparticles obtained following thermolysis of $cis\text{-}[\text{Pd}^{\text{II}}(\text{L}^{2a}\text{-S},\text{O})_2]$ at 200 °C for 40 minutes.

In the crystal structure of this phase, the planar coordination of the metal atoms by four chalcogens and the tetrahedral coordination of the chalcogen atoms by four metal atoms, is evident (Fig. 3.345).^[79]

EDAX analysis of the nanoparticles revealed a Pd:S ratio of 1.33:1 suggesting a Pd₄S₃ phase of palladium sulfide, however no such phase is known and given the low concentration of the two elements in the nanoparticulate matter, precise determination of the elemental ratios is unlikely and the formation of the PdS phase seems more probable.

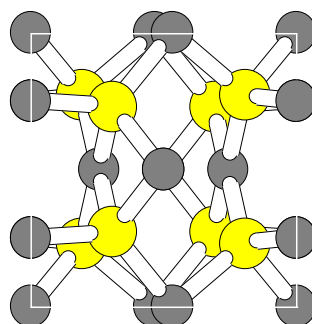


Fig. 3.345 Structure of PdS where \bullet = Pd, and \bullet = S, viewed down the a axis. Obtained using Ref [80].

Several applications of palladium sulfides have been documented including their catalytic use in hydrogenation reactions such as the hydrogenation of thiophenes to tetrahydrothiophenes where PdS on an aluminosilicate support showed markedly higher activity than other PGM sulfides. The hydrogenation of gasoline pyrolysis residue over palladium sulfide on aluminium oxide and that of naphthalene to tetralin over carbon supported palladium sulfide has also been reported.^[81] Both PdS and PtS have been engaged as light image receiving materials with silver halides and palladium sulfide has also been employed for lithographic plates and films with high resolution.^[81] Only one other report could be found documenting the synthesis of PdS nanoparticles where separate PdCl₂ and Na₂S precursors resulted in the formation of PdS nanoparticles 20 – 30 nm in diameter when grown in acidic medium and nanoparticles 2-5 nm when grown in alkaline medium. No PXRD data was reported, however the nanoparticles were deposited onto circuit boards and facilitated the electroplating of copper.^[82] Calculations performed by Raybaud and co-workers suggest semiconducting properties for PdS (band gap ~ 2.0 eV) as well as PtS^[81, 83] and this confirms previous reports by Hulliger where semiconductivity in Ni-group compounds of the type M_mX_x is only possible if $m < x$, hence palladium sulfide phases such as Pd₄S are not expected to be semiconducting.^[84] Given the above number of potential applications for nanoparticulate palladium sulfide and the likely formation of PdS using the [Pd^{II}(L^{2a}-S,O)₂] precursor, further examination of thermolysis temperatures and other reaction conditions could yield interesting results from this precursor.

3.3.5.7 Thermolysis of *cis*-[Pt^{II}(L^{2a}-S,O)₂], 214

The uses of platinum sulfide are very similar to those given above for palladium sulfide, such as catalytic use in hydrogenation reactions and as a light image receiving material.^[81] Platinum sulfide has also been used in the catalytic dehydrogenative polycondensation of 1,2,3,4-tetrahydroquinoline, providing a direct route to the synthesis of unsubstituted quinoline oligomers.^[81] Platinum sulfide has two stable phases, PtS and PtS₂, where the former has been calculated to have semiconducting properties,^[83] and a band gap of ~1.41 eV,^[81] the solid state structure is shown in Fig. 3.346. The tetragonal cooperate structure is simpler, but closely related to that of PdS.^[79]

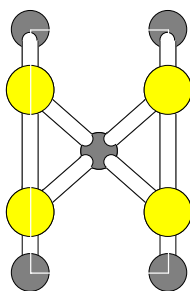


Fig. 3.346 Structure of PtS where \bullet = Pt, and \bullet = S, viewed down the b axis. Obtained using Ref [80].

As with PdS, to the best of our knowledge, only one report exists documenting the synthesis of PtS nanoparticles using the single source precursor route.^[12] A strong excitonic peak at 360 nm and a band edge of 410 nm were reported. Nanoparticles obtained following thermolysis of *cis*-[Pt^{II}(L^{2a}-S,O)₂] exhibited a band edge of 370 nm and an emission spectrum with dual maxima (Fig. 3.347 (A)). The lower wavelength emission at 391 nm is likely to be the band edge emission and the longer wavelength emission at 531.5 nm is most likely due to deep trap emission.

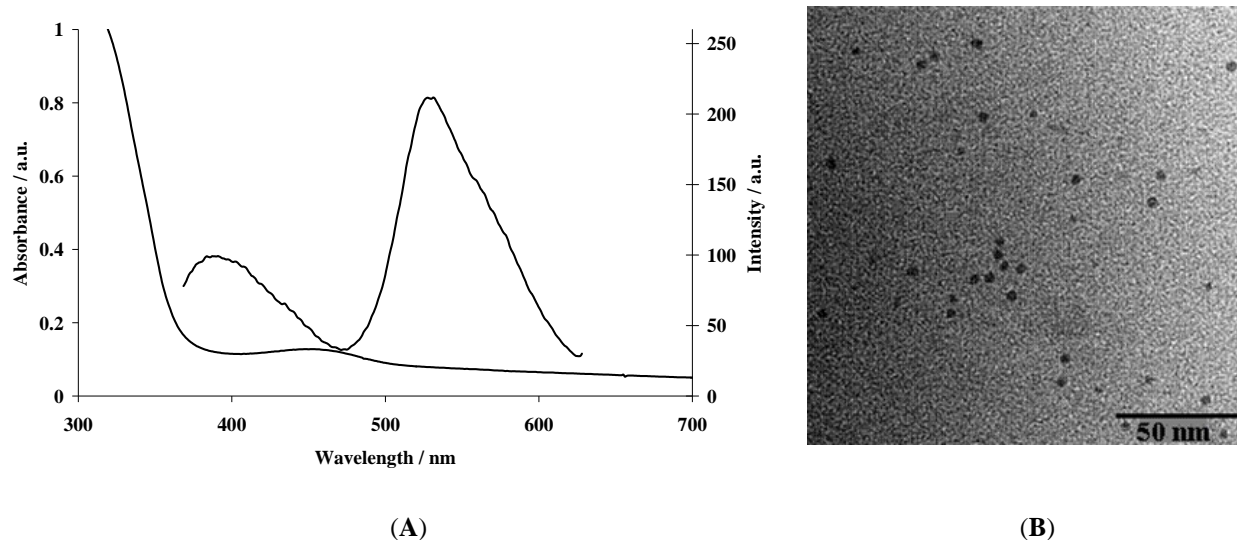


Fig. 3.347 Optical spectra (A) and TEM image (B) of nanoparticles obtained following thermolysis of *cis*-[Pt^{II}(L^{2a}-S,O)₂] at 200 °C for 40 minutes.

As observed previously for *cis*-[Pd^{II}(L^{2a}-S,O)₂] thermolysis, the PXRD of the resulting material showed very poor crystallinity and the presence of largely amorphous material. EDAX analysis of the residue showed a Pt : S ratio of 1 : 1.37, however as explained previously, the elemental ratio is likely to be closer to 1 : 1. TEM analysis showed nanoparticles 3.6 (11) nm in diameter, with a relatively low particle size distribution. The *cis*-[Pt^{II}(L^{2a}-S,O)₂] precursor therefore does show potential for the formation of PtS nanoparticles.

3.3.5.8 Thermolysis of *cis*-[Pd^{II}(L^{1a}-Se,O)₂], 112

Many different phases of palladium selenide are known and these include PdSe,^[85] Pd₃Se, Pd₄Se, Pd₇Se, Pd₈Se, PdSe₂, Pd₇Se₂, Pd₇Se₄, Pd₁₇Se₁₅ and Pd₃₄Se₁₁.^[81] The superconductivity of several of these phases have been reported,^[86, 87] however very little has been documented about the semiconducting ability of these phases. The calculated band gap of PdSe was found to be 0.4 eV, however, as density functional calculations have a tendency to underestimate the experimental band gap, the experimental value could be closer to 1eV.^[88] Recently, several palladium complexes with a variety of different ligand systems have been thermally decomposed in a furnace and the PXRD pattern of the resulting residue found to correspond to that of Pd₁₇Se₁₅. These include palladium complexes of dichalcogenoimidophosphinate ligands,^[89] monoselenocarboxylates,^[90] 3-dimethylaminopropyl selenolates,^[91] 2-methoxycarbonyl ethylselenolates,^[93] and benzoylselenolates.^[94] The structure of PdSe and Pd₁₇Se₁₅ are shown in Fig. 3.348 (A and B) where the former is tetragonal and the latter has cubic symmetry. In each of these phases as with that shown for PdS, the metal ion is bonded to four Se atoms in a square planar geometry and each Se atom is bonded to four Pd atoms which are tetrahedrally orientated around it.

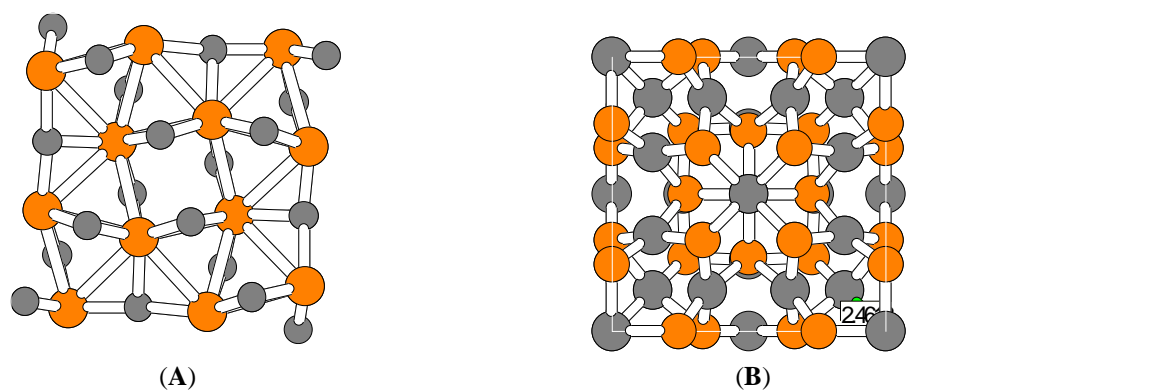


Fig. 3.348 Structure of tetragonal PdSe (A) viewed down the c axis and cubic Pd₁₇Se₁₅ (B), where \bullet = Pd and \bullet = Se. Obtained using Ref [80].

To the best of our knowledge, no report exists on the thermolysis of a single source precursor to form capped palladium selenide nanoparticles. It was therefore with interest that cis -[Pd^{II}(L^{1a}-Se₂O)₂] was injected into HDA at 200 °C. The absorbance spectrum and TEM image of the resulting nanoparticles are shown in Fig. 3.349 (A and B).

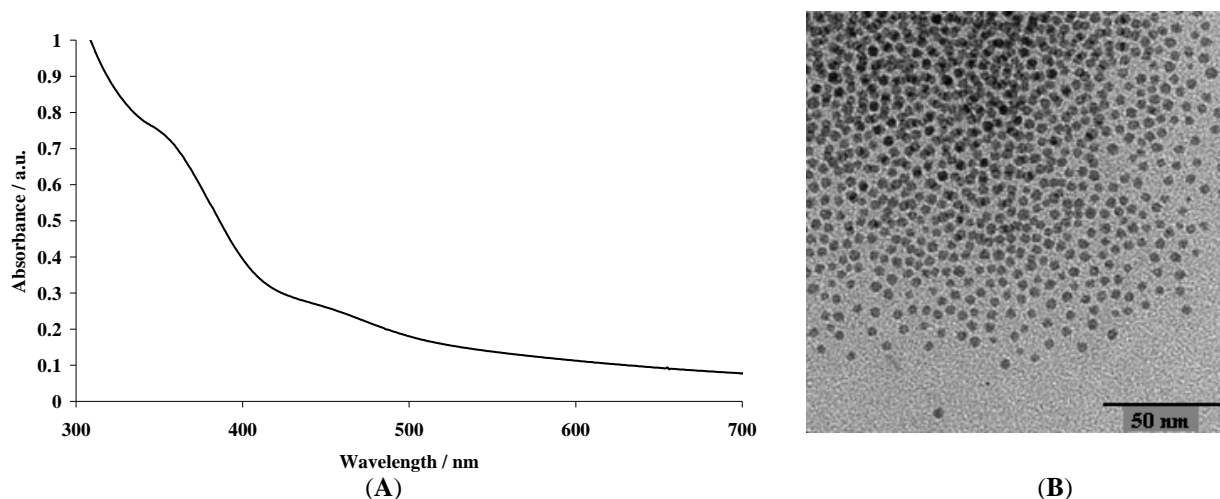


Fig. 3.349 Absorbance spectrum (A) and TEM image (B) of nanoparticles obtained following 200 °C thermolysis of cis -[Pd^{II}(L^{1a}-Se₂O)₂] for 40 minutes.

A band edge of 450 nm (2.76 eV) was calculated for the 40 minute sample and no emission could be observed. As with the sulfur analogue, the PXRD pattern revealed largely amorphous material, making assignment of the palladium selenide phase difficult. The TEM image shows beautifully defined spherical nanoparticles, 3.9 (11) nm in diameter, the particle size distribution being significantly improved relative to that exhibited by nanoparticles obtained following decomposition of the sulfur analogue. EDAX analysis of the nanoparticles revealed a Pd : Se ratio of 8.11 : 1. Whilst a Pd₈Se phase is known, only one report could be found documenting this phase with very little information regarding its properties and stability.^[81] Given the 2:1 Se : Pd ratio of the precursor, it is unlikely that this phase formed, in addition, Se and its varying compounds are usually accompanied by a strong and distinctive smell, if excess Se had been removed during the nanoparticle washing process, it is likely that this would have been noted, however no such observation was made. It is also possible that the low Se concentration could be attributed to oxidation of surface Se atoms over time. This degradation could take place if the surface of the nanoparticle is poorly passivated and as HDA is known to be a weakly coordinating ligand and the EDAX analysis took place several months after the nanoparticle synthesis, it is likely that this oxidation could have contributed to the low Se concentration detected.^[95]

The *cis*-[Pd^{II}(L^{1a}-Se,O)₂] precursor and its possible products are discussed further in the next chapter.

The reduced crystallinity observed for the nanoparticles obtained from thermolysis of the square-planar *d*⁸ metal complexes, suggests that the increased stability of these precursors, necessitates the need for higher thermolysis temperatures as well as longer reaction times to allow the formation of crystalline material.

3.3.6 Core-shell nanoparticle synthesis

The synthesis of heterostructured nanoparticles of varying composition has been fairly widely reported,^[64, 96-100] and two basic types of structures exist (Fig. 3.350). Type I nanoheterostructures consist of a semiconductor core, covered by a second semiconducting material, this usually having a larger band gap than that of the core material. Nanoparticles of this type are usually accompanied by an increase in the quantum yield due to passivation of free valences at the nanoparticle surface resulting in the suppression of radiationless recombination that occurs here.^[101] The efficacy of this is increased by using an epitaxially grown inorganic material rather than ionically or Van Der Waal's bound organic surfactants. In the second structure type, nanoparticles of different compositions are brought into such close contact, that it becomes possible for charge carrier transport between the materials to occur. Whilst both structure types have been reviewed, more emphasis will be placed on Type I structures in this work.^[102]

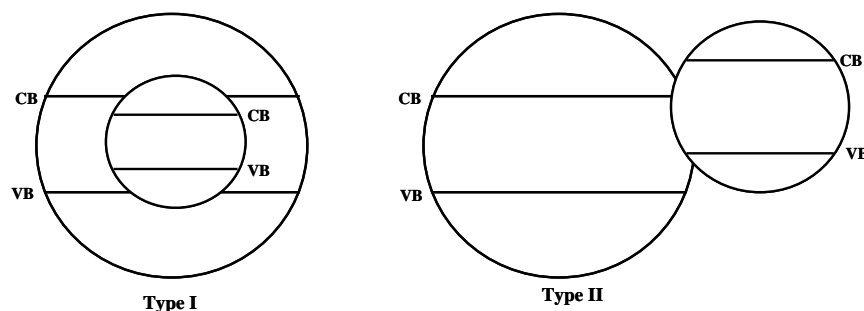


Fig. 3.350 Typology of semiconductor nanoheterostructures, VB = valence band and CB = conduction band. Taken from Ref [102].

3.3.6.1 Synthesis of CdSe/CdS nanoparticles

Several studies detailing the synthesis of nanoheterostructures with CdSe cores and a larger band gap, CdS shell have been reported.^[59, 63, 101] Core-shell type structures have been synthesised using both the single source precursor route,^[103, 104] and separate metal and chalcogen sources.^[63] Interestingly, in all these reports, both the CdSe and CdS are in the wurtzite phase where the lattice mismatch is only 3.9 %, this being small enough for epitaxial growth without significant alteration of nanoparticle morphology or any structure defects and large enough to confine charge carriers to the core, to suppress radiative recombination to a degree.^[99] Both the CdSe and CdS nanoparticles formed from the thermolysis of [Cd^{II}(L^{1a}-Se,O)₂] and [Cd^{II}(L^{2a}-S,O)₂] respectively, are cubically phased where the lattice mismatch in this case is 4.4 %,‡ however this should still be small enough to allow for epitaxial growth of the larger band gap material. Following Peng's report where TOPO was found to bind too strongly to the nanoparticle surface, thereby preventing epitaxial shell growth, our well established system using HDA was thought to be ideal for the synthesis of core/shell nanoparticles. As HDA is not such a strongly binding ligand,^[60] it is likely to behave as a dynamic capping agent, providing both access to the nanoparticle surface and chemical stability in much the same way as pyridine,^[63] thus allowing for the epitaxial growth of a larger band gap material.

‡ This was calculated using the lattice parameters of each material, where $a_0 = 5.82$ nm for CdS and 6.08 nm for CdSe at 300K.

In an attempt to synthesise CdSe/CdS core/shell nanoparticles, previously synthesised CdSe nanoparticles were re-suspended in HDA and heated to 150 °C, followed by the injection of a TOP solution of $[\text{Cd}^{\text{II}}(\text{L}^{2\text{a}}\text{-S},\text{O})_2]$ and a 60 minute reaction period. The temperature of 150 °C was chosen as good quality CdS and CdSe nanoparticles had previously been obtained from both precursors at this temperature and the temperature was thought to be low enough to allow epitaxial growth of CdS (as opposed to separate nucleation and growth of CdS) and high enough to ensure material with a reasonable crystallinity. The optical spectra of the nanoparticles obtained are shown in Fig. 3.351.

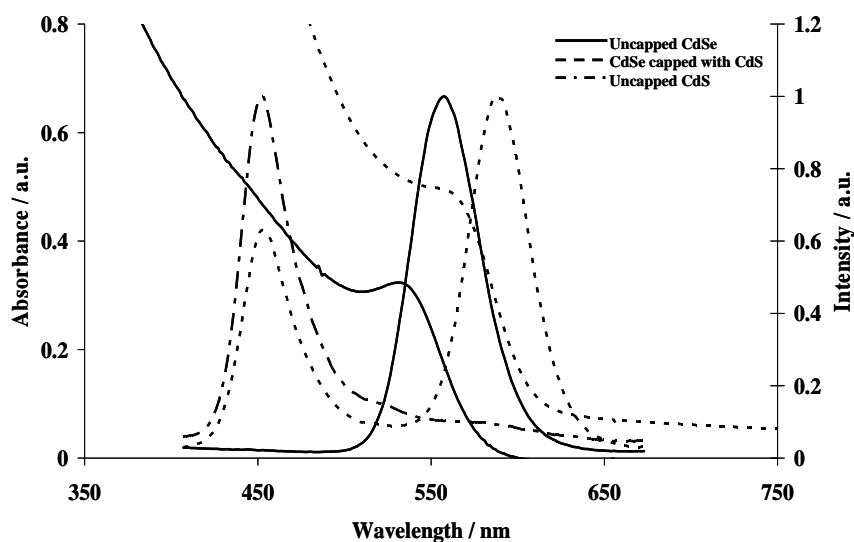


Fig. 3.351 Comparison of the optical spectra of —uncapped CdSe nanoparticles, ----CdS capped CdSe nanoparticles and the - · - · - emission spectrum of CdS nanoparticles.

The band edge of the previously uncoated CdSe is 575 nm and that of the CdS coated nanoparticles is 616 nm, indicating a red shift of 41 nm. This is reflected in the emission spectra where a red shift from 557.5 nm to 587.5 nm is evident for the uncoated and coated nanoparticles respectively. It may be argued that the observed red shifts are a result of normal nanoparticle growth and not necessarily due to capping by CdS, however from previous experiments, it can be deduced that 60 minute growth never results in such a large red shift in either absorption or emission spectra, the reason for this observation must therefore lie elsewhere. The wave functions of the excited electron and hole in the nanocrystals spread into the shell (or coating), the kinetic energy of both the excited electron and hole decreases resulting in the observed red shift and this is therefore clear evidence for the CdS capping of the CdSe nanoparticle cores.^[63, 103] This observation also limits the possibility of alloying having occurred.^[63, 104] Quantum yield determinations indicated an approximate two fold increase in emission efficiency and this is further evidence for the passivation of surface states by CdS capping. A second lower wavelength emission at 452.5 nm is however clearly evident in Fig. 3.351. Comparison with previously synthesised CdS following thermolysis of $[\text{Cd}^{\text{II}}(\text{L}^{2\text{a}}\text{-S},\text{O})_2]$ for 60 minutes shows exactly the same emission maximum. It is therefore likely that two sets of nanoparticles are present in the sample, CdS coated CdSe giving rise to the longer wavelength emissions and CdS formed by the separate nucleation of the precursor upon injection giving rise to the shorter wavelength emission. The PXRD pattern of the nanoparticles obtained as well as those of separately prepared CdS and CdSe for comparison purposes are shown in Fig. 3.352.

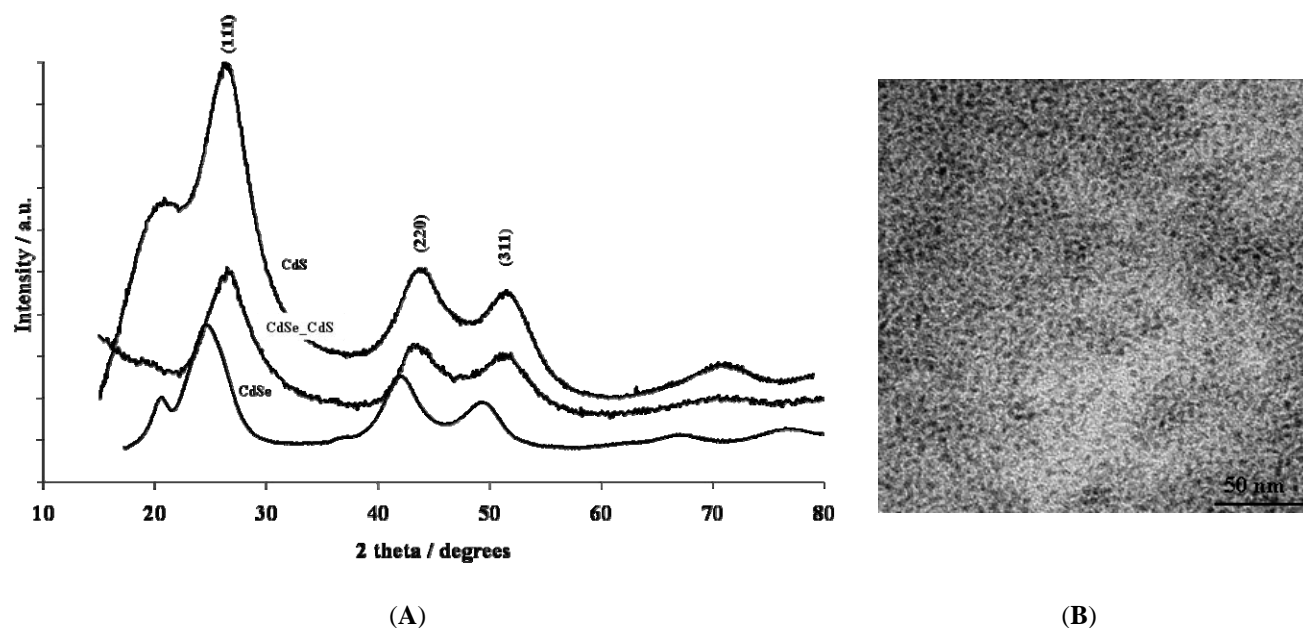


Fig. 3.352 PXRD patterns of CdS, CdSe/CdS and CdSe nanoparticles (A) and TEM image of the obtained nanoparticles (B).

The PXRD pattern of the coated nanoparticles obtained strongly resembles that of separately prepared CdS, with only a slight variation in d spacing. The nanoparticle size calculated using the Scherrer equation is 3.0 nm and agrees very well with that obtained from the TEM image (2.9 (15) nm), where spherical nanoparticles are clearly evident. The size of the CdSe cores was previously found to be 2.5 (15) nm and the formed nanoparticles are clearly larger. This suggests further evidence for coated nanoparticles, however comparison with CdS nanoparticles synthesised by the 60 minute thermolysis of $[\text{Cd}^{\text{II}}(\text{L}^{2\text{a}}\text{-S},\text{O})_2]$ shows nanoparticles 3.0 (15) nm in diameter (Table 3.32). Therefore, it is likely that the majority of the sample is composed of CdS nanoparticles formed by separate nucleation and growth upon injection of the precursor. This accounts for the nanoparticle sizes observed in the TEM image as well as the PXRD data. A second smaller set of nanoparticles is also present however, and these are most likely CdS coated CdSe nanoparticles as observed from the optical spectra. The separate nucleation and growth of CdS nanoparticles implies that a lower reaction temperature could yield a greater proportion of coated nanoparticles and minimise the extent of separate CdS nucleation and growth.

3.3.6.2 Synthesis of CdSe/ZnS nanoparticles

Whilst the lattice mismatch of only 3.9 % between CdS and CdSe allows for the epitaxial growth of the former on the latter, the relatively small difference in band edges can allow for the tunnelling of charge carriers from the cores to the surface atoms of the shell, in other words lowering the electronic passivation of the nanoparticles and reducing their emission efficiencies. This can be avoided by use of a material with a significantly larger band gap such as ZnS.^[99] Hines *et al.* reported a 50 % quantum yield for ZnS capped CdSe nanoparticles,^[105] and Talapin and co-workers later reported similar results.^[106] Varying sizes of CdSe/ZnS nanoparticles have been incorporated into silica beads with the concurrent introduction of biological functional groups^[107] and Gill and co-workers report on the potential application of CdSe/ZnS nanoparticles in the monitoring of biocatalytic transformations.^[108] In 2002 Malik *et al.* reported on the use of metal complexes as single source precursors for the synthesis of CdSe/ZnS quantum dots^[103] and in the same year Cumberland and co-workers used inorganic clusters for the same purpose.^[123]

The lattice mismatch between CdSe and ZnS is 12 % for both wurtzite and zinc-blende phases, considerably larger than that between CdS and CdSe.^[99] In order to investigate the effect of this on our system, the synthesis of CdSe/ZnS nanoparticles was attempted and the optical spectra of the resulting nanoparticles are shown in Fig. 3.353.

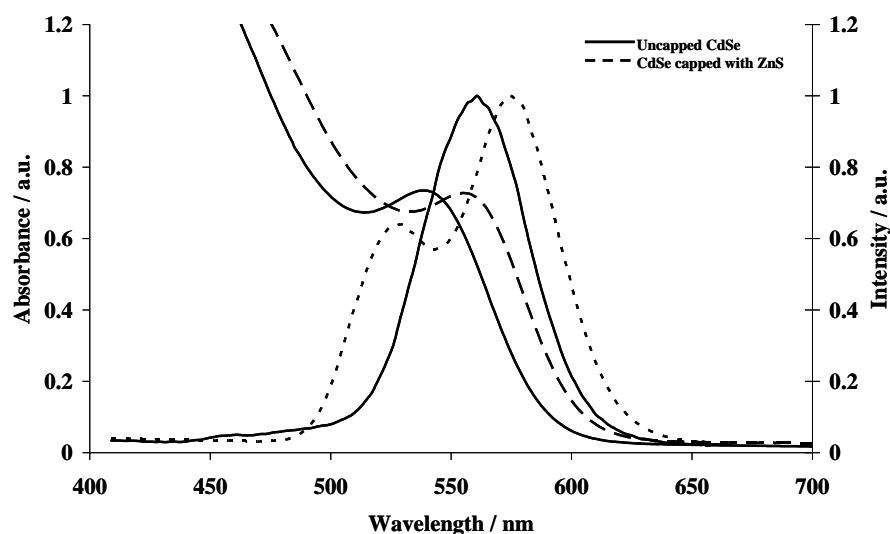


Fig. 3.353 Comparison of the optical spectra of —uncapped CdSe nanoparticles, ----ZnS capped CdSe nanoparticles.

The absorption spectra show a clear red shift in the band edge from 595 nm to 605 nm, indicating the presence of a ZnS coating on the CdSe nanoparticles.^[95] A slightly larger red shift of 14 nm is seen in the emission spectra where the maxima shift from 561 nm to 575 nm following injection of $[\text{Zn}^{\text{II}}(\text{L}^{2\text{a}}\text{-S}_2\text{O})_2]$, similar results having been reported previously.^[95] As in the previous case, quantum yield determinations show an increase in emission efficiency, however in this case an approximate 4.5 fold increase was observed. This signifies ZnS capping of the CdSe cores and can be taken as further evidence for the increased electronic passivation exhibited by a material with a larger band gap. Once again, a second lower wavelength emission becomes evident following injection of the capping material precursor, however in this case the origin of the emission is less facile to understand. If, as in the previous case, injection of the capping material precursor results in separate nucleation and growth of nanoparticles, a close to band edge emission can be expected as evidence of this. The band edge of ZnS is in the region of 340 nm and hence the second smaller emission at 529 nm is too red shifted to account for this. It should be noted here that no emission was evident at shorter wavelengths than those shown in Fig. 3.353. A subset of very small CdSe nanoparticles can be expected to exhibit emission in a similar region (529 nm), however their formation at a temperature of 150 °C with an emission in this wavelength region is highly unlikely (Table 3.31) as is their appearance 60 minutes into the reaction. The appearance of the emission maxima therefore remains something of an anomaly. The PXRD data and TEM image of the resulting nanoparticles are shown in Fig. 3.354 (A and B). The PXRD pattern of the resulting nanoparticles strongly resembles that of CdSe although a slight shift in d spacing towards that of ZnS is evident. The TEM image indicates spherical nanoparticles approximately 2.4 (13) nm in diameter and that calculated from the PXRD data indicates a diameter of 3.2 nm. Uncoated CdSe nanoparticles synthesised under similar condition exhibit diameters in the region of 2.5 (15) nm and it is therefore likely that the CdSe nanoparticles are coated by only a few monolayers of ZnS, making a significant size distinction between that of coated and uncoated nanoparticles using TEM difficult.

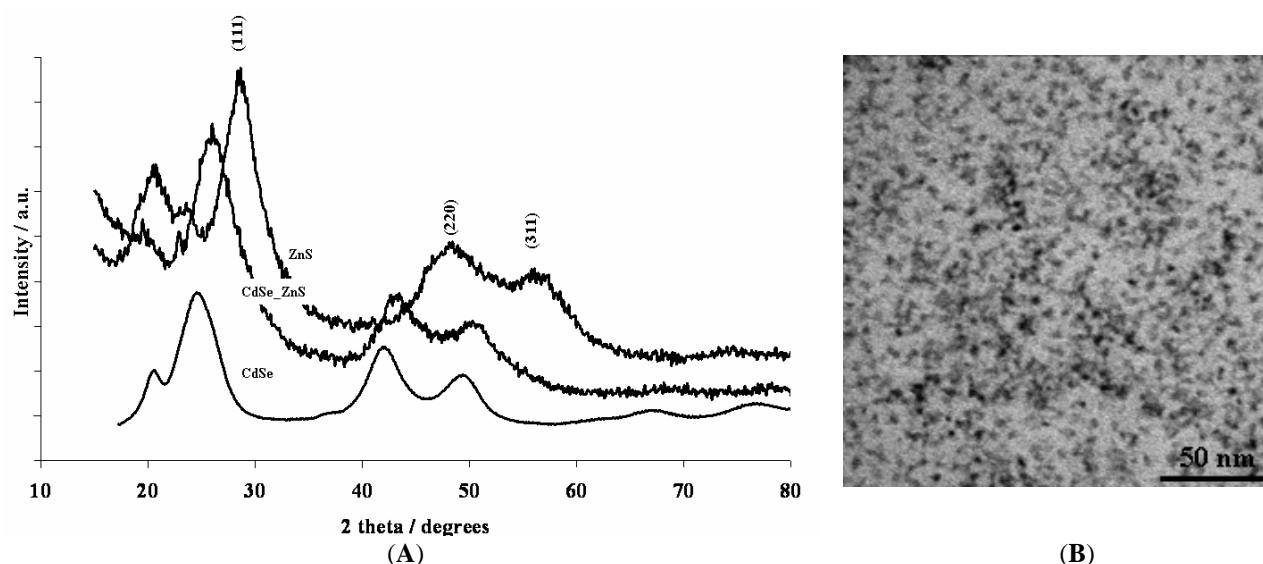


Fig. 3.354 PXRD data (A) of CdSe/ZnS nanoparticles as well as those of separately prepared CdSe and ZnS for comparison and TEM image (B) and CdSe/ZnS nanoparticles.

Whilst the majority of nanoparticles are spherical, some do exhibit slightly irregular shapes and these can be attributed to the larger mismatch between CdSe and ZnS. Where the coating of ZnS becomes thicker than approximately 1.3 monolayers, the interface strain increases and is eventually released through the formation of misfit dislocations, these leading to irregular shapes and degradation in the optical properties of the nanoparticles.^[95]

3.3.6.3 Synthesis of CdSe/ZnSe nanoparticles

Very few reports exist detailing the synthesis of ZnSe capped CdSe nanoparticles,^[103] and given the formation of ZnO nanoparticles resulting from the thermolysis of $[\text{Zn}^{\text{II}}(\text{L}^{\text{Ia}}\text{-Se}, \text{O})_2]$, it was with interest that this material was used as a potential ZnSe capping agent of CdSe nanoparticles. The optical spectra of the resulting nanoparticles are shown in Fig. 3.355. A clear 40 nm red shift in the band edge from 575 nm to 615 nm can be taken as clear evidence for capping of the CdSe nanoparticles. This is reflected in the emission spectra, where the maximum red shifts from 546 nm to 578 nm.^[103] An approximate 18 fold increase in emission efficiency was observed for this sample, this being considerably higher than that observed for CdSe/CdS and CdSe/ZnS nanoparticles. The TEM image and PXRD data are shown in Fig. 3.356 (A and B). Spherical nanoparticles 2.5 (14) nm in diameter are evident from the TEM image, whereas that of uncapped CdSe is almost identical 2.5 (15) nm. This suggests a very thin capping of the CdSe nanoparticles, such that an increased diameter is not easily measurable using TEM. The PXRD pattern reveals some very interesting peaks and clearly more than one type of material is present in the sample. Peaks labelled with * correspond closely to the (111), (220) and (311) peaks expected for cubically phased CdSe. Those labelled with ‡ correspond to cubically phased CdO and the broadness of the peaks suggests that this material should also be in the “nano” size domain, although precise determination of the particle size is complicated by peak overlap. The formation of both CdO and CdSe was previously observed from the thermolysis of $[\text{Cd}^{\text{II}}(\text{L}^{\text{Id}}\text{-Se}, \text{O})_2]$. The very sharp peaks labelled with # correspond to the (100), (002), (101), (102), (110), (103) and (112) peaks of wurtzite ZnO, the peak sharpness indicating the formation of fairly large particles, not necessarily in the “nano” size domain. There is no evidence supporting the formation of ZnSe.

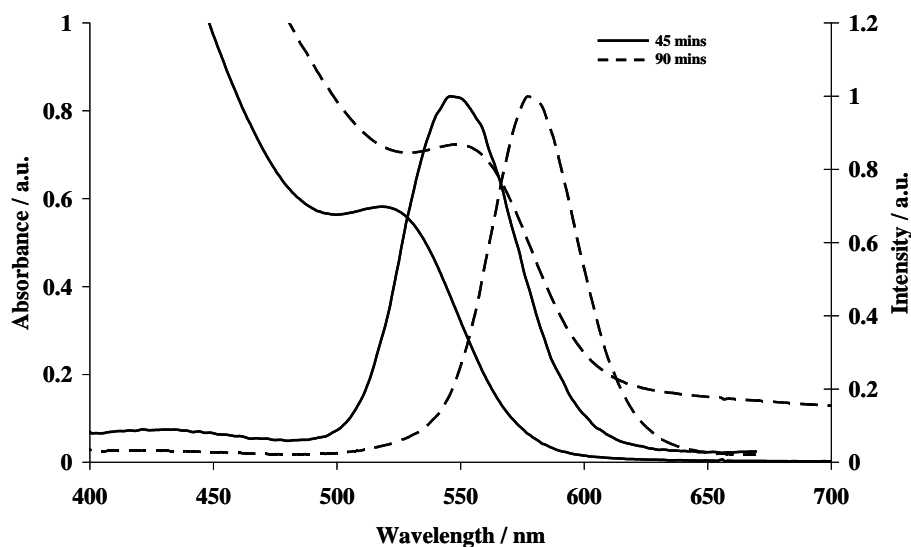
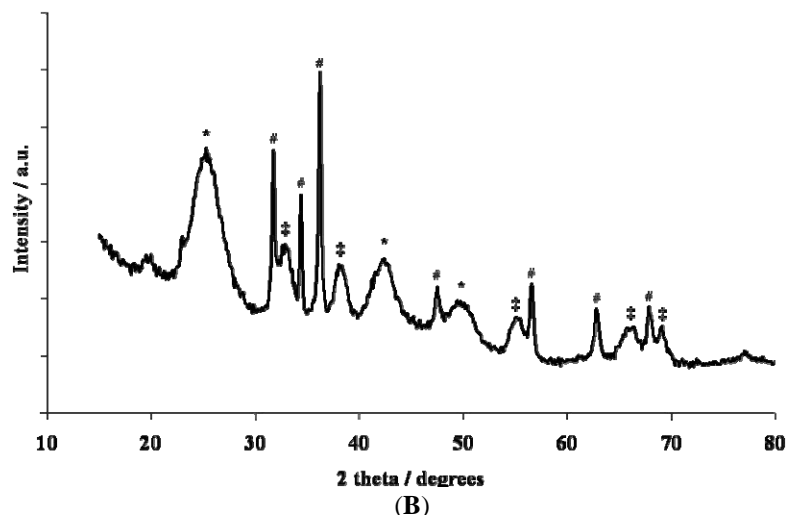
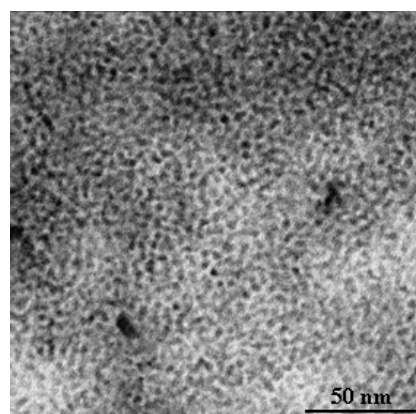


Fig. 3.355 Optical spectra of CdSe nanoparticles obtained prior to (45 minutes) and following (90 minutes) injection of $[\text{Zn}^{\text{II}}(\text{L}^{1\text{a}}\text{-Se},\text{O})_2]$.



(A)

(B)

Fig. 3.356 TEM image (A) and PXRD pattern (B) of nanoparticles obtained following injection of $[\text{Zn}^{\text{II}}(\text{L}^{1\text{a}}\text{-Se},\text{O})_2]$ into a solution of CdSe nanoparticles where * denotes CdSe, #, ZnO and ‡, CdO.

The PXRD data points towards the separate nucleation and growth of ZnO upon injection of $[\text{Zn}^{\text{II}}(\text{L}^{1\text{a}}\text{-Se},\text{O})_2]$ as well as the separate nucleation and growth of CdO and CdSe nanoparticles. The optical spectra do however give a clear indication of CdSe capping, although the composition of the capping agent is difficult to determine. Based on the marked increase in quantum efficiency it is possible that a large band gap material is responsible. The lattice mismatch between CdSe and ZnO is very large, in the region of 28 % and that between CdO and CdSe is in the region of 25 %. Based on these figures alone it is unlikely that capping of the CdSe cores by either material would take place. On the other hand the lattice mismatch between ZnSe and CdSe is only 7 % making this a far more likely alternative. As a single source precursor, $[\text{Cd}^{\text{II}}(\text{L}^{1\text{a}}\text{-Se},\text{O})_2]$ resulted in the formation of both CdO and CdSe, it is not unreasonable to propose a similar occurrence using $[\text{Zn}^{\text{II}}(\text{L}^{1\text{a}}\text{-Se},\text{O})_2]$ and the formation of both ZnO and ZnSe. Whilst there is no direct evidence for the formation of the latter, HRTEM may resolve this, by determining the nature of the capping agent from the lattice plane spacing at the edges of each nanoparticle.

These preliminary studies in core-shell nanoparticle synthesis indicate that the $[\text{Cd}^{\text{II}}(\text{L}^{2\text{a}}-\text{S},\text{O})_2]$, $[\text{Zn}^{\text{II}}(\text{L}^{2\text{a}}-\text{S},\text{O})_2]$ and $[\text{Zn}^{\text{II}}(\text{L}^{1\text{a}}-\text{Se},\text{O})_2]$ metal complexes can be used as capping agent precursors for the synthesis of core-shell quantum dots. Further work, focussing on the variation of thermolysis temperature, is necessary to optimise the conditions for CdSe core coating and to minimise the separate nucleation and growth of nanoparticles derived from the capping agent precursors.

3.4 Conclusion

The Cd(II) complex, $[\text{Cd}^{\text{II}}(\text{L}^{1\text{a}}-\text{Se},\text{O})_2]$ and its sulfur analogue, $[\text{Cd}^{\text{II}}(\text{L}^{2\text{a}}-\text{S},\text{O})_2]$ can successfully be used as single source precursors for the synthesis of CdSe and CdS nanoparticles respectively, both of these nanoparticle types exhibiting quantum confinement. Thermolysis of $[\text{Cd}^{\text{II}}(\text{L}^{1\text{a}}-\text{Se},\text{O})_2]$ over a range of temperatures allows the synthesis of CdSe nanoparticles with varying diameters, a direct correlation being established between nanoparticle size and thermolysis temperature. Emission spectra obtained from these nanoparticles clearly demonstrate the size dependant emission of CdSe and the zinc-blende phase of the CdSe nanoparticles is independent of thermolysis temperature under the reaction conditions investigated. Thermolysis of $[\text{Cd}^{\text{II}}(\text{L}^{2\text{a}}-\text{S},\text{O})_2]$ over a similar range of temperatures allows the synthesis of CdS nanoparticles with varying diameters exhibiting a similar correlation between nanoparticle diameter and thermolysis temperature to their Se analogues, although the degree of size control is less than that exhibited by CdSe. The increased stability of $[\text{Cd}^{\text{II}}(\text{L}^{2\text{a}}-\text{S},\text{O})_2]$ relative to $[\text{Cd}^{\text{II}}(\text{L}^{1\text{a}}-\text{Se},\text{O})_2]$ necessitates the use of slightly higher thermolysis temperatures to achieve even nucleation and monodispersity in the resulting CdS nanoparticles. Over the temperature range investigated, the zinc-blende phase of CdS is consistent. Thermolysis of both $[\text{Cd}^{\text{II}}(\text{L}^{1\text{a}}-\text{Se},\text{O})_2]$ and $[\text{Cd}^{\text{II}}(\text{L}^{2\text{a}}-\text{S},\text{O})_2]$ over a range of temperatures forms CdSe and CdS nanoparticles with predominantly spherical morphology and thermolysis temperature therefore exerts little control over final nanoparticle morphology for these single source precursors.

Thermolysis of the *N,N*-dialkyl-*N'*-benzoylselenourea Cd(II) complexes, $[\text{Cd}^{\text{II}}(\text{L}^{1\text{b}}-\text{Se},\text{O})_2]$, $[\text{Cd}^{\text{II}}(\text{L}^{1\text{c}}-\text{Se},\text{O})_2]$, $[\text{Cd}^{\text{II}}(\text{L}^{1\text{d}}-\text{Se},\text{O})_2]$, $[\text{Cd}^{\text{II}}(\text{L}^{1\text{e}}-\text{Se},\text{O})_2]$ and $[\text{Cd}^{\text{II}}(\text{L}^{1\text{f}}-\text{Se},\text{O})_2]$ shows that each can be used as a single source precursor for the synthesis of CdSe nanoparticles. Thermolysis of these complexes under similar conditions results in the formation of CdSe nanoparticles exhibiting a red shifted band edge and emission maximum, with increasing precursor alkyl chain length. The presence and intensity of a shorter wavelength emission also appears to be related to precursor alkyl chain length. An increase in anisotropic morphology of the resulting nanoparticles appears to be correlated to the alkyl chain length of the precursor complex, this trend being consistent up to a C8 alkyl chain length in $[\text{Cd}^{\text{II}}(\text{L}^{1\text{d}}-\text{Se},\text{O})_2]$. Thermolysis of $[\text{Cd}^{\text{II}}(\text{L}^{1\text{f}}-\text{Se},\text{O})_2]$ with a C10 alkyl chain length results in the formation of spherical nanoparticles. The zinc-blende phase of CdSe is consistent for the thermolysis of each precursor, a sharpening of the (220) peak relative to that of the (311) peak being evident where nanoparticles exhibit an increased anisotropy. Elucidation of the growth mechanism for the formation of the tripodal structures obtained following thermolysis of $[\text{Cd}^{\text{II}}(\text{L}^{1\text{d}}-\text{Se},\text{O})_2]$ is difficult due to the limited resources available, however it is likely to follow that of a zinc-blende phased core, where epitaxial growth of wurtzite phased arms takes place on the {111} surfaces of the core. Bipodal and tripodal structures are likely to be formed by the faster growth of the (001) wurtzite faces relative to the remaining (111) surfaces of the zinc-blende core.

Thermolysis of $[\text{Cd}^{\text{II}}(\text{L}^{1\text{d}}-\text{Se},\text{O})_2]$ over a range of temperatures results in the formation of anisotropic structures between 80 and 200 °C. A red shift in the band edge and emission maximum with increasing thermolysis temperature is evident, although less consistent than that observed for the shorter alkyl chain analogue, $[\text{Cd}^{\text{II}}(\text{L}^{1\text{a}}-$

$\text{Se}, \text{O})_2$]. Reduced nanoparticle crystallinity is observed at lower thermolysis temperatures however the presence of cubically phased CdSe appears to be largely consistent over the temperature range studied.

Comparison of the decomposition profiles of $[\text{Cd}^{\text{II}}(\text{L}^{1\text{a}}-\text{Se}, \text{O})_2]$ and $[\text{Cd}^{\text{II}}(\text{L}^{1\text{d}}-\text{Se}, \text{O})_2]$ shows an approximate three step decomposition for each, where the second mass loss appears to be a first order process for both precursors. Coats Redfern analysis of this data allows the calculation of the activation energy for this decomposition process where the 48.1 kJ mol^{-1} of $[\text{Cd}^{\text{II}}(\text{L}^{1\text{d}}-\text{Se}, \text{O})_2]$ is more than twice the 21.4 kJ mol^{-1} of the shorter alkyl chain analogue, $[\text{Cd}^{\text{II}}(\text{L}^{1\text{a}}-\text{Se}, \text{O})_2]$. This suggests the involvement of factors other than a growth regime under kinetic control for the formation of anisotropic structures. The relatively larger nanoparticles ensuing from $[\text{Cd}^{\text{II}}(\text{L}^{1\text{d}}-\text{Se}, \text{O})_2]$ decomposition fall within the size regime where branching of the nanoparticle to form bi-, tri- and tetrapodal structures results in a decrease in the number of surface atoms, and hence internal energy of the system, this possibly being the driving force for the development of multiarmed structures.

Thermolysis of the *N,N*-dialkyl-*N'*-benzoylthiourea Cd(II) complexes, $[\text{Cd}^{\text{II}}(\text{L}^{2\text{b}}-\text{S}, \text{O})_2]$, $[\text{Cd}^{\text{II}}(\text{L}^{2\text{c}}-\text{S}, \text{O})_2]$, $[\text{Cd}^{\text{II}}(\text{L}^{2\text{d}}-\text{S}, \text{O})_2]$ and $[\text{Cd}^{\text{II}}(\text{L}^{2\text{e}}-\text{S}, \text{O})_2]$ illustrates that each can be used as a single source precursor for the synthesis of CdS nanoparticles. Thermolysis of these complexes under similar conditions results in CdS nanoparticles where a red shift in the band edge with increasing precursor alkyl chain length is evident. This trend is comparable to that observed for the emission maxima and no shorter wavelength emission observed in the formation of CdSe nanoparticles was evident here. The formation of zinc-blende CdS appears to be independent of precursor alkyl chain length, for the precursors studied and in this series, the relative sharpness of the (220) and (311) peaks remains consistent. The exclusive formation of spherical nanoparticles indicates that under these conditions, the morphology of CdS nanoparticles is independent of the precursor alkyl chain length.

Increasing the concentration of $[\text{Cd}^{\text{II}}(\text{L}^{2\text{a}}-\text{S}, \text{O})_2]$ at $150 \text{ }^\circ\text{C}$ thermolysis, results in the formation of larger CdS nanoparticles with a red shifted band edge and emission maxima and spherical morphology. A similar experiment performed at $200 \text{ }^\circ\text{C}$ indicates that quantum confinement in the ensuing CdS nanoparticles is no longer conserved. "Ageing" of this sample allows the development of anisotropic structures from previously spherical CdS nanoparticles, where the growth mechanism responsible is likely to be that of "orientated attachment."

Nanoparticles derived from the thermolysis of $[\text{Cd}^{\text{II}}(\text{L}^{1\text{a}}-\text{Se}, \text{O})(\text{L}^{2\text{a}}-\text{S}, \text{O})]$ exhibit optical spectra similar to those of CdSe. The PXRD patterns of these nanoparticles however resemble that of CdS.

Thermolysis of $[\text{Zn}^{\text{II}}(\text{L}^{1\text{a}}-\text{Se}, \text{O})_2]$ results in the formation of nanoparticles most likely composed of ZnO, roughly spherical in shape, and exhibiting a bimodal emission. Thermolysis of the sulfur analogue, $[\text{Zn}^{\text{II}}(\text{L}^{2\text{a}}-\text{S}, \text{O})_2]$ results in the formation of ZnS nanoparticles with a cubic crystallinity. These nanoparticles exhibit a spherical morphology and blue shifted band edge relative to that of bulk ZnS. The emission spectrum is dominated by a longer wavelength emission arising from structural defects, this being commonly associated with ZnS. Consequently both Zn(II) complexes synthesised show potential as single source precursors.

Nanoparticles derived from the thermolysis of *cis*- $[\text{Ni}^{\text{II}}(\text{L}^{2\text{a}}-\text{S}, \text{O})_2]$ are spherical in shape as are those derived from the thermolysis of $[\text{Co}^{\text{III}}(\text{L}^{2\text{a}}-\text{S}, \text{O})_3]$. Further investigation of these complexes as single source precursors could lead to the formation of nanoparticles with interesting and varied compositions.

Thermolysis of *cis*- $[\text{Pd}^{\text{II}}(\text{L}^{2\text{a}}-\text{S}, \text{O})_2]$ results in the formation of well defined, fairly polydisperse, spherical nanoparticles with a band edge of 454 nm. Although the PXRD pattern indicates amorphous material, EDAX analysis suggests the formation of PdS.

Nanoparticles obtained following thermolysis of *cis*-[Pt^{II}(L^{2a}-S,O)₂] exhibit a 370 nm band edge and dual maxima emission. Well defined spherical nanoparticles are obtained, although PXRD analysis indicates poor crystallinity, this making absolute nanoparticle composition difficult to ascertain. EDAX analysis indicates that PtS formation is possible.

Thermolysis of *cis*-[Pd^{II}(L^{1a}-Se,O)₂] results in the formation of well defined, monodisperse, spherical nanoparticles with a band edge of 450 nm. PXRD analysis indicates the formation of amorphous material, precluding the determination of absolute nanoparticle composition.

Nanoparticles derived from the thermolysis of [Cd^{II}(L^{1a}-Se,O)₂] followed by injection of [Cd^{II}(L^{2a}-S,O)₂] consist of a mixture of materials. The reaction conditions used allow the separate nucleation and growth of CdS nanoparticles as well as the capping of the previously synthesised CdSe nanoparticles resulting in the formation of core/shell, CdSe/CdS material. The latter nanoparticles account for the increased emission efficiency exhibited by this sample.

Thermolysis of [Cd^{II}(L^{1a}-Se,O)₂] followed by injection of [Zn^{II}(L^{2a}-S,O)₂] results in the formation of irregularly shaped nanoparticles most likely of the form CdSe/ZnS. The PXRD data obtained is consistent with that expected for nanoparticles of this type and the red shifted optical spectra and increased quantum yield corroborate this.

Thermolysis of [Cd^{II}(L^{1a}-Se,O)₂] and consequent injection of [Zn^{II}(L^{2a}-S,O)₂] results in the formation of CdO, CdSe as well as ZnO nanoparticles. Red shifted optical spectra and a marked increase in the quantum yield, suggest the capping of the CdSe nanoparticles, possibly by ZnSe.

Given the potential shown by the *N,N*-dialkyl-*N'*-benzoylseleno(thio)ureas as single source precursors for the synthesis of a variety of different nanoparticles, their use as single source precursors for the deposition of nanophased material onto a glass substrate was of interest. The results of the complexes investigated are discussed in the next chapter.

References

- [1] M. A. Malik, P. O'Brien, *Chemistry of Materials* **1991**, *3*, 999.
- [2] B. Ludolph, M. A. Malik, P. O'Brien, N. Revaprasadu, *Chemical Communications (Cambridge)* **1998**, 1849.
- [3] T. Trindade, P. O'Brien, X.-m. Zhang, *Chemistry of Materials* **1997**, *9*, 523.
- [4] M. A. Malik, N. Revaprasadu, P. O'Brien, *Chemistry of Materials* **2001**, *13*, 913.
- [5] M. Azad Malik, P. O'Brien, N. Revaprasadu, *Journal of Materials Chemistry* **2001**, *11*, 2382.
- [6] M. Lazell, P. O'Brien, *Chemical Communications (Cambridge)* **1999**, 2041.
- [7] A. A. Memon, M. Afzaal, M. A. Malik, C. Q. Nguyen, P. O'Brien, J. Raftery, *Dalton Transactions* **2006**, 4499.
- [8] M. Lazell, S. J. Norager, P. O'Brien, N. Revaprasadu, *Materials Science & Engineering, C: Biomimetic and Supramolecular Systems* **2001**, *C16*, 129.
- [9] M. Chunggaze, M. Azad Malik, P. O'Brien, *Journal of Materials Chemistry* **1999**, *9*, 2433.
- [10] S.-M. Lee, Y.-w. Jun, S.-N. Cho, J. Cheon, *Journal of the American Chemical Society* **2002**, *124*, 11244.
- [11] N. Revaprasadu, M. Azad Malik, J. Carstens, P. O'Brien, *Journal of Materials Chemistry* **1999**, *9*, 2885.
- [12] M. A. Malik, P. O'Brien, N. Revaprasadu, *Journal of Materials Chemistry* **2002**, *12*, 92.
- [13] P. S. Nair, T. Radhakrishnan, N. Revaprasadu, G. Kolawole, P. O'Brien, *Journal of Materials Chemistry* **2002**, *12*, 2722.
- [14] Y. Li, X. Li, C. Yang, Y. Li, *Journal of Materials Chemistry* **2003**, *13*, 2641.
- [15] N. Pradhan, B. Katz, S. Efrima, *Journal of Physical Chemistry B* **2003**, *107*, 13843.
- [16] P. Sreekumari Nair, T. Radhakrishnan, N. Revaprasadu, G. A. Kolawole, P. O'Brien, *Polyhedron* **2003**, *22*, 3129.
- [17] P. S. Nair, T. Radhakrishnan, N. Revaprasadu, G. A. Kolawole, P. O'Brien, *Chemical Communications (Cambridge, United Kingdom)* **2002**, 564.
- [18] P. Sreekumari Nair, N. Revaprasadu, T. Radhakrishnan, G. A. Kolawole, *Journal of Materials Chemistry* **2001**, *11*, 1555.
- [19] P. S. Nair, M. M. Chili, T. Radhakrishnan, N. Revaprasadu, P. Christian, P. O'Brien, *South African Journal of Science* **2005**, *101*, 466.

- [20] Y. Hasegawa, M. Afzaal, P. O'Brien, Y. Wada, S. Yanagida, *Chemical Communications (Cambridge, United Kingdom)* **2005**, 242.
- [21] M. T. Ng, C. Boothroyd, J. J. Vittal, *Chemical Communications (Cambridge, United Kingdom)* **2005**, 3820.
- [22] G. Kedarnath, L. B. Kumbhare, V. K. Jain, P. P. Phadnis, M. Nethaji, *Dalton Transactions* **2006**, 2714.
- [23] S. L. Cumberland, K. M. Hanif, A. Javier, G. A. Khitrov, G. F. Strouse, S. M. Woessner, C. S. Yun, *Chemistry of Materials* **2002**, *14*, 1576.
- [24] Y. Li, M. Afzaal, P. O'Brien, *Journal of Materials Chemistry* **2006**, *16*, 2175.
- [25] B. D. Cullity, *Elements of X-Ray Diffraction. 2nd Ed*, **1978**.
- [26] J. Olmsted, III, *Journal of Physical Chemistry* **1979**, *83*, 2581.
- [27] C. Parker, W. Rees, *Analyst* **1960**, *85*, 587.
- [28] S. Russo, *Journal of Chemical Education* **1969**, *46*, 6.
- [29] P. Hrdlovic, S. Chmela, *Journal of Photochemistry and Photobiology A* **2001**, *143*, 59.
- [30] C. B. Murray, D. J. Norris, M. G. Bawendi, *Journal of the American Chemical Society* **1993**, *115*, 8706.
- [31] R. J. Bandaranayake, G. W. Wen, J. Y. Lin, H. X. Jiang, C. M. Sorensen, *Applied Physics Letters* **1995**, *67*, 831.
- [32] M. G. Bawendi, A. R. Kortan, M. L. Steigerwald, L. E. Brus, *Journal of Chemical Physics* **1989**, *91*, 7282.
- [33] X. Peng, J. Wickham, A. P. Alivisatos, *Journal of the American Chemical Society* **1998**, *120*, 5343.
- [34] P. S. Nair, T. Radhakrishnan, N. Revaprasadu, P. O'Brien, *Materials Science and Technology* **2005**, *21*, 237.
- [35] M. J. Moloto, N. Revaprasadu, P. O'Brien, M. A. Malik, *Journal of Materials Science: Materials in Electronics* **2004**, *15*, 313.
- [36] I. U. Arachchige, S. L. Brock, *Journal of the American Chemical Society* **2007**, *129*, 1840.
- [37] G. Zlateva, Z. Zhelev, R. Bakalova, I. Kanno, *Inorganic Chemistry* **2007**, *46*, 6212.
- [38] J. C. Bruce, N. Revaprasadu, K. R. Koch, *New Journal of Chemistry* **2007**, *31*, 1647.
- [39] O. Zelaya-Angel, J. J. Alvarado-Gil, R. Lozada-Morales, H. Vargas, A. Ferreira da Silva, *Applied Physics Letters* **1994**, *64*, 291.
- [40] O. Zelaya-Angel, R. Lozada-Morales, *Physical Review B: Condensed Matter and Materials Physics* **2000**, *62*, 13064.
- [41] F. Dumestre, B. Chaudret, C. Amiens, M.-C. Fromen, M.-J. Casanove, P. Renaud, P. Zurcher, *Angewandte Chemie (International ed. in English)* **2002**, *41*, 4286.
- [42] Y. Li, X. Li, C. Yang, Y. Li, *Journal of Physical Chemistry B* **2004**, *108*, 16002.
- [43] C. B. Murray, C. R. Kagan, M. G. Bawendi, *Annual review of Materials Science* **2000**, *30*, 545.
- [44] S. A. Blanton, R. L. Leheny, M. A. Hines, P. Guyot-Sionnest, *Physical Review Letters* **1997**, *79*, 865.
- [45] M. Shim, P. Guyot-Sionnest, *Journal of Chemical Physics* **1999**, *111*, 6955.
- [46] N. Chestnoy, T. D. Harris, R. Hull, L. E. Brus, *Journal of Physical Chemistry* **1986**, *90*, 3393.
- [47] L. Brus, *Journal of Physical Chemistry* **1986**, *90*, 2555.
- [48] J. J. Ramsden, M. Gratzel, *J. Chem. SOC., Faraday Trans. 1*, **1984**, *80*, 919.
- [49] L. Manna, E. C. Scher, A. P. Alivisatos, *Journal of the American Chemical Society* **2000**, *122*, 12700.
- [50] K.-T. Yong, Y. Sahoo, M. T. Swihart, P. N. Prasad, *Journal of Physical Chemistry C* **2007**, *111*, 2447.
- [51] D. Berhanu, K. Govender, D. Smyth-Boyle, M. Archbold, D. P. Halliday, P. O'Brien, *Chemical Communications (Cambridge, United Kingdom)* **2006**, 4709.
- [52] Y.-W. Jun, S.-M. Lee, N.-J. Kang, J. Cheon, *Journal of the American Chemical Society* **2001**, *123*, 5150.
- [53] Y.-W. Jun, J.-H. Lee, J.-S. Choi, J. Cheon, *Journal of Physical Chemistry B* **2005**, *109*, 14795.
- [54] A. W. Coats, J. P. Redfern, *Nature (London, United Kingdom)* **1964**, *201*, 68.
- [55] P. S. Nair, G. D. Scholes, *Journal of Materials Chemistry* **2006**, *16*, 467.
- [56] J. Yang, J.-H. Zeng, S.-H. Yu, L. Yang, G.-e. Zhou, Y.-t. Qian, *Chemistry of Materials* **2000**, *12*, 3259.
- [57] P. J. Thomas, P. O'Brien, *Journal of the American Chemical Society* **2006**, *128*, 5614.
- [58] C. J. Murphy, *Analytical Chemistry* **2002**, *74*, 520A.
- [59] P. D. Cozzoli, T. Pellegrino, L. Manna, *Chemical Society Reviews* **2006**, *35*, 1195.
- [60] H. Yu Jung, J. Joo, M. Park Hyun, S.-I. Baik, W. Kim Young, C. Kim Sung, T. Hyeon, *Journal of the American Chemical Society* **2005**, *127*, 5662.
- [61] Z. Tang, N. A. Kotov, M. Giersig, *Science (Washington, DC, United States)* **2002**, *297*, 237.
- [62] L. A. Swafford, L. A. Weigand, M. J. Bowers, II, J. R. McBride, J. L. Rapaport, T. L. Watt, S. K. Dixit, L. C. Feldman, S. J. Rosenthal, *Journal of the American Chemical Society* **2006**, *128*, 12299.
- [63] X. Peng, M. C. Schlamp, A. V. Kadavanich, A. P. Alivisatos, *Journal of the American Chemical Society* **1997**, *119*, 7019.
- [64] L. Ouyang, N. Maher Kristin, L. Yu Chun, J. McCarty, H. Park, *Journal of the American Chemical Society* **2007**, *129*, 133.
- [65] N. Pradhan, D. Goorskey, J. Thessing, X. Peng, *Journal of the American Chemical Society* **2005**, *127*, 17586.

- [66] O. Madelung, *Semiconductors*, 1st ed., Springer-Verlag, Berlin, **1996**.
- [67] P. D. Cozzoli, L. Manna, M. L. Curri, S. Kudera, C. Giannini, M. Striccoli, A. Agostiano, *Chemistry of Materials* **2005**, *17*, 1296.
- [68] M. A. Malik, M. M. Zulu, P. O'Brien, G. Wakefield, *Journal of Materials Chemistry* **1998**, *8*, 1885.
- [69] W. Bensch, M. Schuster, *Zeitschrift fuer Anorganische und Allgemeine Chemie* **1993**, *619*, 786.
- [70] R. G. Pearson, *Journal of Chemical Education* **1968**, *45*, 581.
- [71] J. S. Matthews, O. O. Onakoya, T. S. Ouattara, R. J. Butcher, *Dalton Transactions* **2006**, 3806.
- [72] J. Hambrock, S. Rabe, K. Merz, A. Birkner, A. Wohlfart, R. A. Fischer, M. Driess, *Journal of Materials Chemistry* **2003**, *13*, 1731.
- [73] Y. S. Wang, P. J. Thomas, P. O'Brien, *Journal of Physical Chemistry B* **2006**, *110*, 4099.
- [74] J. Auld, D. J. Houlton, A. C. Jones, S. A. Rushworth, M. A. Malik, P. O'Brien, G. W. Critchlow, *Journal of Materials Chemistry* **1994**, *4*, 1249.
- [75] B. Y. Geng, X. W. Liu, J. Z. Ma, Q. B. Du, L. D. Zhang, *Applied Physics Letters* **2007**, *90*, 183106/1.
- [76] W. Liu, *Materials Letters* **2006**, *60*, 551.
- [77] H. Zhang, B. Chen, B. Gilbert, J. F. Banfield, *Journal of Materials Chemistry* **2006**, *16*, 249.
- [78] A. Zubkov, T. Fujino, N. Sato, K. Yamada, *Journal of Chemical Thermodynamics* **1998**, *30*, 571.
- [79] G. Kliche, *Infrared Physics* **1985**, *25*, 381.
- [80] FindIt, *ICSD Database* **2007**, (FIZ)(NIST).
- [81] S. Dey, V. K. Jain, *Platinum Metals Review* **2004**, *48*, 16.
- [82] M. Schultz, E. Matijevic, *Colloids and Surfaces, A: Physicochemical and Engineering Aspects* **1998**, *131*, 173.
- [83] P. Raybaud, J. Hafner, G. Kresse, H. Toulhoat, *Journal of Physics: Condensed Matter* **1997**, *9*, 11107.
- [84] F. Hulliger, *Physics and Chemistry of Solids* **1965**, *26*, 639.
- [85] I. Ijjaali, J. A. Ibers, *New Crystal Structures* **2001**, *216*, 485.
- [86] C. J. Raub, V. B. Compton, T. H. Geballe, B. T. Matthias, J. P. Maita, G. W. Hull, Jr., *Physics and Chemistry of Solids* **1965**, *26*, 2051.
- [87] S. Sato, T. Takabatake, M. Ishikawa, *Acta Crystallographica Section C* **1989**, *C45*, 1.
- [88] R. Seshadri, *Personal communication* **2007**.
- [89] A. Singhal, D. P. Dutta, S. K. Kulshreshtha, S. M. Mobin, P. Mathur, *Journal of Organometallic Chemistry* **2006**, *691*, 4320.
- [90] L. B. Kumbhare, V. K. Jain, B. Varghese, *Inorganica Chimica Acta* **2006**, *359*, 409.
- [91] S. Dey, V. K. Jain, B. Varghese, T. Schurr, M. Niemeyer, W. Kaim, R. J. Butcher, *Inorganica Chimica Acta* **2006**, *359*, 1449.
- [92] S. Dey, L. B. Kumbhare, V. K. Jain, T. Schurr, W. Kaim, A. Klein, F. Belaj, *European Journal of Inorganic Chemistry* **2004**, 4510.
- [93] L. B. Kumbhare, V. K. Jain, P. P. Phadnis, M. Nethaji, *Journal of Organometallic Chemistry* **2007**, *692*, 1546.
- [94] S. Dey, V. K. Jain, B. Varghese, *Journal of Organometallic Chemistry* **2001**, *623*, 48.
- [95] B. O. Dabbousi, J. Rodriguez-Viejo, F. V. Mikulec, J. R. Heine, H. Mattoussi, R. Ober, K. F. Jensen, M. G. Bawendi, *Journal of Physical Chemistry B* **1997**, *101*, 9463.
- [96] J. W. Stouwdam, J. Shan, F. C. J. M. Van Veggel, A. G. Pattantyus-Abraham, J. F. Young, M. Raudsepp, *Journal of Physical Chemistry C* **2007**, *111*, 1086.
- [97] A. C. Bartnik, F. W. Wise, A. Kigel, E. Lifshitz, *Physical Review B: Condensed Matter and Materials Physics* **2007**, *75*, 245424/1.
- [98] Y. Yang, O. Chen, A. Angerhofer, Y. C. Cao, *Journal of the American Chemical Society* **2006**, *128*, 12428.
- [99] R. Xie, U. Kolb, J. Li, T. Basche, A. Mews, *Journal of the American Chemical Society* **2005**, *127*, 7480.
- [100] T. Uematsu, S. Maenosono, Y. Yamaguchi, *Journal of Physical Chemistry B* **2005**, *109*, 8613.
- [101] M. C. Schlamp, X. Peng, A. P. Alivisatos, *Journal of Applied Physics* **1997**, *82*, 5837.
- [102] A. Eychmueller, *Journal of Physical Chemistry B* **2000**, *104*, 6514.
- [103] M. A. Malik, P. O'Brien, N. Revaprasadu, *Chemistry of Materials* **2002**, *14*, 2004.
- [104] N. Revaprasadu, M. Azad Malik, P. O'Brien, G. Wakefield, *Chemical Communications (Cambridge)* **1999**, 1573.
- [105] M. A. Hines, G.-S. Philippe, *Journal of Physical Chemistry* **1996**, *100*, 468.
- [106] D. V. Talapin, A. L. Rogach, A. Kornowski, M. Haase, H. Weller, *Nano Letters* **2001**, *1*, 207.
- [107] D. Gerion, F. Pinaud, S. C. Williams, W. J. Parak, D. Zanchet, S. Weiss, A. P. Alivisatos, *Journal of Physical Chemistry B* **2001**, *105*, 8861.
- [108] R. Gill, R. Freeman, J.-P. Xu, I. Willner, S. Winograd, I. Shweky, U. Banin, *Journal of the American Chemical Society* **2006**, *128*, 15376.

Chapter 4

Use of the *N,N*-dialkyl-*N'*-benzoyl(thio)selenourea metal complexes as single source precursors for the Aerosol Assisted Chemical Vapour Deposition (AACVD) of CdSe, CdS, ZnSe, ZnS and other materials.

The use of (*N,N*-diethyl-*N'*-benzoylselenourea)Cd(II) as a single source precursor for the AACVD of CdSe on glass substrates is reported. Crystalline, wurtzite CdSe is formed at deposition temperatures as low as 225 °C using this complex. AACVD of the longer alkyl chain derivatives, [Cd^{II}(L^{1b-e}-Se,O)₂] allows the deposition of CdSe at 250 °C. Use of the sulfur analogue, (*N,N*-diethyl-*N'*-benzoylthiourea)Cd(II) as a single source precursor for the deposition of CdS is also described where deposition of crystalline wurtzite CdS occurs between 325 and 475 °C. The AACVD of the longer alkyl chain derivatives [Cd^{II}(L^{2b-e}-S,O)₂] at 250 °C is briefly discussed. The AACVD of (*N,N*-diethyl-*N'*-benzoylselenourea)Zn(II) is investigated over a range of temperature, lower temperatures favouring the deposition of zinc-blende ZnSe and higher temperatures favouring the deposition of wurtzite ZnSe. The deposition of ZnS is investigated using (*N,N*-diethyl-*N'*-benzoylthiourea)Zn(II) as a single source precursor, deposition temperatures of 400 and 475 °C allowing the formation of crystalline, wurtzite ZnS. Crystalline heazelwoodite, Ni₃S₂, results from the AACVD of *cis*-bis(*N,N*-diethyl-*N'*-benzoylthiourea)Ni(II) at 400 °C. The morphology of the deposit is examined and discussed in detail. Use of *cis*-bis(*N,N*-diethyl-*N'*-benzoylthiourea)Pd(II) for the AACVD of PdS is discussed and post deposition treatment of the thin films allows the formation of crystalline palladium. The AACVD of *cis*-bis(*N,N*-diethyl-*N'*-benzoylthiourea)Pt(II) is described for the first time and the deposition of crystalline platinum is reported. Use of *cis*-bis(*N,N*-diethyl-*N'*-benzoylselenourea)Pd(II) as a single source precursor allows the deposition of crystalline Pd₁₇Se₁₅. This is the first time that palladium selenide has been deposited using the AACVD technique. The thin films obtained are investigated in detail and certain electronic properties are reported.

4.1 Introduction

Many different techniques and variations exist for the production of thin films. Chemical vapour deposition is an advanced technology used in the manufacturing of thin films, and is currently the focus of intense research.^[1] Fig. 4.1.1 illustrates the chemical vapour deposition process, and focuses on the use of metal organic precursors, leading to the term MOCVD (Metal Organic Chemical Vapour Deposition). During the CVD process, the precursor is transported by a carrier gas (usually Ar or N₂) to the substrate inside the reactor (1). Once at the substrate, adsorption of the precursor occurs (2), followed by its reaction (3) and the subsequent desorption of by-products that are formed (6). The carrier gas transports the formed by-products out of the reactor (7) and the atoms of interest (*e.g.* Cd and S or Zn and Se) diffuse to form nuclei of the desired material (4), followed by its growth on the substrate (5).^[2, 3]

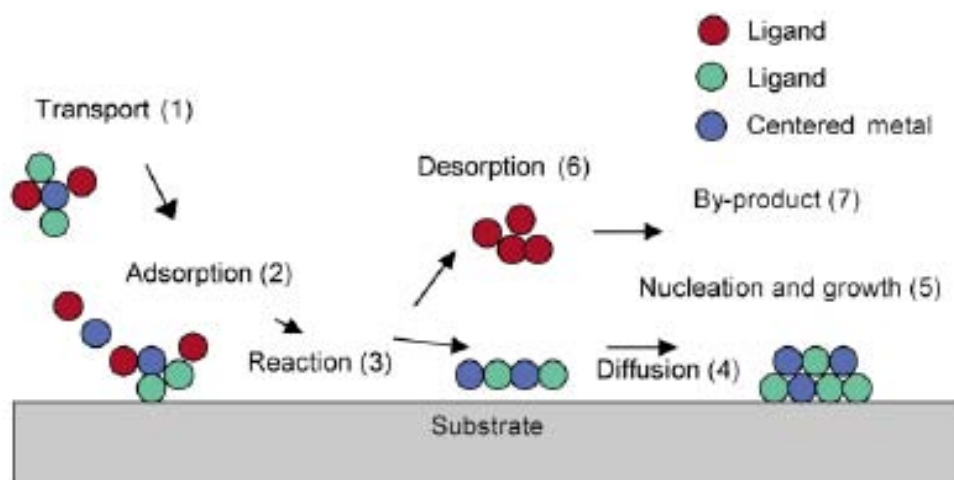


Fig. 4.1.1 Schematic diagram illustrating the CVD process. Taken from Ref [2].

Conventional CVD processes usually involve the use of volatile precursors and where these are multiple source precursors, they are highly reactive and susceptible to gas phase reactions.^[4] These can lead to powder formation and loss of control over film composition and structure. In addition, a large imbalance in molar ratios of the precursor materials is often required as differences in thermal reactivity and volatility of the precursors necessitates this for the ultimate formation of good quality thin films. Single source precursors with preformed M-E bonds (where M = Cd, Zn or other metal, E = S, Se or other chalcogen) are therefore a feasible alternative as their advantages include stoichiometry control, reduced pre-reactions and reduced air and moisture sensitivity.^[2]

Several different materials have been deposited using single source precursors and MOCVD, such as the use of bis[methyl(*n*-hexyl)-diselenocarbamate]Zn(II) for the deposition of ZnSe, as well as the deposition of CdSe using the Cd(II) analogue.^[5] Further studies on the MOCVD of CdSe have made use of Cd(SeR_f)₂ (R_f = 2,4,6-(CF₃)₃C₆H₂),^[6] Cd[(SePPh₂)₂N]₂,^[7] and [MeCd{(SePⁱPr₂)₂N}]₂,^[8] as single source precursors. In[(SePⁱPr₂)₂N]₂Cl^[9] and [R₂In(SePⁱPr₂)₂N]^[10] (where R = Me, Et) have also been investigated for the LP-MOCVD of In₂Se₃. Cadmium dipropyldithiocarbamate successfully deposited CdS onto GaAs substrates,^[11] and use of Ni(S₂CNRR')₂ complexes where RR' = Et₂, MeEt, MeⁿBu and MeⁿHex as single source precursors resulted in the successful deposition of nickel sulfide, although the phase composition sometimes varied.^[12] The deposition of CuS and CuSe was investigated using bis[methyl(*n*-hexyl)-dithio-diselenocarbamate]Cu(II) as single source precursors,^[13] and chalcopyrite thin films of the type CuME₂ (where M = In or Ga; E = S, Se) were grown using bis[methyl(*n*-hexyl)-dithio-diselenocarbamate]Cu(II) and bis[methyl(*n*-hexyl)-dithio-diselenocarbamate]M as single source

precursors.^[14] The LP-MOCVD of ZnSe has been studied using related diselenocarbamates, $[\text{RZnSe}_2\text{CNET}_2]_2$ where $\text{R} = \text{Me}, \text{Et}$,^[15] as well as the neopentyl and tert-butyl analogues, where $\text{R} = \text{Me}_3\text{CCH}_2$ and Me_3C .^[16] The sulfur analogues of the latter two complexes, *i.e.* $[\text{RZnS}_2\text{CNET}_2]_2$ where $\text{R} = \text{Me}_3\text{CCH}_2$ and Me_3C ,^[16] as well as zinc-bis(*O*-ethylxanthate) have been examined for the LP-MOCVD of ZnS thin films.^[17]

The use of LP-MOCVD is however sometimes problematic, as precursor volatility is required for successful deposition and frequently, potential single source precursors are not sufficiently volatile, or are polymeric compounds.^[6] In addition, LP-MOCVD depends on the delivery of the precursor at its equilibrium vapour pressure at the source temperature, where precursor complexes could decompose when subjected to the extended heating periods necessary to elevate the vapour pressure.^[2] In contrast, Aerosol Assisted Chemical Vapour Deposition (AACVD) allows the transport of an aerosol directly into the reactor, where both the precursor and solution evaporate. In AACVD (Fig. 4.1.2), the single source precursor is dissolved in an organic solvent (1), and using a piezoelectric modulator, converted into droplets containing both solvent and precursor (2). Use of a carrier gas allows the transport of this aerosol into the furnace or reactor, where evaporation takes place (3). The precursor vapour is transported to the substrate where it reacts and absorbs to form the film and organic by-products are removed by the carrier gas (4). This technique is suitable to form thin films from single source precursors with lower thermal stability and insufficient volatility to allow their use in LP-MOCVD.^[2, 4]

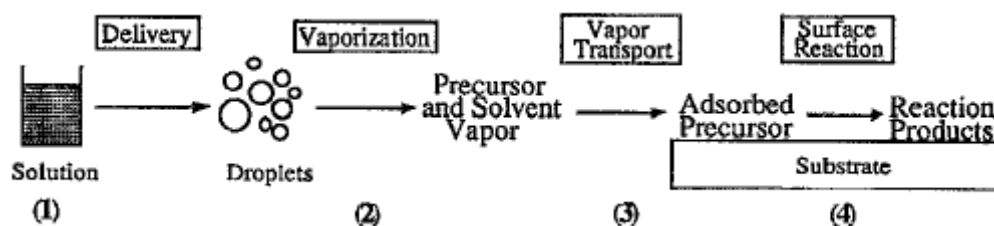


Fig. 4.1.2 Schematic representation of the AACVD process. Taken from Ref [3].

Calcium phosphate^[18] and magnesium oxide coatings have successfully been prepared with AACVD, the latter making use of magnesium ethoxide as a single source precursor.^[19] Examination of dialkyl dithiocarbamate metal complexes has led to the AACVD of MoS_2 ,^[20] cobalt sulfide and manganese sulfide.^[21] Deposition of $\beta\text{-In}_2\text{S}_3$ was affected using the novel precursor, $[\text{HL}]^+ [\text{In}(\text{SCOCH}_3)_4]^-$, where $\text{L} = 3,5\text{-dimethyl pyridine}$,^[22] with the same material being deposited using $\text{In}[(\text{SP}^i\text{Pr}_2)_2\text{N}]_2\text{Cl}$ as a precursor.^[23] Use of the closely related $\text{M}[\text{TeP}^i\text{Pr}_2)_2\text{N}]_2$, where $\text{M} = \text{Cd}, \text{Hg}$ has allowed the deposition of CdTe, and interestingly, where $\text{M} = \text{Hg}$, deposition of hexagonal telluride took place.^[24] AACVD of $[\text{Ti}(\text{O}^i\text{Pr})_4]$ and $[\text{W}(\text{O}^i\text{Ph})_6]$ has been investigated and deposition of titanium dioxide and tungsten trioxide was successfully affected, where the WO_3 thin films exhibited photochromic behaviour.^[25] Single source precursors of the type, $(\text{PPh}_3)_2\text{CuIn}(\text{SEt})_4$, have been used for the AACVD of CuInS_2 thin films.^[26] Ternary thin films of the type, $\text{Cd}_x\text{Zn}_{1-x}\text{S}$ have been formed from the AACVD of $\text{M}(\text{SOCC}(\text{CH}_3)_3)_2\text{TMEDA}$ metal complexes, where TMEDA = *N,N,N,N*-tetramethylethylenediamine, $\text{M} = \text{Cd}, \text{Zn}$. These syntheses exploited one of the advantages of AACVD, in that use of more than one precursor in the initial solution is possible, leading to the deposition of films with compositions not necessarily possible where only a single source precursor could be used.^[27] In this way thin films of Sn doped In_2O_3 were deposited, where $\text{In}(\text{III})$ acetylacetonate and $\text{Sn}(\text{IV})$ -bis-acetylacetonate-dibromide were used as precursor compounds.^[28]

As the *N,N*-dialkyl-*N'*-benzoyl(thio)selenoureas could successfully be used as single source precursors for the synthesis of a variety of different nanoparticles, selected metal complexes were investigated for their potential as single source precursors for the AACVD of thin films with an array of compositions.

4.2 Experimental

4.2.1 General methods and instrumentation

Single source precursors were synthesised according to methods described in Chapter 2. All other solvents and reagents were commercially available and used without further purification.

Thin film deposition was performed via Aerosol Assisted Chemical Vapour Deposition (AACVD) and a general procedure is as follows. A set amount of precursor was dissolved in toluene and placed in a 2 neck round bottomed flask. On one side, the flask was connected via tubing to a quartz reactor loaded with 2.5 x 1 cm glass substrates inside a Carbolite tube furnace and a flow of argon gas (flow rate: 160 sccm) was regulated using a Platon flow gauge on the other. The flask was set in an ultrasonic humidifier equipped with a piezoelectric modulator which generated droplets of the precursor solution which were then transferred by the carrier gas into the reactor chamber. Glass substrates were washed in concentrated nitric acid, before being successively washed with deionised water and oven dried. The quartz reactors were subjected to the same cleaning procedure. Substrate temperatures were varied according to the details given below.

The composition of the deposited films was examined by PXRD using a Bruker AXS D8 diffractometer equipped with monochromatic Cu-K α radiation (University of Manchester). The morphology was examined using a FEG-SEM Philips XL30 (University of Manchester), samples were carbon coated and EDAX-DX4 was used to confirm the film composition. Several films were reanalysed using a LEO 1430VP SEM (University of Stellenbosch), samples were gold coated and EDAX analysis was used to confirm the film composition. In certain cases, the required magnification could not be obtained using the LEO 1430VP SEM, despite alterations in beam spot size and voltage. Where the necessary resolution to examine film morphology could not be attained using SEM, Atomic Force Microscopy (AFM) (Nanosurf, easyScan 2 using a 10 μ m scan head in contact mode at the University of Stellenbosch) was used. Particle size was determined by measuring the diameter of selected particles using a software (freeware) programme called ImageJ. Transmission electron microscopy (TEM) was performed on a LEO 912 Omega (Zeiss, Oberkochen) instrument fitted with a 2k x 2k digital camera.

Voltage – current characteristics of selected films were determined using a Jandel Voltmeter, Model RM3, using the four-point probe method. This consists of four collinear and equally spaced electrodes, pressed into the surface of the film. Current is passed through the outer two electrodes and the voltage is measured between the inner two electrodes.^[29] In each case three different areas of the same film were tested for each current used and the results were averaged to obtain the values finally used. Film thickness measurements performed on selected films were done using a Dektak 8 Stylus profilometer. Both these instruments were only available at the University of Manchester.

4.2.2 Deposition conditions

4.2.2.1 Deposition using $[\text{Cd}^{\text{II}}(\text{L}^{1\text{a-e}}-\text{Se},\text{O})_2]$

The precursor, $[\text{Cd}^{\text{II}}(\text{L}^{1\text{a}}-\text{Se},\text{O})_2]$, (0.2 g) was dissolved in toluene (20 ml) and deposited for 120 minutes onto glass substrates at 7 different temperatures; 200, 225, 275, 325, 375, 425 and 475 °C.

The precursors, $[\text{Cd}^{\text{II}}(\text{L}^{1\text{b-e}}-\text{Se},\text{O})_2]$, (0.15 g) were dissolved in toluene (10 ml) and deposited for 90 minutes onto glass substrates at 250 °C.

4.2.2.2 Deposition using $[\text{Cd}^{\text{II}}(\text{L}^{2\text{a-e}}-\text{S},\text{O})_2]$

The precursor, $[\text{Cd}^{\text{II}}(\text{L}^{2\text{a}}-\text{S},\text{O})_2]$, (0.15 g) was dissolved in toluene (10 ml) and deposited for 90 minutes onto glass substrates at 4 different temperatures; 250, 325, 400 and 475 °C.

The precursors, $[\text{Cd}^{\text{II}}(\text{L}^{2\text{b-e}}-\text{S},\text{O})_2]$, (0.15 g) were dissolved in toluene (10 ml) and deposited for 90 minutes onto glass substrates at 250 °C.

4.2.2.3 Deposition using $[\text{Zn}^{\text{II}}(\text{L}^{1\text{a}}-\text{Se},\text{O})_2]$

The precursor, $[\text{Zn}^{\text{II}}(\text{L}^{1\text{a}}-\text{Se},\text{O})_2]$ (0.08 g), was dissolved in toluene (10 ml) and deposited for 90 minutes onto glass substrates at 4 different temperatures: 250, 325, 400 and 475 °C.

4.2.2.4 Deposition using $[\text{Zn}^{\text{II}}(\text{L}^{2\text{a}}-\text{S},\text{O})_2]$

The precursor, $[\text{Zn}^{\text{II}}(\text{L}^{2\text{a}}-\text{S},\text{O})_2]$ (0.15 g), was dissolved in toluene (10 ml) and deposited for 90 minutes onto glass substrates at 4 different temperatures: 250, 325, 400 and 475 °C.

4.2.2.5 Deposition using *cis*- $[\text{Ni}^{\text{II}}(\text{L}^{2\text{a}}-\text{S},\text{O})_2]$

The precursor *cis*- $[\text{Ni}^{\text{II}}(\text{L}^{2\text{a}}-\text{S},\text{O})_2]$ (0.08 g), was dissolved in toluene (10 ml) and deposited for 90 minutes onto glass substrates at 400 °C.

4.2.2.6 Deposition using *cis*- $[\text{Pd}^{\text{II}}(\text{L}^{2\text{a}}-\text{S},\text{O})_2]$

The precursor, $[\text{Pd}^{\text{II}}(\text{L}^{2\text{a}}-\text{S},\text{O})_2]$ (0.15 g), was dissolved in toluene (10 ml) and deposited for 90 minutes onto glass substrates at 4 different temperatures: 250, 325, 400 and 475 °C.

Material deposited at 325 °C was annealed under nitrogen overnight at 425 °C.

4.2.2.7 Deposition using *cis*- $[\text{Pt}^{\text{II}}(\text{L}^{2\text{a}}-\text{S},\text{O})_2]$

The precursor, $[\text{Pt}^{\text{II}}(\text{L}^{2\text{a}}-\text{S},\text{O})_2]$ (0.15 g), was dissolved in toluene (15 ml) and deposited for 120 minutes onto glass substrates at 4 different temperatures: 250, 325, 400 and 475 °C.

4.2.2.8 Deposition using *cis*- $[\text{Pd}^{\text{II}}(\text{L}^{1\text{a}}-\text{Se},\text{O})_2]$

The precursor, $[\text{Pd}^{\text{II}}(\text{L}^{1\text{a}}-\text{Se},\text{O})_2]$ (0.15 g), was dissolved in toluene (10 ml) and deposited for 90 minutes onto glass substrates at 5 different temperatures: 200, 250, 325, 400 and 475 °C.

4.3 Results and Discussion

4.3.1 Deposition of CdSe

Several single source precursors have been used for the Low Pressure – Metal Organic Chemical Vapour Deposition (LP-MOCVD) of CdSe thin films.^[5, 7, 30, 31] These include asymmetrically substituted diselenocarbamate complexes,^[5] as well as their symmetrically substituted counterparts.^[32] Separate Cd(II) and Se sources have been used for the synthesis of CdSe films using Chemical Bath Deposition (CBD), room temperature deposition of CdSe occurred on glass substrates, however high annealing temperatures were required to improve the crystallinity of the deposit.^[33, 34] The synthesis of several single source precursors such as $\text{MeCdSe}_2\text{CNEt}_2$ is not facile and requires the use of inert reaction conditions.^[31] Thin films synthesised using the LP-MOCVD of single source precursors, frequently require high reaction temperatures before deposition takes place, in the case of $\text{Cd}[(\text{SePPh}_2)_2\text{N}]_2$, thin film growth did not occur at temperatures lower than 475 °C.^[7] In addition, use of this and other related precursors frequently results in the phosphorous contamination of the resulting thin films, where this could have negative effects for the potential applications of these materials.

$[\text{Cd}^{\text{II}}(\text{L}^{\text{Ia}}\text{-Se},\text{O})_2]$ can be used to form crystalline CdSe nanoparticles at temperatures as low as 150 °C, and therefore shows potential for the relatively low temperature chemical vapour deposition of CdSe thin films.

4.3.1.1 Deposition using $[\text{Cd}^{\text{II}}(\text{L}^{\text{Ia}}\text{-Se},\text{O})_2]$

The precursor, $[\text{Cd}^{\text{II}}(\text{L}^{\text{Ia}}\text{-Se},\text{O})_2]$ was dissolved in toluene and 7 different temperatures were tested for deposition onto glass substrates. The PXRD patterns of the deposited material are shown in Fig. 4.3.1.

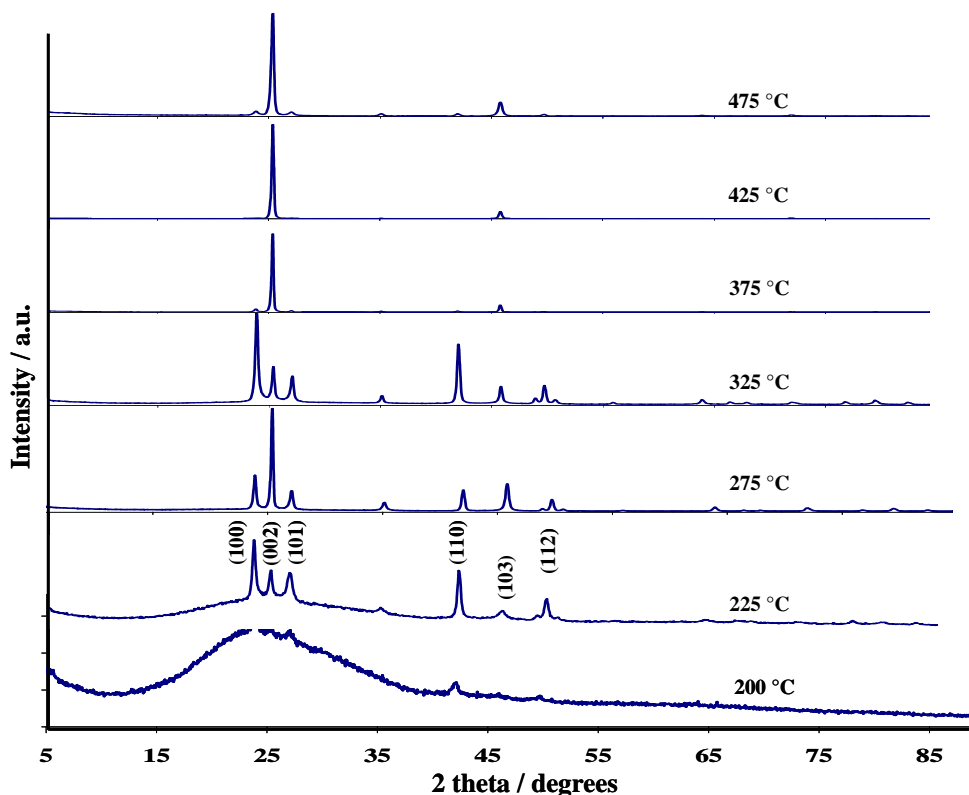


Fig. 4.3.1 PXRD patterns of CdSe following AACVD of $[\text{Cd}^{\text{II}}(\text{L}^{\text{Ia}}\text{-Se},\text{O})_2]$ at 200, 225, 275, 325, 375, 425 and 475 °C.

The lower temperature limit of deposition is clearly 225 °C as the PXRD pattern for material deposited at 200 °C is largely amorphous. A 25 °C higher temperature results in the deposition of hexagonally phased CdSe, the increased

intensity of the (100) peak indicating preferential orientation of the material along this plane. At 275 °C, the deposited phase is the same, however under these conditions, preferential alignment occurs along the (002) plane. A higher deposition temperature of 325 °C once again indicates preferred growth along the (100) plane. At the three highest reaction temperatures tested, 375, 425 and 475 °C the deposited phase remains consistent and the material is highly crystalline and ordered along the (002) plane, to such a degree that diffraction peaks from the remaining planes, although present are barely visible in Fig. 4.3.1. The morphology of the deposited material was examined using SEM and selected images are shown in Fig. 4.3.2.

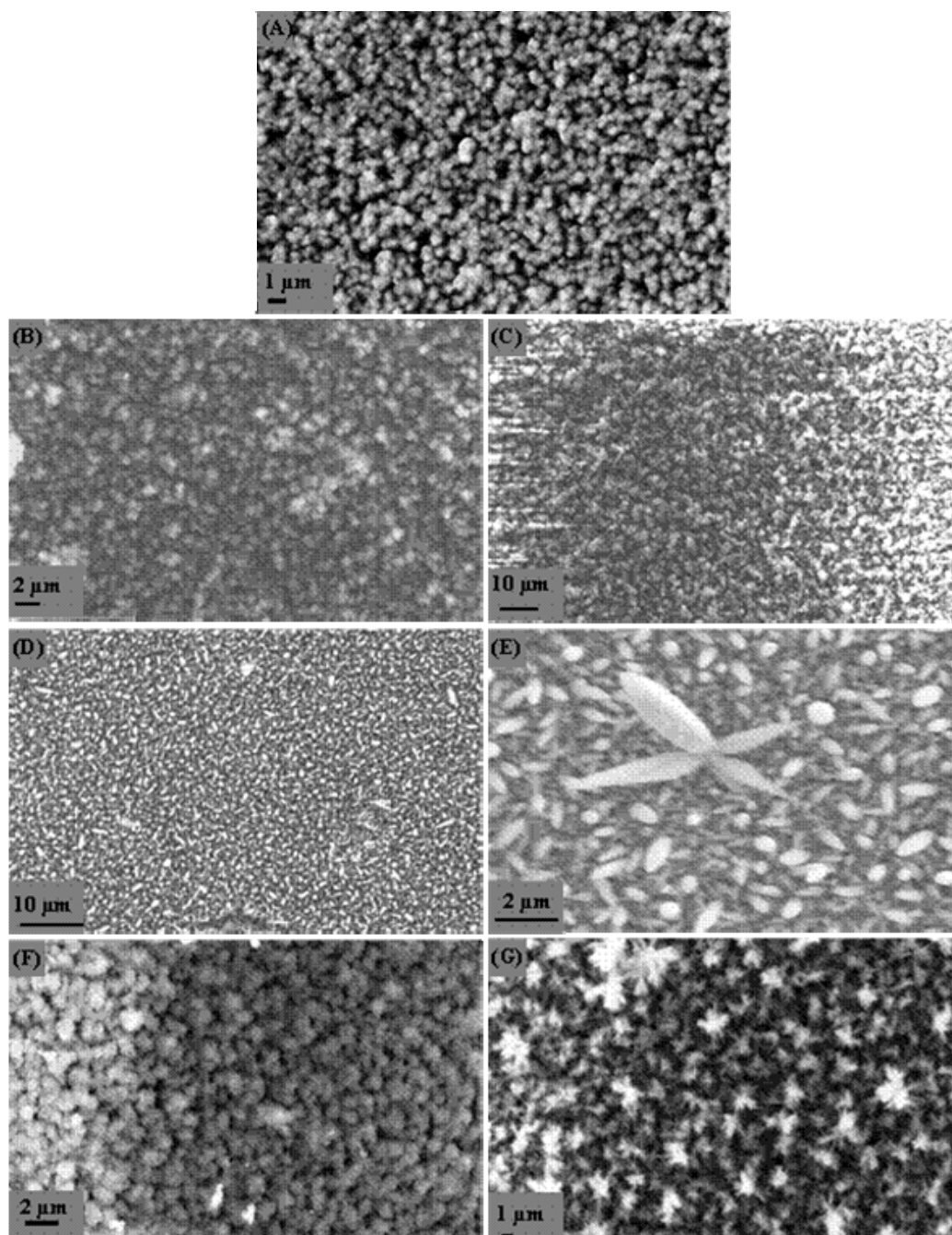


Fig. 4.3.2 SEM images showing morphology of CdSe obtained at deposition temperatures of (A) 225 °C, (B) 275 °C, (C) 325 °C, (D) 375 °C, (E) 375 °C, (F) 425 °C, (G) 475 °C.

Material deposited at 225 °C exhibits a roughly spherical morphology and crystallite sizes of approximately 0.3 (15) μm in diameter. The presence of the substrate in certain areas seen by the darker areas in the SEM image indicates relatively poor film coverage; EDAX analysis confirmed a 1:1 ratio of Cd to Se (Table 4.3.1). Higher deposition temperature (275 °C), results in roughly spherical crystallites, 0.8 (16) μm in diameter and substrate coverage appears to be slightly increased relative to that at 225 °C. A slight excess of selenium is present in the thin films formed at this temperature. Deposition at 325 °C yields small, spherical crystallites, 0.7 (13) μm in diameter that appear to cluster together to form slightly larger, roughly spherical crystallites, 1.4 (17) μm in diameter that are visible in Fig. 4.3.2. Similarly to the films deposited at 275 °C, excess selenium is present in the thin films deposited at 325 °C. In Fig. 4.3.2 both images (D) and (E) are different magnifications of films deposited at 375 °C. Two size regimes of crystallites are clearly present, larger oblate crystallites, 3.2 (20) μm in length (E) and numerous smaller crystallites approximately 1.4 (12) μm in length with a rice-like morphology. EDAX analysis of both the larger and smaller structures indicated that both are of similar composition (Cd:Se, 1:1). Substrate coverage at this temperature is clearly improved relative to that at lower temperatures. Deposition temperatures of 425 °C and 475 °C both exhibit good substrate coverage and the morphology of the 475 °C deposition is quite different to that obtained at any previous temperature. Roughly spherical crystallites, 1.0 (11) μm in diameter obtained at 425 °C, now appear to resemble snowflakes at 475 °C. The composition is also slightly altered from favouring cadmium at 425 °C, to a slight selenium excess at 475 °C.

Table 4.3.1 Composition of CdSe thin films obtained at varying deposition temperatures

Deposition Temp	Ratio of Cd:Se	Crystallite size / μm
225 °C	0.99	0.3 (15)
275 °C	0.89	0.8 (16)
325 °C	0.83	0.7 (13) and 1.4 (17)
375 °C	1.00	3.2 (20) and 1.4 (12)
425 °C	1.07	1.0 (11)
475 °C	0.93	1.1 (34)

Film thickness measurements performed on samples of film obtained at each deposition temperature are graphically depicted in Fig. 4.3.3. As expected, the thinnest films are obtained at the lower deposition temperatures, where the thickest films were deposited at 325 °C (38.1 kÅ) and 425 °C (52.2 kÅ). Increasing the temperature to 475 °C significantly reduced the amount of CdSe deposition. Unexpectedly thin films result from deposition at 375 °C, where SEM analysis indicates fair substrate coverage and density and PXRD analysis shows the presence of significantly crystalline material. The value used is however the average of three readings, each of which are very similar, suggesting that this result is not artificial.

Absorption spectra of the deposited material at selected temperatures could be determined, and in each case the band gap was found to be smaller than that of bulk CdSe (1.73 eV).^[35]

This precursor was also used to investigate the potential of these compounds for use in LP-MOCVD however the reaction proved unsuccessful as no deposition was observed on the glass substrate.

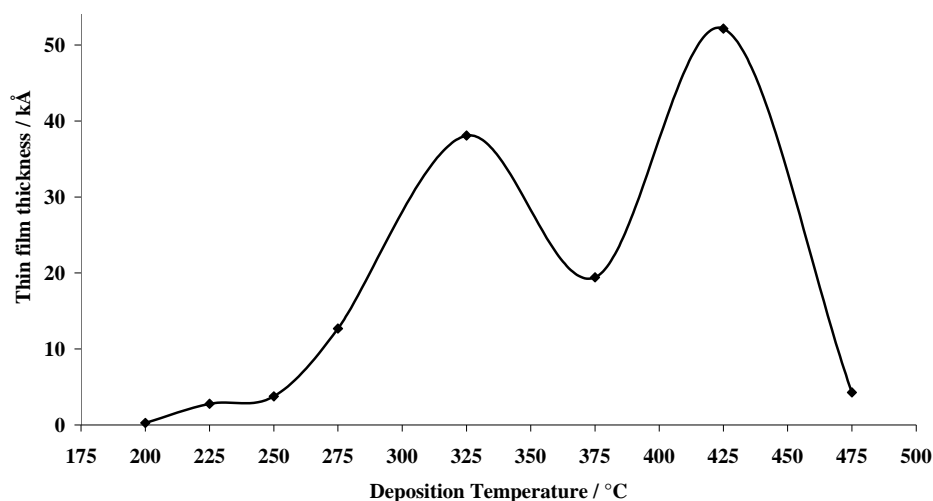


Fig. 4.3.3 Variation of CdSe film thickness with deposition temperature.

Therefore as expected, significantly more crystalline material and better coverage of the substrate was obtained at higher temperatures however it is very interesting to note that deposition of crystalline CdSe did occur at a temperature as low as 225 °C allowing for the potential deposition on a wide variety of less heat resistant materials. Kapton, a flexible polyimide film manufactured by Du Pont is known to be stable at temperatures as high as 260 °C for extended periods of time. Given the fairly good quality CdSe obtained by AACVD at 250 °C this material could most likely be used as a substrate. The structure of Kapton is shown in Fig. 4.3.4 where the presence of the carbonyl groups implies a degree of polarity. As CdSe appears to adhere relatively well to the polar surface of the glass substrates used, kapton or other related polybenzimidazole polymeric tapes hold potential as alternative substrates for lower CdSe deposition temperatures.

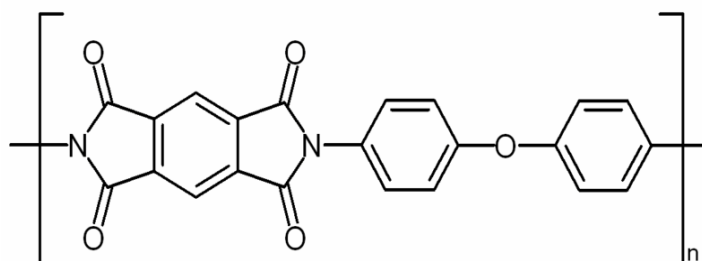


Fig. 4.3.4 Structure of Kapton.^[36]

It is also interesting to note that the phase of CdSe remained consistently different to that obtained for the HDA capped nanoparticles formed from the same precursor (Section 3.3.2.1). The temperature range of these sets of experiments overlap, where nanoparticle synthesis was examined between 100 and 250 °C, over which the zinc-blende phase remained consistent and thin film deposition took place between 225 and 475 °C over which the wurtzite phase remained consistent.^[37] This illustrates, to a degree, the vastly different reaction environments of the two processes and the effects these can have on the obtained material, from the same precursor. This observation is continually made throughout the chapter where in almost every case, AACVD of the precursor gives rise to material different to that obtained from its thermolysis.

4.3.1.2 Deposition using $[\text{Cd}^{\text{II}}(\text{L}^{\text{1b-e}}-\text{Se},\text{O})_2]$

As a continuation of the thermolysis work in the previous chapter, the precursors $[\text{Cd}^{\text{II}}(\text{L}^{\text{1b-e}}-\text{Se},\text{O})_2]$ were tested under similar conditions to the diethyl analogue, however due to time constraints on the available instrumentation, only 1 temperature (250 °C) could be tested. The PXRD data obtained are shown in Fig. 4.3.5.

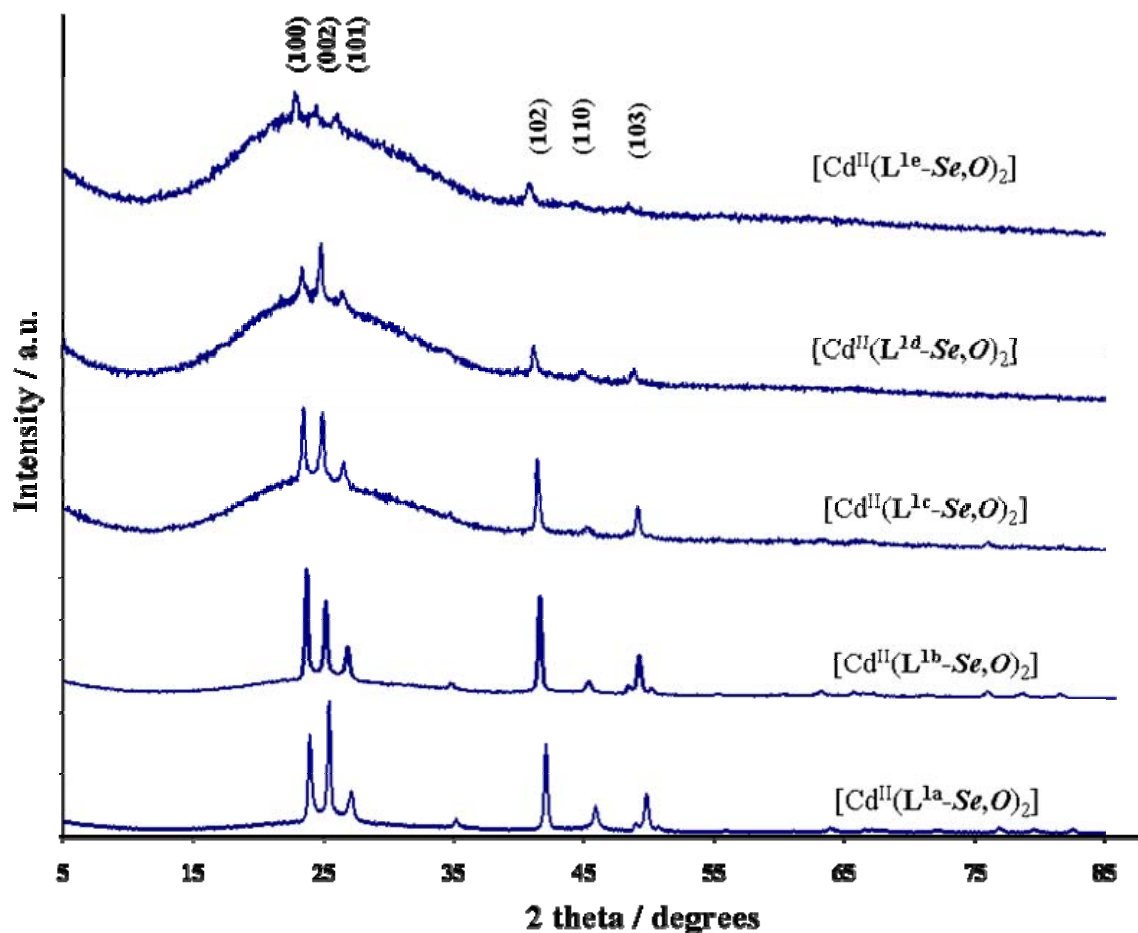


Fig. 4.3.5 PXRD patterns of CdSe following AACVD of $[\text{Cd}^{\text{II}}(\text{L}^{\text{1a-e}}-\text{Se},\text{O})_2]$ at 250 °C.

From the PXRD patterns obtained it appears as though precursor alkyl chain length does indeed affect the quality of the deposited material, where the longest chain precursor $[\text{Cd}^{\text{II}}(\text{L}^{\text{1d}}-\text{Se},\text{O})_2]$ deposited CdSe with a significantly reduced crystallinity relative to that deposited using $[\text{Cd}^{\text{II}}(\text{L}^{\text{1a}}-\text{Se},\text{O})_2]$. Interestingly however, the asymmetrically substituted $[\text{Cd}^{\text{II}}(\text{L}^{\text{1e}}-\text{Se},\text{O})_2]$ resulted in the deposition of material with the lowest crystallinity. Retrospectively, the increased alkyl chain length in the precursor most likely results in increased hydrophobic interactions between the dialkyl residues, necessitating the need for higher deposition temperatures and aromatic interactions in $[\text{Cd}^{\text{II}}(\text{L}^{\text{1e}}-\text{Se},\text{O})_2]$ may play a role in the observations made for material deposited from this precursor. It is interesting to note however that hexagonally phased CdSe is consistently deposited from each precursor, despite each of these resulting in the formation of zinc-blende phased CdSe nanoparticles. The preferred orientation however, is slightly altered as the chain length increases, from a favoured (002) orientation for material deposited using $[\text{Cd}^{\text{II}}(\text{L}^{\text{1a}}-\text{Se},\text{O})_2]$, to a favoured (100) orientation for material deposited using both $[\text{Cd}^{\text{II}}(\text{L}^{\text{1b}}-\text{Se},\text{O})_2]$ and $[\text{Cd}^{\text{II}}(\text{L}^{\text{1c}}-\text{Se},\text{O})_2]$. $[\text{Cd}^{\text{II}}(\text{L}^{\text{1d}}-\text{Se},\text{O})_2]$ depositing CdSe exhibits preferential alignment along the (002) plane.

Given the poor quality films obtained following AACVD of the precursors $[\text{Cd}^{\text{II}}(\text{L}^{\text{1b-e}}\text{-Se}, \text{O})_2]$, SEM analysis was not performed on any of the films, due to the costly nature of this method and the limited information that would likely be obtained.

4.3.2 Deposition of CdS

The deposition of CdS has been widely investigated and several single source precursors have been reported. Malandrino *et. al.* used $\text{Cd}(\text{tta})_2\text{tmeda}$ (where $\text{tta} = 2\text{-thenoyl-trifluoroacetone}$, and $\text{tmeda} = N,N,N,N\text{-tetramethylethylenediamine}$) for the deposition of CdS,^[38] and several reports describe the use of dialkyldithiocarbamate Cd(II) complexes for the LP-MOCVD of CdS onto GaAs^[11] and quartz substrates.^[39] Cadmium complexes of the type, $[\text{Cd}\{(\text{SPiPr})_2\text{N}\}_2]$ have also been used in the LP-MOCVD of CdS, however the resulting thin films exhibited a fair degree (2 %) of phosphorous contamination.^[30] Use of monomeric thioacetate complexes, $\text{Cd}(\text{SOCCH}_3)_2\text{tmeda}$ for the AACVD of CdS have also been investigated.^[4]

Similarly to its selenium analogue, the ability of $[\text{Cd}^{\text{II}}(\text{L}^{\text{2a}}\text{-S}, \text{O})_2]$ to form crystalline nanoparticles, indicated its potential for use as a single source precursor for the deposition of CdS thin films using AACVD.

4.3.2.1 Deposition using $[\text{Cd}^{\text{II}}(\text{L}^{\text{2a}}\text{-S}, \text{O})_2]$

$[\text{Cd}^{\text{II}}(\text{L}^{\text{2a}}\text{-S}, \text{O})_2]$ was dissolved in toluene and 4 different temperatures were used to examine the deposition onto glass substrates. Fig. 4.3.6 shows the PXRD patterns of the deposited material.

Reaction of $[\text{Cd}^{\text{II}}(\text{L}^{\text{2a}}\text{-S}, \text{O})_2]$ at 250 °C results in the poor deposition of CdS as seen from the quality of the PXRD pattern. This is in contrast to the selenium analogue, $[\text{Cd}^{\text{II}}(\text{L}^{\text{1a}}\text{-Se}, \text{O})_2]$, where reaction at this temperature results in the deposition of significantly more crystalline CdSe (Fig. 4.3.5), reflecting the relative stability of both precursor complexes. Deposition at 325 °C clearly shows the formation of hexagonally phased CdS, where orientation along the (002) plane is slightly favoured. Interestingly, deposition of CdSe at this temperature indicates preferential alignment along the (100) plane. CdS deposition occurs at temperatures of both 400 and 475 °C, where in each case, the material is highly ordered along the (002) plane. Generally, different temperatures led to altering preferential phase alignment in the case of CdSe, where this is less evident for CdS, although it must be mentioned that fewer temperatures were tested for this material. The morphology of the deposited material was examined using SEM and selected images are shown in Fig. 4.3.7 for material deposited at 250 and 325 °C. Very poor quality images were obtained for material deposited at 400 and 475 °C, and these films were then analysed using AFM, where selected images are shown in Fig. 4.3.7.

As indicated by the PXRD pattern, deposition of material at 250°C is very poor, and this is reflected in the SEM image where large areas of the substrate remain uncoated. The isolated areas of deposited material are spherical in shape with an average diameter of 0.62 (28) μm, and EDAX analysis indicates a Cd:S ratio very close to unity (Table 4.3.2). A higher deposition temperature (325 °C), indicates significantly improved substrate coverage, where smaller spherical crystallites 0.32 (14) μm in diameter agglomerate to form larger irregularly shaped crystallites, 0.76 (9) μm in diameter. The Cd:S ratio in this case is slightly cadmium deficient.

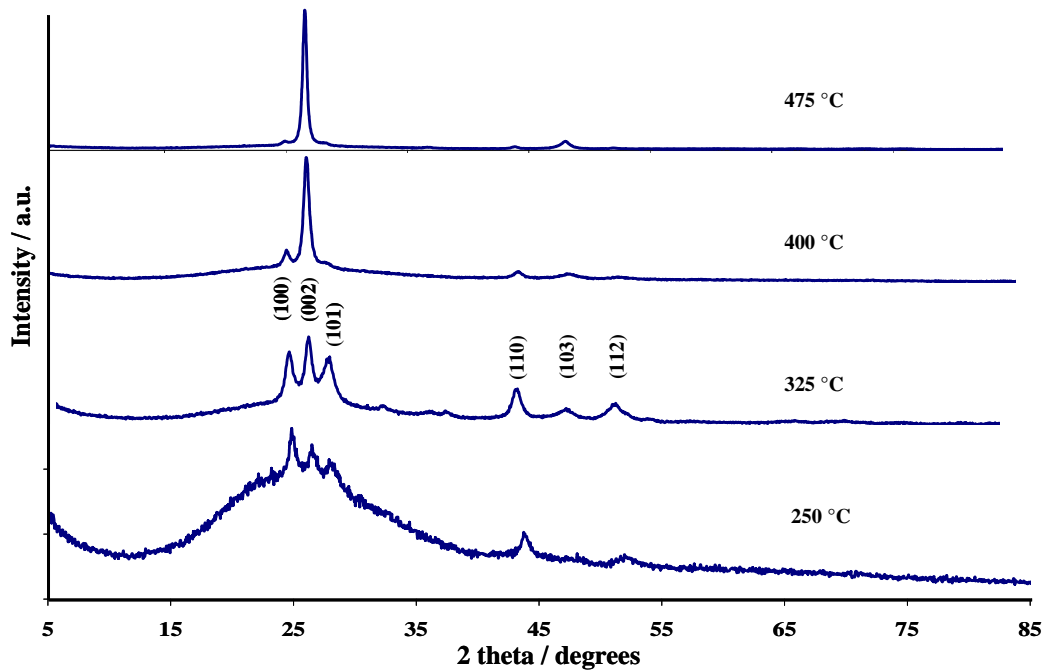


Fig. 4.3.6 PXRD patterns of CdS following AACVD of $[\text{Cd}^{\text{II}}(\text{L}^{2\text{a}}-\text{S},\text{O})_2]$ at 250, 325, 400 and 475 °C.

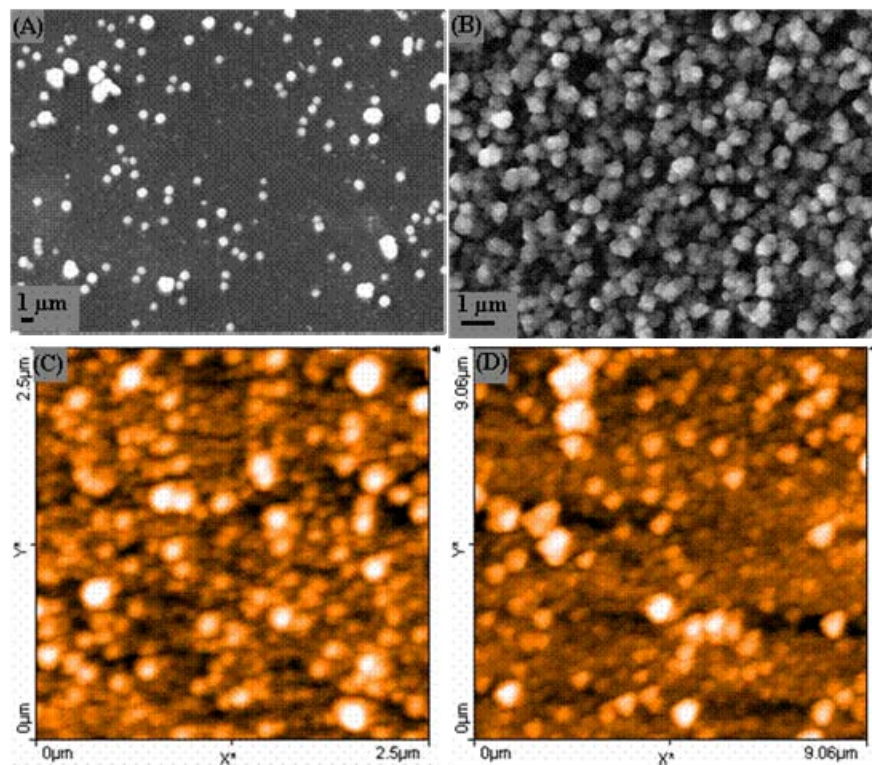


Fig. 4.3.7 SEM images showing morphology of CdS obtained at deposition temperatures of (A) 250 °C, (B) 325 °C, and AFM images of CdS obtained at deposition temperatures of (C) 400 °C and (D) 475 °C.

The absorption spectrum of material deposited at 325 °C was examined and the band edge calculated to be 2.2 eV, smaller than the 2.53 eV of bulk CdS.^[30] AFM analysis of the two higher deposition temperatures both show that the spherical morphology of the crystallites is maintained, however the size distribution appears slightly smaller at 400 °C, where crystallites range between 0.08 and 0.17 μm, larger crystallites and a larger size distribution resulting

from deposition at 475 °C, (0.018 – 0.45 μm). A slight sulfur deficiency is evident in the EDAX analysis of the material deposited a 400 °C, however deposition at 475 °C returns the Cd:S ratio to unity.

Table 4.3.2 Composition of CdS thin films obtained at varying deposition temperatures

Deposition Temp	Ratio of Cd:S	Crystallite size / μm
250	0.94	0.62 (28)
325	0.91	0.32 (14) and 0.76 (9)
400	0.75	0.08 – 0.17
475	1.00	0.18 – 0.45

Similarly to $[\text{Cd}^{\text{II}}(\text{L}^{1\text{a}}\text{-Se}, \text{O})_2]$, deposition of $[\text{Cd}^{\text{II}}(\text{L}^{2\text{a}}\text{-S}, \text{O})_2]$ results in better substrate coverage and significantly more crystalline material at higher reaction temperatures. In each case the formation of hexagonally phased CdS is consistent, contrasting to the zinc blende nanoparticles obtained from thermolysis of this precursor (Section 3.3.2.2). The temperature range of these sets of experiments overlap, where nanoparticle synthesis took place between 125 and 300 °C, over which the zinc blende phase remained consistent, despite reports indicating a possible phase transition from zinc blende to wurtzite at 300 °C.^[40] Deposition experiments performed between 250 and 475 °C, consistently indicate the presence of hexagonally phased CdS, suggesting that the reaction environment in the AACVD process favours the formation of the stable hexagonal phase, whilst the reaction environment in the thermolysis reactions supports the formation of the metastable cubic phase of CdS, and that reaction temperature alone, in the case of thermolysis reactions, may play a less crucial role in phase determination.

4.3.2.2 Deposition using $[\text{Cd}^{\text{II}}(\text{L}^{2\text{b-e}}\text{-S}, \text{O})_2]$

As a continuation of the thermolysis work in Chapter 3, the precursors $[\text{Cd}^{\text{II}}(\text{L}^{2\text{b-e}}\text{-S}, \text{O})_2]$ were reacted under similar conditions to the diethyl analogue, and as time on the instrumentation was limited, a deposition temperature of 250 °C was tested. The PXRD patterns obtained are shown in Fig. 4.3.8. As in the case of the complexes, $[\text{Cd}^{\text{II}}(\text{L}^{1\text{b-e}}\text{-Se}, \text{O})_2]$, alkyl chain length of the precursor does indeed appear to effect the quality of the resulting material, where CdS with very poor crystallinity was deposited following reaction of $[\text{Cd}^{\text{II}}(\text{L}^{2\text{b-e}}\text{-S}, \text{O})_2]$. The poorest quality material was obtained following reaction of $[\text{Cd}^{\text{II}}(\text{L}^{2\text{d}}\text{-S}, \text{O})_2]$, where the increased hydrophobic interactions between the dioctyl residues may necessitate a higher deposition temperature to obtain crystalline material. Given the poor quality of the material, little comment can be made regarding CdS orientation following reaction of the various precursors. It is however clear that hexagonally phased material is deposited following reaction of $[\text{Cd}^{\text{II}}(\text{L}^{2\text{a-c,e}}\text{-S}, \text{O})_2]$, the crystalline quality of CdS deposited using $[\text{Cd}^{\text{II}}(\text{L}^{2\text{d}}\text{-S}, \text{O})_2]$ being too poor to allow phase differentiation. This is again in contrast to the phase of material obtained following thermolysis of each of these precursors, where zinc blende CdS was consistently formed; these results reflect observations made for the selenium analogues.

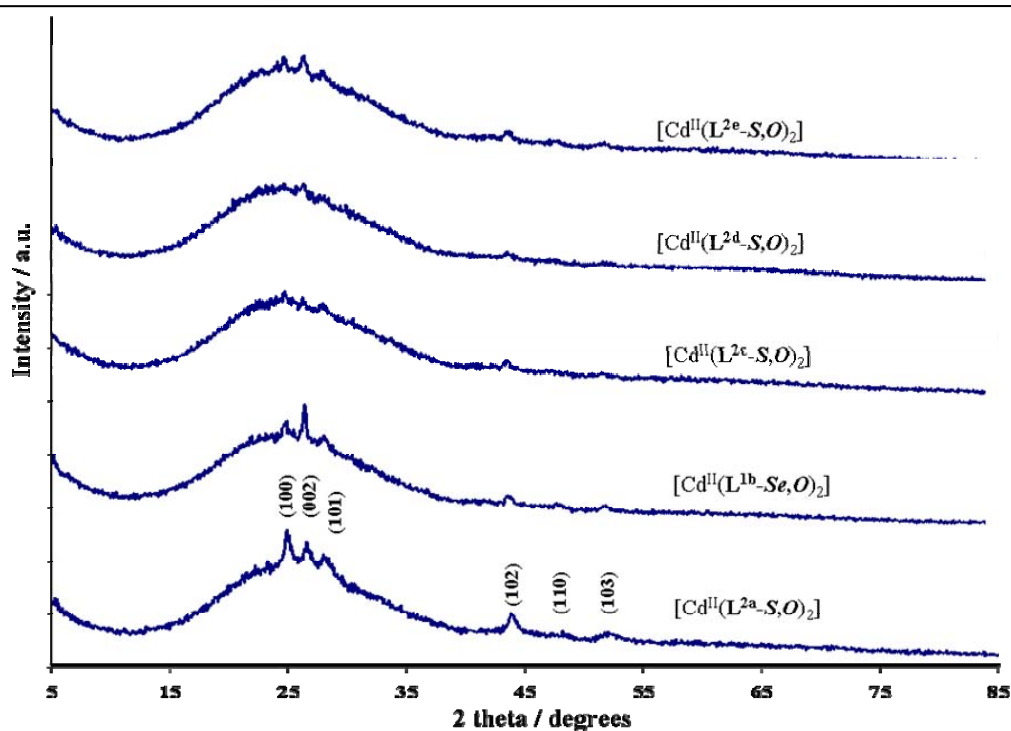


Fig. 4.3.8 PXRD patterns of CdS following AACVD of $[\text{Cd}^{\text{II}}(\text{L}^{2\text{a-e}}-\text{S},\text{O})_2]$ at 250 °C.

The poor crystalline quality of the films obtained following AACVD of the precursors $[\text{Cd}^{\text{II}}(\text{L}^{2\text{a-e}}-\text{S},\text{O})_2]$ did not warrant their SEM analysis, given the costly nature of this method and the limited information that would likely be obtained.

4.3.3 Deposition of ZnSe

Separate sources of zinc and selenium (diethyl zinc and diisopropyl selenide) have been used in the MOCVD of ZnSe nanowires, where the deposited material exhibited zinc blende crystallinity.^[41] Single source precursors have also been employed in the LP-MOCVD of ZnSe, and these include $[\text{EtZnSe}_2\text{CNEt}_2]_2$,^[31] $[\text{MeZnSe}_2\text{CNEt}_2]_2$,^[15] $[\text{Zn}\{\text{SePPh}_2\}_2\text{N}]_2$,^[7] and $[\text{Zn}\{\text{SePiPr}_2\}_2\text{N}]_2$.^[30] Frequently however, high temperatures are needed before deposition occurs,^[7] and in some cases the use of a phosphorous containing precursor results in phosphorous contamination of the resulting thin film.^[30] The absence of phosphorous in the air stable precursor, $[\text{Zn}^{\text{II}}(\text{L}^{1\text{a}}-\text{Se},\text{O})_2]$, could lead to the deposition of high quality ZnSe thin films from this complex. Thermolysis of $[\text{Zn}^{\text{II}}(\text{L}^{1\text{a}}-\text{Se},\text{O})_2]$ resulted in the formation of ZnO nanoparticles (Section 3.3.5.2) and it was therefore with interest that the AACVD of this precursor was investigated at four different temperatures, 250, 325, 400 and 475 °C. The PXRD patterns obtained are illustrated in Fig. 4.3.9.

At the lower deposition temperature of 250 °C, largely amorphous material was obtained. Interestingly, the Cd(II) analogue allows the deposition of crystalline material at this temperature, reflecting observations made in Section 2.3.6.1 where the thermal decomposition profile of $[\text{Cd}^{\text{II}}(\text{L}^{1\text{a}}-\text{Se},\text{O})_2]$ indicates a decomposition onset at lower temperature than that of its Zn(II) counterpart. Reaction of $[\text{Zn}^{\text{II}}(\text{L}^{1\text{a}}-\text{Se},\text{O})_2]$ at 325 °C allows the deposition of crystalline ZnSe. The 2 theta values obtained experimentally correspond closely (although not 100 %) to those expected for cubically phased ZnSe. As the deposition temperature is increased to 400 °C, the crystallinity is maintained, and again corresponds largely to zinc blende ZnSe, although the presence of hexagonally phased material is likely. This trend continues as the deposition temperature increases, where at 475 °C, the ZnSe corresponds more closely to that of wurtzite phased material than cubic. Rietveld refinement of the data would be

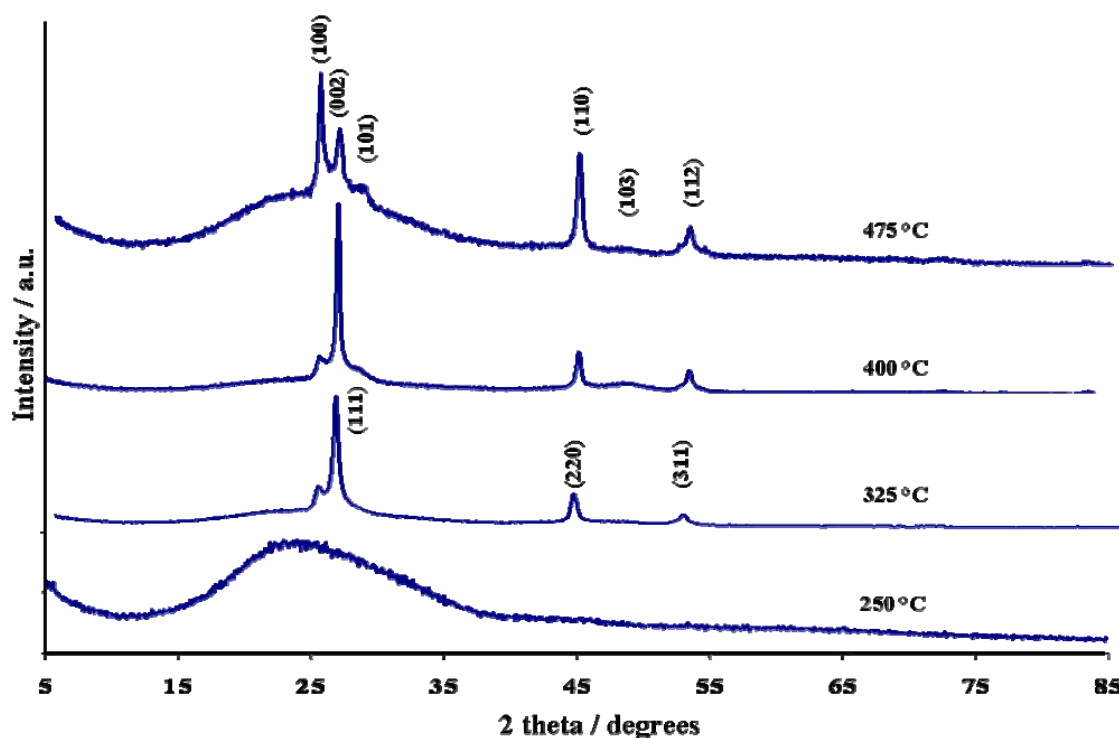


Fig. 4.3.9 PXRD patterns of ZnSe following AACVD of $[\text{Zn}^{\text{II}}(\text{L}^{\text{Ia}}\text{-Se},\text{O})_2]$ at 250, 325, 400 and 475 °C.

necessary to conclusively confirm this observation; however the data quality resulting from the instrument detector precludes this possibility. Despite this, semi-quantitative values of the relative percentage of each phase present can be obtained. To perform this analysis, the most intense peaks of each phase were used in the scaling process. For cubic material the maximum intensity is expected at 2θ values of 27.49 ° and 45.68 °, and for hexagonal material maximum intensities are expected at 2θ values of 25.99 ° and 45.66 °. Because the second values for each phase are so close together, the first 2θ values for each phase were used in the scaling process and the results are shown in Table 4.3.3. As this analysis is semi-quantitative, only integer values have been quoted and these can merely be used as an indication of the relative percentages. It is clear that material deposited at 325 and 400 °C is mostly cubically phased with similar quantities of hexagonally phased material being present. As the deposition temperature increases to 475 °C the relative percentages are exchanged and the deposited material is now largely hexagonally phased with approximately 1/3 of cubically phased ZnSe being present. These observations are not unexpected for ZnSe systems, where LP-MOCVD of $[\text{MeZnSe}_2\text{CNEt}_2]_2$ results in the deposition of cubically phased material^[15] and $[\text{Zn}\{\text{SePiPr}_2\text{N}\}_2]$ allows the formation of hexagonally phased ZnSe.^[30] Whilst the phase transition from zinc blende to wurtzite material occurs between 1411 and 1420 °C for bulk material,^[42, 43] the difference in total energy between the two phases is only 5.3meV/atom,^[43] therefore the presence of both phases following a single deposition does not seem unlikely. Indeed, Cozzoli *et al.* have reported the presence of both phases in ZnSe nanoparticles, allowing the development of unusual anisotropic structures.^[43]

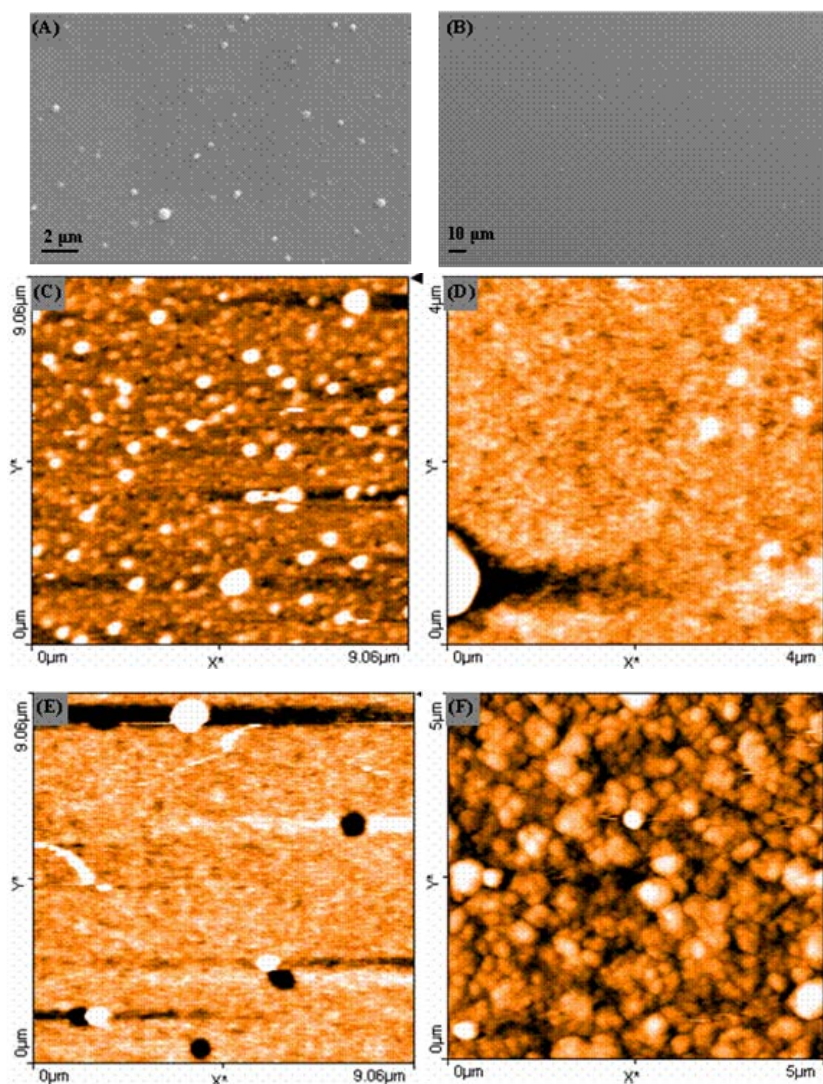
Absorption spectra indicated a band gap value of 3.07 eV for the material deposited at 250 °C, and 2.82 eV for that deposited at 325 °C. Deposition temperatures of 400 and 475 °C indicate band gap values of 2.52 and 2.44 eV respectively where all these values compare well with the 2.58 eV of bulk ZnSe.^[30]

Sections of the films obtained at each deposition temperature were carbon or gold coated and SEM analysis was attempted, however in each case, poor resolution and insufficient magnification prevented useful images from being obtained, however EDAX analysis could be performed and the results are given in Table 4.3.3.

Table 4.3.3 Semi-quantitative analysis of ZnSe phases and composition of thin films obtained at varying deposition temperatures of $[\text{Zn}^{\text{II}}(\text{L}^{\text{Ia}}-\text{Se},\text{O})_2]$.

Deposition temp. / °C	% cubic phase present	% hexagonal phase present	Spot analysis Zn:Se ratio	Area analysis Zn:Se ratio	Crystallite size / μm
325	83	17	0.77	0.96	0.19 (16) and 0.05 (24)
400	87	13	0.93	0.92	0.06 (19)
475	33	67	1.20	1.22	0.35 (31) and 0.14 (29)

Spot and area analysis were obtained for each sample. Fig. 4.3.10 does show 2 of the SEM images obtained from deposition at 325 and 475 °C (A and B). In each case large, approximately spherical crystallites were observed randomly distributed on the surface of the film, these were analysed using a spot analysis and sections of the film where unclear smaller crystallites were visible under the SEM were analysed using the area analysis. Table 4.3.3 shows that the larger crystallites visible using the SEM are actually ZnSe, although slightly Zn deficient crystallites are obtained at deposition temperatures of 325 and 400 °C. Area analysis indicates approximate 1:1 Zn:Se ratios for all three temperatures shown. As SEM proved unsuitable for analysis of these samples, AFM was used to obtain some indication of film coverage and surface morphology. The images are shown in Fig. 4.3.10 (C-F).

**Fig. 4.3.10** SEM images of ZnSe films deposited at 325 and 475 °C (A, B). AFM images of ZnSe films deposited at (C) 250, (D) 325, (E) 400 and (F) 475 °C.

At a deposition temperature of 250 °C, despite the PXRD pattern not showing the presence of any ZnSe, two clear size distributions of spherical crystallites appear to be present; the larger approximately 0.32 (18) μm in diameter and the smaller varying between 0.14 and 0.16 μm in diameter with an average value of 0.15 (15) μm. Thin film coverage appears to be better than expected at such a low deposition temperature, however areas of uncovered substrate (indicated by the darker shading in the AFM image) are present. At a higher deposition temperature of 325 °C larger (0.19 (16) μm) and smaller crystallites (0.05 (24) μm) are still present although it appears that the larger crystallites are less numerous than those obtained at 250 °C. It appears as though deposition at the higher temperature is more uniform and that substrate coverage is slightly better than that observed for the 250 °C sample. Deposition at 400 °C also gives crystallites with a spherical morphology and 2 size regimes are evident; larger crystallites, 0.42 – 0.52 μm in diameter and smaller crystallites with an average diameter of 0.06 (19) μm. Substrate coverage appears to be very good at this deposition temperature however it is interesting to note that spherical holes appear in the thin film corresponding in size to those of the larger crystallites and Fig. 4.3.10 (E) shows 2 larger crystallites next to two of these holes, suggesting that these were formed by the removal of the larger crystallites. The morphology of the deposition obtained at 475 °C appears spherical in nature however the degree of agglomeration is greater than that observed at lower temperatures. Distinct size regimes of crystallites are no longer visible; rather they appear more evenly distributed and range in size between 0.17 and 0.26 μm in diameter. Substrate coverage appears to be slightly worse at this higher temperature than previously observed at 400 °C, reflecting the poorer quality of the PXRD pattern obtained from deposition at 475 °C.

The deposition of ZnSe using $[\text{Zn}^{\text{II}}(\text{L}^{\text{1a}}\text{-Se},\text{O})_2]$ as a single source precursor is quite remarkable, given that thermolysis of the same precursor at 150 °C yields ZnO nanoparticles. Clearly under the different reaction conditions present during the AACVD process, formation of ZnSe is favourable.

4.3.4 Deposition of ZnS

Of the II-VI compound semiconductors, the ~3.7 eV band gap of ZnS is the largest at room temperature making ZnS one of the materials with considerable potential for applications in optoelectronic devices operating in the UV or blue region of the UV/Visible spectrum.^[44] Several different techniques based on vapour deposition have been employed in the synthesis of crystalline ZnS thin films. These include the growth of ZnS thin films on yttria-stabilised-zirconia substrates using Pulsed Laser Deposition (PLD),^[44] and the use of separate sources of zinc and sulfur (dimethyl zinc and hydrogen sulfide) for the Plasma Assisted Metal Organic Chemical Vapour Deposition (PA-MOCVD) of cubically phased ZnS on silica glass substrates.^[45] The employment of single source precursors has also been reported, where the polymeric zinc dithiocarbamate, $[\{\text{Zn}[\text{S}_2\text{CN}(\text{Me})\text{CH}_2\text{CH}_2\text{CH}_2\text{NMe}_2\}_2]_n$, has been used for the LP-MOCVD of ZnS film growth.^[46] Very thin films of ZnS have been grown from the CVD of zinc bis(*O*-ethylxanthate) although the crystalline phase of the deposit could not be established;^[17] the isopropyl analogue, zinc bis(*O*-isopropylxanthate) also shows potential as a single source precursor.^[47] Use of $[\text{Zn}\{\text{SPiPr}_2\}_2]$ as a single source precursor however results in a slight phosphorous contamination of the deposited thin film and fairly high deposition temperatures are needed.^[30] The use of $[\text{Zn}^{\text{II}}(\text{L}^{\text{2a}}\text{-S},\text{O})_2]$ as a single source precursor for the synthesis of ZnS nanoparticles showed great potential and AACVD of this metal complex was therefore investigated over a range of 4 different temperatures. The PXRD patterns of the obtained material are shown in Fig. 4.3.11.

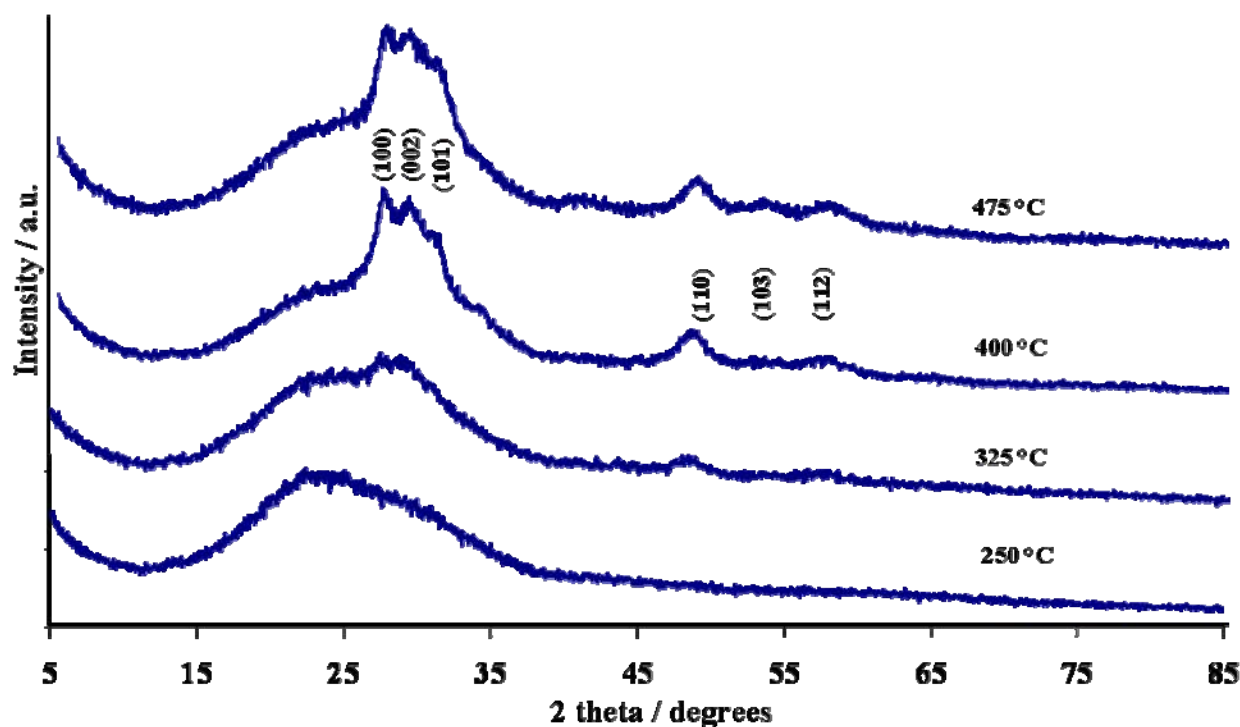


Fig. 4.3.11 PXRD patterns of ZnS following AACVD of $[\text{Zn}^{\text{II}}(\text{L}^{2\text{a}}\text{-S},\text{O})_2]$ at 250, 325, 400 and 475 °C.

The lower deposition temperature of 250 °C yielded largely amorphous material and only a slight indication of crystallinity is evident from deposition at 325 °C. As the deposition temperature increases the film quality appears to improve, where deposition at 475 °C yields the best results. In each case the PXRD patterns resemble hexagonally phased ZnS, but the 2 theta values obtained experimentally do not correspond exactly to those of the known standard. The d spacing does not vary by the same amount at both high and low angles, precluding the possibility of sample height accounting for this difference, and it is therefore possible that the presence of small percentages of cubically phased material could alter the 2 theta values slightly, as in the case of ZnSe, however the data quality prohibits both Rietveld refinement and semi-quantitative calculations to confirm this. Comparison with results obtained following deposition of ZnSe, indicate the deposition of significantly more crystalline material at lower temperatures (325 °C) following reaction of $[\text{Zn}^{\text{II}}(\text{L}^{1\text{a}}\text{-Se},\text{O})_2]$ than observed here following reaction of the sulfur analogue. This could possibly reflect the stability difference of the two precursors, where higher temperatures are needed for the decomposition of $[\text{Zn}^{\text{II}}(\text{L}^{2\text{a}}\text{-S},\text{O})_2]$ and deposition of crystalline material.

SEM images of samples obtained at deposition temperatures of 250 and 325 °C are shown in Fig. 4.3.12 (A and B respectively). Deposition at 250 °C resulted in very poor substrate coverage as expected from the amorphous nature of the PXRD pattern, however spherical crystallites are present and vary in size with an average diameter of 0.65 (20) μm . Spherical crystallites between 0.19 and 0.48 μm in diameter with an average size of 0.4 (19) μm were obtained from deposition at 325 °C and in this case the substrate coverage can be seen to be significantly improved relative to that obtained from deposition at 250 °C. Whilst suitable images could not be obtained for films grown at 400 and 475 °C, EDAX analysis could be performed on each sample and indicated an approximate 1:1 Zn:S ratio, although in each case the films grown appeared to be slightly S deficient. The large difference in vapour pressure between zinc and sulfur frequently results in the deposition of non-stoichiometric thin films, and therefore an exact 1:1 ratio is rarely obtained.^[45] AFM was performed on the samples from 400 and 475 °C deposition and the results

are shown in Fig. 4.3.12 (C and D respectively). At both temperatures approximately spherical crystallites were obtained; those deposited at 400 °C appearing in the size range 0.13 – 0.3 μm with an average of 0.2 (18) μm, slightly smaller than those obtained at the higher temperature where sizes vary between 0.27 – 0.41 μm in diameter with an average of 0.3 (20) μm. In both cases substrate coverage appears significantly increased relative to that at lower deposition temperatures as expected from the PXRD patterns. The band gap of material deposited at 475 °C, was calculated as 3.5 eV, this comparing well with that of the bulk value of ~ 3.7 eV.

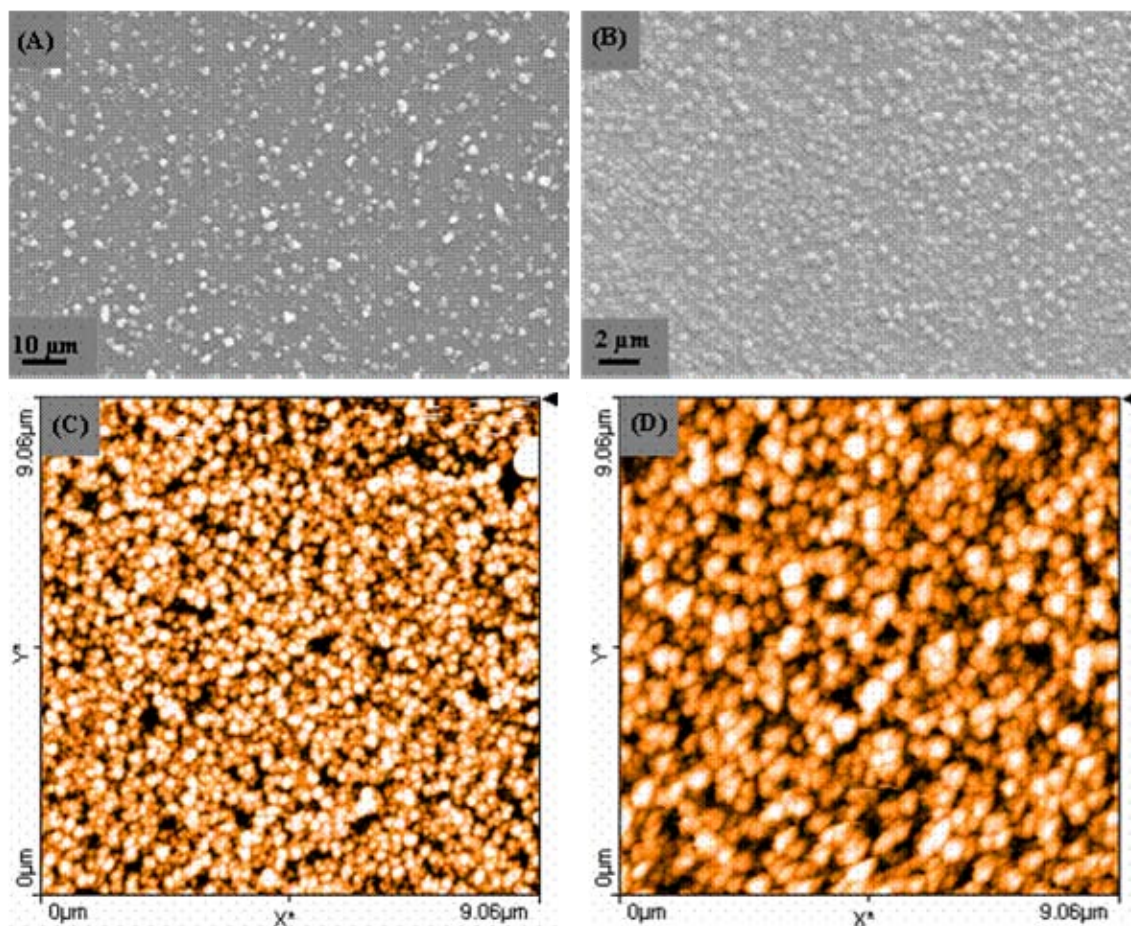


Fig. 4.3.12 SEM images of ZnS films deposited at 250 and 325 °C (A, B). AFM images of ZnS films deposited at 400 (C) and 475 (D) °C.

It is interesting to note that thermolysis of $[\text{Zn}^{\text{II}}(\text{L}^{2\text{a}}-\text{S},\text{O})_2]$ resulted in the formation of cubically phased nanoparticles, whereas hexagonally phased ZnS was deposited onto the glass substrates using the same precursor. Both cubic and hexagonally phased material have been formed following chemical vapour deposition procedures,^[30, 45] although the cubic phase is generally considered to be the more stable, where the zinc-blende – wurtzite transition takes place in the region of 1023 °C.^[44] The phase transformation of nanocrystalline material may however differ to that of the bulk, allowing the formation of stable wurtzite nanocrystals under the experimental conditions used.^[48, 49]

The precursor, $[\text{Zn}^{\text{II}}(\text{L}^{2\text{a}}-\text{S},\text{O})_2]$, therefore shows potential for the deposition of crystalline ZnS onto glass substrates.

4.3.5 Deposition of Ni_3S_2

Only a single report detailing the use of single source precursors for the AACVD of nickel sulfide thin films could be found.^[50] In this report Waters *et. al.* made use of nickel dithiocarbamate precursors and the deposited material consisted of mixtures of various nickel sulfide phases such as Ni_7S_6 , NiS_2 and $\text{NiS}_{1.03}$. As previously mentioned, Section 3.3.5.4, several phases of nickel sulfide exist such as Ni_3S_2 , Ni_7S_6 , Ni_9S_8 , $\alpha\text{-NiS}$, $\beta\text{-NiS}$, Ni_3S_4 and NiS_2 .^[51] As nanoparticles were formed from thermolysis of *cis*- $[\text{Ni}^{\text{II}}(\text{L}^{2a}\text{-S},\text{O})_2]$, it was with interest that this complex was used as a precursor in the AACVD process. Due to time constraints on the instrumentation, only one deposition temperature could be tested and the PXRD pattern of the material obtained following reaction of *cis*- $[\text{Ni}^{\text{II}}(\text{L}^{2a}\text{-S},\text{O})_2]$ at 400 °C is shown in Fig. 4.3.13.

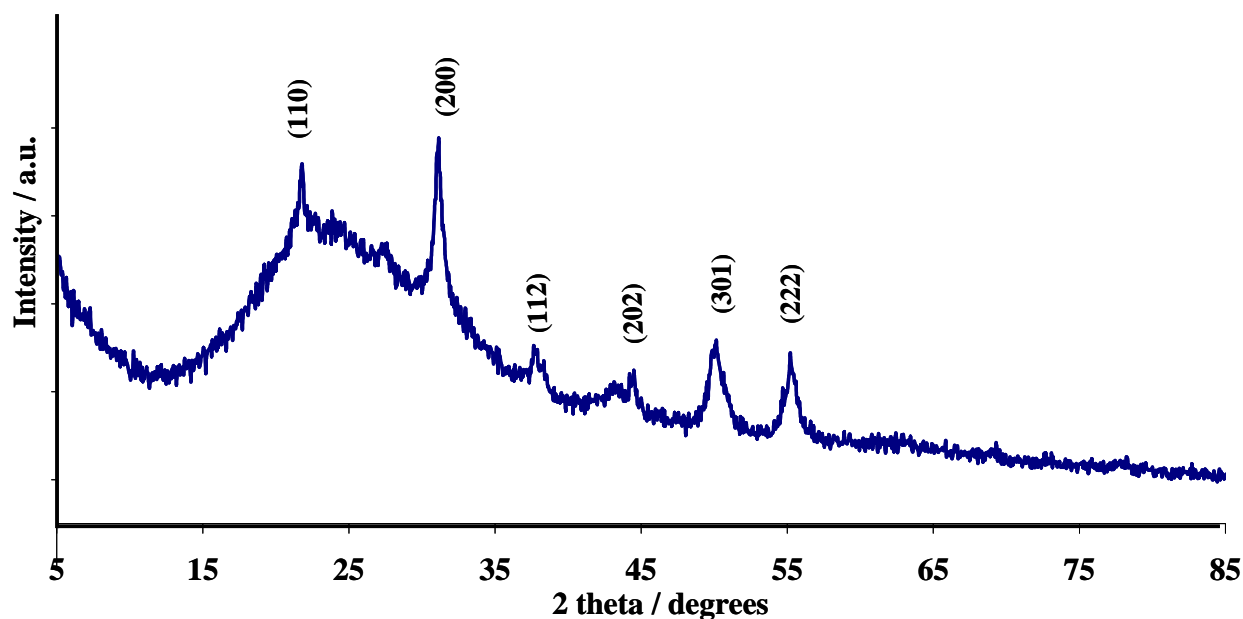


Fig. 4.3.13 PXRD pattern of Ni_3S_2 deposited, following AACVD of *cis*- $[\text{Ni}^{\text{II}}(\text{L}^{2a}\text{-S},\text{O})_2]$ at 400 °C.

This PXRD pattern corresponds to that of heazewoodite, Ni_3S_2 , a rhombohedral phase of nickel sulfide, where this phase appears to be relatively pure with no evidence of a second phase being present. This observation is remarkable given the experience of Waters *et. al.* where mixtures of nickel sulfide phases were obtained.^[50] The SEM images are shown in Fig. 4.3.14 (A and B). A lower magnification (A) indicates good substrate coverage, and a higher magnification (B), reveals an interesting morphology. The deposit appears to resemble a wire mesh, the nature of the morphology makes exact measurement difficult, however the fibres are estimated to be between 1 and 5 μm in length and no significant ordering of the mesh is evident. EDAX analysis indicated an approximate 1.8 Ni:S ratio, very close to the expected 1.5 for Ni_3S_2 . Sections of the deposited material were removed from the glass substrate, suspended in toluene and analysed using TEM. The images obtained are shown in Fig. 4.3.14 (C and D). Remarkably, triangular nanoparticles, are present in the mesh and in (C), their aggregation around the length of a central fibre is evident. At least 3 different morphologies are illustrated in (D). Triangular nanoparticles are present in the centre of the image, with an average length of 14.8 (12) nm. Darker fibres are evident in the bottom half, and thicker, lighter fibres are present in the top half of the image. The dark fibre in the bottom right hand corner is remarkably uniform, 7.3 (4) nm in diameter. That of the dark fibre in the left hand corner is similar at 6.1 nm (12), however slightly less uniform as indicated by the larger standard deviation. The two thinner, lighter fibres are 4.9 (7) and 6.9 (7) nm in diameter, whilst those of the two thicker fibres are 12 (11) nm and 15 (3) nm in diameter, where

the most left hand fibre is significantly less uniform than the right hand fibre as indicated by the standard deviation. The microscope resolution is not sufficient to allow lattice spacing determination, however HRTEM would give very interesting insight into the nature of these materials, *i.e.* whether they are all crystalline and the same phase of nickel sulfide, if so, the formation of the uniform 2 dimensional fibres has potential applications. Differing morphologies of nickel sulfide have been reported, where Yu *et. al.* investigated the synthesis of nickel sulfides using soft solution processing techniques. Reaction of a nickel salt, and sulfur in the presence of ethylenediamine led to the formation of both spherical and rod shaped morphologies for the same procedure, EDAX analysis confirming the NiS₂ phase of the spherical particles and the NiS phase of the rods.^[52]

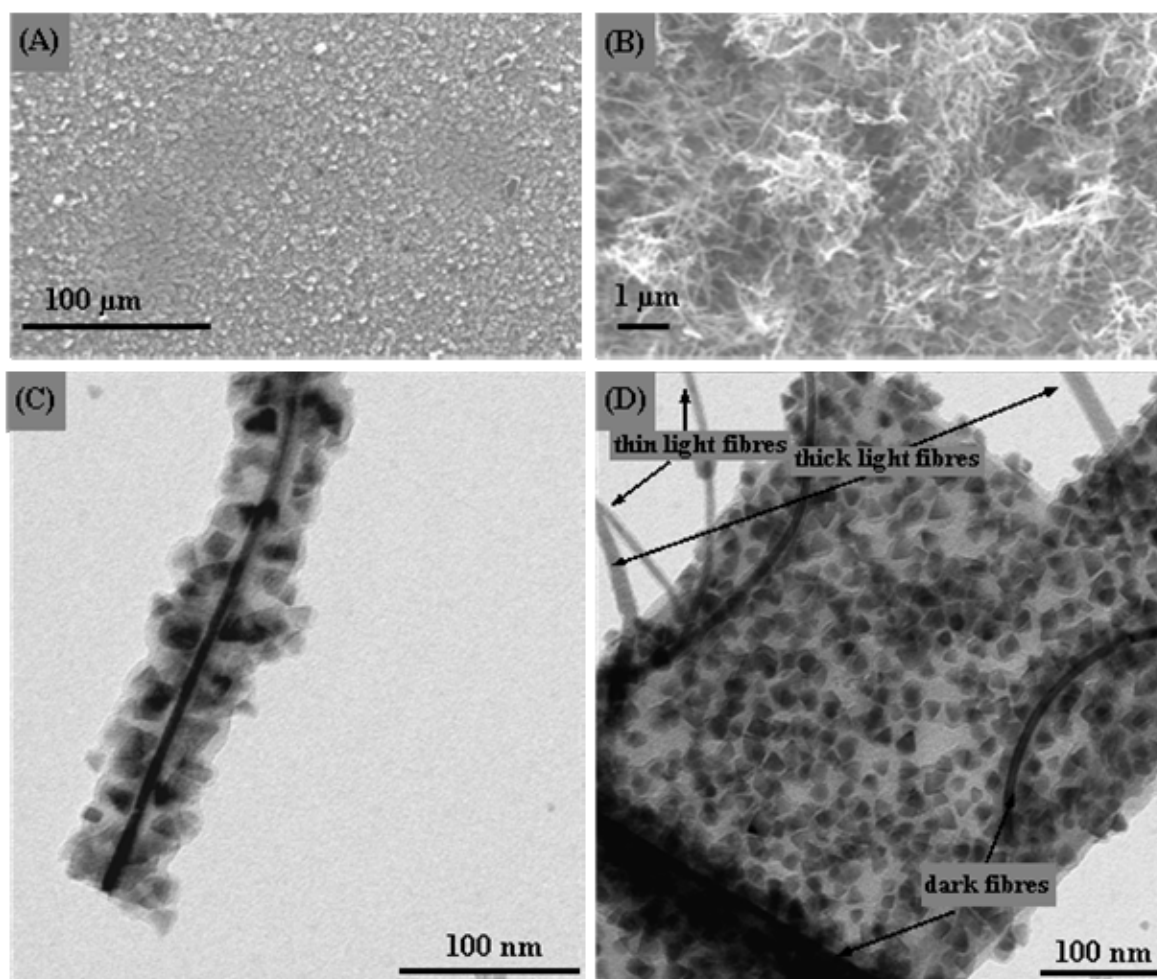


Fig. 4.3.14 SEM images of Ni₃S₂ deposited following AACVD of *cis*-[Ni^{II}(L^{2a}-S,O)₂] at 400 °C (A and B). TEM images of deposited material (C and D).

Thermolytic decomposition of nickel thiolate precursors in the presence of octanoate has led to the formation of a mixture of triangular and rod shaped morphologies, both composed of NiS (millerite). From the same reaction, misshaped needles and other particulates were also formed, and these were found to be composed of Ni₃S₄, thought to have formed as a byproduct.^[53] Altering the deposition conditions, using *cis*-[Ni^{II}(L^{2a}-S,O)₂] as a single source precursor, could therefore lead to the deposition of a variety of different morphologies of nickel sulfides with varying compositions

Film thickness measurements were performed using a profilometer, and showed an average film thickness of 14.08 kÅ.

The deposition of crystalline Ni₃S₂ following reaction of *cis*-[Ni^{II}(L^{2a}-S,O)₂] is interesting, given the unknown composition of nanoparticles formed following thermolysis of the same precursor. Further work using this complex could yield very interesting results regarding the phase of the different morphologies evident in Fig. 4.3.14 (D), as well as their potential application.

4.3.6 Deposition using *cis*-[Pd^{II}(L^{2a}-S,O)₂]

Similarly to the case of nickel sulfide, only a single report detailing the use of palladium dithiocarbamate complexes as single source precursors for the synthesis of palladium sulfide thin films via AACVD could be found.^[50] Reaction of these precursors resulted in the deposition of a mixture of palladium sulfide phases, reminiscent of the results obtained for their nickel analogues. LP-MOCVD of bis(*n*-hexyl(methyl)dithiocarbamato)palladium(II) however, resulted in the formation of PdS thin films.^[54] As a continuation of our interest in the PGM's, the precursor *cis*-[Pd^{II}(L^{2a}-S,O)₂] was reacted at four different temperatures, in an attempt to deposit palladium sulfide. The PXRD patterns of the resulting material are shown in Fig. 4.3.15.

These results reflect those reported in Section 3.3.5.6, where well defined spherical nanoparticles were obtained following thermolysis of *cis*-[Pd^{II}(L^{2a}-S,O)₂], however PXRD analysis did not indicate the formation of any crystalline material. In Fig. 4.3.15, the most crystalline material appears to be that deposited at 400 °C, however the pattern can not be matched to any of those in the database, and the identity of the material could not be established. To improve the crystallinity of the deposit, samples obtained at a deposition temperature of 325 °C were annealed at 425 °C and reanalysed. The resulting PXRD pattern is illustrated in Fig. 4.3.16.

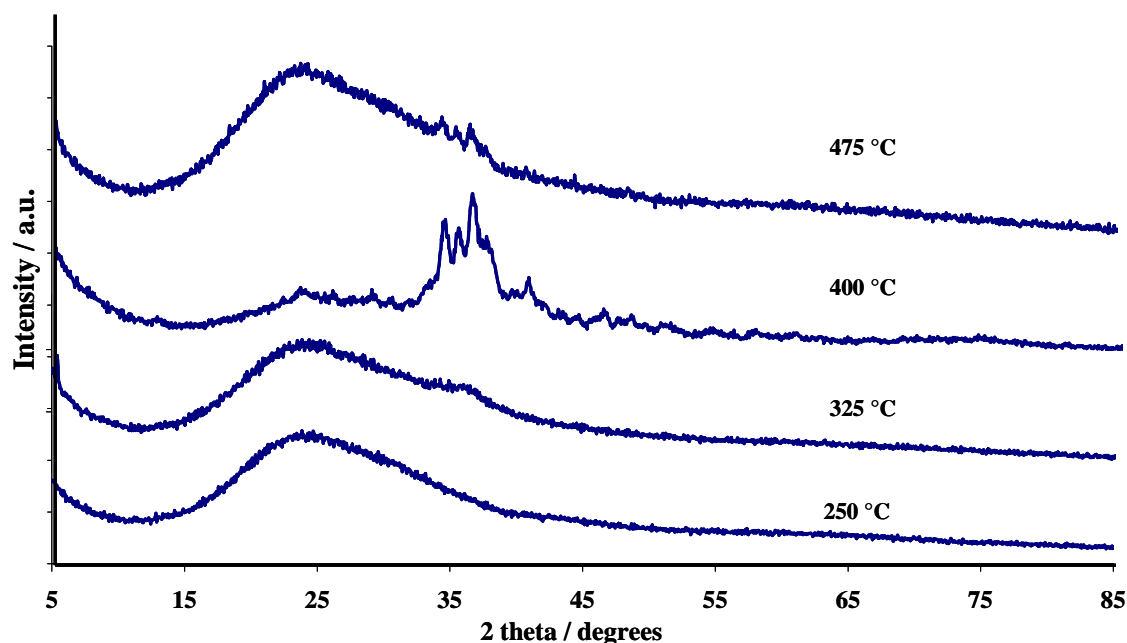


Fig. 4.3.15 PXRD patterns obtained following AACVD of *cis*-[Pd^{II}(L^{2a}-S,O)₂] at 250, 325, 400 and 475 °C.

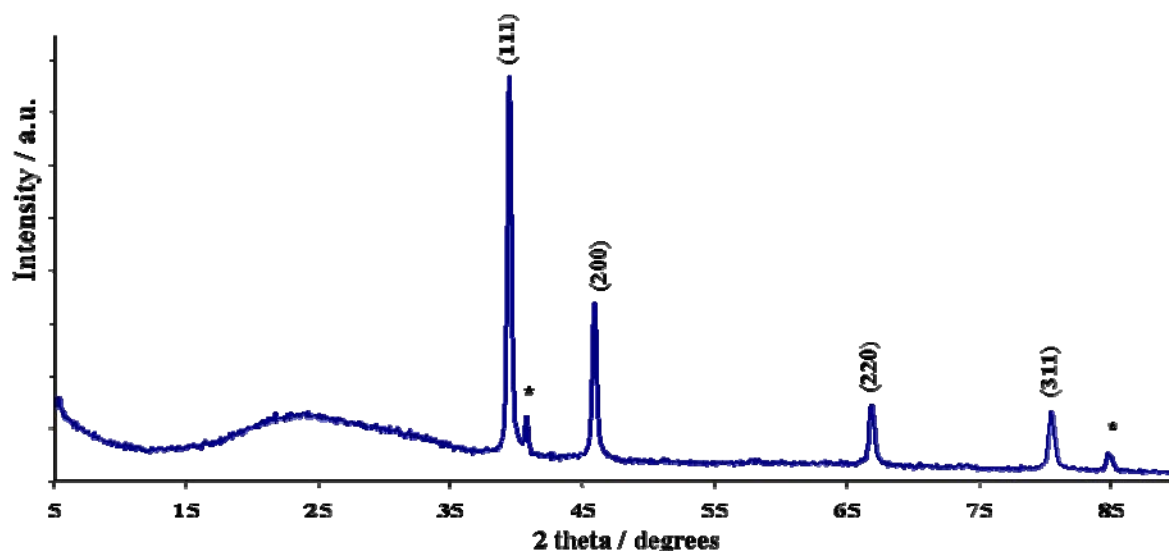


Fig. 4.3.16 XRD patterns of Pd, following AACVD of *cis*-[Pd^{II}(L^{2a}-S,O)₂] at 325 °C and annealing at 425 °C.* indicate peaks of unknown origin.

The crystallinity of the deposit was significantly improved and the XRD pattern corresponds to that of palladium metal. The appropriate Miller indices are indicated above each peak, however * indicates two peaks of unknown origin at 40.8 and 85 °. The deposition of palladium is quite remarkable given the 2:1, S:Pd ratio present in the precursor.

The morphology of the films was investigated using SEM, before and after annealing and the images are shown in Fig. 4.3.17. Approximately spherical crystallites are clearly visible prior to annealing (A and B) and range in size between 1.37 and 1.84 μm. Spot EDAX analysis on one of these particles indicated a large palladium percentage relative to that of sulfur, Pd:S = 2.3:1. Following annealing (C and D), the number of spherical crystallites present is clearly reduced, and the surface of the films appear more uniform. A spot EDAX analysis on the large crystallite clearly visible in Fig. 4.3.17 (C), indicates a significantly increased palladium percentage, where the Pd:S ratio increased to 13.8:1. An area EDAX analysis on this sample (not including the crystallite) indicated only the presence of palladium as no sulfur was observed, these results reflecting those obtained from XRD analysis. A magnified area of the film obtained following annealing (Fig. 4.3.17 (D)), indicates the presence of holes, 0.3 – 0.5 μm in diameter, in a mat of more finely formed crystallites. It is interesting to note that the small white crystallites evident in (D) are of approximately the same size. Annealing of the thin film clearly reduces the sulfur concentration and improves the crystallinity of the remaining palladium.

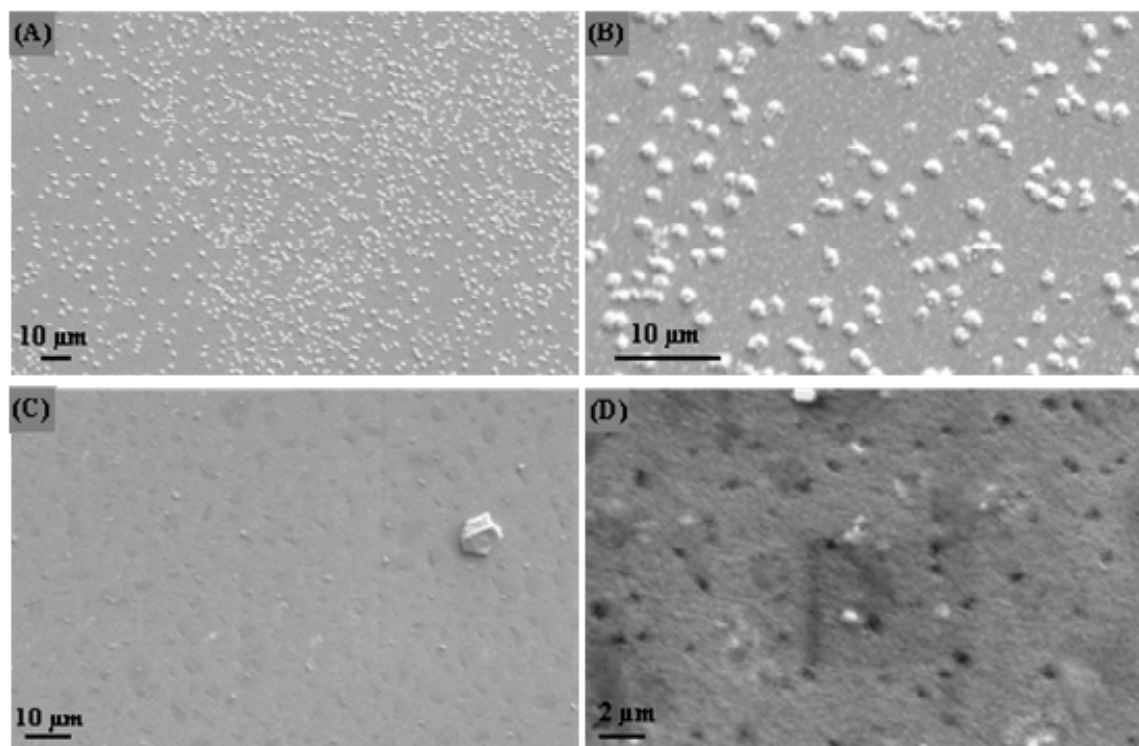


Fig. 4.3.17 SEM images of deposit obtained following AACVD of $cis\text{-}[\text{Pd}^{\text{II}}(\text{L}^{2a}\text{-S},\text{O})_2]$ at 325 °C (A and B), followed by annealing at 425 °C, (C and D).

As further focussed magnification of these films was not possible using SEM, AFM analysis was performed and the image obtained is shown in Fig. 4.3.18.

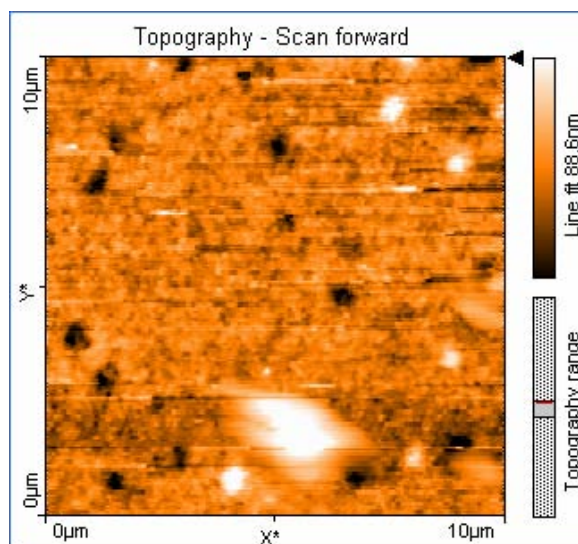


Fig. 4.3.18 AFM image of Pd following AACVD of $cis\text{-}[\text{Pd}^{\text{II}}(\text{L}^{2a}\text{-S},\text{O})_2]$ at 325 °C and annealing at 425 °C.

This image shows fair substrate coverage although sections of the substrate are still visible through the holes previously mentioned. Whilst the image quality does not allow size determination of the smaller crystallites, they are more clearly visible than in the SEM image (Fig. 4.3.17 (D)) of the same sample.

The precursor, $cis\text{-}[\text{Pd}^{\text{II}}(\text{L}^{2a}\text{-S},\text{O})_2]$ can therefore be used for the chemical vapour deposition of palladium under the appropriate conditions. A number of organometallic precursors have reportedly been used for the CVD of palladium including the use of $\text{Pd}(\eta^3\text{-C}_3\text{H}_5)\text{Cp}$ (Cp = cyclopentadienyl), for palladium deposition onto glass,^[55] and porous

divided supports.^[56] The deposition mechanism of this precursor onto a palladium substrate has recently been elucidated.^[57] Several studies detail the use of $[\text{Pd}(\text{hfac})_2]$ (where $\text{hfac} = 1,1,1,5,5,5\text{-hexafluoro-2,4-pentanedionate}$),^[58-60] as well as $\text{Pd}(\text{allyl})(\text{hfac})$ as precursor complexes.^[61] Palladium complexes of β -diketones, such as $\text{Pd}(\text{acac})_2$,^[62] $\text{Pd}(\eta\text{-allyl})(\beta\text{-diketonate})$,^[63, 64] and β -ketoiminates, such as $\text{allyl}(\beta\text{-ketoiminato})\text{Pd}(\text{II})$,^[65, 66] have also been used in a similar context. This is however, to the best of our knowledge, the first time that an N,N -dialkyl- N' -benzoylthiourea Pd(II) complex has been employed as a single source precursor for the AACVD of palladium.

4.3.7 Deposition using $\text{cis-}[\text{Pt}^{\text{II}}(\text{L}^{2a}\text{-S,O})_2]$

As in the case of palladium sulfide, very little has been reported on the deposition of platinum sulfide. Only a single paper reports the use of $[\text{Pt}(\text{S}_2\text{CNMe}(\text{Hex}))_2]$ as a single source precursor for the LP-MOCVD of PtS onto GaAs substrates.^[54] No report could be found on the synthesis of Pt or PtS thin films using AACVD. To further our investigations into the synthesis of PGM based materials, $\text{cis-}[\text{Pt}^{\text{II}}(\text{L}^{2a}\text{-S,O})_2]$ was reacted at four different temperatures, and the PXRD patterns of the resulting material are shown in Fig. 4.3.19.

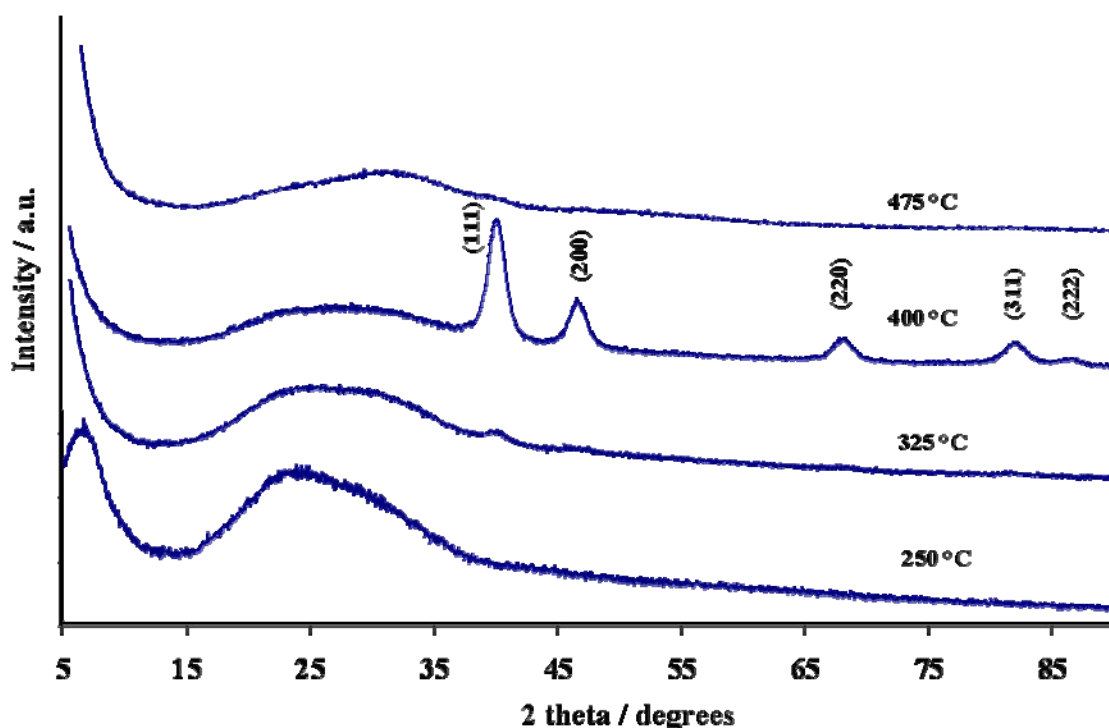


Fig. 4.3.19 PXRD patterns of deposit following AACVD of $\text{cis-}[\text{Pt}^{\text{II}}(\text{L}^{2a}\text{-S,O})_2]$ at 250, 325, 400 and 475 °C.

Amorphous deposits were obtained following reactions at 250, 325 and 475 °C, however pure platinum was deposited at 400 °C. This reflects observations made in the previous sections for $\text{cis-}[\text{Pd}^{\text{II}}(\text{L}^{2a}\text{-S,O})_2]$, however in this case annealing was not necessary to obtain the crystalline metal as a deposit. The broadness of the peaks in the PXRD pattern (Fig. 4.3.19) indicates the presence of small crystallites in the deposit. SEM images of the films obtained following deposition at 250 and 325 °C are shown in Fig. 4.3.20 (A and B respectively). Little surface detail is visible even at fairly high magnifications, however the spherical particles visible are approximately between 0.74 μm and 1.39 μm in diameter. EDAX analysis was performed on both samples and approximate 1:1 ratios of Pt:S were detected in the sample obtained at 250 °C. Spot EDAX analysis on the spherical particle in the 325 °C sample indicated a slight Pt excess (Pt:S - 1.335:1) and an area analysis indicated a slight excess of sulfur (Pt:S -

1:1.20). However, from PXRD data it is clear that no long range crystallinity is evident in samples deposited at these temperatures. SEM images of the thin films deposited at 400 and 475 °C are shown in Fig. 4.3.20 (C,D and E,F).

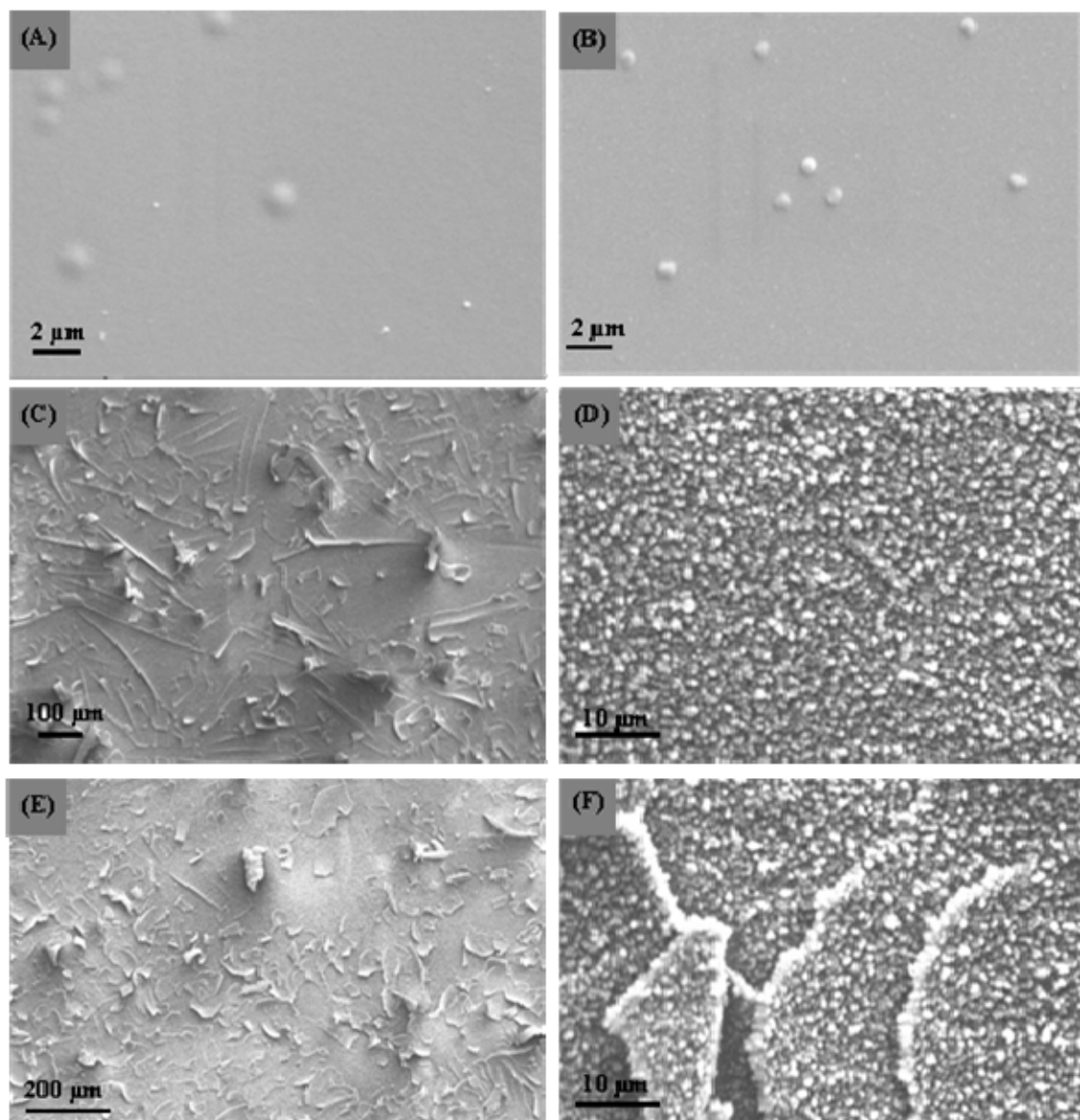


Fig. 4.3.20 SEM images of deposit obtained following AACVD of $cis\text{-}[\text{Pt}^{\text{II}}(\text{L}^{2a}\text{-S,O})_2]$ at 250 °C (A), 325 °C (B), 400 °C, (C and D), and 475 °C (E and F).

Images of both films obtained at low magnification clearly show sections of the film peeling off the substrate appearing similar to paint peeling off a surface. This may be due to excessive strain in the film causing it to buckle and lift off the substrate surface. Higher magnification however shows that these sections are composed of approximately spherical crystallites, ranging in size from 0.46 – 0.93 μm for the samples obtained at 400 °C and slightly larger particles, 0.72 – 1.2 μm in diameter for the sample obtained at 475 °C. EDAX analysis showed that a significant amount of sulfur was present in the film obtained at 400 °, however due to the quality of the PXRD pattern (indicating crystalline platinum) it is unlikely that all of this material is incorporated into the lattice of the crystallites, but may be adsorbed onto the surface of the film. Film thickness measurements showed the deposition to be approximately 1.47 kÅ in thickness at this deposition temperature. EDAX analysis of the film obtained at 475

°C deposition also indicated the presence of sulfur however this was significantly less than that detected for the film following 400 °C deposition.

The precursor, $cis-[Pt^{II}(L^{2a}-S,O)_2]$ can therefore be used for the deposition of metallic platinum under certain reaction conditions. The synthesis of platinum thin films using chemical vapour deposition techniques has been studied in detail given the myriad of potential applications in the fields of catalysis and electronics for materials of this type.^[1] Various families of precursors have been employed such as $Pt(acac)_2$,^[67] $cis-Pt(CO)_2Cl_2$, $Pt(PF_3)_4$, $CpPtMe_3$, $Pt(\eta^3-C_3H_5)_2$, $Pt(C_2H_4)_3$, $[Pt(COD)Me_2]$,^[56, 60, 61] as well as $Pt(MeNC)_2Me_2$ and $Pt(hfa)_2$ (where hfa = hexafluoroacetylacetoate).^[1, 59] This is however, to the best of our knowledge, the first time that a cis -bis(N,N -dialkyl- N' -benzoylthioureato)Pt(II) complex has been employed for the AACVD of metallic platinum. Further work involving this precursor could yield interesting results. A focus area would be the apparent film strain leading the film peeling off the substrate as observed in the SEM images. Use of a different substrate with potential epitaxial growth of the platinum could reduce this apparent strain. For example, GaAs with a [100] surface leads to the growth of zinc-blende CdS, a [111] surface leading to the growth of wurtzite CdS.^[11] Studies indicate that substrate quality is more important than lattice mismatch to the layer being grown,^[6] and therefore a similar effect could be obtained for the growth of platinum, where the relative orientation of the substrate could be altered to minimise the film strain, leading to better and more adherent platinum deposition.

4.3.8 Deposition of $Pd_{17}Se_{15}$

As no report on the chemical vapour deposition of any phase of palladium selenide could be found, it was with interest that $cis-[Pd^{II}(L^{1a}-Se,O)_2]$ was reacted at four different temperatures, the PXRD patterns of the resulting material are shown in Fig. 4.3.21.

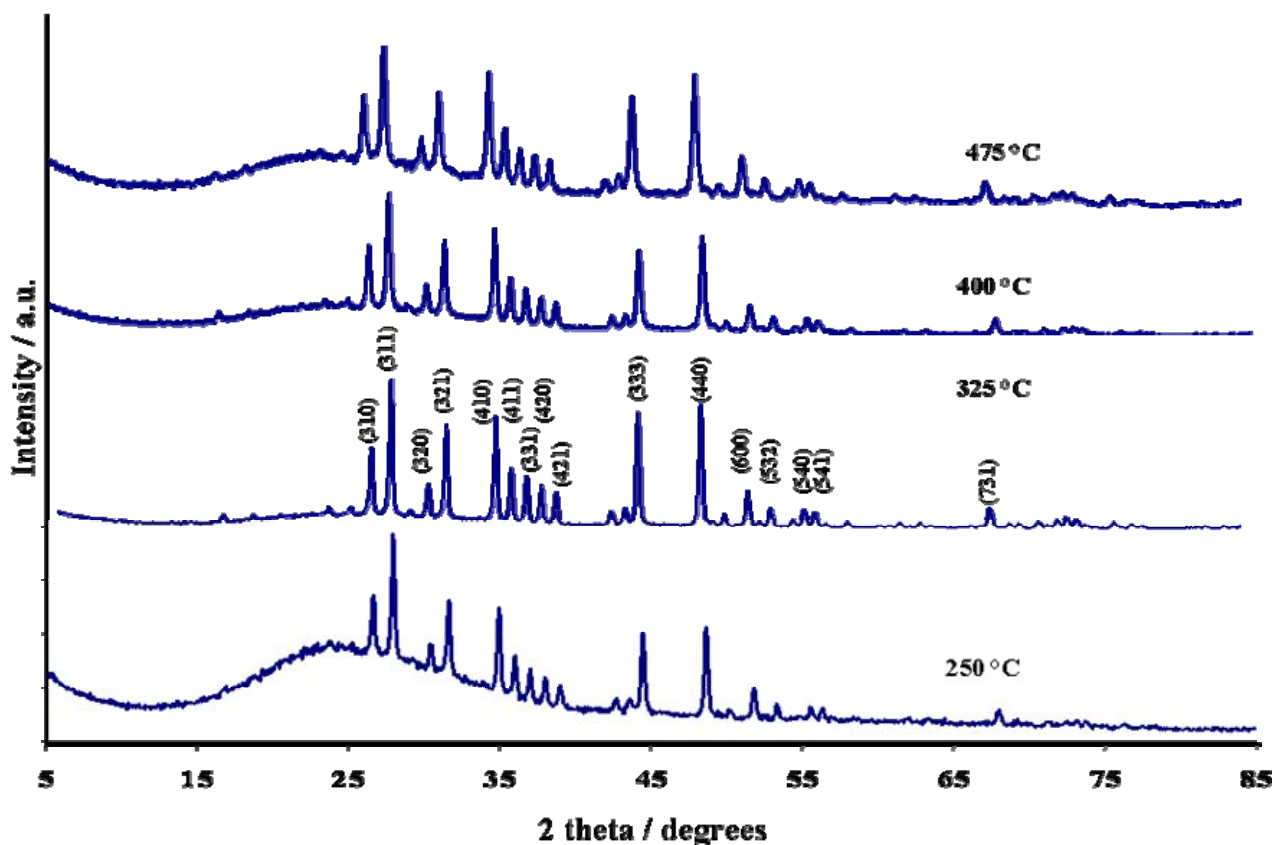


Fig. 4.3.21 PXRD patterns of $Pd_{17}Se_{15}$ following AACVD of $cis-[Pd^{II}(L^{1a}-Se,O)_2]$ at 250, 325, 400 and 475 °C.

The deposition of crystalline material at each temperature is clearly evident. The relatively good crystalline quality of the film deposited at 250 °C led to testing the precursor at a deposition temperature of 200 °C, however, this resulted in an amorphous deposit and the results are not shown here. The PXRD pattern of the crystalline material corresponds to that of a cubic phase of palladium selenide called palladseite, Pd₁₇Se₁₅. At each temperature, the relative intensities of the peaks remain consistent, indicating that the crystallographic orientation of the deposited material is maintained in each case.

SEM images of each sample are shown in Fig. 4.3.22. The image of material deposited at 250 °C is of fairly poor quality, making particle size determination difficult, however spherical particles approximately 0.1 μm in diameter are present. Deposition at 325 °C results in reasonable substrate coverage, although small sections of the substrate are still visible. Two size regimes of crystallites are present, lighter larger crystallites, ranging in size from 0.41 – 0.47 μm in diameter, and a smaller darker set, 0.12 – 0.19 μm in diameter. Deposition at 400 °C results in improved substrate coverage, although this is not 100 %, and roughly spherical crystallites 0.4– 0.6 μm in diameter are visible. The upper growth limit tested of 475 °C indicates spherical crystallites ranging in size from 0.43 – 1.7 μm in diameter.

EDAX analysis was performed on each sample and the results are summarised in Table 4.3.4. The expected ratio of Pd:Se for a thin film composition of Pd₁₇Se₁₅ is 1.13, and thin films deposited at 325 and 400 °C are within experimental error of this value, confirming their composition as being that of palladseite. Film deposition at 250 °C, indicates a slight palladium excess and that deposited at 475 °C, a slight selenium excess. Interestingly, the presence of sulfur was detected in the films deposited at 325 and 400 °C.

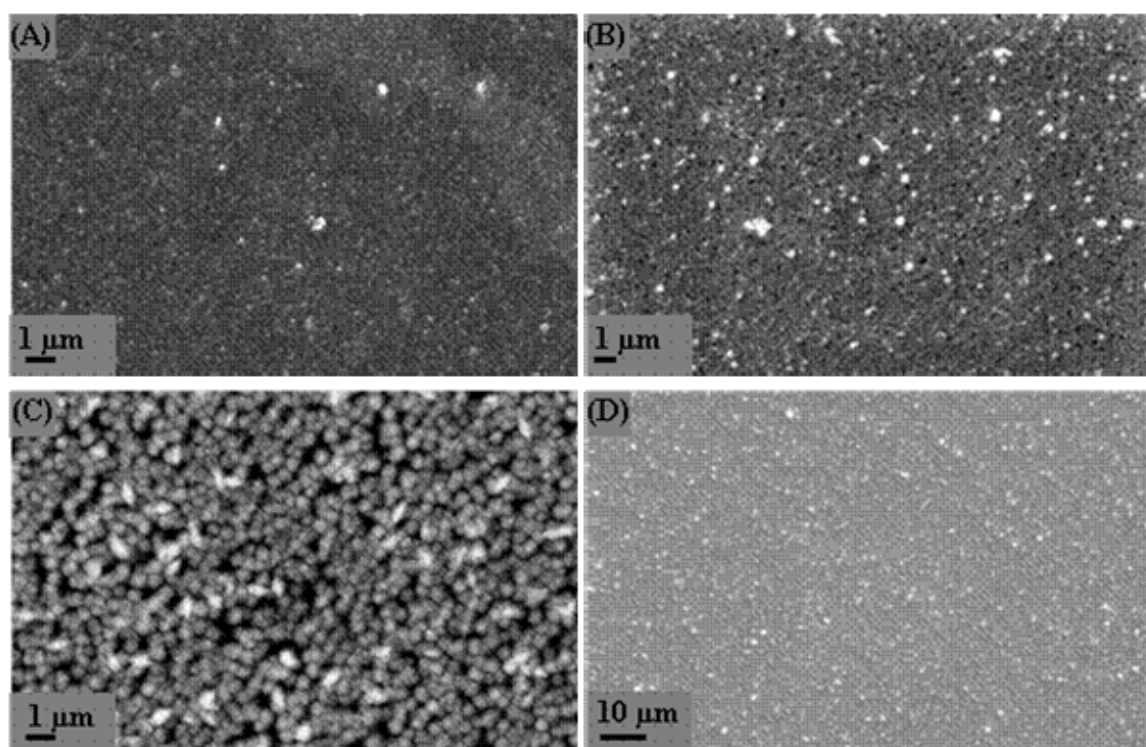


Fig. 4.3.22 SEM images of Pd₁₇Se₁₅ thin films obtained following AACVD of *cis*-[Pd^{II}(L^{1a}-Se,*O*)₂] at 250 (A), 325 (B), 400 (C) and 475 °C (D).

Table 4.3.4 Composition of Pd₁₇Se₁₅ thin films obtained at varying deposition temperatures.

Deposition temp. / °C	Atomic % (Pd)	Atomic % (Se)	Atomic % (S)	Pd:Se ratio
250	2.25	1.87		1.20
325	24.43	21.16	1.11	1.16
400	24.43	21.16	1.11	1.16
475	27.78	29.34		0.95

The atomic percentages of palladium and selenium increase with increasing deposition temperature indicating a temperature dependant thin film thickness. This was confirmed with thin film thickness measurements performed using a profilometer, where the average of three readings per sample were recorded and the results are summarised in Table 4.3.5.

Table 4.3.5 Properties of Pd₁₇Se₁₅ thin films obtained at varying deposition temperatures.

Deposition temp. / °C	250	325	400	475
Resistance / Ω	70.58	16.19	5.93	79.55
Film thickness / kÅ	1.55	1.85	4.60	64.49
Resistivity / Ωm	4.96 x 10 ⁻⁴	1.36 x 10 ⁻⁴	1.24 x 10 ⁻⁴	2.32 x 10 ⁻²

The thickness of the deposit increases with deposition temperature where the thickest deposit of 64.49 kÅ was obtained at 475 °C. This reflects observations made during experimentation where at higher temperatures, deposition occurred at the mouth of the reactor over a very small area, but as the temperature decreased, the deposition area became larger and spread through the reactor, although at 200 °C where deposition appeared to be the most uniformly distributed, the material had a significantly reduced crystallinity.

As little is known about this phase of palladium selenide, conductivity measurements were performed on samples grown at each temperature and the data is graphically depicted in Fig. 4.3.23.

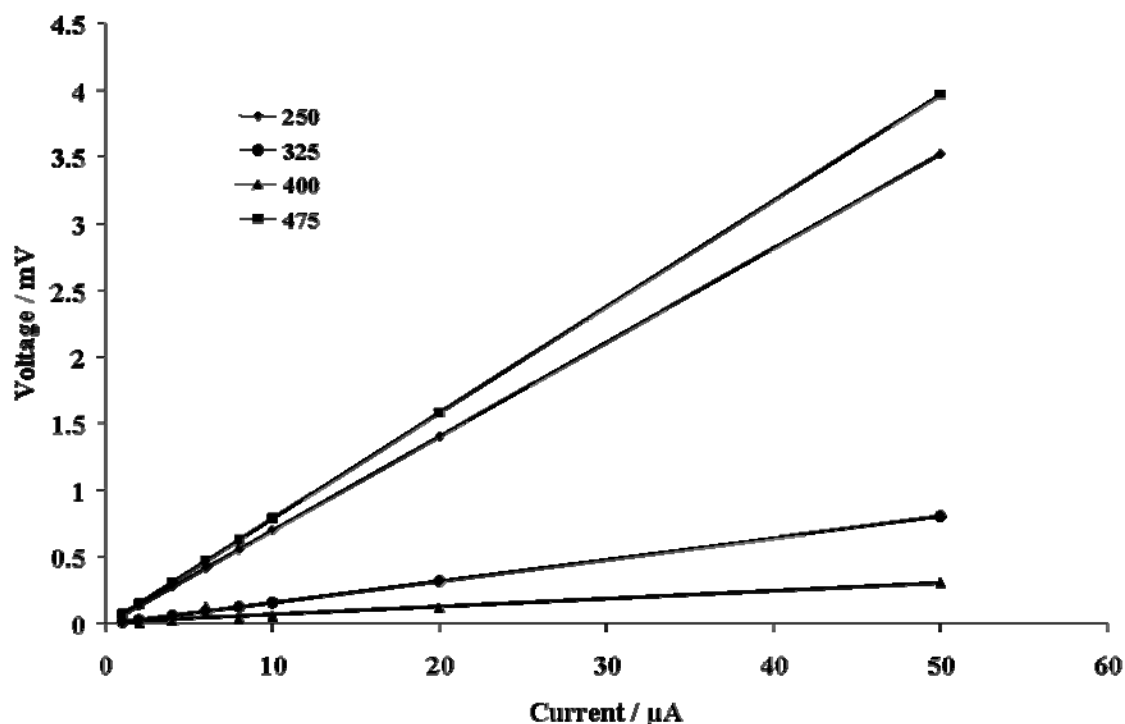


Fig. 4.3.23 Graph illustrating measured potential difference against applied current on Pd₁₇Se₁₅ films obtained at various deposition temperatures.

In each case a linear correlation between the applied potential difference and measured current indicates that the material obtained at each deposition temperature is ohmic. The resistance obtained from the slope of each curve is given in Table 4.3.5, where it is apparent that it does not vary linearly with deposition temperature. The lowest and highest deposition temperatures (475 and 250 °C) gave comparable resistance values of 79.55 and 70.58 Ω respectively, whereas deposition of temperatures of 325 and 400 °C give much lower resistance values of 16.19 and 5.93 Ω respectively. Table 4.3.5 also gives values for the resistivity of films obtained at each deposition temperature. According to Hu *et.al.* resistivity can be calculated as:

$$\rho = 4.532(V/I) \times d$$

where ρ = resistivity in Ωm , 4.532 = instrument constant,* (V/I) = slope of the line in Fig. 4.3.23 in Ω , d = film thickness in m.

The values shown in Table 4.3.5 indicate that the highest resistivity is exhibited by the material deposited at 475 °C and the lowest by that deposited at 400 °C, however the difference between the two is approximately two orders of magnitude. The reason for this is the significantly thicker film obtained at 475 °C relative to the other three deposition temperatures. As mentioned previously it was observed that deposition at this temperature was mainly localised around the mouth of the reactor and very little distribution was evident. At lower temperatures (250 °C) deposition was more distributed but the film was much thinner. Therefore, at higher temperatures (475 °C) decomposition of the precursor most likely occurs immediately on entrance to the reactor, leading to a much thicker localised deposition at the mouth of the reactor and very little in the remaining area whereas lower temperatures allows more continual precursor decomposition and more uniform deposition throughout the reactor, although this necessarily leads to the deposition of thinner films.

Resistivity is the reciprocal of conductivity, and hence films deposited at 325 and 400 °C are the most conductive. It is interesting that this property does not appear to be linearly related to the deposition temperature. The reason for this remains unclear as the material obtained at both 325 and 400 °C is clearly crystalline and of a consistent phase. One possible explanation however, may be the presence of sulfur as indicated by the EDAX analysis. Films deposited at 250 and 475 °C exhibiting higher resistance, do not appear to contain sulfur, whereas those deposited at 325 and 400 °C, with lower resistance do. The quality of the PXRD patterns of these films (325 and 400 °C), makes it unlikely that the detected sulfur forms part of the crystal lattice, rather it is more likely located on the surface of the thin film. It is therefore possible that the presence of sulfur contributes in some way to the flow of electrons through the film, in so doing, lowering the natural resistance exhibited by the material in the absence of sulfur.

The precursor *cis*-[Pd^{II}(L^{1a}-Se,O)₂] can therefore be used for the deposition of Pd₁₇Se₁₅ over a variety of different deposition temperatures. No other reports on the deposition of any palladium selenide phase could be found.

4.4 Conclusions

AACVD of [Cd^{II}(L^{1a}-Se,O)₂] results in the deposition of wurtzite phased, crystalline CdSe over a range of different temperatures. At higher deposition temperatures of 375 – 475 °C, the deposited material is highly orientated along the (002) plane. It is remarkable that crystalline CdSe is deposited at temperatures as low as 225 °C, allowing for the potential deposition of CdSe onto less heat resistant materials such as Kapton, using [Cd^{II}(L^{1a}-Se,O)₂] as a single source precursor. Preliminary experiments indicate that [Cd^{II}(L^{1a}-Se,O)₂] shows little potential as a single source

* The same instrument as Hu *et. al.* was used at the University of Manchester, therefore, the reported instrument constant was maintained in the calculations performed using our own data.

precursor for the LP-MOCVD of CdSe. Deposition of CdSe was observed following the AACVD of $[\text{Cd}^{\text{II}}(\text{L}^{\text{1b-e}}-\text{Se},\text{O})_2]$ at 250 °C, although the film quality appears poor under these reaction conditions. PXRD thin film analysis indicates that precursor alkyl chain length does affect the nature of the deposited material where the poorest quality films were obtained following use of $[\text{Cd}^{\text{II}}(\text{L}^{\text{1d}}-\text{Se},\text{O})_2]$ as a single source precursor. Interestingly, the observation made for $[\text{Cd}^{\text{II}}(\text{L}^{\text{1a}}-\text{Se},\text{O})_2]$ is reflected in the longer alkyl chain analogues, where wurtzite CdSe is deposited following reaction of $[\text{Cd}^{\text{II}}(\text{L}^{\text{1b-e}}-\text{Se},\text{O})_2]$.

CdS can successfully be deposited using $[\text{Cd}^{\text{II}}(\text{L}^{\text{2a}}-\text{S},\text{O})_2]$ as a single source precursor where, similarly to the case of CdSe, wurtzite phased material is deposited. Fair substrate coverage and crystallinity is obtained between deposition temperatures of 325 and 475 °C. Low temperature deposition (250 °C) however, results in the formation of poor quality thin films in contrast to those obtained following AACVD of $[\text{Cd}^{\text{II}}(\text{L}^{\text{1a}}-\text{Se},\text{O})_2]$ under similar reaction conditions. This reflects the relative stabilities of the two single source precursors. Deposition of CdS was also observed following reaction of $[\text{Cd}^{\text{II}}(\text{L}^{\text{2b-e}}-\text{S},\text{O})_2]$ at 250 °C, although poor quality films were obtained at this deposition temperature. In each case, as for the diethyl analogue, wurtzite phased CdS was deposited.

AACVD of $[\text{Zn}^{\text{II}}(\text{L}^{\text{1a}}-\text{Se},\text{O})_2]$ allows the deposition of crystalline ZnSe between 325 and 475 °C. At lower deposition temperatures 325 and 400 °C, the deposition of zinc-blende ZnSe is favoured and deposition at 475 °C results in the formation of predominantly wurtzite phased ZnSe. At each deposition temperature, spherical crystallites are formed and optimal substrate coverage is obtained at a deposition temperature of 400 °C. Given the formation of ZnO nanoparticles following thermolysis of $[\text{Zn}^{\text{II}}(\text{L}^{\text{1a}}-\text{Se},\text{O})_2]$, the deposition of ZnSe thin films is quite remarkable from the same single source precursor.

Use of $[\text{Zn}^{\text{II}}(\text{L}^{\text{2a}}-\text{S},\text{O})_2]$ as a single source precursor allows the deposition of ZnS over a range of temperatures. Although not crystalline, deposition does occur at temperatures of 250 and 325 °C, higher deposition temperatures of 400 and 475 °C allowing the deposition of wurtzite phased ZnS. Poor substrate coverage is also evident at the lower deposition temperatures, the optimal substrate coverage being obtained at 400 °C. The poorer quality films obtained using $[\text{Zn}^{\text{II}}(\text{L}^{\text{2a}}-\text{S},\text{O})_2]$ as a single source precursor relative to its selenium analogue, reflect observations made for the cadmium precursors, $[\text{Cd}^{\text{II}}(\text{L}^{\text{1a}}-\text{Se},\text{O})_2]$ and $[\text{Cd}^{\text{II}}(\text{L}^{\text{2a}}-\text{S},\text{O})_2]$ where the increased stability of the *N,N*-diethyl-*N'*-benzoylthiourea metal complexes requires higher reaction temperatures for the deposition of crystalline material than for the less stable *N,N*-diethyl-*N'*-benzoylselenourea metal complexes.

Deposition of crystalline heazewoodite, Ni_3S_2 , can successfully be affected using *cis*- $[\text{Ni}^{\text{II}}(\text{L}^{\text{2a}}-\text{S},\text{O})_2]$ as a single source precursor. Good quality substrate coverage can be obtained at deposition temperatures of 400 °C where high magnification of the material illustrates wire mesh type morphology. Even higher magnification reveals the presence of distinct, well formed triangular nanoparticles, with an average length of 14.8 (12) nm, adhering to the wires as well as loosely located in the mesh. Fibres of varying diameters and densities are also evident. HRTEM analysis could provide very interesting information regarding the phase and crystallinity of these different morphologies.

AACVD of *cis*- $[\text{Pd}^{\text{II}}(\text{L}^{\text{2a}}-\text{S},\text{O})_2]$ at temperatures ranging between 250 and 475 °C results in the deposition of largely amorphous material. Annealing of the thin films at 425 °C however, significantly enhances the crystallinity and results in the formation of highly crystalline palladium with no evidence of sulfur contamination in the PXRD pattern. Substrate coverage of these films is good, although the presence of 0.3-0.5 μm holes in the crystallite matt is evident.

Metallic platinum can be deposited via AACVD using *cis*- $[\text{Pt}^{\text{II}}(\text{L}^{\text{2a}}-\text{S},\text{O})_2]$ as a precursor complex. Reaction at 400 °C results in deposition of the crystalline metal and unlike the palladium analogue, no film annealing is necessary to

obtain these results. The metal is deposited as small spherical crystallites 0.46 – 0.93 μm in diameter, where sections of this deposit appear to lift off the substrate most likely due to excessive strain in the film. EDAX analysis indicates the presence of sulfur in the deposit obtained at 400 °C where this is possibly adsorbed onto the surface of the film. This is the first time that a *cis*-bis(*N,N*-dialkyl-*N'*-benzoylthioureato)Pt(II) complex has been employed for the AACVD of metallic platinum.

Pd₁₇Se₁₅ can successfully be deposited using *cis*-[Pd^{II}(L^{1a}-Se,O)₂] as a single source precursor. Crystalline material is obtained at deposition temperatures as low as 250 °C and as high as 475 °C. The crystallographic orientation of the deposit remains largely consistent over this temperature range. Thin film thickness increases with deposition temperature, the thickest film of 64.49 kÅ being obtained at a temperature of 475 °C. Conductivity measurements indicate little correlation between deposition temperature and the conductivity of the resulting thin films. Material deposited at 325 and 400 °C appears to exhibit greater conductance than that deposited at either 250 or 475 °C and this is attributed to the presence of sulfur thought to be adsorbed onto the film surface and contributing to an electron flow through the material. This is the first time that an (*N,N*-dialkyl-*N'*-benzoylselenoureato)Pd(II) complex as been engaged as a single source precursor for the deposition of palladium selenide. In addition, this is believed to be the first time that palladium selenide has been deposited using the AACVD technique.

References

- [1] C. Thurier, P. Doppelt, *Coordination Chemistry reviews* **2008**, 252, 155.
- [2] M. Lazell, P. O'Brien, D. J. Otway, J.-H. Park, *Dalton Transactions* **2000**, 4479.
- [3] C. Roger, T. S. Corbitt, M. J. Hampden-Smith, T. T. Kodas, *Applied Physics Letters* **1994**, 65, 1021.
- [4] M. Nyman, M. J. Hampden-Smith, E. N. Duesler, *Chemical Vapor Deposition* **1996**, 2, 171.
- [5] M. Chunggaze, J. McAleese, P. O'Brien, D. J. Otway, *Chemical communications (Cambridge, England)* **1998**, 833.
- [6] H. S. Park, M. Mokhtari, H. W. Roesky, *Chemical Vapor Deposition* **1996**, 2, 135.
- [7] M. Afzaal, S. M. Aucott, D. Crouch, P. O'Brien, J. D. Woollins, J.-H. Park, *Chemical Vapor Deposition* **2002**, 8, 187.
- [8] M. Afzaal, D. Crouch, M. A. Malik, M. Motevalli, P. O'Brien, J. H. Park, *Journal of Materials Chemistry* **2003**, 13, 639.
- [9] M. Afzaal, D. Crouch, P. O'Brien, *Materials Science & Engineering, B: Solid-State Materials for Advanced Technology* **2005**, B116, 391.
- [10] J.-H. Park, M. Afzaal, M. Helliwell, M. A. Malik, P. O'Brien, J. Raftery, *Chemistry of Materials* **2003**, 15, 4205.
- [11] I.-H. Choi, P. Y. Yu, *Physica Status Solidi b* **2005**, 242, 1610.
- [12] P. O'Brien, J. H. Park, J. Waters, *Thin Solid Films* **2003**, 431-432, 502.
- [13] M. Kemmler, M. Lazell, P. O'Brien, D. J. Otway, M. Park Hyun, J. R. Walsh, *Journal of Materials Science: Materials in Electronics* **2002**, 13, 531.
- [14] J.-H. Park, M. Afzaal, M. Kemmler, P. O'Brien, D. J. Otway, J. Raftery, J. Waters, *Journal of Materials Chemistry* **2003**, 13, 1942.
- [15] M. A. Malik, P. O'Brien, *Chemistry of Materials* **1991**, 3, 999.
- [16] M. A. Malik, M. Motevalli, J. R. Walsh, P. O'Brien, *Organometallics* **1992**, 11, 3136.
- [17] D. Barreca, E. Tondello, D. Lydon, T. R. Spalding, M. Fabrizio, *Chemical Vapor Deposition* **2003**, 9, 93.
- [18] M. V. Cabanas, M. Vallet-Regi, *Journal of Materials Chemistry* **2003**, 13, 1104.
- [19] J.-G. Yoon, H. K. Oh, S. J. Lee, *Physical Review B: Condensed Matter* **1999**, 60, 2839.
- [20] A. Adeogun, M. Afzaal, P. O'Brien, *Chemical Vapor Deposition* **2006**, 12, 597.
- [21] F. Srouji, M. Afzaal, J. Waters, P. O'Brien, *Chemical Vapor Deposition* **2005**, 11, 91.
- [22] G. Shang, K. Kunze, M. J. Hampden-Smith, E. N. Duesler, *Chemical Vapor Deposition* **1996**, 2, 242.
- [23] M. Afzaal, D. Crouch, P. O'Brien, J.-H. Park, *Journal of Materials Science: Materials in Electronics* **2003**, 14, 555.
- [24] S. S. Garje, J. S. Ritch, D. J. Eisler, M. Afzaal, P. O'Brien, T. Chivers, *Journal of Materials Chemistry* **2006**, 16, 966.
- [25] R. G. Palgrave, I. P. Parkin, *Journal of Materials Chemistry* **2004**, 14, 2864.
- [26] M. Jin, H.C., K. K. Banger, J. D. Harris, A. F. Hepp, *Materials Science & Engineering, B*: **2005**, 116, 395.

- [27] M. Nyman, K. Jenkins, M. J. Hampden-Smith, T. T. Kodas, E. N. Duesler, *Chemistry of Materials* **1998**, *10*, 914.
- [28] K. Maki, N. Komiya, A. Suzuki, *Thin Solid Films* **2003**, *445*, 224.
- [29] R. T. Shuey, *Semiconducting Ore Minerals*, Elsevier Scientific, Amsterdam, **1975**.
- [30] M. Afzaal, D. Crouch, M. A. Malik, M. Motevalli, P. O'Brien, J.-H. Park, J. D. Woollins, *European Journal of Inorganic Chemistry* **2004**, 171.
- [31] M. B. Hursthouse, M. A. Malik, M. Motevalli, P. O'Brien, *Journal of Materials Chemistry* **1992**, *2*, 949.
- [32] M. Chunggaze, M. Azad Malik, P. O'Brien, *Journal of Materials Chemistry* **1999**, *9*, 2433.
- [33] R. B. Kale, C. D. Lokhande, *Journal of Physical Chemistry B* **2005**, *109*, 20288.
- [34] H. Cachet, H. Essaïdi, M. Froment, G. Maurin, *Journal of Electroanalytical Chemistry* **1995**, *396*, 175.
- [35] C. B. Murray, D. J. Norris, M. G. Bawendi, *Journal of the American Chemical Society* **1993**, *115*, 8706.
- [36] <http://www.kaptontape.com/default.php>.
- [37] J. C. Bruce, K. R. Koch, N. Revaprasadu, *New Journal of Chemistry* **2007**.
- [38] G. Malandrino, S. T. Finocchiaro, P. Rossi, P. Dapporto, I. Fragala, *Chemical communications (Cambridge, England)* **2005**, 5681.
- [39] Y.-J. Hsu, S.-Y. Lu, *Langmuir* **2004**, *20*, 194.
- [40] O. Zelaya-Angel, J. J. Alvarado-Gil, R. Lozada-Morales, H. Vargas, A. Ferreira da Silva, *Applied Physics Letters* **1994**, *64*, 291.
- [41] X. T. Zhang, Z. Liu, Y. P. Leung, Q. Li, S. K. Hark, *Applied Physics Letters* **2003**, *83*, 5533.
- [42] H. Okada, T. Kawanaka, S. Ohmoto, *Journal of Crystal Growth* **1996**, *165*, 31.
- [43] P. D. Cozzoli, L. Manna, M. L. Curri, S. Kudera, C. Giannini, M. Striccoli, A. Agostiano, *Chemistry of Materials* **2005**, *17*, 1296.
- [44] H. Hiramatsu, H. Ohta, M. Hirano, H. Hosono, *Solid State Communications* **2002**, *124*, 411.
- [45] Z. Z. Zhang, D. Z. Shen, J. Y. Zhang, C. X. Shan, Y. M. Lu, Y. C. Liu, B. H. Li, D. X. Zhao, B. Yao, X. W. Fan, *Thin Solid Films* **2006**, *513*, 114.
- [46] P. O'Brien, J. R. Walsh, I. M. Watson, M. Motevalli, L. Henriksen, *Dalton Transactions* **1996**, 2491.
- [47] D. Barreca, A. Gasparotto, C. Maragno, R. Seraglia, E. Tondello, A. Venzo, V. Krishnan, H. Bertagnolli, *Applied Organometallic Chemistry* **2005**, *19*, 1002.
- [48] F. Huang, J. F. Bandfield, *Journal of the American Chemical Society* **2005**, *127*, 4523.
- [49] S. Li, J. S. Lian, Q. Jiang, *Chemical Physics Letters* **2008**, *455*, 202.
- [50] P. O'Brien, J. Waters, *Chemical Vapor Deposition* **2006**, *12*, 620.
- [51] R. D. Tilley, D. A. Jefferson, *Journal of Physical Chemistry B* **2002**, *106*, 10895.
- [52] S.-H. Yu, M. Yoshimura, *Advanced Functional Materials* **2002**, *12*, 277.
- [53] A. Ghezelbash, M. B. Sigman, Jr., B. A. Korgel, *Nano Letters* **2004**, *4*, 537.
- [54] M. A. Malik, P. O'Brien, N. Revaprasadu, *Journal of Materials Chemistry* **2002**, *12*, 92.
- [55] J.-C. Hierso, C. Satto, R. Feurer, P. Kalck, *Chemical Materials* **1996**, *8*, 2481.
- [56] J.-C. Hierso, R. Feurer, P. Kalck, *Chemical Materials* **2000**, *12*, 390.
- [57] A. Niklewski, T. Strunskus, G. Witte, C. Woll, *Chemistry of Materials* **2005**, *17*, 861.
- [58] V. Bhaskaran, M. J. Hampden-Smith, T. T. Kodas, *Chemical Vapor Deposition* **1997**, *3*, 85.
- [59] N. L. Jeon, W. Lin, M. K. Erhardt, G. Girolami, S., R. G. Nuzzo, *Langmuir* **1997**, *13*, 3833.
- [60] M. Feng, R. J. Puddephatt, *Canadian Journal of Chemistry* **2007**, *85*, 645.
- [61] J.-C. Hierso, P. Serp, R. Feurer, P. Kalck, *Applied Organometallic Chemistry* **1998**, *12*.
- [62] G. Y. Meng, L. Huang, M. Pan, C. S. Chen, D. K. Peng, *Materials Research Bulletin* **1997**, *32*, 385.
- [63] Y. Zhang, Z. Yuan, R. J. Puddephatt, *Chemical Materials* **1998**, *10*, 2293.
- [64] Y. Zhang, R. J. Puddephatt, *Chemical Vapor Deposition* **1997**, *3*, 81.
- [65] Y.-L. Tung, W.-C. Tseng, C.-Y. Lee, P.-F. Hsu, Y. Chi, S.-M. Peng, G.-H. Lee, *Organometallics* **1999**, *18*, 864.
- [66] Y.-H. Liu, Y.-C. Cheng, Y.-L. Tung, Y. Chi, Y.-L. Chen, C.-S. Liu, S.-M. Peng, G.-H. Lee, *Journal of Materials Chemistry* **2002**, *13*, 135.
- [67] I. K. Igumenov, N. V. Gelfond, N. B. Morozova, H. Nizard, *Chemical Vapor Deposition* **2007**, *13*, 633.

Chapter 5

Conclusions

The synthesis and structural characterization of several novel *N,N*-dialkyl-*N'*-benzoyl(thio)selenourea ligands has successfully been completed. In general, the characteristic intermolecular interactions present in the solid state structures of both ligand types are Resonance Assisted Hydrogen Bonding (RAHB) between the selenium or sulfur atom of one molecule and the seleno(thio)amidic proton of a neighbouring molecule, a reciprocal hydrogen bond leading to the formation of 8 membered dimers in the crystal lattice. The longer alkyl chain derivatives such as *N,N*-dihexyl-*N'*-benzoyl(thio)selenourea, *N,N*-dioctyl-*N'*-benzoyl(thio)selenourea and *N,N*-didecyl-*N'*-benzoylselenourea also exhibit intermolecular π - π interactions between the benzene residues of neighbouring molecules. Interestingly, despite the presence of two benzene residues in each of the asymmetrically substituted *N*-benzyl-*N*-methyl-*N'*-benzoylseleno- and -thiourea ligands, no intermolecular π - π interactions are apparent in the solid state structures. Crystal structure analysis of these two ligands does however reveal that the *Z* isomer is the most stable in the solid state, where the structural characterization of *N*-benzyl-*N*-methyl-*N'*-benzoylselenourea is, to the best of our knowledge, the first of an asymmetrically substituted selenourea ligand of this type. Two separate products could be isolated and structurally characterized from the attempted synthesis of *N,N*-dicyclohexyl-*N'*-benzoylselenourea, a novel 1,3,5-oxaselenazine salt and dicyclohexylaminobenzoate. Attempts to synthesise the sulfur analogue, *N,N*-dicyclohexyl-*N'*-benzoylthiourea revealed the isolation of the “enol” form of the ligand in the solid state. Preparation of *N,N*-diphenyl-*N'*-benzoylselenourea disclosed a particularly short intermolecular Se-Se distance in the crystal structure, leading to the classification of this ligand as a diselenide, rather than a selenourea. These observations coupled with those regarding the use of dicyclohexylamine indicate that the choice of amine substituents in ligand synthesis can have a significant influence over the reaction progression and the consequent product formation. The first structural characterization of a “bipodal” selenourea ligand, namely that of 3,3,3',3'-tetra(*n*-butyl)-1,1'-isophthaloylbis(selenourea) reflects trends exhibited by the “monopodal” analogue, *N,N*-dibutyl-*N'*-benzoylselenourea, where RAHB between the selenium atom and selenoamidic proton of a neighbouring molecule are the dominant intermolecular interactions in the solid state.

Complexation of the *N,N*-dialkyl-*N'*-benzoyl(thio)selenoureas to Pd(II) allowed the formation of a number of potential single source precursors, several of which could be structurally characterized. The preparation of square planar complexes with coordination taking place through the O and Se donor atoms was evident following the solid state characterizations of *cis*-bis(*N,N*-dibutyl-*N'*-benzoylselenoureato)palladium(II), *cis*-bis(*N,N*-dihexyl-*N'*-benzoylselenoureato)palladium(II), and *cis*-bis(*N*-benzyl-*N*-methyl-*N'*-benzoylselenoureato)palladium(II). The structure of the latter indicating that the *EZ* isomer is the most stable in the solid state, this being, to the best of our knowledge, the first report of a structural characterisation of an asymmetrically substituted selenourea Pd(II) complex. Crystal structure analysis of *cis*-bis(*N,N*-dibutyl-*N'*-benzoylthioureato)palladium(II), *cis*-bis(*N,N*-dihexyl-*N'*-benzoylthioureato)palladium(II) and *cis*-bis(*N*-morpholine-*N'*-benzoylthioureato)palladium(II), reflect observations made for the selenium analogues, in the formation of square planar metal complexes with coordination taking place through the O and S donor atoms. Structural elucidation of the novel (*N,N*-diphenyl-*N'*-benzoylselenoureato)cadmium(II) reveals a bimetallic complex in the solid state, where the expected 2:1 ligand : metal ratio is maintained, and the two Cd(II) centres are 5 and 6 coordinated, with O and Se donor atoms.

The potential single source precursors were extensively studied using Nuclear Magnetic Resonance (NMR) Spectroscopy. $^1J(^{13}\text{C}-^{77}\text{Se})$ coupling constants could be determined from the ^{77}Se satellites present in the ^{13}C NMR

spectra of the *N,N*-dialkyl-*N'*-benzoylselenoureas, these ranging between 217.8 Hz and 222.1 Hz for the *N,N*-dialkyl-*N'*-benzoylselenourea ligands and 175.8 and 181.3 Hz for the Pd(II) complexes. The Cd(II) and Zn(II) complexes of *N,N*-diethyl-*N'*-benzoylselenourea exhibiting values of 164.9 and 166.6 Hz respectively. The reduction in the coupling constants upon complexation reflecting the reduction in C=Se bond order in the metal complexes. ¹H NMR spectroscopy allowed an indication of the relative isomer distributions (*EE*, *EZ* and *ZZ*) of *cis*-bis(*N*-benzyl-*N*-methyl-*N'*-benzoyl(thio)selenoureato)palladium(II) to be obtained. ⁷⁷Se NMR spectroscopy indicates a decrease in the nuclear shielding of the ⁷⁷Se nucleus as the “hardness” of the central metal ion increases *i.e.* Pd(II) > Zn(II) > Cd(II). A similarity in the chemical shift environment of the Cd(II) metal centre in [Cd^{II}(**L**^{1a}-**Se**,**O**)₂] and [Cd^{II}(**L**^{1a}-**Se**,**O**)(**L**^{2a}-**S**,**O**)] was revealed using ¹¹³Cd NMR spectroscopy, this indicating the preferential binding of *N,N*-diethyl-*N'*-benzoylselenourea to Cd(II) over that of its sulfur analogue and initial studies indicate a form of chelate metathesis taking place in solution. The coordination of *N,N*-diethyl-*N'*-benzoylselenourea to Pt(II) in solution was investigated using ³¹P NMR spectroscopy, where evidence was gained to support coordination of the ligand to the metal centre.

Studies on the thermal decomposition profiles of (*N,N*-diethyl-*N'*-benzoyl(thio)selenoureato)cadmium(II) complexes suggest the formation of CdSe and CdS residues, confirming their potential as single source precursors for the synthesis of CdSe and CdS quantum dots. Preliminary investigations into the thermolysis of these complexes confirmed the formation of spherical CdSe and CdS nanoparticles exhibiting quantum confinement. Further studies revealed that the formation of CdSe and CdS nanoparticles from the thermolysis of their respective precursors takes place over a range of different temperatures. In the case of CdSe, a direct correlation between thermolysis temperature and nanoparticle diameter was evident, this being further reflected in the size dependant emission of the nanoparticles. Although not as clear as in the case of CdSe, a correlation between nanoparticle diameter and thermolysis temperature could also be established in the case of CdS nanoparticles derived from (*N,N*-diethyl-*N'*-benzoylthioureato)cadmium(II) although the degree of size control was less than that exhibited by the selenium counterparts. In both cases, the formation of zinc-blende nanoparticles appeared to be consistent and independent of the thermolysis temperature. The lower stability of (*N,N*-diethyl-*N'*-benzoylselenoureato)cadmium(II) relative to its sulfur analogue, allows the use of lower thermolysis temperatures to achieve even nucleation and monodispersity in the resulting sample. From these investigations it was apparent that little morphological control over the final nanoparticles was possible through regulation of the thermolysis temperature of (*N,N*-diethyl-*N'*-benzoyl(thio)selenoureato)cadmium(II).

The effect on nanoparticle morphology by tailoring the alkyl chain length of the precursors was investigated by thermolysing [Cd^{II}(**L**^{1b-f}-**Se**,**O**)₂], and in each case, the formation of CdSe nanoparticles was successful. As precursor alkyl chain length increased a red shift in the band edge and emission maxima of the resulting nanoparticles was evident. In addition, the degree of anisotropy exhibited by the CdSe nanoparticles could be correlated to precursor alkyl chain length up to a limit of a C8 alkyl chain after which the morphology returned to being spherical upon the thermolysis of the C10 alkyl chain length derivative, (*N,N*-didecyl-*N'*-benzoylselenoureato)Cd(II). Interestingly the phase of resultant nanoparticles remained consistently zinc-blende irrespective of the precursor alkyl chain length. Thermolysis of (*N,N*-dioctyl-*N'*-benzoylselenoureato)Cd(II) resulted in the formation of anisotropic nanoparticles, this being affected over a range of different thermolysis temperatures. Limited instrumentation complicates elucidation of the growth mechanism, however the epitaxial growth of hexagonally phased arms on the {111} faces

of a cubically phased core appear to be the most likely mechanism leading to the structures observed. To gain insight into the apparent effect of precursor alkyl chain length on the morphology of the resultant nanoparticles, the decomposition profiles of (*N,N*-diethyl-*N'*-benzoylselenoureato)Cd(II) and (*N,N*-dioctyl-*N'*-benzoylselenoureato)Cd(II) were investigated further. Approximate three step profiles were apparent for each, where in both cases the second mass loss appeared to be a first order process, allowing calculation of the activation energy for this particular stage in the decomposition. (*N,N*-diethyl-*N'*-benzoylselenoureato)Cd(II) yielding spherical nanoparticles exhibited an activation energy of 21.4 kJmol⁻¹, half that of the tripod yielding (*N,N*-dioctyl-*N'*-benzoylselenoureato)Cd(II) exhibiting an activation energy of 48.1kJmol⁻¹. These observations propose the involvement of factors other than a growth regime under kinetic control, where the relatively larger nanoparticles resulting from thermolysis of (*N,N*-dioctyl-*N'*-benzoylselenoureato)Cd(II) fall within a size regime where branching of the nanoparticles to form multiarmed structures decreases the surface atom number. This consequently maximises the lattice energy, and is possibly the driving force for the development of multiarmed structures.

A parallel investigation into the effect of nanoparticle morphology by tailoring of the precursor alkyl chain length was undertaken for the (*N,N*-dialkyl-*N'*-benzoylthioureato)Cd(II) complexes, [Cd^{II}(L^{2b-e}-S,O)₂], and in each case the formation of CdS nanoparticles was successfully achieved. Similarly although less marked than the Se analogues, a red shift in the band edge of the resulting CdS nanoparticles with increasing precursor alkyl chain length is apparent. In addition, the formation of zinc-blende phased nanoparticles appears to be independent of precursor alkyl chain length as does nanoparticle morphology as the formation of spherical nanoparticles was consistently observed for each of the (*N,N*-dialkyl-*N'*-benzoylthioureato)Cd(II) precursors.

An investigation into the use of other *N,N*-dialkyl-*N'*-benzoyl(thio)selenourea metal complexes as single source precursors revealed that both (*N,N*-diethyl-*N'*-benzoylselenoureato)Zn(II) and its sulfur analogue show potential as single source precursors for the formation of ZnO and ZnS nanoparticles respectively. Thermolysis of both *cis*-bis(*N,N*-diethyl-*N'*-benzoylthioureato)Ni(II) and (*N,N*-diethyl-*N'*-benzoylthioureato)Co(III) resulted in the formation of spherical nanoparticles where further investigation of these complexes could lead to nanoparticles with modifiable compositions and consequently tuneable properties. As part of a continued interest in the Platinum Group Metal (PGM) ions, the potential of *cis*-bis(*N,N*-diethyl-*N'*-benzoylthioureato)Pd(II), its selenium analogue as well as *cis*-bis(*N,N*-diethyl-*N'*-benzoylthioureato)Pt(II) as single source precursors was investigated. While in each case, thermolysis resulted in the formation of well defined spherical nanoparticles, absolute nanoparticle composition could not be obtained with the instrumentation available.

Preliminary investigations into the use of *N,N*-dialkyl-*N'*-benzoyl(thio)selenourea metal complexes as single source precursors for the synthesis of core-shell nanoparticles revealed the formation of CdSe/CdS nanoparticles resulting from the thermolysis of (*N,N*-diethyl-*N'*-benzoylthioureato)Cd(II) in the presence of preformed CdSe nanoparticles. The conditions used also allowed the separate nucleation and growth of CdS nanoparticles resulting in a mixture of materials being obtained. The use of (*N,N*-diethyl-*N'*-benzoylthioureato)Zn(II) and (*N,N*-diethyl-*N'*-benzoylselenoureato)Cd(II) yielded promising results for the formation of CdSe/ZnS nanoparticles, where further investigation could lead to the optimisation of this synthesis and the preparation of monodisperse, evenly passivated material.

Given the success with which the *N,N*-dialkyl-*N'*-benzoyl(thio)selenourea metal complexes could be used as single source precursors for the synthesis of a variety of nanoparticles, their use as precursors for the Aerosol Assisted Chemical Vapour Deposition (AACVD) was investigated.

Use of (*N,N*-diethyl-*N'*-benzoylselenourea)Cd(II) allowed the deposition of crystalline CdSe over a temperature range of 225 to 475 °C. Interestingly, despite the formation of CdSe nanoparticles with a zinc-blende phase upon thermolysis of this complex, deposition reaction conditions led to the formation of exclusively wurtzite phased material, this being highly orientated along the (002) plane at deposition temperatures between 375 and 475°C. Crystalline deposition of CdSe occurred at a temperature as low as 225 °C, allowing this complex significant potential for the deposition of CdSe onto less heat resistant materials. Preliminary experiments indicated little possibility of using (*N,N*-diethyl-*N'*-benzoylselenourea)Cd(II) as a single source precursor for the deposition of CdSe using Low Pressure Metal Organic Chemical Vapour Deposition (LPMOCVD). The effect of precursor alkyl chain length on the nature of the deposited material was briefly investigated at 250 °C for $[\text{Cd}^{\text{II}}(\text{L}^{\text{1b-e}}\text{-Se}, \text{O})_2]$ where initial studies indicated that longer precursor alkyl chain lengths resulted in poorer deposition quality under the conditions used. Similarly to its selenium analogue, use of (*N,N*-diethyl-*N'*-benzoylthiourea)Cd(II) allowed the deposition of crystalline CdS over a range of temperatures between 325 and 475 °C. The largely amorphous deposition obtained at lower temperatures relative to those obtained for its selenium analogue, reflects the differing stabilities of the two metal complexes. As in the case of (*N,N*-diethyl-*N'*-benzoylselenourea)Cd(II), thermolysis of (*N,N*-diethyl-*N'*-benzoylthiourea)Cd(II) resulted in the formation of CdS nanoparticles with a zinc-blende phase, however material obtained following AACVD exhibited a wurtzite phase.

The AACVD of (*N,N*-diethyl-*N'*-benzoylselenourea)Zn(II) was investigated where the deposition of crystalline ZnSe could successfully be affected at deposition temperatures between 325 and 475 °C. Lower temperatures favour the deposition of zinc-blende material, with wurtzite phased material being deposited at higher temperatures. Interestingly, thermolysis of the same precursor resulted in the formation of ZnO nanoparticles, illustrating the effect that the differing reaction conditions can have on the resultant material. Use of the sulfur analogue, (*N,N*-diethyl-*N'*-benzoylthiourea)Zn(II) allowed the deposition of crystalline ZnS in the hexagonal phase at temperatures of 400 and 475 °C, lower temperature deposition resulting in largely amorphous material. These observations confirm those made regarding (*N,N*-diethyl-*N'*-benzoylselenourea)Cd(II) and its sulfur analogue, where the increased stability of the acylthiourea derivatives requires higher deposition and thermolysis temperatures than necessary for their selenium counterparts.

Cis-bis(*N,N*-diethyl-*N'*-benzoylthiourea)Ni(II) was successfully used as a single source precursor for the deposition of crystalline heazelwoodite (Ni_3S_2) at 400 °C, where in addition to the deposition of material with a wire mesh type morphology, TEM analysis revealed triangular nanoparticles adhering to the wire mesh. In addition fibres of varying length, density and thickness were also visible, where accurate phase determination using HRTEM could provide interesting results. As a continuation of our interest in the PGM's, the AACVD of *cis*-bis(*N,N*-diethyl-*N'*-benzoylthiourea)Pd(II) was investigated where amorphous material was deposited over temperatures ranging from 250 to 475 °C. Annealing at 425 °C of thin films deposited at 325 °C resulted in the formation of highly crystalline palladium. Metallic platinum was deposited from the AACVD of *cis*-bis(*N,N*-diethyl-*N'*-benzoylthiourea)Pt(II) at 400 °C, where no annealing was necessary to obtain a crystalline deposit. AACVD of *cis*-bis(*N,N*-diethyl-*N'*-benzoylselenourea)Pd(II) allowed the deposition of crystalline $\text{Pd}_{17}\text{Se}_{15}$ at temperatures ranging between 250 and

475 °C. The conductivity measurements performed suggest little correlation between deposition temperature and the conductivity of the resulting thin films. This, to the best of our knowledge, is the first time that AACVD has been performed, using the *N,N*-dialkyl-*N'*-benzoyl(thio)selenourea metal complexes as single source precursors, in addition, we believe it to be the first time that palladium selenide has been deposited using the AACVD technique.

Addendum A

Cadmium(II) complexes of *N,N*-diethyl-*N'*-benzoylthio(seleno)urea as single-source precursors for the preparation of CdS and CdSe nanoparticles

Jocelyn C. Bruce, Neerish Revaprasadu† and Klaus R. Koch*

Received (in Durham, UK) 15th December 2006, Accepted 10th May 2007

First published as an Advance Article on the web

DOI: 10.1039/b618254b

Cadmium complexes of *N,N*-diethyl-*N'*-benzoylthiourea and *N,N*-diethyl-*N'*-benzoylselenourea have been used as single-source precursors for the synthesis of HDA capped CdS and CdSe nanoparticles in a predominantly cubic phase, respectively. Both types of particles show quantum confinement effects and close to band edge luminescence. The particle morphology of CdS and CdSe nanoparticles obtained from the thermolysis of *N,N*-diethyl-*N'*-(benzoylthioureato)cadmium(II) and *N,N*-diethyl-*N'*-(benzoylselenoureato)cadmium(II) was found to be independent of the thermolysis temperature and monomer concentration in the ranges examined. The structure of the *N,N*-diethyl-*N'*-benzoylthiourea ligand was determined by single-crystal X-ray diffraction.

Introduction

The synthesis of highly crystalline, well coated, semiconducting nanocrystals of uniform shape and size has been the focus of considerable research interest in recent years.¹ These particles have a wide variety of promising applications due to their unique chemical and optical properties, particularly their size dependant emission.^{2–6} The use of organometallic precursor compounds for the controlled synthesis of semiconducting quantum dots was pioneered by Bawendi and co-workers, however the noxious and hazardous nature of some of the starting compounds necessitates the need for safer synthetic routes.⁷ To this end the use of single-source precursors has attracted significant attention and a variety of precursor complexes have been reported.^{1,8–12} These include the cadmium complexes of alkyl substituted thioureas.¹³

As part of our long-standing interest in the coordination chemistry of *N,N*-dialkyl-*N'*-acyl(aryl)thioureas, we here explore the synthesis of CdS and CdSe quantum dots from single-source precursor *N,N*-diethyl-*N'*-(benzoylthioureato)cadmium(II)¹⁴ and *N,N*-diethyl-*N'*-(benzoylselenoureato)cadmium(II)¹⁵ derived from ligands HL¹ and HL² in Fig. 1. These ligands readily form stable, bidentate O, S(Se) bound complexes with a wide variety of transition metal ions, following loss of the thioamidic proton or the selenoamidic proton.^{16,17}

To our knowledge these complexes have not been used as single-source precursors before. Both ligands and metal complexes can be easily prepared in high yields from relatively inexpensive and only mildly hazardous starting materials, making them ideal for the potential large scale synthesis of CdS and CdSe nanoparticles.

Experimental

Precursor synthesis

N,N-Diethyl-*N'*-benzoylthiourea (HL¹) and *N,N*-diethyl-*N'*-benzoylselenourea (HL²) were synthesised and recrystallised according to literature methods.^{18,19} The cadmium complexes of HL¹ and HL² were synthesised and recrystallised according to the method described in the literature.¹⁵

Chemicals

Sodium acetate, ethanol, toluene, methanol, hexadecylamine (HDA), tri-*n*-octylphosphine (TOP) and cadmium nitrate tetrahydrate were used as obtained from Aldrich. KSCN and KSeCN were dried in a vacuum oven immediately prior to use and acetone, diethyl amine and benzoyl chloride were distilled before use.

N,N-Diethyl-*N'*-benzoylthiourea. Yield (87%); mp 99.8–100.7 °C. Found: C, 61.8; H, 5.9; N, 11.4. C₁₂H₁₆N₂OS requires C, 61.1; H, 6.8; N, 11.9%. δ_{H} (400 MHz; CDCl₃): 1.28 (unres. t, 3H, H10/H12), 1.35 (unres. t, 3H, H10/H12), 3.59 (unres. q, 2H, H9/H11), 4.02 (unres. q, 2H, H9/H11), 7.45 (m, 2H, H3, H5), 7.56 (t, 1H, ³J_{HH} = 7.5 and ⁴J_{HH} = 1.3, H4), 7.82 (d, 2H, ³J_{HH} = 7.5, H2, H6), 8.40 (br s, 1H, N–H). δ_{C} (100 MHz; CDCl₃): 11.4, 13.1 (C10, C12), 47.7, 47.9 (C9, C11), 127.8 (C3, C5), 128.8 (C2, C6), 132.6 (C1), 132.8 (C4), 163.7 (C7) 179.2 (C8).

N,N-Diethyl-*N'*-benzoylselenourea. Yield (39.0%); mp 111.1–112.5 °C. Found: C, 51.0; H, 5.7; N, 9.9. C₁₂H₁₆N₂OSe requires C, 50.9; H, 5.7; N, 9.9%. δ_{H} (600 MHz; CDCl₃): 1.30 (t, 3H, ³J_{HH} = 7.2, H10/H12), 1.40 (t, 3H, ³J_{HH} = 7.0, H10/H12), 3.59 (q, 2H, ³J_{HH} = 7.2, H9/H11), 4.13 (q, 2H, ³J_{HH} = 7.0, H9/H11), 7.46 (m, 2H, H3, H5), 7.57 (t, 1H, ³J_{HH} = 7.4, H4), 7.83 (d, 2H, ³J_{HH} = 7.6, H2, H6), 8.59 (br s, 1H, N–H). δ_{C} (150 MHz; CDCl₃): 11.7, 12.8 (C10, C12), 48.4, 51.2 (C9, C11), 127.8 (C3, C5), 128.8 (C2, C6), 132.6 (C1), 132.9 (C4), 162.2 (C7), 180.4 (C8), ¹J(¹³C–⁷⁷Se) = 220.3.

Department of Chemistry and Polymer Science, University of Stellenbosch, P Bag X1, Matieland, 7602, South Africa. E-mail: krk@sun.ac.za; Fax: 021-8083342; Tel: 021 8083020

† Present address: Department of Chemistry, University of Zululand, Private Bag X1001, Kwadlangezwa, 3386, South Africa. Fax: 035 9026568; Tel: 035 9026152.

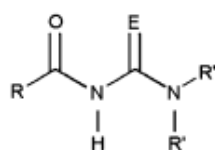


Fig. 1 Structure of the *N,N*-dialkyl-*N'*-acyl(aryl)thio(seleno)urea ligands where R = alkyl or aryl, R' = alkyl. E = S (HL¹), Se (HL²).

(*N,N*-Diethyl-*N'*-benzoylthiourea)cadmium(II). Yield (92.7%); mp 158.0–159.5 °C. Found: C, 49.3, H, 5.1, N, 9.5, S, 10.8. C₂₄H₃₀N₄O₂S₂Cd requires C, 49.4, H, 5.2, N, 9.7, S, 11.0%. δ_{H} (400 MHz; CDCl₃): 1.17 (t, 3H, ³J_{HH} = 7.1, H10/H12), 1.26 (t, 3H, ³J_{HH} = 7.1, H10/H12), 3.70 (q, 2H, ³J_{HH} = 7.1, H9/H11), 3.84 (q, 2H, ³J_{HH} = 7.1, H9/H11), 7.29 (m, 2H, H3, H5), 7.39 (t, 1H, ³J_{HH} = 7.4, H4), 8.03 (d, 2H, ³J_{HH} = 7.1 Hz, H2, H6). δ_{C} (100 MHz; CDCl₃): 12.9, 13.0 (C10, C12), 45.7, 46.1 (C9, C11), 127.5 (C3, C5), 129.4 (C2, C6), 130.8 (C4), 138.1 (C1), 170.9 (C8), 176.6 (C7).

(*N,N*-Diethyl-*N'*-benzoylselenourea)cadmium(II). Yield (78.5%); mp 160.1–161.5 °C. Found: C, 42.7; H, 4.4; N, 8.2. C₂₄H₃₀N₄O₂Se₂Cd requires C, 42.6; H, 4.4; N, 8.3%. δ_{H} (400 MHz; CDCl₃): 1.24 (t, 3H, ³J_{HH} = 7.1, H10/H12), 1.35 (t, 3H, ³J_{HH} = 7.1, H10/H12), 3.78 (q, 2H, ³J_{HH} = 7.1, H9/H11), 3.98 (q, 2H, ³J_{HH} = 7.1, H9/H11), 7.33 (m, 2H, H3, H5), 7.44 (t, 1H, ³J_{HH} = 7.3, ⁴J_{HH} = 2.0, H4), 8.07 (d, 2H, ³J_{HH} = 7.8, H2, H6). δ_{C} (100 MHz; CDCl₃): 13.0, 13.5 (C10, C12), 45.8, 48.0 (C9, C11), 127.6 (C3, C5), 129.5 (C2, C6), 131.1 (C4), 137.9 (C1), 167.8 (C8), 170.9 (C7), ¹J(¹³C–⁷⁷Se) = 164.9.

Synthesis of CdS and CdSe nanoparticles

A typical synthesis was as follows. A specified mass of the precursor complex was dissolved in TOP and injected into a three-neck flask containing HDA at the specified temperature, under a flow of nitrogen. Samples were withdrawn at various time intervals. Following a 60 min reaction period the solution was cooled to 70 °C and excess methanol added to precipitate the nanoparticles. These were isolated by centrifugation and redispersed in toluene to enable further characterisation. No size selective precipitation was performed.

Synthesis of CdSe nanoparticles. The precursor (0.58 g) was suspended in TOP (4 ml) and injected into HDA (5 g) and reacted for 60 min. An initial temperature of 200 °C was used, followed by 100, 125, 150 and 250 °C.

Synthesis of CdS nanoparticles. The precursor (0.5 g) was suspended in TOP (4 ml) and injected into HDA (5 g) and reacted for 60 min. An initial temperature of 200 °C was used, followed by 125, 150 and 240 °C.

Varying precursor concentration for CdS nanoparticles. The precursor (1.25 g) was suspended in TOP (4 ml) and injected into HDA (6 g) at 150 °C followed by a 60 min reaction period.

General experimental

¹H and ¹³C NMR spectra were recorded on either a 400 MHz Varian^{Unity} Inova spectrometer equipped with an Oxford

magnet (9.4 T) operating at 400 MHz for ¹H and 100 MHz for ¹³C or a 600 MHz Varian^{Unity} Inova spectrometer equipped with an Oxford magnet (14.09 T) operating at 600 MHz for ¹H and 150 MHz for ¹³C. All samples were measured in deuterated chloroform at concentrations in the order of 10⁻² M. Proton chemical shifts are quoted relative to the residual CHCl₃ solvent resonance at 7.26 ppm, and ¹³C chemical shifts relative to the CDCl₃ triplet at 77.0 ppm (centre peak). *J* values are given in Hz. Elemental analyses were performed on a Heraeus Universal Combustion Analyser, Model CHN-Micro. UV-Vis absorption spectra were obtained using an Agilent 8453 spectrometer and quartz cuvettes (1 cm path length) were used. Samples were determined in toluene which was also used as a reference solvent. Emission spectra were obtained using a Perkin Elmer LS50B Luminescence Spectrometer where the excitation and emission slit widths were set to 5 and 10 nm, respectively. An excitation wavelength of 350 nm was used. X-Ray powder diffraction (XRD) patterns were recorded on an Oxford Xcalibur 2 diffractometer using Mo-K α radiation (λ = 0.71073 Å) at a temperature of 100 K and with X-ray power = 2.0 kW. Thermogravimetric analyses (TGA) of the precursor compounds were performed using a TG Instruments Q500 thermogravimetric analyser where the samples were maintained in a nitrogen atmosphere and heated at a rate of 10 °C min⁻¹. Transmission electron microscopy (TEM) was performed on either a JEM 1200 EXII (Jeol, Japan) instrument or a LEO 912 Omega (Zeiss, Oberkochen) instrument, fitted with a 2k × 2k digital camera. Samples were prepared by placing a drop of the dilute toluene solution of the sample onto a carbon coated copper grid at room temperature. Excess sample was wicked away using filter paper.

Crystallography

Data collection for the single-crystal determination for *N,N*-diethyl-*N'*-benzoylselenourea was performed on a SMART APEX CCD (Bruker-Nonius). Cell refinement and data reduction was performed using SAINT (Bruker-Nonius). Initial structure solution was performed using SHELXS 97²⁰ and atomic positions were located from a difference fourier map. The refinement method was full matrix least squares on *F*² using SHELXL 97. Molecular graphics were generated via X-Seed²¹ using POV-Ray. All hydrogen atoms were placed in geometrically calculated positions with C–H = 0.99 Å, (for –CH₂); 0.98 Å, (for –CH₃); 0.95 Å, (for phenyl) and refined using a riding model with *U*_{iso}(H) = 1.2 *U*_{eq} (parent), for –CH₂ and phenyl or *U*_{iso}(H) = 1.5 *U*_{eq} (parent) for –CH₃.

Crystallographic data are presented in Table 1.

CCDC reference number 622749.

For crystallographic data in CIF or other electronic format see DOI: 10.1039/b618254b

Results and discussion

Structural characterisation of *N,N*-diethyl-*N'*-benzoylselenourea, (HL²)

Despite several structural characterisations of metal complexes of *N,N*-diethyl-*N'*-benzoylselenourea being available

Table 1 Crystal data for *N,N*-diethyl-*N'*-benzoylselenourea

Compound	HL ²
Empirical formula	C ₁₂ H ₁₆ N ₂ OSe
Formula weight/g mol ⁻¹	283.2314
Crystal system	Monoclinic
Space group	C2/c
<i>a</i> /Å	20.562(4)
<i>b</i> /Å	8.442(2)
<i>c</i> /Å	14.824(3)
β /°	106.93(3)
<i>V</i> /Å ³	2461.7(9)
<i>Z</i>	8
<i>D</i> _c /g cm ⁻³	1.528
<i>F</i> (000)	1152
Temperature/K	173(2)
Absorption coefficient/mm ⁻¹	3.032
θ Range for data collection/°	2.07–28.24
Limiting indices, <i>hkl</i>	–26 to 26; –11 to 9; –19 to 18
Reflections collected/unique	7430/2851
Radiation	Mo-K α , graphite monochromated
Refinement method	Full-matrix-least-squares on <i>F</i> ²
Data/restraints/parameters	2851/0/148
Goodness-of-fit on <i>F</i> ²	1.095
Final <i>R</i> indices $> I > 2\sigma(I)$	0.228, 0.0585
<i>R</i> Indices (all data)	<i>R</i> = 0.0247, <i>wR</i> ₂ = 0.0592

in the literature,^{15,22–24} no structural characterisation of the ligand could be found. Fig. 2 shows the molecular structure of HL² and Table 2 gives the relevant bond lengths for the compound as well as those of the sulfur analogue.²⁵

Table 2 shows that the N–C(O), N–C(E) and (E)C–NR₂ bonds are all shorter than the average C–N single bond length of 1.472(5) Å, consistent with the observed trend for the *N,N*-dialkyl-*N'*-aroylthioureas, for which the C–N bond lengths decrease in the order N–C(S) > N–C(O) > S(C)–N.²⁶ It is noteworthy that the corresponding bond lengths N–C(O) and N–C(E) for HL¹ (E = S) and HL² (E = Se), respectively, differ significantly, the N–C(O) for HL¹ being shorter than for HL², while the opposite is observed for the N–C(E) bond. This suggests a differing degree of double bond character in these bonds in HL¹ compared to HL². In the sulfur analogue HL¹ an intermolecular hydrogen bond between the oxygen atom of the carbonyl group and the thioamidic proton of the neighbouring molecule (symmetry operator; *x*, 1 + *y*, *z*) N(H)⋯O = 2.012 Å and N–O = 2.871(3) Å, is present,²⁵ which however is not observed in the selenium analogue. In the case of HL², the selenoamidic proton is involved in a weak hydrogen bond with the selenium atom of a neighbouring molecule (symmetry operator 1 – *x*, 1 – *y*, –*z*) N(H)⋯Se = 2.70 Å and N–Se = 3.532(2) Å, and the selenoamidic proton of this molecule in turn forms a weak hydrogen bond with the selenium atom of the original molecule, so resulting in a weakly hydrogen bonded dimer in the crystal structure. In terms of hydrogen bonding, the acylselenourea moiety consists of a donor–acceptor pair connected by a delocalized π -system reflected in the shorter amide and acyl-substituted C–N bonds. The formation of a dimer in the crystal lattice by HL² therefore represents an example of resonance-assisted hydrogen bonding (RAHB) or π -bond cooperativity.²⁷ In structures of related acylthiourea ligands, C₁₄H₉C(O)NHC(S)N(C₂H₅)₂ and C₁₆H₉(CH₂)₃C(O)NHC(S)N(C₂H₅)₂ we have observed a similar RAHB effect,²⁸ although it is interesting that HL¹

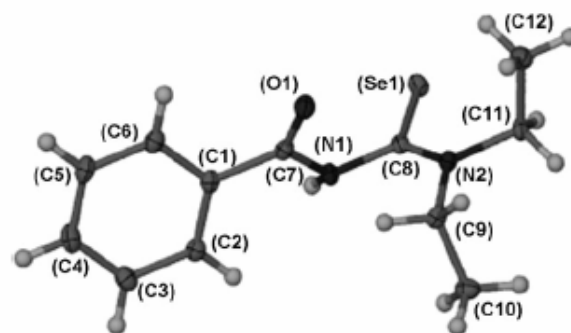


Fig. 2 Molecular structure of *N,N*-diethyl-*N'*-benzoylselenourea (HL²). Displacement ellipsoids are drawn at the 50% probability level.

exhibits different hydrogen bonding in the crystal lattice to its selenium counterpart. The relative orientations of the S and O atoms in HL¹ and the Se and O atoms in HL² can be defined using the following torsion angles: O–C(O)–N(H)–C(S) = –12.5(4)° and C(O)–N(H)–C(S)–S = –100.4(3)° for HL¹ and O–C(O)–N(H)–C(Se) = 6.9(2) and 108.5(1)° for HL². These values show that the coordinating atoms have similar orientations in both HL¹ and HL² (Table 2).

NMR spectroscopy

Assignment of the proton and carbon resonances of both the ligands and metal complexes is relatively straightforward, although an interesting aspect of HL² and its Cd complex is the presence of the NMR active ⁷⁷Se nucleus, which couples to the selenocarbonyl carbon atom giving rise to clear satellites, enabling the unambiguous assignment of the selenocarbonyl resonances. As shown in Fig. 3 there are relatively larger differences between the chemical shifts of the C(Se) and C(O) peaks in the ligand compared to the cadmium complex. The C(Se) resonance of HL² is more downfield (180.4 ppm) relative to the C(O) resonance (162.2 ppm). In the cadmium complex, the relative chemical shifts are exchanged and the C(Se) resonance is more upfield (167.8 ppm) relative to the C(O) resonance (170.9 ppm). This is probably due to increased electron density and changes in the electronic delocalisation in the chelate ring following loss of H⁺ upon coordination to the metal centre. The lower ¹*J*(¹³C–⁷⁷Se) coupling of 164.9 Hz in the cadmium complex relative to 220.3 Hz observed in the unbound ligand, also reflects this. Similar observations have been made for *N,N*-dialkyl-*N'*-benzoylthioureas in which ¹³C enrichment was used to assign the thiocarbonyl and carbonyl carbons resonances unambiguously.^{29,30}

Table 2 Relevant bond lengths (Å) of HL¹ and HL²

Bond length	HL ¹ , ²⁵ E = S	HL ² E = Se
C=O	1.230(3)	1.221(2)
N–C(O)	1.362(4)	1.388(2)
N–C(E)	1.448(4)	1.416(2)
C=E	1.672(3)	1.834(2)
(E)C–NR ₂	1.320(4)	1.320(2)

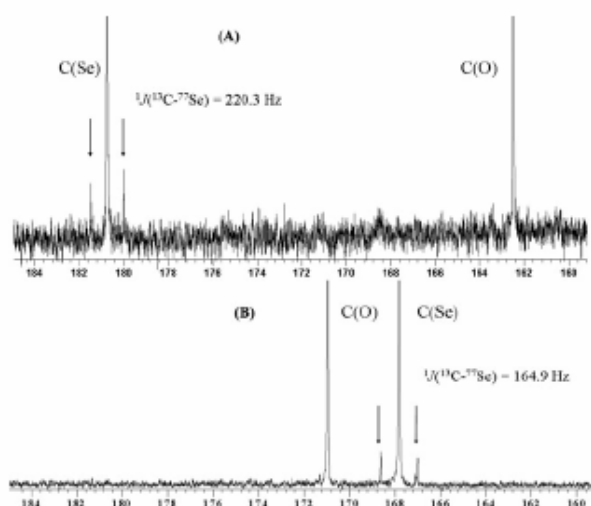


Fig. 3 Expansions of ^{13}C NMR spectra of $\text{C}_6\text{H}_5\text{CONCSeNC}_2\text{H}_5$ (A) and $\text{Cd}(\text{C}_6\text{H}_5\text{CONCSeNC}_2\text{H}_5)_2$ (B), showing $^1J(^{13}\text{C}-^{77}\text{Se})$ coupling satellites.

Nanoparticle synthesis

Cadmium complexes of *N,N*-dialkyl-*N'*-benzoylthio(seleno)ureas HL¹ and HL² readily result in CdS or CdSe nanoparticles on controlled thermolysis. Initially the *N,N*-diethyl-*N'*-(benzoylthioureato)cadmium(II) precursor was thermolysed in TOP and HDA at an injection temperature of 200 °C, to establish whether previously well characterised CdS nanoparticles could be formed. This was found to be the case.

The band edge of 494 nm for the CdS particles formed (Fig. 4) was calculated using the linear regression method and was significantly blue shifted relative to that of bulk CdS (515 nm), indicating quantum confinement.³¹ Close to band edge luminescence was observed from the photoluminescence (PL) spectrum and the full width at half maximum height (FWHM) was calculated to be 31.5 nm indicating a relatively narrow particle size distribution. This was confirmed by a relative standard deviation in the particle size distribution obtained using the TEM image of only 15%.

Spherical nanoparticles of CdS could clearly be seen in the TEM image (Fig. 5) and the average particle size calculated

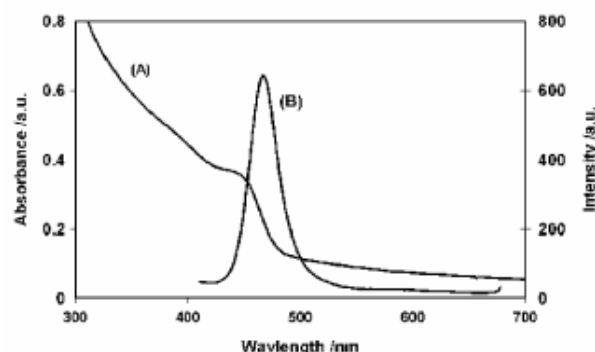


Fig. 4 Optical spectra of CdS nanoparticles: (A) absorption spectrum and (B) photoluminescence spectrum (200 °C, 60 min).

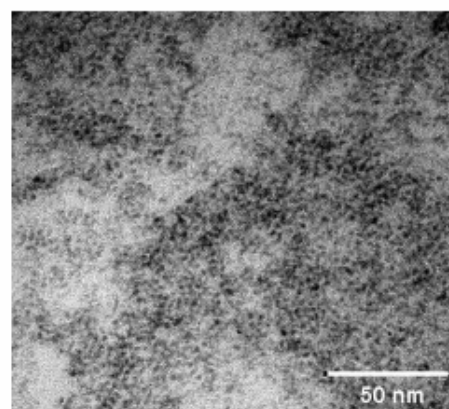


Fig. 5 TEM image of CdS nanoparticles (200 °C, 60 min).

from the TEM data is given in Table 3 as well as data from the optical spectra.

The corresponding selenium analogue, $\text{Cd}(\text{C}_6\text{H}_5\text{CONCSeNC}_2\text{H}_5)_2$, was thermolysed under similar conditions to those of the sulfur derivative. Well formed, monodispersed spherical nanoparticles of CdSe with an average size of 3.3 (14%) nm were obtained as clearly seen in the TEM image (Fig. 6).

A band edge of 639 nm for the CdSe was obtained from the UV spectrum, this being significantly blue shifted relative to that of bulk CdSe at 716 nm.⁷ The PL spectrum (Fig. 7) showed close to band edge luminescence, with the FWHM being slightly larger than in the case of the sulfur analogue at 51 nm. This indicates a larger particle size distribution although this is not reflected in the standard deviation obtained from the TEM image.

It is well known that both bulk CdS and CdSe have stable wurtzite phases at room temperature,³² however both types of crystallites can exist in either the cubic or hexagonal phases. The small particle size of both the CdS and CdSe nanoparticles however complicates the assignment of a specific phase and it becomes difficult to exclusively assign a particular phase to each sample. Bawendi *et al.* have also reported that a mixture of the two phases is possible for CdSe nanoparticles where one phase can dominate the other.³³ The X-ray diffraction patterns of the CdS and CdSe nanoparticles synthesised here (Fig. 8 and 9) are interestingly consistent with a predominantly cubic phase in both cases, although this phase is not necessarily exclusive.

The broad peaks in both the CdS and CdSe diffraction patterns are indicative of particles in the nanosize domain and the (111), (220) and (311) planes of cubic CdS and CdSe are clearly visible.

Effects of variation of thermolysis conditions

Recent reports in the literature have shown that variations in reaction temperature can significantly affect the morphology of the resulting nanoparticles.^{34,35} We examined the role of temperature on the thermolysis of *N,N*-diethyl-*N'*-(benzoylselenoureato)cadmium(II) and *N,N*-diethyl-*N'*-(benzoylthioureato)cadmium(II), results of which are shown in Table 3.

Table 3 Properties of CdS and CdSe nanoparticles obtained at various temperatures from thermolysis of *N,N*-diethyl-*N'*-(benzoylselenoureto)cadmium(II) and *N,N*-diethyl-*N'*-(benzoylthioureto)cadmium(II)

	Temp./°C	Band edge/nm	Band edge/eV	Average size ^a /nm (std. dev. %)	Average size/nm (Scherrer equation ³⁶)	Emission maxima/nm
CdSe	100	515	2.41	2.0 (14)	—	504 453 ^b
	125	539	2.30	2.2 (13)	1.3	522.5 451.5 ^b
	150	575	2.15	2.5 (15)	1.7	557.5
	200	639	1.94	3.3 (14)	1.6	589.5
	250	688	1.80	3.8 (15)	1.7	611
CdS	125	480	2.58	3.1 (18)	—	441.5 516.5 ^b
	150	464	2.67	3.0 (15)	1.6	452.5
	200	494	2.51	3.5 (15)	1.9	467.0
	240	562	2.21	3.9 (13)	—	474.0

^a From TEM data. ^b Second, smaller maximum.

For *N,N*-diethyl-*N'*-(benzoylselenoureto)cadmium(II) formation, it is remarkable that CdSe nanoparticle formation occurred at a temperature as low as 100 °C. Samples withdrawn from the reaction vessel at varying times resulted in particles for which the band edge (502 nm) and the emission maximum (487 nm) at this temperature was only marginally red shifted over time. A second smaller emission maximum appeared however at 453 nm, the intensity of which increased with time. This phenomenon was also observed at 125 °C at which temperature the band edge red shifted only marginally over time as did the emission maxima; however the smaller emission maximum at 453 nm persisted and grew in intensity as the reaction progressed. Nevertheless the overall intensity of the latter minor emission band decreased with increasing temperature (21.5% of the emission maxima at 100 °C to 8.2% of the emission maxima at 125 °C and was no longer observable at temperatures > 150 °C). At temperatures > 150 °C good quality nanoparticles with comparable optical spectra were obtained. Surprisingly quantum confinement still occurred at 250 °C since the band edge of 699 nm remained blue shifted relative to that of bulk CdSe although (at 250 °C) the emission broadened significantly over time suggesting the formation of a polydisperse distribution of CdSe particle sizes.

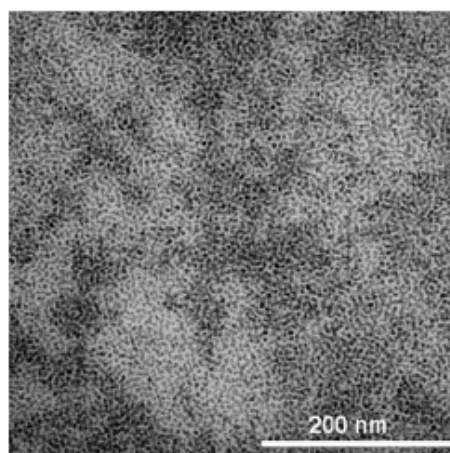


Fig. 6 TEM image of CdSe nanoparticles (200 °C, 60 min).

Particle sizes estimated from the TEM images as well as the (220) peak in the XRD data³⁶ are shown in Table 3. The reduced crystallinity of the particles obtained at 100 °C precluded particle size estimation and no data is shown. Particle sizes calculated using the Scherrer equation³⁶ are consistently smaller than those obtained from the TEM images, although the trend of increasing particle size with increasing temperature is consistent with TEM observation. It is noteworthy that the particle morphology remained similar throughout the temperature study; essentially only spherical particles were obtained.

Examining data obtained for CdS nanoparticle formation shows that at an injection temperature of 125 °C, relatively poor quality CdS nanoparticles were obtained. It is likely that at this relatively low decomposition temperature slow nucleation occurs, and this is supported by the yellow colour due to nucleation in the solution only being observed 12 min into the reaction, whereas at higher temperatures (200 °C) this yellow colour is immediately observable. The uneven nucleation results in a broad particle size distribution reflected in the higher standard deviation of 18% and the bimodal emission evident in the PL spectrum. An injection temperature of 150 °C resulted in nanoparticles with the smallest diameter and a band gap of 464 nm. This is significantly blue shifted relative to that of bulk CdS at 515 nm indicating quantum confinement. The absorption spectrum obtained from a sample withdrawn 10 min into the reaction at 150 °C, was very similar to

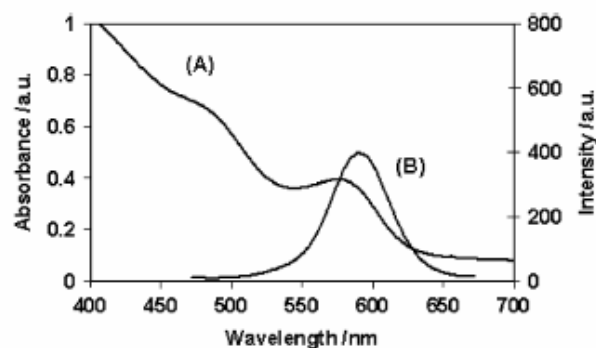


Fig. 7 Optical spectra of CdSe nanoparticles: (A) absorption spectrum and (B) photoluminescence spectrum (200 °C, 60 min).

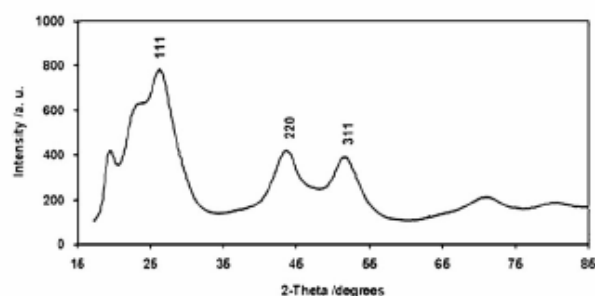


Fig. 8 X-Ray diffraction pattern of CdS nanoparticles (200 °C, 60 min).

that from the 60 min sample indicating that nucleation occurs more rapidly at a higher temperature. The PL spectrum obtained from the same 10 min sample, showed an emission maximum at 447 nm, but with clear evidence of longer wavelength emission. As the reaction time increased this emission was significantly reduced and is barely observable in the spectrum obtained at 60 min. This indicates that annealing and passivation of the semiconducting surface occurs as the reaction proceeds. At an even higher injection temperature of 240 °C, the reaction becomes uncontrollable as within 20 min the particles are no longer in the region of quantum confinement. In contrast the formation of relatively good quality CdSe nanoparticles starts at relatively lower temperatures (100 °C) but results in particles with a relatively narrow size distribution over the entire temperature range, the CdSe particles retaining quantum confinement up to 250 °C.

Particle sizes estimated from the (220) peak in the XRD data using the Scherrer equation are given in Table 3.³⁶ CdS particle sizes for the 125 and 240 °C samples are not given due to the reduced crystallinity observed in these samples. It is interesting to note that whilst the average diameter of the nanoparticles did vary with the injection temperature, the final morphology of the particles remained unaltered for both CdS and CdSe obtained in this manner.

The effect of monomer concentration was investigated using *N,N*-diethyl-*N'*-(benzoylthioureaato)cadmium(II) where a 2.5-fold increase in the precursor concentration (0.5–1.25 g of precursor) led to the optical spectra shown in Fig. 10. A red shift in the band edge and a broader emission indicate larger and more polydisperse nanoparticles, however, the morphol-

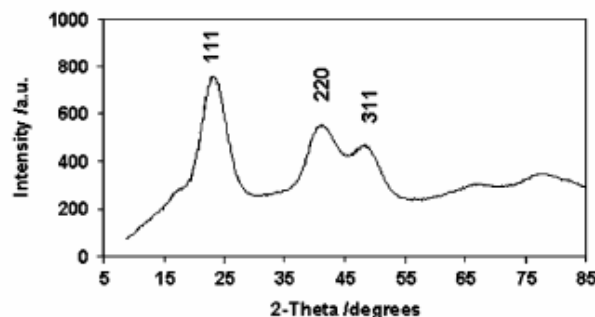


Fig. 9 X-Ray diffraction pattern of CdSe nanoparticles (200 °C, 60 min).

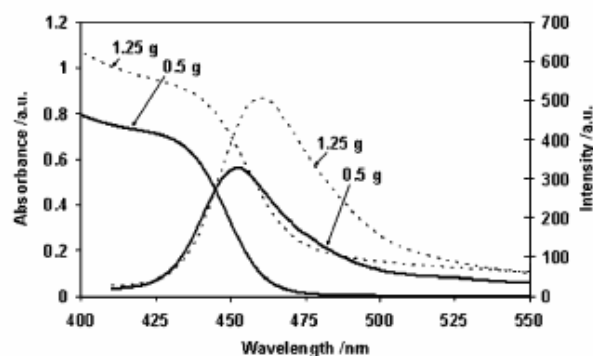


Fig. 10 Optical spectra of CdS at varying precursor concentrations: (A) absorption and (B) photoluminescence spectra (200 °C, 60 min).

ogy of the particles remained constant with increased precursor concentration.

The thermogravimetric (TGA) decomposition data for both *N,N*-diethyl-*N'*-(benzoylselenoureaato)cadmium(II) and *N,N*-diethyl-*N'*-(benzoylthioureaato)cadmium(II) is shown in Fig. 11. Thermal decomposition of *N,N*-dialkyl-*N'*-benzoylselenourea metal complexes have not been reported, although there are reports on the thermal decomposition of the related *N,N*-dipropyl- and dihexyl-*N'*-(benzoylthioureaato)cadmium(II) complexes indicating that the mass loss and residue formed correspond to the formation of cadmium sulfide.³⁷ Our data is consistent with these findings, as shown in Table 4 for the formation of CdS as well as CdSe.

Assuming that the mass loss during thermal decomposition is a first-order process, a Coats–Redfern analysis³⁸ can be performed to estimate the activation energy of our precursors resulting in cubic phases of either CdSe or CdS. This analysis gave activation energies in the range of 18–23 kJ mol⁻¹ for the selenourea complex Cd(C₆H₅CONCSeNC₂H₅)₂, and 28–39 kJ mol⁻¹ for the thiourea complex, Cd(C₆H₅CONCSNC₂H₅)₂. Activation energies between 10.9 and 18.2 kJ mol⁻¹ for several, related single-source precursors, resulting in the formation of only *spherical* nanoparticles have recently been published.³⁹ In this context, Nair and Scholes recently suggested that single compound precursors with much lower activation energies, in the region of 2.1 kJ mol⁻¹, were shown to result in particles showing anisotropic growth as a result of *kinetically controlled growth*, giving rise to CdS nanorods, rather than spherical CdS particles, resulting from more thermodynamically stable precursors such as ours. It should be emphasized here that the non-spherical particles obtained were hexagonally phased, whereas those described in this paper form in a cubic phase, so that any inference from these finding should be made with caution.

Table 4 TGA results of precursors

Precursor	Temp. range/°C	Found mass (%)	Calc. mass [for CdE] (%)
Cd(C ₆ H ₅ CONCSeNC ₂ H ₅) ₂	175–377	31.0	28.3
Cd(C ₆ H ₅ CONCSNC ₂ H ₅) ₂	200–501	25.8	24.8

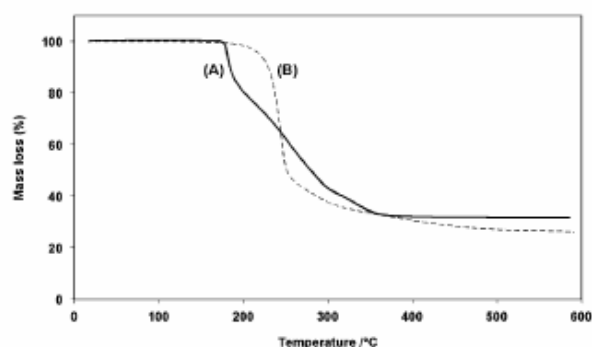


Fig. 11 Thermal decomposition of $\text{Cd}(\text{C}_6\text{H}_5\text{CONCSNC}_2\text{H}_5)_2$ (A) and $\text{Cd}(\text{C}_6\text{H}_5\text{CONCSNC}_2\text{H}_5)_2$ (B) precursors.

Conclusions

In conclusion the conveniently prepared *N,N*-diethyl-*N'*-(benzoylthiourea)cadmium(II) and its corresponding selenourea analogue, *N,N*-diethyl-*N'*-(benzoylselenourea)cadmium(II), may be used as single-source precursors for the synthesis of HDA stabilised, spherical CdS and CdSe nanoparticles, respectively, which show quantum confinement. From the XRD data it is clear that both CdS and CdSe particles are readily formed from these precursors which are predominantly in the cubic phase. Thermolysis of *N,N*-diethyl-*N'*-(benzoylthiourea)cadmium(II) and, the somewhat thermodynamically less stable *N,N*-diethyl-*N'*-(benzoylselenourea)cadmium(II), over a range of increasing temperatures (100–200 °C) shows that essentially only spherical CdS and CdSe nanoparticles were obtained, independent of the reaction temperature and the precursor concentration employed. This suggests thermodynamic growth control of CdS and CdSe from these precursors, respectively.

Acknowledgements

Financial support from the University of Stellenbosch, the NRF, (GUN 2046827), THRIP (project 2921) and Angloplatinum Ltd, is gratefully acknowledged. J. B. acknowledges a Harry Crossley bursary.

References

- 1 M. A. Malik, N. Revaprasadu and P. O'Brien, *Chem. Mater.*, 2001, 13, 913–920.
- 2 M. C. Schlamp, X. Peng and A. P. Alivisatos, *J. Appl. Phys.*, 1997, 82, 5837–5842.
- 3 W. C. W. Chan and S. Nie, *Science (Washington, D. C.)*, 1998, 281, 2016–2018.
- 4 V. I. Klimov, A. A. Mikhailovsky, S. Xu, A. Malko, J. A. Hollingsworth, C. A. Leatherdale, H. J. Eisler and M. G. Bawendi, *Science (Washington, D. C.)*, 2000, 290, 314–317.

- 5 S. Coe, W.-K. Woo, M. Bawendi and V. Bulovic, *Nature (London)*, 2002, 420, 800–803.
- 6 W. U. Huynh, J. J. Dittmer and A. P. Alivisatos, *Science (Washington, D. C.)*, 2002, 295, 2425–2427.
- 7 C. B. Murray, D. J. Norris and M. G. Bawendi, *J. Am. Chem. Soc.*, 1993, 115, 8706–8715.
- 8 M. Azad Malik, P. O'Brien and N. Revaprasadu, *J. Mater. Chem.*, 2001, 11, 2382–2386.
- 9 Y.-w. Jun, S.-M. Lee, N.-J. Kang and J. Cheon, *J. Am. Chem. Soc.*, 2001, 123, 5150–5151.
- 10 P. S. Nair, T. Radhakrishnan, N. Revaprasadu, G. Kolawole and P. O'Brien, *J. Mater. Chem.*, 2002, 12, 2722–2725.
- 11 P. S. Nair, T. Radhakrishnan, N. Revaprasadu, G. A. Kolawole and P. O'Brien, *Chem. Commun.*, 2002, 564–565.
- 12 P. Sree Kumari Nair, T. Radhakrishnan, N. Revaprasadu, G. A. Kolawole and P. O'Brien, *Polyhedron*, 2003, 22, 3129–3135.
- 13 M. J. Moloto, N. Revaprasadu, P. O'Brien and M. A. Malik, *J. Mater. Sci.: Mater. Electron.*, 2004, 15, 313–316.
- 14 M. Merdivan, N. Kulcu and S. Aygun, *Kim. Kim. Muhendisligi Semp. 8th*, 1992, 1, 31–34.
- 15 W. Bensch and M. Schuster, *Z. Anorg. Allg. Chem.*, 1993, 619, 791–795.
- 16 L. Beyer, E. Hoyer, H. Hennig, R. Kirmse, H. Hartmann and J. Liebscher, *J. Prakt. Chem.*, 1975, 317, 829–839.
- 17 M. Schuster and K. H. Koenig, *Fresenius' Z. Anal. Chem.*, 1988, 331, 383–386.
- 18 I. B. Douglass, *J. Am. Chem. Soc.*, 1937, 59, 740–742.
- 19 I. B. Douglass and F. B. Dains, *J. Am. Chem. Soc.*, 1934, 56, 1408–1409.
- 20 G. M. Sheldrick, *Suite of programs for crystal structure determination and refinement*, University of Gottingen, Germany, 1997.
- 21 L. J. Barbour, *J. Supramol. Chem.*, 2003, 1, 189.
- 22 W. Bensch and M. Schuster, *Z. Anorg. Allg. Chem.*, 1993, 619, 786–790.
- 23 W. Bensch and M. Schuster, *Z. Anorg. Allg. Chem.*, 1994, 620, 1479–1482.
- 24 W. Bensch and M. Schuster, *Z. Anorg. Allg. Chem.*, 1994, 620, 177–182.
- 25 M. Bolte and L. Fink, personal communication to CCDC, 2003 (CCDC 214315).
- 26 K. R. Koch, C. Sacht, T. Grimmacher and S. Bourne, *S. Afr. J. Chem.*, 1995, 48, 71–77.
- 27 T. Steiner, *Angew. Chem., Int. Ed.*, 2002, 41, 48–76.
- 28 J. C. Bruce and K. R. Koch, unpublished results, 2004.
- 29 K. R. Koch and M. C. Matoetoe, *Magn. Reson. Chem.*, 1991, 29, 1158–1160.
- 30 A. N. Mautjana, J. D. S. Miller, A. Gie, S. A. Bourne and K. R. Koch, *Dalton Trans.*, 2003, 1952–1960.
- 31 T. Trindade, P. O'Brien and N. L. Pickett, *Chem. Mater.*, 2001, 13, 3843–3858.
- 32 R. J. Bandaranayake, G. W. Wen, J. Y. Lin, H. X. Jiang and C. M. Sorensen, *Appl. Phys. Lett.*, 1995, 67, 831–833.
- 33 M. G. Bawendi, A. R. Kortan, M. L. Steigerwald and L. E. Brus, *J. Chem. Phys.*, 1989, 91, 7282–7290.
- 34 Y. Li, X. Li, C. Yang and Y. Li, *J. Mater. Chem.*, 2003, 13, 2641–2648.
- 35 A. A. Memon, M. Afzaal, M. A. Malik, C. Q. Nguyen, P. O'Brien and J. Raftery, *Dalton Trans.*, 2006, 4499–4505.
- 36 B. D. Cullity, *Elements of X-ray Diffraction*, Addison-Wesley Publishing Company, New York, 2nd edn, 1978.
- 37 M. Merdivan, F. Karipcin, N. Kulcu and R. S. Aygun, *J. Therm. Anal. Calorim.*, 1999, 58, 551–557.
- 38 A. W. Coats and J. P. Redfern, *Nature (London)*, 1964, 201, 68–69.
- 39 P. S. Nair and G. D. Scholes, *J. Mater. Chem.*, 2006, 16, 467–473.

Addendum B

***N*-Benzoyl-*N,N'*-dibutylselenourea
and its palladium(II) complex**

Jocelyn C. Bruce and Klaus R. Koch*

Department of Chemistry, University of Stellenbosch, Private Bag X1, Matieland
7602, South Africa

Correspondence e-mail: krk@sun.ac.za

Received 11 September 2007

Accepted 27 October 2007

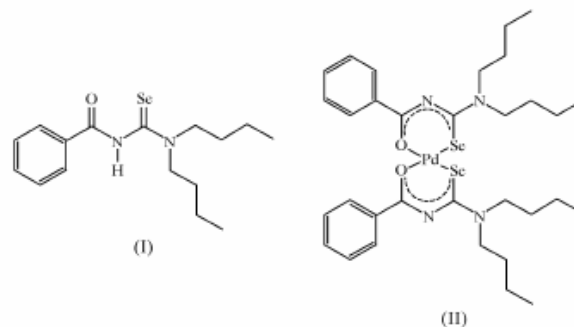
Online 14 December 2007

The crystal and molecular structures of *N*-benzoyl-*N,N'*-dibutylselenourea (HL), C₁₆H₂₄N₂OSe, and the corresponding complex bis(*N*-benzoyl-*N,N'*-dibutylselenoureaato-κ²Se,O)-palladium(II), [Pd(C₁₆H₂₃N₂OSe)₂], are reported. The selenourea molecule is characterized by intermolecular hydrogen bonds between the selenoamidic H atom and the Se atom of a neighbouring molecule forming a dimer, presumably as a consequence of resonance-assisted hydrogen bonding or π-bonding co-operativity. A second dimeric hydrogen bond is also described. In the palladium complex, the typical square-planar coordination characteristic of such ligands results in a *cis*-[Pd(*L-Se,O*)₂] complex.

Comment

The use of metal complexes in which the ligands contain either S or Se as single-source precursors for the synthesis of semi-conducting quantum dots has recently attracted interest (Nair *et al.*, 2005; Malik *et al.*, 2005). In this context, we have recently reported the use of [*N'*-benzoyl-*N,N*-diethylthio(seleno)urea]cadmium(II) complexes as single-source precursors for the successful synthesis of CdS and CdSe nanoparticles (Bruce *et al.*, 2007). As part of our interest in extending this study to include other metal ions, we have prepared several *N,N*-dialkyl-*N'*-benzoylselenoureas and corresponding metal complexes with a view to using these as single-source precursors for nanoparticle synthesis. The related *N,N*-dialkyl-*N'*-benzoylthiourea ligands have been studied extensively and are well known to coordinate to a wide variety of first-row transition metal ions (Schuster & Koenig, 1987; Dietze *et al.*, 1991; Beyer *et al.*, 1981). The corresponding *N,N*-dialkyl-*N'*-benzoylselenoureas are relatively rare, although some metal complexes of Ni^{II} and Pd^{II} derived from *N,N*-dialkyl-*N'*-benzoylselenourea have been structurally characterized (Kampf *et al.*, 2004; Bensch & Schuster, 1994). Generally, both *N,N*-dialkyl-*N'*-benzoylthioureas and *N,N*-dialkyl-*N'*-benzoylselenoureas readily coordinate to metal ions with loss of a thioamidic or selenoamidic H atom, resulting in bidentate coordination through the S(Se) and O donor atoms. Surpris-

ingly, relatively few crystal structures of the unbound ligand *N,N*-dialkyl-*N'*-benzoylthiourea and analogous *N,N*-dialkyl-*N'*-benzoylselenoureas are available in the literature. We report here the crystal and molecular structures of *N,N*-dibutyl-*N'*-benzoylselenourea (HL), (I) (Figs. 1 and 2), and its Pd^{II} complex, *cis*-[Pd(*L-Se,O*)₂], (II) (Fig. 3).



Compound (I) (Fig. 1) crystallizes in the space group *P*2₁/*c*. The O and Se donor atoms adopt an *anti* orientation relative to each other as a result of twisting about the N1–C8 bond, to give torsion angles O1–C7–N1–C8 = 0.5 (4)° and C7–N1–C8–Se1 = 121.1 (2)°. The C–N bonds are all shorter than the average C–N bond length of 1.472 (5) Å (Allen *et al.*, 1987) (Table 1); the alkyl-substituted selenourea C–N bond [C8–N2 = 1.316 (3) Å] is significantly shorter than the amide bond [C7–N1 = 1.397 (3) Å] and the acyl-substituted selenourea C–N bond [C8–N1 = 1.399 (3) Å]. This reflects the trend observed in the sulfur analogues, where *N,N*-dibutyl-*N'*-naphthoylthiourea (Koch *et al.*, 1995) and, more recently, *N*-acetyl-*N,N'*-(butane-1,4-diyl)thiourea (Dillen *et al.*, 2006a) and *N,N*-di-*n*-butyl-*N'*-pivaloylthiourea (Dillen *et al.*, 2006b), show that the *R,RN*–C(S) bond length is, on average, the shortest, followed by the amidic *R'C*(O)–N bond, while the *HN*–C(S) thiourea bond is the longest. Moreover, these molecules usually adopt a conformation in the solid state such that the S and O donor atoms assume opposing orientations, the molecule being usually significantly twisted around the longest *HN*–C(S) thiourea bond.

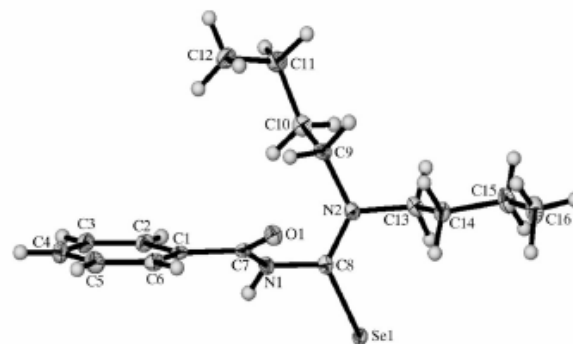


Figure 1
The molecular structure of (I), showing the atomic numbering scheme. Displacement ellipsoids are drawn at the 50% probability level.

metal-organic compounds

As shown in Fig. 2, the molecules of (I) are linked through a hydrogen bond between the selenoamidic H atom of one molecule and the Se atom of its neighbour (see Table 2), so giving rise to a dimer linked through such hydrogen bonds in the crystal structure. The formation of this dimer represents an example of resonance-assisted hydrogen bonding (RAHB) or π -bond co-operativity (Steiner, 2002) since, in terms of hydrogen bonding, the selenourea moiety consists of donor-acceptor pairs which are connected by a resonant π system, manifested by the shortening of the amide and acyl-substituted C—N bonds. Such an arrangement is also observed in the closely related diethyl analogue, *N*'-benzoyl-*N,N*-diethylselenourea (Bruce *et al.*, 2007). This dimer forms an eight-membered ring structure where atoms H1/N1/C8/Se1/H1ⁱ/N1ⁱ/C8ⁱ/Se1ⁱ [symmetry code: (i) $-x, 1-y, 1-z$] lie in a plane, with a maximum deviation of 0.119 (2) Å for atom H1. A second dimeric hydrogen bond is present in (I) between the carbonyl O atom and a H atom on the benzene residue at $(-x, 1-y, -z)$ (see Table 2). Similarly to the first dimer, this forms a ten-membered ring structure where atoms O1/C7/C1/C6/H6/O1ⁱⁱ/C7ⁱⁱ/C1ⁱⁱ/C6ⁱⁱ/H6ⁱⁱ [symmetry code: (ii) $-x, 1-y, -z$] again lie in a plane, with a maximum deviation of 0.241 (2) Å for atom O1, the angle between these two planes being

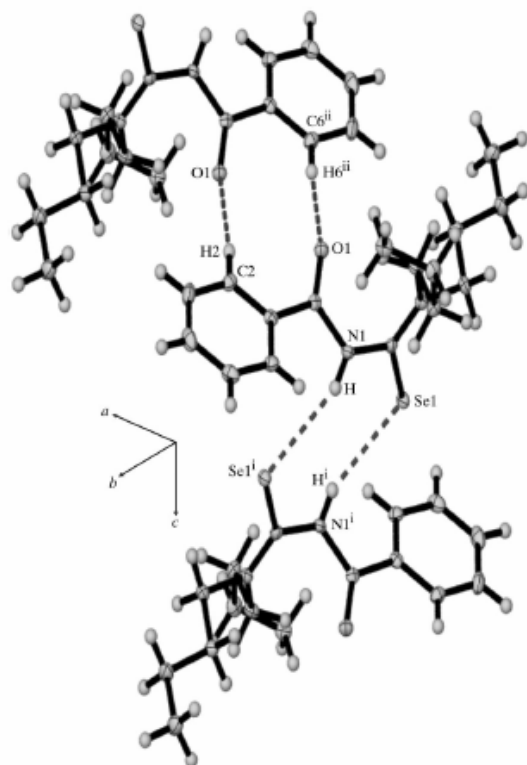


Figure 2
Neighbouring molecules of (I), showing the weak N—H...Se and C=O...H...O intermolecular hydrogen bonds (dashed lines). Displacement ellipsoids are drawn at the 50% probability level. [Symmetry codes: (i) $-x, 1-y, 1-z$; (ii) $-x, 1-y, -z$.]

82.36 (2)°. It is interesting to note that the second hydrogen bond is not evident in the solid-state structures of other *N*'-benzoyl-*N,N*-dialkylselenoureas that have previously been analysed (*N*'-benzoyl-*N,N*-dihexylselenourea, *N*'-benzoyl-*N,N*-dioctylselenourea and *N*'-benzoyl-*N*-benzyl-*N*-methylselenourea; Bruce & Koch, 2007). These two dimers give rise to the hydrogen-bonded chains shown in Fig. 2 that form in the direction of the *c* axis. There is little interaction apparent between these chains.

The molecular structure of *cis*-[Pd(*L*-Se,O)₂], (II), which crystallizes in the space group *P* $\bar{1}$, is shown in Fig. 3. The generally expected mode of coordination of HL, with loss of an H atom and yielding a *cis*-square-planar complex, is observed. The four donor atoms and Pd metal centre lie in a single coordination plane involving atoms Se1A/O1A/Pd1/Se1B/O1B, with a mean deviation from planarity of only 0.024 Å; the two chelate rings are twisted at an angle of 4.6 (1)° relative to each other, and deviate slightly from perfect planarity by 0.096 and 0.085 Å for atoms Se1A/C8A/N1A/C7A/O1A and Se1B/C8B/N1B/C7B/O1B, respectively. The reduced planarity in the chelate rings is reflected in a puckering of the C7A/N1A/C8A and the C7B/N1B/C8B planes, with atoms N1A and N1B, respectively, lying 0.486 (2) Å below and 0.336 (2) Å above the Se1A/O1A/Pd1/Se1B/O1B plane.

The average Pd—Se and Pd—O bond lengths (Table 3) of 2.345 (3) and 2.041 (1) Å, respectively, in (II) compare well with those reported previously for bis[*N*'-(2-fluorobenzoyl)-*N,N*-diisobutylselenoureaato]palladium(II) (Kampf *et al.*, 2004) and its difluoro analogue, bis[*N*'-(2,6-difluorobenzoyl)-*N,N*-diisobutylselenoureaato]palladium(II) (Kampf *et al.*, 2005). The C=O and C=Se bonds in (II) are somewhat longer than the corresponding bonds in the ligand HL, as a result of a slight loss of double-bond character in these bonds, presumably due to electron delocalization in the six-membered chelate ring of the metal complex. The relative reduction in the C=Se bond

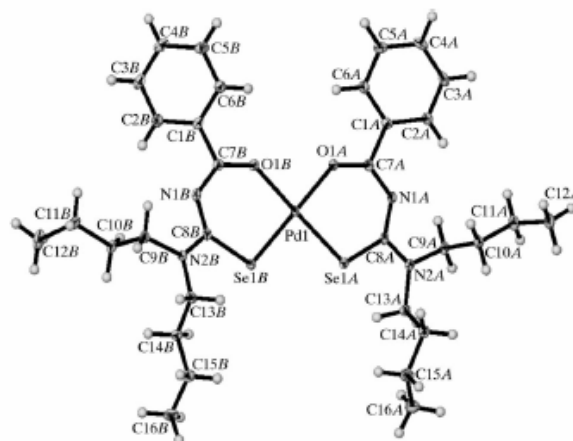


Figure 3
The molecular structure of (II), showing the atomic numbering scheme. Displacement ellipsoids are drawn at the 50% probability level.

order of (I) on coordination to Pd^{II} in the complex is also reflected by a significant reduction of the $^1J(^{77}\text{Se}-^{13}\text{C})$ coupling constant, from 222 Hz in the ligand to 177 Hz in (II), in the ^{13}C NMR spectra of these substances in CDCl_3 . The electron delocalization in the chelate ring of (II) is, in turn, shown by the slight shortening of the C–N bond lengths compared with the corresponding bonds in the unbound ligand.

Experimental

The ligand synthesis was formed according to a previously published procedure (Douglass, 1937).

For the synthesis of (II), a dichloromethane solution (25 ml) of (I) (1.278 mmol) was added to an aqueous solution (25 ml) of K_2PdCl_4 (0.639 mmol). The solutions were shaken together in a separating funnel after which an aqueous solution (10 ml) of sodium acetate (2.558 mmol) was added, followed by gentle shaking. Extraction and drying of the organic layer was followed by the addition of ethanol. Slow evaporation from this mixture yielded crystals suitable for analysis. ^1H NMR chemical shifts are quoted relative to the residual CHCl_3 solvent resonance at 7.26 p.p.m., and ^{13}C NMR chemical shifts are quoted relative to the CDCl_3 triplet at 77.0 p.p.m. (centre peak). Elemental analyses were performed on a Heraeus Universal Combustion Analyser, model CHN-Micro.

For *N*-benzoyl-*N,N'*-dibutylselenourea, (I): yield 57.5%, m.p. 392.5–394.0 K. Analysis found: C 56.6, H 7.1, N 8.2%; $\text{C}_{16}\text{H}_{24}\text{N}_2\text{OSe}$ requires: C 56.6, H 7.1, N 8.3%. ^1H NMR (400 MHz, CDCl_3): δ 0.90 (*t*, 3H, $^3J_{\text{HH}} = 7.4$ Hz, H12/H16), 0.99 (*t*, 3H, $^3J_{\text{HH}} = 7.4$ Hz, H12/H16), 1.28 (*m*, 2H, $^3J_{\text{HH}} = 7.5$ Hz, H11/H15), 1.45 (*m*, 2H, $^3J_{\text{HH}} = 7.5$ Hz, H11/H15), 1.67 (*q*, 2H, $^3J_{\text{HH}} = 7.4$ Hz, H10/H14), 1.83 (*q*, 2H, $^3J_{\text{HH}} = 7.4$ Hz, H10/H14), 3.55 (*t*, 2H, $^3J_{\text{HH}} = 7.4$ Hz, H9/H13), 4.08 (*t*, 2H, $^3J_{\text{HH}} = 7.6$ Hz, H9/H13), 7.46 (*t*, 2H, H3, H5), 7.57 (*t*, 1H, H4), 7.83 (*d*, 2H, H2, H6), 8.54 (*br s*, 1H, N–H); ^{13}C NMR (100 MHz, CDCl_3): δ 13.6 (C12/C16), 13.8 (C12/C16), 19.9 (C15/C11), 20.0 (C15/C11), 28.7 (C14/C10), 29.7 (C14/C10), 53.7 (C13/C9), 56.4 (C13/C9), 127.8 (C3, C5), 128.8 (C2, C6), 132.5 (C4), 133.0 (C1), 162.1 (C7), 180.9 (C8); $^1J(^{77}\text{Se}-^{13}\text{C}) = 222.1$ Hz.

For *cis*-bis(*N*-benzoyl-*N,N'*-dibutylselenourea)opalladium(II), (II): yield 94.2%, m.p. 423.5–424.4 K. Analysis found: C 49.1, H 5.8, N 7.1%; $\text{C}_{32}\text{H}_{46}\text{N}_4\text{O}_2\text{PdSe}_2$ requires: C 49.1, H 5.9, N 7.2%. ^1H NMR (400 MHz, CDCl_3): δ 0.93 (*t*, 6H, $^3J_{\text{HH}} = 7.4$ Hz, H12A/B or H16A/B), 0.98 (*t*, 6H, $^3J_{\text{HH}} = 7.4$ Hz, H12A/B or H16A/B), 1.38 (*m*, 8H, $^3J_{\text{HH}} = 7.6$ Hz, H11A/B, H15A/B), 1.67 (*q*, 4H, $^3J_{\text{HH}} = 7.7$ Hz, H10A/B or H14A/B), 1.76 (*q*, 4H, $^3J_{\text{HH}} = 7.8$ Hz, H10A/B or H14A/B), 3.78 (*m*, 8H, $^3J_{\text{HH}} = 7.8$ Hz, H9A/B, H13A/B), 7.40 (*t*, 4H, H3A/B, H5A/B), 7.49 (*t*, 2H, H4A/B), 8.23 (*d*, 4H, H2A/B, H6A/B); ^{13}C NMR (101 MHz, CDCl_3 , δ): 13.8, 13.9 (C12A/B, C16A/B), 20.2, 20.3 (C11A/B, C15A/B), 29.9, 30.0 (C10A/B, C14A/B), 51.8, 54.7 (C9A/B, C13A/B), 127.9 (C3A/B, C5A/B), 129.7 (C2A/B, C6A/B), 131.4 (C4A/B), 137.2 (C1A/B), 166.7 (C8A/B), 170.8 (C7A/B). $^1J(^{77}\text{Se}-^{13}\text{C}) = 176.5$ Hz.

Compound (I)

Crystal data

$\text{C}_{16}\text{H}_{24}\text{N}_2\text{OSe}$	$V = 1639.4$ (5) \AA^3
$M_r = 339.33$	$Z = 4$
Monoclinic, $P2_1/c$	Mo $K\alpha$ radiation
$a = 10.3880$ (17) \AA	$\mu = 2.29$ mm^{-1}
$b = 15.715$ (3) \AA	$T = 273$ (2) K
$c = 10.1518$ (16) \AA	$0.20 \times 0.16 \times 0.14$ mm
$\beta = 98.423$ (3) $^\circ$	

Data collection

Bruker APEX CCD area-detector diffractometer	10228 measured reflections
Absorption correction: multi-scan (SADABS; Bruker, 2002)	3775 independent reflections
$T_{\text{min}} = 0.651$, $T_{\text{max}} = 0.732$	3031 reflections with $I > 2\sigma(I)$
	$R_{\text{int}} = 0.038$

Refinement

$R[F^2 > 2\sigma(F^2)] = 0.037$	H atoms treated by a mixture of independent and constrained refinement
$wR(F^2) = 0.085$	
$S = 1.02$	$\Delta\rho_{\text{max}} = 0.55$ e \AA^{-3}
3775 reflections	$\Delta\rho_{\text{min}} = -0.33$ e \AA^{-3}
187 parameters	

Table 1

Selected bond lengths (\AA) for (I).

Se1–C8	1.848 (2)	N1–C8	1.399 (3)
O1–C7	1.212 (3)	N2–C8	1.314 (3)
C7–N1	1.397 (3)	N2–C13	1.470 (3)
C7–Cl	1.492 (3)	N2–C9	1.480 (3)

Compound (II)

Crystal data

$[\text{Pd}(\text{C}_{16}\text{H}_{24}\text{N}_2\text{OSe})_2]$	$\gamma = 81.867$ (1) $^\circ$
$M_r = 783.05$	$V = 1632.0$ (2) \AA^3
Triclinic, $P\bar{1}$	$Z = 2$
$a = 9.9302$ (8) \AA	Mo $K\alpha$ radiation
$b = 10.9315$ (9) \AA	$\mu = 2.83$ mm^{-1}
$c = 15.4119$ (13) \AA	$T = 173$ (2) K
$\alpha = 80.216$ (1) $^\circ$	$0.09 \times 0.08 \times 0.08$ mm
$\beta = 88.291$ (1) $^\circ$	

Data collection

Bruker APEX CCD area-detector diffractometer	18809 measured reflections
Absorption correction: multi-scan (SADABS; Bruker, 2002)	7329 independent reflections
$T_{\text{min}} = 0.785$, $T_{\text{max}} = 0.797$	6802 reflections with $I > 2\sigma(I)$
	$R_{\text{int}} = 0.017$

Refinement

$R[F^2 > 2\sigma(F^2)] = 0.022$	374 parameters
$wR(F^2) = 0.056$	H-atom parameters constrained
$S = 1.05$	$\Delta\rho_{\text{max}} = 0.55$ e \AA^{-3}
7329 reflections	$\Delta\rho_{\text{min}} = -0.38$ e \AA^{-3}

Table 2

Hydrogen-bond geometry (\AA , $^\circ$) for (I).

$D-H\cdots A$	$D-H$	$H\cdots A$	$D\cdots A$	$D-H\cdots A$
N1–H1 \cdots Se1 ⁱ	0.83 (3)	2.76 (3)	3.539 (2)	159 (2)
C6–H6 \cdots O1 ⁱⁱ	0.93	2.48	3.407 (3)	174

Symmetry codes: (i) $-x, -y+1, -z+1$; (ii) $-x, -y+1, -z$.

Table 3

Selected bond lengths (\AA) for (II).

Pd1–O1A	2.0395 (12)	N2A–C13A	1.469 (2)
Pd1–O1B	2.0439 (12)	N2A–C9A	1.478 (2)
Pd1–Se1B	2.3411 (3)	C9B–N2B	1.481 (2)
Pd1–Se1A	2.3489 (3)	N1B–C8B	1.334 (2)
Se1A–C8A	1.9076 (17)	N1B–C7B	1.335 (2)
Se1B–C8B	1.9006 (16)	N2B–C8B	1.338 (2)
O1B–C7B	1.260 (2)	N2B–C13B	1.473 (2)
O1A–C7A	1.266 (2)	C8A–N1A	1.333 (2)
N2A–C8A	1.341 (2)	C7A–N1A	1.329 (2)

metal-organic compounds

H atoms involved in hydrogen bonding were located in difference electron-density maps and all other H atoms were placed in geometrically calculated positions, with C–H = 0.99 (for CH₂), 0.98 (for CH₃) or 0.95 Å (for aromatic H), and refined using a riding model, with $U_{30}(\text{H}) = 1.2U_{\text{eq}}(\text{C})$ for CH₂ and aromatic, or $1.5U_{\text{eq}}(\text{C})$ for CH₃ H atoms.

For both compounds, data collection: *SMART* (Bruker, 2001); cell refinement: *SAINT* (Bruker, 2002); data reduction: *SAINT*; program(s) used to solve structure: *SHELXS97* (Sheldrick, 1997); program(s) used to refine structure: *SHELXL97* (Sheldrick, 1997); molecular graphics: *X-SEED* (Barbour, 2001); software used to prepare material for publication: *X-SEED*.

Financial support from the University of Stellenbosch, the NRF (GUN 2046827), THRIP (project No. 2921) and Angloplatinum Ltd is gratefully acknowledged. JB acknowledges a Harry Crossley Bursary.

Supplementary data for this paper are available from the IUCr electronic archives (Reference: SF3058). Services for accessing these data are described at the back of the journal.

References

- Allen, F. H., Kennard, O., Watson, D. G., Brammer, L., Orpen, A. G. & Taylor, R. (1987). *J. Chem. Soc. Perkin. Trans. 2*, pp. S1–19.
- Barbour, L. J. (2001). *J. Supramol. Chem.* **1**, 189–191.
- Bensch, W. & Schuster, M. (1994). *Z. Anorg. Allg. Chem.* **620**, 177–182.
- Beyer, L., Hoyer, E., Liebscher, J. & Hartmann, H. (1981). *Z. Chem.* **21**, 81–91.
- Bruce, J. C. & Koch, K. R. (2007). Unpublished results.
- Bruce, J. C., Koch, K. R. & Revaprasadu, N. (2007). *New J. Chem.* **31**, 1647–1653.
- Bruker (2001). *SMART* (Version 5.625) and *SADABS* (Version 2.05). Bruker AXS Inc., Madison, Wisconsin, USA.
- Bruker (2002). *SAINT*. Version 6.36a. Bruker AXS Inc., Madison, Wisconsin, USA.
- Dietze, F., Lerchner, J., Schmidt, S., Beyer, L. & Koehler, R. (1991). *Z. Anorg. Allg. Chem.* **600**, 37–46.
- Dillen, J., Woldu, M. G. & Koch, K. R. (2006a). *Acta Cryst. E* **62**, o5228–o5229.
- Dillen, J., Woldu, M. G. & Koch, K. R. (2006b). *Acta Cryst. E* **62**, o4819–o4820.
- Douglass, I. B. (1937). *J. Am. Chem. Soc.* **59**, 740–742.
- Kampf, M., Richter, R., Griebel, J., Weller, A. & Kirmse, R. (2005). *Z. Anorg. Allg. Chem.* **631**, 698–708.
- Kampf, M., Richter, R., Hennig, L., Eidner, A., Baldamus, J. & Kirmse, R. (2004). *Z. Anorg. Allg. Chem.* **630**, 2677–2686.
- Koch, K. R., Sacht, C., Grimmacher, T. & Bourne, S. (1995). *S. Afr. J. Chem.* **48**, 71–77.
- Malik, M., O'Brien, P. & Revaprasadu, N. (2005). *Phosphorus Sulfur Silicon Relat. Elem.* **180**, 689–712.
- Nair, P. S., Radhakrishnan, T., Revaprasadu, N. & O'Brien, P. (2005). *Mater. Sci. Technol.* **21**, 237–242.
- Schuster, M. & Koenig, K. H. (1987). *Fresenius Z. Anal. Chem.* **327**, 102–104.
- Sheldrick, G. M. (1997). *SHELXS97* and *SHELXL97*. University of Göttingen, Germany.
- Steiner, T. (2002). *Angew. Chem. Int. Ed.* **41**, 48–76.

Addendum C

Bipodal 1,1'-acyl-3,3,3',3'-tetraalkyl-
bis(thiourea) ligands with flexible
C₃, C₄ and C₆ spacer groupsSusanne Stockmann,^a Jocelyn Bruce,^b Jorn Miller^b and
Klaus R. Koch^{b*}^aInstitut für Anorganische Chemie, Fakultät für Chemie und Mineralogie, Johannis-
sallee 29, 04103 Leipzig, Germany, and ^bDepartment of Chemistry and Polymer
Science, University of Stellenbosch, Private Bag XI, Matieland 7602, South Africa
Correspondence e-mail: krk@sun.ac.za

Received 8 January 2008

Accepted 24 January 2008

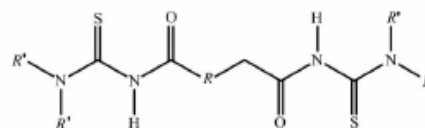
Online 23 February 2008

In the structures of 3,3,3',3'-tetraethyl-1,1'-(propane-1,3-diyldicarbonyl)bis(thiourea), C₁₅H₂₈N₄O₂S₂, (I), 3,3,3',3'-tetraethyl-1,1'-(butane-1,4-diyldicarbonyl)bis(thiourea), C₁₆H₃₀N₄O₂S₂, (II), and 3,3,3',3'-tetrabutyl-1,1'-(hexane-1,6-diyldicarbonyl)bis(thiourea), C₂₆H₅₀N₄O₂S₂, (III), compound (I) displays resonance-assisted hydrogen bonding, (II) exhibits an inversion centre, and both (II) and (III) are characterized by intermolecular hydrogen bonds between the carbonyl O atoms and thioamide H atoms, leading to chains of hydrogen-bonded molecules throughout the structures. The accurate structural data for these molecules is expected to assist in molecular modelling and other studies currently in progress.

Comment

N,N-Dialkyl-*N'*-aryl(aroyl)thioureas coordinate to a diverse array of transition metal ions, usually in an *S,O*-bidentate manner, although several examples of coordination through the S atom and an *S,N*-donor-atom set have been reported (Koch *et al.*, 2001). In view of the interesting practical applications of metal complexes of this class of ligands, a considerable number of both ligands and metal complexes have been studied, and several have been structurally characterized (Sacht *et al.*, 2000; Hernandez *et al.*, 2005). Potentially 'bipodal' derivatives of *N,N*-dialkyl-*N'*-aroylthioureas in which two potentially *S,O*-chelating acylthiourea motifs are linked through a 'spacer' *R* (see scheme) were reported as early as 1965 (Goerdeler & Stadelbauer, 1965). More recently, work on bipodal derivatives based on *para*-substituted phenyl ring spacers [as in 3,3,3',3'-tetraethyl-1,1'-terephthaloylbis(thiourea) or 3,3,3',3'-tetra-*n*-butyl-1,1'-terephthaloylbis(thiourea)] has shown that, with *d*⁸ metal ions, such ligands form almost exclusively 3:3 metallamacrocycles of Ni^{II} (Köhler *et al.*, 1986), Pt^{II} (Koch *et al.*, 1999) and Pd^{II} (Koch *et al.*, 2001). In this context, we showed that the corresponding *meta*-substituted

phenyl ligands [3,3,3',3'-tetraethyl-1,1'-isophthaloylbis(thiourea)] undergo 'self-assembly' with *d*⁸ metal ions to form exclusively the corresponding 2:2 metallamacrocycles, largely as a result of the strong tendency of these ligands to form *cis*-coordinated metal complexes (Koch *et al.*, 1999). The pyridine adducts of 2:2 and 3:3 nickel(II) complexes of 3,3,3',3'-tetraethyl-1,1'-terephthaloylbis(thiourea) show some interesting host-guest chemistry in the solid state (Hallale *et al.*, 2005). Recently, the corresponding diiodidoplatinum(IV) adducts were prepared and characterized after electrochemically induced oxidative addition of I₂ to the corresponding 2:2 and 3:3 Pt^{II} complexes of 3,3,3',3'-tetraethyl-1,1'-isophthaloylbis(thiourea) and 3,3,3',3'-tetraethyl-1,1'-terephthaloylbis(thiourea) (Westra *et al.*, 2005). A similar bipodal ligand with a 2,6-substituted pyridine ring as spacer and its Ag^I coordination polymer has been described (Schröder *et al.*, 2000). In all these bipodal ligands the *spacer unit* was a planar 'rigid' phenyl or pyridyl ring.

(I) *R* = (CH₂)₂, *R'* = -CH₂CH₃(II) *R* = (CH₂)₃, *R'* = -CH₂CH₃(III) *R* = (CH₂)₅, *R'* = -CH₂CH₂CH₂CH₃

As part of our continuing interest in such bipodal ligands, we have prepared a series of *N,N*-dialkyl-*N'*-(acyl)thioureas with flexible C₃, C₄ and C₆ spacers and report here the crystal and molecular structures of 3,3,3',3'-tetraethyl-1,1'-glutaryl-bis(thiourea), (I), 3,3,3',3'-tetraethyl-1,1'-adipoylbis(thiourea), (II), and 3,3,3',3'-tetrabutyl-1,1'-suberoylbis(thiourea), (III). König *et al.* (1987) reported the synthesis of a variety of 3,3,3',3'-tetraalkyl-1,1'-alkanedioylbis(thioureas) and the Ni^{II}, Cu^{II}, Pd^{II} and Pt^{II} metal complexes of 3,3,3',3'-tetraethyl-1,1'-adipoylbis(thiourea), although no structural characterization was carried out.

In view of the nomenclature and atom-numbering schemes of compounds of this type reported in the literature historically being inconsistent, we here follow an atom-numbering scheme for molecules (I)–(III) to correspond to the bipodal molecules with rigid 'spacers' as reported by Westra *et al.* (2005), as this method offers the most clarity.

Compound (I) crystallizes in the *P2₁/n* space group and the molecule adopts a conformation such that the two acylthiourea motifs are at an approximate right angle to one another, owing to the flexible nature of the spacer group (Fig. 1). The donor O and S atoms in each acylthiourea unit assume opposing orientations indicated by the O–C(O)–N–C(O)–C(S) and S–C(S)–N–C(S)–C(O) torsion angles (Table 1). Table 1 shows that the N–C bond lengths are all shorter than the average C–N single bond length of 1.472 (5) Å (Allen *et al.*, 1987), but follow the expected order in which the thioamide N1–C12 bond length is relatively the

longest, followed by the amide N1—C11 bond; the second thioamide N2—C12 bond is the shortest. This trend is consistent with that generally observed for a variety of related simple *N,N*-dialkyl-*N*'-benzoylthioureas (Koch *et al.*, 1995; Dillen *et al.*, 2006).

In the crystal structure, molecules of (I) are linked by two intermolecular hydrogen bonds (Table 2) between the S atom of one molecule and the thioamide H atom of a neighbouring molecule (Fig. 2). The acylthiourea unit consists of a donor-acceptor pair connected by a 'resonant π system', evident from the shortening of the amide and thioamide C—N bonds. This leads to one molecule being hydrogen bonded to two others, as shown in Fig. 2, and this type of hydrogen-bond formation represents an example of π -bond co-operativity or resonance-assisted hydrogen bonding (Steiner, 2002). This, to the best of our knowledge, is the first time that hydrogen bonding of this type has been reported for these compounds. Similar observations have been made for the closely related *N,N*-diethyl-*N*'-benzoylselenourea (Bruce *et al.*, 2007).

The relative orientations of the acylthiourea units are such that, if a plane is defined by C11/C1—C3/C31 along the length of the spacer group, the O atom of one acylthiourea unit is above the plane and the corresponding S atom below, while in the second acylthiourea unit, the O atom is below the plane while the corresponding S atom lies above the plane.

Compound (II) crystallizes in the $P\bar{1}$ space group, exhibiting an inversion centre located midway between atoms C2 and C2', resulting in only half the molecule appearing in the asymmetric unit. The remainder of the molecule can be

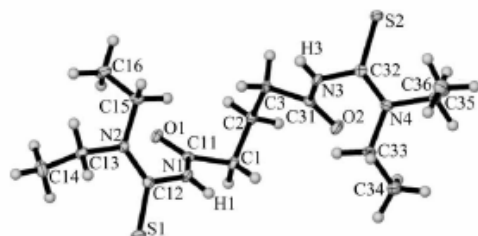


Figure 1
The molecular structure of (I), with the atomic numbering shown. Displacement ellipsoids are drawn at the 50% probability level.

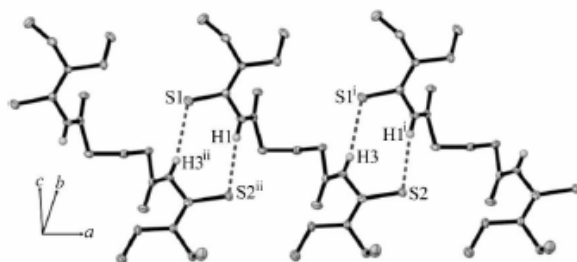


Figure 2
A view of the structure of (I), showing the intermolecular N—H...S hydrogen bonds (dashed lines). Displacement ellipsoids are drawn at the 50% probability level. H atoms, except H1 and H3, have been omitted for clarity. [Symmetry codes: (i) $x + 1, y, z$; (ii) $x - 1, y, z$.]

generated with the symmetry operator $(-x, -y, -z + 1)$ and the whole molecule is shown in Fig. 3. The C—N bond lengths of (II) (Table 3) are similar to those in (I) in that the C—N bond lengths in the acylthiourea unit are all shorter than the average C—N single bond length of 1.472 (5) Å and are consistent with the trend described previously for (I). It is noteworthy that the molecule of (II) with the C₄ flexible spacer assumes an approximately linear conformation in the solid state, in contrast to that of (I) in which the molecule with the C₃ spacer is significantly 'bent'. Moreover, the relative *anti* orientations of the S and O donor atoms in (I) are not observed in (II), for which the O1—C11—N1—C12 [7.1 (4)°] and S1—C12—N1—C11 [45.5 (3)°] torsion angles are substantially different from the corresponding angles [12.6 (4) and 125.7 (2)°] in (I). This is most likely due to the involvement of the O-atom donor in the intramolecular hydrogen bond exhibited by (II) (see below).

The intermolecular hydrogen-bonding pattern observed for (II) is quite different from that seen in (I). In (II) the thioamide H atoms (H1 and H1') hydrogen bond to the carbonyl O atoms (O1 and O1') of a neighbouring molecule (Table 4), as shown in Fig. 4, thus precluding the formation of resonance-

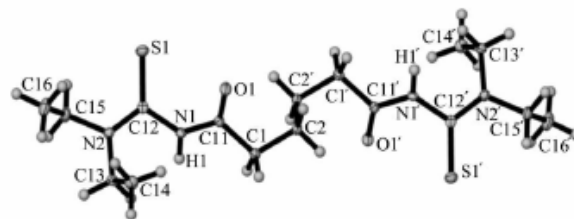


Figure 3
The molecular structure of (II), with the atomic numbering shown. Displacement ellipsoids are drawn at the 50% probability level. [Symmetry code: (i) $-x, -y, -z + 1$.]

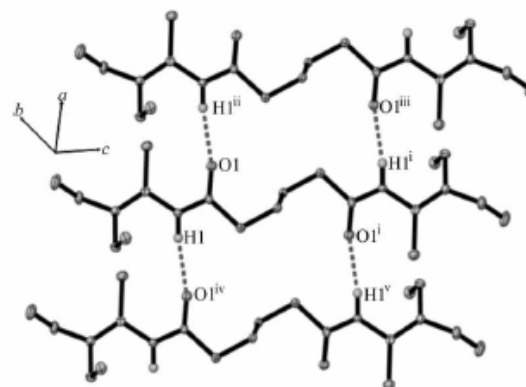


Figure 4
The structure of (II), showing intermolecular N—H...O hydrogen bonds (dashed lines). Displacement ellipsoids are drawn at the 50% probability level. H atoms, except H1, have been omitted for clarity. [Symmetry codes: (i) $-x, -y, -z + 1$; (ii) $x + 1, y, z$; (iii) $-x + 1, -y, -z + 1$; (iv) $x - 1, y, z$; (v) $-x - 1, -y, 1 - z$.]

assisted hydrogen bonding as observed in the crystal structure of (I).

Despite crystallizing in the same space group as (II), the molecule of (III) with the C_6 spacer does not exhibit an inversion centre, the whole molecule being contained in the asymmetric unit (Fig. 5). The overall conformation that molecule (III) adopts differs from that of both (I) and (II); while the C_6 spacer of the molecule remains reasonably linear, the molecule assumes an overall U shape with the two butyl groups of the terminal thioamide units extending above and below this conformation (Fig. 5). As for the previous compounds, the relative orientations of the S and O donor atoms of the acylthiourea groups on either side of the C_6 spacer differ in that the carbonyl O atom of one acylthiourea residue is situated above the C11/C1–C6/C61 plane, while the other carbonyl O atom is below the plane. In each case, the S atom of the thiocarbonyl group has an *anti* orientation relative

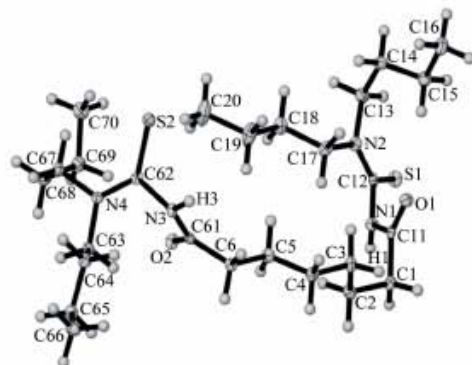


Figure 5
The molecular structure of (III), with the atomic numbering shown. Displacement ellipsoids are drawn at the 50% probability level.

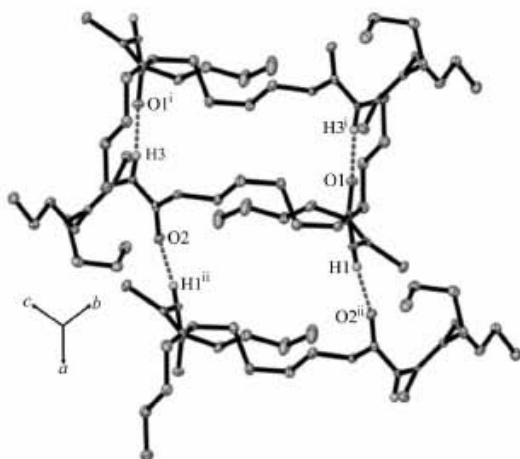


Figure 6
The structure of (III), showing intermolecular N–H...O hydrogen bonds (dashed lines). Displacement ellipsoids are drawn at the 50% probability level. H atoms, except H1, have been omitted for clarity. [Symmetry codes: (i) $-x + 1, -y + 1, -z$; (ii) $-x + 2, -y + 1, -z$.]

to that of the carbonyl O atom, as indicated by the torsion angles in Table 5. This is reminiscent of (I) and different from (II), which interestingly exhibits similar hydrogen bonding.

Similar to (I), the C–N bond lengths in each chelate ring are not identical to the corresponding C–N bonds in the second ring; however, they are all shorter than the average single C–N bond length of 1.472 (5) Å, and the trend described for (I) is maintained here. Intermolecular hydrogen bonding (Table 6) between the carbonyl O atom of one molecule and thioamide H atom of a neighbouring molecule is evident, and the molecular arrangement in this compound is similar to that in (II), in that each molecule has two hydrogen bonds to each neighbour on either side of the central molecule, as shown in Fig. 6.

Experimental

All reactions were carried out under an inert N_2 atmosphere. All reagents and solvents were commercially available and used without further purification, except for the acetone which was distilled prior to use. One molar equivalent of the appropriate acid dichloride in acetone was added dropwise to two molar equivalents of KSCN in acetone. The mixture was heated under reflux for 45 min, after which it was cooled to room temperature and the dropwise addition of two molar equivalents of the appropriate secondary amine in acetone followed. The mixture was heated under reflux for a further 45 min and cooled to room temperature, with subsequent addition of water (*ca* 15–25% *v/v*) to dissolve the KCl which formed as a by-product. Slow evaporation of the acetone afforded a crystalline product and recrystallization from water/acetone solutions (variable ratio of 5–20% *v/v*) yielded crystals suitable for analysis. Analysis for (I) (yield 53%, m.p. 392.6–393.4 K). 1H NMR (400 MHz, $CDCl_3$): δ 9.58 (*s*, 2H, –NH–), 3.96 [*br s*, 4H, –N(CH₂CH₃)₂], 3.61 [*br s*, 4H, –N(CH₂CH₃)₂], 2.39 (*t*, 4H, –CH₂–CH₂–CH₂–), 2.19 (*m*, 2H, –CH₂–CH₂–CH₂–), 1.30 [*m*, 12H, –N(CH₂CH₃)₂]. ^{13}C NMR (100 MHz, $CDCl_3$): δ 179.4 (CS), 170.6 (CO), 47.6 [–N(CH₂CH₃)₂], 47.3 [–N(CH₂CH₃)₂], 34.7 [CH₂–CH₂–CH₂], 24.0 (–CH₂–CH₂–CH₂–), 13.4 [–N(CH₂CH₃)₂], 11.2 [–N(CH₂CH₃)₂]. Analysis for (II) (yield 58%, m.p. 394.7–395.5 K). 1H NMR (400 MHz, $CDCl_3$): δ 7.96 (*s*, 2H, –NH–), 3.94 [*br s*, 4H, –N(CH₂CH₃)₂], 3.53 [*br s*, 4H, –N(CH₂CH₃)₂], 2.40 [*t*, 4H,

Table 1
Selected geometric parameters (Å, °) for (I).

S1–C12	1.687 (3)	O2–C31	1.208 (3)
O1–C11	1.215 (3)	N2–C12	1.319 (3)
N1–C11	1.373 (3)	N3–C31	1.390 (3)
N1–C12	1.411 (3)	N3–C32	1.406 (3)
S2–C32	1.682 (3)	N4–C32	1.326 (3)
C12–N1–C11–O1	12.6 (4)	C32–N3–C31–O2	26.3 (4)
C11–N1–C12–S1	125.7 (2)	C31–N3–C32–S2	113.9 (2)

Table 2
Hydrogen-bond geometry (Å, °) for (I).

<i>D</i> –H... <i>A</i>	<i>D</i> –H	H... <i>A</i>	<i>D</i> ... <i>A</i>	<i>D</i> –H... <i>A</i>
N1–H1...S2 ⁽ⁱ⁾	0.82 (3)	2.58 (3)	3.393 (2)	173 (3)
N3–H3...S1 ⁽ⁱ⁾	0.77 (3)	2.60 (3)	3.344 (2)	165 (2)

Symmetry codes: (i) $x + 1, y, z$; (ii) $x - 1, y, z$.

—CH₂—(CH₂)₂—CH₂—, 1.74 [*q*, 4H, —CH₂—(CH₂)₂—CH₂—], 1.29 [*s*, 12H, —N(CH₂CH₃)₂]. ¹³C NMR (100 MHz, CDCl₃): δ 178.9 (CS), 169.8 (CO), 47.6 [N(CH₂CH₃)₂], 36.3 [CH₂—(CH₂)₂—CH₂], 24.2 [CH₂—(CH₂)₂—CH₂], 13.2 [N(CH₂CH₃)₂], 11.6 [N(CH₂CH₃)₂]. Analysis for (II) (yield 76.1%, m.p. 353.2–355.2 K. ¹H NMR (400 MHz, CDCl₃): δ 8.82 (*s*, 2H, —NH—), 3.88 [*br t*, 4H, —N(CH₂CH₂CH₂CH₃)₂], 3.44 [*br t*, 4H, —N(CH₂CH₂CH₂CH₃)₂], 2.34 [*t*, 4H, —CH₂—(CH₂)₄—CH₂—], 1.67 [*m*, 12H, —CH₂—(CH₂)₄—CH₂— and —N(CH₂CH₂CH₂CH₃)₂], 1.36 [*m*, 12H, —CH₂—(CH₂)₄—CH₂— and —N(CH₂CH₂CH₂CH₃)₂], 0.92 [*m*, 12H, —N(CH₂CH₂CH₂CH₃)₂]. ¹³C NMR (100 MHz, CDCl₃): δ 179.5 (CS), 169.9 (CO), 53.1 [—N(CH₂CH₂CH₂CH₃)₂], 52.9 [—N(CH₂CH₂CH₂CH₃)₂], 36.1 [—CH₂—(CH₂)₄—CH₂—], 30.0 [—N(CH₂CH₂CH₂CH₃)₂], 28.4 [—N(CH₂CH₂—CH₂CH₃)₂], 28.0 [—CH₂—(CH₂)₄—CH₂—], 24.8 [—CH₂—(CH₂)₄—CH₂—], 20.0 [—N(CH₂CH₂CH₂CH₃)₂], 13.8 [—N(CH₂CH₂CH₂CH₃)₂], 13.7 [—N(CH₂CH₂CH₂CH₃)₂].

Compound (I)

Crystal data

C₁₃H₂₈N₄O₂S₂ $V = 1875.9$ (8) Å³
 $M_r = 360.53$ $Z = 4$
 Monoclinic, $P2_1/n$ Mo $K\alpha$ radiation
 $a = 7.1475$ (18) Å $\mu = 0.30$ mm⁻¹
 $b = 27.999$ (7) Å $T = 100$ (2) K
 $c = 9.387$ (2) Å $0.22 \times 0.21 \times 0.18$ mm
 $\beta = 93.026$ (5)°

Data collection

Bruker APEX-I CCD area-detector diffractometer 10628 measured reflections
 Absorption correction: multi-scan 3685 independent reflections
 (SADABS; Bruker, 2002) 2845 reflections with $I > 2\sigma(I)$
 $T_{\min} = 0.937$, $T_{\max} = 0.948$ $R_{\text{int}} = 0.050$

Refinement

$R[F^2 > 2\sigma(F^2)] = 0.052$ H atoms treated by a mixture of independent and constrained refinement
 $wR(F^2) = 0.129$ $S = 1.05$ $\Delta\rho_{\text{max}} = 0.66$ e Å⁻³
 3685 reflections $\Delta\rho_{\text{min}} = -0.47$ e Å⁻³
 220 parameters

Compound (II)

Crystal data

C₁₆H₃₀N₄O₂S₂ $\gamma = 81.894$ (3)°
 $M_r = 374.56$ $V = 477.09$ (16) Å³
 Triclinic, $P\bar{1}$ $Z = 1$
 $a = 4.8287$ (9) Å Mo $K\alpha$ radiation
 $b = 6.3977$ (12) Å $\mu = 0.30$ mm⁻¹
 $c = 15.661$ (3) Å $T = 100$ (2) K
 $\alpha = 85.532$ (3)° $0.47 \times 0.21 \times 0.05$ mm
 $\beta = 86.985$ (3)°

Data collection

Bruker APEX-I CCD area-detector diffractometer 4902 measured reflections
 Absorption correction: multi-scan 1847 independent reflections
 (SADABS; Bruker, 2002) 1611 reflections with $I > 2\sigma(I)$
 $T_{\min} = 0.874$, $T_{\max} = 0.985$ $R_{\text{int}} = 0.059$

Refinement

$R[F^2 > 2\sigma(F^2)] = 0.062$ 111 parameters
 $wR(F^2) = 0.156$ H-atom parameters constrained
 $S = 1.16$ $\Delta\rho_{\text{max}} = 0.90$ e Å⁻³
 1847 reflections $\Delta\rho_{\text{min}} = -0.30$ e Å⁻³

Table 3

Selected geometric parameters (Å, °) for (II).

S1—C12	1.666 (3)	N1—C12	1.421 (3)
O1—C11	1.223 (3)	N2—C12	1.336 (4)
N1—C11	1.353 (3)		
C12—N1—C11—O1	7.1 (4)	C11—N1—C12—S1	45.5 (3)

Table 4

Hydrogen-bond geometry (Å, °) for (II).

<i>D</i> —H... <i>A</i>	<i>D</i> —H	H... <i>A</i>	<i>D</i> ... <i>A</i>	<i>D</i> —H... <i>A</i>
N1—H1...O1 ^{iv}	0.88	2.05	2.921 (3)	170.5

Symmetry code: (iv) $x - 1, y, z$.

Table 5

Selected geometric parameters (Å, °) for (III).

S1—C12	1.673 (2)	O2—C61	1.229 (3)
O1—C11	1.223 (3)	N2—C12	1.330 (3)
N1—C11	1.383 (3)	N3—C61	1.363 (3)
N1—C12	1.408 (3)	N3—C62	1.423 (3)
S2—C62	1.667 (2)	N4—C62	1.331 (3)
C12—N1—C11—O1	9.0 (4)	C62—N3—C61—O2	-10.6 (4)
C11—N1—C12—S1	122.3 (2)	C61—N3—C62—S2	-106.2 (2)

Table 6

Hydrogen-bond geometry (Å, °) for (III).

<i>D</i> —H... <i>A</i>	<i>D</i> —H	H... <i>A</i>	<i>D</i> ... <i>A</i>	<i>D</i> —H... <i>A</i>
N3—H3...O1 ⁱ	0.85 (2)	2.09 (2)	2.902 (3)	160 (2)
N1—H1...O2 ⁱⁱ	0.82 (2)	2.01 (2)	2.828 (3)	172 (2)

Symmetry codes: (i) $-x + 1, -y + 1, -z$; (ii) $-x + 2, -y + 1, -z$.

Compound (III)

Crystal data

C₂₆H₅₀N₄O₂S₂ $\gamma = 92.111$ (3)°
 $M_r = 514.82$ $V = 1473.7$ (4) Å³
 Triclinic, $P\bar{1}$ $Z = 2$
 $a = 9.3206$ (15) Å Mo $K\alpha$ radiation
 $b = 10.6717$ (17) Å $\mu = 0.21$ mm⁻¹
 $c = 15.537$ (2) Å $T = 100$ (2) K
 $\alpha = 105.164$ (3)° $0.41 \times 0.37 \times 0.05$ mm
 $\beta = 97.767$ (3)°

Data collection

Bruker APEX-I CCD area-detector diffractometer 10961 measured reflections
 Absorption correction: multi-scan 5709 independent reflections
 (SADABS; Bruker, 2002) 3751 reflections with $I > 2\sigma(I)$
 $T_{\min} = 0.961$, $T_{\max} = 0.990$ $R_{\text{int}} = 0.059$

Refinement

$R[F^2 > 2\sigma(F^2)] = 0.053$ H atoms treated by a mixture of independent and constrained refinement
 $wR(F^2) = 0.085$ $S = 0.87$ $\Delta\rho_{\text{max}} = 0.36$ e Å⁻³
 5709 reflections $\Delta\rho_{\text{min}} = -0.28$ e Å⁻³
 319 parameters

H atoms involved in hydrogen bonding were located from a difference electron-density map and all other H atoms were placed in geometrically calculated positions. H atoms bonded to N atoms in compounds (I) and (III) were refined freely (refined distances are given in Tables 2 and 6). All other H atoms were treated as riding [C–H = 0.99 (for –CH₂) or 0.98 Å (for –CH₃), N–H = 0.88 Å, and $U_{\text{iso}}(\text{H}) = 1.2U_{\text{eq}}(\text{C},\text{N})$ for –CH₂ and amine or $1.5U_{\text{eq}}(\text{C})$ for –CH₃ H atoms].

For all compounds, data collection: *SMART* (Bruker, 2002); cell refinement: *SAINT* (Bruker, 2002); data reduction: *SAINT*; program(s) used to solve structure: *SHELXS97* (Sheldrick, 2008); program(s) used to refine structure: *SHELXL97* (Sheldrick, 2008); molecular graphics: *X-SEED* (Barbour, 2001); software used to prepare material for publication: *X-SEED*.

Financial support from the University of Stellenbosch, the NRF (grant No. GUN 2046827), THRIP (project No. 2921) and Angloplatinum Ltd is gratefully acknowledged. JB acknowledges a Harry Crossley bursary.

Supplementary data for this paper are available from the IUCr electronic archives (Reference: TR3036). Services for accessing these data are described at the back of the journal.

References

- Allen, F. H., Kennard, O., Watson, D. G., Brammer, L., Orpen, A. G. & Taylor, R. (1987). *J. Chem. Soc. Perkin Trans 2*, pp. S1–19.
- Barbour, L. I. (2001). *J. Supramol. Chem.* **1**, 189–191.
- Bruce, I. C., Revaprasadu, N. & Koch, K. R. (2007). *New J. Chem.* **31**, 1647–1653.
- Bruker (2002). *SMART* (Version 5.628), *SAINT* (Version 6.36a) and *SADABS* (Version 2.05). Bruker AXS Inc., Madison, Wisconsin, USA.
- Dillen, J., Woldu, M. G. & Koch, K. R. (2006). *Acta Cryst E* **62**, o4819–o4820.
- Goerdeler, J. & Stadelbauer, K. (1965). *Chem. Ber.* **98**, 1556–1561.
- Hallale, O., Bourne, S. A. & Koch, K. R. (2005). *CrystEngComm*, **7**, 161–166.
- Hernandez, W., Spodine, E., Beyer, L., Schröder, U., Richter, R., Ferreira, J. & Pavani, M. (2005). *Bioinorg. Chem. Appl.* **3**, 299–316.
- Koch, K. R., Bourne, S. A., Coetzee, A. & Müller, J. (1999). *J. Chem. Soc. Dalton Trans.* pp. 3157–3161.
- Koch, K. R., Hallale, O., Bourne, S. A., Müller, J. & Baesa, J. (2001). *J. Mol. Struct.* **561**, 185–196.
- Koch, K. R., Sacht, C., Grimmbacher, T. & Bourne, S. (1995). *S. Afr. J. Chem.* **48**, 71–77.
- Köhler, R., Kirmse, R., Richter, R., Sieler, J., Hoyer, E. & Beyer, L. (1986). *Z. Anorg. Allg. Chem.* **537**, 133–144.
- König, K. H., Kuge, M., Kaul, L. & Pletsch, H. I. (1987). *Chem. Ber.* **120**, 1251–1253.
- Sacht, C., Datt, M. S., Otto, S. & Roodt, A. (2000). *J. Chem. Soc. Dalton Trans.* pp. 727–733.
- Schröder, U., Beyer, L. & Sieler, J. (2000). *Inorg. Chem. Commun.* **3**, 630–633.
- Sheldrick, G. M. (2008). *Acta Cryst. A* **64**, 112–122.
- Steiner, T. (2002). *Angew. Chem. Int. Ed.* **41**, 48–76.
- Westra, A. N., Bourne, S. A. & Koch, K. R. (2005). *Dalton Trans.* pp. 2916–2924.

Addendum D

Titanoxycarbene complexes of Ti(IV) with O- and N-donor ligands†

Stefan D. Nogai, Oliver Schuster, Jocelyn Bruce and Helgard G. Raubenheimer*

Received (in Durham, UK) 1st October 2007, Accepted 11th December 2007

First published as an Advance Article on the web 8th January 2008

DOI: 10.1039/b715075j

Heterobimetallic complexes of the general formula $[(OC)_3M=C(Me)OTi(OiPr)_2(\mu-OiPr)]_2$ with $M = Cr$ (1), W (2) were synthesized by reacting $(OC)_3M=C(Me)OLi$ ($M = Cr, W$) with $ClTi(OiPr)_3$. X-Ray crystallography revealed dimeric molecular structures based on four-membered Ti_2O_2 -rings for both compounds. Most intriguingly crystals of 1 virtually “shattered” upon cooling below -60 °C. Treatment of 1 and 2 with an excess of pyridine did not effect symmetric cleavage of the dimers, but afforded the unique rearrangement products $[(OC)_3M=C(Me)O_2Ti(OiPr)_2(C_5H_5N)_2]$ with $M = Cr$ (3) and W (4). The isomorphous structures, determined by means of X-ray diffraction, are only the second examples of an unrestrained titanium center coordinated by four OR and two N-donor ligands. Complexes 3 and 4 were also accessible from $Cl_2Ti(OiPr)_2(C_5H_5N)_2$ (5) and $(OC)_3M=C(Me)OLi$. Owing to the inherent dynamic behaviour of all complexes, low-temperature NMR studies were undertaken. The formation of nanoparticles upon thermolysis of complex 2 lends support to the notion that the presented (or related) compounds could be useful as single source precursors for nano-sized mixed metal oxides or oxo nitrides.

Introduction

Titanium dioxide has successfully been used as a support for heterogeneous catalysts for decades. Attempts to increase the surface area by scaling down the TiO_2 primary particle size has not only led to improved activity, but also to new materials acting surprisingly different from the bulk material, once the nanometre scale is approached. This has proven to be true for metals, metal oxides, metal sulfides, etc. Since the new and sometimes unique properties are a function of size in this domain, it is vital to develop routes to uniform particles.

While the preparation of nano-sized TiO_2 powder from titanium alkoxides $Ti(OR)_4$ has been studied carefully and a certain control over particle sizes established,¹ difficulties in the synthesis of monodisperse chromium and chromium oxide nanoparticles have been overcome only recently by the application of Fischer-type carbene complexes.²

In an attempt to combine both types of precursors, we synthesized complexes of the fashion $[(OC)_3M=C(Me)O-Ti(OiPr)_2(\mu-OiPr)]_2$ with $M = Cr$ (1), W (2), extending the pioneering work of Sabat *et al.* on related compounds ($M = Cr$).³ Controlled thermal decomposition of such compounds will presumably yield nano-structured mixed metal oxides $MTiO_x$ different from known metal doped titania species.⁴⁻⁶ Similar ligands coordinated to the metal fragment Cp_2ZrCl (in the presence of MAO) have recently shown a propensity to catalyze the copolymerization of ethylene-1-pentene mixtures and to oligomerise 1-pentene or 1-hexene.⁷ Related cyclopentadienyl compounds of titanium have been prepared by Fischer and co-workers in the early 1970s^{8,9} and many other examples in subsequent years.¹⁰ We have recently reported the utilisation of anionic Fischer-type carbene complexes as bidentate N⁻O ligands towards a number of metal centra.¹¹ Since the chemical reactivity of complexes such as 1 and 2 was not known, we investigated conversions with pyridine and discovered an unusual rearrangement that involves *inter alia* carbene oxide ligand transfer to give unprecedented bis-carbene complexes $[(OC)_3M=C(Me)O_2Ti(OiPr)_2(C_5H_5N)_2]$ with $M = Cr$ (3) and W (4). These or related compounds do possibly offer access to rarely studied mixed metal oxo nitrides by thermal activation.¹²⁻¹⁴

While preliminary investigations on the thermolysis of the title compounds confirmed the formation of nano-sized particles (see ESI†), we herein focus on the synthesis and characterisation of the precursors using X-ray crystallography and low-temperature NMR.

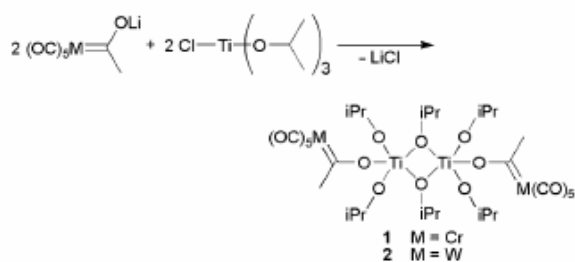
Results and discussion

Initial reactions

Treatment of $ClTi(OiPr)_3$ with equimolar amounts of $(OC)_3M=C(Me)OLi$ ($M = Cr, W$) in diethyl ether gave the heterobimetallic complexes $[(OC)_3M=C(Me)OTi(OiPr)_2(\mu-OiPr)]_2$ in good yields (eqn (1)).

Complexes 1 and 2 were isolated as moisture-sensitive, red crystals by cooling the concentrated reaction mixtures to -20 °C. The compounds dissolve readily in chlorinated solvents and ether. ¹H NMR studies revealed that the products are loosely bound in solution, giving rise to rapid monomer-dimer equilibration at room temperature, but form rather rigid dimers (on the NMR timescale) at low temperatures. Since the NMR-characteristics of both compounds are almost

Department of Chemistry and Polymer Science, University of Stellenbosch, 7602 Stellenbosch, South Africa. E-mail: hgr@sun.ac.za; Fax: +27 21 808 3849; Tel: +27 21 808 3850
† Electronic supplementary information (ESI) available: Crystallographic details for compounds 1–5 in CIF format and preliminary studies of the thermolysis of 2. See DOI: 10.1039/b715075j



identical, the temperature dependence will only be discussed explicitly for the chromium complex **1**. At room temperature the ^1H NMR spectrum of **1** shows two broad resonances for the isopropoxide groups at 4.89 ppm [$\text{OCH}(\text{CH}_3)_2$] and 1.37 ppm [$\text{OCH}(\text{CH}_3)_2$] as well as a singlet for the carbene-methyl protons at 2.79 ppm. At -80°C these signals split into two main sets of resonances with an intensity ratio of 2 : 1. The stronger signals at 4.93 and 1.30 ppm can be assigned to lateral and the weaker ones at 4.59 and 1.21 ppm to bridging isopropoxide groups. ^{13}C NMR spectra recorded at -80°C reveal the expected resonances of the target compounds. In Table 1, a comparison of carbene and carbonyl carbon shifts with those of related methoxycarbene complexes $(\text{OC})_2\text{M}=\text{C}(\text{Me})\text{OMe}$ ($\text{M} = \text{Cr}, \text{W}$)¹³ is given. The data show that substitution of the methyl group by the electron-deficient titanium affects the carbene signals only slightly. No change is observed with regard to the carbonyl ligands. It can be concluded that a significant amount of carbene character of the complexes is maintained in the product.

Molecular structure determinations

The formation of dimers was unambiguously confirmed by X-ray crystal structure determinations. From diethyl ether, compounds **1** and **2** both crystallize in the triclinic space group $P\bar{1}$ with $Z = 1$ formula unit (dimer) in the unit cell. The asymmetric unit contains one half of the dimers related to the other half *via* a center of inversion (Fig. 1 and Fig. 2).

As reported by Sabat *et al.* for similar complexes, $[\{(\text{OC})_2\text{Cr}=\text{C}(\text{R})\text{OTi}(\text{OiPr})_2\}(\mu\text{-OiPr})_2]$ ($\text{R} = n\text{-Bu}, 2\text{-furyl}, \text{CMeCH}_2$),³ the central four-membered Ti_2O_2 rings are skewed with the longer bridging bond $\text{Ti}-\text{O}21$ being diagnostic for the *trans* influence of the isopropoxide ligand (O41A). The coordination geometry around the titanium centers is best described as a distorted trigonal bipyramid with the carbene-oxygen atom, one oxygen atom of a terminal isopropoxide group and one bridging oxygen atom occupying the equatorial

Table 1 ^{13}C NMR chemical shift data (ppm) of the carbene and carbonyl resonances in $[\{(\text{OC})_2\text{M}=\text{C}(\text{Me})\text{OTi}(\text{OiPr})_2\}(\mu\text{-OiPr})_2]$ and $(\text{OC})_2\text{M}=\text{C}(\text{Me})\text{OMe}$ ¹⁵

Complex	$\text{C}_{\text{carbene}}$	<i>trans</i> CO	<i>cis</i> CO
1 ^a	350.7	224.0	216.8
$(\text{OC})_2\text{Cr}=\text{C}(\text{Me})\text{OMe}$ ^b	360.4	223.3	216.3
2 ^a	326.9	204.9	198.0
$(\text{OC})_2\text{W}=\text{C}(\text{Me})\text{OMe}$ ^b	333.0	203.4	197.2

Chemical shifts were measured in CD_2Cl_2 (^a) and CDCl_3 (^b) relative to the solvent.

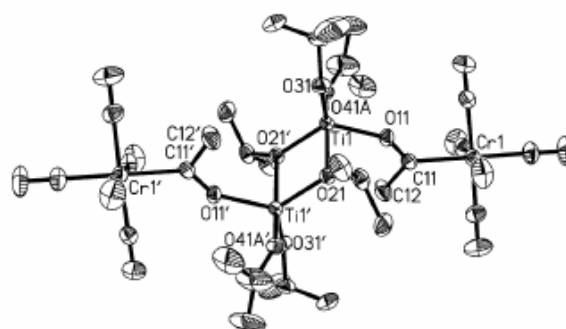


Fig. 1 Molecular structure of **1** (ORTEP, 30% ellipsoids, H atoms omitted). The isopropoxide groups at O31 and O41A are each disordered over two sites. This has been omitted in the drawing for clarity. Selected bond lengths [Å] and angles [°], ' = $(-x, -y, 2-z)$: Cr1–C11 2.043(2), C11–C12 1.508(3), C11–O11 1.272(2), O11–Ti1 1.962(2), Ti1–O21 2.099(2), Ti1–O21' 1.923(2), Ti1–O31 1.767(2), Ti1–O41A 1.757(5); Cr1–C11–O11 123.1(2), C11–O11–Ti1 139.6(2), O11–Ti1–O21 83.82(5), O11–Ti1–O21' 131.86(6), O11–Ti1–O31 109.26(7), O11–Ti1–O41A 93.5(7), O21–Ti1–O31 91.72(6), O21–Ti1–O41A 166.7(7), O21'–Ti1–O31 113.20(6), O21'–Ti1–O41A 99.3(6), O31–Ti1–O41A 101.5(8), O21–Ti1–O21' 73.43(5), Ti1–O21–Ti1' 106.57(5).

positions (O11, O31 and O21' for **1** and **2**). The apical positions are therefore occupied by the oxygen atoms of one bridging and one terminal isopropoxide group (O21 and O41A for **1**; O41 and O21 for **2**). Careful examination of the bond lengths along Cr–C–O–Ti led Sabat *et al.* to the conclusion that these complexes exhibit distinct "acyl" character, while remaining significantly carbenoid (see ^{13}C NMR studies above). This is noteworthy because the two mesomeric forms are usually regarded as competitive in Fischer-type carbene complexes (Scheme 1). As a modification to this simple picture it was rationalised that the O-bound electron-deficient metal increases π -electron delocalization across the carbenoid unit.³ Since compounds **1** and **2** feature very similar structural characteristics (Table 2), this result transfers easily to our work

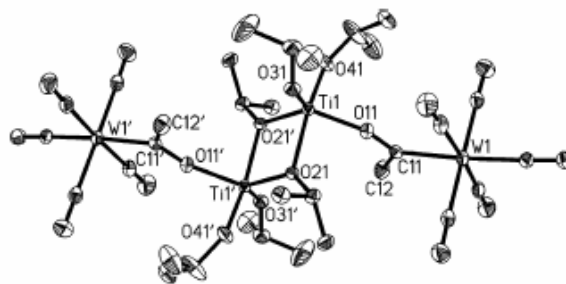


Fig. 2 Molecular structure of **2** (ORTEP, 50% ellipsoids, H atoms omitted). Selected bond lengths [Å] and angles [°], ' = $(-x, -y, -z)$: W1–C11 2.190(2), C11–C12 1.518(5), C11–O11 1.273(5), Ti1–O11 1.941(3), Ti1–O21 2.095(2), Ti1–O21' 1.917(2), Ti1–O31 1.770(3), Ti1–O41 1.760(3); W1–C11–O11 122.0(3), C11–O11–Ti1 150.2(3), O11–Ti1–O21 83.3(2), O11–Ti1–O21' 132.7(2), O11–Ti1–O31 109.7(2), O11–Ti1–O41 90.4(2), O21–Ti1–O31 91.2(2), O21–Ti1–O41 165.8(2), O21'–Ti1–O31 111.9(2), O21'–Ti1–O41 101.2(2), O31–Ti1–O41 102.9(2), O21–Ti1–O21' 74.4(2), Ti1–O21–Ti1' 105.6(2).



Scheme 1 Acyl and carbene resonance forms of Fischer-type carbene complexes (formal charges omitted in the first structure).

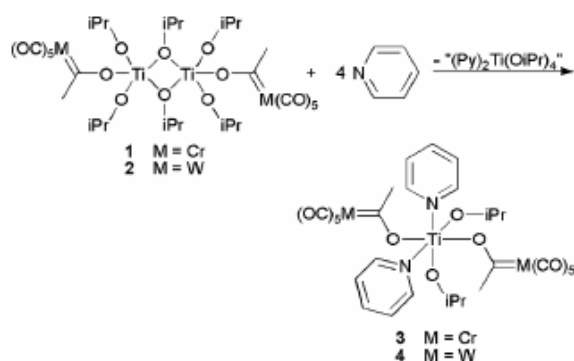
now extending the idea to Fischer carbene complexes derived from tungsten.

Despite their obvious similarities, complexes **1** and **2** are not isomorphous, most likely due to the difference in M–C_{carbene} bond lengths for Cr and W. The biggest difference is found in the torsion of the (OC)₅M moiety around that bond. This is illustrated by a superposition of the two structures (Fig. 3). The chromium compound's torsion angle C5–Cr1–C11–C12 is –32.7(2)° whereas the analogous atoms are almost co-planar in the tungsten compound [1.2(3)°].

This little twist gives rise to significantly different behavior of the crystals upon cooling. While the data collection of **2** was carried out under standard conditions at –173 °C, crystals of **1** had to be measured at –60 °C, because they virtually “exploded” once cooled below this temperature (Fig. 4). This rare behavior is most probably due to a phase transition by the crystals. Unfortunately all attempts to determine the unit cell after the transition or to crystallize **1** in the low temperature modification were unsuccessful.

Subsequent ring cleavage

Dimers of **1** and **2** were readily cleaved by addition of an excess of pyridine to ethereal solutions of these compounds. However, rearrangement to **3** and **4** (both approx. 50% yield) occurs while the expected product of a symmetric cleavage, (OC)₅M=C(Me)OTi(OiPr)₃(C₅H₅N)₂, was not observed (eqn (2)). The by-products in the mother liquor were not identified but it can be assumed that homoleptic Ti(OiPr)₄ and/or its pyridine adducts would be formed. In accordance with the oxophilic character of titanium, even the use of an excess of pyridine did not displace the carbenoxide moieties from the isolated products.

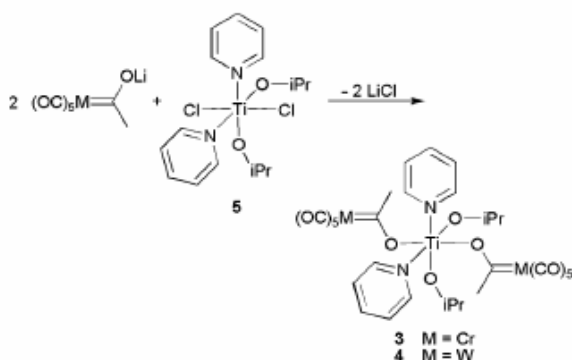


The same complexes **3** and **4** were also deliberately synthesized in satisfactory yields by combining Cl₂Ti(OiPr)₂(C₅H₅N)₂ (**5**) and (OC)₅M=C(Me)OLi (M = Cr, W) (eqn (3)).

Table 2 Bond distances (Å) within the M–C–O–Ti fragment of heterobimetallic Fischer carbene complexes

[{(OC) ₅ M=C(R)O}Ti(OiPr) ₂](μ-OiPr) ₂				
M	R	M–C	C–O	O–Ti
Cr	Me	2.042(2)	1.271(2)	1.961(1)
Cr	<i>n</i> -Bu	2.040(4) ^a	1.272(4) ^a	1.938(2) ^a
Cr	2-Furyl	2.046(8) ^a	1.290(9) ^a	2.016(5) ^a
Cr	CMeCH ₂	2.072(2) ^a	1.284(3) ^a	1.942(2) ^a
W	Me	2.190(2)	1.273(5)	1.941(3)
[{(OC) ₅ M=C(R)O}Ti(OiPr) ₂ (C ₅ H ₅ N) ₂]				
M	R	M–C	C–O	O–Ti
Cr	Me	2.071(2)	1.293(3)	2.010(2)
W	Me	2.190(6)	1.275(7)	1.977(4)

^a Ref. 3.



The pyridine complexes are very sensitive towards moisture. In solution even traces of water result in fast decomposition. Amongst the decomposition products acetaldehyde, (OC)₅Cr(C₅H₅N) and (OC)₄W(C₅H₅N)₂ were verified spectroscopically or by unit-cell determinations. Based on these observations we speculate that H₂O readily substitutes pyridine which in turn coordinates to M(CO)₅ by replacing the anionic carbene ligand affording carbonyl(pyridine)metal(0) complexes. Protonation of the extruded ligand yields acetaldehyde and OH[–] which is able to replace another pyridine and so forth.

The ¹H NMR-spectra of **3** and **4** in CD₂Cl₂ recorded at room temperature show only one set of resonances for the two pyridines (8.75, 7.95 and 7.49 ppm for **3**; 8.78, 7.94 and

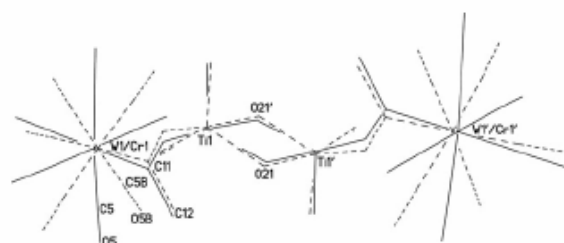


Fig. 3 Superposition of the structures of **1** (broken lines) and **2** (solid lines). The superimposed atoms of both structures are the four-membered Ti–O–ring and W/Cr. The carbon atoms of the isopropoxide groups have been omitted for clarity.

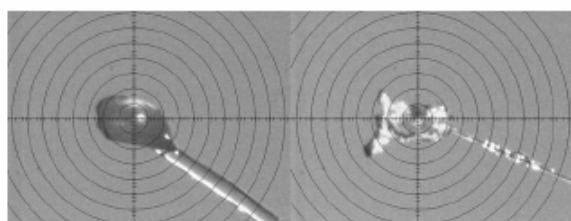


Fig. 4 Crystals of **1** at room temperature (left) and after cooling below $-60\text{ }^{\circ}\text{C}$ (right).

7.50 ppm for **4**), isopropoxide (4.91 and 1.20 ppm for **3**; 4.81 and 1.22 ppm for **4**) and carbenoxide ligands (2.80 ppm **3** and **4**). All signals are broad, indicating rapid ligand exchange. Variable temperature NMR spectroscopy shows that at $-60\text{ }^{\circ}\text{C}$ the resonances split into multiple sets of resonances, most likely representing different possible isomers. Owing to their high complexity no attempts were made to investigate the spectra in more detail.

Molecular structure determinations

Crystallizing **3** and **4** from diethyl ether–pentane or dichloromethane–hexane yielded isomorphous crystals with the monoclinic space group symmetry $P2_1/c$ with $Z = 6$ molecules in the unit cell. The asymmetric unit consists of 1.5 formula units, the incomplete fragment being completed by a twofold rotation axis (C_2 symmetry) passing through Ti1 and intersecting the Ti1–O121 and Ti1–O121' vectors (Fig. 5 and Fig. 6). The central titanium atom is coordinated in a distorted octahedral fashion by two carbenoxide, two isopropoxide and two pyridine ligands, with the two Fischer-type carbene units oriented mutually *trans* towards each other, while the isopropoxy ligands occur in a *cis* arrangement. The bond lengths along M–C–O–Ti (M = Cr, W) show no notable differences compared to the parent complexes **1** (or its analogues)³ and **2** (Table 2), therefore, the same measure of delocalisation can be assumed. The related complex $[(OC)_5Cr=C(Me)O]_2Ti(Cp^*)_2$ exhibits similar features.¹⁶ Note that only one unrestrained

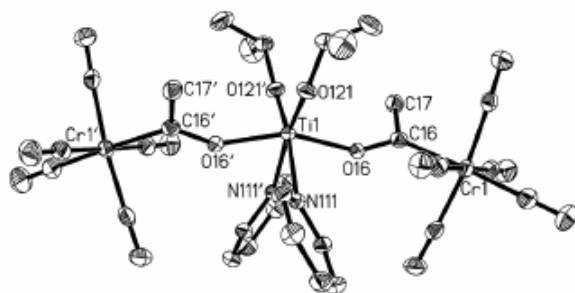


Fig. 5 Molecular structure of **3** (ORTEP, 50% ellipsoids, H atoms omitted). Only the structure of the symmetric molecule is shown. Selected bond lengths [Å] and angles [°], $' = (1 - x, y, 3/2 - z)$: Cr1–C16 2.053(2), C16–C17 1.511(3), C16–O16 1.273(3), O16–Ti1 1.979(2), Ti1–O121 1.769(2), Ti1–N111 2.301(2); Cr1–C16–O16 121.6(2), C16–O16–Ti1 151.1(2), O16–Ti1–O16' 157.73(9), O16–Ti1–N111 83.42(6), O16–Ti1–N111' 80.31(6), O16–Ti1–O121 94.50(7), O16–Ti1–O121' 99.90(7), N111–Ti1–N111' 85.78(9), N111–Ti1–O121 87.68(7), N111–Ti1–O121' 172.07(7), O121–Ti1–O121' 99.2(2).

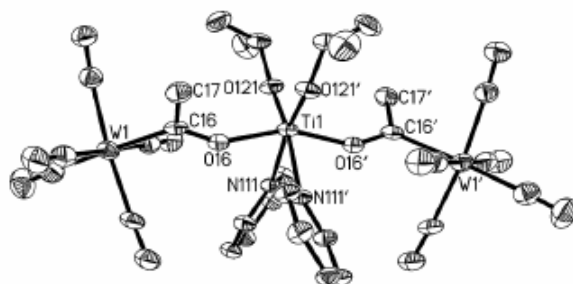


Fig. 6 Molecular structure of **4** (ORTEP, 50% ellipsoids, H atoms omitted). Only the structure of the symmetric molecule is shown. Selected bond lengths [Å] and angles [°], $' = (1 - x, y, 3/2 - z)$: W1–C16 2.171(6), C16–C17 1.503(8), C16–O16 1.255(7), O16–Ti1 1.946(4), Ti1–O121 1.753(4), Ti1–N111 2.288(4); W1–C16–O16 121.1(4), C16–O16–Ti1 150.8(4), O16–Ti1–O16' 157.2(2), O16–Ti1–N111 83.1(2), O16–Ti1–N111' 80.3(2), O16–Ti1–O121 94.1(2), O16–Ti1–O121' 100.6(2), N111–Ti1–N111' 85.3(2), N111–Ti1–O121 87.9(2), N111–Ti1–O121' 171.6(2), O121–Ti1–O121' 99.3(3).

structure (*i.e.* without bidentate ligands) with four alkoxide and two nitrogen donor ligands, $(MeCN)_2Ti[OCH(CF_3)_2]_4$, was hitherto reported.¹⁷ This octahedral compound crystallises readily from an acetonitrile solution of $Ti[OCH(CF_3)_2]_4$, whereas $(iPrO)_2Ti[OCH(CF_3)_2]_2$ yields solely solvent-free crystals. Apparently the oxophilic titanium center becomes susceptible to N-donors only when the donation of the alkoxide ligands is reduced. This enhanced Lewis acidity of the “ TiO_4 ”-moiety in **3** and **4** is also illustrated by the moisture sensitivity discussed before (*vide supra*).

The structure of the starting material $Cl_2Ti(OiPr)_2(C_5H_5N)_2$ (**5**), first reported by Brusilovets *et al.*,¹⁸ was now also determined. This compound crystallizes in the monoclinic space group $P2_1/c$ with $Z = 4$ formula units in the unit cell. The

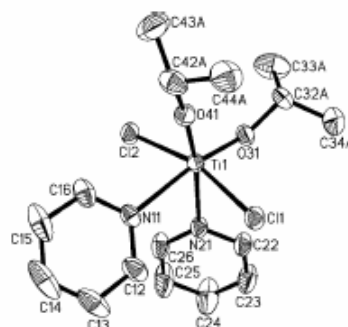


Fig. 7 Molecular structure of **5** (ORTEP, 50% ellipsoids, H atoms omitted). Both isopropoxide ligands are disordered over two sites by a rotation around the O31–C32A and O41–C42A bond, respectively. In the drawing this has been omitted for clarity. Selected bond lengths [Å] and angles [°]: Cl1–Ti1 2.3927(6), Cl2–Ti1 2.3736(6), Ti1–O31 1.775(2), Ti1–O41 1.761(2), Ti1–N11 2.310(2), Ti1–N21 2.293(2); Cl1–Ti1–Cl2 164.42(2), Cl1–Ti1–N11 82.90(4), Cl1–Ti1–N21 84.41(4), Cl1–Ti1–O31 94.27(5), Cl1–Ti1–O41 94.20(5), Cl2–Ti1–N11 84.07(4), Cl2–Ti1–N21 85.31(4), Cl2–Ti1–O31 96.93(5), Cl2–Ti1–O41 94.02(5), N11–Ti1–N21 81.79(6), N21–Ti1–O31 87.40(6), O31–Ti1–O41 102.04(7), O41–Ti1–N11 88.77(6), N11–Ti1–O31 169.03(6), N21–Ti1–O41 170.55(6).

asymmetric unit consists of one molecule without any crystallographically imposed symmetry (Fig. 7) despite its C_2 -symmetric framework. The central titanium atom is coordinated in a distorted octahedral environment by two chloride, two alkoxide and two pyridine ligands. The chloride ligands are *trans* disposed towards each other, whereas the two pyridine ligands are occupying positions *trans* to the isopropoxide donors. The structure of 5, therefore, reflects a similar situation to that found in the structures of compounds 3 and 4 but with chlorides replaced by the anionic carbene-complex ligands.

Conclusion

This study has established a convenient synthesis of hetero-bimetallic Fischer-type carbene complexes of the type $[(OC)_5M=C(Me)OTi(OiPr)_2](\mu-OiPr)_2$ with $M = Cr$ (1), W (2) with central four-membered Ti_2O_2 rings. X-Ray crystal structure determinations and NMR studies demonstrated that these complexes exhibit distinct "acyl" character, while remaining significantly carbenoid in accordance with the findings of Sabat *et al.*³ VT-NMR studies revealed that, in solution at room temperature, these molecules are highly dynamic systems undergoing rapid monomer-dimer equilibration, whereas at low temperatures the dimers are rather rigid on the NMR timescale. In the presence of suitable donor ligands (in this study pyridine) these dimers are readily cleaved. Surprisingly the expected products of a symmetric cleavage, $(OC)_5M=C(Me)OTi(OiPr)_3(C_5H_5N)_2$ were not observed, but instead unique rearrangement products $[(OC)_5M=C(Me)O]_2-Ti(OiPr)_2(C_5H_5N)_2$ with $M = Cr$ (3) and W (4) were obtained. In the latter complexes each Ti-center is now coordinated by two oxycarbene units.

Preliminary thermal decomposition experiments with complex 2 led to the formation of nanoparticles (ESI†). This supports the notions that complexes such as 1 and 2 could be useful single source precursors for mixed metal oxides of the type $MTiO_x$. Furthermore, complexes like 3 and 4 with appropriate N-donor ligands could in a similar fashion provide useful precursors for elusive mixed metal oxo nitrides $M_xTiN_yO_z$. Systematic investigations of these possibilities are under way in our laboratories.

Experimental

General methods

All manipulations were performed in a dry argon atmosphere using standard Schlenk techniques. $Cl_2Ti(OiPr)_2$ was prepared from $TiCl_4$ and $Ti(OiPr)_4$ via a literature procedure.¹⁸ All other chemicals were commercially available. Diethyl ether, hexane and pentane were distilled under N_2 from sodium wire, CH_2Cl_2 from CaH_2 and pyridine from KOH. Melting points (uncorrected) were determined on a Stuart SMP3 apparatus. The infrared spectra were recorded on a Nicolet 380 FTIR instrument and the NMR spectra on a Varian UnityInova 400 spectrometer (chemical shifts reported relative to the solvent resonance).

Preparations

$[(OC)_5Cr=C(Me)OTi(OiPr)_2](\mu-OiPr)_2$ (1). $(OC)_5Cr=C(Me)OLi$ was prepared from 2.1 ml of MeLi (3.3 mmol; 1.6 M in diethyl ether) and 0.73 g $Cr(CO)_6$ (3.3 mmol).¹⁹ The resulting solution was added drop-wise to 0.87 g $ClTi(OiPr)_3$ (3.3 mmol) in diethyl ether with stirring at 0 °C. After the addition was completed, the deep red solution was warmed to room temperature and stirred for another 30 minutes. LiCl was removed by filtration. The filtrate was slowly evaporated under reduced pressure (about 2/3 of the solvent) until a precipitate formed which redissolved upon warming to room temperature. Orange-red crystals of the product were obtained by slow cooling of the remaining solution to -20 °C. The crystals were filtered off, washed with cold hexane (2 × 10 ml, -20 °C) and dried *in vacuo* (yield: 0.87 g, 63%). Mp 41 °C (dec.). IR (ATR, neat, cm^{-1}): 2050 m, 1973 s, 1892 vs (all ν_{CO}). 1H -NMR (CD_2Cl_2 , 25 °C): 4.89 [3H, s(br), $OCH(CH_3)_2$], 2.79 [3H, s, $Cr=C(CH_3)O$], 1.37 [18H, m, $OCH(CH_3)_2$]. 1H -NMR (CD_2Cl_2 , -80 °C): 4.93 [2H, m, $OCH(CH_3)_2$], 4.59 [1H, m, $\mu-OCH(CH_3)_2$], 2.67 [3H, s, $Cr=C(CH_3)O$], 1.30 [12H, m, $OCH(CH_3)_2$], 1.21 [6H, m, $\mu-OCH(CH_3)_2$]. ^{13}C -NMR (CD_2Cl_2 , -80 °C): 350.7 [s, $Cr=C(CH_3)O$], 224.0 [s, CO_{trans}], 216.8 [s, CO_{cis}], 83.0 [s, $OCH(CH_3)_2$], 76.3 [s, $\mu-OCH(CH_3)_2$], 24.1 [s, $OCH(CH_3)_2$], 22.3 [s, $\mu-OCH(CH_3)_2$]; $Cr=C(CH_3)O$ obscured by solvent. Anal. calc. for $C_{32}H_{48}Cr_2O_{18}Ti_2$: C 41.76; H 5.26. Found: C 41.47; H 5.15%.

$[(OC)_5W=C(Me)OTi(OiPr)_2](\mu-OiPr)_2$ (2). The compound was prepared following the route for 1. Amounts used: $W(CO)_6$ (0.94 g; 2.7 mmol), MeLi 1.6 M (1.7 ml; 2.7 mmol), $ClTi(OiPr)_3$ (0.70 g; 2.7 mmol); (yield: 1.01 g; 64%). Mp 81 °C (dec.). IR (ATR, neat, cm^{-1}): 2060 m, 1957 s, 1882 vs (all ν_{CO}). 1H -NMR (CD_2Cl_2 , 25 °C): 4.88 [3H, s(br), $OCH(CH_3)_2$], 2.69 [3H, s, $Cr=C(CH_3)O$], 1.36 [18H, m, $OCH(CH_3)_2$]. 1H -NMR (CD_2Cl_2 , -80 °C): 4.91 [2H, m, $OCH(CH_3)_2$], 4.56 [1H, m, $\mu-OCH(CH_3)_2$], 2.63 [3H, s, $Cr=C(CH_3)O$], 1.29 [12H, m, $OCH(CH_3)_2$], 1.21 [6H, m, $\mu-OCH(CH_3)_2$]. ^{13}C -NMR (CD_2Cl_2 , -80 °C): 326.9 [s, $Cr=C(CH_3)O$], 204.9 [s, CO_{trans}], 198.0 [s, CO_{cis}], 82.9 [s, $OCH(CH_3)_2$], 76.4 [s, $\mu-OCH(CH_3)_2$], 56.2 [s, $Cr=C(CH_3)O$], 24.3 [s, $OCH(CH_3)_2$], 22.3 [s, $\mu-OCH(CH_3)_2$]. Anal. calc. for $C_{32}H_{48}O_{18}Ti_2W_2$: C 32.46; H 4.09. Found: C 32.28; H 3.97%.

$[(OC)_5Cr=C(Me)O]_2Ti(OiPr)_2(C_5H_5N)_2$ (3). (A) To a solution of $[(OC)_5Cr=C(Me)OTi(OiPr)_2](\mu-OiPr)_2$ (1) (0.28 g; 0.30 mmol) in diethyl ether (15 ml), an excess of pyridine (0.14 g; 1.8 mmol) was added at room temperature and the mixture was stirred for 20 min. After evaporation of about half the solvent, 20 ml of pentane was slowly added. The red precipitate was filtered off, washed with pentane (2 × 10 ml) and dried *in vacuo* (yield: 0.13 g; 54%). (B) $(OC)_5Cr=C(Me)OLi$ was prepared from 1.5 ml of MeLi (2.4 mmol; 1.6 M in diethyl ether) and 0.52 g $Cr(CO)_6$ (2.4 mmol).¹⁹ The resulting solution was added drop-wise to a stirred solution of 0.47 g $Cl_2Ti(OiPr)_2(C_5H_5N)_2$ (5) (1.2 mmol) in diethyl ether (15 ml) at 0 °C. A deep red solution was formed and allowed to warm to room temperature. After another 30 minutes of stirring, the solution was filtered to remove precipitated LiCl. Removal of about 2/3 of the solvent *in vacuo* and addition of pentane

Table 3 Crystal data, data collection and structure refinement for compounds 1, 2, 3, 4 and 5

	1	2	3	4	5
Empirical formula	C ₃₂ H ₄₈ Cr ₂ O ₁₈ Ti ₂	C ₃₂ H ₄₈ O ₁₈ Ti ₂ W ₂	C ₃₀ H ₃₀ Cr ₂ N ₂ O ₁₄ Ti	C ₃₀ H ₃₀ N ₂ O ₁₄ TiW ₂	C ₁₆ H ₂₄ Cl ₂ N ₂ O ₂ Ti
<i>M</i>	920.50	1184.20	794.46	1058.16	395.17
Crystal system	Triclinic	Triclinic	Monoclinic	Monoclinic	Monoclinic
Space group	<i>P1</i>	<i>P1</i>	<i>P2/c</i>	<i>P2/c</i>	<i>P2₁/c</i>
<i>a</i> /Å	10.4677(6)	9.6870(5)	23.528(2)	23.520(2)	8.7977(5)
<i>b</i> /Å	10.9006(6)	10.6893(6)	15.423(1)	15.415(1)	13.4237(7)
<i>c</i> /Å	11.5402(7)	11.7611(6)	14.9208(8)	14.9223(9)	16.4837(9)
α /°	87.771(1)	108.787(1)	90	90	90
β /°	67.023(1)	107.558(1)	100.695(2)	100.704(1)	97.906(1)
γ /°	70.163(1)	91.644(1)	90	90	90
<i>V</i> /Å ³	1133.7(2)	1088.5(2)	5320.3(5)	5316.2(6)	1928.2(2)
ρ_{calc} /g cm ⁻³	1.348	1.807	1.488	1.983	1.361
<i>Z</i>	1	1	6	6	4
<i>FM</i> (000)	476	576	2436	3036	824
<i>T</i> /K	213(2)	100(2)	100(2)	100(2)	100(2)
Refls. measured	8280	6461	29084	31409	10977
Refls. unique [<i>R</i> _{int}]	4401 [0.0147]	4503 [0.0147]	10099 [0.0285]	11164 [0.0318]	3908 [0.0200]
Parameters/restraints	320/11	251/0	702/9	702/16	270/8
<i>R</i> [<i>I</i> ≥ 2σ(<i>I</i>)]	0.0333	0.0250	0.0402	0.0380	0.0373
<i>wR</i> ²	0.0961	0.0635	0.1051	0.0955	0.0991
Weighting scheme	<i>a</i> = 0.0583 <i>b</i> = 0.1961	<i>a</i> = 0.0326 <i>b</i> = 2.5027	<i>a</i> = 0.0560 <i>b</i> = 1.9762	<i>a</i> = 0.0436 <i>b</i> = 16.2353	<i>a</i> = 0.0558 <i>b</i> = 1.0083
σ_{int} (max/min)/e Å ⁻³	0.352/−0.186	2.352/−0.801	1.360/−0.491	3.152/−4.027	0.596/−0.245

$$^a wR2 = \{\sum[w(F_o^2 - F_c^2)]^2 / \sum[w(F_o^2)^2]\}^{1/2}; w = 1/[\sigma^2(F_o^2) + (ap)^2 + bp]; p = (F_o^2 + 2F_c^2)/3.$$

(50 ml) yielded a crude product. The solution was filtered off and the residue washed with pentane (2 × 30 ml) and dried *in vacuo*. A pure second batch of crystalline product can be recovered from the mother liquor by cooling the diethyl ether–pentane solution to −20 °C (combined yield: 0.54 g; 58%). The product can be recrystallized from ether–pentane or dichloromethane–hexane. Mp 73 °C (dec.). IR (ATR, neat, cm⁻¹): 2047 m, 1959 w (shoulder), 1870 vs (all ν_{CO}). ¹H-NMR (CD₂Cl₂, 25 °C): 8.75 [2H, s(br), *o*-C₅H₅N], 7.95 [1H, s(br), *p*-C₅H₅N], 7.49 [2H, s(br), *m*-C₅H₅N], 4.91 [1H, s(br), OC-*H*(CH₃)₂], 2.80 [3H, s, Cr=C(CH₃)O], 1.20 [6H, m, OCH(CH₃)₂]. Anal. calc. for C₃₀H₃₀Cr₂N₂O₁₄Ti: C 45.36; H 3.81; N 3.53. Found: C 45.24; H 3.76; N 3.59%.

[(OC)₅W=C(Me)O]₂Ti(OiPr)₂(C₅H₅N)₂ (4). The compound can be prepared following the routes described for 3. Amounts used: (A) [(OC)₅W=C(Me)O]Ti(OiPr)₂(μ-OiPr)₂ (2) (0.35 g; 0.30 mmol), pyridine (0.14 g; 1.8 mmol); (yield: 0.16 g; 51%). (B) W(CO)₆ (0.88 g; 2.5 mmol), MeLi 1.6 M (1.6 ml; 2.5 mmol), Cl₂Ti(OiPr)₂(C₅H₅N)₂ (5) (0.49 g; 1.2 mmol); (yield: 0.75 g; 57%). Mp 76 °C (dec.). IR (ATR, neat): 2057 m, 1962 w, 1866 vs (all ν_{CO}). ¹H-NMR (CD₂Cl₂, 25 °C): 8.78 [2H, s(br), *o*-C₅H₅N], 7.94 [1H, m br, *p*-C₅H₅N], 7.50 [2H, m br, *m*-C₅H₅N], 4.81 [1H, s(br), OCH(CH₃)₂], 2.80 [3H, s, W=C(CH₃)O], 1.22 [6H, m, OCH(CH₃)₂]. Anal. calc. for C₃₀H₃₀N₂O₁₄TiW₂: C 34.05; H 2.86; N 2.65. Found: C 33.91; H 2.80; N 2.70%.

Preparation of Cl₂Ti(OiPr)₂(C₅H₅N)₂ (5). To a solution of Cl₂Ti(OiPr)₂ (0.62 g; 2.6 mmol) in diethyl ether (15 ml), an excess of pyridine (0.29 g; 3.7 mmol) was added at room temperature and the mixture was stirred for about 20 minutes. A small amount of precipitate was filtered off. Cooling the filtrate to −20 °C yielded colorless crystals that were filtered off, washed with pentane (2 × 20 ml) and dried *in vacuo* (yield: 0.71 g; 69%). Analytical data have been reported before.¹⁸

Anal. calc. for C₁₆H₂₄Cl₂N₂O₂Ti: C 48.63; H 6.12; N 7.09. Found: C 48.52; H 6.15; N 7.13%.

Crystal structure determinations

Specimens of suitable quality and size of 1, 2, 3, 4 and 5 were mounted on the ends of glass fibers in inert oil and used for intensity data collection on a Bruker SMART Apex CCD diffractometer,²⁰ employing graphite-monochromated Mo Kα radiation. Data reduction was carried out using the SAINT²¹ suite of programs and multi-scan absorption corrections were performed with SADABS.²² The structures were solved by a combination of direct methods (SHELXS-97) and difference-Fourier syntheses and refined by full matrix least-squares calculations on *F*² (SHELXL-97)²³ within the X-Seed environment.²⁴ The thermal motion was treated anisotropically for all non-hydrogen atoms. All hydrogen atoms were calculated in ideal positions and refined using a riding model. Some of the isopropoxide groups in the structures of 1, 3, 4 and 5 are disordered. Similarity restraints were applied to model the disorder as best as possible. Details of the data collections and structure determinations are listed in Table 3. CCDC reference numbers 670773–670777. For crystallographic data in CIF or other electronic format, see DOI: 10.1039/b715075j

Acknowledgements

We gratefully acknowledge Feodor Lynen Fellowships awarded to SN and OS by the Alexander von Humboldt Foundation.

References

- 1 B. L. Cushing, V. L. Kolesnichenko and C. J. O'Connor, *Chem. Rev.*, 2004, **104**, 3893.

-
- 2 U. Son Seung, Y. Jang, Y. Yoon Ki, C. An, Y. Hwang, J.-G. Park, H.-J. Noh, J.-Y. Kim, J.-H. Park and T. Hyeon, *Chem. Commun.*, 2005, 86.
 - 3 M. Sabat, M. F. Gross and M. G. Finn, *Organometallics*, 1992, 11, 745.
 - 4 M. Fernandez-Garcia, A. Martinez-Arias, A. Fuerte and J. C. Conesa, *J. Phys. Chem. B*, 2005, 109, 6075.
 - 5 Z. Ma, S. She, S. Min, L. Zhang and B. Su, *J. Lanzhou Univ., Nat. Sci.*, 2005, 41, 64.
 - 6 X.-M. Yin and Y.-Q. Cheng, *J. Synth. Cryst.*, 2006, 35, 45.
 - 7 N. Luruli, V. Grumel, R. Bruell, A. Du Toit, H. Pasch, A. J. van Reenen and H. G. Raubenheimer, *J. Polym. Sci., Part A: Polym. Chem.*, 2004, 42, 5121 and references therein.
 - 8 E. O. Fischer and S. Fontana, *J. Organomet. Chem.*, 1972, 40, 159.
 - 9 H. G. Raubenheimer and E. O. Fischer, *J. Organomet. Chem.*, 1975, 91, C23.
 - 10 J. Barluenga and F. J. Fañanás, *Tetrahedron*, 2000, 56, 4597 and references therein.
 - 11 H. G. Raubenheimer, A. du Toit, M. du Toit, L. van Niekerd, S. Cronje, C. Esterhuysen and A. M. Crouch, *Dalton Trans.*, 2004, 1173-1180.
 - 12 Y. Li and L. Gao, *J. Am. Ceram. Soc.*, 2002, 85, 3090.
 - 13 Y. Li and L. Gao, *Mater. Lett.*, 2003, 57, 1062.
 - 14 Y. Li, L. Gao and S. J. Zheng, *J. Chin. Ceram. Soc.*, 2004, 32, 734.
 - 15 G. M. Bodner, S. B. Kahl, K. Bork, B. N. Storhoff, J. E. Wuller and L. J. Todd, *Inorg. Chem.*, 1973, 12, 1071.
 - 16 E. V. Anslyn, B. D. Santarsiero and R. H. Grubbs, *Organometallics*, 1988, 7, 2137.
 - 17 C. Campbell, S. G. Bott, R. Larsen and W. G. Van Der Sluys, *Inorg. Chem.*, 1994, 33, 4950.
 - 18 A. I. Brusilovets, E. B. Rusanov, A. N. Chernega and V. G. Bdzholo, *Russ. J. Gen. Chem.*, 1996, 66, 228.
 - 19 C. T. Lam, C. D. Malkiewich and C. V. Senoff, *Inorg. Synth.*, 1977, 17, 95.
 - 20 SMART: Data collection software (version 5.629), Bruker AXS Inc., Madison, WI, 2003.
 - 21 SAINT: Data reduction software (version 6.45), Bruker AXS Inc., Madison, WI, 2003.
 - 22 SADABS (version 2.05), Bruker AXS Inc., Madison, WI, 2002.
 - 23 G. M. Sheldrick, *SHELX-97: Programs for crystal structure analysis*, University of Göttingen, Germany, 1997.
 - 24 L. J. Barbour, *J. Supramol. Chem.*, 2001, 1, 189.